Anti-Vibration Theory and Technology in Underground Tunnels

Lead Guest Editor: Zhigang Tao
Guest Editors: Chun Zhu, Qingxiang Meng, Yun Lin, and Yuanchao Zhang
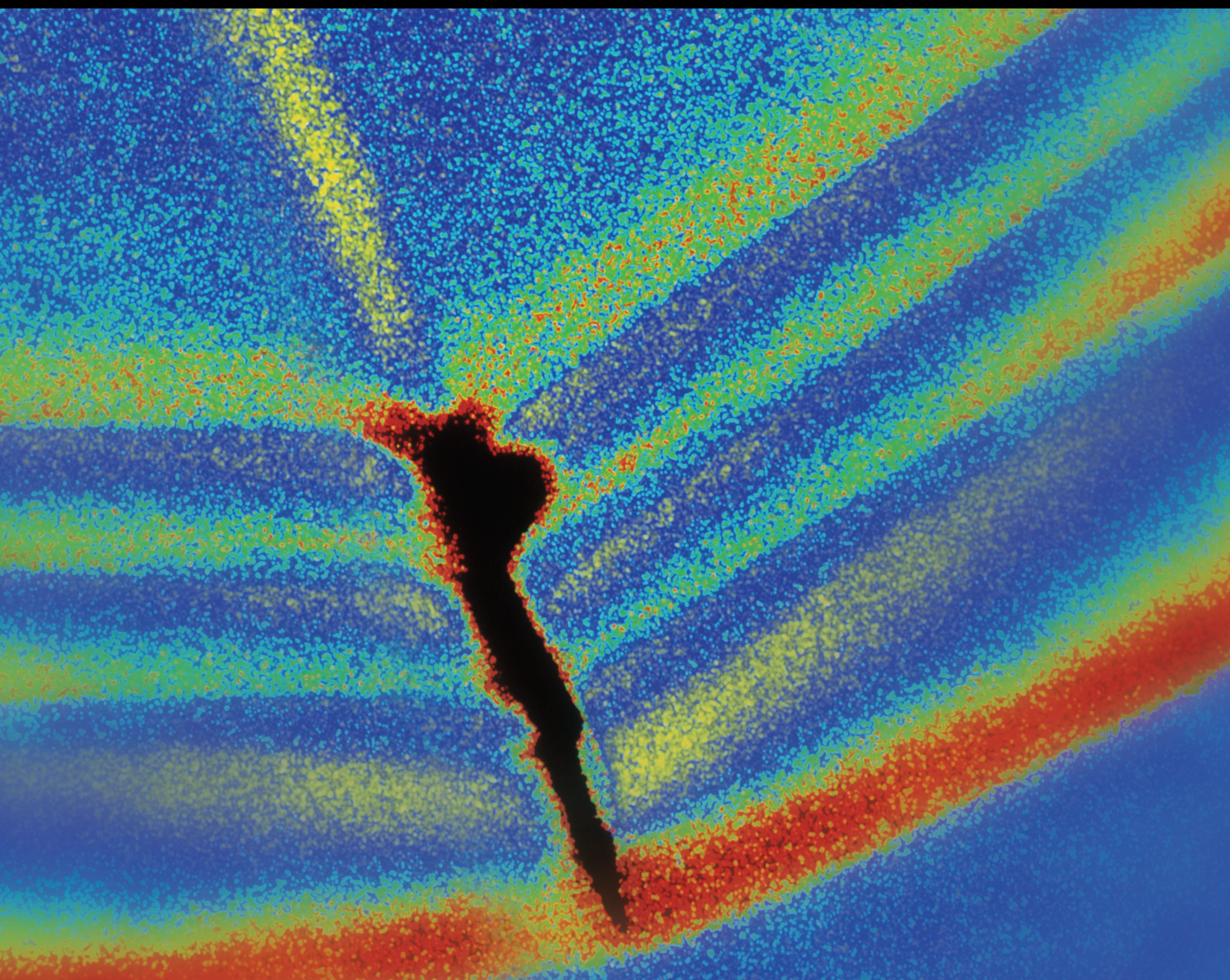
Anti-Vibration Theory and Technology in Underground Tunnels

Anti-Vibration Theory and Technology in Underground Tunnels

Lead Guest Editor: Zhigang Tao
Guest Editors: Chun Zhu, Qingxiang Meng, Yun Lin, and Yuanchao Zhang

Didier Rémond, France
Dario Richiedei, Italy
Fabio Rizzo, Italy
Carlo Rosso, Italy
Riccardo Rubini, Italy
Salvatore Russo, Italy
Giuseppe Ruta, Italy
Edoardo Sabbioni, Italy
Pouyan Roodgar Saffari, Iran
Filippo Santucci de Magistris, Italy
Fabrizio Scozzese, Italy
Abdullah Seçgin, Turkey
Roger Serra, France
S. Mahdi Seyed-Kolbadi, Iran
Yujie Shen, China
Bao-Jun Shi, China
Chengzhi Shi, USA
Gerardo Silva-Navarro, Mexico
Marcos Silveira, Brazil
Kumar V. Singh, USA
Jean-Jacques Sinou, France
Isabelle Sochet, France
Alba Sofi, Italy
Jussi Sopanen, Finland
Stefano Sorace, Italy
Andrea Spaggiari, Italy
Lei Su, China
Shuaishuai Sun, Australia
Fidelis Tawiah Suorineni, Kazakhstan
Cecilia Surace, Italy
Tomasz Szolc, Poland
Iacopo Tamellin, Italy
Zhuhua Tan, China
Gang Tang, China
Chao Tao, China
Tianyou Tao, China
Marco Tarabini, Italy
Hamid Toopchi-Nezhad, Iran
Carlo Trigona, Italy
Federica Tubino, Italy
Nerio Tullini, Italy
Nicolò Vaiana, Italy
Marcello Vanali, Italy
Christian Vanhille, Spain

Dr. Govind Vashishtha, Poland
F. Viadero, Spain
M. Ahmer Wadee, United Kingdom
C. M. Wang, Australia
Gaoxin Wang, China
Huiqi Wang, China
Pengfei Wang, China
Weiqiang Wang, Australia
Xian-Bo Wang, China
YuRen Wang, China
Wai-on Wong, Hong Kong
Yuanping XU, China
Biao Xiang, China
Qilong Xue, China
Xin Xue, China
Diansen Yang, China
Jie Yang, Australia
Chang-Ping Yi, Sweden
Nicolo Zampieri, Italy
Chao-Ping Zang, China
Enrico Zappino, Italy
Guo-Qing Zhang, China
Shaojian Zhang, China
Yongfang Zhang, China
Yaobing Zhao, China
Zhipeng Zhao, Japan
Changjie Zheng, China
Chuanbo Zhou, China
Hongwei Zhou, China
Hongyuan Zhou, China
Jiaxi Zhou, China
Yunlai Zhou, China
Radoslaw Zimroz, Poland

Contents

Research Article

Study of Gob-Side Entry Retaining Technology with Roof Cutting under Upper Roadway Condition

Xingen Ma [ID],[1,2,3] **Manchao He,**[3] **Xuewei Sun,**[4] **Jianfeng Li,**[1] **Gang He,**[1] **and Enze Zhen** [ID][5]

[1]*Coal Burst Research Center of China, Jiangsu, Xuzhou 221000, China*
[2]*Huaneng Coal Technology Research Co., China, Huaneng, Beijing 100070, China*
[3]*State Key Laboratory for Geomechanics and Deep Underground Engineering,*
 China University of Mining and Technology (Beijing), Beijing 100083, China
[4]*Yixin Coal Mine, Longmei Group, Hegang 154100, China*
[5]*School of Architecture and Civil Engineering, Huangshan University, Huangshan 245041, China*

Correspondence should be addressed to Xingen Ma; 294185559@qq.com and Enze Zhen; zhenenze0@163.com

Gob-side entry retaining technology with roof cutting (GERRC) has been widely used in flat and near-flat coal seam conditions, but its application under inclined coal seam is still very deficient. In order to further improve the application system of GERRC and overcome the application difficulties under special geological conditions, this paper takes the 43073 working face of Yixin coal mine as an example to research the GERRC with upper roadway under gently inclined thick coal seam. Firstly, the difficulties in the upper entry retaining with inclined coal seam are analyzed and the corresponding key technologies and system designs are put forward. Subsequently, the roof cutting and upper entry retaining are designed in detail according to geological conditions of test working face, and the roof cutting and pressure releasing effect is analyzed by numerical simulation to expound the stress distribution and pressure releasing mechanism of surrounding rock. Finally, the upper entry retaining field test is carried out to verify the feasibility and applicability of the technology and related designs. Through field monitoring, it is found that the weighting step increases significantly, the weighting strength decreases effectively on the roof cutting side, and the pressure relief effect is obvious. Meanwhile, the maximum roof to floor convergence is 361 mm and the maximum shrinkage of both sides is 280 mm, so the retained entry can meet the reuse requirement of adjacent working face.

1. Introduction

In the gob-side entry retaining technology of longwall mining, only one entry needs to be excavated during one working face mining and another entry is obtained by retaining during the adjacent working face mining. So the technology has the advantages of saving section coal pillars, reducing the amount of entry excavation, and prolonging the mine service life [1, 2]. Under the current increasingly tense situation of coal resources, this mining technology has high research and popularization value, and related scholars have also carried out a lot of research work [3, 4]. For example, Zhu Haotian takes the 9307 working face of Yangmei group as an example and successfully carries out gob-side

entry retaining test by pier-column method, and the deformation of pier-column is controlled within 150 mm [5]. Zhang Sheng takes the 9301 working face of Tangkou coal mine as an example, using coal gangue, fly ash, and cement as filling materials, and successfully carries out gob-side entry retaining test by solid filling method [6]. Li Youcun takes the 21001 working face of Wangcun coal mine as an example and successfully carries out the gob-side entry retaining test in fully mechanized caving face by adopting entry roof reinforcement support measures using wooden stack, gangue bag high prestressing anchor cable, and so on [7].

The above achievements have greatly enriched the research idea and practical experience of gob-side entry

retaining technology in China, but there are still many restrictive factors hindering its wide application. First, the price of filling materials is usually high and the filling efficiency is limited. Second, the backfilling process of goaf is often complex, which has great influences on the mining and succession of working faces [8, 9]. In order to seek a more efficient and economical way of entry retaining, Professor He Manchao puts forward the gob-side entry retaining technology with roof cutting (GERRC) based on the theory of short arm beam on the basis of the existing research in 2008 [10].

After the development in recent years, the GERRC has been successfully tested and popularized in many mines. Sun Xiaoming takes the 1610 working face of Nantun coal mine as an example and studies the design method of key parameters for gob-side entry retaining by roof cutting pressure releasing under the condition of thin coal seam [11]. Zhang Guofeng takes the 2422 working face of Baijiao coal mine as an example and elaborates the implementation process and matching monitoring method of the roof cutting pressure releasing gob-side entry retaining technology [12]. Guo Zhibiao takes the 3118 working face of Jiayang coal mine as an example and analyzes the stress field evolution of surrounding rock with roof cutting pressure releasing by numerical simulation [13, 14]. It can be seen that this technology is mainly used on near-flat thin or medium-thick coal seam in the existing research, but the application in thick coal seam or inclined coal seam is still insufficient because of the influences of rock pressure, entry support, goaf filling effect, and other factors. Therefore, in order to further improve the application system of this technology and overcome the application difficulties under special geological conditions, this study takes the 43073 working face of Yixin coal mine as an example to carry out the adaptability study of GERRC with upper roadway under gently inclined thick coal seam condition.

2. Research Background

2.1. Technical Characteristics.
The GERRC can realize automatic roadway formation without coal pillars by roof cutting along the entry. The technology has been successfully tested in many mines under the condition of near-flat coal seam (as shown in Figure 1(a)). However, there are still many limitations in the application of this technology under the condition of inclined coal seam. The GERRC under the condition of inclined coal seam can be divided into two types, that is, upper and lower entry retaining as shown in Figure 1(b) and 1(c) [15].

Among them, the difficulty of lower entry retaining is that when the goaf roof caves, the caving gangue will gather along the inclination angle of the coal seam to the lower entry direction, which will cause a greater impact on the gangue retaining support. While the difficulty of upper entry retaining is that the gangue caving from goaf roof will accumulate away from the upper entry direction, the gangue wall of retained entry cannot be formed well to support the overlying strata. The main solutions of lower entry retaining are to increase the strength of gangue retaining support and

reduce the height of roof cutting properly, which has been successfully tested in Fucheng coal mine. However, the upper entry retaining is more difficult. The key parameters such as the roof cutting height and angle should be adjusted accordingly and the supporting design should also be improved appropriately. So taking the 43073 working face of Yixin coal mine of Longmei group as an example, this paper carries out the first test of roof cutting pressure releasing bob-side entry retaining technology with upper roadway under gently inclined thick coal seam condition.

2.2. Project Overview.
The 43073 working face of Yixin coal mine Longmei group is located in the third mining level of Hegang coalfield. The strike length of the working face is 400 m, the inclination length is 170 m, and the layout plan is shown in Figure 2(a). The basic parameters of the 43073 working face are shown in Table 1, the roof lithology column diagram is shown in Figure 2(b), and the related parameters of each stratum are shown in Table 2.

Comprehensive mechanized mining method is adopted in the test face. The test entry is the auxiliary roadway of the 43073 working face, and the retaining section is 380 m long in front of open-off cut. The adjacent working face intends to use this retained entry section for reverse direction mining. The reverse mining of adjacent working faces has no impact on the entry retaining procedure, but after the entry retaining is completed, the mining of adjacent working face needs to wait until the retained entry is stable, so as to avoid the entry damage caused by mining impact.

3. Design of Key Technical Parameters

The biggest difference of entry retaining in inclined working face lies in the lateral accumulation of gangue in goaf; that is, gangue will accumulate to the side close to or away from the roadway due to the existence of dip angle. Therefore, the key of entry retaining in inclined working face lies in retaining roadway gangue support and roof cutting height, which will directly affect the effect of entry retaining. When entry retaining with the upper roadway, the gangue retaining support is weakened and the roof cutting height is increased; when entry retaining with the lower roadway, the gangue retaining support is strengthened and the roof cutting height is reduced.

3.1. Roof Cutting Design.
Roof cutting design directly affects the success and effect of entry retaining in the new technology. The reasonable roof cutting parameter design should meet the filling demand of goaf on the entry retaining side as far as possible under the condition of saving the roof cutting workload. Under normal near-flat coal seam condition, the roof cutting height can be calculated according to the bulking coefficient of goaf roof rocks as[16]

$$H_F = \frac{(H_M - \Delta H_1 - \Delta H_2)}{(K-1)}, \tag{1}$$

where H_F is the roof cutting height, m; H_M is the coal seam thickness, m; ΔH_1 is the amount of roof subsidence, m; ΔH_2

(a)

(b)

(c)
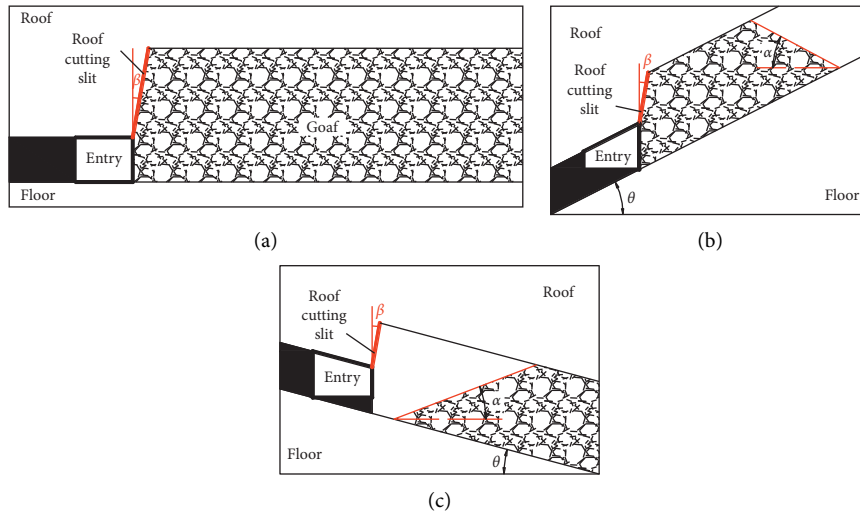
FIGURE 1: Classification of roof cutting pressure releasing gob-side entry retaining. (a) Entry retaining with near-flat coal seam. (b) Lower entry retaining. (c) Upper entry retaining.

(a)

Columnar	Thickness (m)	Lithology
	6.25	Medium sandstone
	5.50	Middle conglomerate
	1.20	Fine sandstone
	1.45	Siltstone
	3.60	Coal

(b)
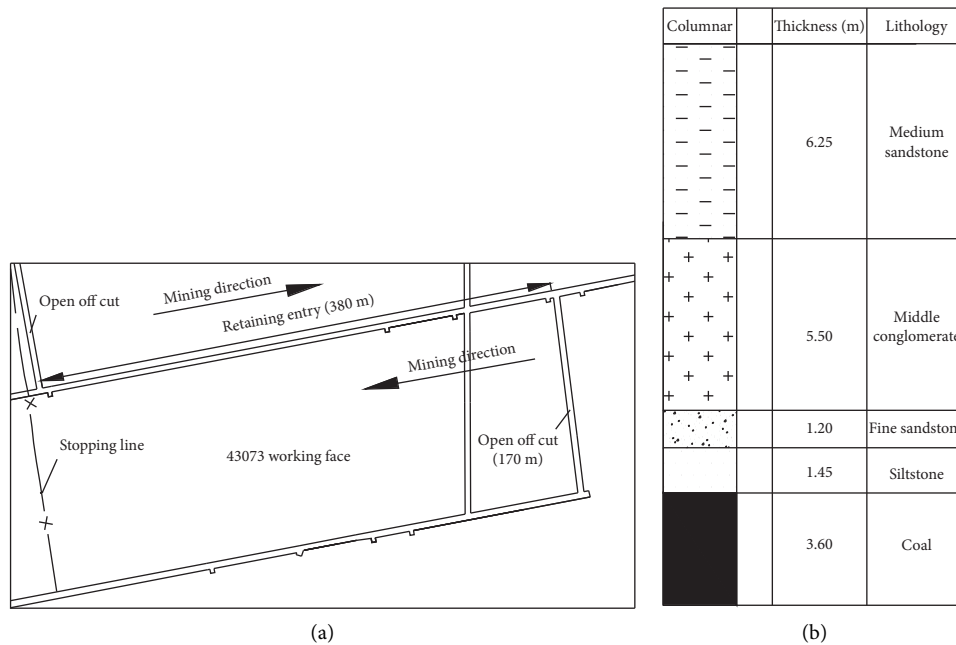
FIGURE 2: Layout and roof lithology of the 43073 working face. (a) Layout of the working face. (b) Lithological profile.

is the amount of floor heave, m; K is the bulking coefficient of roof.

According to the roof condition of the 43073 working face, the bulking coefficient of roof is taken as 1.4 in this study [16]. Without considering the roof subsidence and floor heave, the roof cutting height is designed as 9.0 m according to the mining height and above equation. Under the upper entry retaining process with inclined coal seam, the gangue collapsing from the goaf roof will slide away from the entry retaining side, so the roof cutting height should be increased appropriately. However, from the roof lithology column of the working face, it can be seen that there is a thick stable medium sandstone rock layer above the coal

seam 8.15 m. If increasing the roof cutting height with 1–2 m, not only is the roof cutting workload greatly increased, but also the medium sandstone strata in the roof cutting height increasing range is still difficult to collapse, which has little significance for the filling of goaf on the entry retaining side. Therefore, the ultimate design of roof cutting height is maintained at 9.0 m, and the goaf filling is mainly relying on the strata within lower 8.15 m range of roof.

Another key parameter of roof cutting design is the cutting angle. As shown in Figure 1, the design of roof cutting angle under normal conditions should mainly consider two aspects: one is to minimize the friction effect of goaf roof caving on the roof of retained entry; another is to

TABLE 1: Basic parameters of the 43073 working face.

Coal seam thickness (m)	3.6
Mining height (m)	3.6
Strike length (m)	400
Immediate roof/thickness (m)	Siltstone/1.45
Main roof/thickness (m)	Middle conglomerate/5.50
Depth (m)	440–574
Dig angle/average dip angle (°)	16∼20/18
Inclination length (m)	170
Immediate floor/thickness (m)	Fine sandstone/6.00
Main floor/thickness (m)	Coarse sandstone/19.30

TABLE 2: Parameters of the rock layers.

Lithology	Density (kN/m^3)	Tensile strength (MPa)	Internal friction angle (°)	Cohesion (MPa)	Bulk modulus (GPa)	Shear modulus (GPa)
Fine sandstone	23	7.3	28	1.0	3.81	3.05
Medium sandstone	24	8.4	32	2.6	11.49	7.26
Siltstone	22	4.3	28	0.8	2.11	1.86
Middle conglomerate	26	10.2	35	3.3	14.16	9.21
Coal	13	3.3	29	0.2	0.35	0.18
Coarse sandstone	25	9.6	33	2.9	13.21	8.75

minimize the damage of roof cutting blasting to the original roof bolt cable support [15]. Under the condition of upper entry retaining, the gangue collapsing from the goaf roof will accumulate far away from the retained upper entry, so the friction on the roof cutting surface is usually small and the roof cutting angle can only be designed from the protection of bolt cable support. To sum up, according to the previous test experience, the roof cutting angle is designed as 10° in the roof cutting design of the 43073 working face. At the same time, the smaller roof cutting angle can also cut off the larger volume of goaf roof, which can make up for the shortcoming of goaf insufficient filling on the upper entry retaining side to a certain extent.

3.2. Blasting Design. In the upper entry retaining process with gently inclined coal seam, the roof cutting still needs to be realized by bidirectional shaped charge tension blasting technology, and the technical equipment and principle are shown in Figure 3 [17]. The size of single shaped charge tube is $\varphi 36.5 \, mm \times 1500 \, mm$, and some tubes can be connected and installed by connecting sleeves according to the requirement of blasting depth. There is a row of holes on each side of the tube, and the locked groove at two ends can ensure that the tube always faces a certain direction when connecting and installing. When cutting the roof, a certain amount of explosive rolls are loaded into the shaped charge tubes, then putting them into the blasting hole in the roof and sealing the holes. The blasting energy of the explosive can be directionally transmitted along the shaped charge direction, effective tension force can be formed in the direction of nonshaped energy, and the directional tension presplitting can be formed making use of the poor tensile capacity of rock mass.

The charge quantity and structure of the explosive roll in the shaped charge tube, the blasting hole spacing, and the amount of blasting hole at single initiation should all be determined by field test. The blasting test examines the blasting effect, but there are no special requirements for explosives. The test procedure is shown in Figure 4 [18, 19]. Firstly, a single-hole blasting test is carried out to determine the reasonable charge of a single hole, and the reasonable charge should be able to form effective cracks in the blasting hole without collapse. Secondly, an interval-hole blasting test is carried out to determine the reasonable hole spacing, usually including 300 mm, 400 mm, 500 mm, and 600 mm four types. In this step, the peephole between each two blasting holes should be checked to observe the penetration of the cracks in the hole. Finally, a continuous-hole blasting test is carried out to determine the amount of blasting hole at single initiation, and the main index is harmful gas concentration at this step.

Through the single-hole blasting test in the 43073 working face, the charge structure of the blasting hole is designed as 43210 and the sealing length is designed as 2 m. That is, each blasting hole is filled with five shaped charge tubes, the bottom tube is cut to be 1 m long, and from top to bottom of blasting hole, each tube is charged 4, 3, 2, 1, and 0 rolls of explosive, respectively. The statistical analysis of crack rate per meter in peephole of interval-hole blasting test is shown in Figure 5. It can be seen that hole collapse occurs in 5–6 m section of peephole under 300 mm spacing condition, and the average crack rates under 400 mm, 500 mm, and 600 mm spacing conditions are 87%, 82%, and 74%, respectively. In order to reduce the workload of roof cutting blasting and ensure the effect, the blasting spacing is ultimately selected as 400 m. Combining with the requirements of mining speed and upper limit of harmful gas concentration in entry, the amount of blasting hole at single
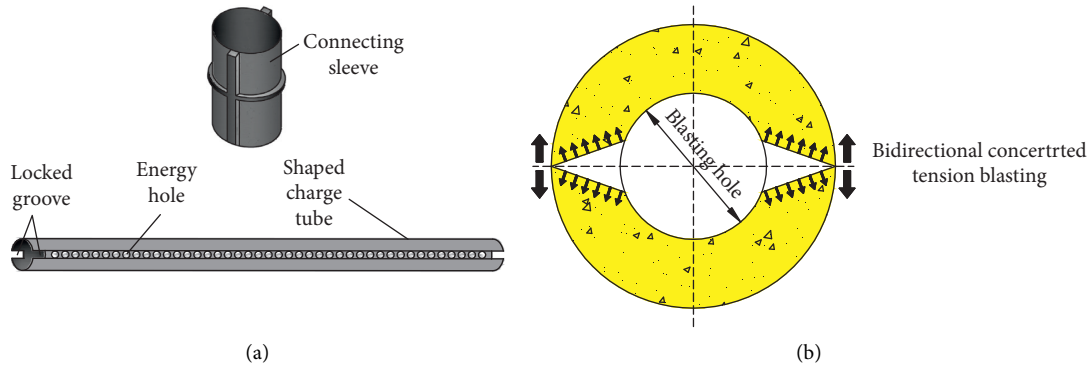
FIGURE 3: Devices and principle of bilateral bidirectional shaped charge tension blasting technology. (a) Connecting sleeve and shaped charge tube. (b) Blasting principle.
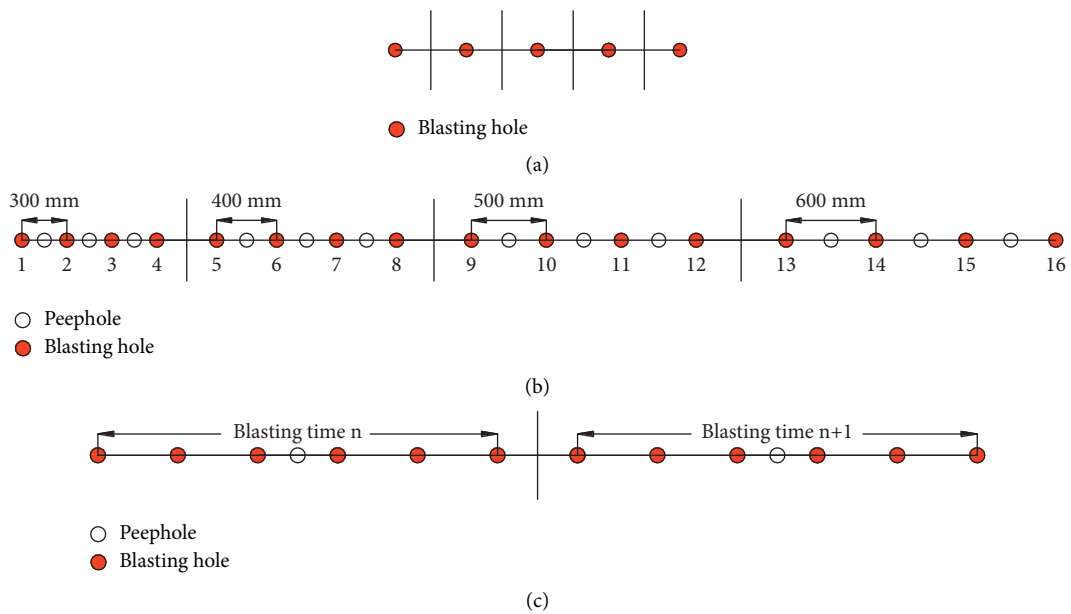
FIGURE 4: Holes layout in blasting test. (a) Single-hole blasting test. (b) Interval-hole blasting test. (c) Continuous-hole blasting test.

initiation is determined to be 6 holes. The common presplitting effect in peephole is shown in Figure 6.

3.3. Design of Reinforcement Support. In the GERRC, the entry roof needs to undergo several disturbances, such as tunneling, mining, entry retaining, and secondary mining. The deformation of the roof is usually large, and the conventional anchor cable support cannot effectively meet the needs of the field support demand under dynamic pressure and large deformation conditions. Therefore, the entry reinforcement support of entry retaining test in the 43073 working face uses the constant resistance large deformation anchor cable [20, 21].

The structure of constant resistance large deformation anchor cable is shown in Figure 7, whose supporting principle is shown in Figure 8 and constitutive relation and energy model are shown in Figure 9 [22]. When the tension of cable is greater than the constant resistance value, the

anchor cable lock head can be retracted into the constant resistance device to provide a certain amount of constant resistance deformation for the anchor cable. The anchor cable can be regarded as an ideal model of elastic and plastic components. When the pull force is less than the constant resistance of anchor cable, the anchor cable is in the elastic stage: $P = K_{gx}$, where P is the anchor cable load, K_g is the stiffness coefficient, and x is the amount of elastic extension. When the pull force increases to the constant resistance value, the anchor lock exhibits plastic slip, then $P = P_0$, where P_0 is the constant resistance value. Therefore, when the plastic slip occurs, the energy absorbed by the constant resistance anchor cable is

$$W = \frac{P_0 x_0}{2 + P_0 (x' - x_0)}, \tag{2}$$

where x_0 is the maximum amount of elastic deformation and x' is the total deformation amount.
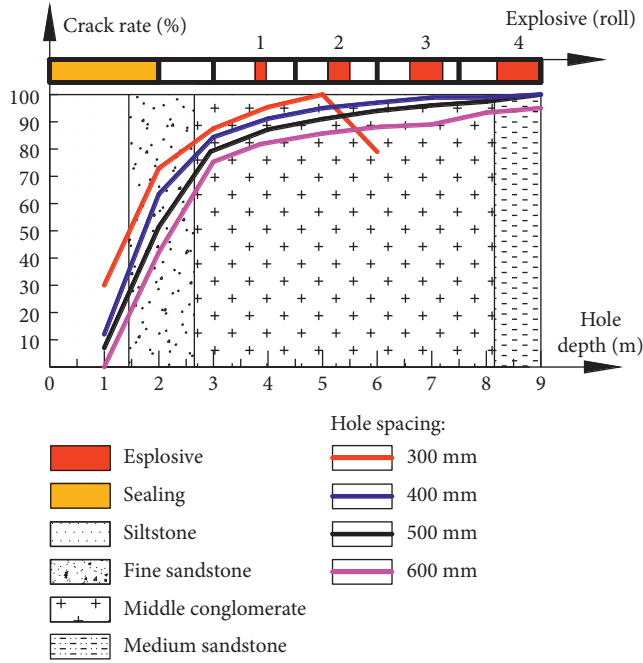
Figure 5: Result of interval-hole blasting test.

The main reinforcement support area of the retained entry roof is also the roof cutting range, so the length of the anchor cable should be 1-2 m longer than the height of roof cutting. That is, the length of the anchor cable used in the 430743 working face is 11 m long. According to the theory of suspension, the support strength of anchorage cable can be calculated according to the following formula [7]:

$$P \geq H_F \rho_d \left(1 + \frac{H_F \tan \beta}{2L_h}\right), \tag{3}$$

where P is the pull force of anchor cable; L_h is the width of entry; ρ_d is the roof density in the roof cutting range. When there are several layers in the roof cutting range, then

$$\rho_d = \sum_{i=1}^{n} \rho_i \frac{D_i}{H_F}, \tag{4}$$

where n is the number of rock layers; ρ_i is single layer density; D_i is single layer thickness. According to the roof lithology of the 43073 working face, it is calculated that $\rho_d = 24.8 \, KN/m^3$ and $P < 261.7 \, KN/m^2$. As the design, the constant resistance value of this anchor cable used in coal mine is 350 KN; that is, the support density of this anchor cable is 0.75/m² at least. Therefore, there are designed three anchor cables on each row and the row spacing is 0.8 m in the upper entry reinforcement support of the 43073 working face. As shown in Figure 10, the roof cutting side of entry suffers strong disturbances of blasting and roof caving, so the anchor cables on this side are all adopted constant resistance large deformation anchor cable; the row of anchor cables on the middle of entry roof is alternately arranged with common steel anchor cable and constant resistance anchor cable; the coal wall side of entry suffers little disturbances of blasting and roof caving, so the anchor cables on this side are all adopted steel anchor cable.

3.4. Design of Gangue Retaining Support.

Gangue retaining support is the special link of GERRC, and the effective gangue retaining support should be carried out in time behind the working face to prevent gangue from rushing into the retained entry when the goaf roof caving [23–25]. At present, the commonly used method of gangue retaining support is U-shaped steel + metal mesh support. In terms of the pressure of gangue retaining support, the pressure is the highest under the low entry retaining with inclined coal seam, the pressure is middle under the near-flat coal seam, and the pressure is the lowest under the upper entry retaining with inclined coal seam. The U-shaped steel type used for gangue retaining support is usually 36U, and the support spacing of it is usually 500 mm in gangue retaining support under near-flat coal seam. Under lower entry retaining, the support spacing should be reduced appropriately according to the mining height and coal seam dip angle, and under upper entry retaining, the support spacing can be increased appropriately to save material consumption.

As shown in Figure 11(a), the U-shaped steel support spacing of the 43073 working face in Yixin coal mine is designed as 600 mm. In order to determine whether the spacing is reasonable, a pressure sensor is installed between the U-shaped steel and gangue wall to measure the gangue retaining support pressure as shown in Figure 11(b). The measuring result is shown in Figure 12(a), and the field effect of gangue retaining support is shown in Figure 12(b). It can be seen that the pressure of gangue retaining begins to appear at 20 m behind the working face and reaches a peak value of 0.28 MPa when it is 73 m behind. Then the pressure of gangue retaining gradually stabilizes after 160 m behind the working face; that is, the gangue wall is effectively formed gradually. As the field effect shows, the crushed gangue wall is denser, and U-shaped steels do not appear obvious compression deformation, so the design of gangue retaining support is reasonable and the formed gangue wall can support overburden effectively.

3.5. Temporary Support Design.

In the GERRC, the temporary support includes two parts: the advance temporary support and the lagging temporary support. Among them, the purpose of advance temporary support is to prevent the disturbance and destruction to the entry caused by the stress concentration in front of the working face. The advance temporary support of the 43073 working face follows the support mode of adjacent working face using leaving coal pillars mining method. As shown in Figure13(a), the DW40-300/110x single prop is selected for support, the support row spacing is 1 m, each row contains three props, and the support range is 0–30 m in advance of working face.

The lagging temporary support is also a special link of GERRC. The key area of lagging temporary support is the dynamic pressure area, so the parameters of this temporary support can be calculated according to the
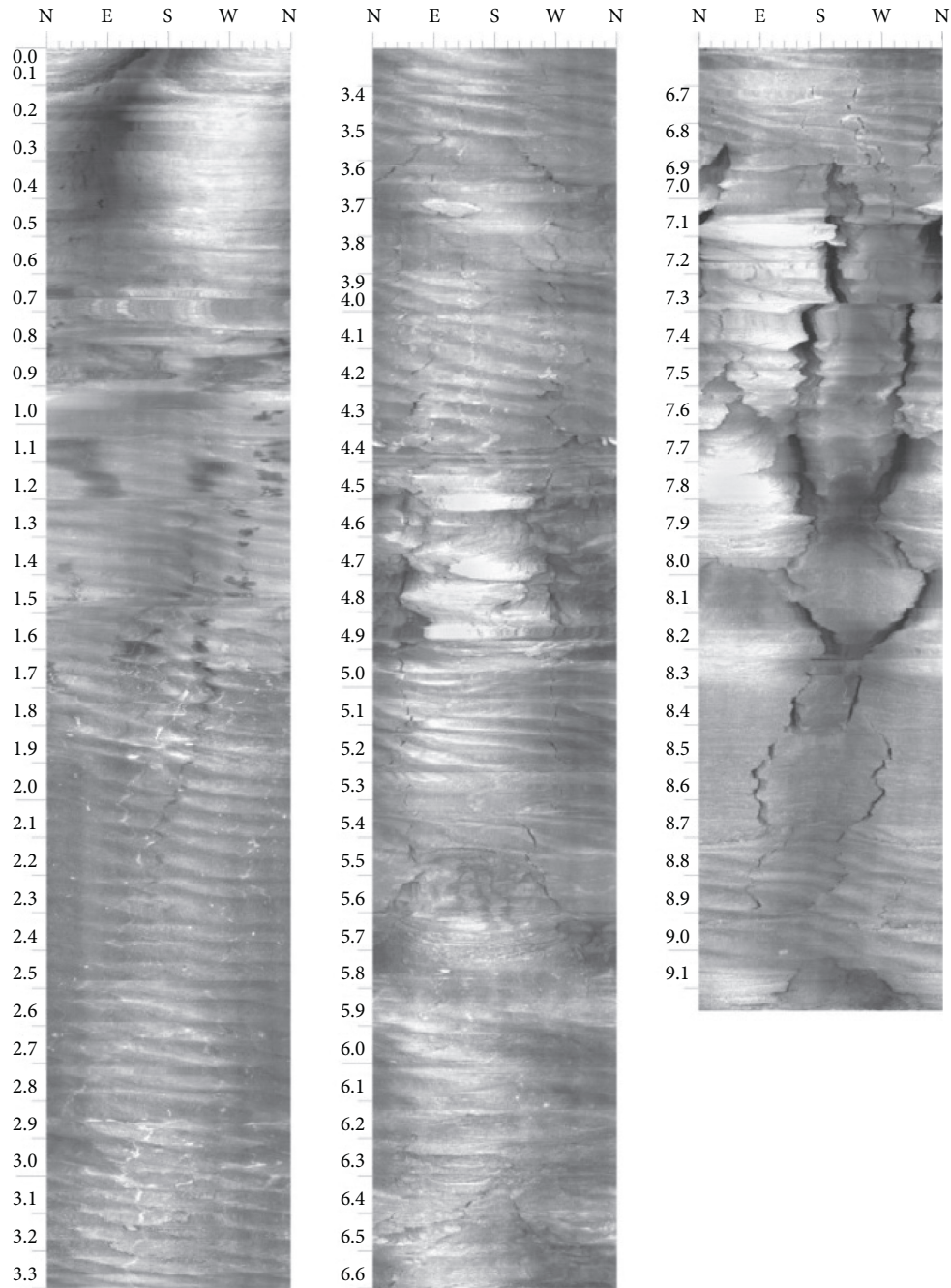
FIGURE 6: Common presplitting effect in peephole.
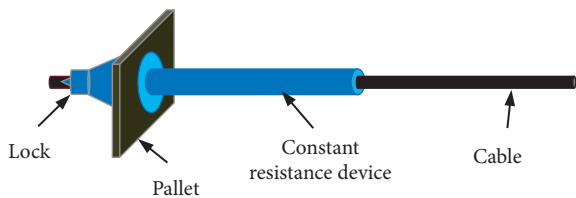
FIGURE 7: Structure of constant resistance large deformation anchor cable.

surrounding rock structure of the dynamic pressure area. As shown in Figure 14, two sides of the retained entry in the dynamic pressure area are supported by the coal wall and the gangue wall, respectively, and the gangue wall is not stable yet. Among them, T_A is the horizontal thrust of block A; N_A is the shear force of block A; M_A is the bending moment of block A at point A'; T_B, N_B, and M_B have the corresponding meanings as T_A, N_A, and M_A, respectively, but for block B; M_0 is the immediate roof
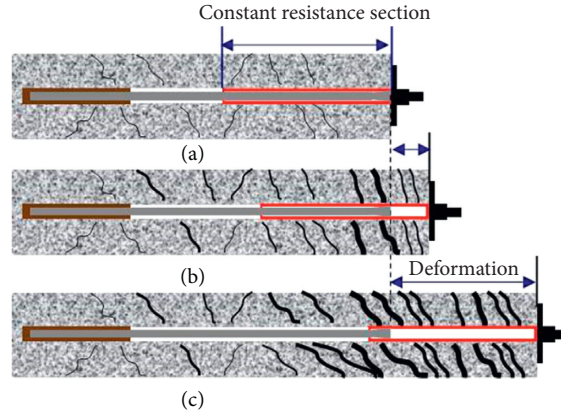
Figure 8: Principle of the anchor cable. (a) Before deformation. (b) Under deformation. (c) After deformation.
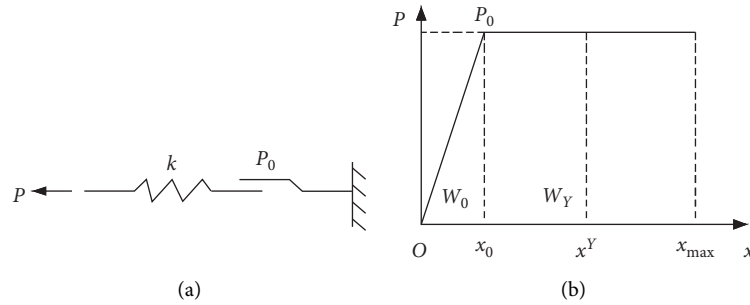
Figure 9: Constitutive and energy model of the anchor cable. (a) Constitutive relation. (b) Energy model.
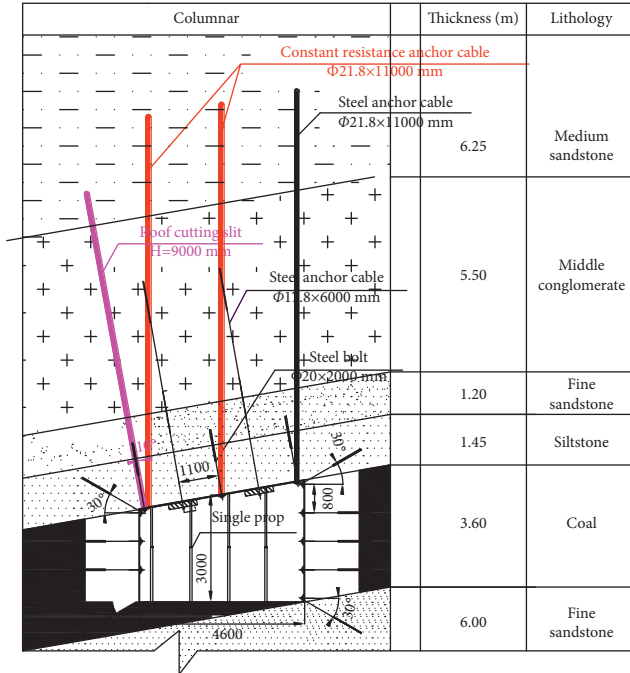
Figure 10: Design of roof cutting and entry supporting in the 43073 working face.

limit bending moment; x_S is the lateral width of the limit equilibrium zone in the coal wall; σ is the coal wall plastic zone support; and F_2 is the gangue wall support. In this area, the gangue wall is not stable, so F_2 is small. Particularly in a certain area close to the working face, F_2 is approximately 0. When calculating the entry support force F_1, the rotary deformation at the elastic-plastic boundary A′ of block A should be considered first, and the width of the limit equilibrium zone in the coal wall and the support force of the plastic zone to roof are [26, 27]

$$x_s = \frac{H_M k_a}{x} \ln\left(\frac{k\gamma H + c'/\tan\varphi'}{c'/\tan\varphi' + p_x/k_a}\right),$$

$$\sigma = (c'/\tan\varphi' + p_x/k_a)e^{2x\tan\varphi'/mk_a} - \frac{c'}{\tan\varphi'},$$

(5)

where c' and φ' are the cohesive force and internal friction angle, respectively, of the interface between the coal seam and the roof; k_a is the lateral pressure coefficient; k is the maximum stress concentration coefficient; H is the mining depth; and p_x is the coal wall support strength. The stress states of blocks A and B are analyzed by the static equilibrium method [26]:
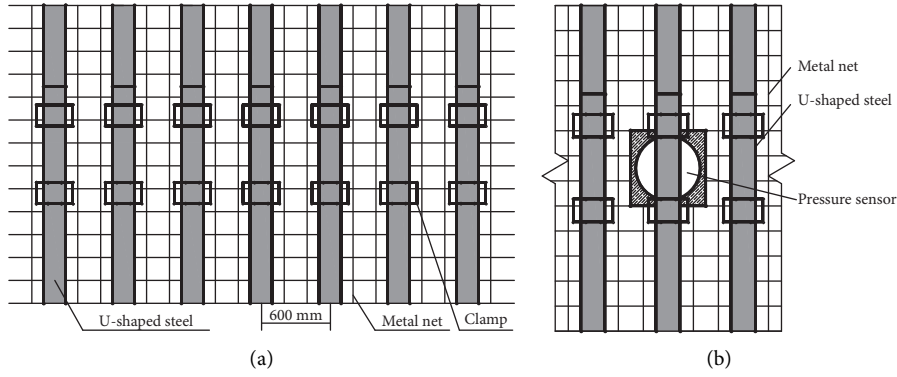
FIGURE 11: Design of gangue retaining support. (a) Support design with U-shaped steel. (b) Pressure monitoring of gangue retaining support.
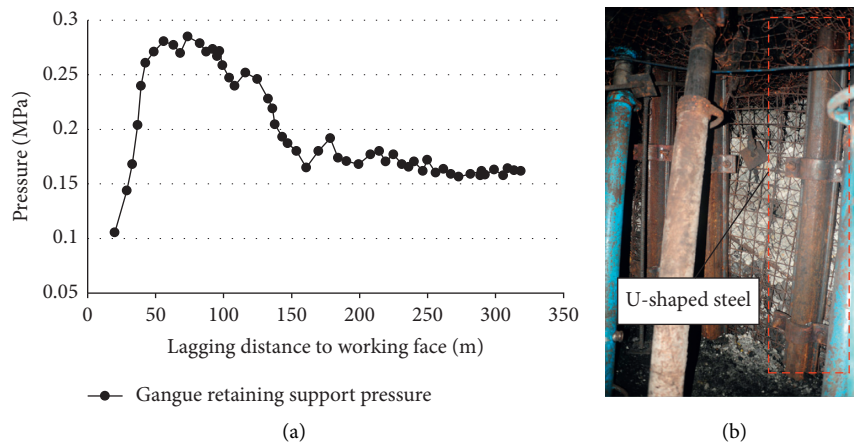
FIGURE 12: Monitoring results of gangue retaining support. (a) Gangue retaining support pressure. (b) Field effect of gangue retaining support.
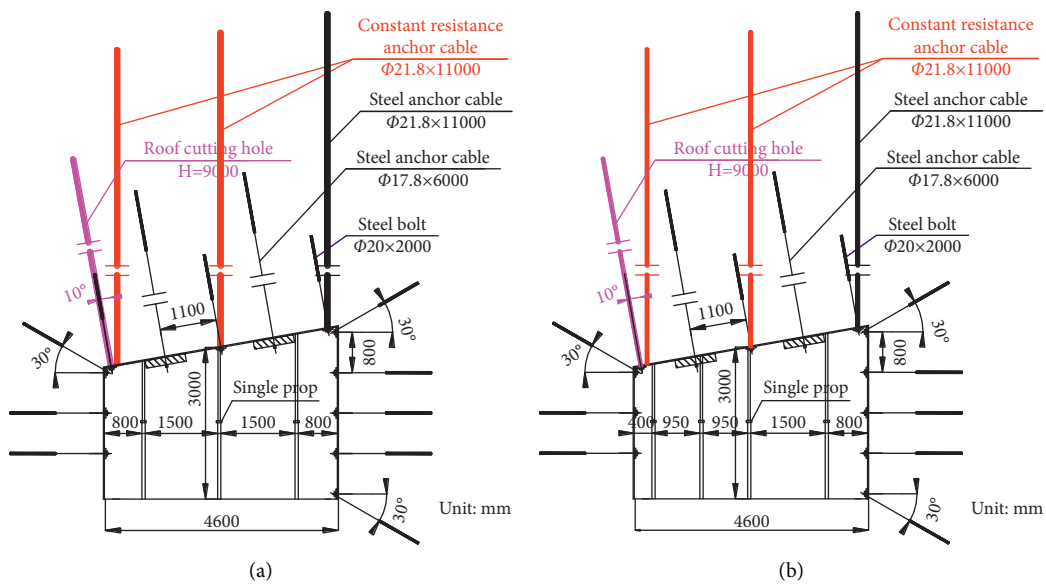
FIGURE 13: Advance and lagging temporary support design of the 43073 working face. (a) Advance temporary support. (b) Lagging temporary support.
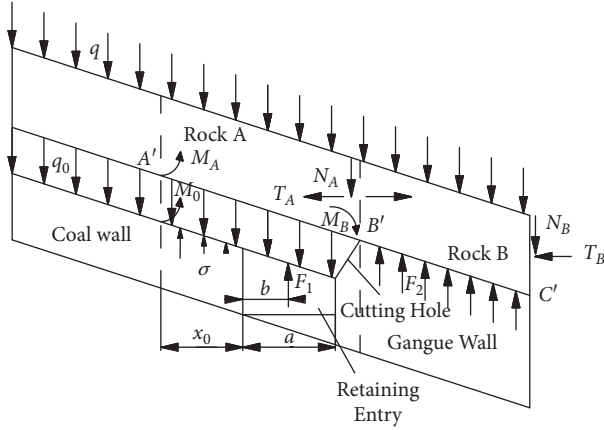
Figure 14: Simplified mechanical model of dynamic pressure area.

Block B:
$$\begin{cases} \sum F_X = 0 \\ \sum F_y = 0 \\ \sum M_{B_l} = 0 \end{cases}, \qquad \text{then}$$

$$\begin{cases} T_A = T_B \\ N_A = N_B + qL \\ M_B + T_B(H - \Delta S_C) - N_B L - qL^2/2 = 0 \end{cases}, \quad \text{then}$$

$$N_B = \frac{M_B + T_A(H - \Delta S_B) - qL^2/2}{L},$$

$$N_A = \frac{M_B + T_A(H - \Delta S_B) - qL^2/2}{L}. \tag{6}$$

Rock A: $\sum M_A = 0$, then

$$M_A + M_0 + F_1(x_s + b) + \int_0^{x_s} \sigma(x_s - x)dx + T_A(H - \Delta S_A)$$

$$- \frac{M_B - qL^2/2 - q_0(x_s + L_h)^2}{2 - N_A(x_s + L_h) = 0},$$

$$T_A = T_B = \frac{qL}{2(H - \Delta S_B)}, \tag{7}$$

where L is the lateral breaking span of the basic roof; ΔS_A is the subsidence of rock A at point B'; and ΔS_B is the subsidence of rock B at point C'. F_1 is determined as follows:

$$F_1 = \left[\frac{M_B(L + x_s + L_h) + q(x_s + L_h)^2/2 + qL(x_s + L_h)/2 + q_0(x_s + L_h)^2/2 + q(x_s + L_h)}{2 - M_A - M_0 - qL/4 - \int_0^{x_s} \sigma(x_s - x)dx/(x_s + b)}\right]. \tag{8}$$

Taking $c' = 0.1$ MPa, $\varphi' = 18°$, $K_a = 2$, $L = 15$ m, $\gamma = 13$, 25 KN/m^3, and $p_x = 0.03, 0.04$ MPa into the above calculation, the entry roof supporting demand of per meter is 1430 KN. The working resistance of the selected single prop is 300 kN, so its support density is 1.04/m^2 at least behind the working face. Therefore, as shown in Figure 13(b), in the upper entry retaining test of 43043 working face, each support row of lagging temporary support is designed as four single props, the row spacing is 0.5 m on the roof cutting side, and it is 1 m to other three rows. In addition, according to the monitoring of the gangue retaining pressure, the gangue wall tends to be stable when it is behind the working face more than 160 m, so the lagging temporary support range is 0–160 m behind the working face at least.

4. Simulation Analysis of Pressure Releasing

Based on the above design, this section firstly uses numerical simulation software to simulate the stress distribution of surrounding rock under the condition of roof cutting and pressure releasing in the mining process and predicts and analyzes the effect of roof cutting from the theoretical point of view.

4.1. Model Establishment. In order to verify the design about the key technical parameters by numerical simulation, on the basis of considering actual engineering conditions and simplified calculation, the calculation

model is established as 200 m × 210 m × 50 m by Flac 3D numerical simulation software. In this model, the entry excavation size is 200 m × 4.6 m × 3.6 m, and the working face mining size is 100 m × 170 m × 3.6 m. The calculation model is shown in Figure 15, which includes roof about 30 m thick, floor about 17 m thick, 1656800 grid units, and 1764670 nodes. The parameters of each rock layer are referenced in Table 2, and the roof cutting and no cutting conditions are simulated, respectively, to be compared [28, 29].

4.2. Simulation Analysis. The simulation results of section A-A are shown in Figure 16. Under the no roof cutting condition, there is an obvious stress concentration zone in the coal wall of entry, the maximum vertical stress is 57.8 MPa, and the stress concentration zone is closer to the entry wall (about 2.0 m), which can easily lead to the adverse phenomenon of coal wall slice. Meanwhile, the entry roof is greatly influenced by the collapse of the goaf roof, whose subsidence is larger on the goaf side and smaller on the coal wall side, and the maximum subsidence is about 2500 mm. However, under the roof cutting condition, the stress concentration range in the coal wall is smaller, the maximum vertical stress is 52.1 MPa, and the stress concentration zone is far from the entry wall (about 4.0 m). Besides, the maximum vertical displacement of the entry roof is 1570 mm, which is far less than the maximum value under no roof cutting condition. The above result shows that the roof cutting can effectively cut off the stress transfer between the

(a)

(b)

(c)
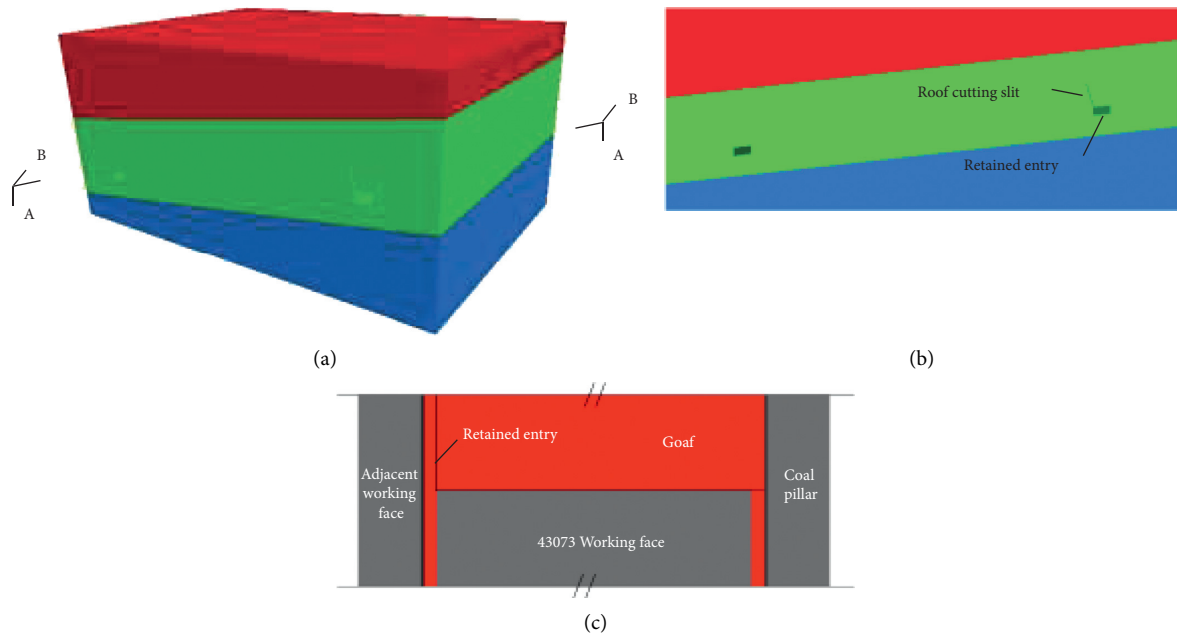
FIGURE 15: Numerical calculation model. (a) Three-dimensional model. (b) Section A-A. (c) Section B-B.

(1) Vertical stress distribution (Unit: Pa)   (2) Vertical displacement distribution (Unit: m)

(a)

(1) Vertical stress distribution (Unit: Pa)   (2) Vertical displacement distribution (Unit: m)

(b)
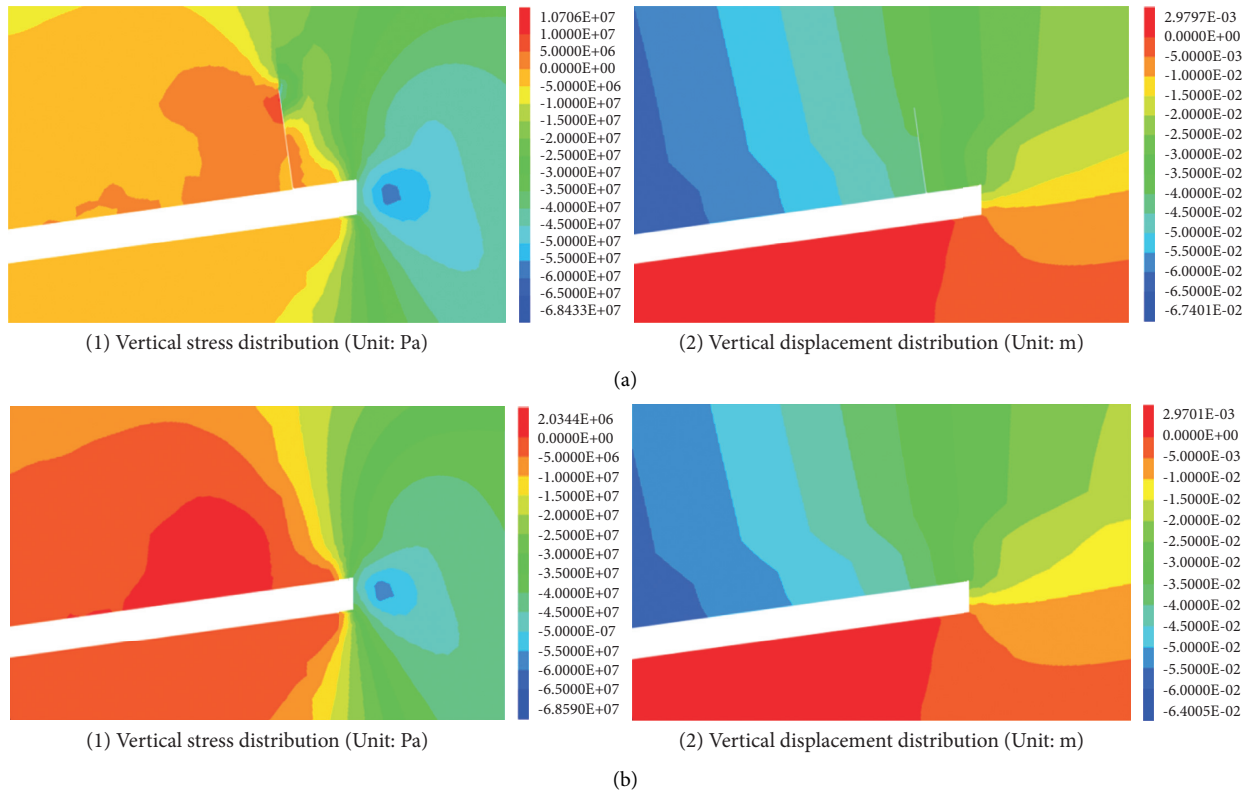
FIGURE 16: The simulation results of A-A section. (a) Simulation results of vertical stress and displacement under roof cutting. (b) Simulation results of vertical stress and displacement under no roof cutting.

entry roof and goaf roof, which can effectively control the deformation of retained entry roof.

In addition, the vertical stress distribution simulation result of the B-B section under roof cutting condition is shown in Figure 17. The distribution characteristics of the vertical stress field in the working face can be seen from the graph: (1) Vertical stress peak appears in front of the working face, and the peak stress value on the roof cutting side is less than that on the no cutting side. (2) Comparing the stress distribution of the coal seam at both sides of goaf, it
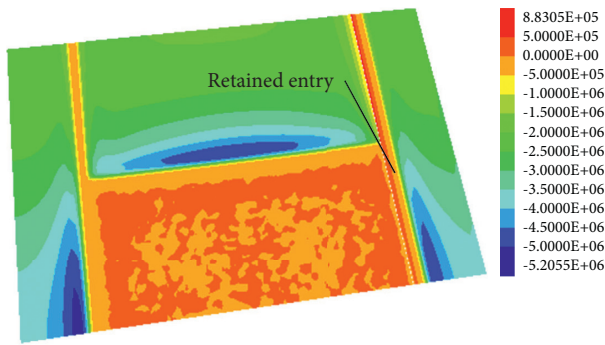
FIGURE 17: The vertical stress distribution simulation results of the B-B section (unit: Pa).

can be seen that the stress concentration range on the no roof cutting side is larger than that on the roof cutting side and the stress concentration value is also higher.

5. Effect of Field Application

Based on the above design and theoretical analysis, the characteristics of roof cutting effect under upper roadway have been analyzed systematically, which can effectively guide the field roof cutting test in the 43073 working face of Yixin coal mine. In the test process, the effect of entry retaining is evaluated by pressure monitoring of the working face and entry deformation monitoring. The relevant monitoring results and analysis are as follows.

5.1. Pressure Monitoring of Working Face. The 43073 working face is mined and its auxiliary entry is retained as the above design. There are 10 GPD60 W mine intrinsically safe wireless pressure sensors distributed in the working face to monitor the change of hydraulic support working resistance. The serial numbers of supports that installed sensors are 1, 12, 23, 34, 45, 56, 67, 78, 89, and 100. In order to analyze the effect of roof cutting pressure releasing, the working resistance monitoring data of hydraulic support near the no roof cutting side (1# support), the middle of working face (45# support), and the roof cutting side (100# support) are chosen as Figures 18(a)–18(c) for comparison.

The statistical results of the weighting step and weighting strength about the above three typical supports are shown in Table 3. It can be seen that the weighting step is shortest and the weighting strength is highest in the middle of the working face. Affected by the roof cutting pressure releasing, the periodic weighting step on the entry retaining side is longer than that of the no roof cutting side, and the average increase is 3 m. And the periodic weighting strength is lower on the roof cutting side, the decrease of average strength is 1.4 MPa, and the decrease of peak strength is 6.8 MPa. The effect of roof cutting pressure releasing is obvious according to the above analysis.

Besides, according to the monitoring results of 10 marked hydraulic supports, the first weighting step, the periodic weighting step, the peak weighting strength, and the

average weighting strength of the working face are statistically analyzed. The results are shown in Figure 19.

It can be seen that the weighting step and weighting strength distribution laws of the working face are consistent with the analysis results of the above three typical supports, and the weighting step and strength distributions are asymmetrical due to the influence of roof cutting at the entry retaining side. Compared to the no roof cutting side, the periodic weighting step is longer and weighting strength is weaker on the roof cutting side. The pressure releasing effect is obvious from the 78# hydraulic support, so the lateral influence range of roof cutting is approximately 37.4 m in the working face (the width of single hydraulic support is 1.7 m), and the more close to the roof cutting line, the more significant the pressure releasing effect. What is more, affected by the roof cutting, on the entry retaining side of the working face, the peak weighting strength of hydraulic support is more affected than the average weighting strength. Specifically, compared to the no roof cutting side, the maximum releasing ratio of peak weighting strength is 17.5% and the maximum releasing ratio of average weighting strength is 4.1% on the roof cutting side of 43073 working face.

5.2. Entry Deformation Monitoring. As shown in Figure 20, the entry deformation monitoring uses the cross point method, and the length of line segment AO, OC, BO, and OD should be measured every day at the monitoring section of entry. The entry deformation should be monitored from the monitoring section entering the advanced temporary support section until the deformation becomes stable. In the entry retaining and monitoring process, the deformation is the most severe at mining footage 130 m and the monitoring result of this section is shown in Figure 21.

According to the monitoring results above, the following can be seen: (1) The final deformation of retained entry floor heave is 143 mm, the final deformation of roof subsidence is 218 mm, and the final deformation of roof to floor convergence is 361 mm. The change trends of roof subsidence and floor heave are the same basically, and the roof to floor convergence becomes stable when the retained entry is behind the working face more than 207 m. (2) The final convergence deformation of the entry two sides is 280 mm. The convergence is mainly manifested as the deformation of the coal wall in the early stage, and then with the gradually compacting of the gangue wall, the convergence is mainly manifested as the deformation of the gangue wall in the latter stage. The final lateral deformation of the gangue wall is 79 mm, the final lateral deformation of coal wall is 201 mm, and the convergence of two sides becomes stable when the retained entry is behind the working face more than 226 m. In this section of retained entry, the final height on the roof cutting side is 1892 mm and the final width is 4320 mm. The field effect of entry retaining is shown in Figure 22, and the retained entry is enough to meet the reuse demand of adjacent working face mining.

(a)

(b)

(c)
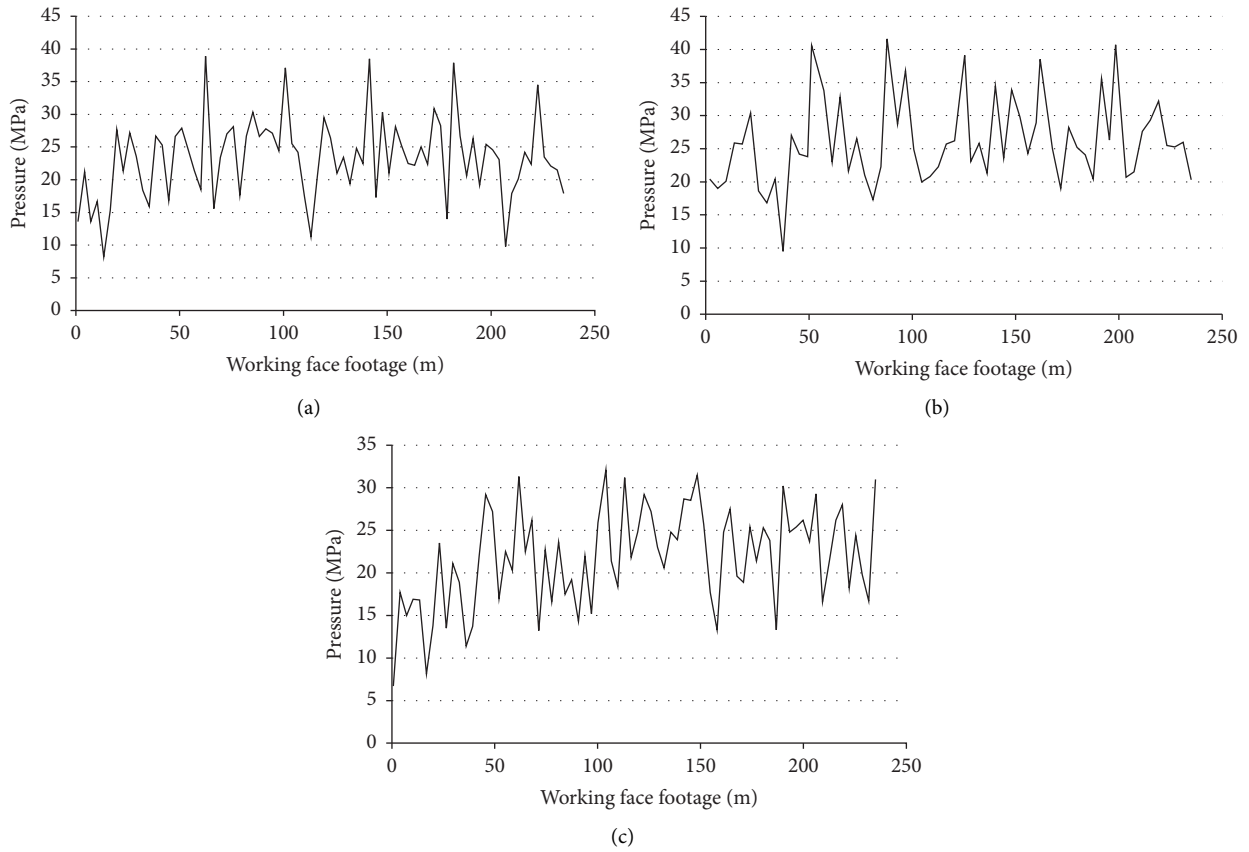
FIGURE 18: Monitoring diagram of typical hydraulic support. (a) 1# support (near the no roof cutting side). (b) 45# support (near the middle of the working face). (c) 100# support (near the roof cutting side).

TABLE 3: Hydraulic support resistance statistic.

Support number	First weighting step (m)	Periodic weighting step (m)				Average pressure (MPa)	Peak pressure (MPa)
		1	2	3	Average		
1	62	39	40	41	40	23.2	38.9
45	51	37	37	38	37	26.1	41.6
100	61	43	44	42	43	21.8	32.1

(a)

△ First weighting step
■ Periodic weighting step

(b)

△ Peak pressure
■ Average pressure
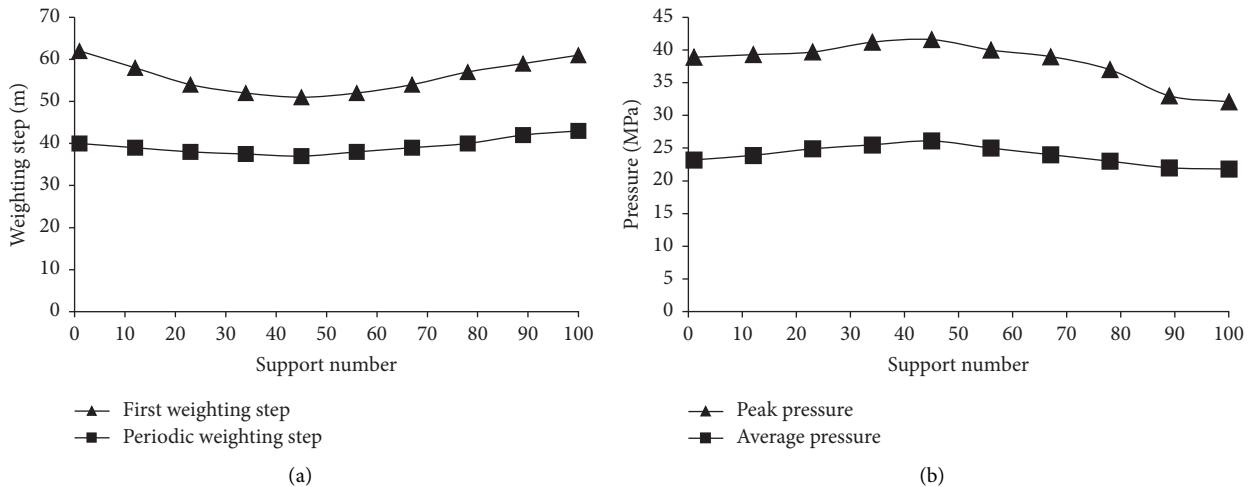
FIGURE 19: Pressure statistics of hydraulic support in working face. (a) Weighting step statist. (b) Weighting strength statistic.
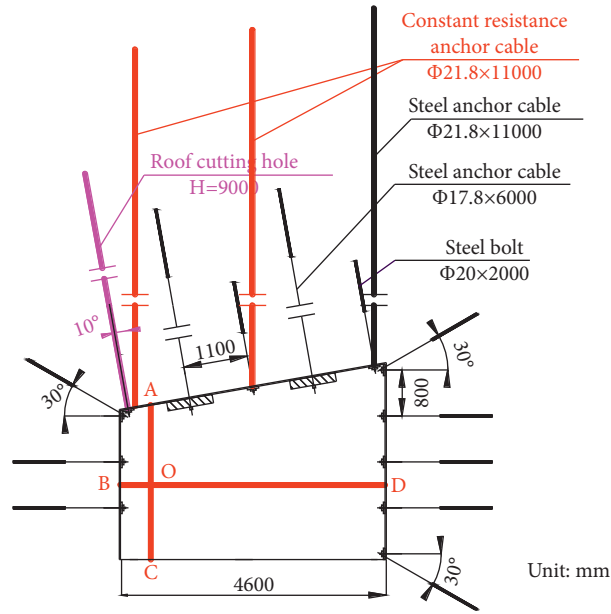
FIGURE 20: Monitoring design of roadway.

(a)

(b)
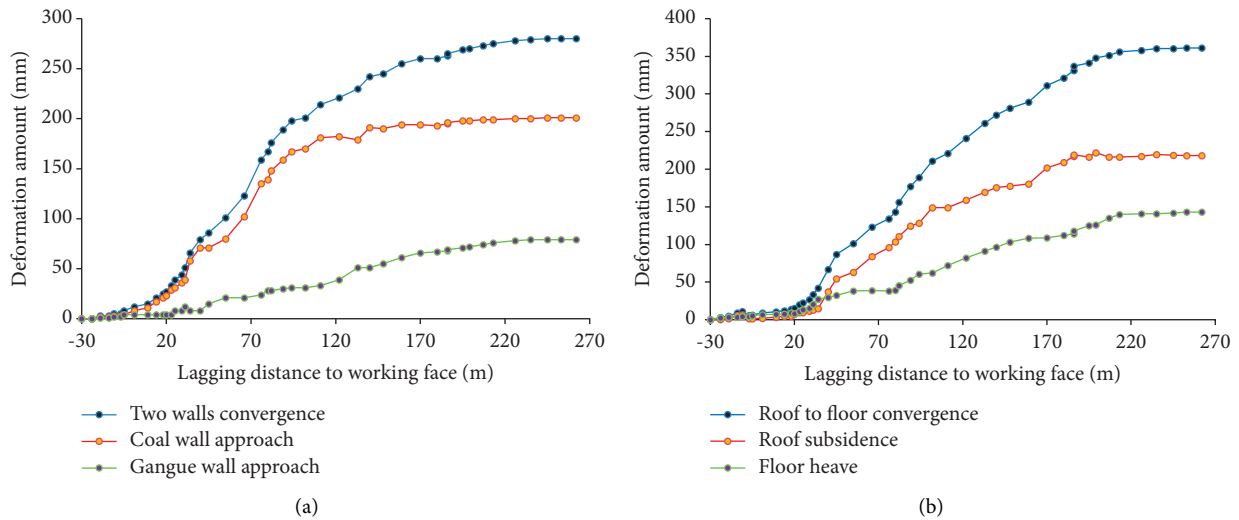
FIGURE 21: Monitoring results at 130 m footage section. (a) Two walls convergence. (b) Roof to floor convergence.

FIGURE 22: Field retaining effect.

6. Conclusions

(1) This paper analyzes the difficulties of upper entry retaining by roof cutting under inclined coal seam condition and puts forward the key technologies and system design to the special condition, which includes five parts: roof cutting, blasting, reinforcement support, gangue retaining support, and temporary support.

(2) Taking the 43073 working face of Yixin coal mine as an example, this paper makes the detail design of GERRC with upper entry under gently inclined thick coal seam condition, analyzes the roof cutting and pressure releasing effect by numerical simulation, and expounds the stress distribution and pressure

releasing mechanism of surrounding rock under roof cutting.

(3) Entry retaining field test is carried out to verify the feasibility and applicability of the upper entry retaining design. Through the field monitoring, it is found that the weighting step increases significantly and the weighting strength decreases effectively on the roof cutting side; namely, the pressure releasing effect is obvious. Meanwhile, the maximum roof to floor convergence is 361 mm and the maximum shrinkage of both sides is 280 mm, so the retained entry can meet the reuse requirement of adjacent working face.

Data Availability

All the data used to support the findings of this study are available from Xingen Ma upon request.

Conflicts of Interest

The authors declare that they have no conflicts of interest.

Acknowledgments

References

[1] H. Kang, D. Niu, Z. Zhang, J. Lin, Z. Li, and M. Fan, "Deformation characteristics of supporting rock and supporting technology of gob-side entry retaining," *Chinese Journal of Rock Mechanics and Engineering*, vol. 29, no. 10, pp. 1977–1987, 2010.

[2] M. Mahoutian, M. Shekarchi, and N. A. Libre, "Application of steel fiber reinforced lightweight Aggregate concrete in Underground mining," *Journal of Mining Science*, vol. 47, no. 5, pp. 606–617, 2011.

[3] Q. Wang, Y. Wang, M. He et al., "Experimental research and application of automatically formed roadway without advance tunneling," *Tunnelling and Underground Space Technology*, vol. 114, Article ID 103999, 2021.

[4] J. Wang and G. Wang, "Discussion on gateway retained along goaf technology with roof breaking and pressure releasing," *Coal engineering*, vol. 1, pp. 24–26, 2012.

[5] H. Zhu, "Technology and application of reserving pier column method along goaf," *Coal mine modernization*, vol. 147, no. 6, pp. 181–186, 2018.

[6] S. Zhang, Y. Liu, H. Liu, S. Jiang, Z. Liu, and H. Xu, "Optimal design of laneway's side support for gob-side entry retaining with solid cemented backfilling," *Safety In Coal Mines*, vol. 49, no. 3, pp. 48–51, 2018.

[7] Y. Li, "Supporting technology with filling beside roadways in gob-side entry retaining on fully-mechanized working face," *Shanxi coal*, vol. 49, no. 3, pp. 48–51, 2018.

[8] C. Zhu, M. C. He, X. H. Zhang, Z. G. Tao, Q. Yin, and L. F. Li, "Nonlinear mechanical model of constant resistance and large deformation bolt and influence parameters analysis of

constant resistance behavior," *Rock and Soil Mechanics*, vol. 42, no. 7, pp. 1911–1924, 2021.

[9] M. He, X. Ma, F. Niu, J. Wang, and Y. Liu, "Adaptability research and application of rapid gob-side entry retaining formed by roof cutting and pressure releasing with composite roof and medium thick coal seam," *Chinese Journal of Rock Mechanics and Engineering*, vol. 37, no. 12, pp. 1–15, 2018.

[10] M. He, Z. Song, A. Wang, H. Yang, H. G. Qi, and G. Guo Zhi, "Theory of longwall mining by using roof cutting shortwall team and 110 method," *Coal Science & Technology Magazine*, vol. 37, no. 1, pp. 1–9, 2017.

[11] X. Sun, X. Liu, G. Liang, and W. Wenda, "Key Parameters of gob-side entry retaining formed by roof cut and pressure releasing in thin coal seams," *Chinese Journal of Rock Mechanics and Engineering*, vol. 33, no. 7, pp. 1449–1456, 2014.

[12] G. Zhang, M. He, X. Yu, and Z. G. Huang, "Research on the technique of no-pillar mining with gob-side entry formed by advanced roof caving in the protective seam in Baijiao coal mine," *Journal of Mining and Safety Engineering*, vol. 28, no. 4, pp. 511–516, 2011.

[13] Q. Yin, J. Wu, C. Zhu, M. He, and Q. Meng, "Mechanical responses of sandstone exposed to high temperature under constant normal stiffness boundary conditions," *Geomechanics and Geophysics for Geo-Energy and Geo-Resources*, vol. 7, p. 35, 2021.

[14] Z. Guo, J. Wang, T. Cao, and L. Y, "Research on key parameters of gob-side entry retaining automatically formed by roof cutting and pressure release in thin coal seam mining," *Journal of China University of Mining and Technology*, vol. 45, no. 9, pp. 879–885, 2016.

[15] X. Ma, M. He, and J. Sun, "Research on the design of roof Cutting parameters of non coal pillar bob-side entry retaining mining with roof cutting and pressure releasing," *Geotechnical & Geological Engineering*, vol. 8, 2018.

[16] X. Ma, J. Wang, H. Wu, Y. Liu, and Q. Jiang, "Experimental study on blasting of roof cutting with no pillar mining in working face of Tashan Coal Mine," *Coal Science and Technology*, vol. 46, no. 6, pp. 27–32, 2018.

[17] C. Wang, M. He, and S. Wang, "Application of the bidirectional energy-cavity blasting technology in the jointed rock mass," *Blasting*, vol. 21, no. 2, pp. 39–42, 2004.

[18] X. Ma, M. He, J. Wang, and G. Yubing, "Mine strata pressure characteristics and mechanisms in gob-side entry retention by roof cutting under medium-thick coal seam and compound roof conditions," *Energies*, vol. 11, p. 2539, 2018.

[19] F. Gan, Y. Kang, X.-C. Wang, and H. Yaoqing, "Investigation on the failure characteristics and fracture classification of shale under Brazilian test conditions," *Rock Mechanics and Rock Engineering*, vol. 53, no. 7, pp. 3325–3340, 2020.

[20] C. Baosuo, K. Zhou, and M. He, "Optimization research on supporting parameters of roof cutting entry retaining with large mining height face," *Coal Science and Technology*, vol. 45, no. 8, pp. 128–133, 2017.

[21] X. Ma, M. He, W. Li, and L. Lifeng, "Research and application of open-off cut roof cutting pressure releasing technology," *Advances in Civil Engineering*, vol. 2021, Article ID 9989213, 14 pages, 2021.

[22] M.-C. He, C. Li, W. Gong, J. Wang, and Z. Tao, "Support principles of NPR bolts/cables and control techniques of large deformation," *Chinese Journal of Rock Mechanics and Engineering*, vol. 35, no. 8, pp. 1513–1529, 2016.

[23] Y. Gao, M. He, J. Yang, and X. Ma, "Experimental study of caving and distribution laws of gangues influenced by roof fracturing in pillarless mining with gob-side entry retaining,"

Journal of China University of Mining and Technology, vol. 47, no. 1, pp. 116–127, 2018.

[24] F. Gan, X. Wang, M. Wang, and Y. Kang, "Experimental investigation of thermal cycling on fracture characteristics of granite in a geothermal-energy reservoir," *Engineering Fracture Mechanics*, vol. 235, Article ID 107180, 2020.

[25] Y. Gao, J. Yang, M. He, and S. Dingjie, "Mechanism and control techniques for gangue rib deformations in gob-side entry retaining formed by roof fracturing in thick coal seams," *Chinese Journal of Rock Mechanics and Engineering*, vol. 10, no. 36, pp. 2492–2502, 2017.

[26] X. Ma, *Research on Key Technologies and Rock Pressure Law of 110 Mining Method with compound hard Roof in Tashan Coal Mine*, China University of Mining and Technology, Beijing, China, 2019.

[27] M. He, S. Chen, and Z. Guo, "Control of surrounding rock structure for gob-side entry retaining by cutting roof to release pressure and its engineering application," *Journal of China University of Mining and Technology*, vol. 9, no. 46, pp. 959–969, 2017.

[28] G. Ramesh and R. Karpurapu, "Laboratory and numerical studies on the performance of geocell reinforced base layer overlying soft subgrade," *International Journal of Geosynthetics and Ground Engineering*, vol. 7, 2021.

[29] F. Wu, H. Zhang, Q. L. Zou, C. B. Li, J. Chen, and R. B. Gao, "Viscoelastic-plastic damage creep model for salt rock based on fractional derivative theory," *Mechanics of Materials*, vol. 150, Article ID 103600, 2020.

Research Article

Study on the Variation Rule and Characteristics of Pore Water Pressure in the Failure Process of Saturated Rock

Yuezheng Zhang [1,2]

[1]*University of Science & Technology Beijing, Beijing 100083, China*
[2]*Beijing Key Laboratory of Urban Underground Space Engineering, Beijing 100083, China*

Correspondence should be addressed to Yuezheng Zhang; yuezheng20053660@163.com

With the development of tunnels and other engineering constructions into the deep strata, rock masses are more prone to dynamic damage such as rock bursts under in situ conditions and excavation disturbances. The pore water in the rock mass will produce pressure changes during this process. According to the relationship between the change of pore water pressure and the development of rock mass damage, the variation rule and precursor characteristics of pore water pressure in the process of rock mass failure can be found. In this paper, through mechanical analysis, the evolution law of pore water pressure during the failure process of saturated rock is obtained. The study found that, in the process of rock failure, the pore water pressure presents three stages of linear growth, transition, and decrease. The rise and fall of pore water pressure are closely related to rock damage and influence each other. Through the observation of pore water pressure during coal mining, it is found that the coseismic effect of pore water pressure is significant. It is proved that there is a close correlation between the evolution of the stress field in the surrounding area of the stope and the change of pore water pressure in the surrounding area under the effect of mining disturbance. During the engineering practice, dynamic monitoring can be carried out on the change of pore water pressure inside the rock mass according to the law, and the precursor information of rock mass instability and failure can be explored.

1. Introduction

The presence of pore water in the rock has a significant impact on the physical and mechanical properties of the rock, which is mainly reflected in the strength and failure mode of the rock. And the degree of the influence increases with the increase of rock porosity [1, 2]. The macroscopic fracture, instability, and failure of the rock after loaded are closely related to the distribution of internal microcracks and the generation, expansion, and penetration of micro-cracks during deformation. The deformation of the rock has caused the change of its internal pore volume, so the pore water pressure is closely related to the damage of the rock [3–5]. Studies have shown that, during the process of rock failure under pressure, the pore water pressure presents a "rise-decrease" change corresponding to the failure process. According to this finding, the seismic research scholar Che Yongtai and others believe that the water level changes in the aquifer are the anomalous information of earthquake precursors. At the same time, according to the principle of effective stress, the deformation and damage of rock and soil are mainly dominated by effective stress. Under certain conditions of total stress, the pore water pressure and the effective stress will change from one to the other. While the damage development affects the pore water pressure, the pore water pressure also affects the effective stress and then the damage development [6]. Therefore, the interaction relationship between rock damage propagation and pore water pressure changes can be deeply studied to explore the precursor information of critical fracture pore water pressure of rock mass [7–10].

Based on the effective stress, Hooke's law, and damage mechanics principles, this paper theoretically analyzes and establishes the relationship between pore water pressure and rock damage propagation based on the existing experimental research results. The characteristic mode of pore water pressure during the process of elastic deformation, plastic damage, and failure of the rock is obtained.

2. Principle of Pore Water Pressure Change Caused by Rock Mass Deformation

Research shows that the complete process of a seismic event is carried out within a certain range of time and space. The source of the earthquake includes the ruptured body that generates rupture and instability and consumes energy when the earthquake occurs and the surrounding participants that provide energy for the earthquake. In the "relevant area" stratum, the scale of the source is usually much larger than the scale of stratum rupture during the earthquake. The stratum rock mass in a certain area will form a "coordinated seismogenic system" under the action of ground stress. And a certain "structural effect" in the stratum will connect strata on a larger scale to form a "correlation region." In the process of earthquake incubation, a series of characteristics such as ground motion, seismic activity, stress field distribution, and pore water pressure distribution in the relevant area will show a strong "correlation" and "synergy" in a certain spatial range. It also shows different "correlation characteristics" between the physical and mechanical characteristics, spatial scale, stress drop level, source scale, energy consumed and released, and the characteristics of seismic activity related to this seismic activity [11].

When the tectonic stress changes in the ground involve the water-bearing rock and soil layer, the force deformation of the rock and soil will happen. The deformation of the rock and soil will cause the change of the pore volume and then cause the change of the pore water pressure in the rock and soil [12–15]. Zhang and others [16, 17] studied the change pattern of pore water pressure in an ideal confined aquifer under the influence of vertical stress σ_V changes and obtained the relationship between pore water pressure and stress change:

$$\Delta H = \frac{n\beta + (1-n)\alpha}{2\beta\rho g} * \Delta\sigma_V, \tag{1}$$

where ΔH is the change of pore water pressure head caused by the change of the vertical stress of the aquifer σ_V, n is the porosity of the aquifer, α is the vertical compression coefficient of the aquifer framework, β is the volume compression coefficient of water, ρ is the density of water, and g is the acceleration due to gravity.

Che et al. researched that the change of rock volume is mainly caused by the change of porosity, and the change of porosity is related to the nature of the force. Under the action of compressive stress, the porosity becomes smaller; under the action of tensile stress, the porosity becomes larger; under the action of shear stress, the porosity does not change. And the law of sandstone porosity changing with axial compressive stress is

$$\frac{n_\sigma}{n_0} = (1-b)10^{-a\sigma} + b, \tag{2}$$

where n_σ is the changed porosity after being stressed, n_0 is the original porosity, σ is the axial stress, b is an index, and E is the ratio after the area is stabilized.

For saturated rock mass, not only the stress of the rock mass but also the pore water pressure will increase during the compression process. If it is a permeable stratum, the excess pore water pressure will dissipate over time and cause the change of groundwater level. The change of well water level during the earthquake is also a macroscopic phenomenon that reflects this law [18].

It can be seen that the stress and deformation of the rock mass will cause damage to the pore water pressure at the same time. The stress and deformation of the rock mass are closely related to the pore water pressure. The change of pore water pressure can be used as earthquake precursor information. To find this precursory information feature, it is necessary to understand the correlation between the damage propagation and the change of pore water pressure during the rock stress process.

3. Correlation Analysis of Pore Water Pressure and Rock Damage

3.1. The Model of Pore Water Pressure Change during Rock Failure. There is pore water pressure in the rock with saturated water, and the deformation of the rock and soil is determined by the effective stress. The relationship between effective stress, pore water pressure, and total stress is

$$\sigma = \sigma' + p. \tag{3}$$

In the formula, σ, σ', and p, respectively, represent total stress, effective stress, and pore water pressure.

When the rock is compressed under water saturation, the pore water pressure will have a significant impact on the strength and failure mode of the rock. However, there will not be a significant impact on the elastic modulus. The deformation of the water-bearing rock mass causes the change of its pore water volume and then causes the change of pressure in pore water in the rock mass.

Che et al. obtained the pore water pressure p change curve through triaxial test research on fine sandstone. On this basis, this paper drew the "pore water pressure stress" in the rock closed unit body (without hydraulic contact with the outside world). Comparison chart of "strain" change relationship (Figure 1) shows that the "stress-strain" curve corresponds to the elastic stage, the plastic stage, and the failure stage. The pore water pressure presents a-b linear increase, b-c increase-decrease transition, and c-d decrease.

3.1.1. Pore Water Pressure: a-b Linear Growth Stage. The "stress-strain" curve changes linearly. When the deformation is in the elastic stage, the elastic modulus E remains unchanged, there is no damage inside the rock, and the porosity remains unchanged. Therefore, the increase in pore water pressure is due to the reduction of pore space caused by the elastic deformation of the rock under pressure.

Considering that water is compressible, the compressibility is β, and the change in pore water pressure is Δp_1, then the change in water volume ΔV_{W-1} can be expressed as
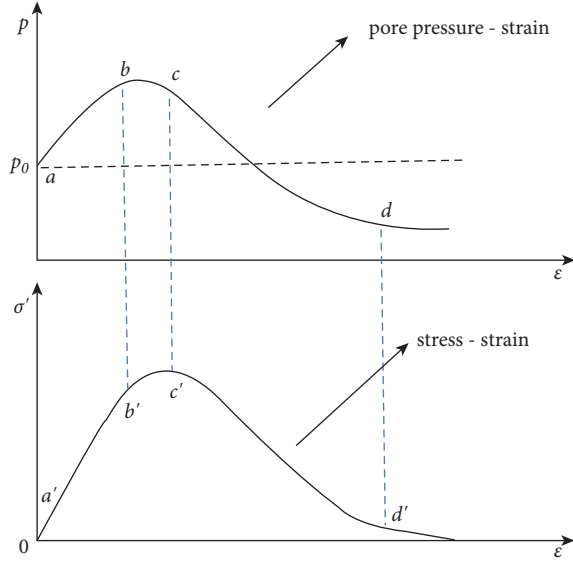
FIGURE 1: "Pore pressure-stress-strain" relation diagram.

$$\Delta V_{W-1} = -\Delta p \beta. \tag{4}$$

The next step is to find the volume change of the rock ΔV. The rock material is a continuous medium material. According to Hooke's law, the volumetric strain θ and volumetric stress Θ in the elastic phase of deformation have the relationship as follows:

$$\theta = \frac{1 - 2\nu}{E}\Theta,$$

$$\Delta\theta = -\frac{(1 - 2\nu)}{E}\Delta\Theta \tag{5}$$

$$= -\frac{(1 - 2\nu)}{E}\Delta\left(\sigma_x' + \sigma_y' + \sigma_z'\right).$$

Triaxial test under constant confining pressure $\sigma_y' = \sigma_z' = $ constant; therefore, $\sigma_y' = \sigma_z' = 0$; in order to facilitate the analysis, $\Delta\sigma' = \Delta\sigma_x'$; formula (5) can also be expressed as follows:

$$\Delta\theta = -\frac{(1 - 2\nu)}{E}\Delta\sigma', \tag{6}$$

where ΔV is the volume change of rock, V is the volume of specimen, and the relationship between them is as follows:

$$\Delta V = \Delta\theta * V. \tag{7}$$

The porosity is n and the relationship between ΔV_{W-1} and ΔV is shown in

$$\Delta V_{W-1} = n\Delta V. \tag{8}$$

Combined with formulas (4), (6), and (7), it can be concluded that

$$-\beta\Delta p_1 = -\frac{(1 - 2\nu)}{E}nV\Delta\sigma', \tag{9}$$

$$\Delta p_1 = \frac{(1 - 2\nu)}{E\beta}nV\Delta\sigma'. \tag{10}$$

By integrating both sides of formula (10), the relationship between pore water pressure and stress in the elastic compression stage is as follows:

$$p = p_0 + \int_{a'}^{\sigma''} \frac{(1 - 2\nu)}{E\beta}nV \, d\sigma'$$

$$= p_0 + \frac{(1 - 2\nu)}{E\beta}nV\sigma'. \tag{11}$$

It can be seen from formula (10) that the pore water pressure p is a one-dimensional linear function about the effective stress σ', so the pore water pressure in the a-b stage is similar to the stress change, showing a linear growth relationship.

3.1.2. Pore Water Pressure: b-c "Increase-Decrease" Transitional Stage.

The "stress-strain" curve shows that the rock deformation enters the plastic stage, and the pore water pressure increases slowly and then decreases after reaching the peak. Similarly, the change of pore water pressure is caused by the change of pore space. At this stage, the change of pores in the rock is mainly composed of two parts. ① The elastic compression of the solid framework causes the reduction of pores. This part of the change is consistent with the a-b elastic stage. ② Damage occurs inside the rock, and the deformation changes from elastic compression to expansion. At the same time, the microcracks continue to develop, the damage increases, the porosity of the rock n increases, and the effective elastic modulus $\bar{E}$ decreases. The sum caused by elastic deformation can be calculated according to formulas (8) and (11). Here, we will focus on the change Δp_2 in pore water pressure caused by plastic deformation.

Rock material is a continuous mechanical medium. Under the action of external load, it will undergo several stages of compaction, elasticity, plasticity, and failure. Reflecting on the damage is that the internal damage produces and develops into a macroscopic crack, which eventually leads to the rupture of the internal structure. It is assumed here that after the rock material is stressed to a certain level, uniform damage occurs, and the change of damage is related to the effective stress acting on the rock structure. Rabonov first introduced the variable corresponding to the continuous variable, namely, the damage variable D [19–21],

$$D = \frac{A^*}{A}, \tag{12}$$

where A is the force-receiving area when there is no initial damage and A^* is the damaged area after damage.

First of all, pay attention to the pore change caused by damage. The volume change of pore water ΔV_{W-2} is proportional to the damage $D(\sigma')$, and the proportional coefficient is m:

$$\Delta V_{W-2} = m * V * D(\sigma'), \tag{13}$$

$$-\beta \Delta p_2 = mV \, D(\sigma'), \tag{14}$$

$$\Delta p_2 = -\frac{mV}{\beta} D(\sigma'), \tag{15}$$

$$p = p_o + \frac{(1-2\nu)}{E\beta} V\sigma' + \int_{b'}^{c'} \frac{mV}{\beta} \left(\frac{\widetilde{E}(\sigma')}{E} - 1 \right) d\sigma', \tag{16}$$

$$p = p_o + \frac{(1-2\nu)}{E\beta} V\sigma' + \int_{b'}^{c'} \frac{mV}{\beta} \left(\frac{\widetilde{E}(\sigma')}{E} - 1 \right) d\sigma'. \tag{17}$$

Formula (17) is the constitutive relationship between pore water pressure and stress in the plastic deformation stage. Damage variables are generally difficult to see from the stress-strain curve. In order to further express this constitutive relationship intuitively, according to the principle of strain equivalence proposed by Lemaitre, the effective stress σ' and damage variable $D(\sigma')$ have the following constitutive relationship:

$$\sigma' = E(1-D)\varepsilon. \tag{18}$$

In the formula, σ', D, E, ε, respectively, represent effective stress, damage variable, rock elastic modulus, and strain. Introducing the effective modulus of elasticity $\widetilde{E}(\sigma') = E(1-D(\sigma'))$, the damage variable can also be expressed as

$$D(\sigma') = 1 - \frac{\widetilde{E}(\sigma')}{E}, \tag{19}$$

$$p = p_o + \frac{(1-2\nu)}{E\beta} V\sigma' + \int_{b'}^{c'} \frac{mV}{\beta} \left(\frac{\widetilde{E}(\sigma')}{E} - 1 \right) d\sigma'. \tag{20}$$

It can be seen intuitively from formula (20) that $\widetilde{E}(\sigma')$ reflects the change in the slope of the "stress-strain" curve. As $\widetilde{E}(\sigma')$ continues to decrease, ΔV_{W-2} continues to increase, and Δp_2 causes a continuous decrease. At that time, when $|\Delta p_1| > |\Delta p_2|$, $\Delta p > 0$, and p increase; at that time, when $|\Delta p_1| = |\Delta p_2|$, $\Delta p = 0$, p reaches the maximum value; when $|\Delta p_1| < |\Delta p_2|$, $\Delta p < 0$, p decrease, so the pore water pressure presents a transition characteristic of "increase-decrease."

3.1.3. Pore Water Pressure: c-d Decreasing Stage. When the stress reaches the peak, the cracks in the rock will be further penetrated, and the rock will enter the failure stage. The internal pore space increases, and the pore water pressure continues to decrease. The relationship between the pore water pressure p and σ' the plastic deformation stage after the peak failure deformation stage is the same as that of the plastic deformation stage:

$$p = p_0 + \frac{(1-2\nu)}{E\beta} V\sigma' - \int_{b'}^{c'} \frac{mV}{\beta} D(\sigma') d\sigma'. \tag{21}$$

At this stage, due to the sudden change of failure and deformation, the pore water pressure continues to decrease, and the nonlinear change is more obvious. When the rock is completely destroyed, the pore space no longer changes, and the pore water pressure will remain at a certain value, which is less than the initial pore water pressure value, $p \le p_0$.

3.2. Precursor Characteristics of Critical Fracture of Pore Water Pressure. Through the analysis of the change relationship of pore water pressure in the process of rock force change, change relationship of stress, damage, and pore water pressure at each stage can be obtained, as shown in Table 1.

Analysis of the change mechanism of pore water pressure during the stress process shows that pore water pressure is closely related to stress and rock damage. Pore water pressure reflects the characteristics of stress and deformation of rock at various stages of loading. The continuous increase of the pore water pressure in the closed rock mass unit reflects the elastic phase of the increased force, and the rock can be regarded as "safe"; when the pore water pressure continues to increase and the "inflection point" decreases, the rock mass causes plastic damage and the force will reach the limit. The change in pore water pressure is a precursor to the occurrence of the primary failure of the rock.

4. The Characteristics of Pore Water Pressure Crack Precursor Information and Its Influence on the Development of Rock Damage

The change of pore water pressure also has an impact on the damage development. According to the principle of effective stress (see formula (3)), during the damage, the pore space inside the rock becomes larger, and the pore water pressure decreases. When the total stress σ remains constant, the pore water pressure p decreases, which in turn causes an instantaneous increase in the effective stress and intensifies the development of damage cracks in the rock. The development of damage cracks in turn causes the pore water pressure to continue to decrease. The interaction of the two accelerates the ultimate rock failure. It can be seen that the development of rock damage affects the change of pore water pressure, and the change of pore water pressure also affects the development of rock damage. The two influence each other [22, 23].

The underground engineering rock mass is a spatial continuous medium, and the stress transmission is continuous. When the local rock mass is damaged due to the stress and energy concentration caused by excavation disturbance, the formation of rock mass in the surrounding area will also produce corresponding stress changes. And the pore water pressure will increase and decrease alternately. The study of the pore water pressure change can be used to

TABLE 1: The mode of "stress-injury-pore pressure."

	Elastic stage	Plastic stage	Destruction stage
Stress	Linear growth	Curve growth	Decline
Damage	None	Development	Rapid development
Pore water pressure	Linear growth	Growth-decrease transition	Rapid decline

analyze its correlation with the rock failure process of adjacent related areas [24, 25].

The test results show that the law of pore water pressure change and permeability can effectively reflect the different stages of the internal damage development of the rock mass [26], the sharp decrease in pore water pressure, and the steep increase in permeability in the CD stage before the main fracture. This is the intuitive information reflection of the changes in the internal physical properties of the rock material. In actual engineering rock masses, when the pore water pressure in the rock mass gradually decreases or sharply decreases from the stable value and the permeability gradually increases or steeply increases from the stable value, large-scale damage and destruction occur inside the rock mass. It will enter a state of instability, which is the precursor information of rock mass rupture. This will provide a new way to predict rock bursts and rock bursts caused by excavation of chambers in rock masses. In actual engineering, it is difficult to measure the permeability inside the rock mass in real time. The pore water pressure monitoring technology developed in the study of seismic monitoring and prediction is becoming more and more mature, which provides an important technical basis for realizing the monitoring of pore water pressure in the rock mass. It is a feasible method to predict rock mass failure by monitoring the change of pore water pressure to predict the deformation of the rock mass in the area.

With the development of technology, the current monitoring accuracy of deep pore water pressure can reach the Pa level. The comprehensive deep borehole observation system popularized in earthquakes can observe information such as formation strain, pore water pressure, ground tilt, and even solid tide, which provides a technical basis for the application in tunnels and mine engineering [27, 28].

5. The Effect of Pore Water Pressure in the Formation in the Relevant Area Caused by Rock Bursts

5.1. Engineering Background. In order to verify the relationship between the change of pore water pressure and the failure of the formation rock mass, the study selected the Yanbei Coal Mine located in the Huating Coalfield in Gansu Province, China, which is frequently subjected to rock bursts, as the engineering background to observe the change of pore water pressure before and after rock burst occurs during mining [29].

The Huating Coalfield is located at the eastern foot of the Liupan Mountains, the southwestern edge of the Ordos block, or the southern end of the fault fold belt on the western edge. This area happens to be located at the intersection of the large fault on the western edge of Liupan Mountain, the thrust belt on the western edge of the Ordos Basin, and the Qingtongxia-Guyuan fault, with a complex geological environment. The Huating Coalfield presents a spinning compound asymmetric syncline structure with a "south-east structure, gentle east and steep west, wide middle, and convergent north and south sections," as shown in Figure 2.

The Huating Coalfield is mainly controlled by horizontal tectonic stress, with folds as the main structure and faults as the auxiliary structure. The thickness and dip of the coal seam change along the direction and tendency of the folds, and the fold structure plays a major role in controlling the transformation, destruction, and shaping of the existing coal measures.

Coal seam mining changes the stress distribution characteristics, causing local rock mass stress concentration, and the surrounding rock accumulates a large amount of elastic energy, which is the main factor that induces the appearance of strong rock pressure in the Yanbei and Huating mining areas. The coal seam is a very thick coal seam with a thickness between 30 m and 40 m. The upper layer is first mined, and then the lower layer is mined. The mining depth reaches 800 m–1000 m. The continuous deep mining of Huating Coal Mine and Yanbei Coal Mine in Huating Coalfield for many years has changed the original structural stress distribution characteristics, causing local stress concentration and increased energy storage [30, 31]. The direction of the working face of the mining area is close to the north-south direction, which is consistent with the direction of the fold structure axis, and is perpendicular to the direction of the maximum principal stress near the east-west in the area.

Yanbei Coal Mine is affected by deep mining and regional structure. Mine earthquakes often occur in the syncline axis, especially in structural change areas, near faults, coal seam dip changes, coal seam buckling, and tectonic stress zones. The 250203 and 250204 working faces passed through the shaft and wings of the fold structure during the mining process, and the rock pressure appeared very obvious.

In order to quantitatively observe the quantitative relationship between mine earthquake disaster source rock mass and regional structure, stress environment, mine depth, mining volume, mining intensity, and other factors in the process of mine earthquakes, the RET-2A high-precision pore water pressure gauge with an accuracy of 10^{-9}-10^{-10} can be used to observe the microdynamic change process of pore water pressure in the crust. The observation site should be installed on the "force chain structure" of the seismogenic system. The
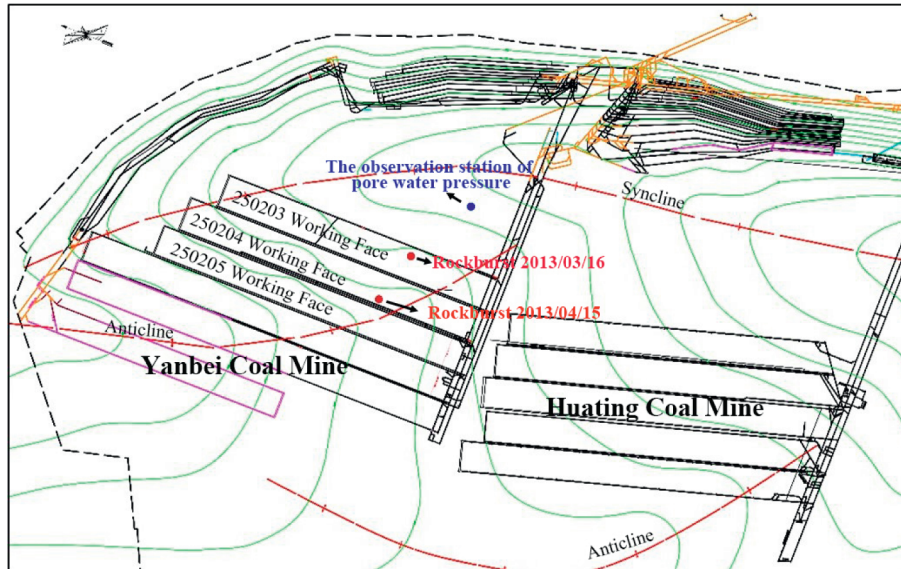
Figure 2: Project overview, location of observation station, and rockburst events.

measurement points and observation characteristic quantities should be jointly arranged according to different characteristic areas such as the core area of the mine earthquake disaster source body, the energy release area, and the surrounding "related areas," as shown in Figure 2. The Yanbei Coal Mine's pore water pressure observation point is installed in the coal seam floor rock at the syncline axis [32, 33].

5.2. Analysis of Measured Data. After the completion of the observatory, continuous observation data of pore water pressure from March 15 to April 19, 2013, were obtained. As shown in Figure 3, the time history data curve of pore water pressure has a significant solid tidal change background, indicating that the expected observation accuracy has been achieved and the equipment is working normally. Due to the high accuracy, in order to obtain an intuitive change rule, no calibration was performed during the analysis process, and the original monitoring data were selected for analysis. During this period of time, mining was carried out at the 250203 working face, and severe rock bursts occurred at 13 : 23 2013/3/16 and 22 : 28 2013/4/15, which had a serious impact on production. The information of the two rockburst events is shown in Table 2.

As shown in Figure 3, the data obtained by the pore water pressure observation station show that, at the same time that the two rock bursts occurred, the pore water pressure has undergone significant synergistic changes, resulting in a significant coseismic effect. It is mainly manifested as a step increase in pore water pressure, but the magnitude of the change is very small, and the impact of the solid tidal stress is an order of magnitude. This microdynamic change can only be measured by high-precision equipment. From the perspective of the change

trend of pore water pressure before and after the occurrence of rockburst, due to the impact of mining, the pore water pressure in the surrounding area has also changed up and down, reflecting that the stress field and pore water pressure in this area are all synergistic variety. This change is mainly manifested as a kind of microdynamic effect, which also shows that the strata in a certain range around the stope and the stope and the rock mass of the seismic source rupture are a coordinated system. The adjustment process of energy accumulation and release in the system can be obtained by observation, and the magnitude is equivalent to that of the Earth tide effect [34].

Since the selection of the observation station is far from the working faces and the location where rock bursts occur, the change of pore water pressure obtained changes with the change of the stress field in the adjacent area of the closed rock mass. This change presents obvious characteristics of microdynamic changes, which proves that there is a close correlation between the evolution of the stress field in the surrounding area of the stope under mining disturbance and the change of the pore water pressure in the surrounding area. Mining dynamic disasters, such as rockburst and mine earthquakes, seriously threaten the safety of the mine. The breeding and inducing processes are the accumulation of factors such as stress and energy, which cause the surrounding rock of the stope to locally reach or exceed the critical state, rupture, and expand to evolve, forming earthquake source or disaster source. The emergence and evolution processes reflect the coaction process of multiple factors such as overburden and stratum structure, original stress field, and mining disturbance and also reflect the synergy mechanism and state evolution process of multiple physical mechanics fields on multiple spatial scales.
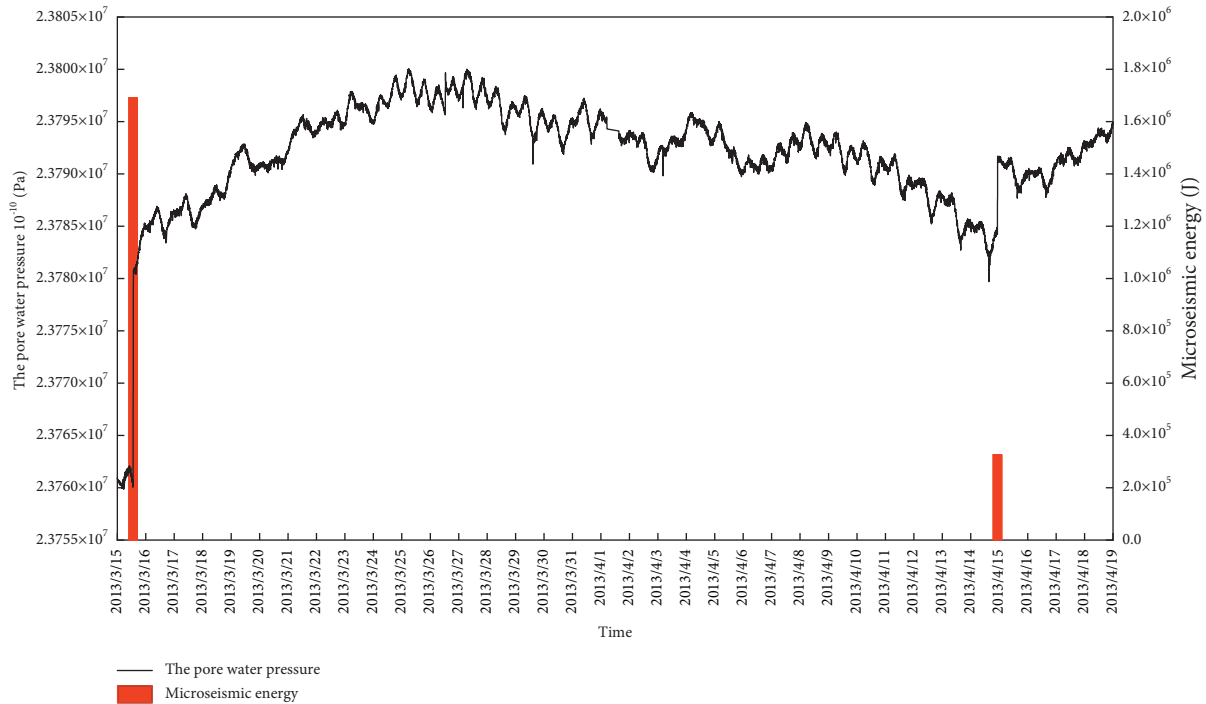
Figure 3: Time history curve of pore water pressure.

Table 2: Information table of rockburst events.

Time	Distance to observing station (m)	Microseismic energy	Damage
2013/3/16 13 : 23	527.5	$1.69E * 10^6$ J	The roadway is deformed, the support is damaged, the top sink is 200–300 mm, the bottom drum is 200–500 mm, 40 anchor cables are broken, and the repair work volume is about 812 m³
2013/4/15 22 : 28	886.6	$3.26E * 10^5$ J	Deformation of the roadway occurred in the transportation lanes and material lanes on both sides of the working face, the bottom drum was 200 mm–600 mm, and the repair works amounted to 353 m³

6. Conclusions and Prospects

(1) In an ideally closed saturated rock unit, the pore water pressure is closely related to the expansion of internal damage. The pore water pressure presents a linear increase, a growth-decrease transition, and a decrease process and reaches a stable value after the rock is completely destroyed.

(2) Based on the analysis of Hooke's law and the principle of damage mechanics, the analytical model between pore water pressure changes and stress changes at various stages is obtained. The "increase-decrease transition" change of pore water pressure is the precursor information of rock fracture.

(3) According to the analysis of the effective stress principle, the pore water pressure and the damage development interact and are related to each other. The damage expansion causes the pore water pressure to decrease, and the decrease of the pore water pressure promotes the damage development.

(4) At present, the monitoring technology of pore water pressure has been relatively maturely applied in seismic monitoring research. On this basis, monitoring the changes of pore water pressure inside the rock mass in deep mining projects can predict dynamic disaster of instability and destruction of rock bursts and other rock masses.

(5) Through the observation of the pore water pressure in the relevant area during the coal mining process, the response of the pore water pressure in the relevant area before and after the occurrence of rockburst in the mine was successfully obtained. The coseismic effect is obvious, which proves that the gestation and induction process of large-scale structural rock bursts or mine shocks is far greater than the range of traditional stope pressure and mining influence. Analyzing the stress field between the rockburst source and the "relevant area" and its multifield correlation is the correct way to reveal the mechanism of the initiation and induction of mine earthquakes.

Data Availability

Conflicts of Interest

The authors declare that they have no conflicts of interest.

Acknowledgments

References

[1] T. H. Yang, C. A. Tang, W. C. Zhu, and Q. Y. Feng, "Coupling analysis of seepage and stresses in rock failure process," *Chinese Journal of Geotechnical Engineering*, vol. 23, no. 4, pp. 489–493, 2001.

[2] X. Li, K. Peng, J. Peng, and H. Xu, "Effect of cyclic wetting-drying treatment on strength and failure behavior of two quartz-rich sandstones under direct shear," *Rock Mechanics and Rock Engineering*, vol. 1, no. 8, 2021.

[3] Y. P. Qin, J. F. Zhang, and L. Wang, "Preliminary discussion on theoretical model of rock damage mechanics," *Chinese Journal of Rock Mechanics and Engineering*, vol. 22, no. 4, pp. 646–650, 2003.

[4] Y. P. Qin, W. B. Sun, and L. Wang, *Analysis 0n damage mechanics model of rock*, vol. 22, no. 5, pp. 702–705, 2003.

[5] J. Yu, H. Li, X. Chen, Y. Cai, N. Wu, and K. Mu, "Triaxial experimental study of associated permeability-deformation of sandstone under hydro-mechanical coupling," *Chinese Journal of Rock Mechanics and Engineering*, vol. 32, no. 6, pp. 1203–1213, 2013.

[6] Y. T. Che, H. N. Yang, and Z. L. Zhang, "Hydrodynamic simulation test and research on the formation process of groundwater microbehavior," *Earthquake*, vol. 9, no. 5, pp. 40–49, 1989.

[7] Q. Yin, J. Y. Wu, C. Zhu, M. He, Q. Meng, and H. Jing, "Shear mechanical responses of sandstone exposed to high temperature under constant normal stiffness boundary conditions," *Geomechanics and Geophysics for Geo-Energy and Geo-Resources*, vol. 7, no. 2, 2021.

[8] K. Sun, L. M. Fan, Y. C. Xia et al., "Impact of coal mining on groundwater of Luohe formation in Binchang mining area," *International Journal Coal Science Technol*, vol. 8, no. 1, pp. 88–102, 2021.

[9] G. D. Cui, W. X. Wang, B. Dou, and Y. Liu, "Geothermal energy exploitation and power generation via a single vertical well combined with hydraulic fracturing," *Journal of Energy Engineering*, vol. 148, 2022.

[10] M. Z. Gao, J. Xie, J. Guo, Y. Lu, Z. He, and C. Li, "Fractal evolution and connectivity characteristics of mining-induced crack networks in coal masses at different depths," *Geomechanics and Geophysics for Geo-Energy and Geo-Resources*, vol. 7, no. 1, 2021.

[11] L. Li, F. M. Li, Y. Zhang, D. Yang, and X. Liu, "Formation mechanism and height calculation of the caved zone and water-conducting fracture zone in solid backfill mining," *International Journal Coal Science Technol*, vol. 7, no. 1, pp. 208–215, 2020.

[12] Y. S. Li Yong, "The main features of groundwater level changes caused by tectonic stress," *Northwestern Seismological Journal*, vol. 1, no. 1, pp. 16–22, 1979.

[13] J. Zhu and J. W. Liang, "Effects of dynamic soil-tunnel interaction on seismic soil pressures and pore pressures," *Journal of Natural Disasters*, vol. 27, no. 6, pp. 66–74, 2018.

[14] C. Zhu, M. C. He, X. H. Zhang, Z. Tao, Q. Yin, and L. Li, "Nonlinear mechanical model of constant resistance and large deformation bolt and influence parameters analysis of constant resistance behavior," *Rock and Soil Mechanics*, vol. 42, no. 7, pp. 1911–1924, 2021.

[15] Z. G. Yi, Z. H. Qiu, and M. Song, "Analysis of data of digitalized borehole strain observation in capital area," *Journal of Geodesy and Geodynamics*, vol. 26, no. 3, pp. 53–58, 2006.

[16] Z. D. Zhang, "Comparison and analysis of observational water-level tide of artesian well and gravity solid tide," *Earthquake*, vol. 11, no. 2, pp. 47–52, 1991.

[17] Z. D. Zhang, J. H. Zheng, C. G. Feng, and G. C. Zhang, "The comparison of the three methods of inversion of stress changes of aquifers using step changes of well level," *North China Earthquake Sciences*, vol. 11, no. 1, pp. 39–44, 1993.

[18] Z. D. Zhang, Q. G. Liu, and J. Geng, "Stress variation of well aquifer inverted by water level behaviors of pressure well," *South China Journal of Seismology*, vol. 19, no. 1, pp. 37–42, 1999.

[19] X. Y. Zhang, H. N. Ruan, and C. H. Jia, "Research development of the rock's damage theory," *Sichuan Building Science*, vol. 36, no. 2, pp. 134–138, 2010.

[20] G. Feng, Y. Kang, X. C. Wang, Y. Hu, and X. Li, "Investigation on the failure characteristics and fracture classification of shale under Brazilian test conditions," *Rock Mechanics and Rock Engineering*, vol. 53, no. 7, pp. 3325–3340, 2020.

[21] G. D. Cui, L. H. Yang, J. C. Fang, Z. Qiu, Y. Wang, and S. Ren, "Geochemical reactions and their influence on petrophysical properties of ultra-low permeability oil reservoirs during water and CO2 flooding," *Journal of Petroleum Science and Engineering*, vol. 203, 2021.

[22] Y. W. Liu, L. Q. Xu, and D. X. Yang, "Pore pressure diffusion characteristics of Longtan reservoir-induced—earthquake," *Chinese Journal of Geophysics*, vol. 54, no. 4, pp. 1028–1037, 2011.

[23] S. L. Liu, Z. N. Li, Y. Yang, J. Shen, Y. Huang, and S. Xu, "Preliminary analysis of the digital observation data quality of borehole body strain in Fujian province," *South China Journal of Selsmology*, vol. 27, no. 4, pp. 79–87, 2007.

[24] Q. Wang, M. C. He, S. C. Li et al., "Comparative study of model tests on automatically formed roadway and gob-side entry driving in deep coal mines," *International Journal of Mining Science and Technology*, vol. 31, no. 4, pp. 591–601, 2021.

[25] Q. Wang, Y. Wang, M. C. He et al., "Experimental research and application of automatically formed roadway without advance tunneling," *Tunnelling and Underground Space Technology incorporating Trenchless Technology Research*, vol. 114, no. 3, 2021.

[26] Y. Z. Zhang and H. G. Ji, "Pore water pressure change-related characteristic and its critical rupture precursor of rock under triaxial compression," *Chinese Journal of Engineering*, vol. 37, no. 4, pp. 399–406, 2015.

[27] D. Issei and K. Toshitaka, "Relationship between earthquake-induced excess pore water pressure and strong ground motion observed in a monitored fill slope," *Engineering Geology*, vol. 266, 2020.

[28] C. J. Meng, X. W. Wang, S. L. Zhang, and S. Y. Yang, "Analysis of shortleveling anomaly in linfen seismic station based on the groundwater change," *Journal of Geodesy and Geodynamics*, vol. 40, no. 11, pp. 1206–1210, 2020.

[29] L. Y. Zhao, H. Zhang, and X. F. Liu, "Study on seismicity characteristics and mechanism in pingliang area Gansu province," *Northwestern Seismological Journal*, vol. 31, no. 2, pp. 186–190, 2009.

[30] H. Jiang, *Research on Fracture Characteristic of Surrounding Rock and the Relationship with Microseismic Actibity in Synclinal axis Region*, Beijing University of science and technology, Beijing, China, 2020.

[31] F. Chen, A. Y. Cao, L. M. Dou, and C. Wang, "Method of coal burst hazard assessment based on region division and identification of main impact factors," *Journal of China Coal Society*, vol. 43, no. 3, pp. 607–615, 2018.

[32] Z. H. Qiu and Y. L. Shi, "Relationchip between theoretic magnitude and longest propagation Distance of seismic strain change," *Journal of Geodesy and Geodynamics*, vol. 24, no. 2, pp. 99–105, 2004.

[33] Y. T. Che, J. Z. Yu, Z. F. Ma, and Q. Wang, "Mining earthquakes and anomalous response of groundwater level in deep well," *Earthquake*, vol. 17, no. 1, pp. 61–66, 1997.

[34] M. Gao, J. Xie, Y. Gao et al., "Mechanical behavior of coal under different mining rates: a case study from laboratory experiments to field testing," *International Journal of Mining Science and Technology*, vol. 31, no. 5, pp. 825–841, 2021.

Research Article

Controlling Vibration Speed in Tunnel Excavation Using Fine Blasting Method under Complex Environmental Conditions

Yingcai Zhang [ID],[1] **Jiyun Zhang** [ID],[1] **Shuren Wang** [ID],[1,2] **and Yubo Chen** [ID][1]

[1]*International Joint Research Laboratory of Henan Province for Underground Space Development and Disaster Prevention, Henan Polytechnic University, Jiaozuo 454003, China*
[2]*School of Minerals and Energy Resources Engineering, University of New South Wales, Sydney, NSW 2052, Australia*

Correspondence should be addressed to Shuren Wang; w_sr88@163.com

It is very important to reduce the impact of blasting vibration on the surrounding structures during the tunnel drilling-blasting excavation. Taking the diversion tunnel of the urban water supply project in Zhumadian, Henan Province, China, as an example, the segmentation linear function between the drilling rig and borehole depth was established by fining blasting design. The test of the blasting number and particle vibration velocity was designed. The propagation and attenuation characteristics of blast vibration velocity in the surrounding rocks of the tunnel were analyzed by using theoretical calculation and field monitoring methods. Results show that the fine blasting design can realize the superposition of negative phase of shock waveform to reduce the vibration speed. With the increase of the blasting number, the attenuation of the particle vibration velocity shows a negative exponential function, and the dimensionless vibration velocity loss increases in a power function. The greater the loss, the greater the energy loss during the shock wave propagation process, which is more conducive to ensuring the stability of the protected buildings. The research results can provide the reference for similar engineering practices.

1. Introduction

At present, the blasting technology still occupies an important position in the construction of various underground engineering and the demolition of various buildings. Particularly in sections where the tunnel length is short and the surrounding rock is relatively broken, the blasting technology can speed up construction, increase production efficiency, and produce significant economic and social benefits [1–3]. However, the secondary disasters caused by the blasting operations, especially the effects of blasting vibration, will bring certain problems to the local environment and residents' lives. The particle vibration effect caused by the explosive explosion is very complicated. Various factors such as construction geological conditions, explosion area topography, and propagation medium will affect the vibration and attenuation characteristics. The amplitude, period, and frequency of different shock waves in time and space are also changing in real time. Generally, the

strength of the blast vibration effect is generally evaluated by the particle vibration velocity [4]. Therefore, the research on the control of blasting vibration is a hot topic of current research.

The high temperature-pressure wave generated by the explosive in the borehole will be converted into a shock wave in a short time to propagate in the medium, and the energy carried by the shock wave will make the surrounding rock shear and tensile stresses, which will further deteriorate the mechanical properties of rock mass in cyclic blasting. To weaken the particle vibration caused by blasting, Kim and Song used abrasive water jet cutting blasting to control particle vibration and found a significant reduction in vibration compared to that caused by the conventional drilling method [5]. Liu et al. concluded that the borehole amount had a significant effect on the optimal differential time and the corresponding maximum synthetic vibration speed, and the effect of vibration reduction could be achieved by designing a reasonable delay time to make the waveform

anisotropic phase dissipation [6]. Yang et al. compared the unloading damage mechanism and rockburst events of the surrounding rock in shield machine and borehole-blasting method, and they found that the scale and frequency of rockburst events generated by shield machine were higher than those of the borehole-blasting method in the stress adjustment process of large burial depth tunnel excavation [7]. To improve the excavation efficiency, Ma et al. obtained the critical distance of the borehole restraint by field test and they proposed a new charging structure without detonating cord and achieved a good smooth blasting effect [8]. Chai et al. studied the effect of the arrangement of cut holes on the control blasting effect and they found that the layout of four empty holes could improve the utilization rate of explosive better than the two, indicating that reasonable reserved compensation space could improve the blasting effect and tunneling efficiency [9]. Duan et al. investigated the influence of blasting excavation on existing tunnels under small spacing [10]. Wang et al. studied the rule of buffer layer on vibration velocity and propagation energy attenuation by constructing a specific shape of loose body, and they found that a reasonable arrangement of buffer layer in oriented blasting could greatly reduce touchdown vibration [11].

For deeply buried underground spaces, Yang et al. studied the effect of differential blasting on the evolution of the rock stress field by establishing a two-dimensional circular excavation model, and they found that two blasts before and after the stress adjustment process would cause a shift in the direction of the maximum and minimum principal stress [12]. Chen et al. believed that the blasting damage zone in the surrounding rock was caused by the redistribution of stress in the surrounding rock after excavation, and the dynamic damage effect caused by the instantaneous unloading of stress after blasting was more significant under high ground stress [13]. Fan et al. compared the influences of quasistatic and transient unloading on the range of damage in the surrounding rock by theoretical calculations and numerical simulations, and they found that the transient unloading had a larger impact range [14]. Taking the practical engineering as an example, Xie et al. conducted a theoretical analysis of strain energy adjustment during blasting and mechanical excavation, and they found that the frequency of secondary disasters caused by blasting excavation was much higher than that of mechanical excavation [15]. While for the shallow buried underground engineering, Xia et al. investigated the influence of blasting vibration on water supply pipelines and found that reducing the water pressure of pipeline could reduce the injury caused by blasting vibration [16]. Jiang et al. optimized the Sadovsky formula by regression analysis of field data to establish a three-dimensional model of gas pipeline under the action of blast vibration and to verify the feasibility [17]. Chen et al. found that the peak vibration velocity of the excavated section was greater than that of the unexcavated section when the tunnel was buried at a shallow depth, and this phenomenon gradually disappeared as the burial depth increased [18]. Shi et al. found that the phenomenon of "hollow effect" existed in the process of excavation blasting, and the intensity of this phenomenon was

proportional to the distance from the excavation face [19]. Liu and Chen established a prediction method for surface vibration waveform caused by the cutting hole blasting in tunnel construction, and they verified the correctness of the prediction method using the field measurement data [20].

In summary, there are few reports on the whole process from equipment selection to blasting effect tracking in tunnel blasting excavation. According to local environmental conditions, the fine blasting design is significant to improve construction efficiency and reduce the impact of blasting shock waves on the environment. This study intends to carry out a fine blasting design from the aspects of equipment selection, the determination of borehole depth, and the design of borehole parameters and obtain the function relationship between the drilling equipment and borehole depth to ensure the construction efficiency. Based on theoretical calculations and field observed values, the monitoring analysis of vibration velocity decay characteristics was conducted, the connection between the particle vibration velocity and the cyclic blasting times was proposed, and the rationality of this fine blasting design was verified.

2. Materials and Methods

2.1. Engineering Background. As shown in Figure 1, taking the new diversion tunnel of the urban water supply project in the eastern part of Zhumadian, Henan province, China, as an example, the diversion tunnel was located 76 m west of the existing diversion tunnel, these two tunnels were parallel to each other, their excavation diameter was 3200 mm, and the design water intake capacity was 2.5 m³/s. There were civil buildings at 40 m on the north and 60 m on the west, the positive operation gate was located 90 m on its east, the reservoir was on the south, and the construction environment was complicated.

Influenced by the geological environment and the project, the engineering was excavated by using the drilling-blasting method. The shaft was constructed first and then the diversion tunnel, and the depth of the shaft was 38.45 m. The blasting vibration effect was more obvious at the same horizontal position with larger elevation, which had an amplification on the particle vibration velocity. Therefore, the fine blasting should be conducted during the construction of the new diversion tunnel to ensure the existing diversion tunnel and the surrounding buildings are not being affected.

The hydrogeology of the construction location directly affects the selection of equipment, the calculation of borehole depth, and the determination of explosive consumption, which is an integral part of the fine blasting. The region was located in the combination of the southern edge of the North China Platform and the Qinling fold belt, with a strong geological structure, influenced by tectonic stress and more folds and joints developed around. The construction site was mainly strongly weathered rock with different thickness of 1.4–2.0 m, conglomerate of 0.5–10.0 m, slightly weathered rock of 0.6–21.6 m, quartzite of 9.0–52.5 m, and gneiss of 0–52 m, respectively.

(a)

(b)
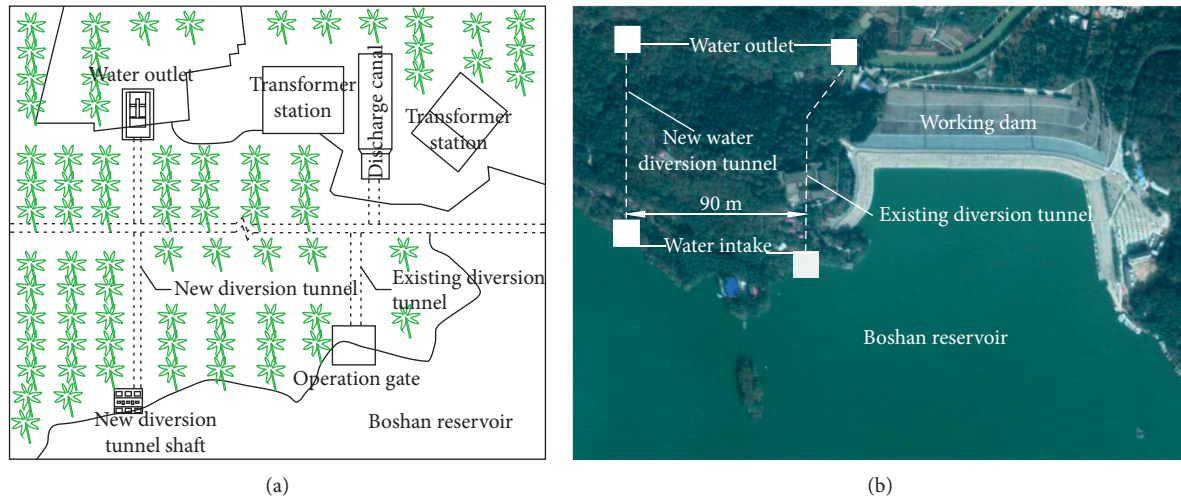
Figure 1: Environmental conditions around water conveying tunnels. (a) Schematic plan. (b) Real map.

2.2. Fine Blasting Evaluation Equipment.

To evaluate the accuracy of the fine blasting design, the vibration velocity was tested at the same measurement points at each blasting to determine the attenuation of the shock wave. The measuring instrument of blasting vibration was Blast-UM, with the resolution of 24-bit A/D, sampling rate of 10 ksps, frequency response range 5–300 Hz, measurement range 0.01–350 mm/s, and working temperature from −10 to 70°C, which can directly measure the vibration signal in three directions simultaneously, and 2G of memory can meet the needs of multistage charge and long delay in tunnel blasting. The detailed operation method is shown in Figure 2. The equipment has the advantages of high precision, large memory, good compatibility, and simple operation, which is widely used in vibration testing caused by human activities.

2.3. Fine Blasting Design

2.3.1. Determination of Borehole Diameter and Depth.

The size of the borehole diameter directly affects the borehole speed, the number of boreholes in the working face, unit explosive consumption, the size of rock block after blasting, and the flatness of the roadway profile. The increase of borehole diameter is conducive to improve the stability of the explosion and increase the explosion speed. While the diameter is too large, the borehole speed decreases, which will reduce the average distribution factor of explosive in the construction area and lead to poor quality of rock crushing under the premise of unchanged construction section, borehole depth, and loading coefficient. The LGU75A mobile air compressor was selected to provide power in this study and the YT18 drilling rig with a 40 mm diameter was used for drilling.

The most suitable borehole depth should be determined according to the mechanical equipment, technology process, rock geology, and organizational management capabilities. To bring out the optimal capacity, improve the efficiency of each process, and reduce the number of man-hours of an effective unit length of roadway, determining the borehole depth according to local conditions was an important part of the fine

blasting. Ignoring the influence of human factors, the drilling test with the selected equipment was carried out and statistical analysis of borehole speed, time-consuming, and hole depth was performed. As seen from Figure 3, the borehole depth is not linearly related to the time-consuming per unit length and the borehole speed. The performance is that the time-consuming per unit length varies slowly and then increases rapidly with increasing borehole depth, and there is a threshold value. The specific performance is that the designed borehole depth increment is 0.2 m, and the node appears when the increment reaches 0.4 m. When the borehole depth is 2.0 m, the time-consuming per unit length is 3.06 min. When the borehole depth is 2.4 m, the time-consuming per unit length is 3.15 min. Under the same conditions, the time-consuming per unit length is 4.10 min when the hole depth is 2.8 m, so the selected equipment will have the highest construction efficiency at a borehole depth of about 2.4 m in the study.

As seen from Figure 4, the time-consuming per unit length keeps increasing with increasing of the borehole depth. The piecewise function can be used to describe the whole process, which can be expressed by the linear equation $y = 0.225x + 2.668$ with a correlation coefficient of 0.832 when the borehole depth is less than 2.4 m, while this can be expressed by the linear relationship of $y = 2.375x - 1.612$ with a correlation coefficient of 0.996 when the borehole depth is greater than 2.4 m. The turning point of time-consuming per unit length is at about 2.4 m borehole depth. Although the two functions are linear equations, the slope of the linear equation is about 10.6 times of the former when the borehole depth is greater than 2.4 m, which means that the time and financial resources of drilling unit length borehole increase significantly when the borehole depth is greater than 2.4 m, and the threshold value of the designed borehole depth should be about 2.4 m, which is the most economical and reasonable.

2.3.2. Design of Borehole Parameters.

The number of boreholes is related to several factors such as excavation section, rock characteristics, borehole diameter, borehole
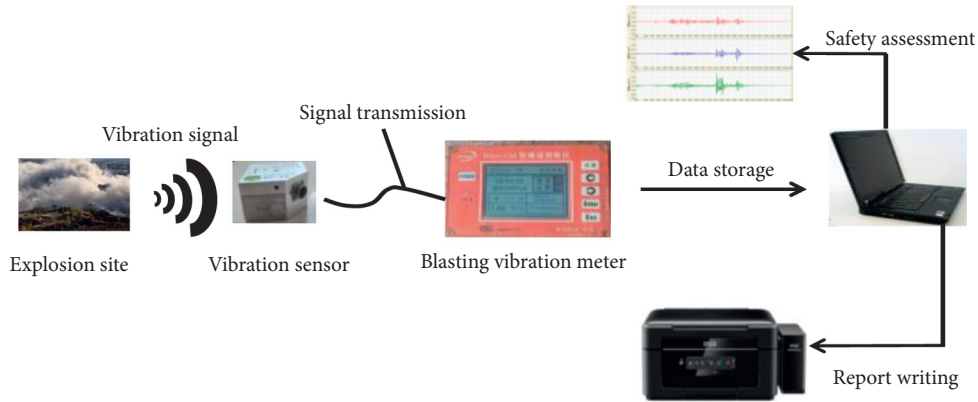
FIGURE 2: Fine blasting evaluation equipment.
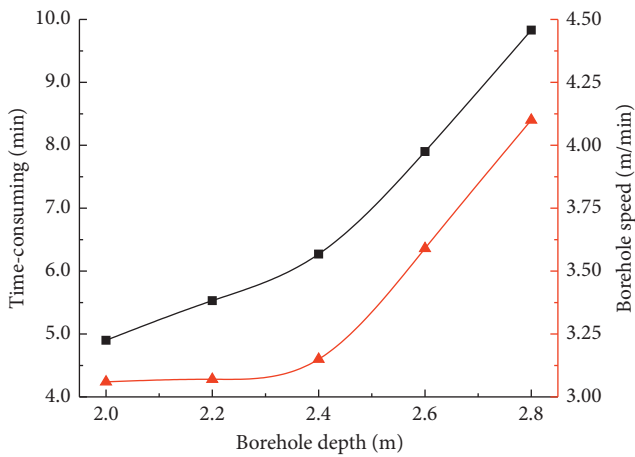
FIGURE 3: Relationship among the borehole depth, time-consuming, and borehole speed.
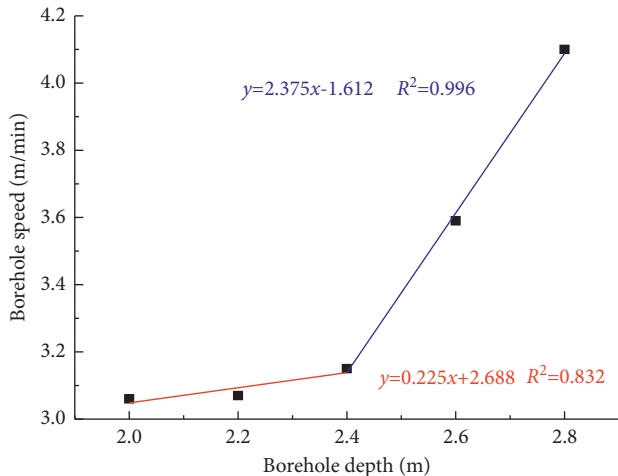
FIGURE 4: Relationship between the borehole depth and borehole speed.

depth, and explosive performance. Under the premise of ensuring a good blasting effect, the number of boreholes should be reduced as much as possible. The number of boreholes can be calculated as follows:

$$N = 3.3\sqrt[3]{fs^2}, \tag{1}$$

where N is the number of boreholes, f is the firmness coefficient of rock, and s represents the cross-sectional area of the excavation section, m^2.

The borehole arrangement is a combination of theoretical calculations and construction experience, the cutting holes and periphery holes are first arranged, and then the auxiliary holes are evenly distributed in the blasted rock. The layout plan and section of the boreholes are shown in Figures 5(a) and 5(b), respectively. The spacing of cutting holes was 500 mm, which were arranged in a wedge shape, inclined inward at an angle of 75°, increased the depth by 150–200 mm, and added the charge mass by 15–20% compared with other boreholes, and the middle cutting hole was not charged. The auxiliary holes were evenly arranged in the excavation section, and the hole spacing was 640–650 mm. To reduce the disturbance to the surrounding rock, reduce the cost of later support, and improve the construction efficiency, the periphery holes were arranged at 100 mm from the edge of the profile, with a hole spacing of 470 mm, and its arrangement and charging structure were carried out according to the standard of smooth blasting.

According to experience, the charge of a single borehole is generally calculated as equation (2):

$$Q = \eta L r, \tag{2}$$

where η is the charge factor of the borehole. L is the depth of the borehole, m. r represents the charge weight of unit length, kg/m.

Since the geological condition of different locations varies greatly, the choice of unit explosive consumption is crucial, which not only is related to the degree of rock fragmentation and scattering distance but also has an important impact on the utilization rate of the borehole, the damage degree of surrounding rock, the quality of contouring, and later support methods [21]. Therefore, on the basis of the comprehensive analysis of explosive performance, rock characteristics, charge diameter, borehole diameter, and borehole depth and the drilling and blasting test in advance, the unit explosive consumption was determined 2.0 kg/m^3, and the specific value could be adjusted

(a)

(b)
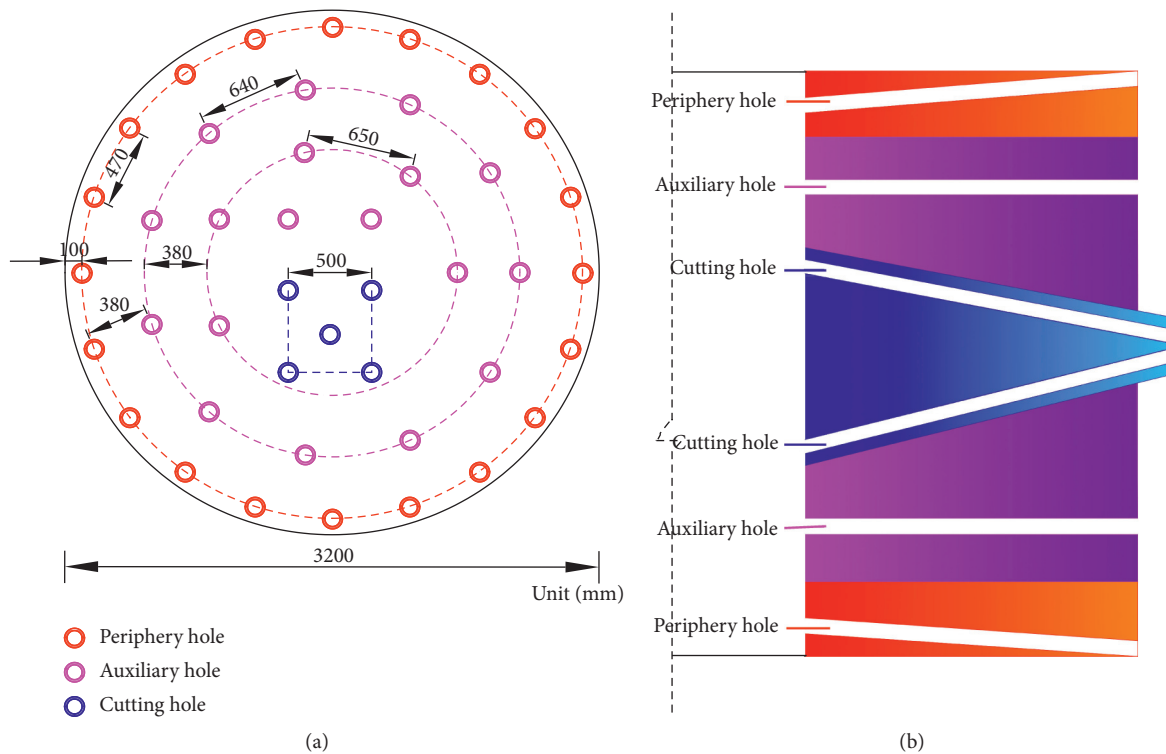
FIGURE 5: Borehole arrangement diagram. (a) Planar graph. (b) Sectional drawing.

appropriately according to the blasting effect during the construction. To ensure the blasting effect, the loading coefficients of the cutting hole, auxiliary hole, and peripheral hole were 0.6, 0.5, and 0.4, respectively. The charge weight of unit length was taken as 1.0 kg/m. As seen from Figures 5 and 6, the number of cutting holes, auxiliary holes, and peripheral holes were 5, 18, and 20, respectively. The depth of the cutting hole was 2.7 m, which was deeper than that of the auxiliary hole and peripheral hole 0.2 m. The single-hole charge of the cutting holes, auxiliary holes, and peripheral holes was 1.6, 1.2, and 1.0 kg, with the single section charge of 6.4, 21.6, and 20 kg, respectively. Therefore, the total charge was 48 kg per cycle and the maximum priming charge of a single section was 21.6 kg (Figure 6).

2.3.3. Design of Charge Structure and Detonation Network. Charge structure has a significant impact on the blasting effect, different charge structure can affect the explosive power, the utilization rate of the released energy, the time of action of the detonation wave, and the surrounding rock. To a certain extent, through the interaction of the shock wave and the surrounding rock joints, the superposition of different shock waves without attenuation of energy can reduce the waveform peaks and troughs, extend the time for the shock wave to reach the particle, achieve the effect of reducing blast vibration, and improve the stability of surrounding rock.

In this study, the axial and radial bidirectional uncoupling charge structure was adopted, the radial uncoupling coefficient was 1.25, and the axial uncoupling coefficients were 1.31, 1.58, and 1.71, respectively. The radial uncoupling can be called natural uncoupling, while the axial uncoupling belongs to artificial uncoupling. Under the premise of determining the amount of charge in a single hole and ensuring the minimal resistance line is not being affected, the axial uncoupling charge can increase the height of charge, and the explosives can be more evenly distributed in the blasting area and weaken the peak pressure of shock wave, which can achieve the purpose of reducing blasting vibration, large lump rate, and blasting shock wave disturbance to the surrounding rock. In addition, it was worth explaining in this study that the boreholes were all of segmented charge structure. After determining the charge of a single borehole, borehole depth, and filling length, the charge of a single borehole calculated in advance was arranged in three equal parts in the boreholes, and one detonator was placed in each concentrated cartridge so that the explosives were evenly distributed in the blasting area and the phenomenon of antiexplosion was eliminated.

The choice of reasonable delay time and charge structure is conducive to weakening the vibration caused by shock waves and reducing the disturbance to surrounding rock. In this study, three segments of second delay detonators were selected, and the fine blasting was realized by means of outhole propagation and in-blasthole delay. Meanwhile, axial uncoupling was realized by air-spaced charge. Specifically, a certain distance of air was reserved between the bottom of the hole and the first explosive cartridge, the interval distance was determined by the charge of a single borehole and the filling length, and the position of the first explosive cartridge was determined by the distance from its end to the
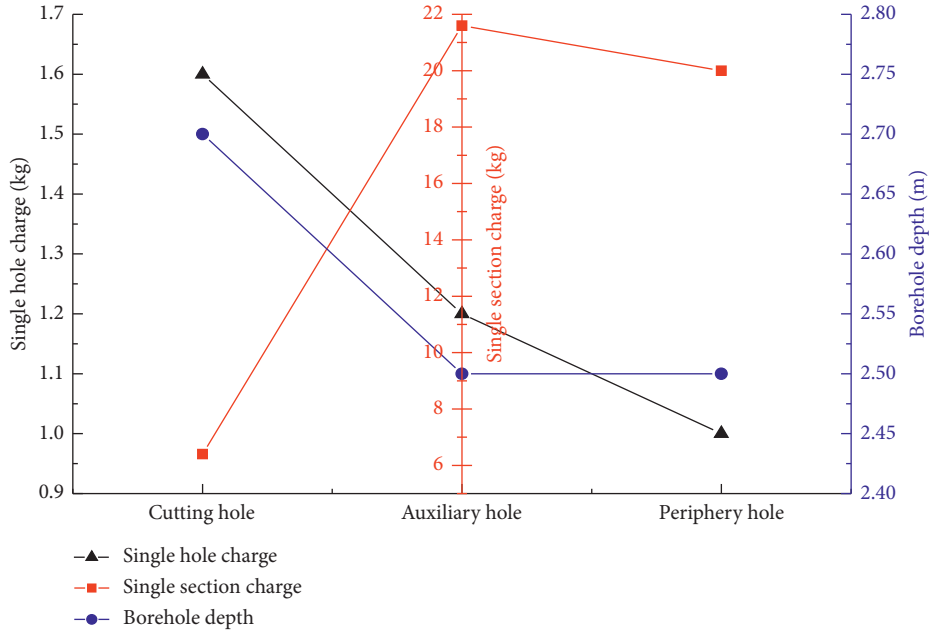
FIGURE 6: Statistics of borehole parameters' design.

orifice. The purpose of increasing the charge height and making the explosives uniformly distributed in the blasting area was realized.

3. Results' Analysis and Discussion

3.1. Attenuation Analysis of Vibration Velocity. The operating floodgate with the highest accuracy to be protected at 90 m east of the blasting site was selected as the vibration monitoring point. The particle vibration velocity can be calculated using equation (3) of Sadovsky to quantitatively determine the reasonable degree of the fine blasting design [22].

$$V = K \left(\frac{\sqrt[3]{Q}}{R} \right)^{\alpha}$$

$$= K\delta^{\alpha}, \tag{3}$$

$$\delta = \frac{\sqrt[3]{Q}}{R}, \tag{4}$$

where V denotes the particle vibration velocity, mm/s. R represents the distance between the protected object and blasting point, m. Q represents the maximum charge of a single section, kg. K denotes the coefficient and α is the attenuation index. $\delta = \sqrt[3]{Q}/R$ is the proportional dosage between the maximum single segment dosage and the effective distance [23].

There are two ways to obtain K and α values. One is selected from the range of empirical values summarized based on the geological topography of the blast area. The other is obtained by the actual monitored particle velocity, the corresponding maximum charge of a single section, and the effective distance between the explosion sources and monitoring point, and the final solution is performed using the least squares method. The specific calculation process is as follows.

Taking the logarithm of both sides of equation (4), then

$$\ln V = \ln K + \alpha \ln \delta. \tag{5}$$

Assuming that $y = \ln V$, $m = \alpha$, $x = \ln \delta$, and $n = \ln K$ and also combining the least squares principle and the extreme value theorem of the function of two variables, then equation (6) can be obtained:

$$\begin{cases} \left(\sum_{i=1}^{h} x_i^2 \right) m + \left(\sum_{i=1}^{h} x_i \right) n = \sum_{i=1}^{h} x_i y_i, \\ \left(\sum_{i=1}^{h} x_i \right) m + hn = \sum_{i=1}^{h} y_i. \end{cases} \tag{6}$$

The solutions of m and n can be obtained from the equation (6). Continuing with the variable substitution, then equation (7) can be obtained:

$$\begin{cases} K = \ln^{-1} \left[\frac{1}{n} \left(\sum_{i=1}^{h} y_i - \alpha \sum_{i=1}^{h} x_i \right) \right], \\ \alpha = h \sum_{i=1}^{h} x_i y_i - \frac{\sum_{i=1}^{h} x_i \sum_{i=1}^{h} y_i}{h \left(\sum_{i=1}^{h} x_i^2 \right) - \left(\sum_{i=1}^{h} x_i \right)^2}. \end{cases} \tag{7}$$

From the above analysis, the theoretical maximum vibration velocity is 13.59 mm/s and the minimum value vibration velocity is 2.87 mm/s. It can be seen from equation (3), under the premise of determining the distance and shock wave propagation medium, that the size of particle vibration velocity is only related to the charge mass. As seen from Figure 7, the maximum vibration velocity of the same
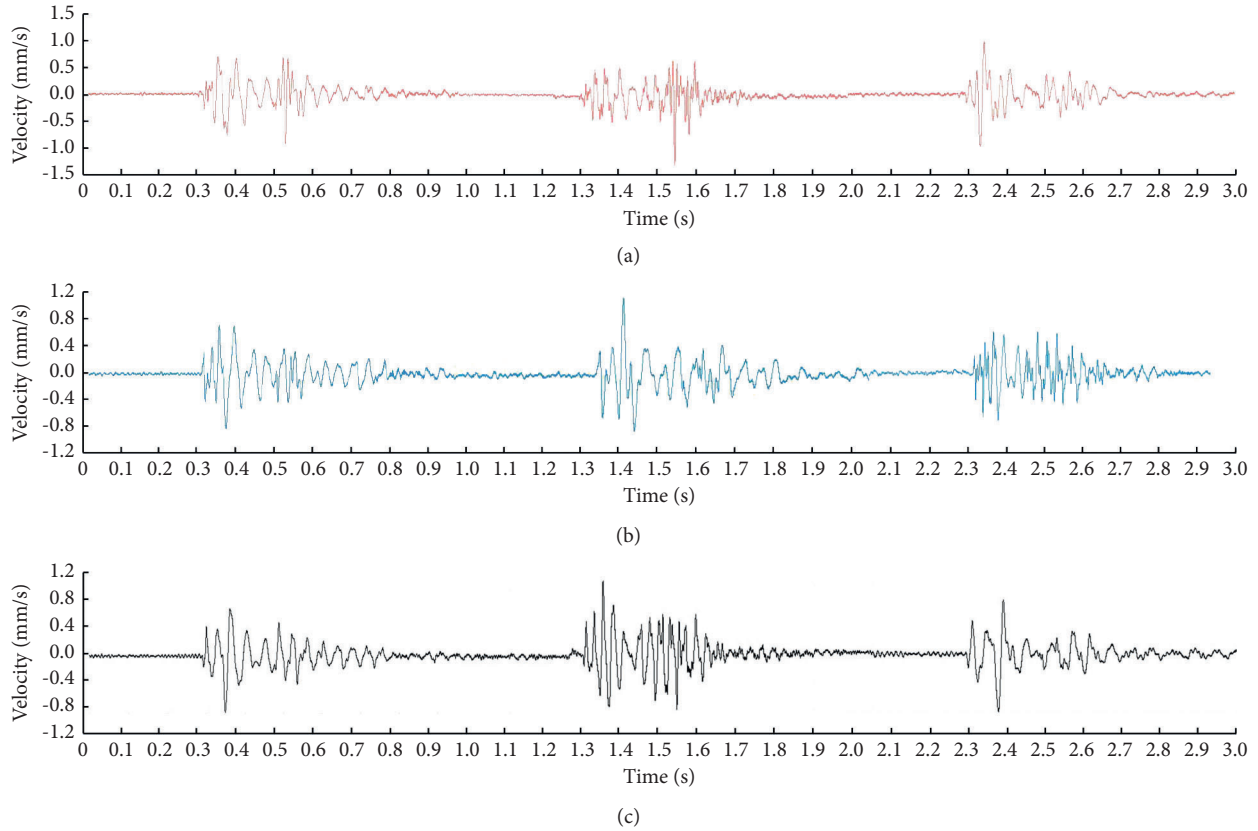
FIGURE 7: Vibration velocity of the same particle under different blasting. (a) First cycle blasting. (b) Second cycle blasting. (c) Third cycle blasting.

particle in three blasts was 1.33, 1.13, and 1.09 mm/s, respectively. To improve the safety factor, the theoretical minimum particle vibration velocity was compared with the measured value, the particle vibration velocity in three cyclic blasts showed a decreasing trend, and the decrease values were 0.20 and 0.05 mm/s, with a decrease of 14.84% and 4.03%, respectively. The decrease of the vibration speed reflects the degree of damage caused by the last blasting to the propagation medium to some extent, and the damage to the rock mass shows an exponential function with the accumulation of the cyclic blasting numbers.

Generally, due to the borehole arrangement, single section detonation charge, and delay time, different blast vibration waveform should be large fluctuations. The fluctuation of the waveform generated by the three delay time points of each blast was not proportional to the size of the charge value, and the overall state of the waveform was relatively smooth. The reason for this phenomenon is the superimposed effect of the vibration waveform caused by the difference of the different delay time of the borehole design; meanwhile, the original and secondary damage to the rock mass between the explosion source and particle has an attenuating effect on the propagation of vibrations. As shown in Figure 7, the superposition is the negative phase superposition of waveform, and the mutual superposition of waveform reduces the propagation of shock wave energy to achieve the purpose of controlling the vibration velocity.

3.2. Effect of Cyclic Blasting on Particle Vibration Velocity. In the local blasting area, assuming that the properties of surrounding rock mass change little after the first blasting, the number of blasting is treated as a variable under the same blast design scheme. The relationship between the particle vibration velocity and blasting times shows a negative exponential function, which can be expressed by equation (8):

$$v = ae^{-bn} + c, \tag{8}$$

where v denotes the particle vibration velocity, mm/s, n denotes the number of blasting cycles, and a, b, and c are regression coefficients.

As seen from Figure 8, the velocity decreases as a negative exponential function with the increase of the number of blasts. The absolute value of the slope of the vibration velocity decay curve between the first and second blasting is 1.97×10^{-2}, the absolute value of the slope of the vibration velocity attenuation curve between the second and third blast is 4.57×10^{-3}, and the former is 4.31 times of the latter.

Each blasting operation will produce different damage to rock mass, the slope of the vibration velocity change curve at the same particle of two adjacent blasts shows that the first blast produces significantly higher damage to the surrounding rock than that of the subsequent blasts, and the

$$v=1.071+1.108e^{-1.462n}$$

$$R^2=0.99$$
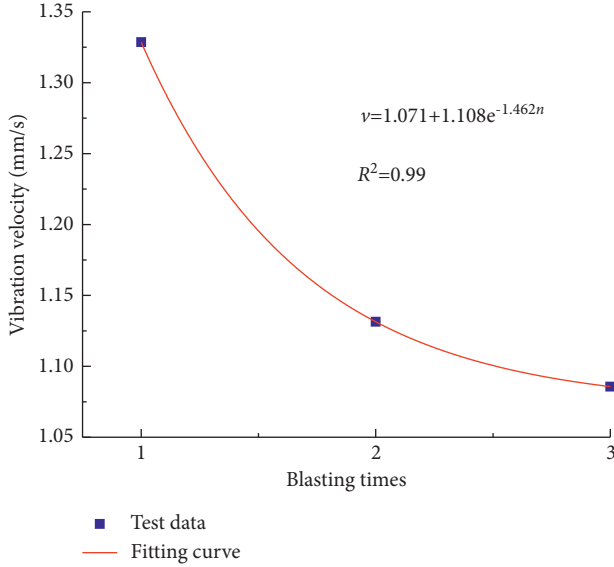
FIGURE 8: Relationship between blasting times and vibration velocity.

FIGURE 9: The difference between measured and theoretical values.

$$y=54.2x^{0.135}$$

$$R^2=0.91$$

FIGURE 10: Relationship between dimensionless vibration velocity and blasting times.

vibration velocity value from subsequent blasts is expected to gradually converge to a constant value. The attenuation of vibration velocity responds to the change of rock integrity; in practice, the difference of the subsequent blasting charge mass, charge structure, and the first blasting design can be adopted. The damage caused to the rock mass by shock wave from the first blast changes the propagation path of the shock wave from the next blast, which in turn achieves the purpose of controlling the particle vibration velocity.

The different damage of rock mass caused by blasting operation can be indirectly expressed by the particle vibration velocity. The greater the difference between the two vibration speeds, the greater the damage caused, while smaller the difference between the two vibration speeds, the smaller the damage caused. The difference between the measured vibration velocity and the theoretical minimum vibration velocity can be used to reflect the attenuation characteristics of vibration velocity, expressed by

$$\nabla v_i = v_{li} - v_{si}, \tag{9}$$

where ∇v_i is the difference between the theoretical value and the measured value of the ith blast vibration velocity, mm/s, v_{li} denotes the theoretical value of the ith blast vibration velocity, mm/s, and v_{si} denotes the measured value of the ith blast vibration velocity, mm/s. As seen from Figure 9, the values of ∇v_1, ∇v_2, and ∇v_3 are 1.54, 1.74, and 1.79 mm/s for the three cycles of blasting counted, respectively. The value of ∇v_i becomes larger as the number of blasts increases, but the increasing trend becomes significantly slower, indicating that the damage inside the surrounding rock tends to stabilize as the number of blasts increases [24].

Under the premise of the constant distance between the explosion sources and particle, the vibration velocity of the same particle varies with the increase of blasting times. To analyze the difference between the number of different blasts and vibration speed, the normalized dimensionless vibration velocity calculation of the particle vibration velocity under different blasting times is expressed by
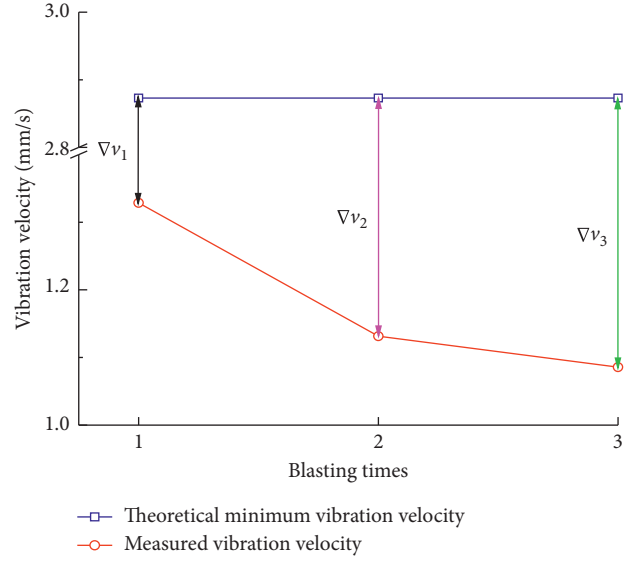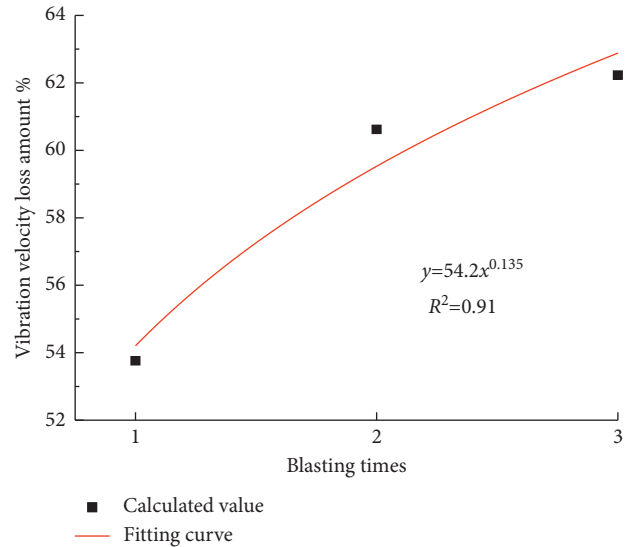
$$\nabla k_i = \frac{v_{li} - v_{si}}{v_{li}}, \tag{10}$$

where ∇k_i is the dimensionless vibration velocity loss.

As seen in Figure 10, the dimensionless vibration speed in the first blasting is the smallest, and the dimensionless vibration speed of the particle gradually increases with the increase of the number of blasting cycles. The trend of the curve can be expressed by the power function $y = 54.2x^{0.135}$, and the specific amount of the loss of dimensionless vibration velocity in three consecutive cyclic blasts is 53.76%, 60.62%, and 62.23%, respectively. The growth trend of the correlation curve becomes slower, indicating that the

sensitivity of the particle vibration velocity to the blasting behavior decreases with the increase of the number of blasts.

4. Conclusions

The concealment of the shock wave propagation generated by blasting in fractured rock determines the complexity and high difficulty of its study. To reduce the effect of blasting vibration on the surrounding structures during the tunnel drilling-blasting excavation, by using the fine blasting design of the tunnel construction, the theoretical and measured values of particle vibration velocity were analyzed. The main results of the study are as follows:

(1) Based on the geological environment, combining with the selected equipment, the appropriate diameter and depth of the borehole are determined. The borehole depth and time-consuming per unit length and borehole velocity are not a linear relationship, and the time-consuming per unit length changes slowly first and then increases rapidly with the increase of the borehole depth. There is an obvious threshold, which can be expressed by the piecewise linear function.

(2) Through the fine blasting design, the negative phase superposition effect of segmented delay blasting shock wave waveform is realized, and reducing energy propagation and particle vibration velocity is achieved. The measured vibration velocities of the same particle in three cycles of blasting are 1.33, 1.13, and 1.09 mm/s, which are 46.24%, 39.39%, and 37.79% of the theoretical minimum vibration velocity, respectively. The rationality of the fine blasting design is verified.

(3) The same particle for multiple blast vibration velocity test shows that the attenuation of vibration velocity is a negative exponential function with the increase of blasting times. The dimensionless vibration velocity loss increases as a power function with the increase of blasting times. The larger the loss is, the more the energy is lost in the process of shock wave propagation, which is conducive to ensuring the stability of protected buildings.

The designed charge directly determines the size of the energy generated by blasting, the physical properties of rock mass between explosion source and particle, the development degree of cracks determine the amount of shock wave energy absorption. In the actual engineering, considering the influence of multiple factors coupling effect with fractured rock mass on shock wave attenuation, the design of construction plans to suit the local conditions to reduce the speed of particle vibration as much as possible should be given great attention, making the blasting construction to environmental protection [25].

Data Availability

Relevant research data can be obtained upon request from the corresponding author.

Conflicts of Interest

The authors declare that they have no conflicts of interest.

Acknowledgments

References

[1] Y. Zhang, M. D. Wei, G. S. Su, Y. Li, J. B. Zeng, and X. Q. Deng, "A novel intelligent method for predicting the penetration rate of the tunnel boring machine in rocks," *Mathematical Problems in Engineering*, vol. 2020, Article ID 3268694, 15 pages, 2020.

[2] M. Koopialipoor, A. Fahimifar, E. N. Ghaleini, M. Momenzadeh, and D. J. Armaghani, "Development of a new hybrid ANN for solving a geotechnical problem related to tunnel boring machine performance," *Engineering with Computers*, vol. 36, no. 1, pp. 345–357, 2020.

[3] G. M. Foderà, A. Voza, G. Barovero, F. Tinti, and D. Boldini, "Factors influencing overbreak volumes in drill-and-blast tunnel excavation. A statistical analysis applied to the case study of the Brenner Base Tunnel-BBT," *Tunnelling and Underground Space Technology*, vol. 105, Article ID 103475, 2020.

[4] C. Yu, H. Z. Yue, H. B. Li, C. B. Zhou, S. C. Chen, and Z. S. Shao, "Analysis of blasting control parameters and reliability based on rock mass quality," *Rock and Soil Mechanics*, vol. 42, no. 8, pp. 1–11, 2021.

[5] J.-G. Kim and J.-J. Song, "Abrasive water jet cutting methods for reducing blast-induced ground vibration in tunnel excavation," *International Journal of Rock Mechanics and Mining Sciences*, vol. 75, pp. 147–158, 2015.

[6] X. Y. Liu, M. Gong, H. J. Wu, and D. An, "Calculation and practice of blasting parameters of electronic detonator in tunnel under the influence of multi-factor coupling," *Journal of Vibration and Shock*, vol. 40, no. 5, pp. 24–32, 2021.

[7] J. Yang, X.-G. Yang, J.-W. Zhou, Y. Liu, B.-S. Dong, and H.-B. Li, "Comparative study of the excavation damage and r of the deeply buried j II diversion tunnels using a TBM and the drilling-blasting method," *Advances in Civil Engineering*, vol. 2020, no. 2, pp. 1–14, 2020.

[8] C. D. Ma, W. B. Xie, Z. L. Liu, Q. Y. Li, J. Q. Xu, and G. S. Tan, "A new technology for smooth blasting without detonating cord for rock tunnel excavation," *Applied Sciences*, vol. 10, no. 19, p. 6794, 2020.

[9] X. W. Chai, S. S. Shi, Y. F. Yan, J. G. Li, and L. Zhang, "Key blasting parameters for deep-hole excavation in an underground tunnel of phosphorite mine," *Advances in Civil Engineering*, vol. 2019, Article ID 4924382, 9 pages, 2019.

[10] B. Duan, W. Gong, G. Ta, X. Yang, and X. Zhang, "Influence of small, clear distance cross-tunnel blasting excavation on existing tunnel below," *Advances in Civil Engineering*, vol. 2019, no. 3, pp. 1–16, 2019.

[11] S. R. Wang, J. Y. Zhang, J. T. Li, F. L. Kong, and J. Q. Fan, "Analysis of vibration attenuation and energy consumption of blasting demolition chimney: a case study," *Tehnički Vjesnik*, vol. 27, no. 3, pp. 826–834, 2020.

[12] J. H. Yang, Q. H. Jiang, Q. B. Zhang, and J. Zhao, "Dynamic stress adjustment and rock damage during blasting excavation

in a deep-buried circular tunnel," *Tunnelling and Underground Space Technology*, vol. 71, pp. 591–604, 2018.

[13] M. Chen, W. B. Lu, P. Yan, and Y. G. Hu, "Blasting excavation induced damage of surrounding rock masses in deep-buried tunnels," *Ksce Journal of Civil Engineering*, vol. 20, no. 2, pp. 933–942, 2016.

[14] Y. Fan, J. W. Zheng, X. Z. Cui, Z. D. Leng, F. Wang, and C. C. Lv, "Damage zones induced by in situ stress unloading during excavation of diversion tunnels for the Jinping II hydropower project," *Bulletin of Engineering Geology and the Environment*, vol. 8, pp. 1–27, 2021.

[15] L. T. Xie, P. Yan, W. B. Lu, M. Chen, and G. H. Wang, "Comparison of seismic effects during deep tunnel excavation with different methods," *Earthquake Engineering and Engineering Vibration*, vol. 17, no. 3, pp. 208–224, 2018.

[16] Y. Xia, N. Jiang, C. Zhou, and X. Luo, "Safety assessment of upper water pipeline under the blasting vibration induced by Subway tunnel excavation," *Engineering Failure Analysis*, vol. 104, pp. 626–642, 2019.

[17] N. Jiang, T. Gao, C. Zhou, and X. Luo, "Effect of excavation blasting vibration on adjacent buried gas pipeline in a metro tunnel," *Tunnelling and Underground Space Technology*, vol. 81, pp. 590–601, 2018.

[18] S. H. Chen, X. M. Liu, Z. H. Zhang, and C. M. Lin, "Analysis of surface vibration effect on tunnel excavation section induced by tunneling blasting," *Chinese Journal of Geotechnical Engineering*, vol. 42, no. 10, pp. 1800–1806, 2020.

[19] L. S. Shi, W. X. Gao, and L. T. Wang, "Experimental and numerical simulation study on blasting seismic effect of subway shallow buried tunnel," *Transactions of Beijing Institute of Technology*, vol. 38, no. 12, pp. 31–37, 2018.

[20] X. M. Liu and S. H. Chen, "Prediction of surface vibration waveform caused by cut hole blasting in tunneling," *Chinese Journal of Geotechnical Engineering*, vol. 41, no. 9, pp. 1731–1737, 2019.

[21] C. Zhu, M. C. He, M. Karakus, X. H. Zhang, and Z. Guo, "The collision experiment between rolling stones of different shapes and protective cushion in open-pit mines," *Journal of Mountain Science*, vol. 18, no. 5, pp. 1391–1403, 2021.

[22] D. Liu, W. B. Lu, M. Chen, and P. Yan, "Attenuation formula of the dominant frequency of blasting vibration during tunnel excavation," *Chinese Journal of Rock Mechanics and Engineering*, vol. 37, no. 9, pp. 2015–2026, 2018.

[23] F. Wu, R. B. Gao, J. Liu, and C. B. Li, "New fractional variable-order creep model with short memory," *Applied Mathematics and Computation*, vol. 380, Article ID 125278, 2020.

[24] F. Wu, H. Zhang, Q. L. Zou, C. B. Li, J. Chen, and R. B. Gao, "Viscoelastic-plastic damage creep model for salt rock based on fractional derivative theory," *Mechanics of Materials*, vol. 150, Article ID 103600, 2020.

[25] C. Zhu, M. He, M. Karakus, X. Zhang, and Z. Tao, "Numerical simulations of the failure process of anaclinal slope physical model and control mechanism of negative Poisson's ratio cable," *Bulletin of Engineering Geology and the Environment*, vol. 80, no. 4, pp. 3365–3380, 2021.

Research Article

Study on Lateral Deformation and Failure Characteristics of Coal Based on Different Confining Pressures

Jian-jun Ren ⬤,[1] **Shan-Yang Wei** ⬤,[2] **Shi-Hai Shu,**[1] **and Wei-Dong Luo**[3]

[1]*College of Physics and Engineering, Xingyi Normal University for Nationalities, Xingyi 562400, China*
[2]*School of Mining, Guizhou University, Guiyang 550025, China*
[3]*Guizhou Panjiang Coal Power and Electricity Group Technology Research Institute Co., Ltd., Guiyang 550081, China*

Correspondence should be addressed to Shan-Yang Wei; sywei1@gzu.edu.cn

To study the lateral deformation characteristics of coal under different confining pressures, coal compression experiments with confining pressures of 0 MPa, 3 MPa, 5 MPa, and 7 MPa were conducted under the same loading rate by using the TAW-2000 electrohydraulic servo rock mechanics experimental machine. The results of the study showed the following: at the initial stage of loading, the lateral strain of coal was about 12.22%–46.9% of the axial strain at the elastic deformation stage and 41.18%–64.96% of the axial strain at the inelastic deformation to peak stress stage. Compared with the experiment under 0 MPa confining pressure, the growth rate of the lateral strain of the coal under 3 MPa, 5 MPa, and 7 MPa confining pressures was much smaller than that of the corresponding axial strain. When the coal was damaged under different confining pressures, the lateral strain was maintained at about 0.6×10^{-2}. Based on the field verification, we proposed that the lateral strain during the coal failure and the nonlinear region of the lateral axis ratio changing with time can be used as potential parameters for predicting the coal failure.

1. Introduction

Because of the impact of excavation, the coal wall of the coal roadway and the coal wall of the working face change from the initial three-way force to the one-way force so that the coal wall of the roadway and the coal near the coal wall of the working face bear the weight of rock strata above the excavation space. The weight causes an increase in the supporting pressure of the coal near the coal wall of the roadway and the working face, causing the coal near the coal wall to expand to the side of the goaf, ultimately resulting in the spalling of roadway coal wall and working face coal wall. That is, under the support pressure, the coal body on one side of the goaf of the coal wall will produce lateral expansion deformation. In practical engineering applications, it is of great significance to study the lateral deformation and lateral deformation characteristics of coal under different surrounding rock pressures to control the expansion deformation of coal rib, to guide roadway support, and to grout reinforcement of coal rib.

Scholars in China and abroad have carried out a lot of research on the lateral deformation characteristics of rocks. Based on the triaxial test results of granite under different confining pressures, Jingxiang et al. analyzed the lateral deformation characteristics of granite and proposed that the brittleness characteristics of rock samples can be comprehensively reflected from the change law and magnitude of brittleness [1]. Guojun et al. believed that, under the continuous action of cyclic loading and unloading, the failure of rock is a cumulative process. The growth trend of axial and lateral cumulative irreversible strains under cyclic loading is linear, and the increase of confining pressure can effectively limit the lateral cumulative irreversible strain of rock [2]. Based on the triaxial unloading seepage test results under different initial confining pressures and unloading rates, Rubin et al. obtained the lateral deformation characteristics. In these tests, volumetric dilatancy characteristics of sandstone changed significantly with the increase of initial confining pressure and unloading rate during unloading failure of sandstone [3]. Using an MTS815 electrohydraulic

servo-controlled rigid testing machine, Memetyusup et al. conducted unloading/decreasing confining pressure tests with constant axial deformation. The test results indicated that, with the decrease of the confining pressure, the lateral expansion of rock samples continued, and the axial stress decreased [4]. Dong et al. proposed that the axial stress of rock can be determined by its axial strain before the peak, and it is controlled by lateral deformation after the peak, and it gradually decreases to residual strength with the increase of lateral deformation [5].

Compared with rock, coal has different characteristics in different directions. It also has low strength and undergoes a large deformation under a given loading process. Zhenqian et al. investigated the lateral deformation characteristics of coal under different loading rates by using the TAW-2000 electrohydraulic servo rock mechanics experimental system. They concluded that the lateral strain was the same when the first axial stress dropped under different loading rates, and the lateral strain was used as the control variable to predict the failure of coal [6]. Yongping carried out uniaxial and triaxial compression tests on typical soft and hard coal rock samples by MTS815 electrohydraulic servo rock mechanics testing machine. The results demonstrated that the strength, yield axial strain, and lateral deformation characteristics of soft and hard coal rock were greatly different due to the different internal structures of soft and hard coal rock and the different development degrees of pores and cracks. The internal damage evolution characteristics of coal and rock can be characterized by lateral plastic deformation damage [7]. Mingqing observed that there was a typical step-like drop after the peak stress of hard coal with impact tendency, and the significant increase of lateral axis ratio was mainly after the peak stress [8]. Tarasov and Potvin believed that the existence of surrounding rock can affect the brittleness of rock [9]. Guo et al. investigated the lateral deformation of strip coal pillar in Tangkou Coal Mine with a mining depth of over 1000 m. They concluded that, in deep mining, the accumulation and release of energy cause discontinuous damage in the heterogeneous coal mass, and the lateral deformation of coal pillar shows discontinuity and mutation characters [10–12].

In summary, the lateral deformation characteristics and laws of rock under triaxial compression [13–15] and the axial deformation characteristics of coal under different confining pressures and loading speeds [16, 17] have been investigated in depth in China and abroad, and some great results have been achieved. However, there are few studies regarding the lateral deformation of coal under the same loading rate and different confining pressures. In this study, the TAW-2000 electrohydraulic servo rock mechanics testing machine was employed to examine the deformation characteristics of coal samples under the same loading rate and different confining pressures. Furthermore, the influence of the confining pressure on the lateral deformation characteristics of the coal body was analyzed. The research results combined with the actual measurement results in the underground mine are of great significance to the analysis of the deformation characteristics of the coal body after excavation at a certain buried depth and the selection of reasonable support schemes. At the same time, they can also be utilized as a basis for evaluating the damage of the coal body [18–21].

2. Sample Preparation and Test Method

The TAW-2000 electrohydraulic servo rock mechanics testing machine was used in this research. The overall stiffness of the test frame was 10 GN/m, the maximum axial force was 2000 kN, and the maximum confining pressure was 100 MPa. The dynamic strain monitor and the triaxial test pressure chamber are shown in Figure 1.

The coal samples were selected from the standard specimen made of coal blocks in a coal mine in Shanxi Province of China. The coal blocks obtained from the underground were processed into standard cylindrical coal samples with a diameter of 50 mm and a height of 100 mm by using drilling, cutting, and grinding [22–24]. The experimental coal samples are shown in Figure 2. The experimental data were monitored by a high-precision extensometer. Since the extensometer could not resist large deformation, the axial deformation control was adopted in the experiments. The loading speed was set to 0.05 mm/min, and the test confining pressures were 0 MPa, 3 MPa, 5 MPa, and 7 MPa, respectively. The data of time, load, displacement, stress, axial strain, radial strain, and confining pressure change in the whole process were obtained during the tests [25–27].

To reduce the influence of the heat shrink tube on the experimental results, the same heat shrink tube was employed to package all coal samples in the experiment. The coal samples after the experiment are exhibited in Figure 3.

3. Analysis of Test Results

3.1. Experimental Data Processing.

(1) Peak strength (σ_c): on the stress-strain curve, the maximum stress (i.e., peak stress) [28, 29] is obtained through the following formula:

$$\delta_c = \frac{P_{\max}}{A}, \tag{1}$$

where $P_{\max}$ is the maximum axial load (N) in the test process and A is the compressed area (m^2) of the sample.

(2) The linear elastic stage: in this stage, the stress and strain on the stress-strain curve have a linear relationship (i.e., their relationship follows Hooke's law).

(3) The nonlinear elastic stage: on the stress-strain curve, it is the section after the linear elastic stage and before the failure of the coal sample.

(4) The plastic deformation stage: in this stage, the weak surface inside the coal body is destroyed, and the stage continues up to the end of the test.

(5) lateral axis ratio: the ratio of the lateral strain to the axial strain of the coal sample during the experiment is called the side axis ratio [30].

(a)   (b)
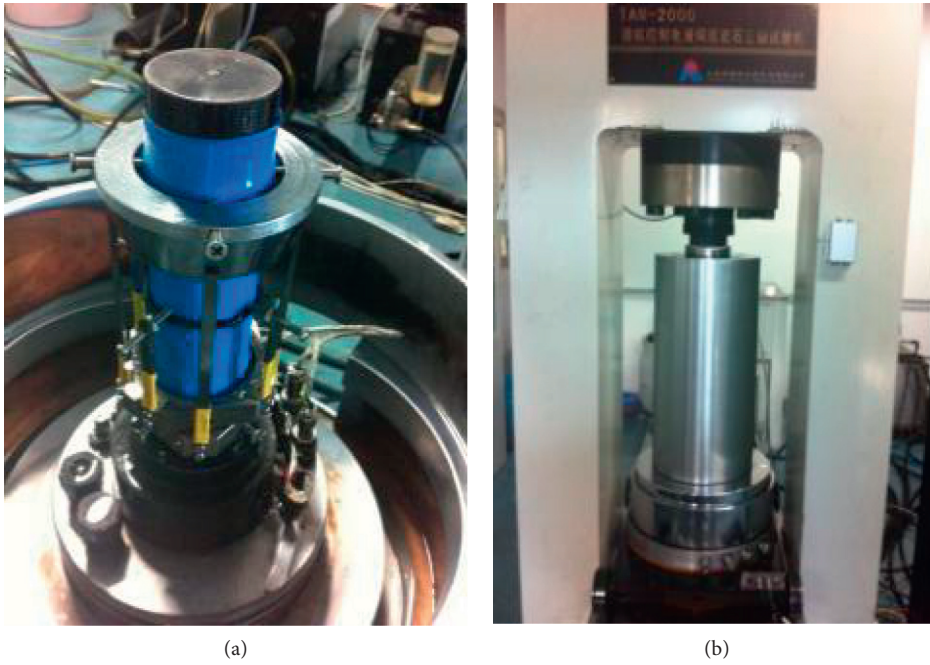
FIGURE 1: Test equipment. (a) Dynamic strain monitoring instrument. (b) Pressure chamber of triaxial test.

FIGURE 2: Experimental coal samples.

FIGURE 3: Coal samples after conducting the tests.

3.2. Analysis of Results. The physical and mechanical parameters of coal samples under different confining pressures are displayed in Table 1. The complete stress-strain curves of coal samples under different confining pressures are shown in Figure 4.

According to the stress-strain curves of coal samples under different confining pressures, coal samples experienced four stages from the beginning of loading to the failure of coal samples (Figure 4): (1) the compaction stage of internal cracks of coal, (2) elastic deformation stage (linear elastic stage and nonlinear elastic stage), (3) plastic deformation stage, and (4) postpeak failure stage.

In the pressure consolidation and compaction stage of cracks, the microcracks inside the coal body were compacted, and the coal had a negative strain in the radial direction, which was characterized as a radial shrinkage. The experimental results indicated that the radial strain developed forward when the stress exceeded 0.83 MPa at 0 MPa confining pressure, 1.36 MPa at 3 MPa confining pressure, 1.78 MPa at 5 MPa confining pressure, and 1.95 MPa at 7 MPa confining pressure.

The coal body entered the linear elastic stage after the pressure consolidation and compaction stage. In this stage, the axial strain and radial strain of the coal body increased according to a certain slope, and the changing trend of the two was consistent. At this stage, the axial and radial stress-strain curves were both straight lines (i.e., the elastic modulus of the coal body was a fixed value). With the increase of stress, the coal entered the nonlinear elastic stage. Compared with the linear elastic stage, the elasticity of coal decreased with the increase of stress, and the strain increased with the increase of stress, which was more obvious with the increase of confining pressure.

With the continuous increase of stress, the weak surface inside the coal body first broke, and the coal body entered the plastic deformation stage. From a large number of experimental test results, we found that there were two types of failure in the loading process of the coal body: (1) The coal body underwent a process of destruction-stabilization-redestruction-restabilization-redestruction caused by the destruction of the weak surface. The stress gradually reached the maximum, and, finally, the main weak surface in the coal body was destroyed, so that the coal body lost its bearing capacity. (2) When the structure of the coal sample was good, there was no stage of restabilization-redestruction, and the failure bearing capacity of the coal from the main weak surface diminished directly. It can be observed from Figure 4 that the first type of failure was more obvious when the confining pressure was 0 MPa, and when the confining pressure was nonzero, the coal body mostly showed the second type of failure.

After the peak failure, the coal sample entered the postpeak failure stage, in which both the axial strain and the radial strain increased sharply.

4. Lateral Deformation Characteristics of Coal under Different Confining Pressures

4.1. Lateral Deformation Characteristics. To clearly describe the lateral deformation characteristics of the coal under the same loading speed and different confining pressures, the total stress-strain curves of the coal under different confining pressures were plotted. It can be observed from Figure 4 that the axial stress-lateral strain curve and the axial stress-axial strain curve of coal samples under different confining pressures maintained the same changing trend in all four stages. The lateral axis ratio of coal samples under the same loading speed and different confining pressure [31] is shown in Figure 5. The four following stages were observed during the performed tests:

(1) The pressure consolidation and compaction stage of the internal cracks in the coal body: the coal body had radial shrinkage in all four cases. The minimum value of lateral deformation at this stage appeared in the uniaxial compression state and was dominated by radial shrinkage. This showed that, no matter whether or not there was confining pressure, there was a pressure consolidation and compaction process in the radial direction of internal cracks in the coal under axial load. The duration of this stage was short, lasting about three seconds.

(2) Elastic stage: according to Figure 4, the lateral strain range of the coal under 0 MPa confining pressure was 0.091×10^{-3}–3.44×10^{-3}, and the corresponding axial strain range was 0.377×10^{-3}–4.01×10^{-3}. Thus, the lateral strain was about 24.1%–85.8% of the axial strain. When the confining pressure was nonzero, the range of the lateral strain and the axial strain of the coal body increased, and the range of the lateral strain of the coal body was the same regardless of the confining pressure, and the lateral strain range was 0.045×10^{-3}–5.06×10^{-3}. The range of the axial strain under nonzero confining pressure was 0.368×10^{-3}–12.44×10^{-3}. Therefore, the lateral strain range was approximately 12.22%–46.9% of the axial strain range under a nonzero confining pressure. At this stage, the lateral strain was at a low level, and the specimen was mainly subjected to axial compression.

(3) Inelastic stage: in this stage, with the increase of the axial load, the increase rate of the axial strain of the coal sample was greater than that of the lateral strain. The lateral strain of coal under 0 MPa confining pressure was 3.413×10^{-3}–4.33×10^{-3}, and the corresponding axial strain was 3.991×10^{-3}–4.494×10^{-3}. Thus, the lateral strain of the specimen was 85.5%–96.35% of the axial strain. Under nonzero confining pressure, the range of lateral strain of coal was 4.107×10^{-3}–10.398×10^{-3}, and the range of axial strain of coal was

TABLE 1: Physical and mechanical parameters of coal samples under different confining pressures.

Number	Loading rate (mm/min)	Diameter (mm)	Height (mm)	Confining pressure (MPa)	Peak strength (MPa)	Peak lateral strain, 10^{-2}	Peak axial strain, 10^{-2}	Maximum lateral strain, 10^{-2}	Maximum axial strain, 10^{-2}
M1	0.05	49.28	98.32	0	12.80	0.7667	0.5351	2.0611	0.997
M2	0.05	49.42	98.89	3	43.95	0.6984	1.2775	1.6062	2.0216
M3	0.05	49.3	100.18	5	53.36	0.852	1.2412	2.6946	2.1174
M4	0.05	49.34	100.11	7	67.43	1.0649	1.8067	2.1468	2.3674
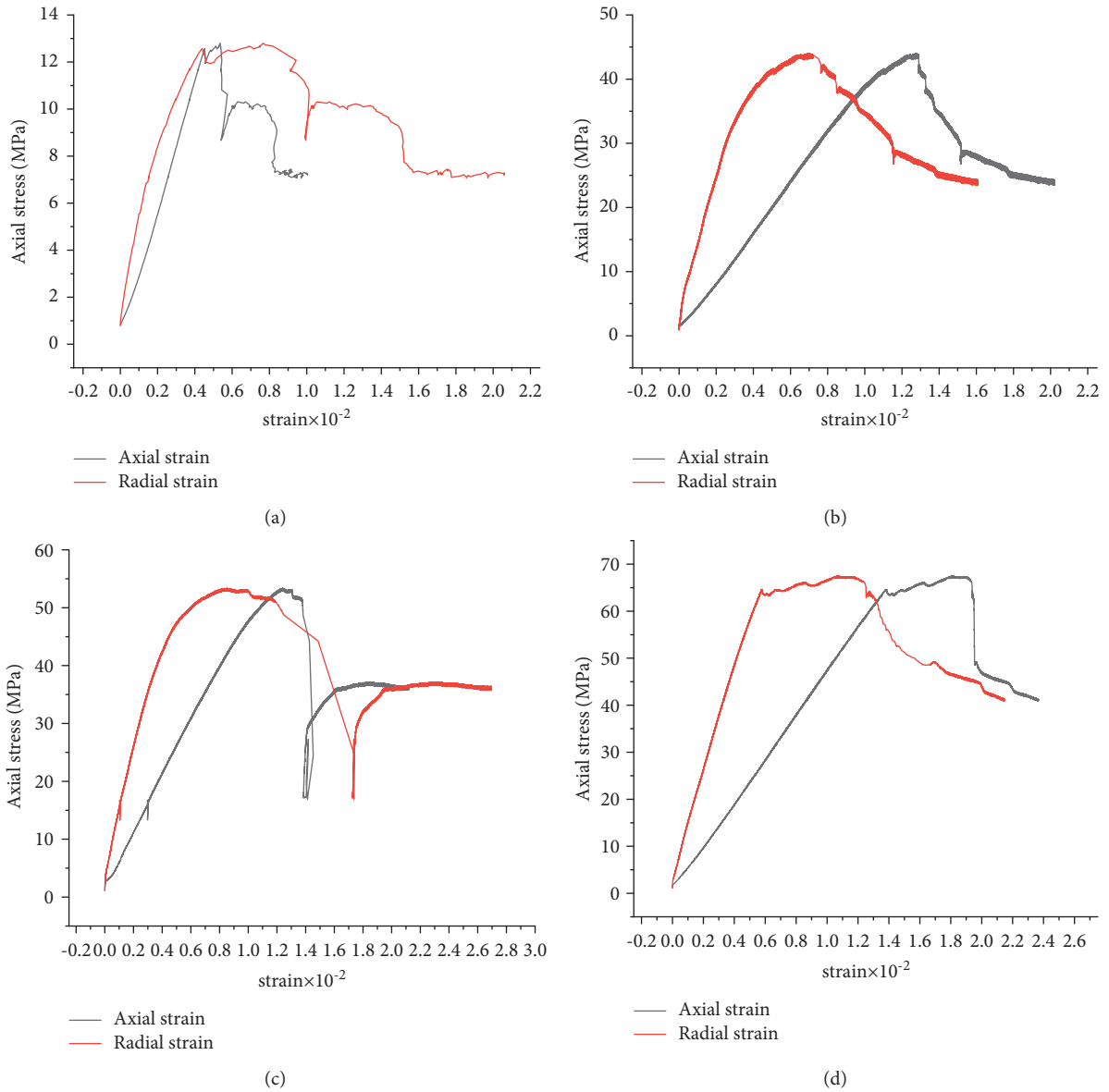
FIGURE 4: Stress-strain curves under different confining pressures. Stress-strain curve under (a) 0 MPa confining pressure, (b) 3 MPa confining pressure, (c) 5 MPa confining pressure, and (d) 7 MPa confining pressure.

9.972×10^{-3}–17.811×10^{-3}. Therefore, the lateral strain of the specimen was 41.18%–64.96% of the axial strain under a nonzero confining pressure. That is, the lateral deformation was slightly smaller than the axial strain at 0 MPa; however, it was significantly smaller than the axial deformation when the confining pressure was nonzero.

(4) Postpeak expansion stage: the damage of the coal sample at this stage was chiefly manifested as the damage caused by the development of the weak

(a)

(b)
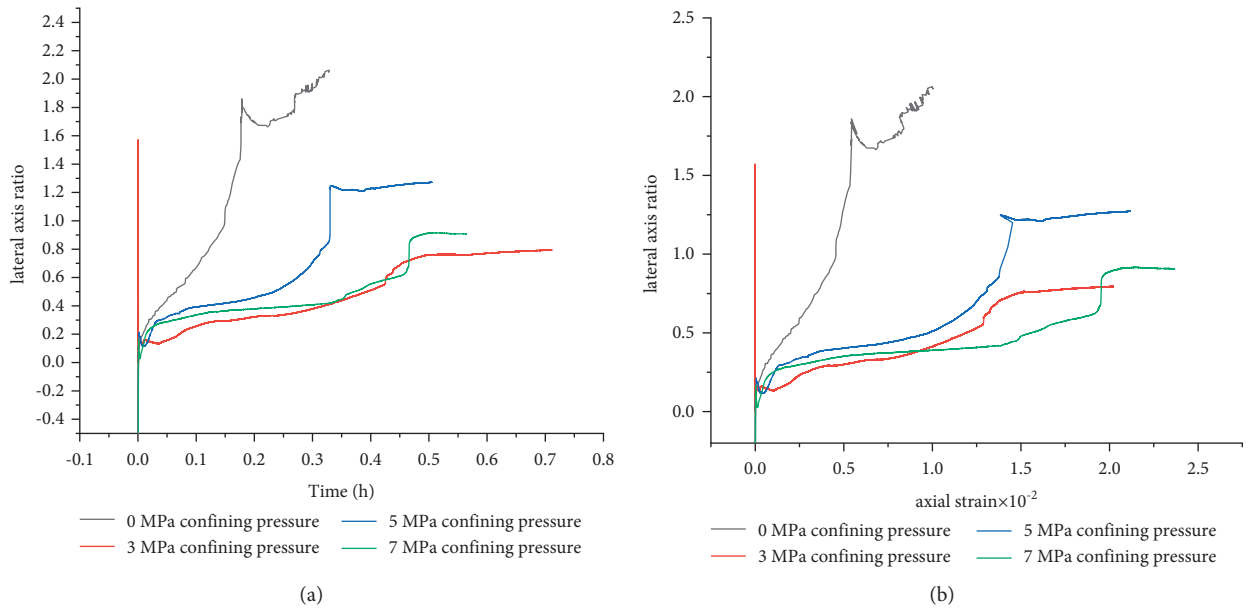
FIGURE 5: Characteristic curves of lateral axis ratio of coal sample under different confining pressures. (a) Characteristic curve of lateral axis ratio versus time. (b) Characteristic curve of lateral axis ratio versus axial strain.

(a)

(b)
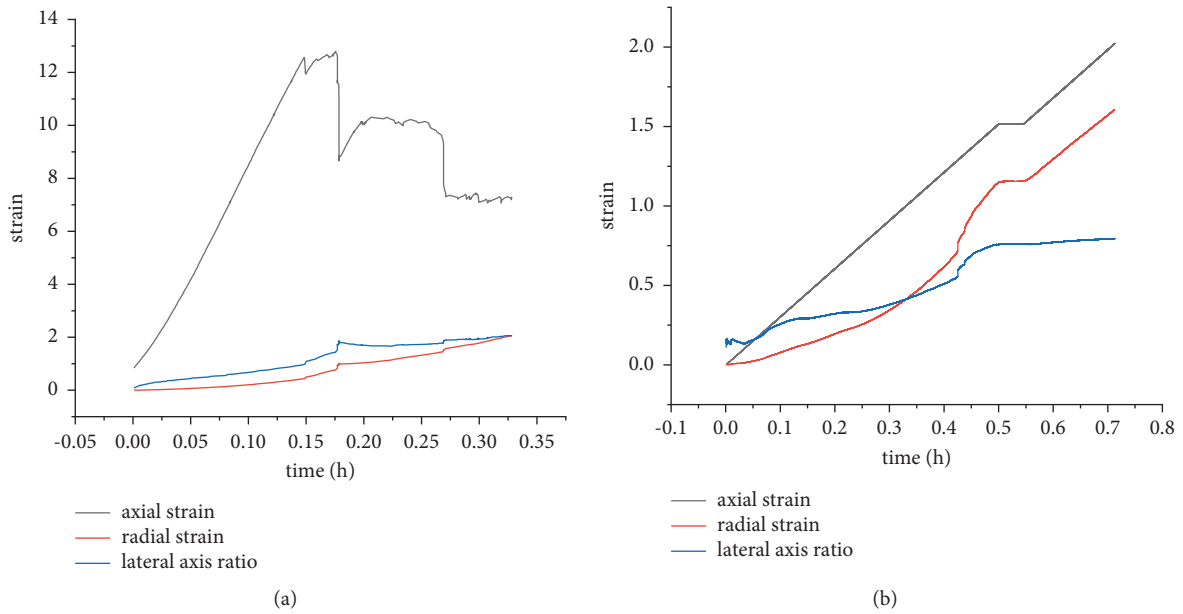
FIGURE 6: Continued.

(c)

(d)
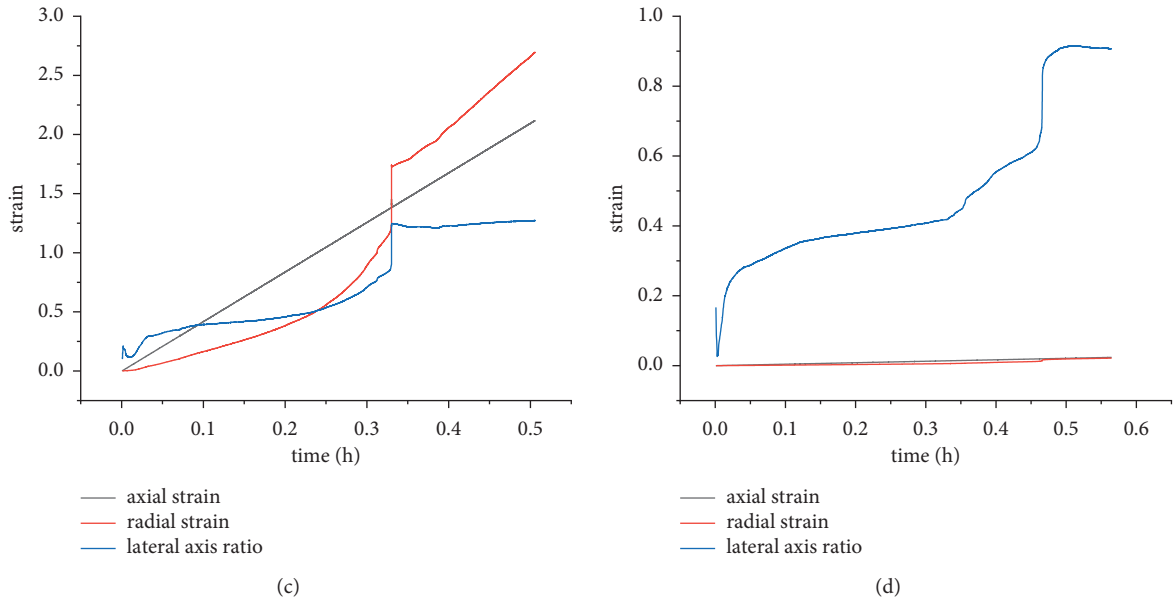
FIGURE 6: Time-strain characteristic diagrams of coal sample. Time-strain characteristic diagram under (a) 0 MPa confining pressure, (b) 3 MPa confining pressure, (c) 5 MPa confining pressure, and (d) 7 MPa confining pressure.

(a)

(b)
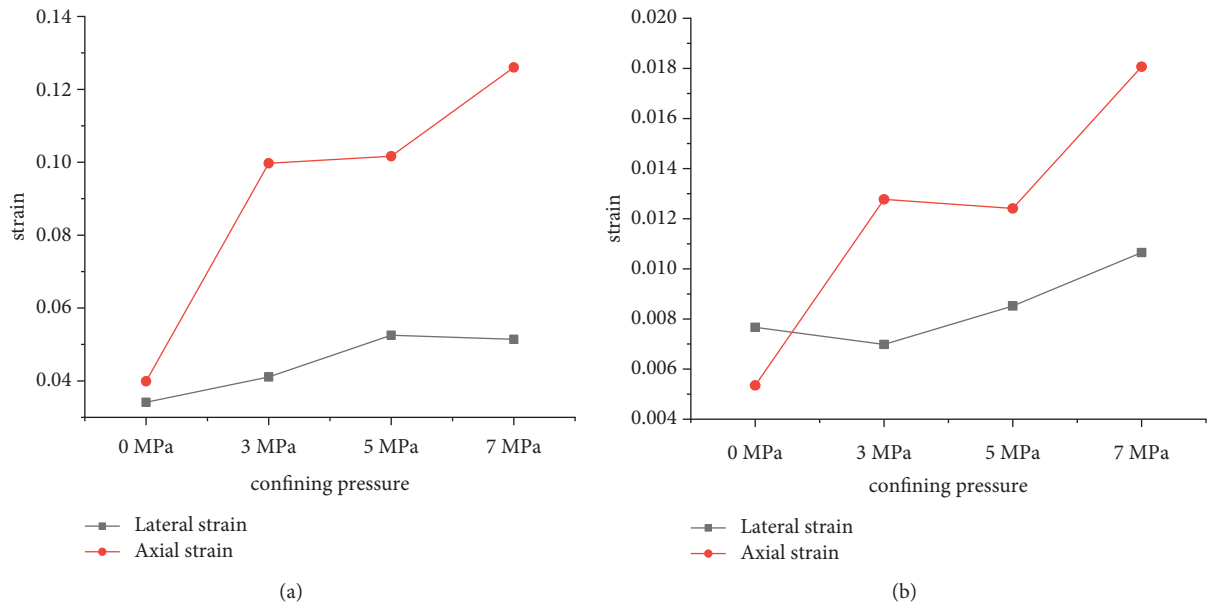
FIGURE 7: Peak strain characteristic diagrams. (a) Lateral strain and axial strain at peak stress of elastic deformation. (b) Lateral strain and axial strain at peak stress.

surface inside the coal body towards the failure surface. At this stage, the strength of the coal body decreased rapidly, and the lateral strain increased quickly. The lateral strain at this stage accounted for more than 50% of the total lateral strain.

4.2. Characteristics of Lateral Axis Ratio. Figures 5(a) and 5(b) show that, before the first stress drop, the lateral axis ratio under 0 MPa confining pressure increased rapidly with time, and the first stress drop occurred in a short time. Furthermore, the lateral axis ratio initially increased slowly

with time under the confining pressures of 3 MPa, 5 MPa, and 7 MPa, and the lateral axis ratio showed the same change rate. After some time, the lateral axis ratio increased with time up to the point of stress drop. That is, the binding effect of the confining pressure had a great influence on maintaining the stability of the coal body.

4.3. Time-Strain Characteristics. Figure 6 displays the variation trend of axial strain, lateral strain, and lateral axis ratio with time when the coal samples fail under four different confining pressures. It can be observed from the figure that
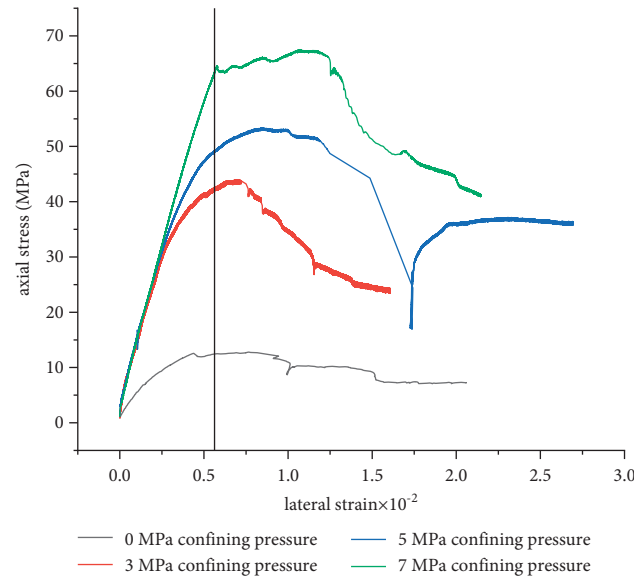
FIGURE 8: Characteristic curves of axial stress versus lateral strain.
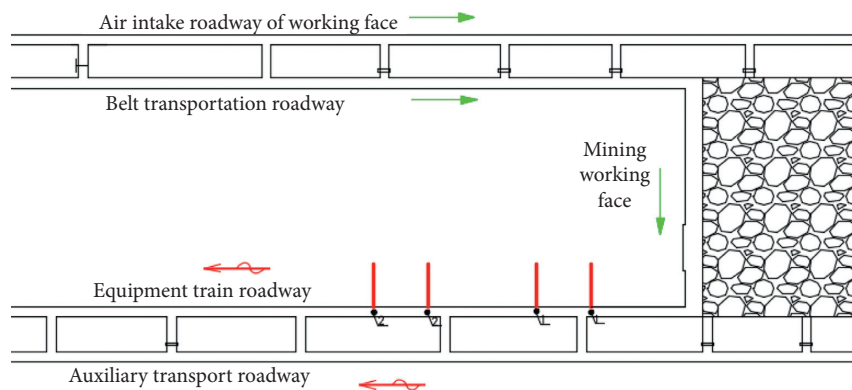
FIGURE 9: Monitoring point layout plan.

the lateral axis ratio curve changed in advance before the lateral failure. At the same time, the linear area where the lateral axis ratio changes with time can be used as a stable area for the deformation of the coal wall of the roadway and the working face, and the area outside the linear area can be utilized as a potential parameter for evaluating the deformation and failure of the coal wall and as a parameter for predicting the failure of the coal body.

4.4. Peak Strain Characteristics. From Figures 7(a) and 7(b) and Figure 8, it can be observed that when the coal body was destroyed under different confining pressures, the lateral strain was maintained at about 0.6×10^{-2}.

5. Engineering Applications

To verify the reliability of the experimental results, the coal wall of a working face of the No. 5 coal seam of the mine was selected for validation. The deformation of the roadway coal wall in the vertical and horizontal directions was monitored by drilling peep and abscission layer instruments. The experimental location is shown in Figure 9. The test was divided into two groups: In the first group, an anchor net was used with certain confining pressure + steel belt and U-shaped support, respectively, before the lateral strain of the coal wall became equal to 41.18% of the axial strain. In the second group, after the lateral strain of the coal wall became equal to 64.96% of the axial strain, the anchor net + steel belt and U-shaped support were used to observe the deformation and failure of the coal wall [32–34]. The destruction of the coal wall is shown in Figure 10 and the monitoring results are displayed in Figure 11.

The field test results showed the following: (1) Supporting before reaching the lateral axis ratio of the failure in the experimental study effectively reduced the deformation and failure of coal wall and increased the stability of coal wall. (2) The existence of confining pressure limited the

Anchor net + steel belt support   U-shaped support

(a)

Anchor net + steel belt support   U-shaped support

(b)
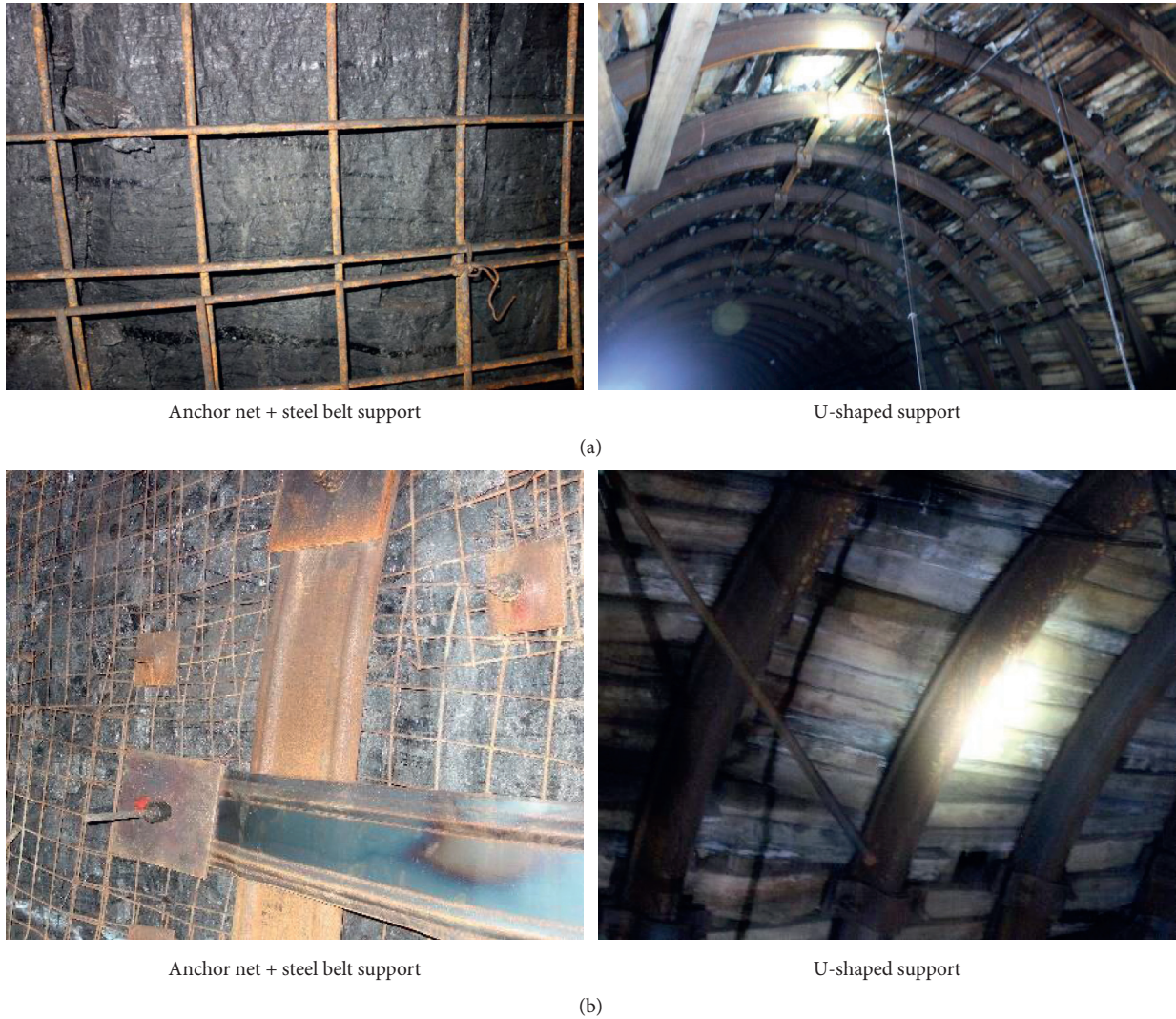
Figure 10: Coal wall failure in monitoring points. (a) The first group. (b) The second group.
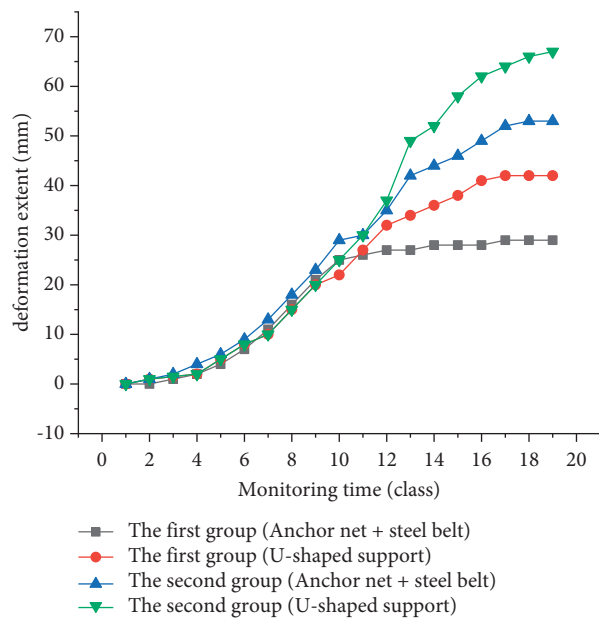
Figure 11: Field curves of deformation versus monitoring time.

deformation of the coal wall and improved the stability of the coal wall.

6. Conclusion

(1) The coal bodies under different confining pressures experienced the whole loading process that ultimately led to the destruction of the coal body. The radial deformation of the coal bodies experienced the internal crack consolidation and compaction stage, the elastic deformation stage, the nonlinear elastic deformation stage, and the postpeak plastic stage. This means that the lateral deformation of the coal body underwent four stages, from shrinkage deformation to linear growth and then to postpeak expansion.

(2) The lateral axis ratios of coal under different confining pressures were different, which could be divided into two categories: under 0 MPa confining pressure, the lateral strain of the coal was about 85.5%–96.35% of the axial strain when it was destroyed. When the confining pressure was nonzero, the lateral strain of the coal mass was about 41.18%–64.96% of the axial strain. When the coal body was destroyed, the lateral strain of the coal was maintained at about 0.6×10^{-2}.

(3) The field test results indicated that the lateral axis ratio can be used as a potential parameter for evaluating the deformation and failure of coal wall and as a basis for designing the support parameters.

(4) The lateral deformation characteristics of coal under different confining pressures explain why when the same coal seam is mined from shallow to deep, the risk of gas outbursts in coal bodies and the risk of coal wall slicing accidents increase, and the necessity of timely support when excavating underground coal mines becomes more prominent.

Data Availability

The data used to support the findings of the study are available within the article.

Conflicts of Interest

The authors declare that they have no conflicts of interest.

Acknowledgments

References

[1] Y Jingxiang, F. Tao, Z. Yawu, M. Dongyu, and Z. Zeqi, "A new method to evaluate the brittleness of granite based on lateral deformation," *Journal of Wuhan University (Engineering Edition)*, pp. 1–7.

[2] C. Guojun, F. Weiqiang, Z. Daan, Z. Yang, C Shihao, C. Yuhang et al., "Experimental study on the deformation and damage mechanics of sandstone under triaxial cyclic loading," *Analysis of Triaxial Cyclic Experimental Results*, vol. 45, no. 10, pp. 44–48+747, 2019.

[3] W. Rubin, X. U. Bo, X. U. Weiya et al., "Experimental research on influence of different unloading stress paths on permeability evolution for sandstone," *Chinese Journal of Rock Mechanics and Engineering*, vol. 38, no. 3, pp. 467–475, 2019.

[4] S. Memetyusup, Z.-d. Zhu, N. I. Xiao-hui, G. Liu, and H. E. Zhi-lei, "Experimental study on deformation failure of sandstone under unloading confining pressure condition," *Journal of Hebei University of Engineering (Natural Science Edition)*, vol. 32, no. 3, pp. 14–30, 2015.

[5] W. Dong, W. Ding, H. Xiaogang et al., "Limestone failure law and post-failure constitutive relation in the control of lateral deformation," *Journal of China Coal Society*, vol. 35, no. 12, pp. 2022–2027, 2010.

[6] M. Zhenqian, X. Liang, E. Chi, P. Zhang, and X. Xie, "Experimental study on lateral deformation characteristics of coal under different loading rates," *Chinese Journal of Applied Mechanics*, vol. 37, no. 5, pp. 2007–2012+2320, 2020.

[7] Y. Wu and G. Xicai, "Experimental comparative study on lateral deformation characteristics of coal sample in different loading path," *Journal of China Coal Society*, vol. 35(S), pp. 44–48, 2010.

[8] Y. Mingqing, *Mechanical Properties of rocks*, Geological Publishing House, Beijing, China, 2007.

[9] B. Tarasov and Y. Potvin, "Universal criteria for rock brittleness estimation under triaxial compression," *International Journal of Rock Mechanics and Mining Sciences*, vol. 59, pp. 57–69, 2013.

[10] W. Guo, H. Wang, and S. Chen, "Coal pillar safety and surface deformation characteristics of wide strip pillar mining in deep mine," *Arabian Journal of Geosciences*, vol. 9, no. 2, pp. 1–9, 2016.

[11] S. Chen, X. Qu, D. Yin et al., "Investigation Lateral Deformation and Failure Characteristics of Strip Coal Pillar in Deep Mining," *Geomechanics and engineering*, vol. 14, 2018.

[12] S. Chen, H. Wang, Y. Zhu et al., "Monitoring method for coalmass lateral deformation in deep mining and characteristics of step deformation," *Chinese Journal of Rock Mechanics and Engineering*, vol. 35, no. S2, pp. 4121–4128, 2016.

[13] Z. Zhang and F. Gao, "Confining pressure effect on rock energy," *Chinese Journal of Rock Mechanics and Engineering*, vol. 34, no. 1, pp. 1–11, 2015.

[14] L. I. Xi-bing, C Zheng-hong, C. A. O. Wen-zhuo, and M. Tao, "ZHOU Jian Time-effect properties and mechanisms of marble failure under different unloading rates," *Chinese Journal of Geotechnical Engineering*, vol. 39, no. 9, pp. 1565–1574, 2017.

[15] Yu Wang, L. I. Xiao, Y. Wu et al., "Research on relationship between crack initiation stress level and brittleness indices for brittle rocks," *Chinese Journal of Rock Mechanics and Engineering*, vol. 33, no. 2, pp. 264–275, 2014.

[16] M. A. Zhen-qian, Y.-d. Jiang, L. I. Yan-wei, Y.-m. Yang, and L. I. Hai-tao, "Experimental research on influence of loading rate and confining pressure on energy evolution of coal," *Chinese Journal of Geotechnical Engineering*, vol. 38, no. 11, pp. 2114–2121, 2016.

[17] Y. Wang, X. Liu, D. Chen, D. Wang, Y. Yang, and D. Chen, "Damage characteristics of outburst coal sample containing gas under different loading rates," *Safety In Coal Mines*, vol. 51, no. 6, pp. 25–30, 2020.

[18] X. Yingjie, L. Lianchong, T. Chun'an et al., "Rock brittleness evaluation based on stress dropping rate after peak stress and energy ratio," *Chinese Journal of Rock Mechanics and Engineering*, vol. 35, no. 6, pp. 1141–1154, 2016.

[19] C. Guo-qing, C. Zhao, W. Tao et al., "Evaluation method of rock brittlecharacteristics based on full stress-strain curve and crack initiation stress," *Chinese Journal of Rock Mechanics and Engineering*, vol. 37, no. 1, pp. 51–59, 2018.

[20] Q. Wang, M. C. He, S. C Li et al., "Comparative study of model tests on automatically formed roadway and gob-side entry driving in deep coal mines," *International Journal of Mining Science and Technology*, vol. 31, no. 4, pp. 591–601, 2021.

[21] Q. Wang, Y. Wang, M. He et al., "Experimental research and application of automatically formed roadway without advance tunneling," *Tunnelling and Underground Space Technology*, vol. 114, Article ID 103999, 2021.

[22] T. Wang, Z. Ma, P. Gong, N. Li, and S. Cheng, "Analysis of failure characteristics and strength criterion of coal-rock combined body with different height ratios," *Advances in Civil Engineering*, vol. 2020, Article ID 8842206, 14 pages, 2020.

[23] Q. Yin, J. Wu, C. Zhu, M. He, Q. Meng, and H. Jing, "Shear mechanical responses of sandstone exposed to high temperature under constant normal stiffness boundary conditions," *Geomechanics and Geophysics for Geo-Energy and Geo-Resources*, vol. 7, no. 2, p. 35, 2021.

[24] F. Gan, Y. Kang, X.-c. Wang et al., "Investigation on the failure characteristics and fracture classification of shale under Brazilian test conditions," *Rock Mechanics and Rock Engineering*, vol. 53, no. 7, pp. 3325–3340, 2020.

[25] C. X. Zhang, B. Dai, and W. U. Qiu-Hong, "Analysis on deformation properties and energy dissipation of rock unloading failure process under different stress path," *Journal of Safety Science and Technology*, vol. 10, no. 10, pp. 35–40, 2014.

[26] F. Wu, H. Zhang, Q. Zou, C. Li, J. Chen, and R. Gao, "Viscoelastic-plastic damage creep model for salt rock based on fractional derivative theory," *Mechanics of Materials*, vol. 150, Article ID 103600, 2020.

[27] F. Gan, X. Wang, M. Wang et al., "Experimental investigation of thermal cycling on fracture characteristics of granite in a geothermal-energy reservoir," *Engineering Fracture Mechanics*, vol. 235, Article ID 107180, 2020.

[28] X. Hao, L. Yuan, Y. Li et al., "Lateral deformation characteristics of coal with bump tendency based on uniaxial compression experiment," *Zhongguo Kuangye Daxue Xuebao/Journal of China University of Mining and Technology*, vol. 47, no. 1, pp. 129–136, 2018.

[29] H. . Wagner, "Determination of the Complete Load-Deformation Characteristics of Coal Pillars," *Congress of the International Society for Rock Mechanics 3*, Lisboa: Laboratório nacional de engenharia civil, Lisbon, Portugal, 1974.

[30] Xianjie, L. Yuan, Y. Li et al., "Lateral deformation characteristics of coal with bump tendency based on uniaxial compressions experiment," *Journal of China university of mining & technology*, vol. 47, no. 1, pp. 129–136, 2018.

[31] pengbo Lv, *Study on Mechanical Characteristics and Damage Laws of Coal Samples under Different loading*, Henan Polytechnic University, Jiaozuo, China, 2018.

[32] L. I. Bin-Yu, M. Bai, and Y. C. Bian, "Analysis on Support Reinforcement for Lateral Deformation of Coal Transporting Trestle," *Coal Engineering*, vol. 47, no. 7, pp. 33–35, 2015.

[33] C. Zhu, M. C. He, X. H. Zhang, Z. G. Tao, Q. Yin, and L. F. Li, "Nonlinear mechanical model of constant resistance and large deformation bolt and influence parameters analysis of constant resistance behavior," *Rock and Soil Mechanics*, vol. 42, no. 7, pp. 1911–1924.

[34] F. Wang, S. Yin, A. Guo et al., "Frame structure and engineering applications of the multisource system cloud service platform of monitoring of the soft rock tunnel," *Geofluids*, vol. 2021, no. 3, 15 pages, Article ID 6672732, 2021.

Research Article

Influence of Chamber Geometrical Parameters on Suppressing Explosion Propagation

Zhuo Yan ![ORCID],[1,2,3] **Shengli Guo,**[3] **Shujie Yuan** ![ORCID],[3] **and Chaomin Mu** ![ORCID][3]

[1]*State Key Laboratory of Mining Response and Disaster Prevention and Control in Deep Coal Mines,
Anhui University of Science and Technology, Huainan 232001, China*
[2]*Institute of Energy, Hefei Comprehensive National Science Center, Anhui, Hefei 230031, China*
[3]*School of Safety Science and Engineering, Anhui University of Science and Technology, Huainan 232001, China*

Correspondence should be addressed to Shujie Yuan; yuansj@aust.edu.cn and Chaomin Mu; chmmu@mail.ustc.edu.cn

In this article, the effect of a chamber's geometrical parameters on suppressing gas explosion propagation was studied. Three rectangular chambers were used in the study, with a constant length of 0.5 m, a constant height of 0.2 m, and a variable width of 0.3 m, 0.5 m, and 0.8 m; each chamber was installed in a pipeline system for experimental research. The experimental results showed that when the chamber length and height were fixed at 0.5 m and 0.2 m, respectively, the suppression effect of the chamber on the explosion shockwave improves with the increase in the chamber width; when the chamber width increases to 0.8 m, the chamber has suppressive effect on explosion shockwave propagation. It was also found that the suppression effect of the chambers on the explosion flame improves with the increase in the chamber width; when the width of the chamber is 0.5 m, the chamber effectively suppresses explosion flames. Based on the experimental results, a numerical model was established to simulate the suppression effect of five types of chambers with a length, width, and height of $0.5 \, m \times 0.3 \, m \times 0.2 \, m$, $0.3 \, m \times 0.5 \, m \times 0.2 \, m$, $0.5 \, m \times 0.5 \, m \times 0.2 \, m$, $0.5 \, m \times 0.8 \, m \times 0.2 \, m$, and $0.8 \, m \times 0.5 \, m \times 0.2 \, m$, respectively. The numerical simulation results indicated that when the chamber length and height are constant at 0.5 m and 0.2 m, respectively, the suppressive effect of the chamber on the shockwave improves as the chamber width increases; when the chamber width increases to 0.8 m, the shockwave overpressure at the chamber outlet is attenuated by 10.61%, indicating that the chamber suppresses the propagation of explosion shockwave, which is consistent with the experimental results obtained in the study. It was also found that when the chamber width and height were constant at 0.5 m and 0.2 m, respectively, as the chamber length increases, the overpressure increases first and then weakens. When the chamber length increases to 0.8 m, the overpressure at the chamber outlet is attenuated by −14.16%, indicating that the chamber is not able to suppress the propagation of explosion shockwave. Finally, a numerical simulation of the propagation process of a methane-air mixture and explosion flames in different chambers was performed to analyse the effect of chamber geometrical parameters on explosion suppression effect.

1. Introduction

When gas explosions occur in coal mine tunnels and urban underground pipeline systems, a strong ultrahigh temperature flame and an enormous shockwave overpressure are generated instantaneously, which then rapidly propagate through the confined space of the tunnel or pipeline system, destroying surrounding facilities, causing a large number of casualties and property losses, and having a highly detrimental social and economic impact [1]. The development of

explosion and flame suppression technology is important for the prevention and control of gas explosion accidents in mining tunnels and underground urban pipeline systems. To this end, much theoretical research and experimental investigations have been conducted in this field both at home and abroad; for example, Thomas, Pawel Kosinski, Mikhail Krasnyansky, Hermanns, Lu Shouxiang, Bi Mingshu, Yu Minggao, Xu Hongli, Wang Xishi, Wen Hu, Luo Zhenmin et al. [2–12] have conducted successful studies on gas explosion suppression using water mist, powder inhibitors, and

inert gas technology. Shao Jiwei et al. [13] demonstrated experimentally that porous materials have an obvious explosion suppression effect. Zhao Kai et al. [14] found that the hollow cylindrical shell structure has a strong shock wave-absorbing and energy-absorbing effect, and it can withstand damage from repeated explosions. Wu and Jiang [15] designed a vacuum chamber based on the negative pressure principle of vacuum and installed it on an experimental pipeline; the study found that when the explosion propagated in the pipeline, the shockwave and flame produced by the explosion were sucked into the vacuum chamber owing to the negative pressure effect, thereby significantly suppressing the explosion overpressure and flames. Shao et al. [16–18] found that the effect of the vacuum chamber in suppressing gas explosion depends on the volume of vacuum chamber; when the chamber volume exceeds the critical volume, the vacuum chamber can effectively suppress gas explosions. On the contrary, when the chamber volume is smaller than the critical volume, not only does the vacuum chamber have no effect in suppressing gas explosion but also the shockwave overpressure and flame intensity are actually stronger than when no vacuum chamber is used. In addition, the vacuum degree has no obvious influence on the effect of the vacuum chamber in suppressing gas explosion. Li et al. [19] used rectangular chambers of different sizes installed on a 36 m-long large-scale pipeline system for gas explosion experiment to conduct an experimental research, and they found that the chamber attached to the pipeline system has effect on shockwave suppression.

In practical applications, the chamber height is usually consistent with the height of a mine tunnel or an underground pipeline system, and the chamber size is changed by adjusting its length or width. However, there are few studies on how the change of chamber length or width affects its detonation suppression performance. The aim of this study is to explore the influence of the chamber width or length on its explosion suppression effect. To this end, we conducted a series of experiments and numerical simulations under the following two sets of conditions: (1) with the chamber height and length fixed and with variable width, and (2) with the chamber height and width fixed and with variable length, in order to better understand the effect of the geometric parameters of different rectangular chambers on the propagation of explosion shock-wave and to analyse the effect of the geometric parameters of chambers on their effectiveness in gas explosion suppression.

2. Experimental Study on the Explosion Suppression Effect of Chambers

In this study, a series of experiments was carried out to investigate shockwave overpressure and flame data and to analyse the suppression effect of different chambers on shockwave propagation in gas explosions. To this end, three rectangular chambers with fixed height and length and a gradually changing width were installed in a gas pipeline system; the length, width, and height of the three chambers were 0.5 m × 0.3 m × 0.2 m, 0.5 m × 0.5 m × 0.2 m, and 0.5 m × 0.8 m × 0.2 m, respectively, and the wall thickness of all three chambers was 0.01 m.

2.1. Experimental System. The design of the experimental system is shown in Figure 1. The 36 m pipeline system for gas explosion experiment consists of five parts: an explosion pipeline section, premixed gas preparation system, ignition system, data acquisition system, and chamber.

① The experimental pipeline is constructed of steel pipes with a diameter of 0.2 m and a thickness of 0.01 m, with a pressure resistance of 20 MPa. The pipes are connected by flange plates with rubber and asbestos gaskets to ensure that the pipeline section is airtight. ② The premixed gas preparation system consists of a gas tank, a vacuum pressure gauge, an air compressor, and a pump for circulating gas. The gas used in the present experiment is high-purity methane (over 99.9% purity). ③ The ignition system consists of a power supply, a fuse, conducting wires, and an ignition electrode. The electrode is placed on the flange at the end of the pipeline section, where it is ignited by the fuse; the ignition voltage is 36 V, and the ignition energy is 10 J. ④ The data acquisition system consists of pressure sensors, flame sensors, a flow transmitter, a data collector, and an operating unit. The pressure sensors P_1 and P_2, which have a detection range of 0 to 3 MPa with an accuracy of 0.5% of FS, are placed at a distance of 13.25 m (0.25 m from the chamber's inlet) and 13.75 + x m (0.25 m from the chamber's outlet, x is the chamber's length), respectively, from the ignition electrode. The flame sensors F_1 and F_2 have a maximum sampling frequency of 20 Msps with an accuracy of 0.1% of FS; they are placed at positions corresponding to the pressure sensors, respectively. ⑤ The length, width, and height of the three chambers are 0.5 m × 0.3 m × 00.2 m, 0.5 m × 0.5 m × 00.2 m, and 0.5 m × 0.8 m × 00.2 m, respectively, as shown in Figure 2.

2.2. Experiment Design. Before starting the experiment, the pipes of the detonation system were connected, and a 0.4 mm-thick polyethylene film was used to seal the detonation segment at a distance of 11 m from the ignition electrode. A positive displacement air compressor was then used to test the airtightness of each joint, and a vacuum pump was used to evacuate the air from the pipes. Next, a methane-air mixture was prepared based on Dalton's partial pressure principle, so that a 10% concentration methane-air mixture was used in each experiment, which is the optimal concentration to produce the highest explosion intensity under experimental conditions [20]. After preparing the gas mixture, a gas circulating pump was used to mix air and methane in the detonation segment into a homogenous mixture for 10 to 20 min. After completing the mixing process, the ignition system was used to initiate the explosion. Once the explosion was initiated, the flame sensors and pressure sensors began to collect data, which were processed using the testing software DAP to generate flame- and pressure-change curves. On completion of the experiment, an air compressor was used to force out any residual exhaust from the pipeline section.

The experiments are divided into four categories: (1) the propagation of gas explosion in a pipeline section without a chamber, where the chamber in Figure 1 is
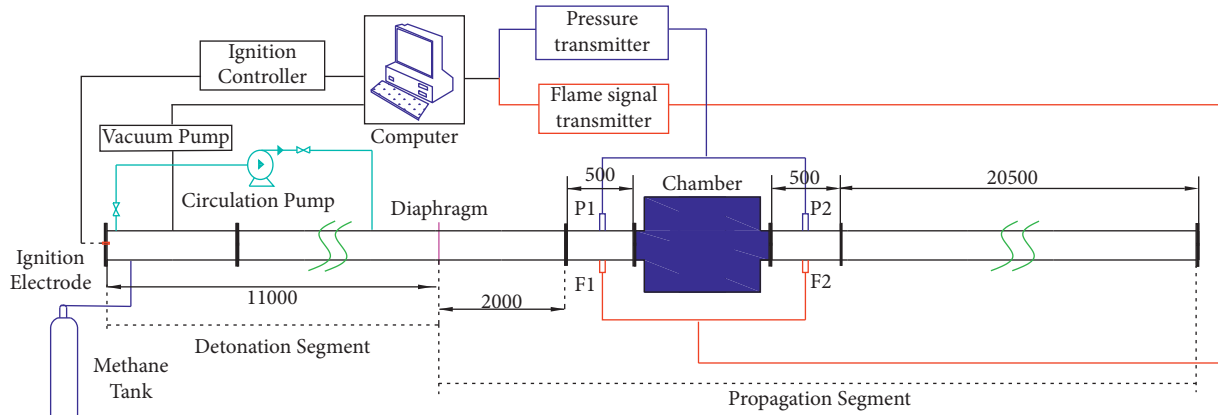
FIGURE 1: Chart of experimental system for gas explosion.

FIGURE 2: Experimental rectangular chambers.

replaced by a 0.2 m-diameter pipe with a length of 0.5 m; (2) gas explosion suppression using a rectangular chamber of L0.5 m × W0.3 m × H0.2 m; (3) gas explosion suppression using a chamber of L0.5 m × W0.5 m × H0.2 m; and (4) gas explosion suppression using a chamber of L0.5 m × W0.8 m × H0.2 m.

2.3. Experimental Results and Analysis

2.3.1. Suppression of Explosion Shockwave by Chambers with Different Geometric Parameters. Figure 3 shows the overpressure-time curve of the gas explosion shockwave at each monitoring point of the propagation experiment of gas explosion in a pipeline section without a chamber and the explosion suppression experiments using different-size chambers.

Figure 3(a) shows that, in the pipeline section without a chamber, the maximum overpressure of the shockwave at the points P1 and P2 is 0.3208 MPa and 0.3319 MPa, respectively; the attenuation ratio of the shockwave overpressure at P2 can be expressed as (0.3208–0.3319)/0.3208 = −3.46%, which means that from P1 to P2, the shockwave overpressure increases, so the explosion overpressure is in the rising phase.

It is evident from Figure 3(b) that when the chamber of L0.5 *m* × W0.3 *m* × H0.2 m is used in the experiment, the maximum overpressure at the points P1 and P2 is 0.4367 MPa and 0.4605 MPa, respectively, and after passing through the chamber, the explosion overpressure at P2 increases slightly and is attenuated by −5.45%. Compared

with the pipeline section without a chamber, the relative overpressure attenuation ratio measured at P1 and P2 can be calculated as (0.3208–0.4367)/0.3208 = −36.15% and (0.3319–0.4605)/0.3319 = −38.7%, respectively, which shows that the chamber actually increased the explosion overpressure.

Figure 3(c) shows that when the chamber of L0.5 m × W0.5 m × H0.2 m is used in the experiment, the maximum overpressure at P1 and P2 is 0.418 MPa and 0.42 MPa, respectively, and after passing the chamber, the magnitude of the overpressure does not change significantly; the overpressure at P2 is attenuated by only −0.47%. Compared with the pipeline section without a chamber, the relative overpressure attenuation ratio at P1 and P2 is −30.3% and −26.5%, respectively, which shows that this chamber causes an increase in the overpressure.

Figure 3(d) shows that when the chamber of L0.5 m × W0.8 m × H0.2 m is used, the maximum overpressure at P1 and P2 is 0.3509 MPa and 0.2927 MPa, respectively, and after the shockwave passes through the chamber, significant overpressure attenuation occurs at P2, with an attenuation ratio of 16.58%. Compared with the pipeline section without a chamber, the overpressure attenuation ratio at P1 and P2 is −9.38% and 11.8%, respectively. Although the shockwave overpressure at the chamber inlet (P1) increased, the shockwave overpressure at the chamber outlet (P2) was significantly attenuated, which shows that this chamber has an attenuation effect on the explosion overpressure.

The results of these experiments show that when the chamber length and height are constant at 0.5 m and 0.2 m,

FIGURE 3: Explosion overpressure-time curve at the chamber inlet and outlet. (a) Pipeline section without a chamber; (b) chamber of L0.5 m × W0.3 m × H0.2 m; (c) chamber of L0.5 m × W0.5 m × H 0.2 m; (d) chamber of L0.5 m × W0.8 m × H0.2 m.

respectively, the effect of the chamber on suppressing explosion propagation improves with the increase in the chamber width. When the chamber width is increased to 0.8 m, the chamber has a suppressing effect on the explosion shockwave propagation.

2.3.2. Suppression of Explosion Flame Propagation by Chambers with Different Geometric Parameters. Figure 4 shows the evolution process of the explosion flame at each monitoring point in the experiment of gas explosion in a pipeline section without a chamber and the explosion suppression experiment using different chambers. The flame size is defined as the time integral of the optical signal collected by the flame sensor.

Figure 4(a) shows that, in the experiment of gas explosion in a pipeline section without a chamber, the flame size measured at the points F1 and F2 is 0.0613 and 0.0579,

respectively, which shows that a slight suppression of the flame occurred at F2, with an attenuation ratio of 5.54%.

In Figure 4(b), in the explosion suppression experiment with the chamber of L0.5 m × W0.3 m × H0.2 m, the flame size measured at the points F1 and F2 is 0.0614 and 0.0594, respectively, which means that after passing through the chamber, the flame at F2 was slightly attenuated, with an attenuation ratio of 3.26%. Compared with the pipeline section without a chamber, the explosion flame measured at points F1 and F2 in this experiment was attenuated by −0.16% and 2.5%, respectively, which shows that the flame size did not change significantly.

Figure 4(c) shows that, with the chamber of L0.5 m × W0.5 m × H0.2 m, the flame size measured at the points F1 and F2 is 0.0409 and 0.0325, respectively, which means that after passing through the chamber, the flame at F2 was significantly attenuated, by approximately 20.5%. Compared with the pipeline section without a chamber, the

(a)

(b)

(c)

(d)

FIGURE 4: Explosion flame-time curve at the chamber inlet and outlet. (a) Pipeline section without a chamber; (b) chamber of L0.5 m × W0.3 m × H0.2 m; (c) chamber of L0.5 m × W0.5 m × H0.2 m; (d) chamber of L0.5 m × W0.8 m × H0.2 m.

explosion flame size at points F1 and F2 was attenuated by 33.27% and 43.8%, respectively. This high attenuation ratio shows that the chamber used in this experiment had a strong suppressing effect on the propagation of the explosion flames.

Figure 4(d) shows that when the chamber of L0.5 m × W0.8 m × H0.2 m is used for flame suppression, the flame magnitude at the points F1 and F2 is 0.0402 and 0.0204, respectively, which means that the flame was significantly attenuated at F2, with an attenuation ratio of 49.2%. Compared with the pipeline section without a chamber, the explosion flame size at points F1 and F2 was attenuated by 34.4% and 64.7%, respectively. This high attenuation ratio shows that the chamber used in this experiment had a strong suppressing effect on the gas explosion flames propagation.

The above experimental results show that when the chamber length and height are constant at 0.5 m and 0.2 m, respectively, the suppressing effect of the chamber on the

propagation of the explosion flames improves as the chamber width increases. When the chamber width is 0.3 m, the chamber has no suppressing effect on flame propagation; when the chamber width is increased to 0.5 m, the chamber has a suppressing effect on flame propagation, and as the chamber width is increased further, its suppression effect is enhanced.

3. Numerical Simulation of the Explosion Suppression Effect of Chambers with Different Geometric Parameters

To further explore the influence rule of chamber geometry on its explosion suppression effect, a numerical model based on the experimental results described in the preceding section was established, and a numerical simulation of the gas explosion propagation process was carried out using five types of chambers with a length, width, and

height of 0.5 m × 0.3 m × 0.2 m, 0.5 m × 0.5 m × 0.2 m, 0.5 m × 0.8 m × 0.2 m, 0.3 m × 0.5 m × 0.2 m, and 0.8 m × 0.5 m × 0.2 m, respectively.

3.1. Geometric Model and Boundary Conditions.
The geometric model and meshing are shown in Figure 5. The X, Y, and Z dimensions of the simulated area are 36 m, 0.8 m (or 0.3 m or 0.5 m), and 0.2 m, respectively, and the number of mesh cells in the corresponding directions is 1800, 40 (or 15 or 25), and 10. In this model, the 11 m-long detonation segment is on the left side of the model; the detonation segment is a pipe filled with a premixed 10% methane-air gas mixture. The propagation segment is on the right side of the model. The propagation segment is 22.5 m long and consists of a pipe with an outer diameter of 0.2 m and a rectangular chamber. The two pressure monitoring points P1 and P2 are located at a distance of 13.25 m (0.25 m from the chamber's inlet) and 13.75 + x m (0.25 m from the chamber's outlet, x is the chamber's length along the X-axis), respectively, from the ignition electrode.

The initial conditions of the model are as follows: The initial pressure, initial density gradient, and initial temperature in the pipeline are 0.1 MPa, 0, and 293 K, respectively. The boundary conditions of the model are as follows: The inner walls of the pipeline and chamber allow for adiabatic flow with no slip.

3.2. Mathematical Model and Numerical Method.
The model is based on the following assumptions: The gas explosion is an adiabatic expansion process of an ideal gas; the gas explosion reaction is assumed to be a single-step reversible process; the thermal radiation is ignored; and the fluid-solid coupling effect between the impact flow and the solid inner wall is ignored.

The gas explosion process satisfies the conditions of the conservation of energy, mass, and momentum equations, as well as of the turbulent kinetic energy, turbulent energy dissipation rate, fuel component, and mixture component equations, which can all be expressed in a unified form as [21]

$$\frac{\partial}{\partial t}(\rho\phi) + \frac{\partial}{\partial x_j}(\rho u_j \phi) = \frac{\partial}{\partial x_j}\left(\Gamma\phi \frac{\partial\phi}{\partial x_j}\right) + S\phi,$$

$$\Gamma\phi = \frac{\mu_{eff}}{\sigma\phi}, \tag{1}$$

where t is time, ρ is the density, ϕ is a general variable, $\partial/\partial t(\rho\phi)$ is an unsteady term, u_j is the velocity component in the x-direction, x_j represents the spatial coordinates ($j = 1,2,3, \ldots$), $\partial/\partial x_j(\rho u_j \phi)$ is a convection term, $\Gamma\phi$ is the exchange coefficient of the flux ϕ, μ_{eff} is the effective viscosity, $\sigma\phi$ is the Prandtl number, $\partial/\partial x_j(\Gamma\phi(\partial\phi/\partial x_j))$ is a diffusion term, and $S\phi$ is the energy source term.

In the numerical simulation, the k-ε turbulence model is used to deal with turbulence in the combustion process; the wall surface function is adopted to treat the variations in the flow field close to the wall area. The control volume integration method, the staggered grid method, and the semi-implicit method for pressure linked equations (SIMPLE) algorithm were used to solve the pressure-velocity coupling based on the segregated approach; the incremental method and the backward difference method were used to discretize the control equations of the chemical reaction field, the material structure field, and the chemical flow field [22].

3.3. Numerical Simulation Results.
Figure 6 shows the explosion overpressure-time curve measured at each monitoring point of the pipeline section without a chamber and with different-size chambers; the maximum value of shockwave overpressure and the attenuation ratio at each monitoring point are listed in Table 1.

Comparing the experimental results with the numerical simulation results, the experimental overpressure measured at each monitoring point is slightly greater than its simulated counterparts. This is because of the polyethylene film installed between the propagation segment and the detonation segment in the experiment; the turbulence generated when the membrane is broken accelerates the reaction. At the same time, owing to the limitations of the processing technology, the inner wall of the pipeline and chambers as well as the connecting joints are not perfectly smooth and flat. For these reasons, the experimental values of the overpressure are greater than the simulated values. Nevertheless, the experimental results and simulation results show consistent trends of explosion overpressure propagation.

3.3.1. Suppression of Shockwave Propagation by Variable-Width Chambers with Constant Length of 0.5 m and Height of 0.2 m.
From Table 1 and Figures 6(a), 6(c)–6(e), it can be observed that when the chamber of L0.5 m × W0.3 m × H0.2 m is used, the attenuation ratio of the overpressure after passing through the chamber is −3.85%. In addition, compared with the corresponding locations on the pipeline section without a chamber, the gas explosion overpressure attenuation ratio at the chamber inlet P1 and outlet P2 is −36.19% and −38.04%, respectively, which shows that this chamber enhances the propagation of explosion shockwave. When the chamber of L0.5 m × W0.5 m × H0.2 m is used, the overpressure attenuation ratio after passing through the chamber is 0.88%, and compared with the pipeline section without a chamber, the attenuation ratio at the inlet P1 and outlet P2 is −30.40% and −26.15%, respectively, which shows that this chamber enhances the propagation of the shockwave. When the chamber of L0.5 m × W0.8 m × H0.2 m is used, the overpressure attenuation ratio after passing the chamber is 13.73%, and compared with the pipeline section without a chamber, the attenuation ratio at P1 and P2 is −6.16% and 10.61%, respectively. Although the shockwave overpressure at the chamber inlet was increased slightly, it was significantly weaker at the chamber outlet, which shows that this chamber had a suppression effect on the explosion overpressure.
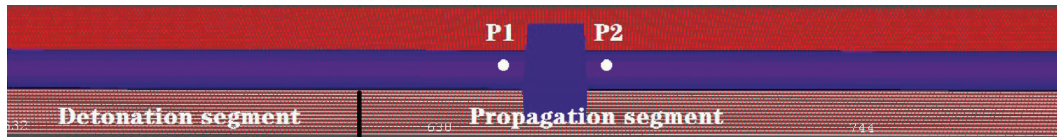
FIGURE 5: Geometric model and meshing.

The above results show that when the chamber length and height are constant at 0.5 m and 0.2 m, respectively, its explosion suppression effect improves with an increase in the chamber width; when the chamber width increases to 0.8 m, the chamber can effectively suppress the propagation of explosion shockwave. The numerical simulation results and the experimental results are consistent, which means that the numerical model is reliable.

3.3.2. Suppression of Shockwave Propagation by Variable-Length Chambers with Constant Width of 0.5 m and Height of 0.2 m. From Table 1 and Figures 6(a), 6(b), 6(d), and 6(f), it can be observed that for the chamber of L0.3 m × W0.5 m × H0.2 m, the overpressure is attenuated by −0.64% after passing through the chamber, and compared with the pipeline section without a chamber, the shockwave overpressure at the inlet P1 is attenuated by −17.46% and at the outlet P2 is attenuated by −16.01%, which shows that this chamber enhanced the propagation of the shockwave. For the chamber of L0.5 m × W0.5 m × H0.2 m, the overpressure is attenuated by 0.88% after passing through the chamber, and compared with the pipeline section without a chamber, the overpressure at P1 is attenuated by −30.40%, and at P2, overpressure is attenuated by −26.15%, which indicates that this chamber also enhanced the propagation of the explosion shockwave. For the chamber of L0.8 m × W0.5 m × H0.2 m, the overpressure attenuation ratio after passing through the chamber is 8.77%, and compared with the pipeline section without a chamber, the overpressure is attenuated by −33.74% at P1 and by −14.16% at P2, which shows that this chamber also enhanced the propagation of shockwave.

These results show that when the chamber height and width are constant at 0.2 m and 0.5 m, respectively, the chamber has an enhancing effect on shockwave at the inlet, and the shockwave overpressure increases as the chamber length increases. The enhancement effect on the overpressure is stronger at the chamber outlet and weaker at its inlet, and as the chamber length increases, the shockwave overpressure first increases and then decreases. Therefore, the three types of chambers with a constant height of 0.2 m and width of 0.5 m are not effective in suppressing the propagation of explosion shockwave.

4. Influence of Chamber Geometrical Parameters on Effect of Explosion Propagation Suppression and Its Mechanism Analysis

The propagation of the explosion flame and the premixed gas in the chamber can be obtained from the numerical simulation. Figure 7 shows the propagation process of the

explosion flame in different chambers at certain times; the colour legend on the far right shows the flame temperature. Figure 8 shows the propagation of the premixed gas in the chamber at the times corresponding to those in Figure 7; the colour bar on the far right shows the mass fraction of methane. It is evident from Figures 7 and 8 that the premixed gas enters the chamber under the impulse of the flame precursor shockwave. Owing to the sudden expansion of the propagation space, the premixed gas is dissipated in the chamber under the action of the shockwave and advances rapidly in the same direction as the propagation segment. Some of the dissipated gas develops turbulent flow under the action of the shockwave, and some of it is diluted by the air in the chamber and ignited by the flame immediately afterwards. This causes an explosion inside the chamber, in which the secondary shockwave generated by the explosion collides with the initial shockwave and then propagates out of the chamber [23]. Therefore, the strength of the secondary shockwave directly affects the explosion suppression effect of the chamber, and the strength of the secondary shockwave is determined by the amount of methane consumed in the chamber.

Figure 9 shows the change over time in the methane mass concentration measured at the outlets of different chambers. The time integral values can be used to characterise the remaining amount of methane after the premixed gas passes through the chamber. Accordingly, the residual amount of methane for the chambers of L0.3 m × W0.5 m × H 0.2 m, L0.5 m × W0.3 m × H0.2 m, L0.5 m × W0.5 m × H 0.2 m, L0.5 m × W0.8 m × H0.2 m, and L0.8 m × W0.5 m × H0.2 m is 0.09337, 0.07571, 0.07615, 0.11193, and 0.04318, respectively. Because the same amount of methane enters each chamber, if there is a reduction in the residual amount of methane after the gas mixture passes through the chamber, then it follows that the more methane reacts in the chamber, the greater will be the explosion energy that is released, and a stronger explosion shockwave will be produced. Figure 9(a) shows that when the chamber length is constant at 0.5 m, as the chamber width increases, the residual amount of methane at the chamber outlet gradually increases; for example, after passing through the chambers of L0.5 m × W0.5 m × H0.2 m and L0.5 m × W0.8 m × H0.2 m, a secondary methane-air mixture appears, but its mass fraction is below the lower explosive limit. The reason for this is that after the premixed methane-air gas enters the chamber, part of the premixed gas is diluted by the air present in the chamber, causing it to lose its explosive characteristics. As the chamber width increases, the amount of methane that reacts in the chamber decreases; hence, the secondary shockwave generated in the reaction weakens. In addition, the explosion relief capacity
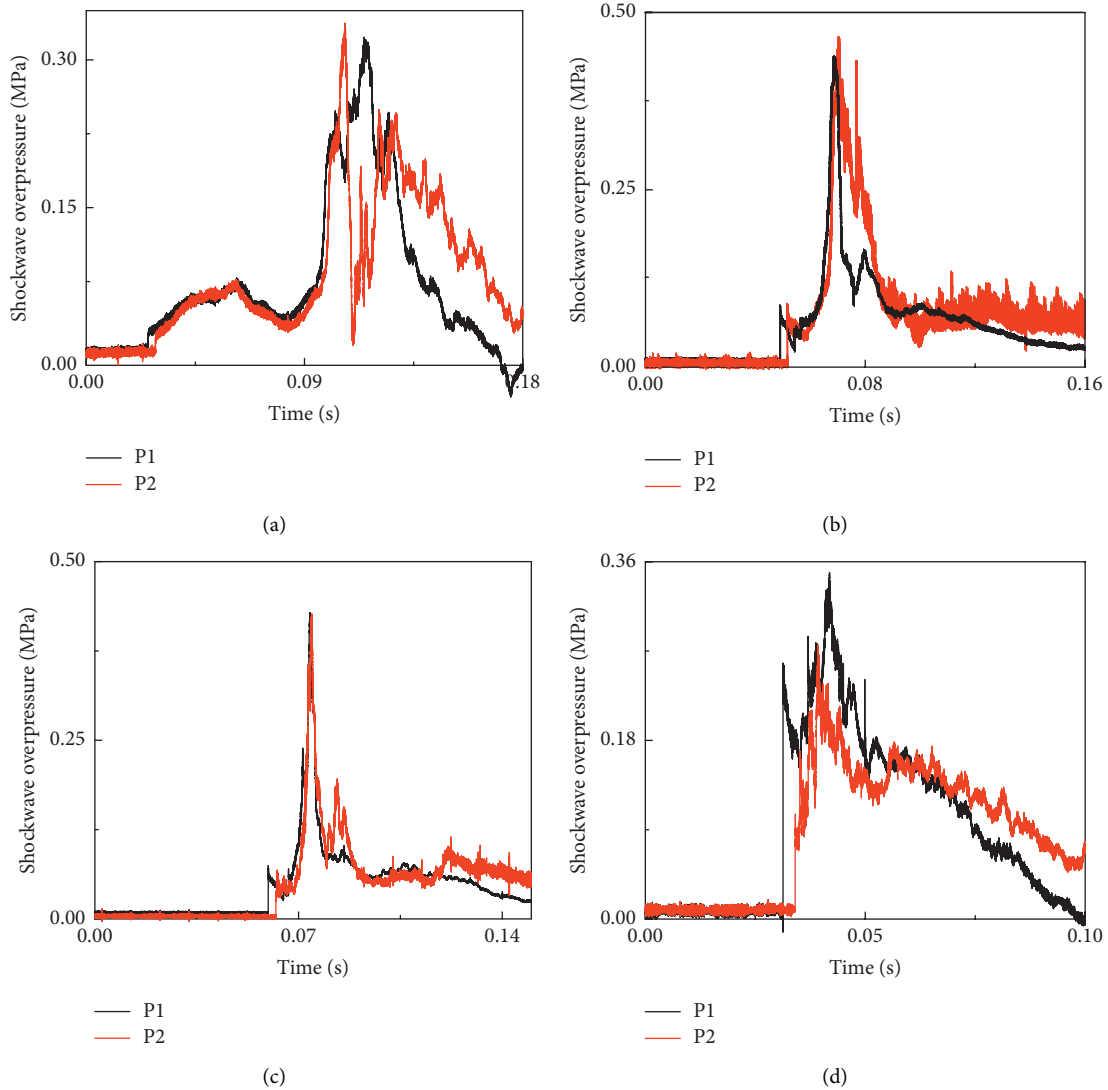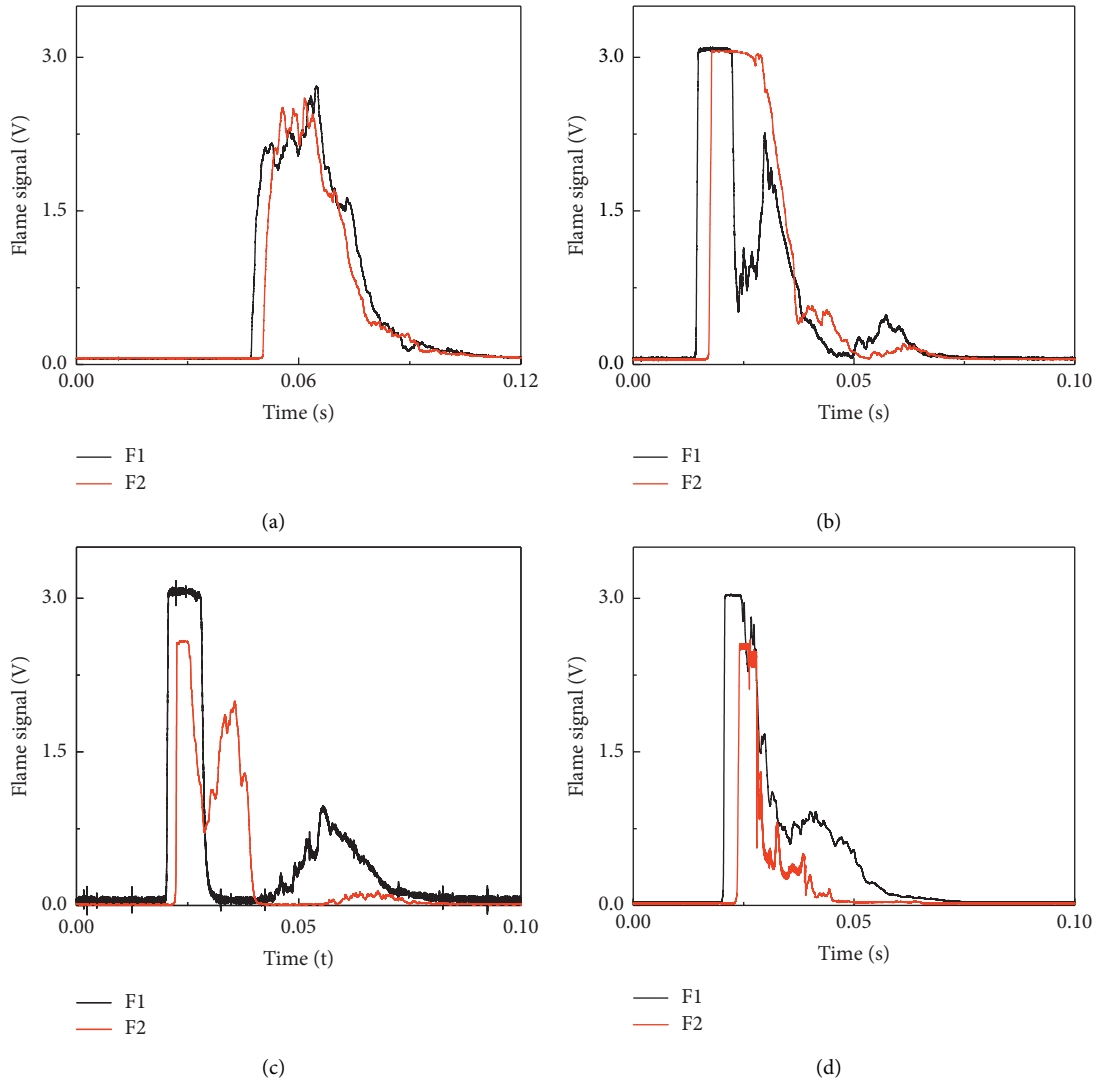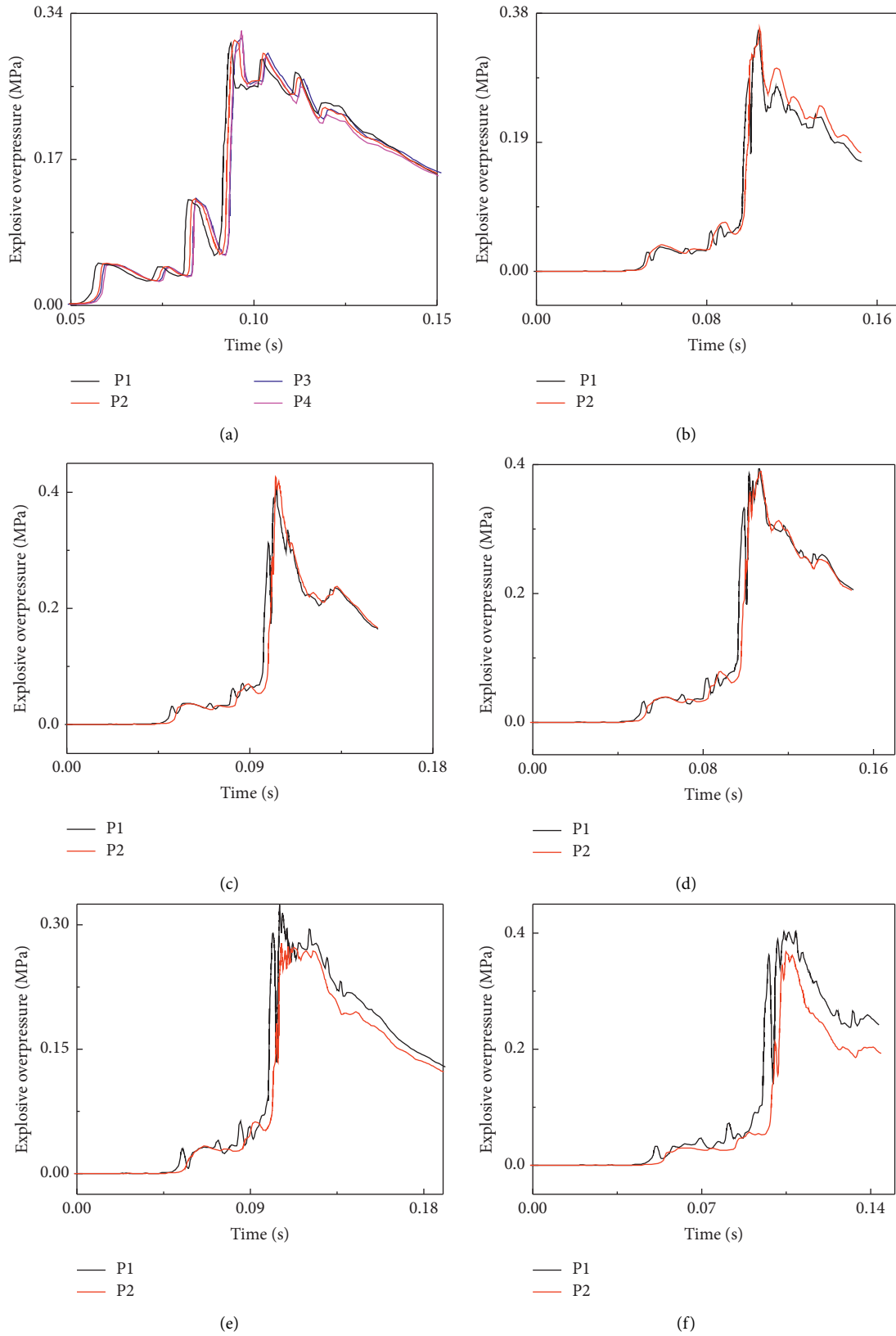
FIGURE 6: Explosion overpressure-time curve at the chamber inlet and outlet. (a) Pipeline section without a chamber; (b) chamber of L0.3 m × W0.5 m × H0.2 m; (c) chamber of L0.5 m × W0.3 m × H0.2 m; (d) chamber of L0.5 m × W0.5 m × H0.2 m; (e) chamber of L0.5 m × W0.8 m × H0.2 m; (f) chamber of L0.8 m × W0.5 m × H0.2 m.

TABLE 1: Maximum overpressure and overpressure attenuation ratio at each monitoring point of the pipeline section without a chamber and with different chambers.

Chamber dimensions (length × width × height)	Maximum overpressure at each monitoring point (MPa)				Overpressure attenuation ratio after passing the chamber (%)	Overpressure attenuation ratio at chamber inlet relative to no-chamber pipeline (%)	Overpressure attenuation ratio at chamber outlet relative to no-chamber pipeline (%)
	13.25 m from the ignition electrode	14.05 m from the ignition electrode	14.25 m from the ignition electrode	14.55 m from the ignition electrode			
Pipeline section only (no chamber)	0.3053	0.3111	0.3128	0.3263	—	—	—
0.3 m × 0.5 m × 0.2 m	0.3586	0.3609	—	—	−0.64	−17.46	−16.01
0.5 m × 0.3 m × 0.2 m	0.4158	—	0.4318	—	−3.85	−36.19	−38.04
0.5 m × 0.5 m × 0.2 m	0.3981	—	0.3946	—	0.88	−30.40	−26.15
0.5 m × 0.8 m × 0.2 m	0.3241	—	0.2796	—	13.73	−6.16	10.61
0.8 m × 0.5 m × 0.2 m	0.4083	—	—	0.3725	8.77	−33.74	−14.16
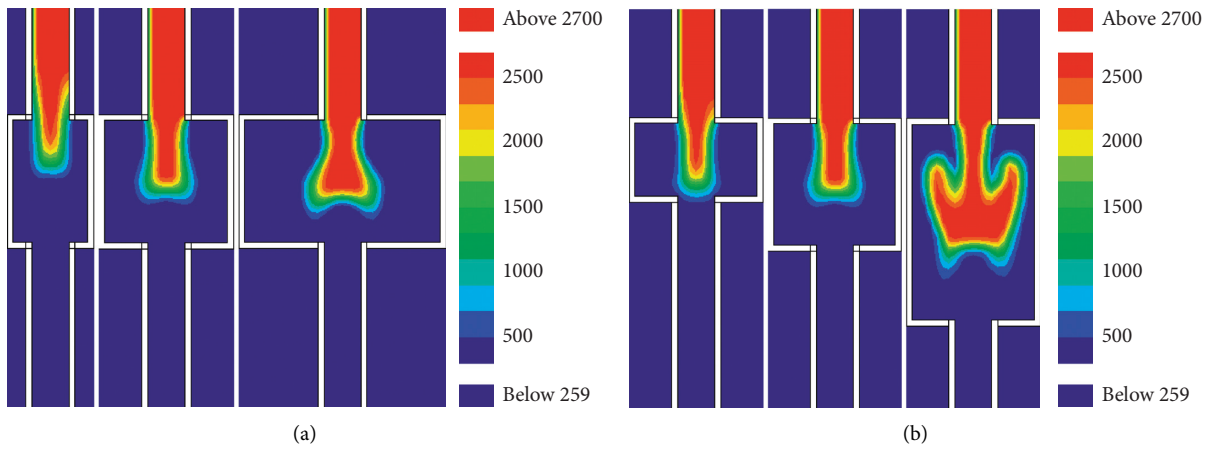
FIGURE 7: Propagation of explosion flame in chambers with different geometric parameters. (a) Variable-width chambers (0.2 m high and 0.5 m long); (b) variable-length chambers (0.2 m high and 0.5 m wide).
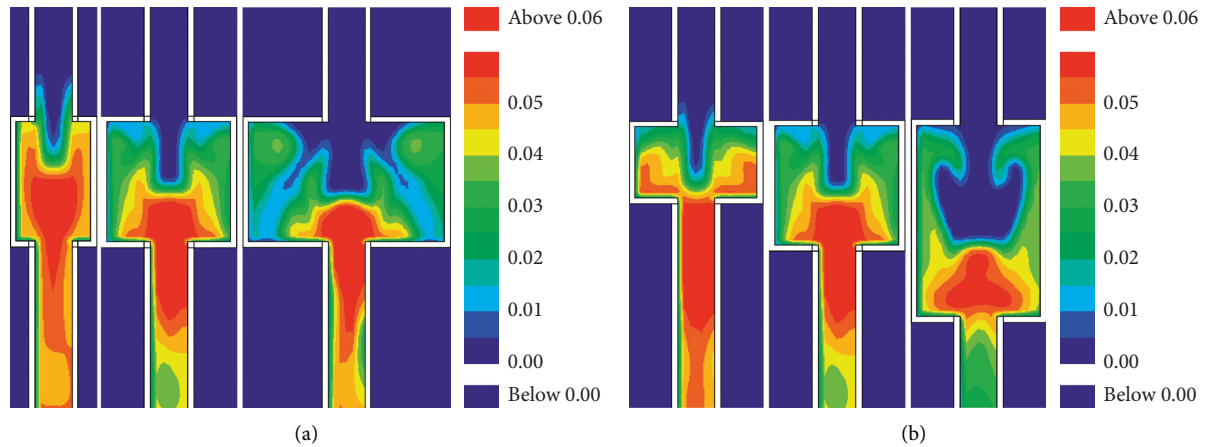
FIGURE 8: Propagation of premixed methane in chambers with different geometric parameters. (a) Variable-width chambers (0.2 m high and 0.5 m long); (b) variable-length chambers (0.2 m high and 0.5 m wide).

of the chamber increases rapidly with the increase in the chamber width, so when the chamber's relief capacity is sufficient to accommodate the secondary shockwave, the chamber has an explosion suppression effect. Accordingly, when the chamber width increases to 0.8 m, the chamber can effectively suppress the propagation of explosion shockwave. It is evident from Figure 9(b) that when the chamber width is fixed at 0.5 m, as the chamber length increases, the amount of premixed gas participating in the chemical reaction inside the chamber gradually increases, and the secondary
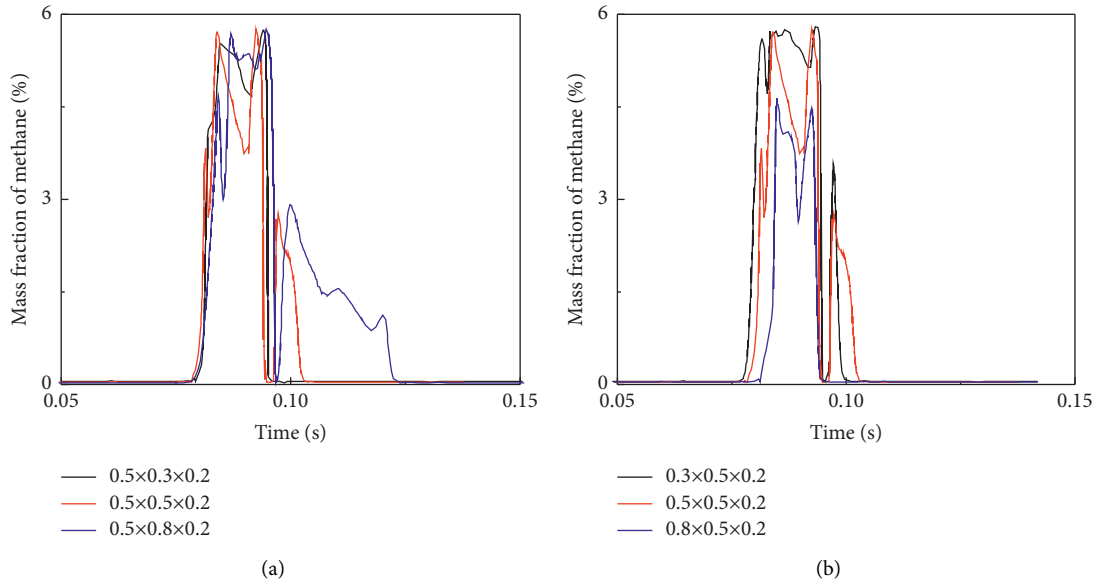
FIGURE 9: Methane mass concentration at the outlet of chambers with different geometric parameters. (a) Variable-width chambers (0.2 m high and 0.5 m long); (b) variable-length chambers (0.2 m high and 0.5 m wide).

shockwave inside the chamber expands. At the same time, even though the explosion relief capacity of the chamber increases rapidly with the increase in its length, its relief capacity is still insufficient to suppress the secondary shockwave generated by the chemical reaction inside the chamber. Therefore, none of the three chambers with different lengths and a constant width of 0.5 m are effective in suppressing the propagation of shockwave from gas explosions.

5. Conclusions

(1) In this study, an experiment involving three types of chambers with fixed heights and lengths and variable widths (with the length, width, and height of $0.5 \, \text{m} \times 0.3 \, \text{m} \times 0.2 \, \text{m}$, $0.5 \, \text{m} \times 0.5 \, \text{m} \times 0.2 \, \text{m}$, and $0.5 \, \text{m} \times 0.8 \, \text{m} \times 0.2 \, \text{m}$, respectively) was carried out with the following results. The suppression effect of chambers on the explosion shockwave improves with the increase in the chamber width; when the chamber width increases to 0.8 m, the chamber inhibits the propagation of explosion shockwave. In addition, the flame suppression effect of the chamber also improves with the increase in the chamber width; when the chamber width increases to 0.5 m, the chamber has a suppressing effect on the propagation of flames.

(2) The numerical simulation results obtained in this study are as follows: when the chamber height and length are constant at 0.2 m and 0.5 m, respectively, the explosion suppression effect of the chamber improves with the increase in the chamber width; when the chamber width increases to 0.8 m, the overpressure at the chamber outlet is attenuated by 10.61%, indicating that the chamber has the effect on

suppressing the propagation of explosion shock-wave, which is consistent with the experimental results in this study. When the chamber height and width are constant at 0.2 m and 0.5 m, respectively, as the chamber width increases, the overpressure suppression effect at the chamber outlet first increases and then weakens. When the chamber width increases to 0.8 m, the overpressure at the outlet is attenuated by −14.16%, which shows that the chamber does not suppress the propagation of shockwave.

(3) Using a numerical simulation of the propagation process of the explosion flames and premixed methane-air gas in different chambers, the effect of the chamber geometry on the explosion suppression mechanism is analysed. It is found that when the chamber height and length are fixed at 0.2 m and 0.5 m, respectively, as the chamber width increases, the amount of the methane mixture participating in the chemical reaction inside the chamber gradually decreases, and hence, the secondary shockwave in the chamber weakens. At the same time, as the chamber width increases, the explosion relief capacity of the chamber increases rapidly. When the explosion relief capacity is sufficient to accommodate the secondary shockwave, the chamber has a suppressing effect on explosion shockwave. When the chamber height and width are fixed at 0.2 m and 0.5 m, respectively, as the chamber length increases, the amount of premixed gas participating in the chemical reaction inside the chamber gradually increases, and the secondary explosion shockwave in the chamber also increases. Although the explosion relief capacity of the chamber increases rapidly with the increase in the chamber length, it is not sufficient

to suppress the secondary shockwave generated in the chemical reaction inside the chamber; therefore, the chamber has no explosion suppression effect.

Data Availability

The data can be obtained by contacting Shujie Yuan and Chaomin Mu (yuansj@aust.edu.cn).

Conflicts of Interest

The authors declare that there are no conflicts of interest regarding the publication of this study.

Acknowledgments

References

[1] Y. J. Liu, L. Yuan, and J. H. Xue, "Analysis on the occurrence law of gas disaster accidents in coal mine from 2007 to 2016," *Mining Safety and Environmental Protection*, vol. 45, no. 3, pp. 124–128, 2018.

[2] G. O. Thomas, A. Jones, and M. J. Edwards, "Influence of water sprays on explosion development in fuel-air mixtures," *Combustion Science and Technology*, vol. 80, no. 1–3, pp. 47–61, 1991.

[3] M. J. Xu and S. X. Lu, "Sprinkler fire suppression experiments in large space," *Ship & Ocean Engineering*, vol. 46, no. 3, pp. 94–97, 2017.

[4] X. S. Wang, X. D. Zhao, and B. H. Cong, "Experimental study on gaseous flame suppression with water mist," *Journal of University of Science and Technology of China*, vol. 1, pp. 26–28, 2006.

[5] H. L. Xu, *Experimental Study on Mitigation of Menthane-Coal Dust Hybird Explosion with Ultra-fine Water Mist*, University of Science and Technology of China, Hefei, China, 2013.

[6] M. S. Bi, Z. Li, and P. P. Zhang, "Experimental investigation on suppression of gas explosion with water mist," *Journal of Mining and Safety Engineering*, vol. 29, no. 3, pp. 440–443, 2012.

[7] M. G. Yu, X. N. Zhu, and B. Pei, "Experimental study on methane explosion suppression using carbon dioxide and ultra-fine water mist," *Journal of China Coal Society*, vol. 40, no. 12, pp. 2843–2848, 2015.

[8] P. Kosinski, "Explosion suppression by a cloud of particles: numerical analysis of the initial processes," *Applied Mathematics and Computation*, vol. 217, no. 11, pp. 5087–5094, 2011.

[9] M. Krasnyansky, "Prevention and suppression of explosions in gas-air and dust-air mixtures using powder aerosol-inhibitor," *Journal of Loss Prevention in the Process Industries*, vol. 19, no. 6, pp. 729–735, 2006.

[10] H. Wen, W. Cao, and K. K. Wang, "Experimental study on ABC dry powder to repress gas explosion," *Journal of Safety Science and Technology*, vol. 7, no. 6, pp. 9–12, 2011.

[11] R. T. E. Hermanns, A. A. Konnov, R. J. M. Bastiaans, and L. P. H. De Goey, "Laminar burning velocities of diluted Hydrogen–Oxygen–Nitrogen mixtures," *Energy & Fuels*, vol. 21, no. 4, pp. 1977–1981, 2007.

[12] H. Wang, L. M. Ge, and J. Deng, "Experimental study of using inert gas to suppress mine gas explosion," *Mining Safety & Environmental Protection*, vol. 35, no. 1, pp. 4–7+91, 2008.

[13] J. W. Shao, C. J. Zhuang, and Z. R. Wang, "Explosion suppression effect of CH4/air by combined porous materials in a container piping system," *Explosion and Shock Waves*, vol. 38, no. 4, pp. 905–912, 2018.

[14] K. Zhao, G. F. Gao, and X. J. Wang, "Dimensional analysis and numerical simulation for impact-resistance performance of cylindrical shell structures," *Journal of Vibration and Shock*, vol. 33, no. 11, pp. 12–16, 2014.

[15] Z. Y. Wu and S. G. Jiang, *Study on Suppression Effect of Gas Explosion under Vacuum Cavity*, pp. 56–112, China University of Mining and Technology Press, Xuzhou, China, 2009.

[16] H. Shao, S. Jiang, X. Zhang, Z. Wu, K. Wang, and W. Zhang, "Influence of vacuum degree on the effect of gas explosion suppression by vacuum chamber," *Journal of Loss Prevention in the Process Industries*, vol. 38, pp. 214–223, 2015.

[17] H. Shao, S. G. Jiang, and Q. H. Li, "Influence of vacuum chamber volume on gas explosion suppression," *Journal of Mining and Safety Engineering*, vol. 31, no. 3, pp. 489–493, 2014.

[18] H. Shao, S. Jiang, X. He, Z. Wu, X. Zhang, and K. Wang, "Numerical analysis of factors influencing explosion suppression of a vacuum chamber," *Journal of Loss Prevention in the Process Industries*, vol. 45, pp. 255–263, 2017.

[19] Z. Q. Li, C. M. Mu, and D. K. Xu, "Influence of cavity length on shock wave propagation of gas explosion," *Journal of Mining and Safety Engineering*, vol. 35, no. 6, pp. 1293–1300, 2018.

[20] X. C. Li, B. S. Nie, and C. L. Yang, "Effect of gas concentration on kinetic characteristics of gas explosion in confined space," *Chinese Journal of High Pressure Physics*, vol. 31, no. 2, pp. 135–147, 2017.

[21] Z. M. Luo, Q. Zhang, and H. Wang, "Numerical simulation of gas explosion in confined space with FLACS," *Journal of China Coal Society*, vol. 38, no. 8, pp. 1381–1387, 2013.

[22] G. -F. Zhang, "Numerical simulation and optimization of reactive extrusion processes for free radical reaction," *Shandong University*, pp. 36–73, 2009.

[23] Z. Yan, S. Yuan, Z. Li, S. Gu, and C. Mu, "Study on inhibitory effect of cavity on gas explosion propagation," *Geofluids*, vol. 2021, no. 8, Article ID 6674425, 9 pages, 2021.

Research Article

Study on the Dynamic Evolution of Through-Crack in the Double Hole of Elliptical Bipolar Linear-Shaped Charge Blasting

Bo Wu,[1,2,3] Shixiang Xu [ID],[1] Guowang Meng [ID],[1] Yaozhong Cui,[1] Junhua Cai [ID],[4] and Yao Zhang[5]

[1]*College of Civil Engineering and Architecture, Guangxi University, Nanning, Guangxi 530004, China*
[2]*School of Civil and Architectural Engineering, East China University of Technology, Nanchang, Jiangxi 330013, China*
[3]*School of Architectural Engineering, Guangzhou City Construction College, Guangzhou, Guangdong 510925, China*
[4]*Sanming Puyan Expressway Co., Ltd., Sanming, Fujian 365000, China*
[5]*China Railway 11th Bureau Group First Engineering Co. Ltd., Xiangyang 441104, China*

Correspondence should be addressed to Shixiang Xu; 603559081@qq.com

Seeking the law of through-crack in the double hole of shaped charge can help reveal the rock failure mechanism of directional controlled blasting. Using LS-DYNA numerical simulation analysis, the dynamic mechanical behaviors of double-hole crack development and double-hole crack penetration in elliptical bipolar linear-shaped charge blasting and ordinary blasting were compared and studied. The results showed that it was difficult to form a straight line through the double holes under ordinary blasting, while easy to cause over-under-excavation problems. The blasting of the elliptical bipolar linear-shaped charge had a significant effect on the formation of directional crack. The crack penetrated along the connecting center line of the two holes. The main crack growth form was tensile fracture mode, and the explosion gas was the important driving force for continuous crack growth. The elliptical bipolar linear-shaped charge blasting produced fewer cracks in the nonenergy-accumulating direction, which could effectively reduce the damage of the retained rock mass.

1. Introduction

The directional fracture controlled blasting of shaped charge changes the structure of the explosive itself and utilizes the energy gathering effect of the energy cavity to form a stream of explosive products with high velocity and pressure after blasting, which directly acts on the wall of the blast hole and makes the rock crack and expand preferentially in the concentrating energy direction and then achieves the purpose of directional fracture blasting. In recent years, scholars at home and abroad have carried out relevant theoretical research, experimental research, and numerical simulation analysis on directional fracture controlled blasting technology. Cho et al. [1] studied the effect of the location of the guide hole and the initiation time lag on the crack propagation control and analyzed the relationship between the applied fracture energy and crack extension. Yang and Wang

et al. [2–5] explored the influence of different cutting angle, depth, and other factors on blasting crack propagation by using a testing system of digital laser dynamic caustics, and specific tests were carried out on the extension and penetration mechanism of cracks. Yue et al. [6–10] analyzed the influence of different intervals between holes of explosive load on the crack propagation through the dynamic caustics test and numerical simulation, which indicated that the growth rate of the main blasting crack, the peak value of the dynamic stress intensity factor, and the stress peak value of the crack meeting area all depended on the blast hole spacing. When the distance between holes is small, the peak value is large, which is conducive to the directional expansion of cracks. Zhang et al. [11] studied the influence of the material of the cut tube and the decoupling coefficient on the crack growth through the mortar model test. He et al. developed a new material of constant resistance and large

deformation bolt in deep rock mass [12] and developed the technology and equipment of energy-gathered roof cutting in deep rock mass, which has achieved precise control of blasting crack propagation and ensured the molding quality around the roadway [13, 14]. Luo et al. [15, 16] based on dynamics of explosion and fracture mechanics studied the mechanism of crack initiation and its expansion of directional fracture controlled blasting by shaped charge with wedge-type liners in rock. Guo et al. [17–19] analyzed the dynamic effect of deep hole-shaped charge blasting and considered that the shaped charge effect of deep hole-shaped charge blasting significantly changed the propagation characteristics of explosion stress wave and the mechanical properties of rock mass. Wu et al. [20–23] conducted a preliminary study on the influencing factor of the formation of the elliptical bipolar line-shaped charge jet and the mechanism of initial crack formation.

However, the stress wave propagation and crack development of single-hole blasting and double-hole blasting are different in shaped charge blasting. To date, there are few studies on the stress wave propagation and crack development law of surrounding rock of shaped energy double-hole blasting. Therefore, this paper combined the theoretical analysis with the numerical simulation to study the stress wave propagation and crack development law of double-hole blasting based on the elliptical bipolar linear-shaped charge blasting technology, whilst compared with those of ordinary blasting. The results are of great significance to the research and application of the technology.

2. Stress Wave Propagation and Crack Mechanism of Shaped Charge Blasting

2.1. Mechanism Analysis of Crack Development in Shaped Charge Blasting. The elliptical bipolar linear-shaped charge blasting technology makes full use of the tensile failure characteristics of rock. Through the combination of PVC shaped charge pipe and explosive, the tangential tensile stress is formed in the concentrating energy direction after the explosion, and the detonation pressure is transformed into the tensile effect on surrounding rock, forming effective directional precracking in the concentrating energy direction. At the same time, due to the buffering effect of PVC pipe in the nonconcentrated energy direction, the damage of rock on the blast hole wall in the nonconcentrated energy direction is avoided. The principle of elliptical bipolar linear-shaped charge blasting and the schematic diagram of shaped charge are shown in Figure 1.

2.2. Fracture Mechanism of Double Hole-Shaped Charge Blasting. In continuous-hole-shaped charge blasting, two adjacent blast holes are detonated simultaneously, and the explosion stress wave propagates to the midpoint of the line connecting the blast hole and superimposes at the midpoint of the line of the two blast holes. Due to a certain energy loss in the propagation of wave and explosive gas in the rock, when the tensile stress at each point of the connecting line in the concentrating energy direction of the adjacent blast holes

is greater than or equal to the tensile strength of the rock, the cracks between the adjacent blast holes can be connected [24]. The mechanical model of the elliptical bipolar linear-shaped charge blasting continuous hole is shown in Figure 2.

As shown in Figure 2, during continuous-hole-shaped charge blasting, the explosive gas enters from the concentrating energy direction of two blasting holes, respectively, for expansion and extrusion. However, the stress superposition surface would be generated at the vertical line of the midpoint of the concentrating energy direction line of two blasting holes in the process of stress wave propagation. Although there is energy loss in the process of stress wave propagation, according to the superposition principle of wave, a tensile stress of 2 times is generated at the stress superposition surface, which can appropriately increase the distance between the two blast holes.

3. Validation of Numerical Solution

3.1. Numerical Model. LS-DYNA was used to carry out numerical simulation analysis. The explosive material model in LS-DYNA was characterized by MAT_HIGH_EXPLO-SIVE_BURN, and the JWL equation was adopted to describe the relationship between the pressure and volume of the explosive after detonation.

$$p = A\left(1 - \frac{\omega}{R_1 V}\right)e^{-R_1 V} + B\left(1 - \frac{\omega}{R_2 V}\right) + \frac{\omega E}{V}, \quad (1)$$

where p is the pressure, A, B, ω, R_1, and R_2 are the basic parameters of the equation of state, V is the relative volume of the detonation product, and E is the initial internal energy density of the detonation product. Properties of explosive and JWL state equation are shown in Table 1.

The mechanical parameter of the shaped charge cover is shown in Table 2.

The HJC constitutive model was used for rock material. The MAT_ADD_EROSION damage criterion was used to determine the damage condition of each element in the simulation of fracture development [25]. The mechanical parameters of rock in the model are shown in Table 3, and the maximum principal stress failure of rock is defined to analyze the crack development.

3.2. Explosion Test of PMMA. PMMA is often used as an ideal experimental material to study the crack initiation process under blasting loading. Its fracture mechanics behavior is similar to that of brittle rock [26, 27]. Che [28] carried out the experimental research on the blasting test of shaped charge with PMMA. The shaped charge cover is a PVC hard plastic tube, with an inner diameter of 0.5 cm. The shaped charge cover thickness is 0.1 cm. The diameter of the blast hole is 1.2 cm, as shown in Figure 3.

3.3. Comparison between Simulation Results and Experimental Results. By establishing the same numerical analysis model as the experiment, the results of numerical simulation and experiment are shown in Figure 4. The numerical
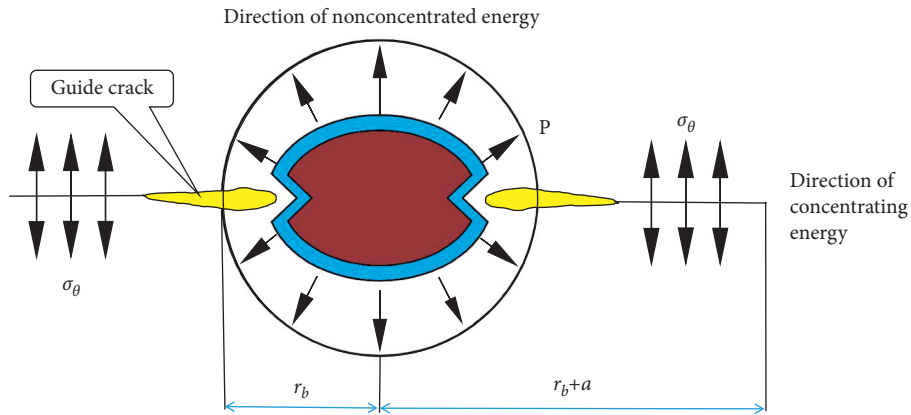
FIGURE 1: Mechanical model of cracking due to shaped charge blasting [23].
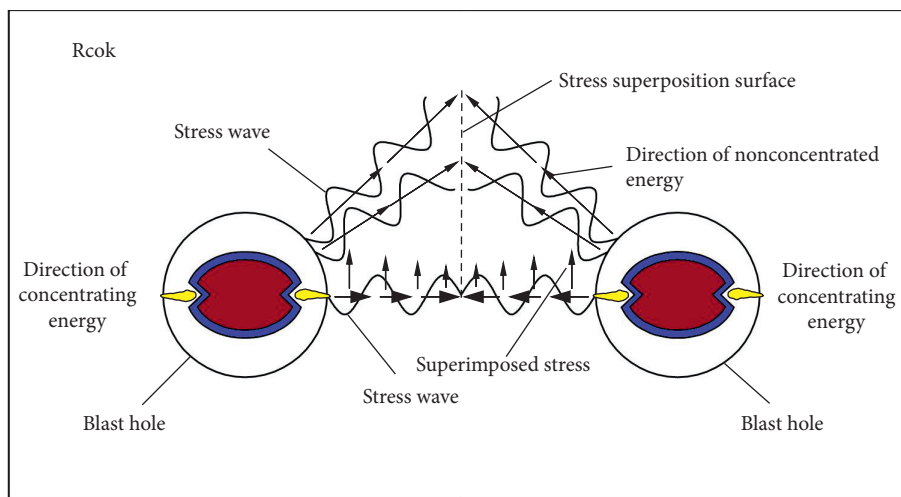
FIGURE 2: Mechanical model of continuous hole due to shaped charge blasting.

TABLE 1: Explosive and parameters of equation of state [23].

ρ (g·cm^{-3})	v_D (cm·μs^{-1})	A (GPa)	B (GPa)	R_1	R_2	ω	E (GPa)
1.3	0.4	214.4	0.182	4.2	0.9	0.15	4.192

TABLE 2: Mechanical parameter of the shaped charge cover [23].

Material	Density (g·cm^{-3})	Elastic modulus (GPa)	Poisson's ratio (μ)
PVC	1.3	3.0	0.38

TABLE 3: Material parameters of rock [23].

Parameters	Property	Value
ρ (g·cm^{-3})	Density	2.18
G (GPa)	Shear modulus	14.86
A	Normalized cohesive strength	0.79
B	Normalized pressure hardening	1.60
C	Strain rate coefficient	0.007
S_{fmax}	Normalized maximum strength	7
ε_{fmin}	Amount of plastic strain before fracture	0.01
N	Pressure hardening exponent	0.61
D_1	Damage constant 1	0.04
D_2	Damage constant 2	1
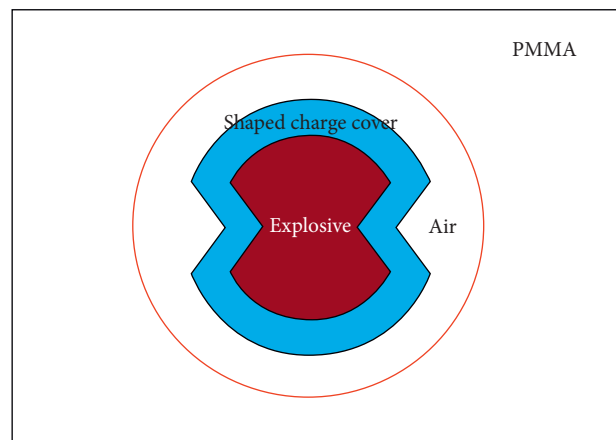
FIGURE 3: PMMA-shaped charge blasting [28].

simulation results perfectly reproduced the test process, the crack development was basically consistent with the test results at 80 μs and 600 μs, and the final distribution pattern of rock crack is consistent with the test results. It was concluded that LS-DYNA could effectively simulate the

(a)

(b)

(c)

(d)
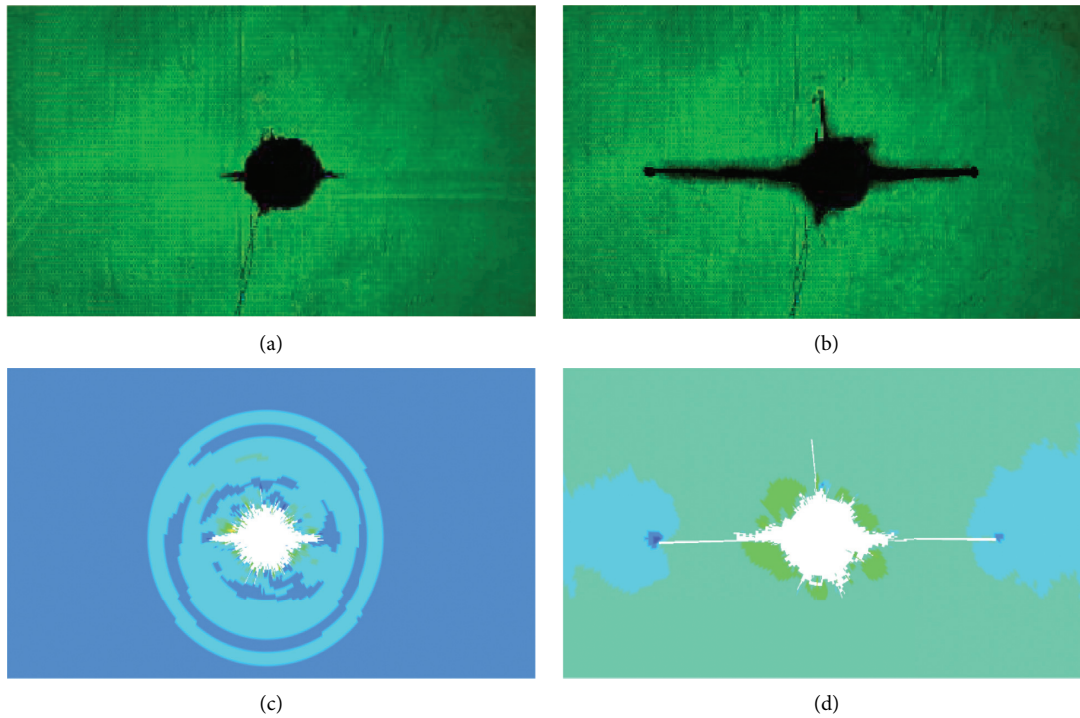
FIGURE 4: Comparison of the simulation results and experiment results (a) at $80\,\mu$s of experiment results [28]; (b) at $600\,\mu$s of experiment results [28]; (c) at $80\,\mu$s of simulation results; (d) at $600\,\mu$s of simulation results.
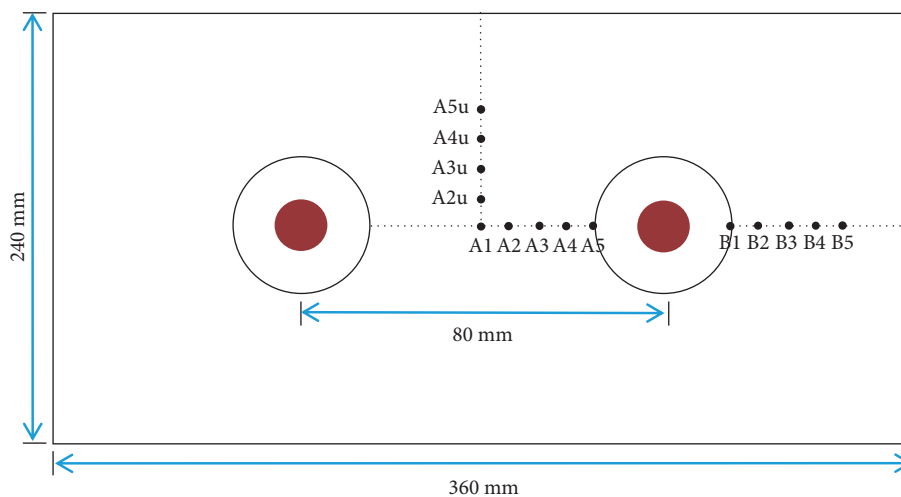
FIGURE 5: Schematic diagram of numerical calculation.

crack development process of rock in the shaped charge blasting process.

4. Numerical Model of Elliptic Bipolar Linear-Shaped Charge Blasting

4.1. Geometric Model of Numerical Calculation. The calculation models of double-hole ordinary blasting and elliptical bipolar linear shaped charge blasting with 90 mm hole diameter were established, respectively, as shown in Figures 5 and 6. The charge mass of the two models is equal, the energy gathering tube is made of PVC material, the thickness of the shell of the energy gathering tube is 2 mm, the thickness of the layer liner is 1.4 mm, and the angle of the shaped charge groove is 70 degrees. Rock mass implies Lagrange unit, and other various materials imply the fluid-solid coupled algorithm. Nonreflecting boundary condition is applied around the model. The layout of measuring points is shown in Figures 5 and 6. Thereinto, A1 measuring point is in the center of the model, and the distance between each two adjacent measuring points is equal.
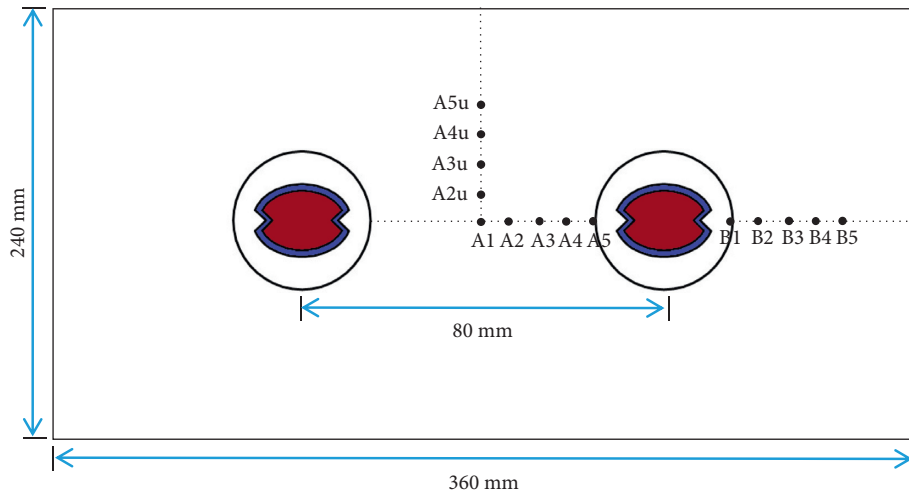
FIGURE 6: Schematic diagram of the numerical calculation model for the ordinary blasting model for shaped charge blasting.
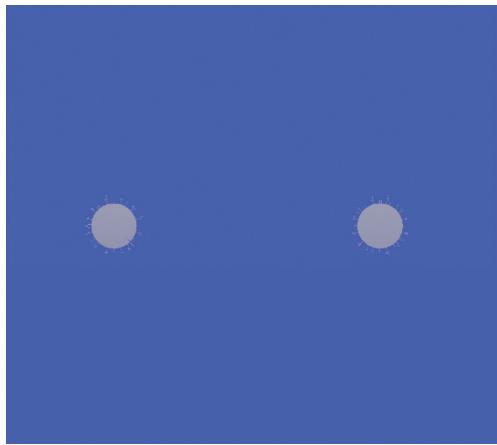
FIGURE 7: Crack development at $30\,\mu$s of ordinary blasting.
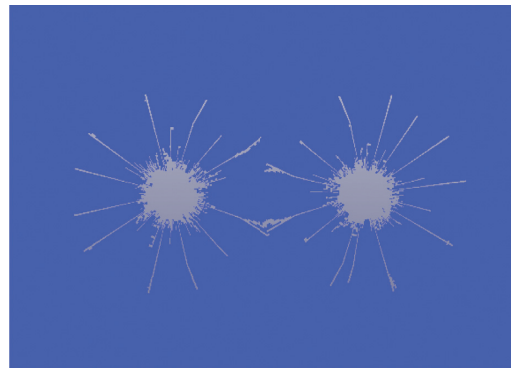
FIGURE 9: Crack penetration of ordinary blasting.

FIGURE 8: Crack development at $30\,\mu$s of shaped charge blasting.
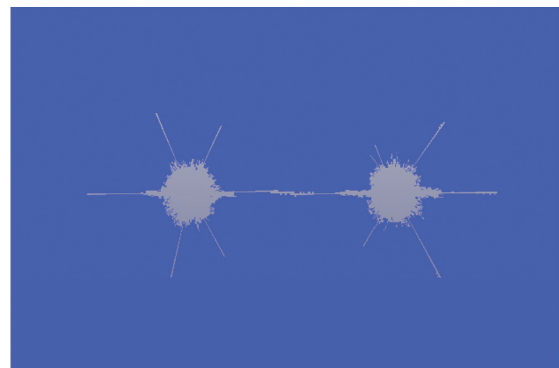
FIGURE 10: Crack penetration of shaped charge blasting.

4.2. Blasting Crack Development. Under ordinary blasting, after the explosives detonate, the detonation product is scattered randomly around the blasthole. Under shaped charge blasting, after the explosives detonate, the detonation wave acts on the shaped charge cover with huge pressure to form a shaped charge jet with high temperature, high pressure, and high energy, and the jet acts on the rock to form guiding crack. At $30\,\mu$s, the cracks develop irregularly in multiple directions under ordinary blasting, as shown in Figure 7, and the shaped charge blasting mainly develops along the concentrating energy direction, as shown in Figure 8.

At $190\,\mu$s, the two cracks of ordinary blasting form a breakthrough, as shown in Figure 9. At $228\,\mu$s, the two main cracks of shaped charge blasting form a breakthrough, as
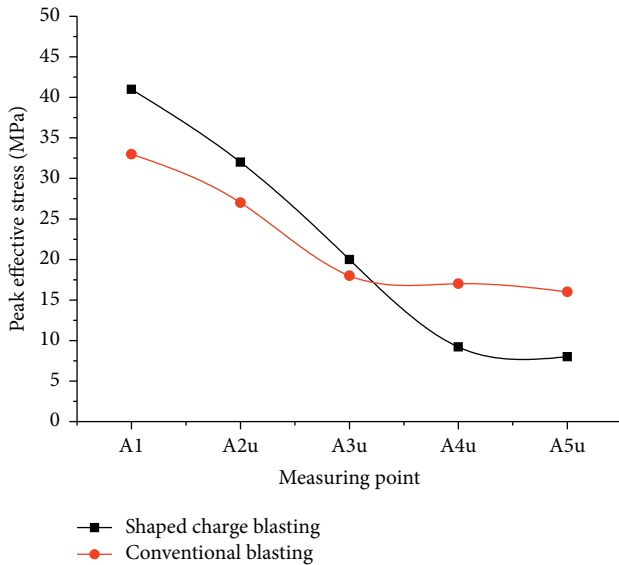
FIGURE 11: Peak effective stress of measuring point at the blast hole center line.
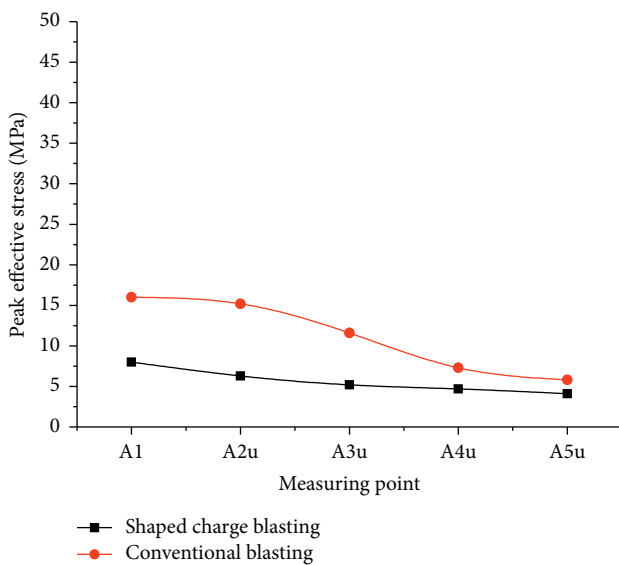
FIGURE 12: Peak effective stress of measuring point at the vertical direction of the blast hole center line.

shown in Figure 10. Generally speaking, there are more multidirectional cracks produced by ordinary blasting, and the two hole cracks are not connected to the two hole centerline, which is easy to cause over-under-excavation problem. There are fewer cracks produced by shaped charge blasting. The two hole cracks are connected to the two hole centerline, and the crack directional development effect is good.

4.3. Comparative Analysis of Effective Stress at Measuring Points. The peak effective stress of each measuring point of shaped charge blasting and ordinary blasting is shown in Figures 11 and 12. The peak effective stress of A1–A5 on the

connecting center line of the blast hole was basically the same as that of B1–B5 on the right side of the blast hole. The peak effective stress is the largest at the wall of the blast hole, and the farther away from the center of the blast hole, the smaller the peak effective stress. The results show that the peak effective stress at the borehole wall of shaped charge blasting is larger than that of ordinary blasting, which is conducive to the development of initial cracks in the concentrating energy direction. In the vertical direction of the blast hole center line, the peak effective stress of the measuring point of ordinary blasting is always larger than that of shaped charge blasting, which shows that shaped charge blasting can reduce the damage of rock in the non-concentrated energy direction. The crack development in the later stage of blasting mainly depends on the effect of blasting gas.

5. Conclusions

(1) Under ordinary blasting, multidirectional random cracks will be formed, and it is difficult for double holes to form a straight line through, which is easy to cause the problem of overbreak and underbreak.

(2) The blasting of the elliptical bipolar linear shaped charge can effectively form directional cracks. The main crack of blasting mainly develops in tensile fracture mode, and the explosive gas is the important driving force for continuous crack growth.

(3) The elliptical bipolar linear-shaped charge blasting can effectively reduce the damage of the retained rock mass. The crack penetration is carried out along the connecting center line of the two holes, and the effect is significant.

Data Availability

The data supporting the results of this study can be obtained upon request to the corresponding author.

Conflicts of Interest

The authors declare that they have no conflicts of interest regarding the publication of this paper.

Acknowledgments

References

[1] S. H. Cho, Y. Nakamura, B. Mohanty, H. S. Yang, and K. Kaneko, "Numerical study of fracture plane control in laboratory-scale blasting," *Engineering Fracture Mechanics*, vol. 75, no. 13, pp. 3966–3984, 2008.

[2] R. S. Yang, Y. B. Wang, Z. W. Yue et al., "Dynamic behaviors of crack propagation in directional fracture blasting with two holes," *Explosion and Shock Waves*, vol. 33, no. 6, pp. 631–637, 2013.

[3] R. S. Yang, Y. B. Wang, D. M. Guo et al., "Experimental research of crack propagation in polymethyl methacrylate material containing flaws under explosive stress waves," *Journal of Testing and Evaluation*, vol. 44, no. 1, pp. 56–60, 2016.

[4] R. S. Yang, Y. B. Wang, H. J. Xue et al., "Dynamic behavior analysis of perforated crack propagation in two-hole blasting," *Procedia Earth and Planetary Science*, vol. 5, pp. 254–261, 2012.

[5] Y. Wang, "Study of the dynamic fracture effect using slotted cartridge decoupling charge blasting," *International Journal of Rock Mechanics and Mining Sciences*, vol. 96, pp. 34–46, 2017.

[6] Z. W. Yue, L. Y. Yang, and Y. B. Wang, "Experimental study of crack propagation in polymethyl methacrylate material with double holes under the directional controlled blasting," *Fatigue and Fracture of Engineering Materials and Structures*, vol. 36, no. 8, pp. 827–833, 2013.

[7] Z. W. Yue, S. C. Zhang, P. Qiu et al., "Influence of charge structures on the slotted cartridge blasting effect," *Journal of Vibration and Shock*, vol. 37, no. 10, pp. 27–34, 2018.

[8] Z. W. Yue, S. Y. Tian, S. C. Zhang et al., "Expanding law of cracks formed by slotted cartridge blast under unidirectional confining pressure," *Journal of Vibration and Shock*, vol. 38, no. 23, pp. 186–195, 2019.

[9] Z. W. Yue, X. B. Hu, Z. Y. Chen et al., "Experimental study of effect of uncoupled charge on energy utilization efficiency of explosives," *Blasting*, vol. 37, no. 3, pp. 34–39, 2020.

[10] Z. W. Yue, S. Y. Tian, and Z. Y. Chen, "Influence of the interval between holes on crack propagation in slit charge blasting," *Chinese Journal of Rock Mechanics and Engineering*, vol. 37, no. 11, pp. 2460–2467, 2018.

[11] Z. X. Zhang, Y. L. Guo, and L. F. Li, "Study on mechanism of crack growth of cutting seam cartridge blasting," *Engineering Blasting*, vol. 2, pp. 11–14, 2007.

[12] C. Zhu, M. C. He, X. H. Zhang et al., "Nonlinear mechanical model of constant resistance and large deformation bolt and influence parameters analysis of constant resistance behavior," *Rock and Soil Mechanics*, vol. 42, no. 7, pp. 1911–1924, 2021.

[13] Q. Wang, M. C. He, S. C. Li et al., "Comparative study of model tests on automatically formed roadway and gob-side entry driving in deep coal mines," *International Journal of Mining Science and Technology*, vol. 31, no. 4, pp. 591–601, 2021.

[14] Q. Wang, Y. Wang, M. He et al., "Experimental research and application of automatically formed roadway without advance tunneling," *Tunnelling and Underground Space Technology*, vol. 114, Article ID 103999, 2021.

[15] Y. Luo, Z. W. Sheng, and X. R. Cui, "ApplicAtion study on blasting with linear cumulative cutting charge in rock," *Chinese Journal of Energetic Materials*, vol. 3, no. 14, pp. 236–241, 2006.

[16] Y. Luo, "Study on application of shaped charge in controlled rock mass blasting technology," *Journal of Disaster Prevention and Mitigation Engineering*, vol. 27, no. 1, pp. 57–62, 2001.

[17] D. Y. Guo, J. C. Zhao, P. F. Lv, and M. Zhai, "Dynamic effects of deep-hole cumulative blasting in coal seam and its application," *Chinese Journal of Engineering*, vol. 38, no. 12, pp. 1681–1687, 2016.

[18] D. Y. Guo, J. C. Zhao, C. Zhang, and T. G. Zhu, "Mechanism of empty borehole on coal crack initiation and propagation under deep-hole cumulative blasting in coal seam," *Chinese Journal of Rock Mechanics and Engineering*, vol. 37, no. 4, pp. 919–930, 2018.

[19] D. Y. Guo, C. Zhang, T. G. Zhu, and J. J. Pan, "Effect of charge structure on deep-hole cumulative blasting to improve coal seam permeability," *Chinese Journal of Engineering*, vol. 40, no. 12, pp. 1488–1494, 2018.

[20] B. Wu, H. Wei, S. Xu et al., "Analysis of the cracking mechanism of an elliptical bipolar linear-shaped charge blasting," *Advances in Civil Engineering*, vol. 2021, Article ID 6669704, 12 pages, 2021.

[21] B. Wu, H. Wei, S. Xu et al., "Numerical study of two-way shaped charge blasting with different charge structures," *Engineering Blasting*, vol. 27, no. 1, pp. 14–21, 2021.

[22] B. Wu, H. Wei, S. Xu et al., "Research on numerical optimization of smooth blasting layer parameters of shaped energy smooth blasting," *Nonferrous Metals Engineering*, vol. 10, no. 12, pp. 113–121, 2020.

[23] B. Wu, S. Xu, G. Meng et al., "Study on dynamic evolution law of blasting cracks in elliptical bipolar linear shaped charge blasting," *Shock and Vibration*, vol. 2021, Article ID 5272878, 10 pages, 2021.

[24] K. Zhang, W. Y. Huang, Q. Y. Chen et al., "Mechanism research of directional fracturing of control hole and application," *Blasting*, vol. 31, no. 1, pp. 16–18, 2014.

[25] N. Meng, Y. Chen, J. Bai, X. Wang, W. Wu, and B. Wu, "Numerical simulation of directional fracturing by shaped charge blasting," *Energy Science & Engineering*, vol. 8, no. 5, pp. 1824–1839, 2020.

[26] Q. Li, Y. Liang, K. K. Ren et al., "Experimental study of propagation of directional cracks with shaped charge under blasting load," *Chinese Journal of Rock Mechanics and Engineering*, vol. 29, no. 8, pp. 1684–1689, 2010.

[27] N. Murphy, M. Ali, and A. Ivankovic, "Dynamic crack bifurcation in PMMA," *Engineering Fracture Mechanics*, vol. 73, no. 16, pp. 2569–2587, 2006.

[28] Y. L. Che, *Study on the Mechanism of Irregular Cartridge and the Damage of Surrounding Rock*, China University of Mining and Technology, Xuzhou, China, 2015.

Research Article

Dynamic Response Analysis of Underground Double-Line Tunnel under Surface Blasting

Pei Zhang [ID],[1] **Jianhua Cai**,[2] **Feng Zong**,[3] **Yanpeng He** [ID],[1] **and Qiong Wang**[4]

[1]*College of Energy Science and Engineering, Xi'an University of Science and Technology, Xi'an, Shanxi 710000, China*
[2]*Pingliang Xin'an Coal Industry Co., Ltd., Pingliang, Gansu 744000, China*
[3]*Shaanxi Jinyuan Zhaoxian Mining Co., Ltd., Baoji, Shanxi 721000, China*
[4]*Department of Emergency Technology and Management, North China Institute of Science and Technology, Beijing 101601, China*

Correspondence should be addressed to Pei Zhang; zhangpei@xust.edu.cn

Blasting has been widely used for economical and rapid rock excavation in civil and mining engineering. In order to study the influence of relative horizontal distance and relative vertical distance between two tunnels on the dynamical response of the two tunnels, 10 numerical simulation cases are done by LS-DYNA 3D models under surface explosion by controlling the clear distance and height difference of double-line tunnel, and the ALE multimaterial fluid structure coupling algorithm is applied to analyze the dynamic response characteristics of double-line tunnel under different conditions. The numerical results show that the dynamic response characteristics of the tunnel lining are affected by the change of the clear distance and height difference of the tunnel. With the increase of the height difference between adjacent tunnels, the peak value of vibration velocity at the top of the lining on the blast face increases, which is due to the upward elevation of the right tunnel, which is more conducive to the reflection and superposition of stress waves. When the height difference of tunnel is 4–6 m, the vibration velocity and displacement of monitoring point C on the back blasting side will change abruptly, and the variation range of vibration velocity is about 25%, while the variation range of displacement is about 60%.

1. Introduction

Blasting is widely used in rock excavation, mining, and other hard rock engineering applications since it has the advantages of strong geological adaptability and economy. However, the blast-induced vibration may do harm to the surrounding buildings, tunnels, and other structures. At present, many studies have been done for blasting-induced damage or effects on surface buildings, while the research studies on underground structures are quite rare relatively. With the increase of underground space building, the underground tunnel engineering are booming and face lots of blasting problems, such as tunnel rock fall. Therefore, it is very important to study how to effectively protect underground structures and minimize the loss under the strong explosion.

Many scholars have done research on the dynamic response characteristics of underground structures under explosive loading. Eitzenberger [1] observed through experimental and numerical investigations that the attenuation of the shock wave is controlled by the texture of the rock mass. Wu et al. [2] investigated the propagation of blast-induced shock wave in jointed rock mass using accelerometers and found that the attenuation of the shock wave is completely dependent on the distance from the charge weight, the angle between the strike of rock strata, and the direction of wave propagation. Yang et al. [3] investigated the response of blast-induced vibration on tunnel surfaces and inside surrounding rock using three-dimensional (3D) numerical analysis procedure. Numerical studies show that compared with the inside vibration, the tunnel surface vibration has a higher, more readily attenuated PPV and a lower frequency with a slower rate of decline in the dominant frequency. Liang et al. [4] investigated the response of an existing tunnel subjected to blast-induced vibrations

from a newly constructed tunnel placed adjacent to the existing tunnel. Mohammad and Rehan Sadique [5] considered an internal blast loading on a rock tunnel constructed in quartzite rock; the results show that the extent of damage in shallow depth tunnels is found to be more than that of the tunnels at higher depth of overburden. Liu et al. [6] investigated the explosion inside tunnel and a formula for the explosion blast wave overpressure at a certain distance from the detonation center point inside the tunnel was derived by using the dimensional analysis theory. Feldgun et al. [7] studied internal blast loading in a buried lined tunnel by the modified Godunov method, which considered all the stages of the process: detonation of the internal charge; the shock wave propagation in the internal gas and its following interaction with the cavity's shell lining including multiple reflections. Yang et al. [8] performed numerical modeling to assess the damage characteristics of an underwater tunnel subjected to blast loads and explore the potential mitigation measures based on coupled Lagrange and Euler (CLE) method. The results show that the rigidity and load-carrying ability of the tunnel are significantly improved by bonding the CFRP cloth. The recommended thickness of the CFRP cloth is 0.5–0.835 mm. Koneshwaran et al. [9] investigated underground transport tunnels in blast loading; the results indicated that several bolts failed in the longitudinal direction due to redistribution of blast loading to adjacent tunnel rings, and the tunnel segments respond as arch mechanisms in the transverse direction and suffered damage mainly due to high bending stresses.

The above researches are of great significance to understand the mechanism and process of underground space dynamic disaster. However, the researches on the dynamic response characteristics of underground double-line tunnel under the surface blasting are relatively rare. The research on the structures under explosive loading mainly adopts the methods of experiment, theoretical analysis, and numerical simulation. The explosion experiment is the most effective and direct method to study the dynamic response characteristics of the structures, but the destructive experimental conditions are harsh and costly. Under the blast impact load, the underground structure is not only affected by the stress waves from all directions, but also influenced by the nonperiodic transient action and considering the plastic strain of the material, which makes the problem become a highly nonlinear problem combining state nonlinearity and material nonlinearity [10–14]. Therefore, it is difficult to realize the blast mechanics analysis of complex structures by theoretical means. For these reasons, the use of numerical method to study the complex progress between wave propagation and tunnel interaction is necessary and effective. In this paper, in order to study the influence of relative horizontal distance and relative vertical distance between two tunnels on the dynamical response of the two tunnels, 10 numerical simulation cases are done by LS-DYNA 3D models under surface explosion. The research results can provide a useful reference for the antiexplosion protection design of underground tunnel.

2. Three-Dimensional Finite Element Modeling

2.1. Finite Element Modeling of Rock and Lining. In order to study the influence of relative horizontal distance and relative vertical distance between two tunnels on the dynamical response of the two adjacent tunnels, 10 numerical simulation cases are done by LS-DYNA 3D models under surface explosion. The model is constructed in cm-g-μs unit system. Figure 1 shows the geometric model of the double-line tunnel. Figures 2 and 3 are the isometric side view and front view of the finite model of the double-line tunnel, respectively. The size of whole model is 80 m × 10 m × 42 m. The outer diameter of the lining is 10 m, the wall thickness of the lining is 0.3 m, and the longitudinal length of the lining is 10 m. The charge of the TNT explosive is 40 kg. The distance between the side and top of the left lining and the center of TNT explosive is 30 m and 20 m, respectively, as shown in Figure 1. Three degrees of freedom (UX, UY, and UZ) of the bottom of the finite element model are constrained. In order to simulate the infinite region and eliminate the influence of the reflected stress wave on the simulation results, except for the top free surface, the other boundary segment of the model is controlled by keyword *Boundary_Non_Reflecting, which can absorb the expansion wave and shear wave passing through the interface.

Considering the influence of lining clear distance and height difference on dynamic response characteristics of double line tunnel under surface blasting, the following parametric analysis scheme is formulated. When analyzing the influence of lining clear distance variable on dynamic characteristics, ensure that the height difference of two linings is 0 m, the position of left lining relative to TNT explosive remains unchanged at the same time, only change the horizontal clear distance of right lining, and the horizontal clear distances of lining are 5 m, 7 m, 9 m, 11 m, and 13 m, respectively. In order to simplify the subsequent analysis, the corresponding conditions are marked as A1, A2, A3, A4, and A5, respectively, as shown in Figure 4 and Table 1. When analyzing the influence of lining height difference variables on dynamic characteristics, the horizontal clear distance between two linings is 9 m, and the position of left lining relative to TNT explosive remains unchanged. The height differences between two linings are 0 m, 2 m, 4 m, 6 m, and 8 m, respectively. In order to simplify the subsequent analysis, the corresponding conditions are marked as A3, B3, C3, D3, and E3, respectively, as shown in Figure 4 and Table 1.

2.2. ALE Multimaterial Fluid Structure Coupling Algorithm. The Arbitrary Lagrange–Euler (ALE) coupling algorithm is used in LS-DYNA 3D to solve the fluid structure coupling problem in this paper, which is the same as the description of Euler algorithm. It can be understood that there are two layers of grids overlapped together, but the difference is that the grid in ALE algorithm is not fixed and can move arbitrarily in space. The ALE algorithm first performs several Lagrange time step calculations, in which the element mesh deforms with the material flow and then performs ALE time
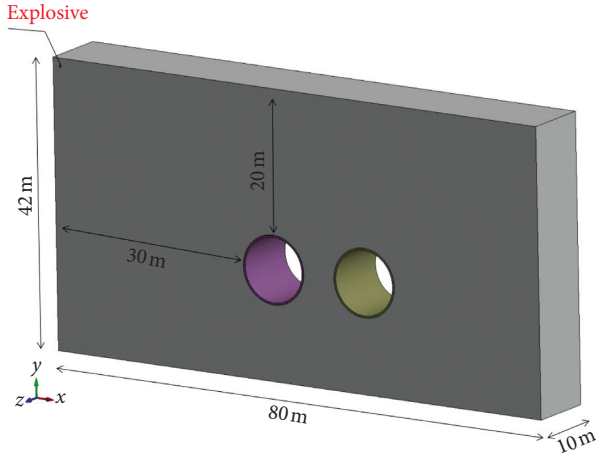
FIGURE 1: Isometric side view of geometric model.

FIGURE 2: Equiaxed side view of finite element model.
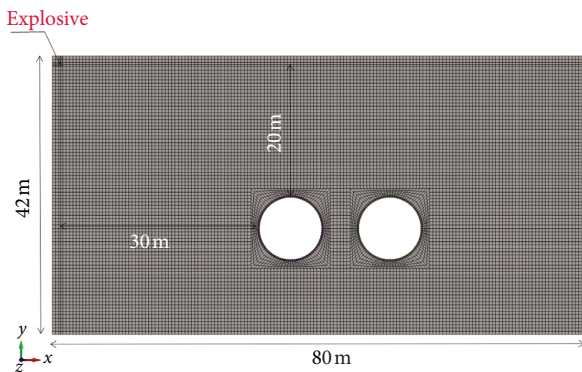
FIGURE 3: Front view of finite element model.

step calculation. (1) The boundary conditions of the modified object remain unchanged, and the internal element is meshed to keep the topological relationship of the mesh unchanged. This step is called smooth step. (2) The element parameters (density, energy, stress tensor, etc.) and node velocity vector in the deformed mesh are transferred to the new mesh, which is called expectation step. ALE algorithm on the one hand retains the advantages of Lagrange
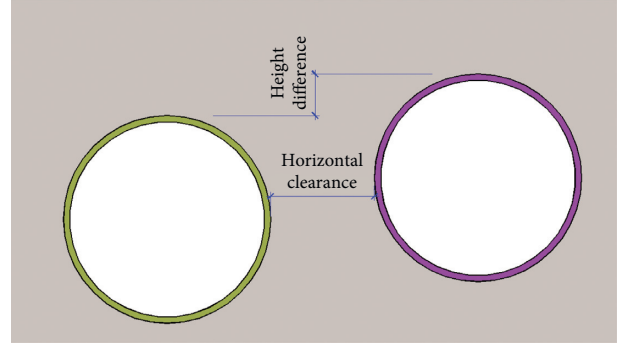
FIGURE 4: Details of numerical simulation cases.

algorithm [10, 15, 16]; that is, it can accurately detect the boundary of the mesh, but also inherits the main advantages of Euler algorithm, which can well solve the problem of element distortion, make up for the shortcomings of the two algorithms, and is very suitable for large deformation analysis.

In this simulation, the rock mass and lining are described by the Lagrange method; the explosive and air are described by the Euler method. This method couples fluid and solid together to realize the nonlinear coupling between fluid medium and rock mass model by keyword *Constrained_Lagrange_In_Solid. The fluid structure coupling algorithm is to couple the structure and fluid together through certain constraint method to realize the transmission of mechanical parameters. The main constraint methods [17] are velocity constraint, acceleration constraint, and penalty function constraint. The advantage of this algorithm is that the fluid element and structural element on the coupling surface do not need to be corresponded one by one, which greatly reduces the workload of mesh generation. The calculation steps of velocity and acceleration constraints are as follows:

The fluid element with structural nodes is searched, and the structural node parameters (mass, momentum, and nodal force) are assigned to the fluid element nodes.

$$m_n (M, F)_{f,i} = m_0 (M, F)_{f,i} + h_i m (M, f)_s. \tag{1}$$

Calculate the new acceleration of fluid node (velocity):

$$a (v)_{f,i} = \frac{F (M)_{f,i}}{m_{fn,i}}. \tag{2}$$

The acceleration (velocity) of constrained structure node is as follows:

$$a (v)_s = \sum_1^i h_i a (v)_{f,i}, \tag{3}$$

where m_n and m_o represent the nodal mass of fluid element before and after distribution, respectively; M and F are the momentum and nodal force, respectively; a and v are the acceleration and velocity of the node; h is the number of nodes contained in a single fluid element; and f and s are symbols of fluid and solid element.

TABLE 1: Details of numerical simulation cases.

Numerical simulation case number	Horizontal clearance of lining (m)	Numerical simulation case number	Height difference of lining (m)
A1	5	A3	0
A2	7	B3	2
A3	9	C3	4
A4	11	D3	6
A5	13	E3	8

2.3. Constitutive Model of Materials

2.3.1. Constitutive Model of TNT Explosive.
Explosive material model is described by keyword *MAT_HIGH_EXPLOSIVE_BURN combined with JWL equation of state provided by LS-DYNA. The P-V relation of the JWL equation of state is as follows:

$$P = A\left(1 - \frac{\omega}{R_1 V}\right)e^{-R_1 V} + B\left(1 - \frac{\omega}{R_2 V}\right)e^{-R_2 V} + \frac{\omega E}{V}, \quad (4)$$

where A, B, R_1, R_2, and ω are material constants for TNT explosive, parameters A and B represent the magnitudes of pressure, ρ is the density of the explosive, and E is the specific internal energy at atmospheric pressure.

For TNT explosive [18], $\rho = 1630\,\text{kg/m}^3$; detonation wave speed $D = 6930\,\text{m/s}$; Chapman–Jouget pressure PCJ = $0.255 \times 10^{11}\,\text{Pa}$; $A = 373800\,\text{MPa}$; $B = 3747\,\text{MPa}$; $R_1 = 4.15$; $R_2 = 0.9$; and $\omega = 0.35$.

2.3.2. Constitutive Model of Air.
The air model [19] is described by keyword *MAT_NULL combined with multi-linear equation of state *EOS_LINEAR_POLYNOMIAL in this study.

$$P = \left[C_0 + C_1\mu + C_2\mu^2 + C_3\mu^2\right] + \left[C_4 + C_5\mu + C_6\mu^2\right]e. \quad (5)$$

For the convenience of calculation, air is regarded as an ideal gas, in which the parameters are as follows: $C_0 = C_1 = C_2 = C_3 = C_6 = 0$, $C_4 = C_5 = 0.4$. For air in cm-g-μs unit system, the parameters of the null material model are as follows: density $\rho = 0.0012\,\text{g/cm}^3$ and dynamic viscosity coefficient $Mu = 0.001$.

2.3.3. Constitutive Model of Concrete.
The concrete material adopts the model which adapts to high pressure and high strain rate by means of keyword *MAT_JOHNSON_HOLMQUIST_CONCRETE (HJC). The material model of HJC consists of state equation, yield equation, and damage equation. The equation of state can be divided into elastic stage, plastic stage (internal porosity compression, porosity reduction), and fully dense stage (internal porosity compression, damage, and fine grain cracks). The characteristic of the HJC model is that it can reflect the dynamic response of brittle materials such as concrete under large strain, high strain rate and high pressure, and material damage effect. It is especially suitable for the study of dynamic response of concrete structure under explosion load. The equations of state of HJC material model are as follows.

Elastic loading and unloading ($p < p_c$) is given by

$$p = k_e\mu. \quad (6)$$

Loading of plastic transition zone ($p_c \leq p \leq p_1$) is given by

$$p = p_1 + \frac{(p_1 - p_c)(\mu - \mu_1)}{\mu - \mu_1}. \quad (7)$$

Unloading of plastic transition zone ($p_c \leq p \leq p_1$) is given by

$$p - p_{\max} = \left[\left(1 - \frac{\mu_{\max} - \mu_c}{\mu_1 - \mu_c}\right)K_e + \frac{\mu_{\max} - \mu_c}{\mu_1 - \mu_c}K_1\right](\mu - \mu_{\max}). \quad (8)$$

Fully compacted loading ($p > p_1$) is given by

$$p = k_1\frac{\mu - \mu_1}{1 + \mu_1} + k_2\left(\frac{\mu - \mu_1}{1 + \mu_1}\right)^2 + k_3\left(\frac{\mu - \mu_1}{1 + \mu_1}\right)^3. \quad (9)$$

In the fully compacted unloading ($p > p_1$) stage, the material is completely destroyed:

$$p - p_{\max} = k_1\left(\frac{\mu - \mu_1}{1 + \mu_1} - \left(\frac{\mu - \mu_1}{1 + \mu_1}\right)_{\max}\right). \quad (10)$$

The yield equation of HJC material model is as follows:

$$\sigma^* = \left[A(1 - D) + BP^{*N}\right](1 + C\ln\varepsilon^*). \quad (11)$$

The damage equation of HJC material model is as follows:

$$D = \sum\frac{\Delta\varepsilon_p + \Delta\mu_p}{D_1\left(P^* + T^*\right)^{D_2}}, \quad (12)$$

where $k_e = p_c/\mu_c$ is the bulk modulus, which is the ratio of crushing volume pressure p_c and crushing volume μ_c strain in uniaxial compression test, p_1 represents compaction pressure of concrete material, and μ_1 is the compaction volume strain. K_1 is the plastic bulk modulus; $p_{\max}$ and $\mu_{\max}$ are the maximum volume pressure and volume strain before unloading. In this stage, the porosity in the material is compressed, the material is damaged, and the crushing crack begins to appear; σ^* is the standardized equivalent stress, D is the damage value ($0 \leq D \leq 1.0$), p^* is the standardized hydrostatic pressure, $\varepsilon^* = (\varepsilon/\varepsilon_0)$ is the dimensionless strain rate, A is the normalized cohesive strength; B is the normalized pressure hardening coefficient; N is the pressure

hardening index; C represents the strain rate coefficient; $\Delta\varepsilon_p$ and $\Delta\mu_p$ are the equivalent plastic strain increment and plastic volume strain increment of an element in a calculation cycle, T^* is the standardized maximum tensile stress, and D_1 and D_2 are the damage constant of the concrete. The parameters of concrete in this study are shown in Table 2.

2.3.4. Constitutive Model of Rock. The rock is simulated by means of the Drucker–Prager model. The yield criteria of the Drucker–Prager model are given by

$$t - p \cdot \tan \beta - d = 0, \tag{13}$$

$$t = \left(\frac{q}{2}\right)\left\{a - b\left(\frac{r}{q}\right)^3\right\}, \tag{14}$$

$$\begin{aligned} a &= \frac{1+1}{K}, \\ b &= \frac{1-1}{K}, \end{aligned} \tag{15}$$

where p is hydrostatic stress, q represents von Mises stress, and K is a scalar parameter that determines the shape of the yield surface and maintains the convexity of the yield surface in the deviatoric (p) plane. r is the third invariant of the deviatoric stress tensor:

$$r = \left(\frac{27\,J_3}{2}\right)^{1/3}, \tag{16}$$

where J_2 and J_3 represent the second and the third deviatoric stress invariants, respectively.

$$\tan \beta = \frac{6 \sin \varphi}{(3 - \sin \varphi)}, \tag{17}$$

$$d = \frac{6C \cos \varphi}{(3 - \sin \varphi)}. \tag{18}$$

where φ is the angle of friction and C is the dilation angle.

The material properties used for quartzite rock mass are given in Table 3, obtained from triaxial test [21].

3. Dynamic Response Characteristics of Double-Line Tunnel during Surface Blasting

3.1. Propagation Law of Stress Wave in Double-Line Tunnel. Figure 5 shows the pressure nephogram of rock mass under A1 condition. At the moment of TNT explosive explosion, the explosive volume expands rapidly in a very short time and rapidly changes from solid state to high-pressure gas state. The high-pressure gas acts on the rock and produces stress wave ($t = 0.5$ ms) on the rock mass, with the peak pressure of about 228 MPa. Due to the nonreflective boundary condition, the shock wave will not be reflected at the rock mass boundary. With the further propagation and diffusion of the shock wave in the rock mass, the amplitude of the stress wave is greatly weakened. When $t = 6.3$ ms, the peak value of the pressure decreases to about 4.32 MPa. Combined with Figure 5 ($t = 10$ ms, $t = 17$ ms, and the

velocity time history curve of lining monitoring points in Figure 6), at $t = 10$ ms, the stress wave propagates to the left lining, and at $t = 17$ ms, the stress wave propagates to the right lining. With the further attenuation of the shock wave, the stress wave gradually becomes elastic wave, which propagates at the elastic wave speed which does not disturb the physical state of the rock mass.

It can also be seen from Figure 7 that the peak velocity of monitoring point A is about 7.5 cm/s at $t = 27$ ms, and the time from stress wave propagation to monitoring point A to reaching the peak velocity of monitoring point A is about 17 ms. The peak velocity of point B is about 6.4 cm/s at $t = 46$ ms, and the time from stress wave propagation to point B to the peak velocity is about 29 ms. It can be seen that the time course of reaching the peak speed is different, and the time difference is about 12 ms. This is because the stress wave produces a series of reflection and diffraction between two tunnels, so its dynamic response process is different from that of a single tunnel. In view of this, this paper starts the follow-up research, that is, by changing the horizontal spacing and height difference of the tunnel to investigate the dynamic response characteristics of the double-line tunnel under the surface explosion load.

3.2. Distribution Law of Equivalent Stress of Lining. Figures 8 and 9 show the equivalent stress nephogram of concrete lining under different conditions (considering horizontal clear distance and height difference) at the same time ($t = 20$ ms), respectively. For the tunnel on the left, the stress distribution on the left side of YOZ symmetry plane of the lining is basically the same. For the right side of the YOZ symmetry plane of the lining, the stress distribution shows obvious differences. According to the color corresponding to the cloud figure, the darker the color of the element is, the smaller the equivalent stress is. It can be seen from Figure 8 that with the increase of the clear distance of the lining (5 m, 7 m, 9 m, 11 m, and 13 m), the stress on the right side of the symmetry plane of YOZ of the lining is not regularly decreasing. It can be seen that under A3 and A4 conditions, the overall value of the equivalent stress in this area is obviously smaller than the other three conditions (A1, A2, and A5). This shows that the influence of the tunnel spacing on the dynamic response characteristics of the lining is not linear. Similarly, it can be seen in Figure 9 that the dynamic response characteristics of the lining also show a nonlinear relationship with the variation of the lining height difference (0 m, 2 m, 4 m, 6 m, and 8 m).

3.3. Parameter Analysis of Monitoring Points. Figure 10 is the layout of monitoring points for the left lining. Monitoring points A, B, C, and D are all located on the left lining. Figure 11 shows the relationship curve between the velocity of the monitoring point and the horizontal clear distance of the tunnel. It can be seen from Figure 11 that the velocity response of the monitoring point at the top of the lining blast facing surface is lower than that of the side wall under the action of explosion load. Taking the clear distance of the lining as an example, the peak vibration velocity of the

TABLE 2: Concrete properties [20].

Mid	Ro (g/cm³)	G (Mbar)	A	B	C	N	Fc (Mbar)
	2.4	0.114	0.79	1.6	0.007	0.61	$3.00E-04$
T (Mbar)	Eps0	Efmin	Sfmax	Pc (Mbar)	Uc (Mbar)	Pl (Mbar)	ul
$4.00E-05$	$1.00E-06$	0.01	7	$1.60E-04$	0.001	0.008	0.1
D_1	D_2	K_1 (Mbar)	K_2 (Mbar)	K_3 (Mbar)	fs		
0.04	1	0.85	−1.71	2.08	0.3		

TABLE 3: Quartzite rock properties [21].

Description	Quartzite rock
Weathering condition	Slightly to moderately
Specific gravity (G)	2.65
Density (ρ) (kg/m³)	2550
Elastic modulus (E) (GPa)	28
Poisson's ratio (v)	0.25
Angle of internal friction (φ)	45°
In situ stress ratio (K_0)	0.5
Dilation angle (ψ)	5°
Cohesion (c) (MPa)	2.3
σ_c (MPa)	40
RQD range	75–80
RMR	47
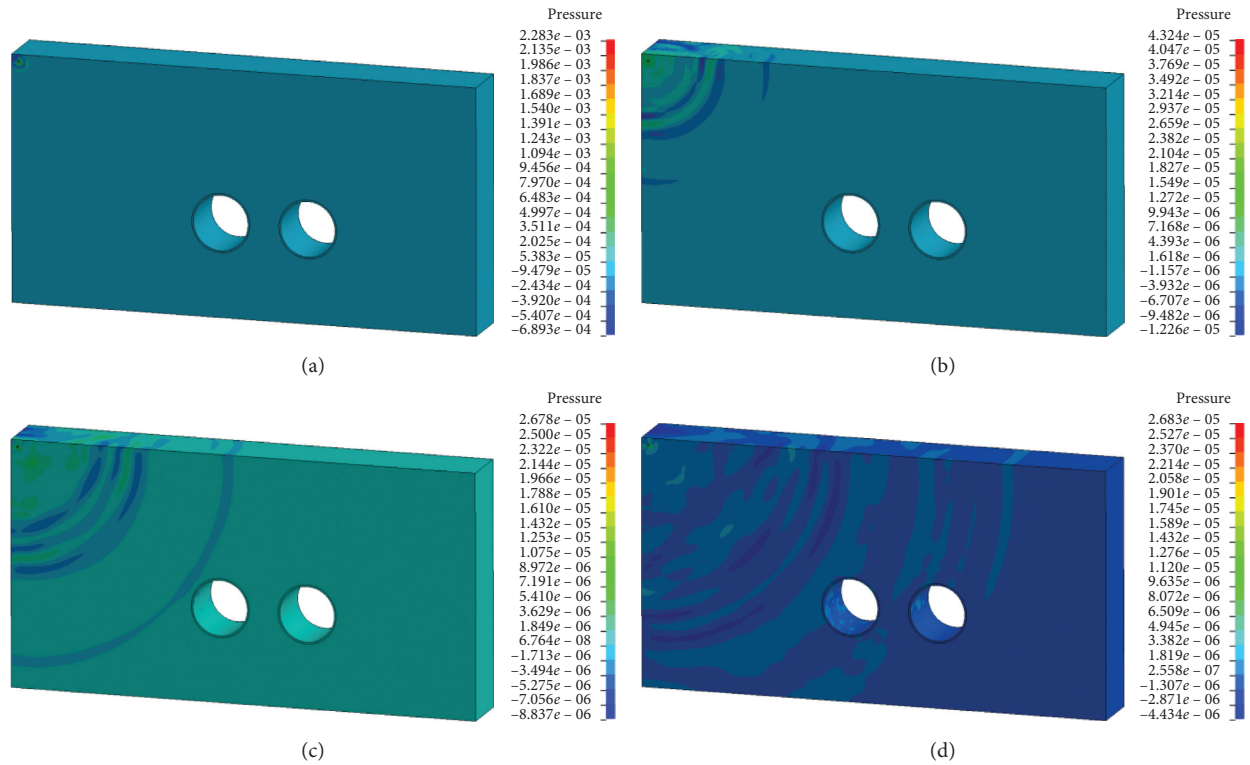
FIGURE 5: Nephogram of geotechnical pressure at typical time (Mbar). (a) $T = 0.5$ ms. (b) $T = 6.3$ ms. (c) $T = 10$ ms. (d) $T = 17$ ms.

monitoring point B at the top of the lining blast facing surface is about 7.5 cm/s, and the peak vibration velocity of the monitoring point A at the side wall of the lining blast facing surface is about 6.5 cm/s. The vibration velocity is about 13% lower than that of B. At the same time, it can be seen that the peak velocity of monitoring points A and B almost does not change with the increase of the horizontal spacing of the lining, which indicates that the influence of the change of the tunnel spacing on the vibration velocity of the top of the lining face and the side wall can be ignored.

As for the monitoring point C on the lining side wall of the back blasting face and the monitoring point D at the bottom of the lining, it can be seen from Figure 11 that the vibration velocity of the monitoring point C is lower than
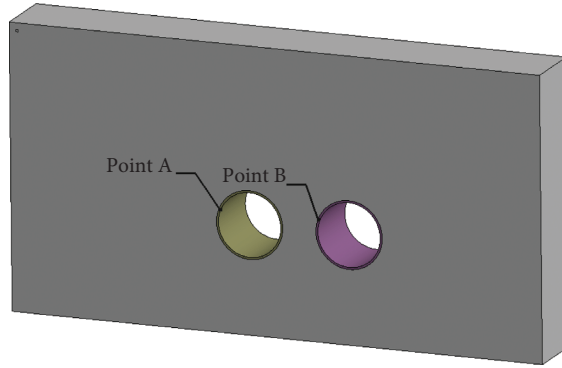
FIGURE 6: Layout of monitoring points.
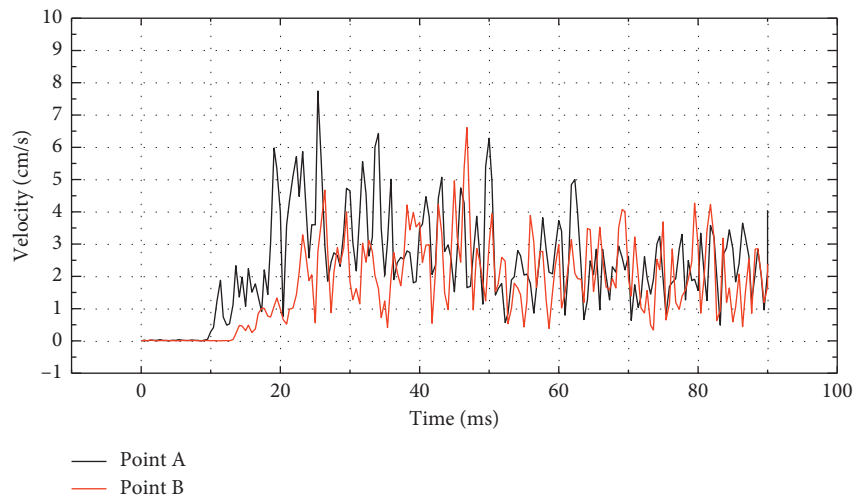
FIGURE 7: Velocity time-history curve of monitoring points.
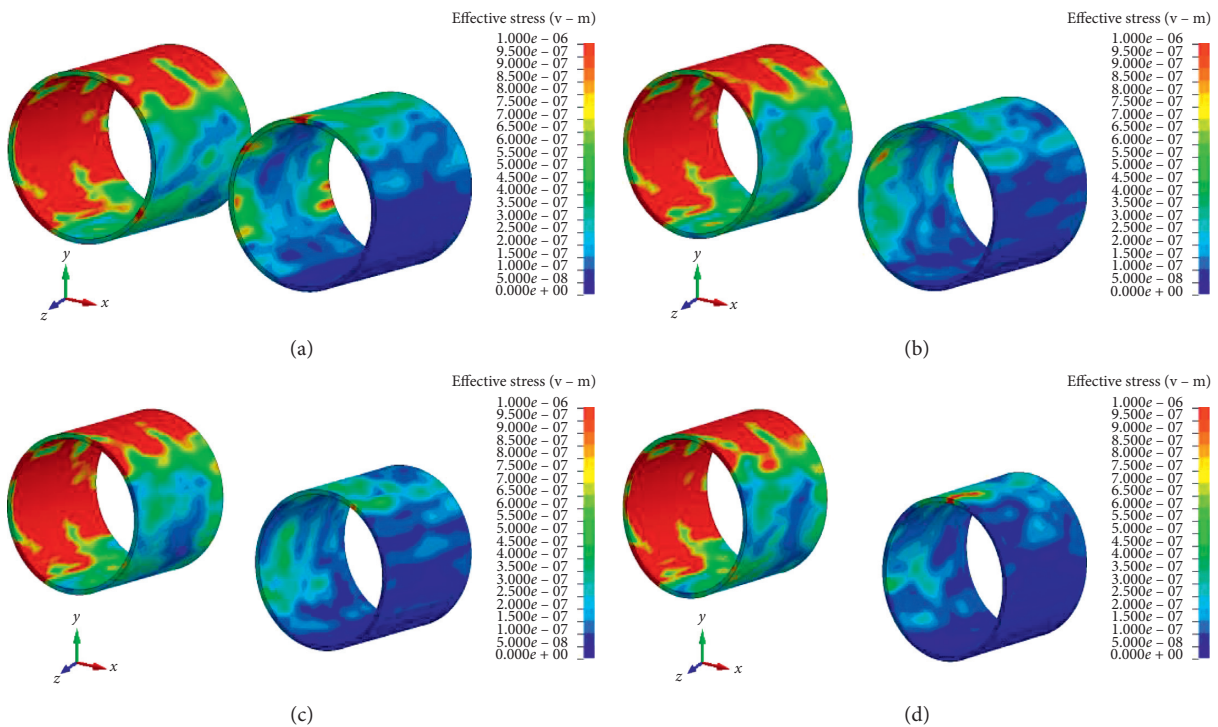
FIGURE 8: Continued.

(e)
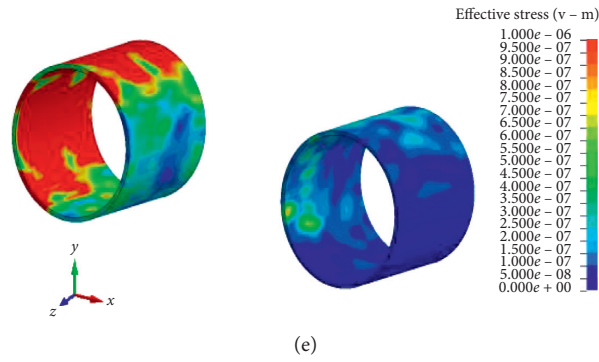
FIGURE 8: Equivalent stress nephogram of lining under condition 1 at $t = 20$ ms (Mbar). (a) A1. (b) A2. (c) A3. (d) A4. (e) A5.

(a)

(b)

(c)

(d)

(e)
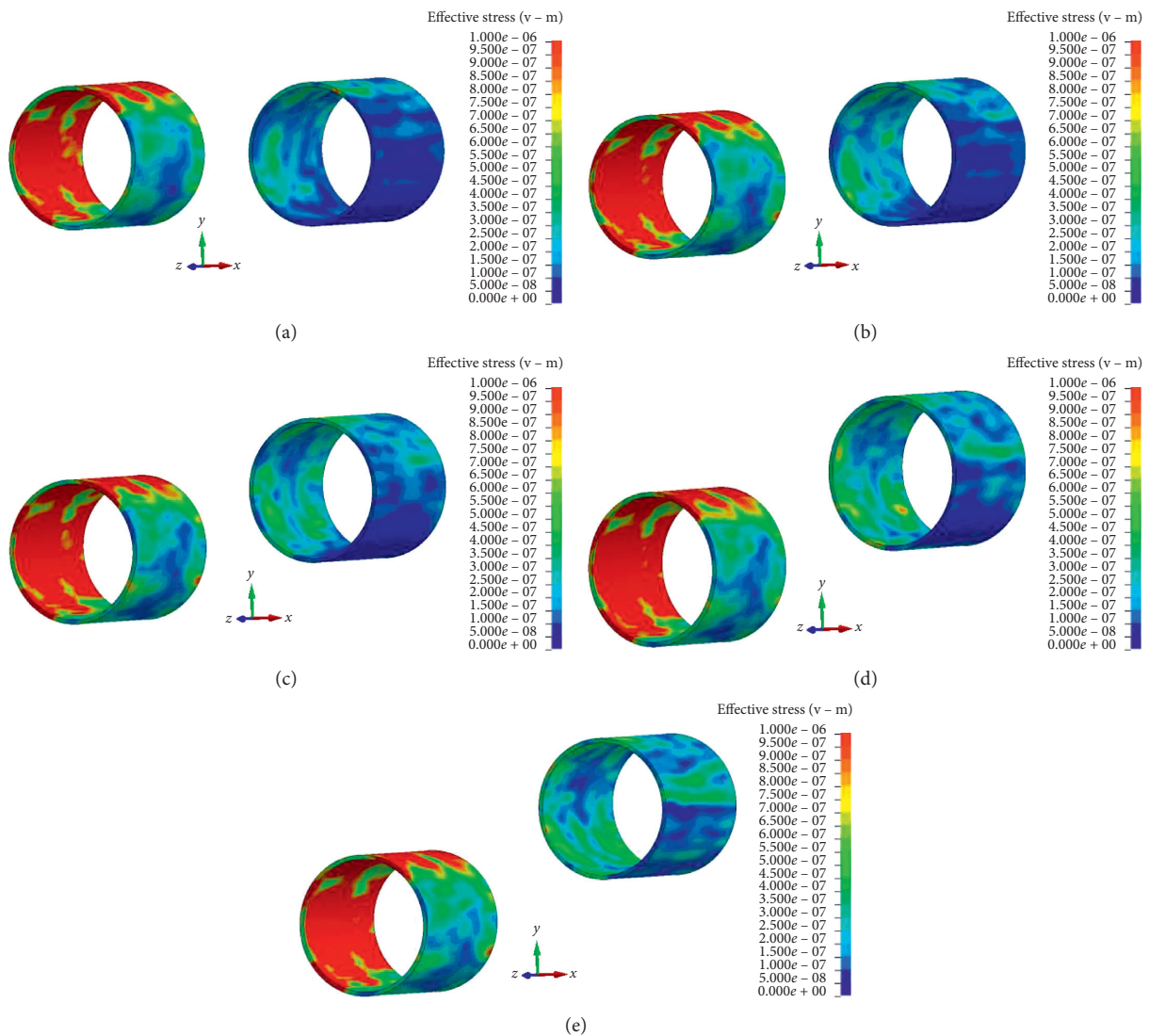
FIGURE 9: Equivalent stress nephogram of lining under condition 2 at $t = 20$ ms (Mbar). (a) A3. (b) B3. (c) C3. (d) D3. (e) E3.

that of the monitoring point D, and with the increase of the horizontal clear distance of the tunnel, the vibration velocity of the monitoring points C and D decreases significantly. For the monitoring point C on the back blasting face, with the increase of the horizontal clear distance of the lining, the vibration velocity of the monitoring point C decreases from 6.4 cm/s to 4.7 cm/s, and the peak velocity decreases by about 26.5%. For point D at the bottom of back blasting surface,
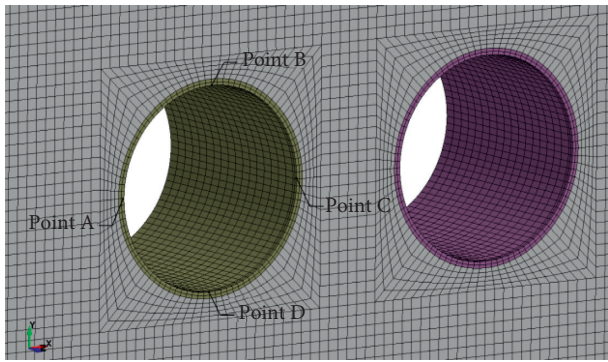
FIGURE 10: Layout of monitoring points.
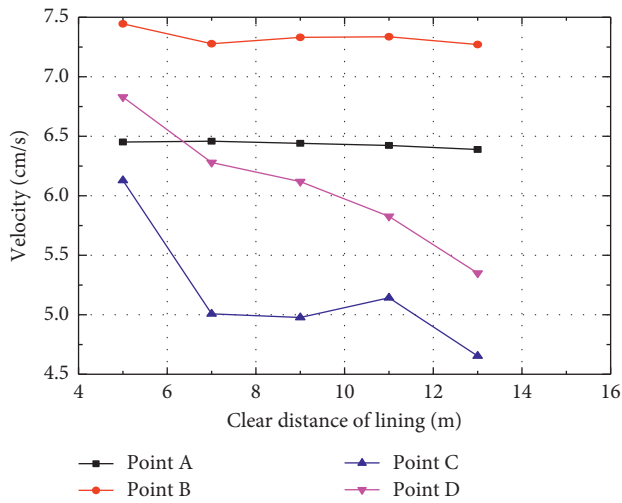
FIGURE 11: Relationship curve between monitoring points speed and horizontal clear distance of tunnel.

FIGURE 12: Relationship curve between equivalent stress of monitoring point and horizontal clear distance of tunnel.

FIGURE 13: Relationship curve between X-direction stress of monitoring points and horizontal clear distance of tunnel.

FIGURE 14: Relationship curve between Y-direction stress of monitoring points and horizontal clear distance of tunnel.

the vibration velocity of point D decreases from 6.7 cm/s to 5.3 cm/s with the increase of horizontal clear distance of lining, and the peak velocity decreases by about 20.9%.

Figures 12–14 are the curves of the relationship between the equivalent stress of the monitoring point and the horizontal clear distance of the tunnel, the relationship between the stress of the monitoring point in the X-direction and the horizontal clear distance of the tunnel, and the relationship between the stress of the monitoring point in the Y-direction and the horizontal clear distance of the tunnel, respectively. It can be seen from Figure 12 that, similar to the variation law of velocity monitoring point, the peak value of equivalent stress of lining side wall monitoring point A and lining top point B on the blast facing face does not change with the increase of horizontal spacing of lining. The peak value of equivalent stress of monitoring point B is about 0.42 MPa, and that of monitoring point A is about 0.36 MPa. The peak value of equivalent stress at point A is reduced by about 14%.

For monitoring point C on lining side wall of back blasting face and monitoring point D on lining bottom, from the overall analysis of Figure 12, it can be seen that with the increase of horizontal spacing of tunnel, the equivalent stress of monitoring point decreases on the whole. For point C, the peak value of equivalent stress decreases from 0.3 MPa to

0.27 MPa, and the peak value of equivalent stress decreases by about 10%. For point D, the peak value of equivalent stress decreases from 0.28 MPa to 0.24 MPa, and the peak value of equivalent stress decreases by about 14%.

As for Figures 13 and 14, it can be seen from the analysis that no matter for the X-direction stress or Y-direction stress of the monitoring point, the peak stress of the monitoring point A has almost no obvious change. This is because although the refraction and diffraction effect of the rock stress wave between the two linings is produced, whose influence is mainly on the lining on the back blasting side, the influence on the monitoring point of the lining side wall on the blast facing side can be ignored. For point C on the blasted side, it can be seen from the analysis of Figures 13 and 14 that the stress components of X and Y are in a downward trend on the whole, while for the monitoring point D on the bottom of the lining, it can be seen that the stress component in the Y-direction has a slight increment with the increase of the net distance of the tunnel, and the stress peak value in the Y-direction increases from 0.15 MPa to 0.18 MPa, an increase of about 20%.

Figure 15 shows the relation between the velocity of the monitoring point and the height difference of the tunnel. It can be seen from Figure 15 that under the action of surface blasting, similar to the previous analysis, the peak value of vibration velocity at monitoring point A on the blast facing surface of lining side wall does not change significantly. For the monitoring point B on the blasting face of lining, with the increase of tunnel height difference, the peak value of vibration velocity increases. This is because as the right tunnel rises upward, which is more conducive to the reflection and superposition of stress wave, so the vibration velocity of measurement point B increases. It can be seen that the vibration velocity of monitoring point B increases from 7.3 cm/s to 7.7 cm/s, with an increase of about 5.5%. When the height difference of lining is between 0 and 4 m, the sensitivity of vibration velocity of side wall monitoring point C is low, and there is almost no significant change in vibration velocity. However, when the height difference is between 4 and 6 m, the vibration velocity changes from 5 cm/s to 5.5 cm/s, and the increase of vibration velocity in this interval is about 10%. For point D at the bottom of the lining, the vibration velocity changes significantly with the increase of tunnel height difference. It can be seen that the vibration velocity of point D increases from 5.7 cm/s to 7.1 cm/s, and the peak velocity increases by about 25%.

Figures 16–18 are the curves of the relationship between the equivalent stress of the monitoring point and the height difference of the tunnel, the relationship between the X-direction stress of the monitoring point and the height difference of the tunnel, and the relationship between the Y-direction stress of the monitoring point and the height difference of the tunnel, respectively. It can be seen from Figure 16 that, with the increase of the tunnel height difference, the equivalent stress of points A and B on the blasting face remains stable, and the peak values of equivalent stress are about 0.36 MPa and 0.43 MPa, respectively. For the back burst surface lining test point C, the peak value
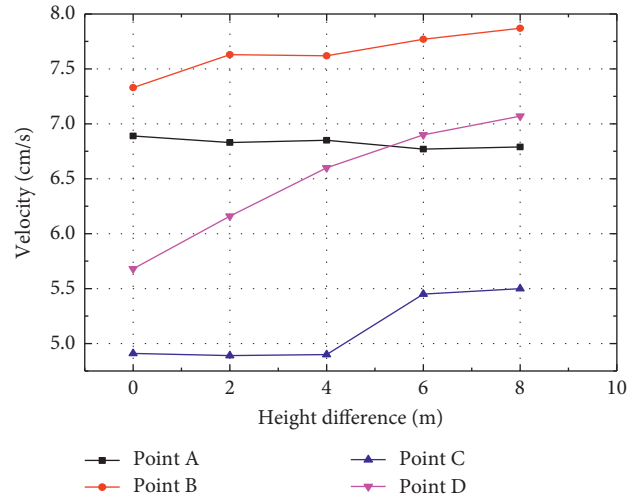
FIGURE 15: Relationship curve between monitoring points speed and horizontal height difference of tunnel.
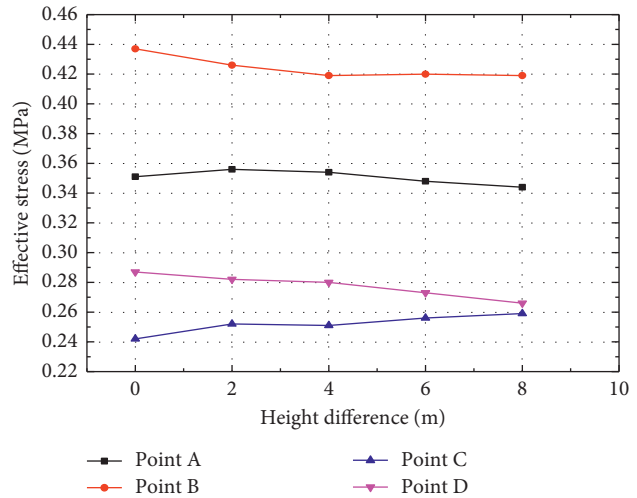
FIGURE 16: Relationship curve between equivalent stress of monitoring point and horizontal height difference of tunnel.
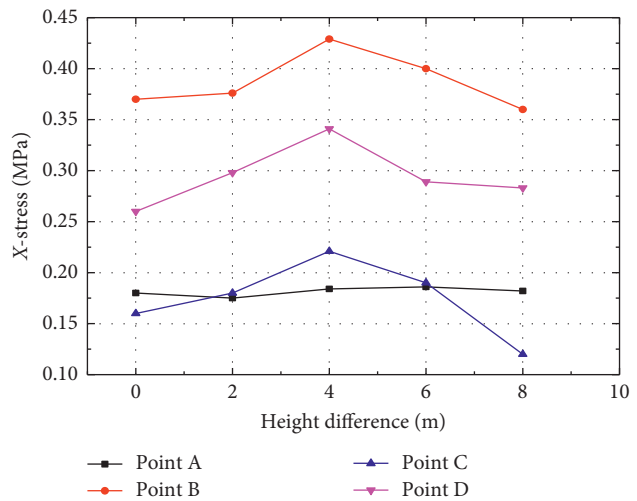
FIGURE 17: Relationship curve between the X-direction stress of monitoring points and tunnel height difference.
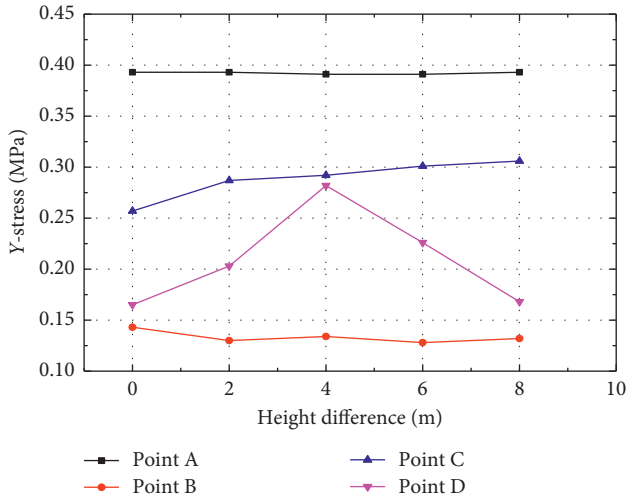
Figure 18: Relationship curve between the Y-direction stress of monitoring points and tunnel height difference.

Figure 19: Path setting of lining monitoring points.

of equivalent stress increases slightly with the increase of tunnel height difference, and the peak value of equivalent stress increases from 0.24 MPa to 0.26 MPa, with an increase of about 8.3%. For the back blasting face lining monitoring point D, with the increase of tunnel height difference, the peak value of equivalent stress of point D presents a small downward trend, and the peak value of equivalent stress decreases from 0.29 MPa to 0.27 MPa, with a decrease of about 6.9%. As for the X-direction stress component of the monitoring points, it can be seen from the analysis of Figure 17 that except for point A on the blasting face, the X-direction stress component of the other monitoring points increases first when the height difference of the lining is 0~4 m and then decreases when the height difference is about 4~8 m. It shows that the reflected shock wave has the greatest influence on the X-direction stress component of the monitoring point on the back blasting surface of the left tunnel when the height difference of the adjacent tunnel is 4 m and the horizontal clear distance is constant. It can be seen from Figure 18 that the peak value of the Y-direction stress at the monitoring point B on the blasting face of the lining decreases slowly with the increase of the tunnel height difference, while for the monitoring point C on the blasting face of the lining, the component of the Y-direction stress decreases slightly with the increase of the tunnel height difference.

Figure 19 is the layout of the monitoring point path of the back burst surface of the left lining. Figures 20 and 21 show the relationship between the displacement along the path (along the negative direction of Z) of the horizontal net distance and the tunnel height difference ($t = 31$ ms), respectively. It can be seen from the figure that the displacement of the lining monitoring point is decreasing along the path direction as a whole. It can also be seen that the displacement of the monitoring points of condition 1, A1 and A5 is larger than A2, A3, and A4, which shows that the variation of displacement of the monitoring points is not very significant due to the lining spacing. For condition 2, it can be seen from Figure 21 that with the increase of the
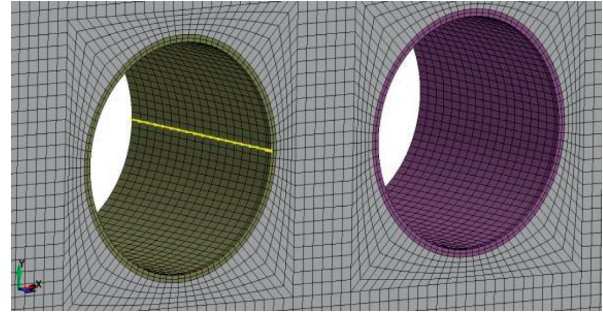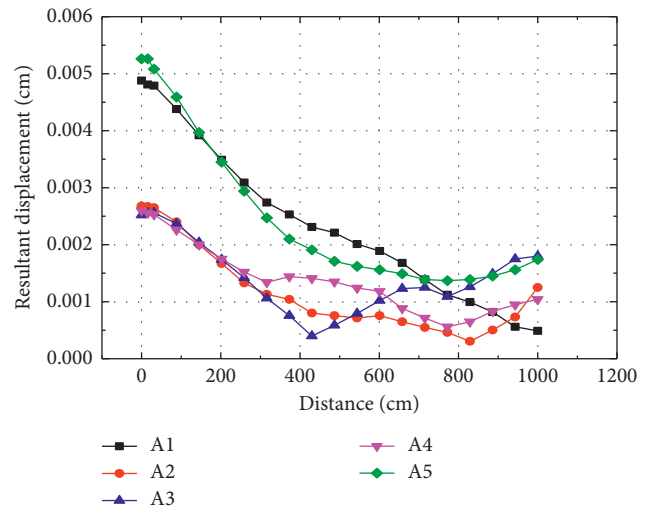
Figure 20: Variation of displacement of lining monitoring points along the path in case 1.
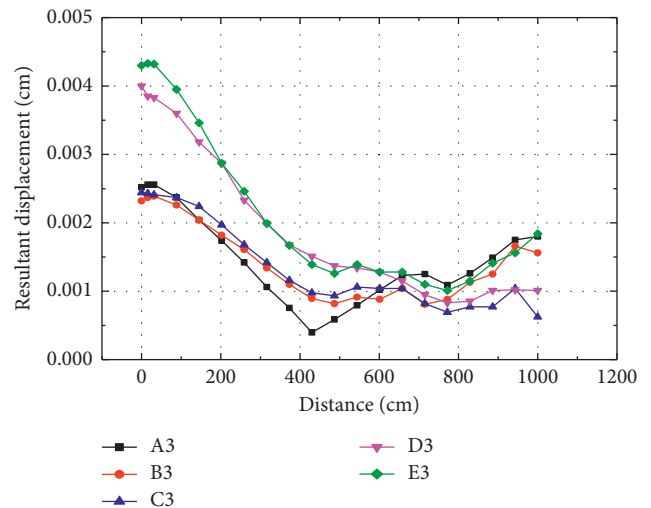
Figure 21: Variation of displacement of lining monitoring points along the path in case 2.

tunnel height difference, the displacement of the monitoring point increases with the increase when the path length is less than 4 m. In addition, the displacement increases obviously in the interval with the tunnel height difference of 4–6 m.
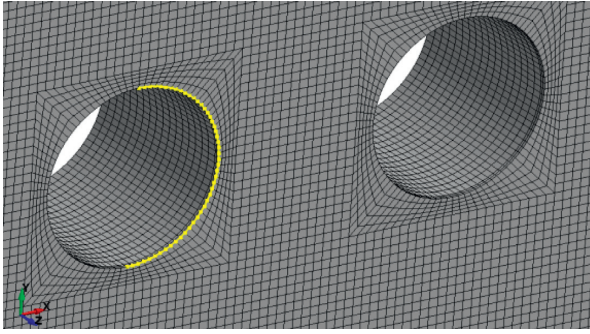
FIGURE 22: Path setting of tunnel rock mass monitoring points.
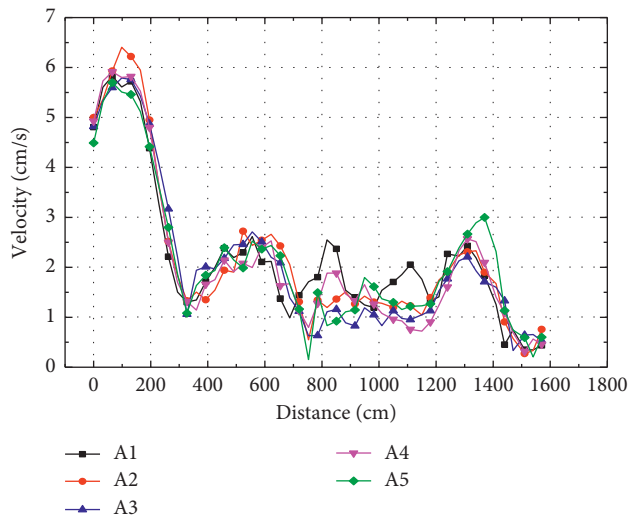
FIGURE 23: Variation velocity of lining monitoring points along the path in case 1.

FIGURE 24: Variation velocity of lining monitoring points along the path in case 2.

Taking the initial point of the path (distance = 0) as an example, the displacement of the monitoring point under C3 condition (height difference = 4 m) is about 0.0025 cm. The displacement of the monitoring point is about 0.004 cm under D3 condition (height difference = 6 m), which is about 60% higher than that of the other.

Figure 22 is the path layout of rock monitoring points. The monitoring points are arranged clockwise along the *z*-axis. It can be seen that the variation law of the vibration velocity along the path of the monitoring points the same no matter in condition 1 or condition 2. The vibration velocity of the tunnel top reaches the peak at about 100 cm along the path, rather than just above the top of the tunnel, as shown in Figures 23 and 24. It can also be seen that the lowest vibration velocity is at the bottom of the tunnel. It can be seen from the dispersion degree of the vibration velocity value of two curves that the dispersion degree of condition 1 will be higher, which indicates that the change of the horizontal spacing of the tunnel will have more significant influence on the vibration velocity of each monitoring point than the change of the tunnel height difference.

4. Conclusions

Based on LS-DYNA 3D nonlinear finite element software, a full coupling model of TNT explosive-surrounding rock-lining structure-air is established. Lagrange algorithm is used for lining and rock mass materials. Euler algorithm is used for air and explosive materials. The nonlinear coupling between Euler fluid domain and Lagrange structure domain is realized by ALE multimaterial fluid structure coupling algorithm. By controlling the clear distance and height difference of double-line tunnel, a variety of numerical simulation cases are formulated. The dynamic response characteristics of double-line tunnel under different conditions and surface explosion load are systematically studied. The main conclusions are as follows:

Under the action of surface blasting, the influence of the tunnel clear distance and height difference on the dynamic response characteristics of the lining presents a nonlinear variation law except for the monitoring point A on the blasting face.

The peak velocity of monitoring points A and B on the blast facing surface hardly changes with the increase of the horizontal spacing of the lining, indicating that the influence of the change of the tunnel spacing on the vibration velocity of the top and side walls of the blast facing surface of the lining can be ignored. For point C on the side wall of back blasting face, the peak velocity of point C decreases about 26.5% with the increase of horizontal clear distance of lining. For point D at the bottom of back blasting face, the peak velocity of point D decreases about 20.9% with the increase of horizontal clear distance of lining. With the increase of the horizontal distance of the tunnel, the equivalent stress of the measuring points decreases on the whole.

With the increase of the height difference between adjacent tunnels, the peak value of vibration velocity of lining monitoring point B increases, which is more conducive to

the reflection and superposition of stress waves due to the upward elevation of the right tunnel. When the height difference between adjacent tunnels is 4 m, the reflected shock wave has the greatest influence on the X-direction stress component of the measuring points on the back blasting surface of the left tunnel. When the tunnel height difference is about 4~6 meters, the vibration velocity and displacement of monitoring point C on the back blasting side will change abruptly, and the variation range of vibration velocity is about 25%, while the variation range of displacement is about 60%.

Data Availability

The data are available and explained in this article; readers can access the data supporting the conclusions of this study.

Disclosure

The authors would like to declare that the work described herein is original research and has not been previously published elsewhere.

Conflicts of Interest

The authors declare that they have no conflicts of interest regarding the publication of this paper.

Acknowledgments

References

[1] A. Eitzenberger, *Wave Propagation in Rock and the Influence of Discontinuities*, Luleå University of Technology, Luleå, Sweden, 2012.

[2] Y. K. Wu, H. Hao, Y. X. Zhou, and K. Chong, "Propagation characteristics of blast-induced shock waves in a jointed rock mass," *Soil Dynamics and Earthquake Engineering*, vol. 17, no. 6, pp. 407–412, 1998.

[3] J. Yang, J. Cai, C. Yao, and P. Li, "Comparative study of tunnel blast-induced vibration on tunnel surfaces and inside surrounding rock," *Rock Mechanics and Rock Engineering*, vol. 52, no. 11, pp. 1–15, 2019.

[4] Q. Liang, J. Li, D. Li, and E. Ou, "Effect of blast-induced vibration from new railway tunnel on existing adjacent railway tunnel in xinjiang, China," *Rock Mechanics and Rock Engineering*, vol. 46, no. 1, pp. 19–39, 2013.

[5] Z. Mohammad and M. Rehan Sadique, "The response of rock tunnel when subjected to blast loading: finite element analysis," *Engineering Reports*, vol. 3, no. 2, 2020.

[6] J. B. Liu, Q. S. Yan, and J. Wu, "Analysis of blast wave propagation inside tunnel," *Transactions of Tianjin University*, vol. 14, no. 5, 2008.

[7] V. R. Feldgun, A. V. Kochetkov, Y. S. Karinski, and D. Z. Yankelevsky, "Internal blast loading in a buried lined tunnel," *International Journal of Impact Engineering*, vol. 35, no. 3, 2007.

[8] G. Yang, G. Wang, W. Lu, Y. Peng, and M. Chen, "Damage assessment and mitigation measures of underwater tunnel subjected to blast loads," *Tunnelling and Underground Space Technology incorporating Trenchless Technology Research*, vol. 94, no. 1, 2019.

[9] S. Koneshwaran, D. P. Thambiratnam, and C. Gallage, "Blast response of segmented bored tunnel using coupled SPH-fe method," *Structure*, vol. 2, no. 1, pp. 58–71, 2015.

[10] F. Wu, H. Zhang, Q. Zou, C. Li, J. Chen, and R. Gao, "Viscoelastic-plastic damage creep model for salt rock based on fractional derivative theory," *Mechanics of Materials*, vol. 150, no. 1, Article ID 103600, 2020.

[11] Y. Wang, W. K. Feng, R. L. Hu, and C. H. Li, "Fracture evolution and energy characteristics during marble failure under triaxial fatigue cyclic and confining pressure unloading (FC-CPU) conditions," *Rock Mechanics and Rock Engineering*, vol. 54, no. 5, pp. 799–818, 2021.

[12] Q. Wang, Y. Wang, M. He et al., "Experimental research and application of automatically formed roadway without advance tunneling," *Tunnelling and Underground Space Technology*, vol. 114, no. 3, Article ID 103999, 2021.

[13] Q.-X. Meng, W.-Y. Xu, H.-L. Wang, X.-Y. Zhuang, W.-C. Xie, and T. Rabczuk, "DigiSim - an open source software package for heterogeneous material modeling based on digital image processing," *Advances in Engineering Software*, vol. 148, no. 3, Article ID 102836, 2020.

[14] C. Zhu, M. C. He, M. Karakus, X.-H. Zhang, and Z. Guo, "The collision experiment between rolling stones of different shapes and protective cushion in open-pit mines," *Journal of Mountain Science*, vol. 18, no. 5, pp. 1391–1403, 2021.

[15] C. Zhu, M. C. He, M. Karakus, X. H. Zhang, and Z. G. Tao, "Numerical simulations of the failure process of anaclinal slope physical model and control mechanism of negative Poisson's ratio cable," *Bulletin of Engineering Geology and the Environment*, vol. 80, no. 7, pp. 3365–3380, 2021.

[16] A. Li, F. Dai, Y. Liu, H. Du, and R. Jiang, "Dynamic stability evaluation of underground cavern sidewalls against flexural toppling considering excavation-induced damage," *Tunnelling and Underground Space Technology*, vol. 112, Article ID 103903, 2021.

[17] Livermore Software Technology Corporation (LSTC), *LS-DYNA Keyword User's Manual Version R 10.0*, Livermore Software Technology Corporation, Livermore, CA, USA, 2017.

[18] M. Larcher and F. Casadei, "Explosions in complex geometries—a comparison of several approaches," *International Journal of Protective Structures*, vol. 1, no. 2, 2010.

[19] X. Huo, X. Shi, X. Qiu et al., "Rock damage control for large-diameter-hole lateral blasting excavation based on charge structure optimization," *Tunnelling and Underground Space Technology*, vol. 106, Article ID 103569, 2020.

[20] J. O. Hallquist, *LS-DYNA Theoretical Manual*, Livemore Software Technology, Livemore, CA, USA, 1998.

[21] H. R. Yadav, *Geotechnical Evaluation and Analysis of Delhimetro Tunnels*, Indian Institute of Technology (IIT), Delhi, India, 2005.

Research Article

Study on Seismic Response and Damping Measures of Surrounding Rock and Secondary Lining of Deep Tunnel

Baoli Tang and Yongqiang Ren [ORCID]

Department of Civil Engineering, Ordos Institute of Technology, Ordos, Inner Mongolia 017010, China

Correspondence should be addressed to Yongqiang Ren; ryongqiang@oit.edu.cn

Tunnel construction is gradually developing to areas with high in situ stress; the deeper the tunnel construction, the more intense the earthquake disturbance. Under the background of frequent earthquakes, the seismic characteristics of tunnels become an important content related to the safety and stability of engineering structures. In view of the key problems of seismic response and vibration reduction measures for complex deep buried tunnels, the methods of advanced grouting and foam concrete aseismic are studied in this paper. Firstly, through geological survey, the in situ stress and geological conditions of the study area are analyzed. The structural characteristics of surrounding rock and related rock mechanics parameters are analyzed. The failure criterion of concrete lining under dynamic load is studied theoretically, and the relevant numerical calculation parameters are modified. A numerical model based on viscous boundary conditions is established. Through numerical calculation, the seismic response of tunnel surrounding rock and lining under different damping measures is analyzed. The research results have theoretical research value and social and economic benefits for ensuring the safety and stability of tunnel structure and improving the seismic fortification level.

1. Introduction

With the gradual transfer of tunnel construction to the high seismic intensity area, tunnel seismic has become a hot and difficult problem. How to put forward reasonable and effective seismic mitigation measures is an important purpose of tunnel seismic response analysis. In view of this, many scholars have carried out a lot of research and discussion on the mechanism and effect of seismic mitigation of tunnels and achieved rich research results. For example, Lai et al. [1] used the tunnel seismic damage investigation method combined with the Wenchuan earthquake to analyze and summarize the tunnel seismic damage. The results show that the seismic damage of fault fracture zone is the most serious, followed by tunnel entrance section and common section. The typical earthquake damages of tunnel are lining cracking, collapse, dislocation, construction joint cracking, and invert uplift. Tunnel lining crack and collapse are significant disasters caused by earthquake. Balkaya and Kalkan [2] carried out a series of modal and nonlinear static analysis

of the tunnel structure, focusing on the characteristic dynamic behavior of the tunnel structure. Shen et al. [3] used the new damage assessment criteria to classify the damage degree of the detection tunnel. Then, the typical seismic damage characteristics and mechanism of mountain tunnel are analyzed from three different damage modes of shallow tunnel damage, deep tunnel structure damage, and pavement damage. Li [4] analyzed the failure characteristics of the tunnel under seismic load and divided it into collapse and landslide near the tunnel, opening cracking, lining, and surrounding rock collapse, lining cracking and dislocation, ground uplift and cracking, and initial support deformation and cracking. Miao et al. [5] adopted the concept of the response displacement method and realized it with a fine free field model and a simplified soil tunnel model in order to efficiently study the seismic characteristics of this special subway tunnel under the action of spatial ground motion. Mayoral et al. [6] used FLAC3D to evaluate the seismic response of a typical tunnel shaft under the condition of increasing seismic intensity. Gan et al. [7] used the discrete

element numerical analysis method to analyze the control effect of the support on the surrounding rock of the tunnel. Vanuvamalai et al. [8] evaluated the seismic performance of tunnel structure by studying the seismic vulnerability of underground tunnel. Hui et al. [9] designed a large-scale shaking table slope model test with the geometric scale of 1 : 10. The Wenchuan earthquake wave was used as the excitation wave in the model test in order to study the mechanical characteristics of shallow bias tunnel with small clear distance under earthquake. Li et al. [10, 11] analyzed the development of plastic zone of surrounding rock under the condition of different grouting thicknesses and calculated the distribution characteristics of in situ stress field by using the neural network inversion method. In terms of numerical computation, Meng et al. [12] established an open source software package for modeling inhomogeneous materials based on digital image processing.

In terms of experiments, Zhu et al. [13] tested the collision of different shapes of rolling stones with protective mats in an open pit mine. Yin et al. [14] analyzed the shear mechanical response of sandstone at high temperature under normal stiffness boundary conditions. In terms of engineering application research, Wang et al. [15, 16] investigated deep mine autocuttings with high-strength bolted grouted roof cuts using numerical simulations, indoor experiments, and other methods. Wang et al. [17] studied the fracture evolution and energy characteristics during marble damage under triaxial fatigue cycling and constrained pressure unloading (FC-CPU) conditions.

In this paper, through geological investigation and numerical analysis, the force characteristics of tunnel surrounding rock and lining under the action of earthquake load are studied and the method to reduce the effect of earthquake on the tunnel and determine the control parameters of the response is proposed.

2. Engineering Geological Conditions

2.1. Geological Characteristics.
Yuelongmen tunnel of China Chenglan railway crosses the Northeast Longmenshan mountain range, and the intersection angle between the tunnel crossing section and the mountain range is about 60°. The Longmenshan structural belt crossed by Yuelongmen tunnel is a huge nappe structural belt with large scale and complex structure. The overall trend is NE 45°. It stretches 500 km and is 25–50 km wide. There are three main faults from east to west: Longmen Qianshan fault, Longmen central fault, and Longmen Houshan fault. The direction of tectonic movement is NW-SE upthrusting, forming three imbricate thrust belts. The terrain is NW-SE descending step by step, and the relative height difference is 600–700 m. The whole tunnel is located in the Longmenshan seismic zone, which is one of the concentrated areas of active faults and strong earthquakes, including the Longmenshan, Minjiang, West Qinling, and other seismic zones, which are prone to high intensity earthquakes in Western China (Figure 1). The famous Wenchuan earthquake still has frequent aftershocks. The lithology of surrounding rock is mainly phyllite, carbonaceous slate, and shale, with local diabase dyke intrusion,

soft rock, broken rock, water saturated surrounding rock, rock softening with water, and low strength.

2.2. In Situ Stress Characteristics.
The in situ stress test was carried out at DK107 + 520 of Yuelongmen tunnel. The designed hole depth is 605 m. The core drilled in this hole is mainly carbonaceous phyllite. The test results are shown in Figure 2.

Based on the test results, the basic characteristics of in situ stress of Yuelongmen tunnel are analyzed. The maximum horizontal principal stress near the tunnel body is about 16 MPa, the minimum horizontal principal stress is about 12 MPa, and the vertical principal stress calculated by overlying strata is about 16 MPa. The relationship between the value of the principal stress in the direction of air near the tunnel body is $S_H > S_V > S_h$. The in situ stress is mainly characterized by regional tectonic stress, while the difference between the vertical stress and the maximum horizontal principal stress is between 4 and 6 MPa. The distribution of principal stress with depth is shown in Figure 2. It can be seen that the three-dimensional principal stress increases with depth. In order to quantitatively analyze the relationship between the stress value and the depth of the hole, the linear regression method is used to calculate the regression of the hole, and the results are as follows [18, 19]:

$$S_H = 0.021\,D + 4.33 \quad R = 0.9016,$$
$$S_h = 0.016\,D + 2.38 \quad R = 0.9309, \qquad (1)$$
$$S_V = 0.0265\,D.$$

2.3. Mechanical Properties of Surrounding Rock.
The surrounding rock of the section is mainly phyllite, with higher mica content, smaller particle size, and directional arrangement. The texture is developed, and the fabric surface can be seen with silk luster. The sandy phyllite is dark gray with crystallite structure and sheet structure. The grain size of mineral particles is small, and the schistosis of rock is developed, and silk luster can be seen on the foliation surface. Phyllite mineral distribution has a strong direction of optimization. According to the mineral analysis, the main minerals of the phyllite sample are as follows: illite content is 14%–59%; quartz content is 3%–68%; and chlorite content is 3%–61%.

The carbonaceous phyllite was studied by 0° and 90°. The stress-strain curve of the triaxial compression test under inclination angle is shown in Figure 3. The confining pressure was set to 5 MPa, 15 MPa, and 20 MPa, respectively. The loaded specimens at 0° and 90° inclination angles exhibit two different deformation characteristics. The former specimens have no obvious peak strength and strain softening stages under different envelope pressures and macroscopically present compression-based ductile expansion damage. The latter has the characteristics of hard rock damage, the peak strength strain is lower, the residual strength increases with the increase in the surrounding pressure, and the specimens mostly have tension damage as

(a)   (b)

(c)
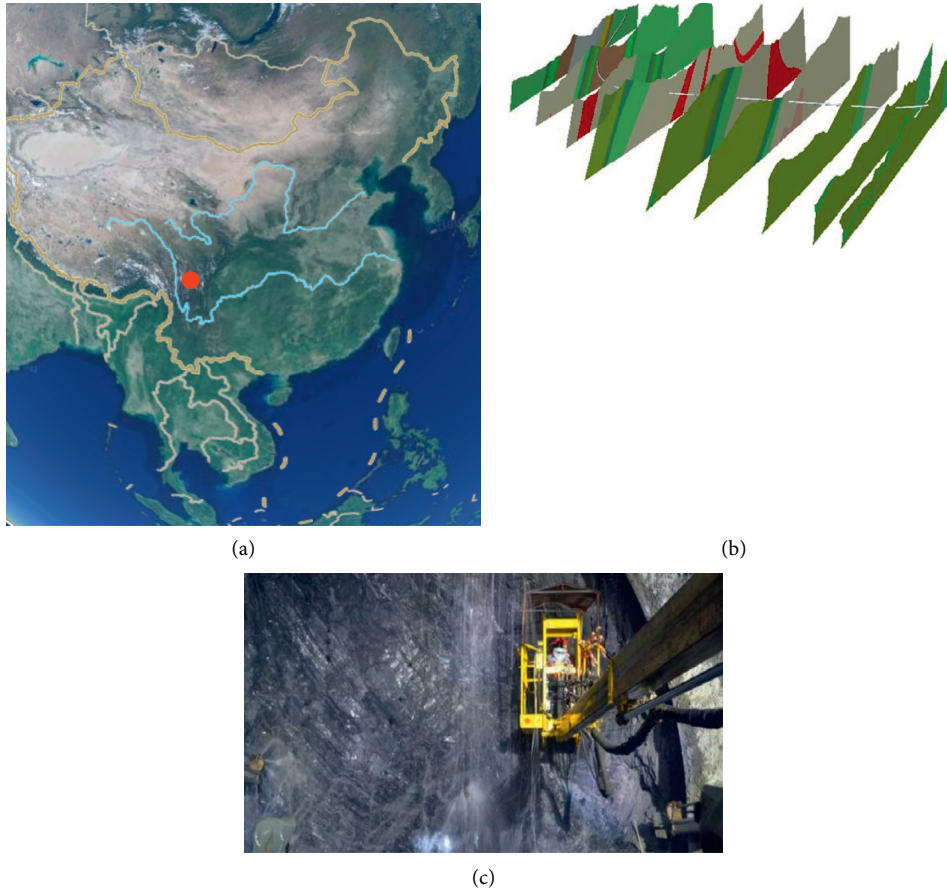
FIGURE 1: Engineering geological characteristics of Yuelongmen deep buried tunnel: (a) tunnel location; (b) tunnel crossing stratum; (c) characteristics of surrounding rock.

(a)   (b)
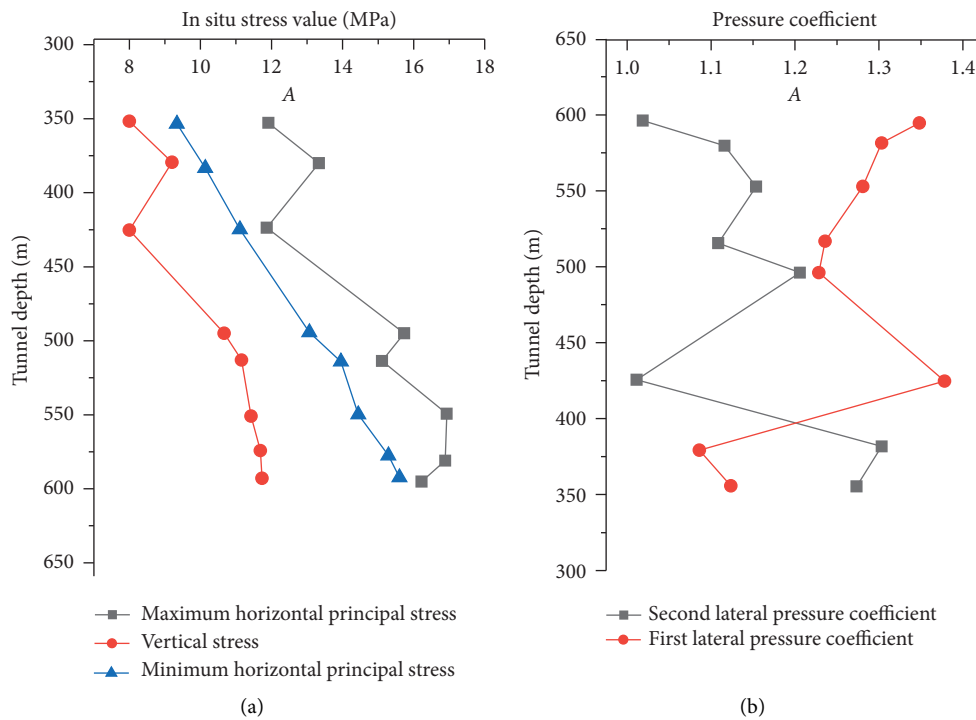
FIGURE 2: In situ stress test results: (a) in situ stress depth relationship; (b) lateral pressure coefficient depth relationship.
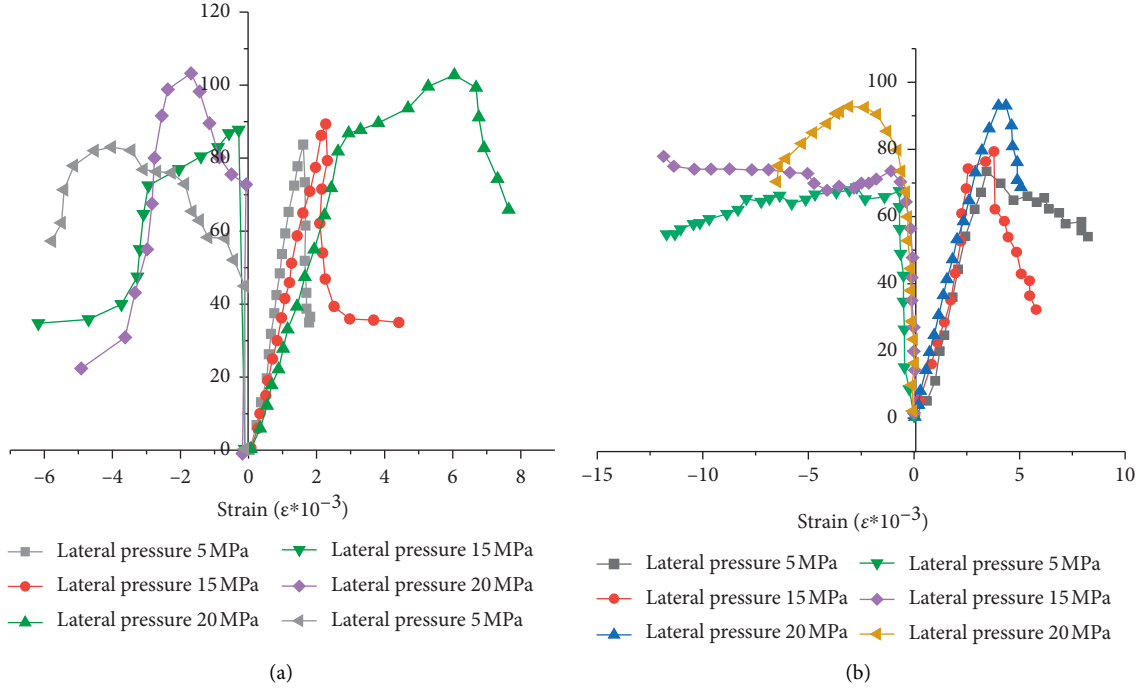
Figure 3: Typical stress-strain curves for triaxial compression of carbonaceous micaceous rocks: (a) joint dip 0°; (b) joint dip 90°.

the main damage mode. According to the experimental results, it is known that when the joints are at 0° dip angle, the peak strength of carbonaceous slate is 85 MPa under the confining pressure of 5 MPa. The peak strength is 90 MPa at a confining pressure of 15 MPa and 104 MPa at a confining pressure of 20 MPa. When the joints are 90° dip, the peak strength of carbonaceous slate is 73 MPa at a confining pressure of 5 MPa, 80 MPa at a confining pressure of 15 MPa, and 95 MPa at a confining pressure of 20 MPa.

3. Tunnel Concrete Lining Dynamic Damage Cracking Model

According to the relevant research results, there are differences between the dynamic and static constitutive models of concrete, as shown in Figure 4. Curve 1 represents the static constitutive model, and curve 2 represents the dynamic constitutive model. The two models satisfy the geometric relation 2.

$$\frac{AB}{Cd} = \frac{OA}{OC}. \tag{2}$$

It is assumed that the constitutive relation of concrete under dynamic load is as follows [20–22]:

$$\sigma_d = E_d \varepsilon (1 - D_d), \tag{3}$$

where E_d is the dynamic elastic modulus of concrete, which can be replaced by the static elastic modulus, and D_d is a dynamic damage variable.

According to formulas (2) and (3), the following formula is obtained:
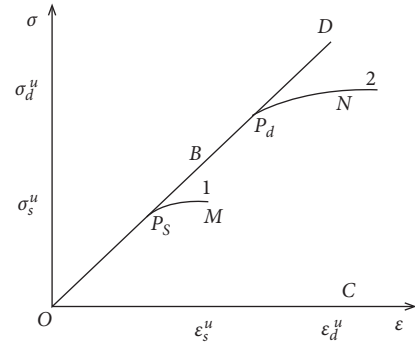
Figure 4: Static and dynamic constitutive relation curve of concrete.

$$[1 - D_d(\varepsilon_d^u)] = \frac{f_\sigma(\dot{\varepsilon})}{f_\varepsilon(\dot{\varepsilon})}[1 - D_s(\varepsilon_s^u)], \tag{4}$$

$$f_\sigma(\dot{\varepsilon}) = \frac{\sigma_d^u}{\sigma_s^u},$$
$$f_\varepsilon(\dot{\varepsilon}) = \frac{\varepsilon_d^u}{\varepsilon_s^u}. \tag{5}$$

In the formula, σ_d^u and ε_d^u are the dynamic damage limit stress and strain of concrete, respectively, and σ_s^u and ε_s^u are the static damage limit stress and strain of concrete, respectively.

The dynamic damage threshold strain of concrete is proportional to the static damage threshold strain, and the static damage threshold strain is ε_s^0 [23, 24]. The concrete dynamic damage threshold value method is shown in

formula (6), and then the concrete dynamic damage constitutive equation (7) is obtained.

$$\varepsilon_d^0 = f_\varepsilon(\dot{\varepsilon})\varepsilon_s^0, \tag{6}$$

$$\begin{cases} \sigma_d = E_d\varepsilon, & \varepsilon \le \varepsilon_d^0, \\ \sigma_d = E_d\varepsilon \dfrac{f_\sigma(\dot{\varepsilon})}{f_\varepsilon(\dot{\varepsilon})}\left[1 - D_s\left(\dfrac{\varepsilon}{f_\varepsilon(\dot{\varepsilon})}\right)\right], & \varepsilon > \varepsilon_d^0. \end{cases} \tag{7}$$

The response process of tunnel lining and surrounding rock under earthquake action involves three kinds of media. The media include surrounding rock, lining, and air in tunnel. There are two kinds of interfaces, the interface between tunnel lining and surrounding rock and the lining free surface.

4. Numerical Calculation Model and Boundary Conditions

4.1. Model Establishment. In the study of vibration load action analysis, the distance between the boundary conditions and the study target has a more serious influence on the calculation results. Theoretically, the smaller the selected range is, the less accurate the analysis results are, but too large a model range will cause inconvenience to the computational analysis and too long analysis time may also lead to interruption of the analysis.

In this paper, we use 3DEC, a computational analysis program based on the discrete unit method as the basic theory to describe the mechanical behavior of discrete media. The rock mass has different lithological properties of rock masses (continuum) and geological structural surfaces (discontinuous features), and under the action of external forces, the rock masses can behave as a continuous media mechanical behavior, while the rock masses interact with each other through the structural surfaces (discontinuous features). When the force on the structural surface exceeds its load-bearing limit, the rock masses will show realistic damage phenomena such as mutual shearing and misalignment or dislocation.

We selected several models with different ranges of surrounding rocks and performed seismic dynamic response analysis to determine the influence of different ranges of surrounding rocks on tunnel stability and concluded that the results of the study tend to be stable when a model with a range greater than 3 times the tunnel width is selected. When the model boundary conditions and the actual situation are different, it will lead to the error of calculation results because of the error of calculating the model boundary conditions, and this calculation error is called the boundary effect. In this paper, the seismic dynamic response analysis of the Leaping Dragon Tunnel cavern section was carried out for the following model ranges: x-direction (horizontal direction) 80 m, y-direction (tunnel direction) 40 m, and z-direction (tunnel vertical direction) 80 m, as shown in Figure 5.

4.2. Selection of Calculation Parameters. Solid units are used to model the tunnel envelope, primary lining, and secondary lining. In order to better simulate the interaction between the tunnel surrounding rock and the lining system, solid units are used. The initial lining is supported by sprayed C30 concrete and the secondary lining by C30 concrete.

For the dynamic analysis of the structure, the mechanical properties of the surrounding rock and materials change under the dynamic load, and the mechanical calculation parameters change accordingly, so the dynamic parameters should be used for the analysis of the seismic dynamic response of the secondary lining of the tunnel opening section.

According to the analysis of the relevant literature, the relationship between the dynamic modulus and static modulus of elasticity satisfies formula (8) where E_s is the static modulus of elasticity and E_d is the dynamic modulus of elasticity, and dynamic parameters are shown in Table 1.

$$E_s = 0.025E_d^{1.7}. \tag{8}$$

4.3. Boundary Conditions and Vibration Load Loading. For this numerical calculation, the viscoelastic artificial boundary is used for the boundary conditions. The elastic artificial boundary condition ensures that its stress state is consistent with the theoretical value obtained from the solution of the fluctuation equation by means of fictitious spring and damper elements. The normal simulation of the artificial boundary is achieved by applying a spring-damper concentrated mass system to the model boundary.

Based on the kinematic principle, the basic differential equations of stress and displacement of the nodes on the artificial boundary after applying the physical system can be derived, as shown in the following equation:

$$\sigma + \frac{M}{C}\frac{\partial\sigma}{\partial t} = K\left(u_R + \frac{M}{C}\frac{\partial u_R}{\partial t} + \frac{M}{C}\frac{\partial^2 u_R}{\partial t^2}\right). \tag{9}$$

The parameters of the applied physical system components satisfy the following:

$$K = \frac{4G}{R},$$
$$C = \rho c_p, \tag{10}$$
$$M = \rho R.$$

In the equation, u_R is the displacement of the artificial boundary node under the load.

The spring + damper system is used to simulate the tangential artificial boundary, and the physical element parameters satisfy the following equation:

$$K = \frac{2G}{R},$$
$$C = \rho c_s. \tag{11}$$

80 m

80 m

(a)

The second lining thickness is 0.55 m

(b)

(c)

(d)
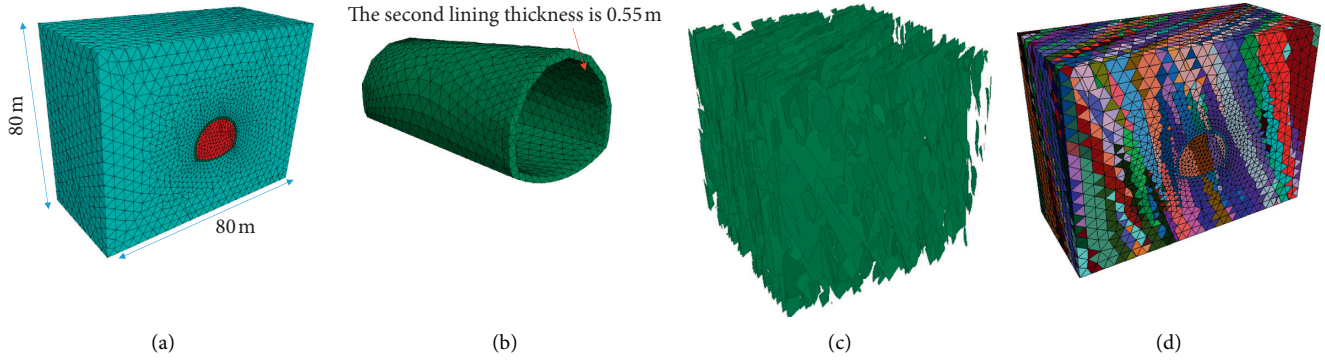
FIGURE 5: Numerical simulation model: (a) numerical calculation model; (b) tunnel lining; (c) distribution characteristics of joints in surrounding rock; (d) tunnel surrounding rock.

TABLE 1: Rock dynamics parameters.

Name	Surrounding rock	Anchor	Initial support	Tunnel lining
Modulus of elasticity E (Pa)	$1.64e^9$	$198e^9$	$23.5e^9$	$30.78e^9$
Poisson's ratio μ	0.42	0.23	0.24	0.22
Weight ρ (kg/m^3)	18.33	25.32	23.16	23.33
Cohesion C (MPa)	0.19			
Angle of internal friction p (°)	23			

Simulating the vertical incidence at the bottom of the P-wave, the seismic intensity of the area where the Yuelongmen tunnel is located is 8 degrees, and the duration of the seismic wave is 5–10 times of the basic vibration period of the structure, and the seismic waveform is shown in Figure 6.

5. Tunnel Seismic Mitigation Measures

5.1. Influence of Grouting Reinforcement of Surrounding Rock on Seismic Effect. The response of grouting thickness to tunnel structure under seismic load is analyzed. Taking different grouting thicknesses under the condition of contact grouting as the research objective, the influence of different grouting thicknesses on surrounding rock is analyzed. After grouting, the elastic modulus of surrounding rock is increased by 55% and the cohesion is increased by 60%. The grouting scheme is shown in Figure 7.

The development law of damage volume of rock around the cave under different grouting thickness conditions is shown in Figure 8. According to the numerical calculation results, it can be seen that with the increase in grouting thickness, the area of plastic zone per unit length of tunnel boring decreases gradually. However, the reduction trend slows down gradually, and the plastic zone decreases by 13% when the grouting thickness is from 0 m to 1 m. From 1 m to 2 m, the plastic zone decreases by 10%. The plastic zone decreases by 6% from 2 m to 3 m. The plastic zone is reduced by 5% from 3 m to 4 m. The plastic zone is reduced by 2.5% when the grouting thickness is from 4 m to 5 m. Considering the economic efficiency, the reasonable grouting thickness should be 4~5 m.

Figure 9 shows the deformation of the second liner under different grouting thicknesses. With the increase in grouting thickness, the deformation of vault top, arch waist, and arch bottom is gradually reduced. Similar to the development of plastic zone, the decrease is gradually reduced.

5.2. Polyethylene Foam Damping Materials on the Seismic Effect of the Tunnel. The polyethylene foam damping material is laid between the lining structure and the rock around the cave, and the lining is separated from the surrounding rock by the damping layer, to reduce and change the intensity and mode of action of the earthquake on the lining structure and to reduce the dynamic response of the lining structure, and its arrangement is shown in Figure 10. The polyethylene foam damping material takes the value of the elastic modulus as 6 MPa and Poisson's ratio as 0.38.

Figures 11 and 12 show the stresses and deformations of the tunnel lining under the protection of different thicknesses of vinyl foam damping materials. The thickness of polyethylene foam is set in four gradients, 0.05 m, 0.1 m, 0.2 m, and 0.3 m. As shown in Figure 11, the maximum principal stress of the second liner decreases gradually with the increase in the thickness of the damping layer. The effect of 0.2 m thickness protective layer and 0.3 m thickness protective layer basically overlaps. Figure 12 shows that the deformation of the tunnel second liner gradually decreases with the increase in the thickness of the damping layer. Taking the right arch waist as an example, the deformation decreases by 5% when the thickness of the damping layer increases from 0 m to 0.05 m. When the thickness of the damping layer increases from 0.05 m to 0.1 m, the deformation decreases by 7%. When the thickness of the damping
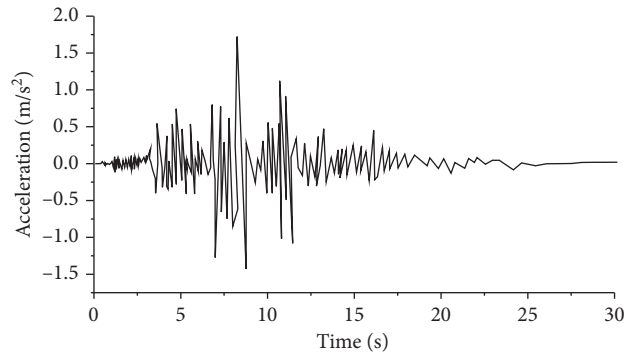
FIGURE 6: Seismic wave P-waveform.
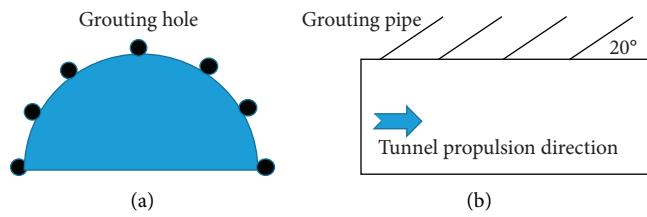
FIGURE 7: Surrounding rock reinforcement grouting process: (a) front view and (b) side view.
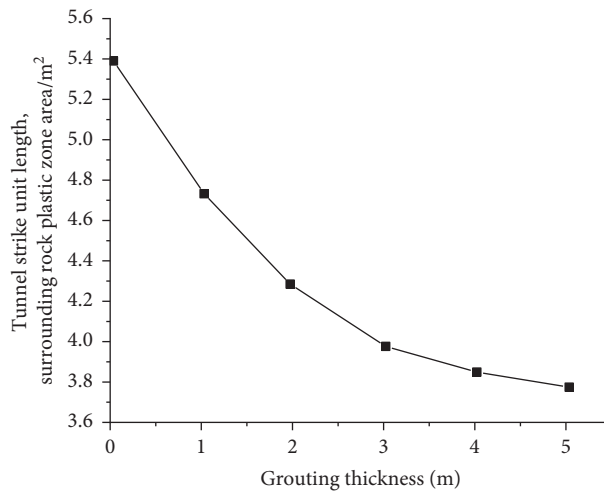
FIGURE 8: Area of plastic zone of surrounding rock under the action of different grouting thicknesses.

layer increases from 0.1 m to 0.2 m, the deformation decreases by 3%. When the thickness of the damping layer is increased from 0.2 m to 0.3 m, the deformation is reduced by 1.4%. Through the analysis of the second liner force and second liner deformation, the selection of 0.2 m thickness of vinyl foam damping material has strong economic value.
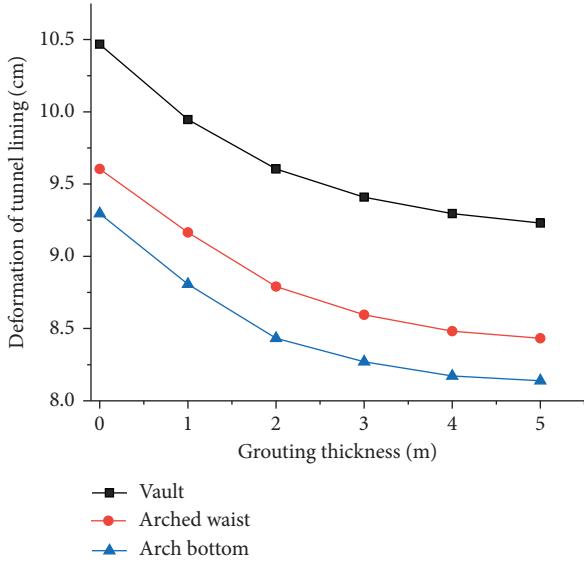
Figure 9: Deformation of the second liner under the action of different grouting thicknesses.
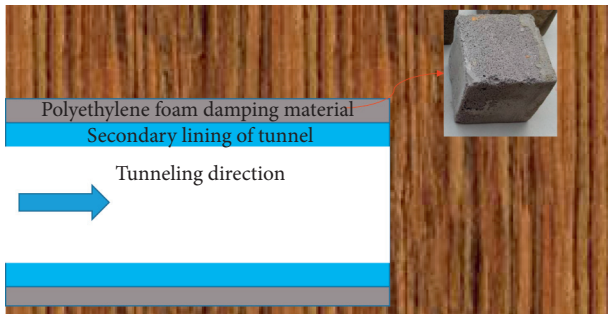
Figure 10: Arrangement of polyethylene foam vibration damping material in the tunnel.
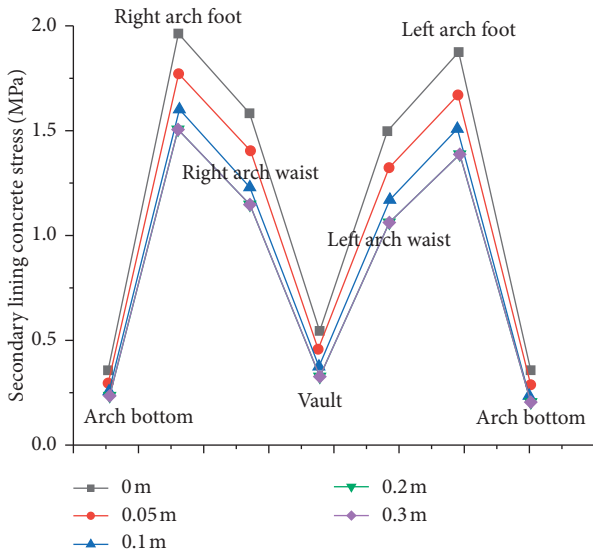
Figure 11: The maximum principal stress of lining structure.
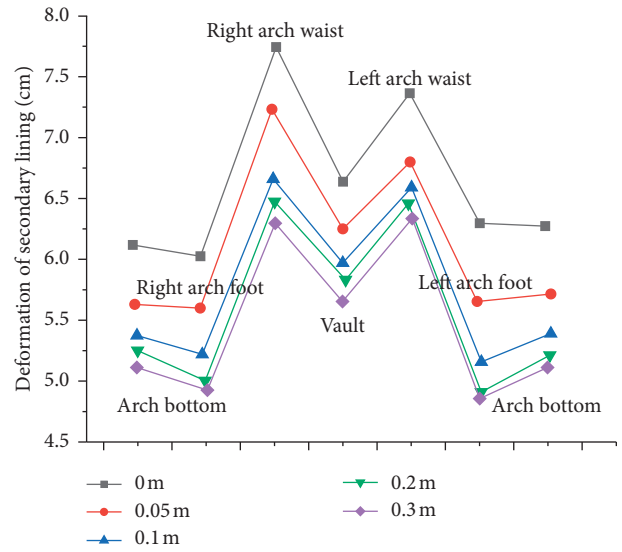
Figure 12: Lining displacement under different thicknesses of the damping layer.

6. Conclusion

Through the analysis of the in situ stress test, the characteristics of in situ stress n of the area of the Yuelongmen tunnel were obtained, and the study concluded that the area is dominated by horizontal in situ stress. The cracking criterion of the second lining concrete under dynamic load was established, and the numerical calculation model was constructed considering the mechanical parameters of the material under dynamic load, and the artificial viscous boundary was adopted as the boundary condition. The effects of two methods, grouting reinforcement and vinyl foam damping material, on the seismic effect of the tunnel were analyzed, and the study showed that both methods had good effects. However, with the increase in tunnel reinforcement area and buffer layer thickness, the seismic damping effect tends to weaken. A reasonable thickness of grouting should be 4~5 m, and the thickness of the buffer layer of damping material should be 0.2 m.

Data Availability

The data used to support the findings of this study are available from the corresponding author upon request.

Conflicts of Interest

The authors declare that they have no conflicts of interest to report regarding the present study.

Acknowledgments

References

[1] J. Lai, S. He, J. Qiu et al., "Characteristics of seismic disasters and aseismic measures of tunnels in Wenchuan earthquake," *Environmental Earth Sciences*, vol. 76, no. 2, p. 94, 2017.

[2] C. Balkaya and E. Kalkan, "Seismic vulnerability, behavior and design of tunnel form building structures," *Engineering Structures*, vol. 26, no. 14, pp. 2081–2099, 2004.

[3] Y. Shen, B. Gao, X. Yang, and S. Tao, "Seismic damage mechanism and dynamic deformation characteristic analysis of mountain tunnel after Wenchuan earthquake," *Engineering Geology*, vol. 180, pp. 85–98, 2014.

[4] T. Li, "Damage to mountain tunnels related to the Wenchuan earthquake and some suggestions for aseismic tunnel construction," *Bulletin of Engineering Geology and the Environment*, vol. 71, no. 2, pp. 297–308, 2012.

[5] Y. Miao, E. Yao, B. Ruan, and H. Zhuang, "Seismic response of shield tunnel subjected to spatially varying earthquake ground motions," *Tunnelling and Underground Space Technology*, vol. 77, pp. 216–226, 2018.

[6] J. M. Mayoral, S. Argyroudis, and E. Castañon, "Vulnerability of floating tunnel shafts for increasing earthquake loading," *Soil Dynamics and Earthquake Engineering*, vol. 80, pp. 1–10, 2016.

[7] L. Gan, M. Weibin, T. Siming, and Z. Wenhao, "Effects of high-pretension support system on soft rock large deformation of perpendicularly crossing tunnels," *Advances in Civil Engineering*, vol. 2020, pp. 1–18, 2020.

[8] A. Vanuvamalai, K. P. Jaya, and V. Balachandran, "Seismic performance of tunnel structures: a case study," *Natural Hazards*, vol. 93, no. 1, pp. 453–468, 2018.

[9] Y. Hui, J. Xueliang, and L. Pengyuan, "Seismic response of tunnel lining for shallow-bias tunnel with a small clear distance under Wenchuan earthquake," *Advances in Civil Engineering*, vol. 2018, pp. 1–10, 2018.

[10] G. Li, W. Ma, S. Tian, Z. Hongbo, F. Huabin, and W. Zou, "Groundwater inrush control and parameters optimization of curtain grouting reinforcement for the jingzhai tunnel," *Geofluids*, vol. 2021, pp. 1–10, 2021.

[11] G. Li, Y. Hu, Q.-B. Li, T. Yin, J.-X. Miao, and M. Yao, "Inversion method of in-situ stress and rock damage characteristics in dam site using neural network and numerical simulation-A case study," *IEEE Access*, vol. 8, pp. 46701–46712, 2020.

[12] Q.-X. Meng, W.-Y. Xu, H.-L. Wang, X.-Y. Zhuang, W.-C. Xie, and T. Rabczuk, "DigiSim - an open source software package for heterogeneous material modeling based on digital image processing," *Advances in Engineering Software*, vol. 148, Article ID 102836, 2020.

[13] C. Zhu, M.-C. He, M. Karakus, X.-H. Zhang, and Z. Guo, "The collision experiment between rolling stones of different shapes and protective cushion in open-pit mines," *Journal of Mountain Science*, vol. 18, no. 5, pp. 1391–1403, 2021.

[14] Q. Yin, J. Wu, C. Zhu, M. He, Q. Meng, and H. Jing, "Shear mechanical responses of sandstone exposed to high temperature under constant normal stiffness boundary conditions," *Geomechanics and Geophysics for Geo-Energy and Geo-Resources*, vol. 7, no. 2, p. 35, 2021.

[15] Q. Wang, Z. Jiang, B. Jiang, H. Gao, Y. Huang, and P. Zhang, "Research on an automatic roadway formation method in deep mining areas by roof cutting with high-strength bolt-grouting," *International Journal of Rock Mechanics and Mining Sciences*, vol. 128, Article ID 104264, 2020.

[16] Q. Wang, Y. Wang, M. He et al., "Experimental research and application of automatically formed roadway without advance tunneling," *Tunnelling and Underground Space Technology*, vol. 114, no. 3, Article ID 103999, 2021.

[17] Y. Wang, W. K. Feng, R. L. Hu, and C. H. Li, "Fracture evolution and energy characteristics during marble failure under triaxial fatigue cyclic and confining pressure unloading (FC-CPU) conditions," *Rock Mechanics and Rock Engineering*, vol. 54, no. 2, pp. 799–818, 2021.

[18] A. Li, F. Dai, Y. Liu, H. Du, and R. Jiang, "Dynamic stability evaluation of underground cavern sidewalls against flexural toppling considering excavation-induced damage," *Tunnelling and Underground Space Technology*, vol. 112, Article ID 103903, 2021.

[19] F. Wu, R. Gao, J. Liu, and C. Li, "New fractional variable-order creep model with short memory," *Applied Mathematics and Computation*, vol. 380, Article ID 125278, 2020.

[20] F. Wu, H. Zhang, Q. Zou, C. Li, J. Chen, and R. Gao, "Viscoelastic-plastic damage creep model for salt rock based on fractional derivative theory," *Mechanics of Materials*, vol. 150, Article ID 103600, 2020.

[21] J. Huang, Y. Zhang, Y. Tian et al., "Research on the dynamic mechanical properties and constitutive models of steel fiber reinforced concrete and polypropylene fiber reinforced concrete," *Advances in Civil Engineering*, vol. 2020, pp. 1–17, 2020.

[22] X. Cong, W. Zhou, and M. Elchalakani, "Experimental study on the engineering properties of alkali-activated GGBFS/FA concrete and constitutive models for performance prediction," *Construction and Building Materials*, vol. 240, Article ID 117977, 2020.

[23] L. Ma, F. Wang, P. Cui, M. Yunusa, and Y. Xiao, "Effect of aging on the constitutive models of asphalt and their mixtures," *Construction and Building Materials*, vol. 272, Article ID 121611, 2021.

[24] J. Lai and W. Sun, "Dynamic behaviour and visco-elastic damage model of ultra-high performance cementitious composite," *Cement and Concrete Research*, vol. 39, no. 11, pp. 1044–1051, 2009.

Research Article

Research on the Influence of Moisture Condition on the Mechanical Properties and Microstructure of Sandstone

Zuosen. Luo [iD],[1,2] **Zuoxiang. Zhu,**[2] **Hao Bai,**[2] **Daxiang Liu,**[1] **and Qiancheng. Sun** [iD][2]

[1]*Engineering Research Center of Eco-environment in Three Gorges Reservoir Region, Ministry of Education, China Three Gorges University, Yichang 443002, China*
[2]*Key Laboratory of Geological Hazards on Three Gorges Reservoir Area of Ministry of Education, China Three Gorges University, Yichang, Hubei 443002, China*

Correspondence should be addressed to Qiancheng. Sun; qc_sun@ctgu.edu.cn

The sandstone from the dry to saturated state shows obvious deterioration characteristics. Taking the sandstone of a slope in the Three Gorges Reservoir area as the research object, uniaxial/triaxial compression of sandstone samples with different water-bearing states (dry, natural, and saturated) is carried out to study the changes in macromechanical properties of sandstone under different water-bearing states. Combined with NMR and SEM, the characteristics of microstructure of sandstone under different moisture conditions were studied. The results show that, with the increase of water content, the macromechanical parameters of sandstone gradually decrease, and the fine and microstructure characteristics are characterized by the gradual increase in the number of pores and the gradual increase in pore size. Based on the PFC2D software, considering the weakening effect of water on the partial cementation from a mesoscopic point of view, it is proposed to use soft and hard contacts to simulate the changes in the degree of cementation between particles under different water-bearing conditions and to study the impact of sandstone micromechanical parameters with changes in water content. Related research results can provide theoretical guidance for the stability evaluation of wading rock mass engineering.

1. Introduction

People's understanding of water-rock interaction in engineering comes from the obvious difference between the physical and mechanical properties of rocks in the saturated state and those in the dry state. It is found that the physical and mechanical properties of rocks in the saturated state have a significant decreasing trend [1, 2]. Water is one of the unavoidable occurrence conditions of rock mass engineering [3]. With the rapid development of rock mass engineering such as slopes [4, 5], tunnels [6, 7], and underground caverns [8–11], water-rock interaction is highly valued. Rocks often contain microscopic defects such as pores and fissures, which become channels for water to enter the rock, thereby deteriorating its mechanical properties. The problem of rock mass engineering disasters caused by water is very common, so studying the mechanical properties of rocks under water-rock interaction is of great significance to rock mass engineering.

With the deepening of research on water-rock interaction, more and more scholars have carried out research on water-rock interaction from the microscopic level. In terms of the research on the change of rock mineral composition under water-rock interaction, Cui et al. [12–15] used X-ray diffraction experiments to study the change law and quantitative analysis of rock mineral content under water-rock interaction. As the water-rock interaction time increases, the clay mineral content generally shows a trend of increasing first and then decreasing. Song et al. [16–18] used the fluorescence spectroscopy test to study the change of the mineral composition of limestone under the action of water and rock and concluded that the content of $CaCO_3$ and SiO_2 changes exponentially as the osmotic pressure increases. In the study of the fine microstructure characteristics of rocks

under water-rock interaction, Qiao et al. [19–21] used CT scanning technology to scan the rock samples damaged by water-rock interaction and found that the water-rock interaction leads to an increase in the mesopores of the rock, and the CT number shows an increasing trend. Zhong et al. [22–24] used nuclear magnetic resonance technology to test the porosity of rocks under different water-rock interaction conditions, found that the increase in water-rock interaction would lead to an increase in porosity, and established a quantitative relationship between porosity and rock mesoscopic damage. Wang et al. [25, 26] studied the influence of water-rock interaction on the microstructure characteristics of rocks based on scanning electron microscopy experiments and found that the damage degree of water and rock continues to increase, and its microscopic pores and cracks continue to increase, and the larger the value of the fractal dimension based on the scanning electron microscope image. The above research shows that the changes in the microscopic structure of rocks after encountering water are the main reason for the deterioration of macromechanical properties.

In recent years, the numerical simulation of particle flow based on the discrete element method has become an important way to study rock mechanics from a mesolevel perspective. Liu et al. [27, 28] studied the influence of water-rock interaction on the contact network, force chain distribution, and crack distribution of sandstone particles based on the particle flow software PFC2D. Jiang et al. [29, 30] analyzed the change law of the mechanical properties and failure modes of rocks under different water content conditions based on the discrete element particle flow method. Based on the particle discrete element method, Hu et al. [31] proposed a parallel bonding water-weakening model and analyzed the heterogeneity of cement, energy dissipation, inclination, failure mode of microcracks, and so on and revealed the mesomechanism of the weakening effect of water on rocks. The above research fully proves the feasibility and applicability of using particle flow software for water-rock interaction analysis.

Based on the abovementioned literature analysis, many scholars have conducted research on the degradation mechanism of rocks under water-rock interaction from the macroscopic and microscopic perspectives, and the research results have provided good guidance for engineering practice. However, in the study of the mechanical properties of sandstone under different water content conditions, based on the results of qualitative and quantitative analysis of rock microlevels, there are few studies on the mechanism of influence of different water content conditions on rock macromicromechanical properties from the perspective of mesoanalysis of the weakening of the cementation between the water-induced mesoparticles. Therefore, this paper selects the more common sandstone in rock mass engineering as the research object. Through uniaxial and triaxial compression tests, the macromechanical properties of sandstone under different water-bearing conditions are studied. Using nuclear magnetic resonance, scanning electron microscope, energy spectrum analysis, and other mesotesting methods, qualitative and quantitative analyses of sandstone mineral composition and microstructure characteristics and

mesopore distribution characteristics were performed. Based on the discrete element software PFC2D, a numerical model considering different water content conditions is established for mesoanalysis. Integrating the macromechanical properties test results and the micro-microtest results reveals the macrofine-micromechanism of rock degradation by water. The research results can provide theoretical guidance for wading rock mass engineering.

2. Test Project

The rock sample used in this test is a slope sandstone from the Three Gorges Reservoir area. The sample used in the test is a standard cylindrical sample with diameter × height = 50 mm × 100 mm, as shown in Figure 1.

Before the test, the quality, height, and diameter of the sample were measured, and the longitudinal wave velocity of the rock sample was measured using RSM-SY5(T) non-metallic acoustic tester. Samples with small size deviations, smooth and flat surfaces, similar densities, and similar wave speeds were selected for use in the test. The selected samples were divided into three groups (A, B, and C), 15 samples in each group, 3 samples in each group are spares, A is the dry group, B is the natural group, and C is the saturated group. The samples of group A were dried in an oven at 105°C for 12 hours, the samples of group B were kept in their natural state, and the samples of group C were dried in an oven at 105°C for 12 hours and then saturated by vacuum soaking in water for 24 hours. The masses after drying and the mass after being saturated with water were measured, and the moisture content of the sandstone in the dry, natural, and saturated states are 0, 1.01%, and 2.53%, respectively.

2.1. Uniaxial/Triaxial Compression Test.
Three samples from each group were taken for uniaxial compression test, nine samples from each were taken, and each three are divided into one type, and triaxial compression test was carried out with a confining pressure of 5, 10, and 15 MPa. The mechanical parameters of sandstone samples under different confining pressures were obtained, and the test equipment is shown in Figure 2. Force- (large-) displacement loading method was used for loading, and the loading rate of displacement is 0.005 mm/s.

2.2. Microstructure Test.
Three samples of group C were selected randomly, and the low-field nuclear magnetic resonance analyzer was used as shown in Figure 2 for nuclear magnetic resonance scanning to obtain the T2 spectrum of rock samples and study the pore distribution in sandstone.

In order to study the microstructure of fracture surface of sandstone under different water-bearing conditions, Prisma E environmental scanning electron microscope was used to obtain SEM scanning images of sandstone fracture surface; EDS analysis system is used to analyze the elements in some areas of sandstone fracture surface, obtain energy spectrum, and study the mineral composition of sandstone. The scanning device of electron microscope is shown in Figure 3.

FIGURE 1: Sandstone sample.

FIGURE 2: Low-field nuclear magnetic resonance analyzer.

FIGURE 3: Prisma E environmental scanning electron microscope + EDS analysis system.
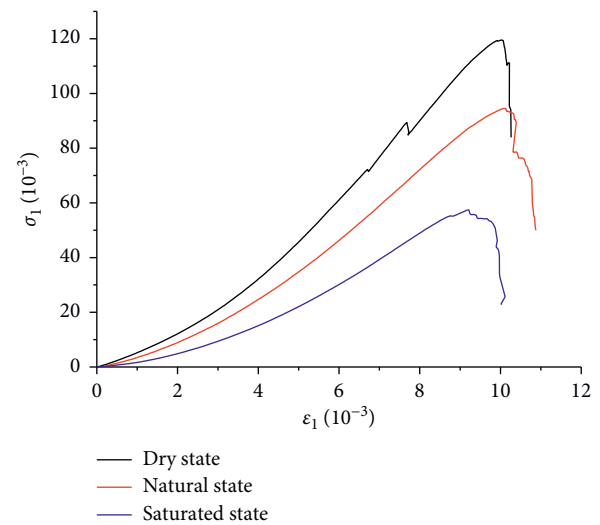
FIGURE 4: Stress-strain curves under uniaxial test.

3. Study on the Change Law of Macromechanical Properties of Sandstone under Different Moisture Conditions

3.1. Variation Law of Macroscopic Mechanical Parameters of Sandstone under Uniaxial Compression. Figure 4 shows the uniaxial compression stress-strain curves of sandstone specimens in three different states. The uniaxial compression curves of all samples have similar compaction stage, elasticity stage, plasticity stage, and failure stage. The difference is that the compaction stage of the dry sample curve is shorter and the plasticity stage is shorter, and the compaction stage of the saturated sample curve is longer, and there is an obvious plasticity stage. As the moisture content increases, the compaction stage gradually increases and the plasticity stage gradually becomes obvious.

According to Figure 4, the mechanical parameters of the rock samples in three states can be obtained. As shown in Table 1, the water content of sandstone increases by 1.01% from the dry state to the natural state, the uniaxial compressive strength decreases by 26.64 MPa, and the elastic modulus decreases by 2.66 GPa. The peak strain increased by 0.26‰; from the natural state to the saturated state, the water content increased by 1.52%, the

uniaxial compressive strength decreased by 35.44 MPa, the elastic modulus decreased by 3.31 GPa, and the peak strain decreased by 1.08%. The strength and elastic modulus of sandstone gradually decrease with the increase of water content, and water has a softening effect on sandstone.

3.2. Variation Law of Macroscopic Mechanical Parameters of Sandstone under Triaxial Compression. The peak strength of sandstone samples under different confining pressures under different water-bearing conditions is shown in Table 2. With the increase of confining pressure, the peak strength of sandstone samples gradually increases; under the same confining pressure, the peak strength of sandstone gradually decreases with the increase of water content.

According to the peak strength value measured by the triaxial compression test of sandstone, combined with the Mohr-Coulomb strength criterion, as shown in formula (1), the internal friction angle and cohesive force of sandstone in three water-bearing states are calculated, as shown in Table 3. With the increase of water content, the internal friction angle and cohesive force of sandstone gradually decrease,

TABLE 1: Mechanical parameters of sandstone in different states.

Sample state	Elastic modulus E (GPa)	Peak intensity $\textrm{б}$ (MPa)	Peak strain ε (‰)
Dry state	15.63	119.54	10.03
Natural state	12.97	92.90	10.29
Saturated state	9.66	57.46	9.21

TABLE 2: Peak strength of sandstone in triaxial compression test.

Confining pressure (MPa)	0	5	10	15
Dry state	119.54	156.12	225.39	240.02
Natural state	92.90	124.02	164.68	201.70
Saturated state	57.46	82.40	120.07	149.76

TABLE 3: Cohesion and internal friction angle of sandstone in different states.

Sample state	Internal friction angle φ (°)	Cohesion c (MPa)
Dry state	52.13	20.52
Natural state	48.21	17.74
Saturated state	44.24	12.36

and the water in the sandstone causes the bonding ability between mineral particles to decrease.

$$\tau = \sigma \tan \varphi + c, \qquad (1)$$

where τ is the shear strength, σ is the main stress, φ is the internal friction angle, and c is the cohesive force.

4. Research on the Fine Microstructure Characteristics of Sandstone under Different Water Content Conditions

4.1. Sandstone Mineral Composition Analysis. The energy spectrum of EDS analysis in some areas of sandstone section is shown in Figure 5. The sandstone contains quartz, feldspar, mica, chlorite, and other minerals. The mineral debris is mainly quartz, mica, and feldspar, chlorite is the main filling mineral, and the larger mineral particles are quartz and feldspar.

4.2. Research on the Structural Characteristics of Sandstone Microfailed Sections under Different Water Content Conditions

4.2.1. Analysis of Failure Section under Uniaxial Compression. Figure 6 shows the scanning electron microscope image of the uniaxial compression failure rock sample with a magnification of 100 times. Figures 6(a)–6(c) show the uniaxial failure cross section diagrams of the sandstone in the dry, natural, and saturated state, using the IPP software. The cross-sectional diameter of broken mineral particles and the particle size of intact mineral particles are measured. According to the analysis of sandstone mineral composition, it can be known that the observed broken minerals and intact minerals are quartz or feldspar. The following can be observed from Figure 6:

(1) Dry sandstone is destroyed by uniaxial compression, and there are a large number of broken fracture surfaces of mineral particles at the section. When dry sandstone is destroyed, the larger mineral particles are mainly broken.

(2) The natural state sandstone is destroyed by uniaxial compression. There are broken sections of mineral particles, complete mineral particles, and pores separated from mineral particles. Larger mineral particles are mainly broken. When the sandstone in the natural state is destroyed, the larger mineral particles are still broken and fractured, and the larger mineral particles are separated from each other due to the separation of the cementing material.

(3) During uniaxial compression failure in the saturated state, the proportion of intact mineral particles and the separation holes of mineral particles at the section increase, and there are also broken minerals, each accounting for 50%. The saturated sandstone is destroyed, the cementation material separates, and the mineral particles separate from each other, and the separation of larger mineral particles is equivalent to the fragmentation.

In the process of uniaxial compression test, due to the inhomogeneity of sandstone material, there are compressive stress, shear stress, and tensile stress inside the sandstone; under the action of three kinds of stress, the rock sample will eventually be destroyed. In the dry and natural state of the rock sample, the larger mineral particles are mainly broken. With the increase of water content, the separation of the cementing material causes the larger mineral particles to not break, and the direct separation phenomenon increases. The direct separation phenomenon of the larger mineral particles in the saturated state reaches the highest. In the process of rock sample compression, it is easier to separate the cementitious material in the saturated state, and it is more difficult to separate the cementitious material in the dry state. As the moisture content increases, the bonding ability of the cementitious material gradually decreases.

4.2.2. Analysis of Fracture Shape and Characteristics. Figure 7 shows the SEM scans of fractures of sandstone in different states, magnified by 1200 times. Figures 7(a)–7(c) show the SEM scans of uniaxial compression failure in dry, natural, and saturated states, respectively. The following can be observed from Figure 7:

(1) In the dry state, the cross section of the rock sample mineral particles is smooth and flat, and there are small areas of fold-type lines and longer continuous

zzx ‖ New sample ‖ Area 1 ‖ EDS spot 2

O: 69.89%

Si: 30.11%

SiO_2

The mineral with the highest content in sandstone is mainly single crystal quartz, which is well rounded.

EDS spot 2

100 um

Det: element

(a)

zzx ‖ New sample ‖ Area 2 ‖ EDS spot 1

O: 65.15%

Al: 8.60%

Si: 22.93%

K: 3.32%

$KAl_2 (AlSi_3O_{10}) (OH)_2$

The mica is mainly layered.

EDS spot 1

100 um

Det: element

(b)

O: 56.64%

Al: 9.78%

Si: 25.36%

K: 8.21%

$K [AlSi_3O_8]$

There are small karst caves in the granules of the analysis point.

EDS spot 1

100 um

Det: element

(c)

FIGURE 5: Continued.

zzx | New sample | Area 2 | EDS spot 2

O: 58.49%

Na: 9.34%

Al: 9.76%

Si: 22.42%

Na [AlSi$_3$O$_8$]

The analysis points were feldspar fragments.

Det: element

(d)

zzx | New sample | Area 4 | EDS spot 2

O: 67.27%

Mg: 8.05%

Al: 6.45%

Si: 15.21%

Fe: 3.03%

(Mg, Fe)$_5$Al (Si$_3$Al) O$_{10}$ (OH)$_8$

Chlorite is filled in the pores at the point of analysis.

Det: element

(e)

FIGURE 5: The results of energy spectrum analysis: (a) quartz, (b) mica, (c) potash feldspar, (d) albite, and (e) chlorite.

lines, both of which are smooth; there are obvious penetrating cracks between the mineral particles, and there are small nonpenetrating mineral particles. Fissures mainly produce mineral particles.

(2) In the natural state, the section of the rock-like mineral particles is smooth and flat, the texture is smooth, and there are angular mineral fragments on the surface. There are continuous cracks between the mineral particles, and the fracture of the mineral particles is straight.

(3) In the saturated state, the section of the rock sample mineral particles is rough, the surface is attached with mineral fragments, and the large area has long stratified roads with tortuous shapes. The mineral particles have large cracks that are completely penetrating, the fractures are tortuous, and the particles are connected. There are penetrating fissures at places, fissures exist in and between mineral particles.

In a word, with the change of water content, the fracture surface of mineral particles is smooth in the dry state and becomes rough and tortuous in the saturated state. The cracks in the mineral particles change from small in the dry state to wide and continuous in the saturated state. It shows that the greater the water content in sandstone, the more obvious the softening of water-soluble mineral particles.

4.3. Research on the Distribution of Micro-Pore Characteristics of Sandstone

4.3.1. NMR T2 Spectrum Analysis. In the NMR T2 spectrum analysis, the size of the relaxed sample T2 is positively related to the pore size, and the area of the T2 spectrum curve is positively related to the number of pores. The larger the spectrum area, the more the number of pores. In Zhang et al.'s study [32], pores are divided into six categories: ultramicropores, with a pore diameter of less than 0.01 μm; micropores, with a pore diameter in the range of 0.01 ~
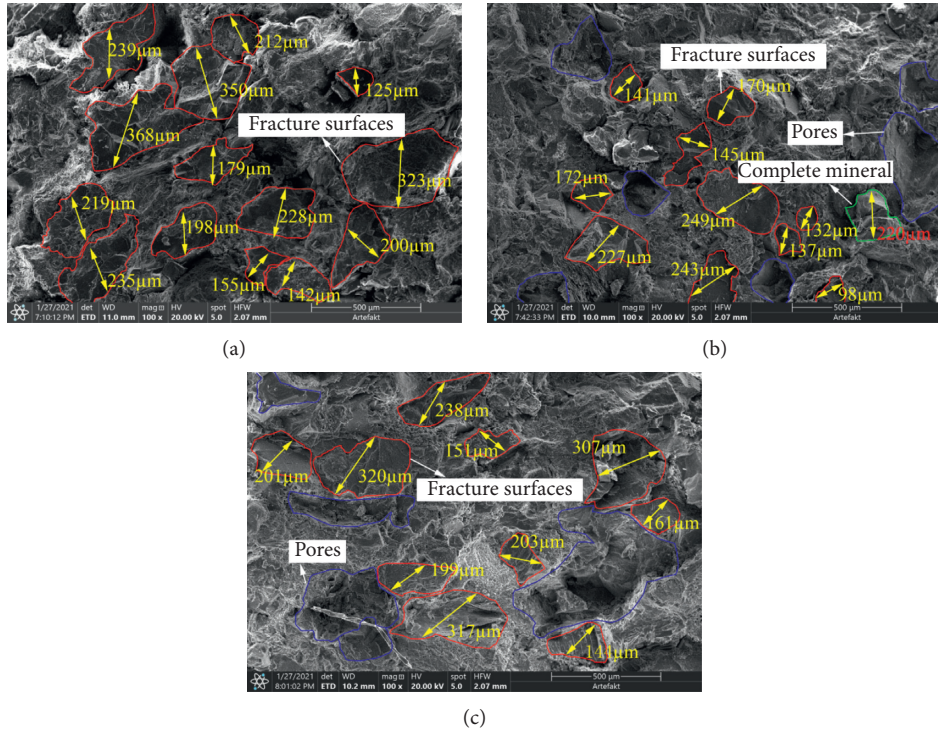
FIGURE 6: Failure section of rock samples in different states under uniaxial compression (×100): (a) dry state, (b) natural state, and (c) saturated state.
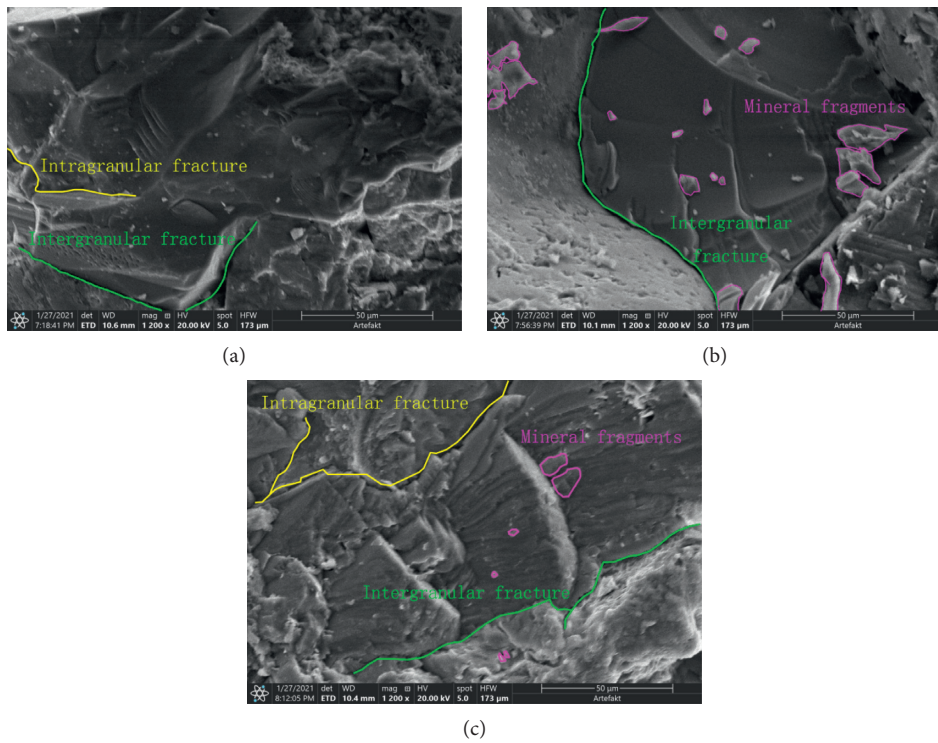
FIGURE 7: Cross section structure of sandstone in different water-bearing states (×1200): (a) dry state, (b) natural state, and (c) saturated state.

0.1 μm; small pores, with a pore diameter in the range of 0.1 ∼ 1 μm; mesopores, with a pore diameter of 1 ∼ 10 μm; large pores, with a pore diameter of 10 ∼ 100 μm; superlarge pores, with pore diameter greater than 100 μm. The T2 spectrum distribution of saturated rock samples is shown in Figure 8. The following can be observed from Figure 8.

There is only one peak in the T2 spectrum distribution curve of the rock, which appears at 0.8 ms, indicating that the pores inside the sandstone are mainly small pores and there are few large pores. The pore size in the sandstone is mainly distributed in the range of 0–0.01 μm. The pores in the sandstone are mainly ultramicropores, and the proportion of mesopores is low. There are no macropores and superlarge pores in the sandstone. The porosity of sandstone is 1.9451%.

4.3.2. Analysis of Pore Structure Changes in Different States.

Sandstone is framed by larger mineral particles such as quartz and feldspar and is filled with smaller clay mineral particles and clastic particles. The cementitious material connects the mineral particles. There are a large number of fine pores and cracks in the sandstone. The difference in the water content of the sandstone will cause the pore structure in the sandstone to be different. Select the SEM scanning images of the cementation sites of the sandstone fragments under uniaxial compression failure in three water-bearing states, and the magnification is 1200 times, as shown in Figure 9. Figures 9(a)–9(c) show dry, natural, and saturated states, respectively. Measure pores with a pore diameter greater than 0.5 μm. The following can be seen from Figure 9:

(1) In the dry state, the cementation material between the debris particles is uniformly filled, with a small amount of primary pores and inconspicuous cracks. The measured pore diameter is in the range of 0.82 μm–3.20 μm, which belongs to the larger pores and the smaller mesopores.

(2) In the natural state, the clastic particles are filled with cement, and large pores appear locally, with a diameter of 1.87 μm–5.82 μm, which are mesopores. In the natural state, the primary pores in the sandstone developed and opened under the action of water, and some of the larger small pores developed into mesopores. The original mesopores were expanded, and the pore diameter and number of mesopores increased.

(3) The clastic particles in the saturated state are loosely arranged, some mineral particles are separated, and many larger pores appear. The pore diameter is 1.75 μm–6.2 μm, which belongs to mesopores. This is consistent with the pore diameter of sandstone measured by nuclear magnetic resonance not greater than 10 μm. After being fully saturated, the number of mesopores in the sandstone further increases, and the pore size distribution of mesopores does not change much.

4.3.3. Pore Fractal Characteristics.

Voss et al. [33] analyzed the relationship between the perimeter and area of the pores
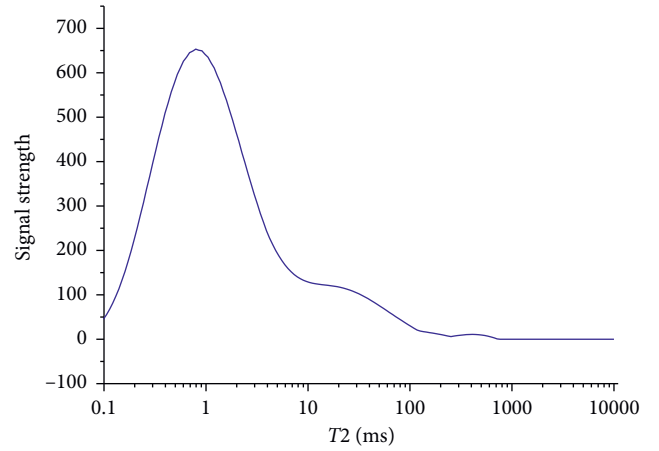
Figure 8: T2 spectrum distribution of full water samples.

in the rock and calculated the fractal dimension of the pores. The pore area, pore perimeter, and fractal dimension in sandstone conform to the following relationship:

$$\lg C = \frac{D}{2} \times \lg A + d_0, \tag{2}$$

where C is the pore circumference, A is the pore area, D is the fractal dimension of the pore shape in the image, and d_0 is a constant.

Select the SEM image (650×) of the fracture section under uniaxial compression, use the IPP software to obtain the perimeter and area of each pore in the slate microscopic image, and draw the relationship between the pore area and the common logarithm of the pore perimeter, as shown in Figure 10. The fractal dimension is twice the slope.

It can be seen from Figure 10 that the fractal dimensions D in dry, natural, and saturated states are 1.42, 1.45, and 1.48, respectively. With the increase of the water content in the sandstone, the fractal dimension is increasing because of the increase in the water content of the sandstone. This leads to the dissolution of the cemented material in the sandstone, the expansion and deformation of the small pore-like circular pores in the dry state, the expansion of the pore size, the variety of shapes, and the increase of fractal dimensions.

5. PFC2D Numerical Simulation and Analysis

Silicate minerals such as feldspar, mica, and chlorite in sandstone are hydrolyzed in contact with water. Water has a softening effect on these minerals. Oxide minerals such as quartz in sandstone are less affected by water. Under the interaction of water and rock, the pore openings in the cemented material increase, the number increases, and the shape becomes diversified. The strength and bonding ability of the cemented material decrease, and the cemented material softens. Part of the cementitious material is little or not affected by the action of water. The pores in the cementitious material do not develop and remain intact. The water-saturated state of the cementitious material is completely in contact with water, and the pores are still dominated by ultramicropores. Short-term immersion in water will cause

(a)

(b)

(c)
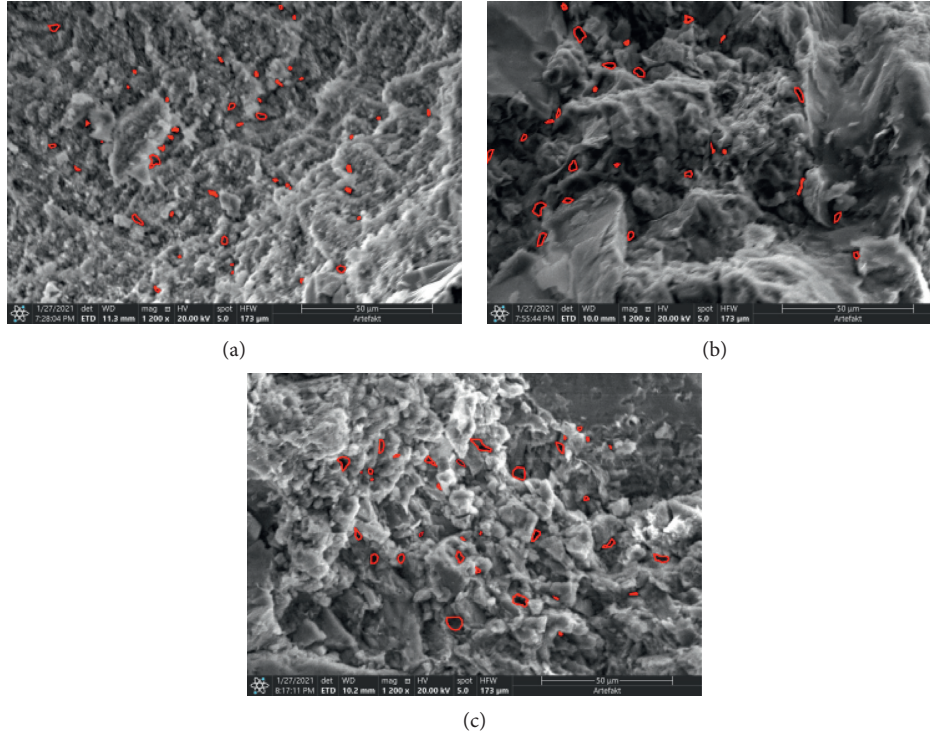
FIGURE 9: Pore structure of sandstone in different water-bearing states (×1200): (a) dry state, (b) natural state, and (c) saturated state.

the sedimentary cementation in the rock to soften, and the diagenetic cementation is not easy to soften. There are soft cementation that is easy to be softened by water and hard cementation that is not easy to be softened by water [34]. With the increase of water content, the softening degree of soft cement gradually increases, resulting in a decrease in the macroscopic mechanical parameters of sandstone. The particle flow discrete element method uses the contact mode between particles to simulate the macromechanical properties and deformation characteristics of materials with different properties. The discrete element software PFC2D is used to analyze the softening of the internal cementation material of sandstone, and the PBM bonding model is used for research. The two types of hard contact are used to simulate soft cementation that is easy to be softened by water and hard cementation that is not easy to be softened by water.

5.1. Model Establishment.
Establish a PFC2D model with a size of 50 mm × 100 mm, set the particle generation radius to 0.3 mm–0.5 mm, containing 8753 particles, the contact between the particles randomly generates 50% soft contact, 50% hard contact, and a total of 23,028 interparticle contacts, as shown in Figure 11 (In Figure 11(b), the green contacts represent soft contact and the blue contacts represent hard contact).

When calibrating the mesoparameters, first calibrate the model parameters in the dry state. The increase in water content will cause the soft cement to soften, that is, the soft contact parameters in the dry state, the natural state, and the saturated state will gradually change. The mesoparameters of

sandstones with different water-bearing states were determined after trial and error and calculation. Table 4 shows the soft contact mesoparameters of sandstone in different water-bearing states. Among which the hard contact parameters do not change, the parallel bonding modulus of hard contact $E_{th} = 39.4$ GPa, linear bonding modulus $E_{ch} = 7.68$ GPa, normal bonding strength $\sigma_{cnh} = 86.4$ MPa, and tangential bond strength $\sigma_{csh} = 72$ MPa.

5.2. Model Loading Stress-Strain Curve Fitting.
The stress-strain curve of uniaxial and triaxial compression has a compaction stage. The compaction stage is obvious during uniaxial compression. The elastic modulus of the compaction section increases with the increase of axial strain. After reaching the elastic stage, the elasticity modulus remains unchanged. In order to simulate the mechanical test results more realistically, a variable modulus model is used for uniaxial compression simulation. In the PFC model, the main parameters affecting the elastic modulus are the parallel bonding modulus E_t and the linear bonding modulus E_c. The constitutive compaction is simulated by simultaneously changing the hard contact and soft contact parallel bonding modulus E_t. The change relationship is as follows:

$$E_t = 0.2E_{t0} + 0.8E_{t0}\frac{\varepsilon}{\varepsilon_0}, \tag{3}$$

where E_t is the parallel bonding modulus, E_{t0} is the parallel bonding modulus after compaction, ε is the axial strain, and ε_0 is the axial strain at the end of compaction, which is determined by the actual constitutive relationship.

(a)

(b)

(c)
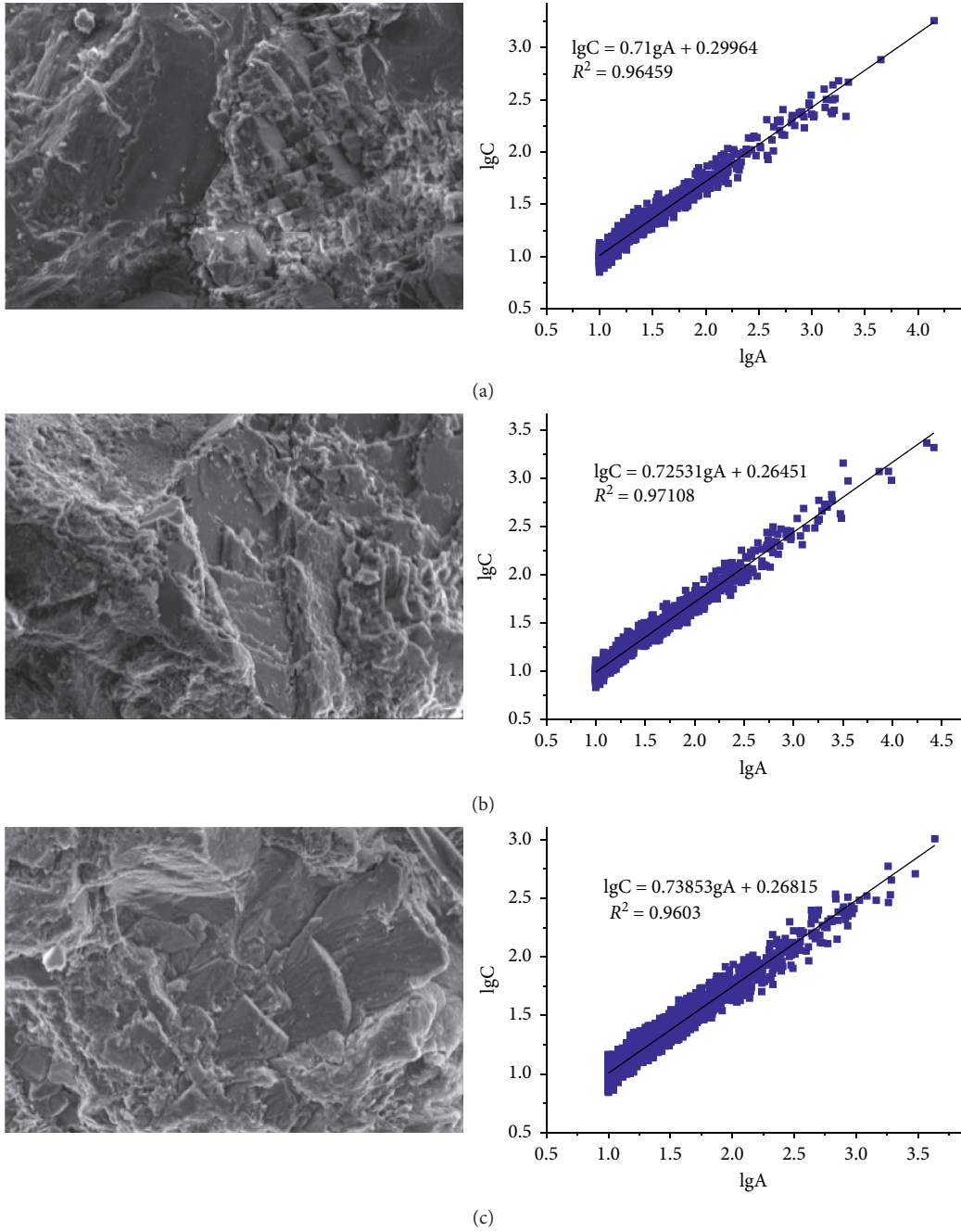
FIGURE 10: Fractal dimension relation between pore circumference and area in sandstone: (a) dry state, (b) natural state, and (c) saturated state.

The elastic modulus of the model is directly proportional to the parallel bond modulus parameters. From formula (3), the stress-strain relationship in the compaction stage can be deduced as follows:

$$\sigma \propto 0.2E_{t0}\varepsilon + 0.8E_{t0}\frac{\varepsilon^2}{\varepsilon_0}. \tag{4}$$

From formula (4), it can be seen that the relationship between stress and strain becomes a quadratic function. The stress-strain curve of the variable modulus uniaxial compression simulation is shown in Figure 12. It can be found that the use of two contact variable modulus models can be very good. It fits the stress-strain curve of uniaxial compression in the dry, natural, and saturated state; in the compaction stage, the dry and natural state model can almost completely fit the actual constitutive relationship. But the actual axial stress in the saturated state is lower than that of the saturated state model, indicating that the actual saturated sandstone stress and strain in the compaction section have a higher-order relationship. The saturated sandstone bears the same axial stress in the early stage of

(a) (b)
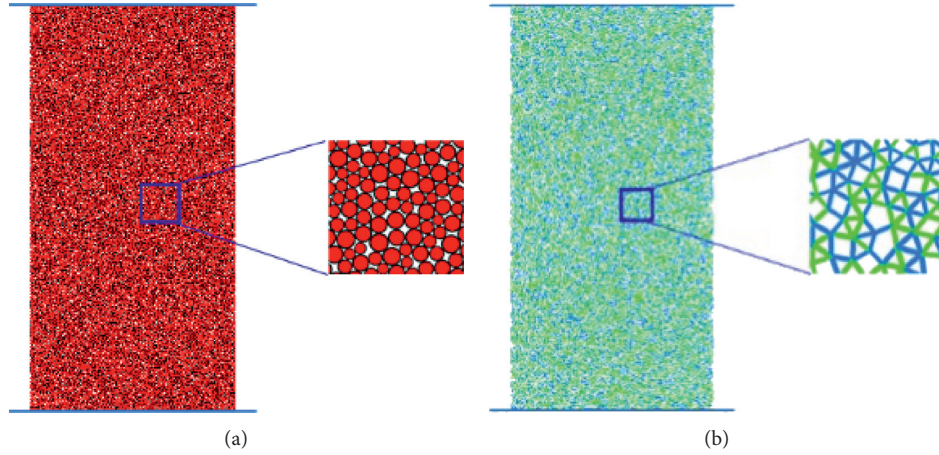
Figure 11: PFC model of sandstone specimen: (a) particle diagram and (b) contact diagram.

Table 4: Mesoparameters of sandstone in different water-bearing states.

Status	E_{ts} (GPa)	E_{cs} (GPa)	σ_{cns} (Pa)	σ_{css} (Pa)
Dry state	23.45	4.36	80.08	72.80
Natural state	15.20	2.72	52.93	48.10
Saturated state	8.91	1.57	8.03	7.30

E_{ts}: soft contact parallel bond modulus; E_{cs}: soft contact linear bond modulus; σ_{cns}: soft contact normal bond strength; σ_{css}: soft contact tangential bond strength.
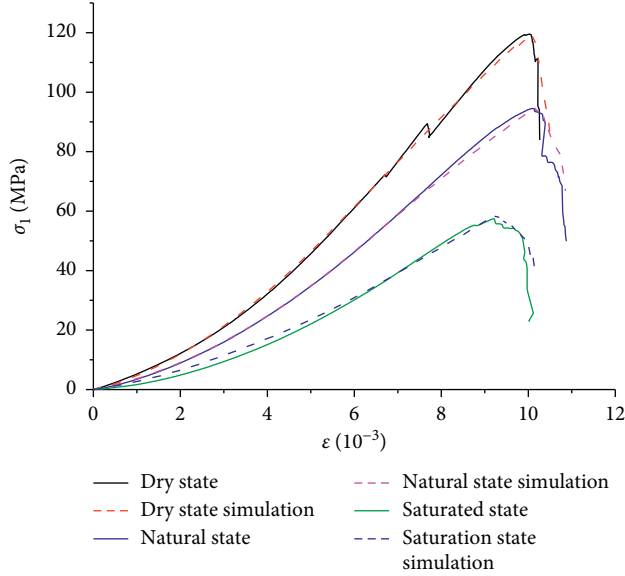
Figure 12: Comparison of variable-modulus uniaxial compression models.

compaction, and the axial strain changes. Larger, that is, the saturated sandstone is more "soft".

Comparing the result of indoor uniaxial compression and numerical simulation, it can be found that the uniaxial compressive strength of the numerical simulation samples under dry, natural, and saturated conditions is 119.34 MPa, 95.34 MPa, and 58.77 MPa, respectively, the relative errors are −0.17%, 0.87%, and 2.3%, and the relative errors are within 3%. Therefore, it is feasible to use the soft-hard double-contact PBM model to simulate the uniaxial test of sedimentary and diagenetic mixed cemented sandstones affected by water deterioration.

Comparing the failure picture of the indoor uniaxial compression test sample with the failure mode of the PFC model, as shown in Figure 13, it can be found that the failure mode of the PFC model is similar to the failure mode of the indoor rock sample, and the simulation situation is in line with the reality; when the sandstone sample is damaged, the sandstone is broken into multiple rock blocks with different stress levels.

5.3. The Influence of Different Water Content Conditions on the Microstructure of Sandstone

5.3.1. Influence on the Distribution of Force Chains Between Particles. Figure 14 shows the distribution of force chains between sample particles in different states of specimen under uniaxial compression and peak stress conditions (the black force chain represents compression, and the red force chain represents tension. The thickness of the force chain is proportional to the magnitude of the bearing and transmitted load). The following can be observed from Figure 14.

For the three hydrated samples, the number and thickness of the pressure chain are much greater than the tension chain. In the peak stress state, the pressure chain is the main load-bearing and load-transmitting force chain, and the overall direction of the pressure chain is along the axial direction. With the increase of moisture content, the proportion of the pressure chain gradually increases, and the proportion of the tension chain gradually decreases; in the dry state, the pressure-strength contact force chain and the tension-strength contact force chain cover the entire sample. With the increase of the rate, the chain of strong contact force gradually decreases, and the distribution gradually disperses. The decreasing trend of the chain of strong contact force under tension is more obvious. This indicates that the higher the water content, the more easily the strength of the
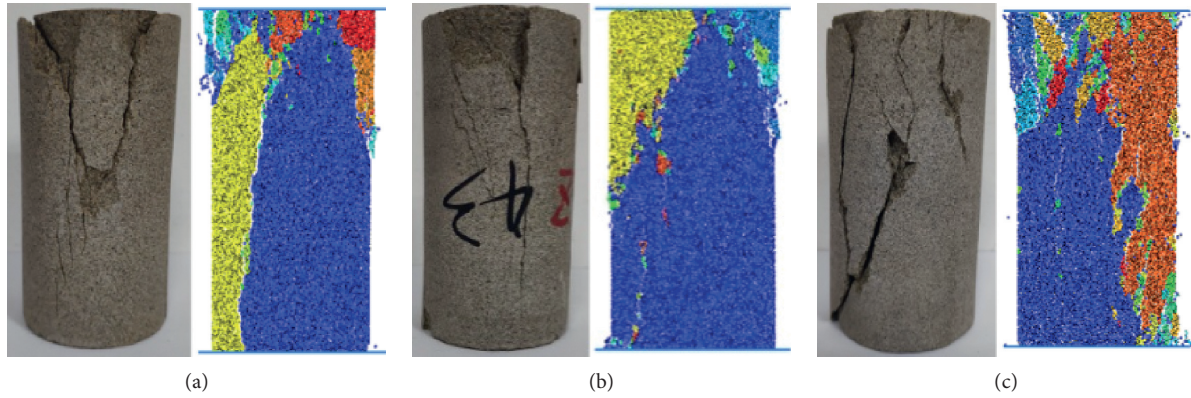
FIGURE 13: The amount of contact varies among different models: (a) dry state, (b) natural state, and (c) saturated state.
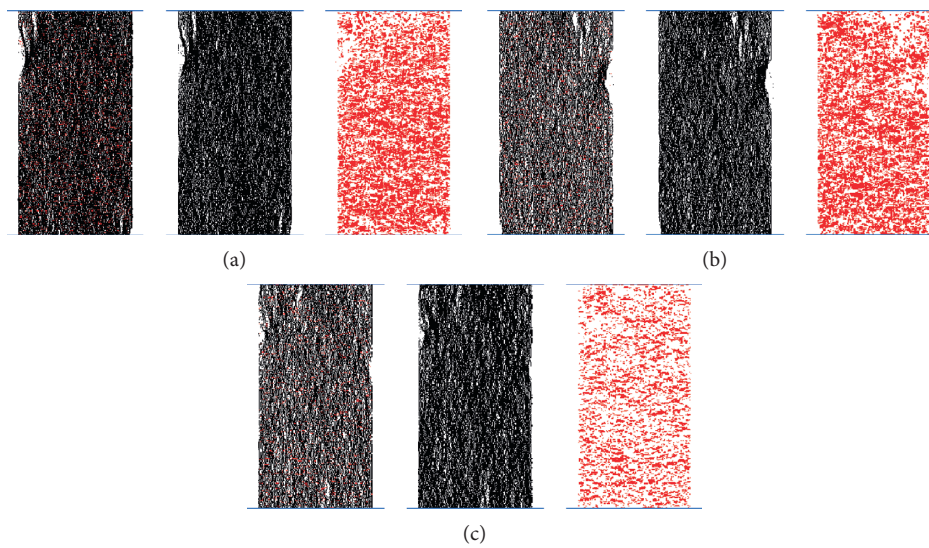
FIGURE 14: Distribution of force chains of specimens in different states: (a) dry state, (b) natural state, and (c) saturated state.

particles and the adhesion between the particles deteriorate. This is consistent with the higher the water content, the more obvious the softening effect of water on the cement and mineral particles.

5.3.2. Influence on the Number of Cracks and Changes in the Number of Contacts. When the postpeak stress is reduced to 20% of the peak value, the sample is completely destroyed. Figure 15 shows the change in the number of cracks and the final distribution of cracks during the uniaxial compression failure of samples in different water-containing states (blue cracks are tensile cracks, and green cracks are shear cracks). It can be seen that the number of uniaxial compression tensile cracks at the final failure is much greater than the number of shear cracks, and the microscopic view of uniaxial compression is dominated by tensile failure. The following can be found from Figure 15.

When the samples were completely destroyed, the numbers of tensile cracks in dry, natural, and saturated samples were 2893, 3129, and 5270, respectively, and the numbers of shear cracks were 1257, 1501, and 3493,

respectively. As the moisture content increases, the final total number of cracks, tensile cracks, and shear cracks continue to increase. The difference between tensile cracks and shear cracks keeps increasing. The distribution area of cracks in the dry state accounts for 60%, and the cracks in the saturated state almost cover the entire sample, indicating that the higher the moisture content, the more obvious the tensile failure.

The occurrence and propagation of tension cracks and shear cracks in dry and natural models are basically the same. After reaching the peak value, it expands rapidly, and the extension of tensile cracks is much faster than that of shear cracks. After the tension cracks and shear cracks of the saturated model appear in the compaction stage, they rapidly expand first, and then the expansion speed slows down. After the axial stress reaches the peak value, the tension cracks expand sharply. The number of tension cracks increases significantly. When the moisture content is low, the crack propagation law in the sandstone is consistent. When the sandstone is fully saturated with water, the cracks in the sandstone expand irregularly.

(a)

(b)

(c)
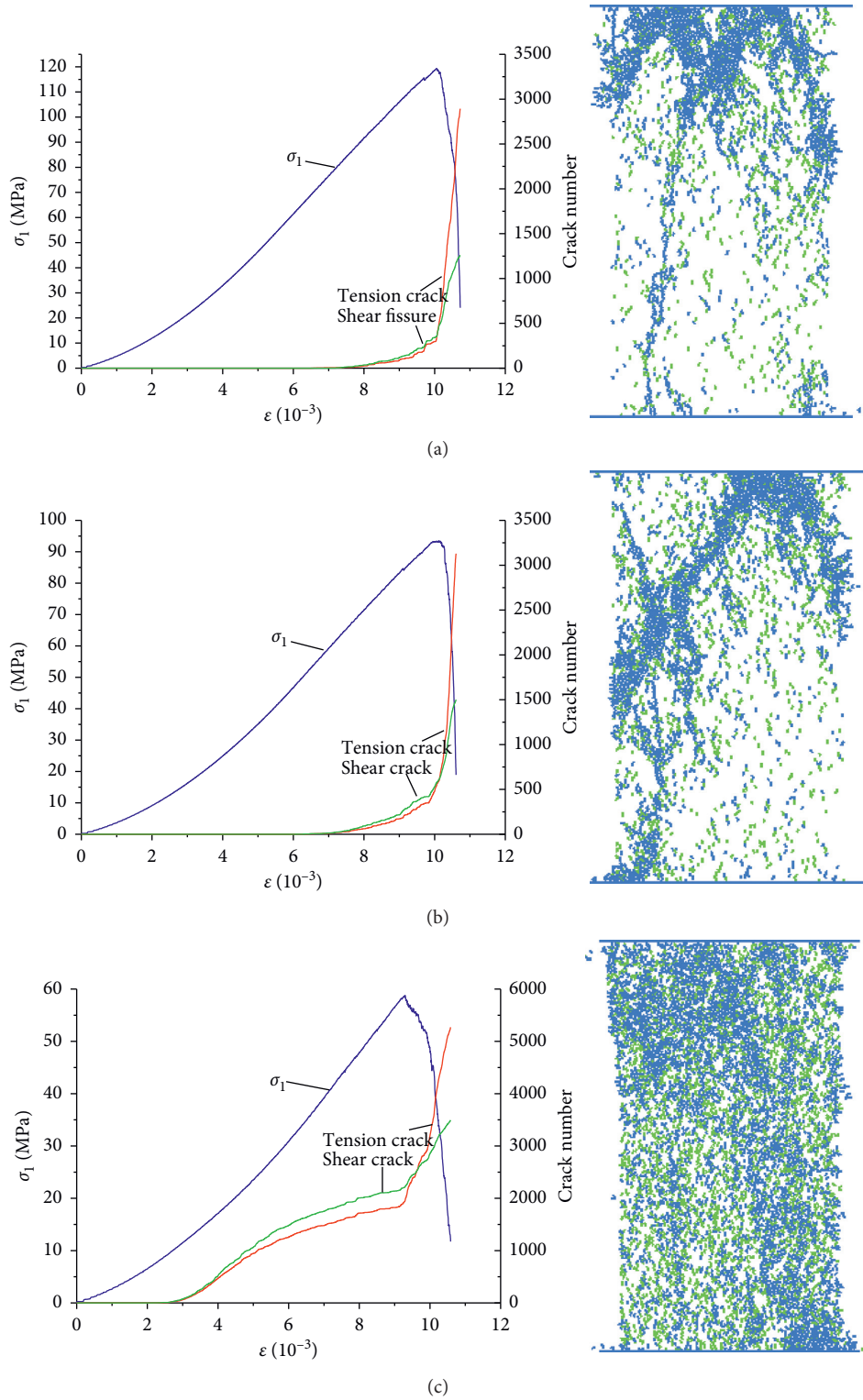
FIGURE 15: The number of cracks developed in different models: (a) dry model, (b) natural model, and (c) saturated model.

Figure 16 shows the changes in the number of soft and hard contacts in the uniaxial compression failure process of the models in different water states. It can be found that the soft contact of the three-state compression model fractures first, and the hard contact occurs after the failure. Comparing Figures 15 with 16, we can find the following.

The dry and natural models start to crack in the elastic stage, and the saturated model cracks in the compaction stage. The higher the moisture content, the easier the crack will appear, and the fracture in the compacted section is soft contact, and the soft cementation is affected by water. With the increase of water content, the bonding ability decreases.
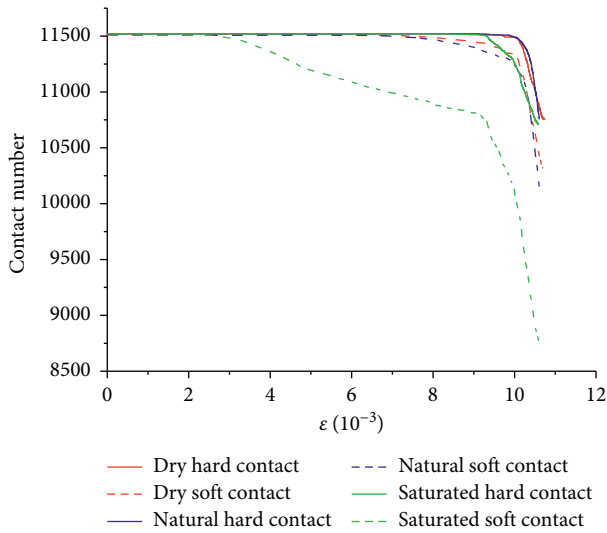
FIGURE 16: The amount of contact varies among different models.

When the water content of sandstone is low, the soft cementation is less affected by water. After the sandstone is saturated with water, the weak cementation is fully softened, and fracture occurs under less load.

Under the peak stress, there are 36 hard contact failures and 181 soft contact failures of the dry samples, 55 hard contact failures and 322 soft contact failures of the natural samples, and 19 hard contact failures and 758 soft contact failures of the saturated samples. The ratio of the number of hard contact damage to soft contact damage in dry, natural, and saturated samples is 0.20, 0.17, and 0.03, respectively. With the increase of water content, the ratio of the number of hard-soft contact fractures decreases gradually under the peak stress state.

6. Conclusion

(1) Water has a weakening effect on sandstone. Water leads to a decrease in the cohesiveness between mineral particles in sandstone and changes in the macromechanical properties of sandstone. The water content of sandstone increases by 1.01% from the dry state to the natural state, the uniaxial compressive strength decreases by 26.64 MPa, and the elastic modulus decreases by 2.66 GPa.

(2) The water in sandstone has a softening effect on cementing materials and mineral particles, and the higher the water content, the more obvious the effect. With the increase of water content, the number of pores increases, the diameter becomes larger, and the shape of the pores becomes diversified. The distribution of pores in natural and saturated sandstone is almost the same, and water has a greater influence on the size of small pores.

(3) Based on the PFC2D discrete element simulation analysis, with the increase of water content, the deterioration of adhesion between particles intensifies. When the water content of sandstone is low,

the soft cementation is less affected by water. After the sandstone is saturated with water, the weak cementation is fully softened, and the load-bearing capacity limit decreases.

Data Availability

The datasets generated and analysed during the current study are available from the first author upon reasonable request.

Conflicts of Interest

The authors declare that they have no conflicts of interest.

Acknowledgments

References

[1] C. G. Dyke and L. Dobereiner, "Evaluating the strength and deformability of sandstones," *The Quarterly Journal of Engineering Geology and Hydrogeology*, vol. 24, no. 1, pp. 123–134, 1991.

[2] A. B. Hawkins and B. J. Mcconnell, "Sensitivity of sandstone strength and deformability to changes in moisture content," *The Quarterly Journal of Engineering Geology and Hydrogeology*, vol. 25, no. 2, pp. 115–130, 1992.

[3] D. Gu, H. Liu, and X. Gao, D. Huang and W. Zhang, "Influence of cyclic wetting–drying on the shear strength of limestone with a soft interlayer," *Rock Mechanics and Rock Engineering*, pp. 1–10, 2021.

[4] C. Zhu, M.-c. He, M. Karakus, X.-h. Zhang, and Z. Guo, "The collision experiment between rolling stones of different shapes and protective cushion in open-pit mines," *Journal of Mountain Science*, vol. 18, no. 5, pp. 1391–1403, 2021.

[5] C. Zhu, M. He, M. Karakus, X. Zhang, and Z. Tao, "Numerical simulations of the failure process of anaclinal slope physical model and control mechanism of negative Poisson's ratio cable," *Bulletin of Engineering Geology and the Environment*, vol. 80, no. 4, pp. 3365–3380, 2021.

[6] C. Yang, Y. Chen, Z. Guo, W. Zhu, and R. Wang, "Surface settlement control in the excavation of a shallow intersection between a double-arched tunnel and a connection tunnel," *International Journal of Geomechanics*, vol. 21, no. 4, pp. 1–11, Article ID 04021035, 2021.

[7] C. Yang, Z. Hu, D. Huang, and F. Guo, "Failure mechanism of primary support for a shallow and asymmetrically loaded tunnel portal and treatment measures," *Journal of Performance of Constructed Facilities*, vol. 34, no. 1, pp. 1–13, Article ID 04019105, 2020.

[8] Q. Wang, Z. Jiang, B. Jiang, H. Gao, Y. Huang, and P. Zhang, "Research on an automatic roadway formation method in deep mining areas by roof cutting with high-strength bolt-grouting," *International Journal of Rock Mechanics and Mining Sciences*, vol. 128, Article ID 104264, 2020.

[9] Y. Wang, W. K. Feng, R. L. Hu, and C. H. Li, "Fracture evolution and energy characteristics during marble failure under triaxial fatigue cyclic and confining pressure unloading (FC-CPU) conditions," *Rock Mechanics and Rock Engineering*, vol. 54, no. 2, pp. 799–818, 2021.

[10] F. Wu, R. Gao, J. Liu, and C. Li, "New fractional variable-order creep model with short memory," *Applied Mathematics and Computation*, vol. 380, Article ID 125278, 2020.

[11] F. Wu, H. Zhang, Q. Zou, C. Li, J. Chen, and R. Gao, "Viscoelastic-plastic damage creep model for salt rock based on fractional derivative theory," *Mechanics of Materials*, vol. 150, Article ID 103600, 2020.

[12] Q. Cui, X. T. Feng, Q. Xue et al., "Mechanism study of porosity structure change of sandstone under chemical corrosion," *Chinese Journal of Rock Mechanics and Engineering*, vol. 27, no. 6, pp. 1209–1216, 2008.

[13] X.-T. Feng and W. Ding, "Experimental study of limestone micro-fracturing under a coupled stress, fluid flow and changing chemical environment," *International Journal of Rock Mechanics and Mining Sciences*, vol. 44, no. 3, pp. 437–448, 2007.

[14] X. Li and X.-S. Li, "Micro-macro quantification of the internal structure of granular materials," *Journal of Engineering Mechanics*, vol. 135, no. 7, pp. 641–656, 2009.

[15] L. L. Wang, M. Bornert, D. S. Yang et al., "Microstructural insight into the nonlinear swelling of argillaceous rocks," *Engineering Geology*, vol. 193, pp. 435–444, 2015.

[16] Z. P. Song, Y. Cheng, T. T. Yang et al., "Experimental study of the influence of osmotic pressure on pore structure evolution in limestone," *Rock and Soil Mechanics*, vol. 13, 2019.

[17] M. Farrokhrouz, M. R. Asef, and R. Kharrat, "Empirical estimation of uniaxial compressive strength of shale formations," *Geophysics*, vol. 79, no. 4, pp. 227–233, 2014.

[18] S. X. Ling, X. Y. Wu, C. W. Sun et al., "Experimental study of chemical damage and mechanical deterioration of black shale due to water-rock chemical action," *Journal of Experimental Mechanics*, vol. 31, no. 4, pp. 511–524, 2016.

[19] L. Qiao, J. Liu, and X. Feng, "Study on damage mechanism of sandstone under hydro-physico-chemical effects," *Chinese Journal of Rock Mechanics and Engineering*, vol. 26, no. 10, pp. 2117–2124, 2007.

[20] J. Fang, F. Dang, Y. Xiao et al., "Quantitative study ON the CT test process OF siltstone under triaxial compression," *Chinese Journal of Rock Mechanics and Engineering*, vol. 34, no. 10, pp. 1976–1984, 2015.

[21] H. Sun, X. L. Liu, and E. Z. Wang, "Prediction on uniaxial compression strength of rocks with X-ray computed tomography," *Chinese Journal of Rock Mechanics and Engineering*, vol. 38, no. S2, pp. 3575–3582, 2019.

[22] Z. L. Zhong, W. K. Luo, X. R. Liu et al., "Experimental study on mechanical properties deterioration of limestone in acid environment based on nuclear magnetic resonance," *Journal of China Coal Society*, vol. 42, no. 7, pp. 1740–1747, 2017.

[23] Y. Song, L. Zhang, J. Ren et al., "Study on damage characteristics of weak cementation sandstone under drying-wetting cycles based on nuclear magnetic resonance technique," *Chinese Journal of Rock Mechanics and Engineering*, vol. 38, no. 4, pp. 825–831, 2019.

[24] N. Li, K. Wang, G. Zhang et al., "Prediction of gas production in carbonates based on CT analysis and nuclear magnetic resonance (NMR) logging," *Petroleum Exploration and Development*, vol. 42, no. 2, pp. 167–174, 2015.

[25] Z. J. Wang, X. R. Liu, Y. Fu et al., "Erosion analysis of argillaceous sandstone under dry-wet cycle in two pH conditions," *Rock and Soil Mechanics*, vol. 37, no. 11, pp. 3231–3239, 2016.

[26] Q.-X. Meng, W.-Y. Xu, H.-L. Wang, X.-Y. Zhuang, W.-C. Xie, and T. Rabczuk, "DigiSim - an open source software package for heterogeneous material modeling based on digital image processing," *Advances in Engineering Software*, vol. 148, Article ID 102836, 2020.

[27] X. R. Liu, D. L. Li, L. Zhang et al., "Influence of wetting-drying cycles on mechanical properties and microstructure of shaly sandstone," *Chinese Journal of Geotechnical Engineering*, vol. 38, no. 7, pp. 1291–1300, 2016.

[28] H. F. Deng, Y. Y. Zhi, L. L. Duan et al., "Research on the mechanical properties of sandstone and the damage evolution of microstructure under water-rock interaction," *Rock and Soil Mechanics*, vol. 40, no. 9, pp. 3447–3456, 2019.

[29] M. J. Jiang, N. Zhang, and H. Chen, "Discrete element simulation of aging effect of chemical weathering on rock," *Rock and Soil Mechanics*, vol. 35, no. 12, pp. 3577–3584, 2014.

[30] M. J. Jiang, P. Zhang, and Z. W. Liao, "DEM numerical simulation of rock under the influence of water softening and chemical weathering and chemical weathering in uniaxial compression test," *Journal of China Institute of Water Resources and Hydropower Research*, vol. 15, no. 2, pp. 89–95, 2017.

[31] J. X. Hu, K. Bian, J. Liu et al., "Discrete element simulation of shale softening based on parallel-bonded water-weakening model," *Chinese Journal of Geotechnical Engineering*, vol. 43, no. 4, pp. 725–733, 2021.

[32] Z. Z. Zhang, F. Gao, Y. N. Gao et al., "Fractal structure and model of pore size distribution of granite under high temperatures," *Chinese Journal of Rock Mechanics and Engineering*, vol. 35, no. 12, pp. 2426–2438, 2016.

[33] R. F. Voss, R. B. Laibowitz, and E. I. Allesandrin, "Fractal geometry of percolation in thin gold films," *Scaling Phenomena in Disordered Systems*, Plenum Press, New York, NY, USA, 1985.

[34] D. M. Gu, *Failure Mechanism and Evolution of the Anaclinal High Carbonatite Rock Slopes with Soft Toes in the Three Gorges Region*, Chongqing University, Chongqing, China, 2018.

Research Article

An Experimental Study on the Creep Characteristics of Sandstone in the Interval of Different Critical Stresses

Chao Yang [ID], Xingchen Dong, Xuan Xu, and Qiancheng Sun [ID]

Key Laboratory of Geological Hazards on Three Gorges Reservoir Area (China Three Gorges University), Ministry of Education, Yichang 443002, China

Correspondence should be addressed to Qiancheng Sun; qc_sun@ctgu.edu.cn

Creep tests on brittle sandstone specimens were performed to investigate the time-dependent characteristics in the interval of different critical stresses. The results showed that failure will not occur when the loaded stress σ_1 is less than the critical stress of dilation σ_{cd}, while all specimens were destroyed when σ_1 is larger than σ_{cd}. In addition, the value of σ_{cd} was very close to the long-term strength obtained by the method of the isochronous stress-strain curve. Therefore, σ_{cd} can be regarded as the long-term strength of the sandstone specimens. When σ_1 is larger than σ_{cd}, the time required for the failure of specimen t_f decreases with the increase of σ_1; the creep rate $d\varepsilon/dt$ increases with time t, and the specimen will be destroyed when it reaches a maximum value $(d\varepsilon/dt)_{max}$. Both relationships t_f and σ_1 and $(d\varepsilon/dt)_{max}$ and σ_1 can be described by the exponential function. Then, a nonlinear damage creep model considering the deformation damage and strength damage in the interval of different critical stresses was established, which can describe the whole creep process and predict the failure time of sandstone specimens.

1. Introduction

Critical stresses (the crack closure stress level σ_{cc}, crack initiation stress level σ_{ci}, critical stress of dilation σ_{cd}, and peak strength σ_c) are important indexes for evaluating hard brittle rocks [1–3], which reflect the internal microfracture activity state of rocks under different stress levels. The failure process of rocks under different compression conditions can be divided into 4 stages, which are crack closure stage ($\sigma_1 < \sigma_{cc}$), elastic region ($\sigma_{cc} < \sigma_1 < \sigma_{ci}$), stable crack growth stage ($\sigma_{ci} < \sigma_1 < \sigma_{cd}$), and unstable crack growth stage ($\sigma_{cd} < \sigma_1 < \sigma_c$). Obviously, the creep characteristics of hard brittle rocks should also be different when under long-term loading in different critical stress intervals.

As the critical point of time-dependent damage under the creep condition, the long-term strength of rocks has always been the focus of researchers [4–6]. Currently, there are mainly two methods to determine the long-term strength. (1) The steady-state creep rate [7]: carrying out creep tests at multiple stress levels by the "Chen method" and determining long-term strength as the maximum load

with zero creep rate. (2) The stress-strain isochronal curves [8, 9]: treating the long-term strength as the yield strength and considering the time effect. Both methods mentioned above are based on a large number of creep tests, which makes the acquisition of long-term strength of rocks relatively complicated. If the results of uniaxial or triaxial tests can be used to establish the correlation with the long-term strength of rocks, the difficulty of the test will be greatly reduced. Some attempts have been made, such as Liu [10] who used the volume expansion method which determines the long-term strength by the volume expansion point and Ding et al. [11] who proposed a method to predict salt rock damage based on the stress corresponding to the damage initiation point as the long-term strength. However, there are few studies on the relationship between critical stresses and long-term strength of hard brittle rocks, as well as creep characteristics under different critical stress intervals.

In this study, a series of laboratory tests, including uniaxial compression test, multistage loading creep test, and single-stage loading creep test, were carried out on sandstone specimens. The creep characteristics of specimens in

the interval of different critical stresses were investigated. The conclusions can provide reference for the analysis of time-dependent behavior of hard brittle rocks.

2. Specimen Preparation and Testing

The sandstones were obtained from Chongqing in China, whose natural dry density was approximately $2.68 \times 10^3 \, \text{kg/m}^3$. Specimens made from sandstones had a columnar shape with a diameter of 50 mm and a height of 100 mm, which were in accordance with the standard recommended by the International Society for Rock Mechanics.

All the tests were performed on a HYZW-500L Rock Mechanics Testing System at the Key Laboratory of Geological Hazards on Three Gorges Reservoir Area, Ministry of Education, China. The loading rate of all tests was maintained at constant 0.2 kN/s. Firstly, uniaxial compression tests were carried out to obtain the critical stresses of the specimens. The axial stress σ_1 was loaded on specimens progressively from 0 MPa until specimens were destroyed. Then, multistage loading creep tests were carried out to obtain the long-term strength. σ_1 was loaded progressively from 0 MPa till the first stage of loading, and then it was increased to the next stage when the deformation was stable. Finally, the single-stage creep tests were performed, in which σ_1 was set based on the results of the first two tests. After reaching the design level with the same loading procedure mentioned above, σ_1 was kept constant until specimens were destroyed or the deformation was stable without increase (in this case, the loading time was at least 200 hours). The load, time, and displacements were recorded in all the tests.

3. Experimental Results

3.1. Critical Stresses. Based on the uniaxial compression test, the crack volumetric strain ε_v^c, the volumetric strain ε_v, and the elastic volumetric strain ε_v^e are calculated as follows [6]:

$$\left. \begin{array}{c} \varepsilon_v^c = \varepsilon_v - \varepsilon_v^e \\[2mm] \varepsilon_v = \varepsilon_1 + 2\varepsilon_3 \\[2mm] \varepsilon_v^e = \dfrac{(1 - 2\mu)\sigma_1}{E} \end{array} \right\}, \tag{1}$$

where ε_1 is the axial strain, ε_3 is the radial strain, σ_1 is the stress level, E is the elastic modulus, and μ is Poisson's ratio.

The σ_1-ε_1-ε_3, ε_v-ε_1, and ε_v^c-ε_1 curves of specimens are shown in Figure 1. According to the crack strain model method, the stress corresponding to the end of the concave section of the σ_1-ε_1 curve is point σ_{cc}, the stress corresponding to the beginning of the negative correlation between ε_v^c and ε_1 in the $\varepsilon_v^c - \varepsilon_1$ curve is point σ_{ci}, and σ_{cd} is the value corresponding to the inflection point of the $\varepsilon v - \varepsilon_1$ curve, after which the whole specimen starts to expand. Therefore, the critical stresses and deformation parameters of the sandstone specimen were $\sigma_{cc} \approx 22.6 \, \text{MPa}$, $\sigma_{ci} \approx 50.3 \, \text{MPa}$, $\sigma_{cd} \approx 72.6 \, \text{MPa}$, $\sigma_c \approx 95.2 \, \text{MPa}$, $E \approx 11.2 \, \text{GPa}$, and $\mu \approx 0.2$.
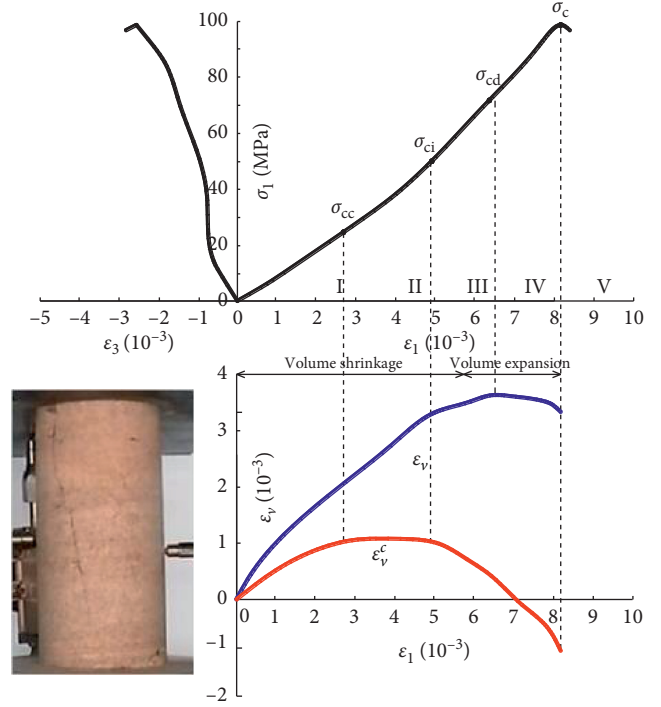
FIGURE 1: Uniaxial compression test curves and failure of the sandstone specimen.

3.2. Long-Term Strength of the Isochronal Curve Method. Based on the multistage loading creep tests, the time-dependent deformation curve under $\sigma_1 = 50, 60, 70$, and 80 MPa is shown in Figure 2. The deformations were stable after 24 h at $\sigma_1 = 50, 60$, and 70 MPa, while creep failure occurred after 17.4 h when $\sigma_1 = 80 \, \text{MPa}$.

The isochronal curve composed of stress and strain values at loading time t of 2, 4, 8, 16, and 24 h is shown in Figure 3. The spacing between curves started to increase gradually from σ_1 of 70 MPa, and the spacing with σ_1 of 80 MPa between curves was significantly different from that of σ_1 of 60 and 70 MPa. Therefore, the long-term strength of specimens was determined to be 70 MPa.

3.3. Creep Rate of the Single-Stage Loading Creep Test. According to critical stresses of specimens and combined with results of the multistage loading creep test, the stress levels σ_1 of the single-stage loading creep tests were designed to be 50, 60, 72, 74, 75, 80, and 85 MPa. From the test curves and specimen failures as shown in Figure 4, specimens did not fail under σ_1 of 50, 60, and 72 MPa, while the accelerated creep stage and failure occurred under σ_1 of 74, 75, 80, and 85 MPa, and the creep failure time gradually decreased to 139.5, 108.7, 42.2, and 17.5 h, respectively. The long-term strength obtained by the stress-strain isochronal curves was about 70 MPa, and the stress of creep failure in the single-stage loading creep tests was between 72 and 74 MPa, which was extremely close to the critical stress of dilation ($\sigma_{cd} \approx 72.6 \, \text{MPa}$) obtained in the uniaxial compression test. Therefore, σ_{cd} can be approximated as the long-term strength of specimens in this paper. It can be considered that
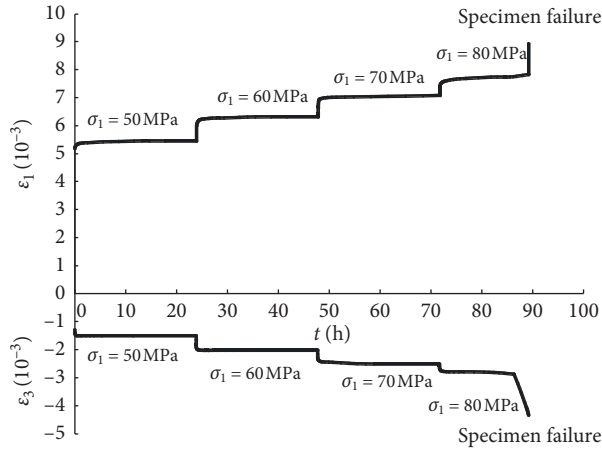
FIGURE 2: Creep deformation curves of the multistage creep test and failure of the specimen.
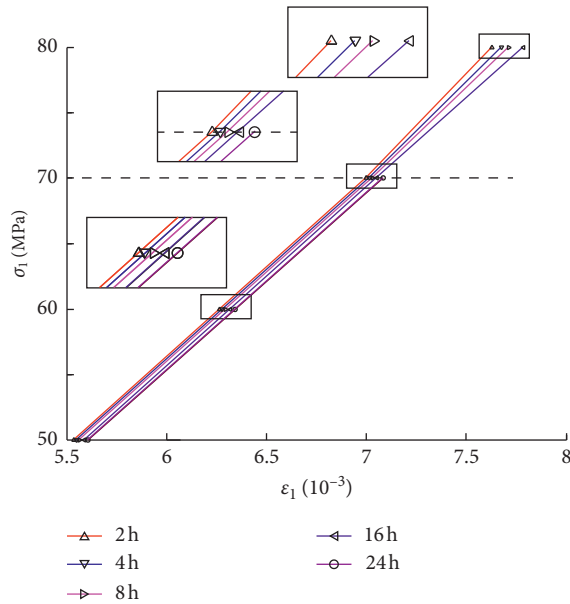
FIGURE 3: Stress-strain isochronal curves.

when σ_1 is less than σ_{cd}, there will be no accelerated creep stage and no creep failure to specimens; when σ_1 is greater than σ_{cd}, the accelerated creep stage and failure of specimens will occur.

As shown in Figure 4, the creep curves only showed characteristics of decay creeping, and the creep rate ($d\varepsilon_1/dt$) finally approaches 0 in the crack closure stage, elastic region, and stable crack growth stage ($\sigma_1 < \sigma_{cd}$).

By analyzing the creep rate variation characteristics of four specimens at the accelerated creep stage shown in Figure 5, the steady-state creep stage of specimens was relatively short, which decreased with an increase of stress levels (the durations under σ_1 of 74, 75, 80, and 85 MPa were 10.1, 6.0, 5.0, and 2.8 h, respectively). Yu et al. [12] showed that the time-dependent deformation exhibited is unstable in the secondary creep stage, and the results of the tests are similar. After the steady-state creep stage, there was a stage
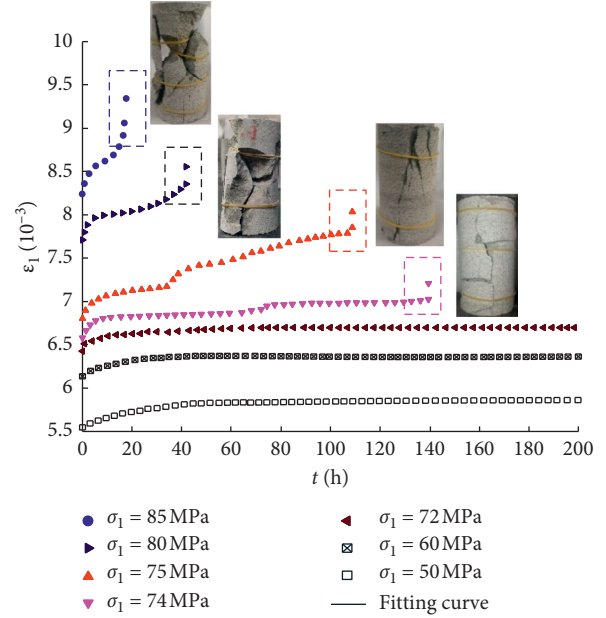
FIGURE 4: Creep deformation curves of the single-stage creep test and failure of the specimens.

of slowly increasing creep rate defined as stage III$_a$ (which is relatively evident in Figures 5(c) and 5(d)) in this paper. After stage III$_a$, there was a stage in which the creep rate increases abruptly defined as stage III$_b$; it was at the end of this stage that specimens failed. Due to the penetration and closure of some microfractures inside specimens under creep conditions, a steep increase and then a steep decrease of creep rate can be found in Figures 5(a) and 5(b). The failure modes of specimens were brittle failure, which is reflected in the creep curve as a sudden vertical ascent of the curve marked in Figure 4. The speed of the ascent was so fast that it presented a folded state rather than a smooth transition. Table 1 summarizes the creep rates and inclination angles of the marked area in Figure 4. There was a maximum creep rate $(d\varepsilon_1/dt)_{max}$ at which specimens failed. And there was a positive correlation between $(d\varepsilon_1/dt)_{max}$ and σ_1; the larger σ_1 was, the larger $(d\varepsilon_1/dt)_{max}$ was.

4. Nonlinear Damage Creep Model

4.1. Damage Variable. Damage variable D is an important mechanical parameter for evaluating material properties and establishing the material damage model. When $D = 0$, there is no damage to the material; when $D = 1$, the material is fully damaged and loses its strength [13–17]. Combined with the test results, it was considered in this paper that when $\sigma_1 < \sigma_{cd}$, the specimens will not fail, and there is no damage to specimens; when $\sigma_1 > \sigma_{cd}$, the specimens will finally fail, and the damage exists in specimens. The damage has the following characteristics: (1) the damage is a time-dependent damage which increases gradually with time and finally reaches complete damage, namely, $D = 1$. (2) The damage is also affected by σ_1. The greater σ_1 is, the shorter the time for specimens to reach the fully damaged state.

(a)

(b)

(c)

(d)
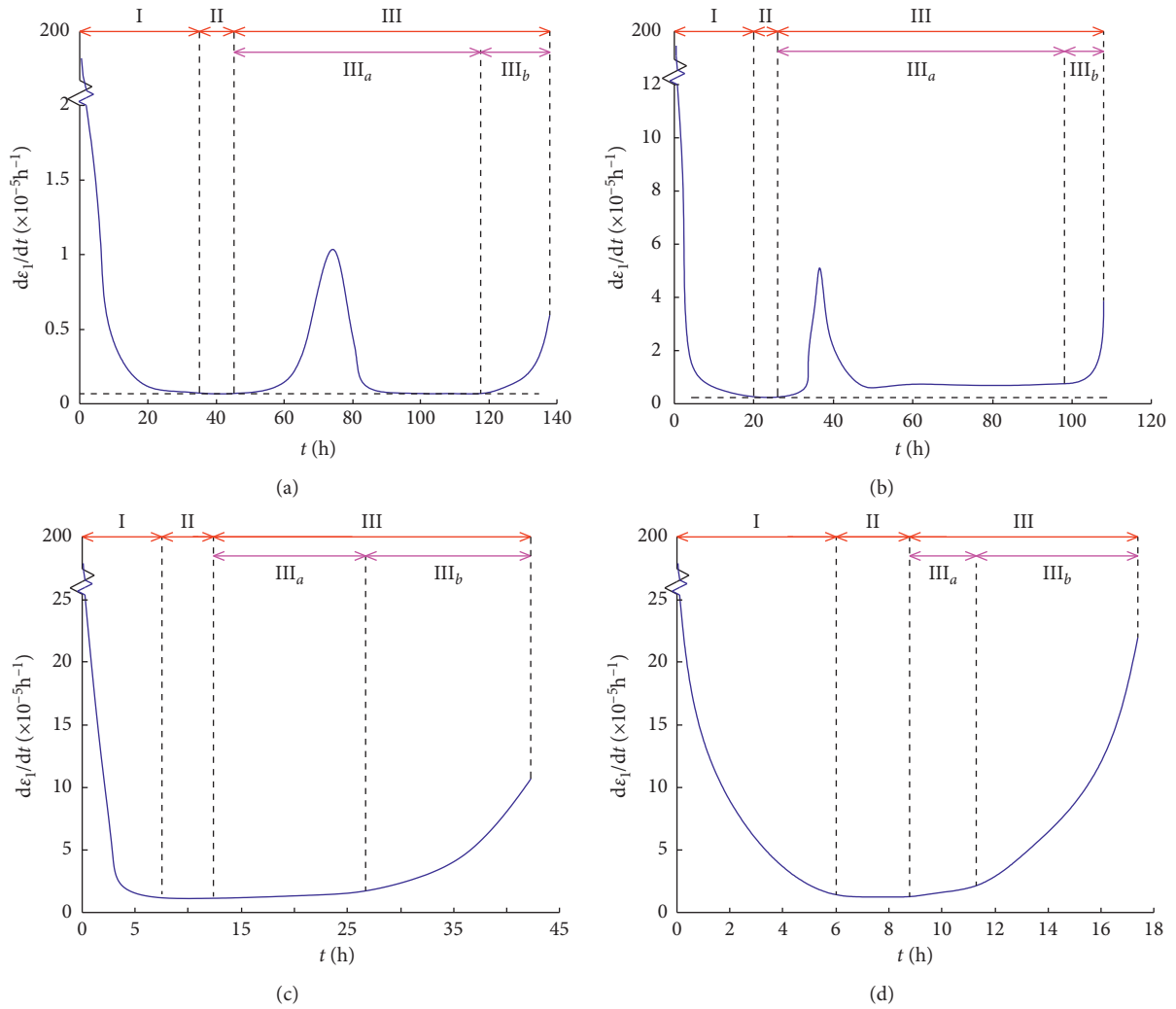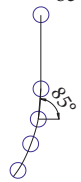
FIGURE 5: Creep rate curves of specimens under different stress levels: (a) $\sigma_1 = 74$ MPa; (b) $\sigma_1 = 75$ MPa; (c) $\sigma_1 = 80$ MPa; (d) $\sigma_1 = 85$ MPa.

TABLE 1: Creep rate and curve inclination before failure.

σ_1 (MPa)	74	75	80	85
$(d\varepsilon_1/dt)_{\max}/h^{-1}$	0.63×10^{-5}	3.67×10^{-5}	10.00×10^{-5}	22.00×10^{-5}
Inclination angles (°)	15	45	50	85
Creep curve before failure				

In terms of the strength of specimens, creep failure occurred in specimens under σ_1 of 74, 75, 80, and 85 MPa, which was reduced by 23%, 21%, 16%, and 10% compared with σ_c.

In terms of the deformation of specimens, the viscosity coefficient η at each time in the creep process can be expressed as

$$\frac{d\varepsilon 1}{dt} = \frac{\sigma 1}{\eta}. \tag{2}$$

When σ_1 is constant, the creep rate $d\varepsilon_1/dt$ is inversely proportional to η. As shown in Figure 5, the creep rate of the specimen was constant in stage II and began to increase as it entered stage III, which indicates that η began to decay with

increasing creep time. Therefore, it can be assumed that no time dependence was produced before stage III, while it started to appear after stage III. When σ_1 was 74, 75, 80, and 85 MPa, η of creep failure was lost about 92%, 90%, 99%, and 95%, respectively.

It was obvious that the damage of the specimen in strength was very different from that in deformation, and the same damage variable cannot be used to describe both. Therefore, two types of damage variables, named strength damage variable and deformation damage variable, were proposed from the analysis above.

The strength damage variable $D_1(\sigma, t)$ can be calculated as

$$D1\,(\sigma, t) = \frac{\sigma_c - \sigma_f(t)}{\sigma_c - \sigma_1}, \tag{3}$$

where σ_1 is the long-term load applied on specimens and $\sigma_f(t)$ is the stress corresponding to the creep failure time t.

When $\sigma_f(t) = \sigma_c$, specimens are instantaneously damaged, namely, $t = 0$. When $\sigma_f(t) = \sigma_{cd}$, the specimen will be permanently undamaged, namely, $t = \infty$. Combined with the stress and time corresponding to the creep failure of specimens in the single-stage loading creep test, the fitting curve is presented in Figure 6.

It can be seen from Figure 6 that the larger σ_1 was, the shorter the time required for the creep failure of specimen t_f was. This relationship can be described as

$$\sigma_f\,(t_f) = \sigma_{cd} + (\sigma_c - \sigma_{cd})\exp(-\alpha t_f), \tag{4}$$

where α is the correlation coefficient of damage degree, which can be fitted according to the test data. For specimens in this paper, $\alpha = -0.025$. By combining equations (3) and (4), the expression of strength time-dependent damage variable $D_1(\sigma, t)$ of specimens can be described as

$$D1\,(\sigma, t) = \frac{(\sigma_c - \sigma_{cd})(1 - \exp(-\alpha t))}{\sigma c - \sigma_1}. \tag{5}$$

The deformation damage variable $D_2(\sigma, t)$ of specimens proposed in this paper is

$$D2\,(\sigma, t) = \begin{cases} 0, & t \le t_w, \\ 1 - [\eta(\sigma, t)/\eta_0], & t > t_w, \end{cases} \tag{6}$$

where $\eta(\sigma, t)$ is the viscosity coefficient function with creep time t, η_0 is the viscosity coefficient at the steady-state creep stage, and t_w is the time required to reach stage III$_a$.

Creep failure of specimens occurred when $D_1(\sigma, t) = 1$, while $D_2(\sigma, t)$ is not strictly equal to 1, and $\eta(\sigma, t)$ corresponded to the maximum creep rate $(d\varepsilon_1/dt)_{max}$ as described in Table 1.

Figure 7 shows the relationship between tw and σ_1 and the variation of $\eta(\sigma, t)$ with time. The larger σ_1 is, the shorter the time experienced before entering the steady-state creep stage is and the small η in the steady-state creep stage is. Moreover, $\eta(\sigma, t)$ decreases gradually with time after stage II; this relationship can also be described as
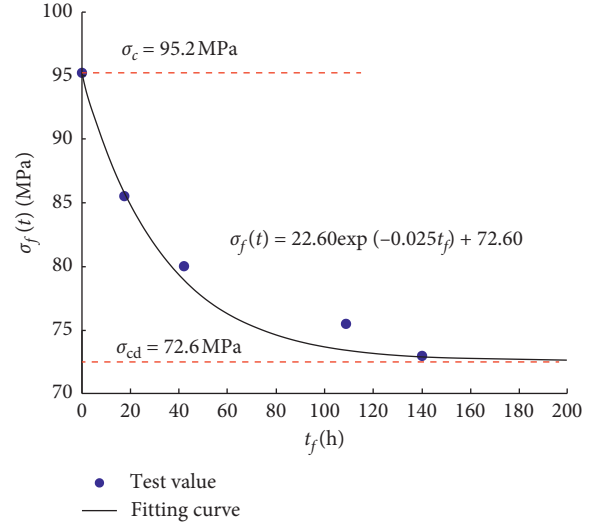
FIGURE 6: Relationship between load and time in the creep failure of specimens.

$$\eta(\sigma, t) = \begin{cases} \eta_0, & t \le t_w, \\ \eta_0 \exp(-\beta t), & t > t_w, \end{cases} \tag{7}$$

where β is the correlation coefficient of damage degree, which is related to σ_1. As σ_1 increases, β increases gradually. The fitting curve combined with η_0, β, and σ_1 is shown in Figure 8.

It can be observed that, with the increase of σ_1, η_0, and β, different variation laws were shown: η_0 decreased with σ_1, while β increased with σ_1. By combining equations (6) and (7), the expression of deformation time-dependent damage variable $D_1(\sigma, t)$ can be described as

$$D2\,(\sigma, t) = \begin{cases} 0, & t \le t_w, \\ 1 - \exp(-\beta t), & t > t_w. \end{cases} \tag{8}$$

4.2. A New Damage Creep Model with Different Critical Stress Intervals.
Based on the creep characteristics and two damage variables of specimens, a new 5-element nonlinear damage creep model was established, in which σ_{cd} is the stress threshold that controls the damaged viscous element, as shown in Figure 9.

According to equation (7), the nonlinear expression of the constitutive equation of the damaged viscous element can be obtained as

$$\frac{d(\varepsilon_1)}{dt} = \frac{\sigma_1}{\eta_0}\exp(\beta t). \tag{9}$$

Taking $\varepsilon_1 = 0$ when $t = 0$, the creep equation of the damaged viscous element can be written as

$$\varepsilon_1 = \frac{\sigma_1}{\eta_0 \beta}[\exp(\beta t) - 1]. \tag{10}$$

(a)

(b)
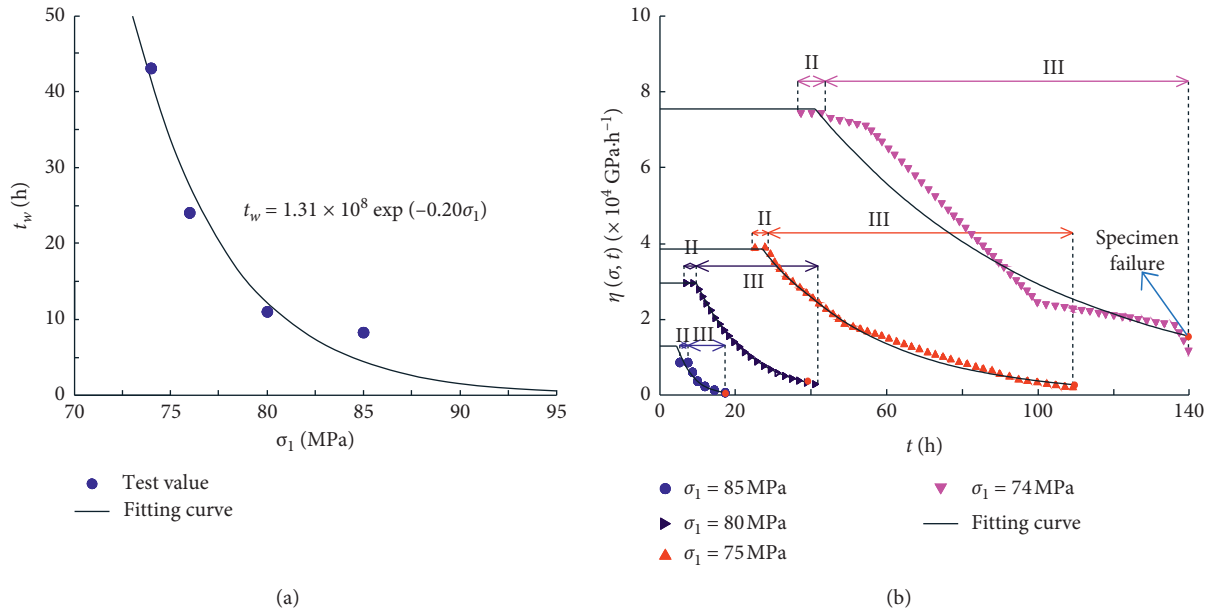
FIGURE 7: Relationship between t_w and σ_1 and $\eta(\sigma, t)$ and t: (a) t_w-σ_1; (b) $\eta(\sigma, t)$-t.

(a)

(b)
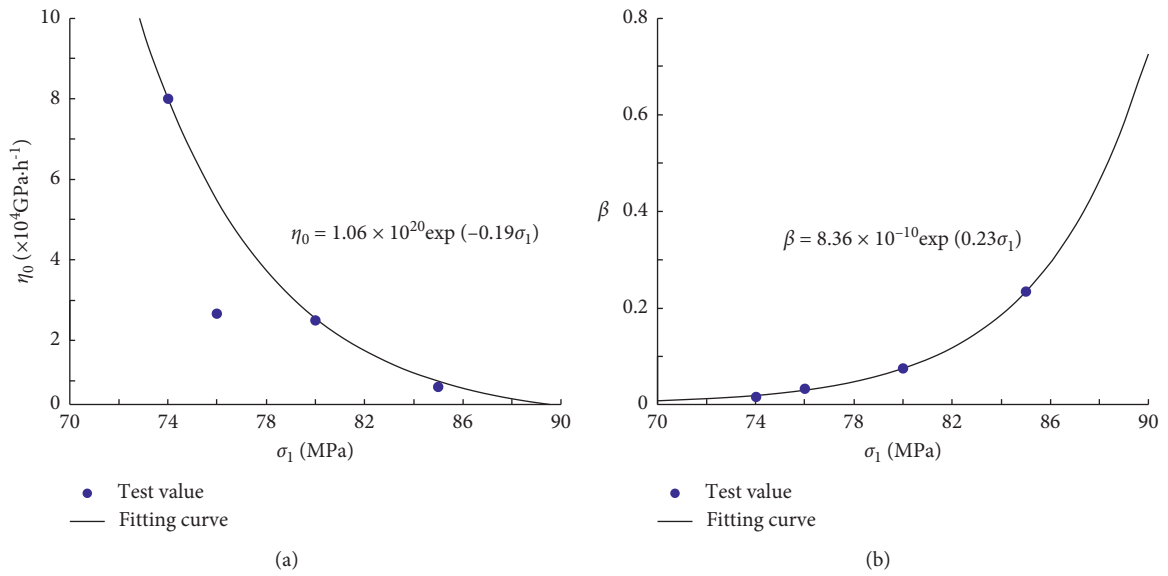
FIGURE 8: The relation graph of viscosity coefficient η_0-σ_1 and β-σ_1 in stage II of the specimen: (a) η_0-σ_1; (b) β-σ_1.
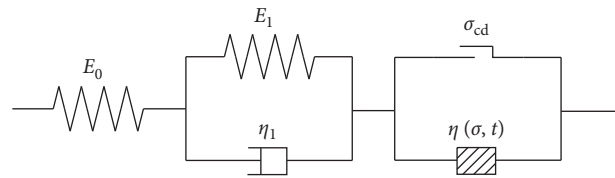
FIGURE 9: Damage creep models with different critical stress intervals.

TABLE 2: The parameters of the damage creep model for specimens.

σ_1 (MPa)	E_0 (GPa)	E_1 (GPa)	$\eta_1 \cdot$ (GPa $\cdot$ h)	$\eta_0 \cdot$ (GPa $\cdot$ h)	β
50	9.3	160	500	—	—
60	9.93	170	600	—	—
72	11.35	195	600	—	—
74	11.03	300	900	80000	0.01884
75	11.11	300	900	55000	0.02978
80	10.45	300	600	25000	0.07400
85	10.39	300	600	9800	0.23350
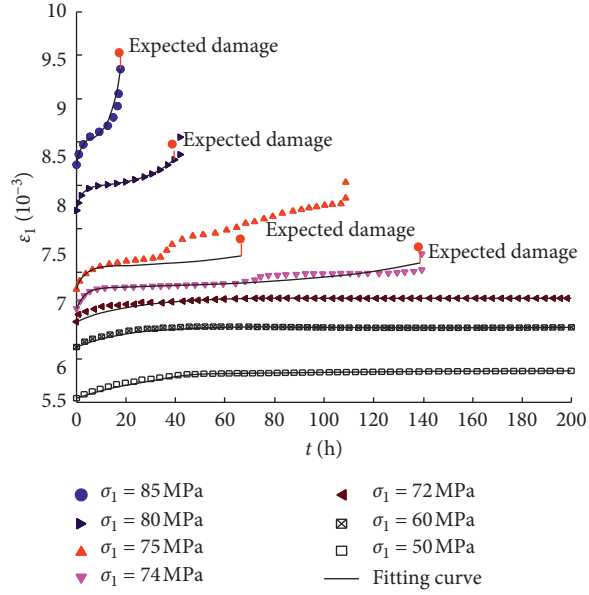
FIGURE 10: The scatter plot of one-step loading creep test and its fitting curve.

Substituting equation (7) into the generalized Kelvin model, the equation of the nonlinear damage creep model can be determined as follows.

(1) When in the crack closure stage, elastic region, and stable crack growth stage ($\sigma_1 < \sigma_{cd}$), the damage creep model is a generalized Kelvin model; then, the equation is

(2) When in the unstable crack growth stage ($\sigma_1 < \sigma_{cd}$), the damage creep model is made up of generalized Kelvin model in series with a damaged viscous element, and the equation is

$$\varepsilon(\sigma, t) = \frac{\sigma_1}{E_0} + \frac{\sigma_1}{E_1}\left(1 - \exp\left(-\frac{E_1}{\eta_0}t\right)\right). \quad (11)$$

$$\varepsilon(\sigma, t) = \begin{cases} \dfrac{\sigma_1}{E_0} + \dfrac{\sigma_1}{E_1}\left(1 - \exp\left(-\dfrac{E_1}{\eta_1}t\right)\right) + \dfrac{\sigma_1}{\eta_0}t, & t \leq t_w, \\[4mm] \dfrac{\sigma_1}{E_0} + \dfrac{\sigma_1}{E_1}\left(1 - \exp\left(-\dfrac{E_1}{\eta_1}t\right)\right) + \dfrac{\sigma_1}{\eta_0\beta}[\exp(\beta t) - 1], & t > t_w. \end{cases} \quad (12)$$

Table 2 shows the fitting values of parameters, and Figure 10 shows the comparison of creep fitting curves and test curves. It can be observed that the damage creep model can better describe all three stages of the creep process and can accurately predict the creep failure time of specimens. Due to the influence of specimen discreteness, the fitting effect under 75 MPa is poor.

5. Conclusions

(1) Creep tests were carried out, and the creep deformation curves of sandstone in the interval of different critical stresses were acquired. The test results showed that the long-term strength is very close to the critical stress of dilation.

(2) Two new damage variables to describe the time-dependent damage of hard brittle rocks were proposed. The creep failure time of specimens was controlled by the strength damage variable, and the deformation of specimens was controlled by the deformation damage variable.

(3) The nonlinear damage creep models with different critical stress intervals can well match the test data and predict the creep failure time and deformation of specimens in the creep process. They can also describe the phenomenon that the creep failure mode of hard brittle rocks was brittle failure.

(4) Further research will be carried out in the numerical calculation of the damage model established in this paper, so as to realize the application in practical engineering.

Data Availability

The datasets generated and/or analysed during the current study are available from the first author upon reasonable request.

Conflicts of Interest

The authors declare that they have no conflicts of interest.

Acknowledgments

References

[1] E. Eberhardt, D. Stead, B. Stimpson, and R. S. Read, "Identifying crack initiation and propagation thresholds in brittle rock," *Canadian Geotechnical Journal*, vol. 35, no. 2, pp. 222–233, 1998.

[2] Y.-H. Gao, X.-T. Feng, X.-W. Zhang, G.-L. Feng, Q. Jiang, and S.-L. Qiu, "Characteristic stress levels and brittle fracturing of hard rocks subjected to true triaxial compression with low minimum principal stress," *Rock Mechanics and Rock Engineering*, vol. 51, no. 12, pp. 3681–3697, 2018.

[3] C. D. Martin and N. A. Chandler, "The progressive fracture of Lac du Bonnet granite," in *Proceedings of International Journal of Rock Mechanics and Mining Science & Geomechanics Abstracts*, Pergamon, Turkey, 1994 December.

[4] N. A. Chandler, "Quantifying long-term strength and rock damage properties from plots of shear strain versus volume strain," *International Journal of Rock Mechanics and Mining Sciences*, vol. 59, pp. 105–110, 2013.

[5] B. Damjanac and C. Fairhurst, "Evidence for a long-term strength threshold in crystalline rock," *Rock Mechanics and Rock Engineering*, vol. 43, no. 5, pp. 513–531, 2010.

[6] C. D. Martin, *The strength of massive Lac du Bonnet granite around underground openings*, UMI Dissertation Services, Michigan, US, 1993.

[7] M. E. Kassner, *Fundamentals of Creep in Metals and Alloys*, Butterworth-Heinemann, Oxford, UK, 2015.

[8] H. Özsen, İ. Özkan, and C. Sensögüt, "Measurement and mathematical modelling of the creep behaviour of Tuzköy rock salt," *International Journal of Rock Mechanics and Mining Sciences*, vol. 66, pp. 128–135, 2014.

[9] R. Wang, Y. Jiang, C. Yang, F. Huang, and Y. Wang, "A nonlinear creep damage model of layered rock under unloading condition," *Mathematical Problems in Engineering*, vol. 2018, pp. 1–8, 2018.

[10] X. Liu, *Rock Rheology Introduction*, Geological Publishing, Beijing, China, 1994.

[11] G. Ding, J. Liu, L. Wang, Z. Wu, and Z. Zhou, "Discussion on determination method of long-term strength of rock salt," *Energies*, vol. 13, no. 10, p. 2460, 2020.

[12] J. Yu, G. Liu, Y. Cai, J. Zhou, S. Liu, and B. Tu, "Time-dependent deformation mechanism for swelling soft-rock tunnels in coal mines and its mathematical deduction," *International Journal of Geomechanics*, vol. 20, no. 3, Article ID 04019186, 2020.

[13] D. Gu, H. Liu, X. Gao, D. Huang, and W. Zhang, "Influence of cyclic wetting–drying on the shear strength of limestone with a soft interlayer," *Rock Mechanics and Rock Engineering*, pp. 1–10, 2021.

[14] Q. Jiang, J. Cui, and J. Chen, "Time-dependent damage investigation of rock mass in an in situ experimental tunnel," *Materials*, vol. 5, no. 8, pp. 1389–1403, 2012.

[15] Q.-X. Meng, W.-Y. Xu, H.-L. Wang, X.-Y. Zhuang, W.-C. Xie, and T. Rabczuk, "DigiSim - an open source software package for heterogeneous material modeling based on digital image processing," *Advances in Engineering Software*, vol. 148, Article ID 102836, 2020.

[16] Y. Wang, W. K. Feng, R. L. Hu, and C. H. Li, "Fracture evolution and energy characteristics during marble failure under triaxial fatigue cyclic and confining pressure unloading (FC-CPU) conditions," *Rock Mechanics and Rock Engineering*, vol. 54, no. 2, pp. 799–818, 2021.

[17] H. Zhao, C. Shi, M. Zhao, and X. Li, "Statistical damage constitutive model for rocks considering residual strength," *International Journal of Geomechanics*, vol. 17, no. 1, Article ID 04016033, 2017.

Research Article

Refinement of a Deflection Basin Area Index Method for Rigid Pavement

Jin Zhang ,[1] Qiuzhen Lv,[1] Wei Shi,[1] Guangsheng Li,[1] and Jiafeng Zhang[2]

[1]*School of Civil Engineering, Qingdao University of Technology, Qingdao 266033, China*
[2]*Shanghai CAAC New Era Airport Design & Research Institute Co., Ltd., Shanghai 200120, China*

Correspondence should be addressed to Jin Zhang; zhangjin@qut.edu.cn

The accuracy of the prediction and reliability of the deflection basin area index method for rigid pavement heavily depend on the sensor layout scheme and the calculation theory. A total of 154 groups of deflection data were generated by the finite element software in different conditions, and the simulated results were in good agreement with the analytical solutions of thin plates on elastic foundation. The accuracy of several types of deflection basin area index methods was assessed with the database of pavement deflection results. It is found that, apart from densifying the distal sensor layouts locally, replacing the deflection value of a specific point with the average of all measured points in the deflection basin area index was also an effective measure to improve the back-calculation accuracy of pavement structural parameters up to 40%. Finally, a new deflection basin area index method was proposed based on the deflection database with the regression analysis. Comparisons between the theoretical calculations of several models and the practical deflection data of an airport in northern China revealed that the newly proposed method performs better on the back-calculation accuracy and efficiency, which can provide a valuable guideline for the practical engineering in the design.

1. Introduction

Sufficient load capacities are essential for the airport runway due to the considerable impact loads during the aircraft landing. The deflection, total deformations of the airport pavement under the load, is a critical parameter to reflect the overall load-bearing capacities of pavement structures. The heavy weight deflectometer (HWD) test, a vital technology for the strength design and performance evaluation of pavement structures, has been widely adopted to determine the deflection value [1–4]. In general, the primary methods for parameter back-calculation of the pavements' structural performance based on deflection values can be classified as follows.

The intelligent optimization method has been developed to find out the optimal solution of pavement structural parameters iteratively, such as neural network algorithm and genetic algorithm [5, 6]. However, the accuracy of these methods heavily depends on the reliability of the algorithm

and the calibration of some internal parameters [7, 8]. Darter et al. [9] have developed the back-calculation technique, like the point-by-point fitting method, to determine the optimal solution by comparing the objective function results of calibration error with the actual deflection basin through an iterative approach. Nevertheless, low efficiency was detected with this method in the iterative process. Besides, Sun et al. [10] have reported that the inherent information of the inert point on deflection curves remained constant regardless of the variations of resilient modulus of pavement slabs. Although the back-calculation of pavement structural parameters can be conducted once the specific inert point was obtained, the deterministic process of this point was relatively complicated [10, 11].

Compared with the back-calculation methods, the derived index method of the deflection basin [12] has been widely recognized by many researchers and engineers mainly due to the simplification of the back-calculation process. The method is also adopted by Chinese code MH/T

5024-2009 [13] and the U.S. Federal Aviation Administration [14] for the back-calculation of pavement structure parameters. This method simplifies the back-calculation process by constructing a deflection basin area index, which includes fitting formula method, back-calculation software method, and graphic method. However, related studies [15, 16] have revealed that the normalization of the basin area index during the aforementioned constructional process with only an assigned measurement point will cause the inferior accuracy and higher variability. To incorporate the effect of different measuring points, Lin et al. [15] have improved the back-calculation method by minimizing the calculated errors of the objective function, but the efficiency has been significantly influenced. However, either the calculation accuracy of these methods is not up to the standard, or the calculation process is too complex, which is not conducive to direct engineering application.

With this background, the finite element (FE) simulation was first applied to generate deflection information under different working conditions. Then, the error analysis was systematically conducted for the existing deflection basin area index methods based on the assembled database, and a new improved approach was developed in this study for practical engineering. By comparing with the measured data of an airport, the prediction accuracy of this method and other selection methods for back-calculation results were evaluated. The result shows that the improved deflection basin area index method has the advantages of simple calculation and high accuracy. In practical engineering application, it can not only save time but also achieve fast and accurate results, which is of great significance.

2. Finite Element Simulation

Considering that multiple variables cannot be considered simultaneously in a practical engineering, the effect of different conditions on the structures cannot be comprehensively estimated. Moreover, the test setup with high costs and measurement strategy may have a great impact on the accuracy of test results. Over the past decades, the FE technique has become increasingly popular in academic researches [17–20] because it can solve the problems that cannot be realized in engineering field. Thus, the finite element software was adopted to simulate the deflections of airport pavement structures under varied working conditions in this study. Studies on parameters were also conducted with the verified FE model for the following theoretical analysis.

2.1. Parameter Setting.
The sectional size of the pavement slab was set as 30 m × 30 m to reduce the influence of edge effect on the simulation because there are no relationships between the deflection value and the slab size for the position beyond 0.7 m away from the slab edge [21]. As per the Chinese code MH/T 5024-2009 [13], some basic parameters of the model were presented as follows: Poisson's ratio ($u = 0.15$); the elastic modulus of the thin concrete plate (32 GPa).

2.2. Boundary Conditions and Mesh.
The spring foundation was added at the bottom surface of pavement slab, and the modulus of subgrade reaction was defined as k to simulate the equivalent reaction modulus of different soil layers under the pavement in actual engineering. Circular uniform load (0.15 m in radius) was applied on the upper surface of the model. No constraints were arranged on the other four sides. The static load of 1.5 MPa was used to simulate the maximum impact load produced by HWD test to obtain the corresponding deflection values according to the literature [19]. The free tetrahedral mesh was chosen, and the mesh element size was smaller than the thickness of the pavement slab h.

2.3. FE Model Results.
One hundred and fifty-four groups of test data (see Table 1) were generated by uniformly extracting the deflection value at the position of 0 cm, 20 cm, 30 cm, 45 cm, 60 cm, 90 cm, 120 cm, 150 cm, and 180 cm away from the load center of the model. In this process, the value of the modulus of subgrade reaction k and the thickness of pavement slab h are continuously changed. Figure 1 shows the layout of the measuring points mentioned above. Figure 2 shows the simulation results of pavement slab with 28 mm in thickness and the modulus of subgrade reaction of 125 MN/m^3. Furthermore, the value of h can be determined from the suggested slab thickness for the FE simulation provided by Cheng et al. [19]. The empirical value of subgrade reaction k can be referred to as the Chinese code GB 50307-2012 [22], and the selected ranges of h and k are presented in Table 2. To facilitate the following discussion, each working condition is given a name composed of letters and numbers. The first letter and the subsequent numbers represent the thickness of the slab (unit: mm). The second letter and the corresponding number stand for the modulus of subgrade reaction (unit: MN/m^3). For example, H28K125 represents the working condition with the pavement thickness of 28 mm and modulus of subgrade reaction of 125 MN/m^3. N represents sensors in Figure 1.

2.4. FE Model Verification

2.4.1. Winkler Foundation Model.
Chen et al. [20] have found that the Winkler foundation model performs better than the elastic half-space foundation model in calculating the structural responses of the pavement. It is assumed that the pressure p at one point on the foundation surface is proportional to the settlement w at the same point in the Winkler foundation model, and the pressure p is also independent of the pressure from surrounding points. The relationship between p and w can be presented as $p = k \cdot w$, which means that every single point of the foundation is supported by a spring, which works separately at different locations.

The analytical equation of the one thin slab deflection value predicted by the Winkler foundation model under uniformly distributed circular load is shown in equation (1) [23], which provides a reliable standard for the verification of deflection results obtained from the FE model.

TABLE 1: Comparison of simulated deflection and theoretical deflection under different working conditions.

Number	w0 (mm)			w20 (mm)			w30 (mm)			w45 (mm)			w60 (mm)			w90 (mm)			w120 (mm)			w150 (mm)			w180 (mm)		
	DFE	Dcal	D%	DFE	Dcal	D%	DFE	Dcal	D%	DFE	Dcal	D%	DFE	Dcal	D%	DFE	Dcal	D%	DFE	Dcal	D%	DFE	Dcal	D%	DFE	Dcal	D%
H20K15	712	725	-1.8	689	707	-2.5	671	687	-2.3	639	651	-2.0	599	610	-1.9	512	521	-1.7	425	431	-1.4	343	347	-1.2	269	272	-1.0
H20K25	550	560	-1.9	528	543	-2.7	511	525	-2.5	481	491	-2.1	445	454	-2.0	368	375	-1.7	293	298	-1.4	226	228	-1.1	168	169	-0.8
H20K35	464	473	-1.9	442	456	-2.9	427	438	-2.7	398	407	-2.1	364	372	-2.0	294	299	-1.7	227	230	-1.3	168	170	-0.9	120	120	-0.5
H20K45	408	416	-1.9	388	400	-3.1	372	383	-2.8	345	353	-2.2	313	319	-2.1	247	251	-1.7	186	188	-1.2	134	135	-0.7	91	92	-0.1
H20K55	369	376	-1.9	348	360	-3.2	334	344	-2.9	307	314	-2.2	277	282	-2.1	214	218	-1.7	158	160	-1.1	110	111	-0.6	73	73	0.2
H20K65	339	345	-1.9	319	330	-3.3	304	314	-3.0	279	285	-2.3	249	255	-2.1	190	193	-1.6	137	138	-1.0	93	94	-0.4	60	59	0.6
H20K75	315	321	-1.9	295	306	-3.4	281	290	-3.1	257	263	-2.3	228	233	-2.1	171	174	-1.6	121	122	-0.9	81	81	-0.2	50	49	1.0
H20K85	296	301	-1.9	276	286	-3.5	262	271	-3.1	238	244	-2.3	210	215	-2.1	156	158	-1.6	108	109	-0.8	71	71	0.0	42	42	1.4
H20K95	279	285	-1.9	260	270	-3.6	247	255	-3.2	223	228	-2.3	196	200	-2.1	143	145	-1.6	98	99	-0.7	62	62	0.2	37	36	1.9
H20K105	265	271	-1.9	246	256	-3.7	233	241	-3.3	210	215	-2.3	184	188	-2.1	133	135	-1.5	89	90	-0.6	56	56	0.4	32	31	2.3
H20K115	253	258	-1.9	235	244	-3.7	222	229	-3.3	199	204	-2.3	173	177	-2.1	124	125	-1.5	82	83	-0.5	50	50	0.6	28	27	2.9
H20K125	243	248	-1.9	224	233	-3.8	211	219	-3.4	189	194	-2.3	164	167	-2.1	116	117	-1.5	76	76	-0.4	46	45	0.8	25	24	3.4
H20K135	234	238	-1.9	215	224	-3.9	202	210	-3.4	181	185	-2.3	156	159	-2.1	109	110	-1.4	70	71	-0.3	42	41	1.0	22	21	4.0
H20K145	225	230	-1.9	207	215	-3.9	194	201	-3.4	173	177	-2.4	148	152	-2.1	103	104	-1.4	66	66	-0.2	38	38	1.2	20	19	4.6
H20K155	218	222	-1.9	200	208	-4.0	187	194	-3.5	166	170	-2.4	142	145	-2.1	97	99	-1.3	61	61	0.0	35	35	1.4	18	17	5.3
H20K165	211	215	-1.8	193	201	-4.0	181	187	-3.5	160	164	-2.4	136	139	-2.1	92	94	-1.3	58	58	0.1	32	32	1.7	16	15	6.0
H20K175	205	208	-1.8	187	195	-4.1	175	181	-3.6	154	158	-2.4	131	134	-2.1	88	89	-1.3	54	54	0.2	30	29	1.9	14	13	6.8
H20K185	199	203	-1.8	181	189	-4.1	169	175	-3.6	149	152	-2.4	126	129	-2.1	84	85	-1.2	51	51	0.3	28	27	2.1	13	12	7.7
H20K195	194	197	-1.8	176	184	-4.2	164	170	-3.6	144	148	-2.4	122	124	-2.1	80	81	-1.2	49	48	0.4	26	25	2.4	12	11	8.6
H20K205	189	192	-1.8	171	179	-4.2	159	166	-3.7	140	143	-2.4	117	120	-2.1	77	78	-1.1	46	46	0.6	24	24	2.6	11	10	9.6
H20K215	184	188	-1.8	167	174	-4.3	155	161	-3.7	136	139	-2.4	114	116	-2.0	74	75	-1.1	44	43	0.7	23	22	2.9	10	9	10.6
H20K225	180	183	-1.7	163	170	-4.3	151	157	-3.7	132	135	-2.3	110	112	-2.0	71	72	-1.1	42	41	0.8	21	21	3.2	9	8	11.8
H24K15	550	553	-0.5	533	542	-1.5	521	530	-1.6	500	507	-1.5	474	481	-1.4	417	423	-1.4	358	363	-1.4	300	304	-1.3	247	250	-1.2
H24K25	426	427	-0.3	410	417	-1.6	399	405	-1.6	379	384	-1.5	355	360	-1.5	304	308	-1.5	252	256	-1.4	204	207	-1.2	161	163	-1.1
H24K35	360	361	-0.1	344	350	-1.7	334	340	-1.7	315	320	-1.5	293	297	-1.5	245	249	-1.5	198	201	-1.4	156	158	-1.2	119	120	-1.0
H24K45	318	318	0.0	302	308	-1.7	292	297	-1.8	274	278	-1.6	253	256	-1.5	208	211	-1.5	165	167	-1.3	126	128	-1.1	93	94	-0.8
H24K55	288	287	0.2	272	277	-1.8	262	267	-1.8	244	248	-1.6	224	228	-1.5	182	184	-1.5	141	143	-1.3	106	107	-1.0	76	77	-0.7
H24K65	265	264	0.3	250	254	-1.8	240	244	-1.8	222	226	-1.6	203	206	-1.5	162	165	-1.5	124	126	-1.3	91	92	-1.0	64	64	-0.5
H24K75	246	245	0.4	232	236	-1.8	222	226	-1.9	205	208	-1.6	186	189	-1.5	147	149	-1.5	111	112	-1.2	80	81	-0.9	55	55	-0.3
H24K85	232	230	0.6	217	221	-1.8	207	211	-1.9	191	194	-1.6	172	175	-1.6	135	137	-1.5	100	101	-1.2	71	72	-0.8	48	48	-0.1
H24K95	219	218	0.7	204	208	-1.9	195	199	-1.9	179	182	-1.6	161	164	-1.6	124	126	-1.5	91	92	-1.1	64	64	-0.7	42	42	0.1
H24K105	208	207	0.8	194	198	-1.9	185	188	-2.0	169	172	-1.6	151	154	-1.6	116	117	-1.5	84	85	-1.1	58	58	-0.6	37	37	0.3
H24K115	199	197	0.9	185	188	-1.9	176	179	-2.0	160	163	-1.7	143	145	-1.6	108	110	-1.5	78	79	-1.1	53	53	-0.5	34	33	0.5
H24K125	191	189	1.0	177	180	-1.9	168	171	-2.0	153	155	-1.7	136	138	-1.6	102	103	-1.5	72	73	-1.0	48	49	-0.4	30	30	0.8
H24K135	184	182	1.1	170	173	-2.0	161	164	-2.0	146	148	-1.7	129	131	-1.6	96	98	-1.5	68	68	-0.9	45	45	-0.3	27	27	1.0
H24K145	178	176	1.1	163	167	-2.0	155	158	-2.0	140	142	-1.7	123	125	-1.6	91	93	-1.5	63	64	-0.9	41	41	-0.2	25	25	1.3
H24K155	172	170	1.2	158	161	-2.0	149	152	-2.1	134	137	-1.7	118	120	-1.6	87	88	-1.4	60	60	-0.8	38	38	-0.1	23	23	1.6
H24K165	167	164	1.3	153	156	-2.0	144	147	-2.1	130	132	-1.7	114	115	-1.6	83	84	-1.4	56	57	-0.8	36	36	0.0	21	21	1.9
H24K175	162	160	1.4	148	151	-2.0	139	142	-2.1	125	127	-1.7	109	111	-1.6	79	80	-1.4	53	54	-0.7	34	34	0.1	19	19	2.2
H24K185	157	155	1.5	144	147	-2.0	135	138	-2.1	121	123	-1.7	106	107	-1.5	76	77	-1.4	51	51	-0.7	32	31	0.3	18	17	2.5
H24K195	153	151	1.6	140	142	-2.0	131	134	-2.1	117	119	-1.7	102	104	-1.5	73	74	-1.4	48	49	-0.6	30	30	0.4	17	16	2.9
H24K205	150	147	1.6	136	139	-2.1	128	130	-2.1	114	116	-1.7	99	100	-1.5	70	71	-1.4	46	46	-0.6	28	28	0.5	15	15	3.2

TABLE 1: Continued.

Number	w0 (mm) DFE	Dcal	D%	w20 (mm) DFE	Dcal	D%	w30 (mm) DFE	Dcal	D%	w45 (mm) DFE	Dcal	D%	w60 (mm) DFE	Dcal	D%	w90 (mm) DFE	Dcal	D%	w120 (mm) DFE	Dcal	D%	w150 (mm) DFE	Dcal	D%	w180 (mm) DFE	Dcal	D%
H24K215	146	144	1.7	132	135	-2.1	124	127	-2.1	111	112	-1.7	96	97	-1.5	67	68	-1.3	44	44	-0.5	26	26	0.6	14	14	3.6
H24K225	143	140	1.8	129	132	-2.1	121	124	-2.2	108	109	-1.7	93	94	-1.5	65	66	-1.3	42	42	-0.4	25	25	0.8	13	13	4.0
H28K15	441	439	0.3	427	432	-1.1	419	424	-1.2	404	409	-1.2	386	391	-1.2	347	351	-1.3	305	309	-1.3	263	266	-1.3	223	226	-1.2
H28K25	342	340	0.7	329	333	-1.0	321	325	-1.2	307	311	-1.2	291	295	-1.2	255	259	-1.4	218	221	-1.3	183	185	-1.3	150	151	-1.2
H28K35	290	287	1.0	277	280	-1.0	269	273	-1.2	256	259	-1.3	241	244	-1.3	207	210	-1.4	174	176	-1.3	142	144	-1.3	113	114	-1.2
H28K45	256	253	1.3	244	246	-1.0	236	239	-1.2	223	226	-1.3	209	211	-1.3	177	179	-1.4	146	147	-1.3	116	118	-1.3	91	92	-1.1
H28K55	232	228	1.6	220	222	-1.0	212	215	-1.2	200	202	-1.3	186	188	-1.3	155	158	-1.4	126	128	-1.3	99	100	-1.2	75	76	-1.0
H28K65	214	210	1.8	201	203	-1.0	194	197	-1.2	182	185	-1.3	169	171	-1.3	139	0	-1.4	111	113	-1.3	86	87	-1.2	64	65	-0.9
H28K75	199	195	2.0	187	189	-0.9	180	182	-1.2	168	170	-1.3	155	157	-1.3	127	129	-1.5	100	101	-1.3	76	77	-1.2	56	56	-0.8
H28K85	187	183	2.2	175	177	-0.9	168	171	-1.2	157	159	-1.3	144	146	-1.3	117	118	-1.5	91	92	-1.3	68	69	-1.1	49	50	-0.7
H28K95	177	173	2.4	166	167	-0.9	159	161	-1.2	147	149	-1.3	135	136	-1.3	108	110	-1.5	84	85	-1.2	62	63	-1.1	44	44	-0.6
H28K105	169	165	2.6	157	159	-0.9	150	152	-1.2	139	141	-1.3	127	128	-1.3	101	102	-1.5	77	78	-1.2	57	57	-1.0	40	40	-0.5
H28K115	162	157	2.7	150	151	-0.9	143	145	-1.2	132	134	-1.3	120	122	-1.3	95	96	-1.5	72	73	-1.2	52	52	-1.0	36	36	-0.4
H28K125	155	151	2.9	143	145	-0.9	137	139	-1.2	126	128	-1.3	114	116	-1.3	89	91	-1.5	67	68	-1.2	48	49	-0.9	33	33	-0.2
H28K135	149	145	3.1	138	139	-0.9	131	133	-1.2	121	122	-1.4	109	110	-1.3	85	86	-1.5	63	64	-1.2	45	45	-0.9	30	30	-0.1
H28K145	144	140	3.2	133	134	-0.9	126	128	-1.2	116	117	-1.4	104	106	-1.3	81	82	-1.5	59	60	-1.1	42	42	-0.8	28	28	0.0
H28K155	140	135	3.3	128	129	-0.9	122	123	-1.2	111	113	-1.4	100	101	-1.3	77	78	-1.5	56	57	-1.1	39	39	-0.7	26	26	0.2
H28K165	136	131	3.5	124	125	-0.9	118	119	-1.3	107	109	-1.4	96	97	-1.3	73	75	-1.5	53	54	-1.1	37	37	-0.7	24	24	0.4
H28K175	132	127	3.6	120	121	-0.8	114	116	-1.3	104	105	-1.4	93	94	-1.3	70	71	-1.5	51	51	-1.0	35	35	-0.6	22	22	0.5
H28K185	128	124	3.8	117	118	-0.8	111	112	-1.3	100	102	-1.4	90	91	-1.3	68	69	-1.5	48	49	-1.0	33	33	-0.5	21	21	0.7
H28K195	125	120	3.9	114	115	-0.8	108	109	-1.3	97	99	-1.4	87	88	-1.3	65	66	-1.5	46	47	-1.0	31	31	-0.5	19	19	0.9
H28K205	122	117	4.0	111	112	-0.8	105	106	-1.3	95	96	-1.4	84	85	-1.3	63	64	-1.5	44	45	-1.0	29	30	-0.4	18	18	1.0
H28K215	119	114	4.1	108	109	-0.8	102	103	-1.3	92	93	-1.4	81	83	-1.3	60	61	-1.5	42	43	-0.9	28	28	-0.3	17	17	1.2
H28K225	117	112	4.2	105	106	-0.8	99	101	-1.3	90	91	-1.4	79	80	-1.3	58	59	-1.5	41	41	-0.9	27	27	-0.3	16	16	1.4
H32K15	363	360	0.7	353	355	-0.4	346	349	-0.9	334	339	-1.2	322	326	-1.3	293	297	-1.3	263	266	-1.2	231	234	-1.3	201	204	-1.2
H32K25	282	278	1.2	273	274	-0.2	266	268	-0.8	255	258	-1.2	243	247	-1.3	217	220	-1.4	190	193	-1.3	163	165	-1.3	138	139	-1.2
H32K35	239	235	1.7	230	230	0.0	224	225	-0.7	213	216	-1.3	202	205	-1.4	178	180	-1.4	153	155	-1.3	128	130	-1.3	106	107	-1.1
H32K45	211	207	2.0	203	202	0.2	196	198	-0.7	186	188	-1.3	175	178	-1.4	152	154	-1.4	129	131	-1.2	106	108	-1.3	86	87	-1.1
H32K55	192	187	2.4	183	183	0.3	177	178	-0.6	167	169	-1.3	156	159	-1.4	134	136	-1.4	112	114	-1.2	91	92	-1.2	72	73	-1.0
H32K65	177	172	2.6	168	168	0.4	162	163	-0.6	152	154	-1.3	142	144	-1.5	121	0	-1.4	100	101	-1.2	80	81	-1.2	63	63	-0.9
H32K75	165	160	2.9	157	156	0.5	150	151	-0.5	141	143	-1.3	131	133	-1.5	110	112	-1.5	90	91	-1.2	71	72	-1.2	55	55	-0.9
H32K85	155	150	3.2	147	146	0.6	141	141	-0.5	131	133	-1.3	122	124	-1.5	102	103	-1.5	82	83	-1.2	64	65	-1.1	49	49	-0.8
H32K95	147	142	3.4	139	138	0.7	133	133	-0.5	123	125	-1.3	114	116	-1.5	95	96	-1.5	76	77	-1.2	59	59	-1.1	44	44	-0.7
H32K105	140	135	3.6	132	131	0.8	126	126	-0.4	117	118	-1.3	108	109	-1.5	89	90	-1.5	70	71	-1.2	54	55	-1.1	40	40	-0.6
H32K115	134	129	3.9	126	125	0.9	120	120	-0.4	111	112	-1.3	102	103	-1.5	83	85	-1.5	66	67	-1.2	50	50	-1.0	37	37	-0.5
H32K125	129	124	4.1	121	120	1.0	115	115	-0.4	106	107	-1.3	97	98	-1.5	79	80	-1.5	62	62	-1.1	46	47	-1.0	34	34	-0.5
H32K135	124	119	4.3	116	115	1.1	111	111	-0.3	101	103	-1.4	93	94	-1.5	75	76	-1.6	58	59	-1.1	43	44	-0.9	31	31	-0.4
H32K145	120	115	4.5	112	111	1.2	106	106	-0.3	97	99	-1.4	89	90	-1.6	72	72	-1.6	55	56	-1.1	41	41	-0.9	29	29	-0.3
H32K155	116	111	4.6	108	107	1.3	102	103	-0.3	94	95	-1.4	85	87	-1.6	68	69	-1.6	52	53	-1.1	38	39	-0.8	27	27	-0.2
H32K165	113	107	4.8	105	103	1.3	99	99	-0.2	90	92	-1.4	82	83	-1.6	65	66	-1.6	50	50	-1.1	36	36	-0.8	25	25	-0.1
H32K175	110	104	5.0	102	100	1.4	96	96	-0.2	87	89	-1.4	79	80	-1.6	63	64	-1.5	47	48	-1.0	34	35	-0.7	24	24	0.0
H32K185	107	101	5.2	99	97	1.5	93	93	-0.2	85	86	-1.4	77	78	-1.6	60	61	-1.5	45	46	-1.0	33	33	-0.6	22	22	0.1

Table 1: Continued.

Number	w0 (mm)			w20 (mm)			w30 (mm)			w45 (mm)			w60 (mm)			w90 (mm)			w120 (mm)			w150 (mm)			w180 (mm)		
	DFE	Dcal	D%	DFE	Dcal	D%	DFE	Dcal	D%	DFE	Dcal	D%	DFE	Dcal	D%	DFE	Dcal	D%	DFE	Dcal	D%	DFE	Dcal	D%	DFE	Dcal	D%
H32K195	104	99	5.3	96	95	1.6	91	91	−0.2	82	83	−1.4	74	75	−1.7	58	59	−1.5	43	44	−1.0	31	31	−0.6	21	21	0.2
H32K205	102	96	5.5	94	92	1.6	88	88	−0.1	80	81	−1.4	72	73	−1.7	56	57	−1.5	42	42	−1.0	30	30	−0.5	20	20	0.4
H32K215	99	94	5.6	92	90	1.7	86	86	−0.1	78	79	−1.4	70	71	−1.7	54	55	−1.5	40	41	−0.9	28	28	−0.5	19	19	0.5
H32K225	97	92	5.8	89	88	1.8	84	84	−0.1	76	77	−1.4	68	69	−1.7	52	53	−1.5	39	39	−0.9	27	27	−0.4	18	18	0.6
H36K15	305	302	1.1	296	298	−0.7	291	294	−0.9	283	286	−1.1	274	277	−1.2	252	256	−1.4	229	232	−1.3	205	208	−1.3	181	184	−1.3
H36K25	238	234	1.8	229	230	−0.6	224	226	−0.9	216	219	−1.2	208	210	−1.	188	191	−1.4	167	169	−1.3	146	148	−1.3	126	128	−1.3
H36K35	202	197	2.3	193	194	−0.6	188	190	−0.9	181	183	−1.2	173	175	−1.2	154	156	−1.4	135	137	−1.3	116	117	−1.3	98	99	−1.2
H36K45	179	174	2.8	170	170	−0.5	165	167	−0.8	158	160	−1.2	150	152	−1.2	133	135	−1.5	115	116	−1.3	97	98	−1.3	80	81	−1.2
H36K55	162	157	3.2	153	154	−0.4	149	150	−0.8	142	144	−1.2	134	136	−1.3	117	119	−1.5	100	102	−1.3	84	85	−1.2	68	69	−1.2
H36K65	150	144	3.5	141	141	−0.4	137	138	−0.8	130	131	−1.2	122	124	−1.3	106	0	−1.5	90	91	−1.3	74	75	−1.2	60	60	−1.1
H36K75	140	134	3.9	131	131	−0.3	127	128	−0.7	120	121	−1.2	113	114	−1.3	97	98	−1.5	81	82	−1.3	66	67	−1.2	53	53	−1.1
H36K85	131	126	4.2	123	123	−0.3	119	120	−0.7	112	113	−1.2	105	106	−1.3	90	91	−1.6	74	75	−1.3	60	61	−1.2	47	48	−1.0
H36K95	125	119	4.5	116	116	−0.2	112	113	−0.7	105	107	−1.2	98	100	−1.3	83	85	−1.6	69	70	−1.3	55	56	−1.1	43	43	−0.9
H36K105	119	113	4.8	110	110	−0.2	106	107	−0.7	100	101	−1.2	93	94	−1.3	78	80	−1.6	64	65	−1.3	51	51	−1.1	39	40	−0.9
H36K115	114	108	5.0	105	105	−0.1	101	102	−0.6	95	96	−1.2	88	89	−1.3	74	75	−1.6	60	61	−1.3	47	48	−1.1	36	36	−0.8
H36K125	109	104	5.3	101	101	−0.1	97	98	−0.6	91	92	−1.2	84	85	−1.3	70	71	−1.6	56	57	−1.3	44	45	−1.0	33	34	−0.7
H36K135	105	100	5.5	97	97	0.0	93	94	−0.6	87	88	−1.2	80	81	−1.3	66	68	−1.6	53	54	−1.3	41	42	−1.0	31	31	−0.7
H36K145	102	96	5.8	93	93	0.0	90	90	−0.6	84	85	−1.2	77	78	−1.3	63	64	−1.6	51	51	−1.3	39	39	−0.9	29	29	−0.6
H36K155	99	93	6.0	90	90	0.0	87	87	−0.6	80	81	−1.2	74	75	−1.3	61	62	−1.6	48	49	−1.2	37	37	−0.9	27	27	−0.6
H36K165	96	90	6.2	87	87	0.1	84	84	−0.6	78	79	−1.2	71	72	−1.3	58	59	−1.6	46	46	−1.2	35	35	−0.8	26	26	−0.4
H36K175	93	88	6.4	85	85	0.1	81	82	−0.5	75	76	−1.2	69	70	−1.3	56	57	−1.6	44	44	−1.2	33	33	−0.8	24	24	−0.3
H36K185	91	85	6.7	82	82	0.1	79	79	−0.5	73	74	−1.2	67	68	−1.3	54	55	−1.6	42	43	−1.2	32	32	−0.8	23	23	−0.2
H36K195	89	83	6.9	80	80	0.2	77	77	−0.5	71	72	−1.2	65	66	−1.3	52	53	−1.6	40	41	−1.2	30	30	−0.7	22	22	−0.1
H36K205	87	81	7.1	78	78	0.2	75	75	−0.5	69	70	−1.2	63	64	−1.4	50	51	−1.7	39	39	−1.2	29	29	−0.7	21	21	0.0
H36K215	85	79	7.3	76	76	0.2	73	73	−0.5	67	68	−1.2	61	62	−1.4	49	49	−1.7	37	38	−1.2	28	28	−0.6	20	20	0.1
H36K225	83	77	7.4	74	74	0.3	71	71	−0.5	65	66	−1.2	59	60	−1.4	47	48	−1.7	36	37	−1.2	27	27	−0.6	19	19	0.2
H40K15	262	258	1.7	254	255	−0.5	250	252	−0.8	243	246	−1.1	236	239	−1.2	220	223	−1.4	202	204	−1.3	183	185	−1.3	164	166	−1.4
H40K25	205	200	2.5	196	197	−0.3	193	194	−0.7	186	188	−1.1	180	182	−1.3	164	167	−1.5	148	150	−1.4	132	133	−1.3	115	117	−1.4
H40K35	174	169	3.2	166	166	−0.2	162	163	−0.6	156	158	−1.1	150	152	−1.3	135	137	−1.5	120	122	−1.4	105	106	−1.4	90	92	−1.4
H40K45	154	149	3.8	146	146	0.0	143	143	−0.5	137	138	−1.1	130	132	−1.3	117	118	−1.6	102	104	−1.4	88	90	−1.4	75	76	−1.4
H40K55	140	134	4.3	132	132	0.1	129	129	−0.4	123	124	−1.1	117	118	−1.3	103	105	−1.6	90	91	−1.5	77	78	−1.4	64	65	−1.4
H40K65	129	123	4.7	121	121	0.2	118	118	−0.4	112	113	−1.1	106	108	−1.3	94	0	−1.6	81	82	−1.5	68	69	−1.4	56	57	−1.3
H40K75	121	115	5.2	113	112	0.3	110	110	−0.3	104	105	−1.1	98	99	−1.4	86	87	−1.7	73	74	−1.5	61	62	−1.4	50	51	−1.3
H40K85	114	108	5.6	106	105	0.3	103	103	−0.3	97	98	−1.1	91	93	−1.4	79	81	−1.7	67	68	−1.5	56	57	−1.4	45	46	−1.3
H40K95	108	102	5.9	100	100	0.4	97	97	−0.2	91	92	−1.1	86	87	−1.4	74	75	−1.7	62	63	−1.5	51	52	−1.4	41	42	−1.2
H40K105	103	97	6.3	95	95	0.5	92	92	−0.2	87	88	−1.1	81	82	−1.4	70	71	−1.7	58	59	−1.5	47	48	−1.3	38	38	−1.2
H40K115	99	93	6.6	91	90	0.6	88	88	−0.2	82	83	−1.1	77	78	−1.4	66	67	−1.7	55	56	−1.6	44	45	−1.3	35	35	−1.2
H40K125	95	89	7.0	87	87	0.6	84	84	−0.1	79	80	−1.1	73	75	−1.4	62	63	−1.8	52	52	−1.6	41	42	−1.3	32	33	−1.1
H40K135	92	85	7.3	84	83	0.7	81	81	−0.1	76	76	−1.1	70	71	−1.4	59	60	−1.8	49	50	−1.6	39	40	−1.3	30	31	−1.1
H40K145	89	82	7.6	81	80	0.8	78	78	0.0	73	73	−1.1	67	68	−1.5	57	58	−1.8	46	47	−1.6	37	37	−1.3	28	29	−1.0
H40K155	86	80	7.9	78	77	0.8	75	75	0.0	70	71	−1.1	65	66	−1.5	54	55	−1.8	44	45	−1.6	35	35	−1.3	27	27	−1.0
H40K165	83	77	8.1	76	75	0.9	73	73	0.0	68	68	−1.1	63	63	−1.5	52	53	−1.8	42	43	−1.6	33	34	−1.2	25	25	−0.9

TABLE 1: Continued.

Number	w0 (mm)			w20 (mm)			w30 (mm)			w45 (mm)			w60 (mm)			w90 (mm)			w120 (mm)			w150 (mm)			w180 (mm)		
	DFE	Dcal	D%	DFE	Dcal	D%	DFE	Dcal	D%	DFE	Dcal	D%	DFE	Dcal	D%	DFE	Dcal	D%	DFE	Dcal	D%	DFE	Dcal	D%	DFE	Dcal	D%
H40K175	81	75	8.4	73	73	0.9	70	70	0.1	65	66	-1.1	60	61	-1.5	50	51	-1.8	40	41	-1.6	32	32	-1.2	24	24	-0.8
H40K185	79	73	8.7	71	71	1.0	68	68	0.1	63	64	-1.1	58	59	-1.5	48	49	-1.9	39	39	-1.6	30	30	-1.2	23	23	-0.8
H40K195	77	71	8.9	69	69	1.0	67	66	0.1	62	62	-1.1	57	58	-1.5	47	48	-1.9	37	38	-1.6	29	29	-1.2	22	22	-0.7
H40K205	76	69	9.2	68	67	1.1	65	65	0.1	60	61	-1.1	55	56	-1.5	45	46	-1.9	36	37	-1.6	28	28	-1.2	21	21	-0.7
H40K215	74	68	9.4	66	65	1.2	63	63	0.2	58	59	-1.1	54	54	-1.5	44	45	-1.9	35	35	-1.6	27	27	-1.1	20	20	-0.6
H40K225	72	66	9.7	65	64	1.2	62	62	0.2	57	58	-1.1	52	53	-1.5	42	43	-1.9	34	34	-1.6	26	26	-1.1	19	19	-0.5
H44K15	228	224	2.1	223	222	0.5	219	219	-0.3	212	215	-1.0	206	209	-1.2	194	196	-1.3	179	182	-1.3	164	166	-1.4	149	151	-1.3
H44K25	178	173	3.0	173	171	0.9	169	169	-0.1	163	164	-1.0	157	159	-1.3	145	147	-1.3	132	134	-1.3	119	121	-1.4	106	107	-1.3
H44K35	152	146	3.8	146	144	1.3	142	142	0.1	137	138	-0.9	131	133	-1.3	120	122	-1.4	108	109	-1.3	96	97	-1.4	84	85	-1.4
H44K45	135	129	4.4	129	127	1.6	125	125	0.3	120	121	-0.9	114	116	-1.4	104	105	-1.4	92	94	-1.3	81	82	-1.5	70	71	-1.4
H44K55	122	116	5.0	117	115	1.8	113	113	0.4	108	109	-0.9	103	104	-1.4	92	94	-1.4	81	82	-1.3	70	71	-1.5	60	61	-1.3
H44K65	113	107	5.5	107	105	2.1	104	103	0.5	98	99	-0.9	94	95	-1.4	84	0	-1.5	73	74	-1.4	63	64	-1.5	53	54	-1.3
H44K75	106	100	6.0	100	98	2.3	96	96	0.6	91	92	-0.9	86	88	-1.4	77	78	-1.5	67	68	-1.4	57	57	-1.5	47	48	-1.3
H44K85	100	94	6.4	94	92	2.5	90	90	0.8	85	86	-0.9	81	82	-1.5	71	72	-1.5	61	62	-1.4	52	52	-1.5	43	43	-1.3
H44K95	95	88	6.8	89	87	2.7	85	85	0.9	80	81	-0.9	76	77	-1.5	66	67	-1.5	57	58	-1.4	48	48	-1.5	39	40	-1.3
H44K105	90	84	7.2	85	82	2.9	81	80	1.0	76	77	-0.9	72	73	-1.5	63	63	-1.5	53	54	-1.4	44	45	-1.5	36	37	-1.2
H44K115	86	80	7.6	81	79	3.1	77	77	1.0.	73	73	-0.9	68	69	-1.5	59	60	-1.5	50	51	-1.4	41	42	-1.5	33	34	-1.2
H44K125	83	77	8.0	78	75	3.3	74	73	1.1	69	70	-0.9	65	66	-1.6	56	57	-1.6	47	48	-1.4	39	39	-1.5	31	32	-1.2
H44K135	80	74	8.3	75	72	3.5	71	71	1.2	66	67	-0.8	62	63	-1.6	54	54	-1.6	45	46	-1.4	37	37	-1.5	29	30	-1.2
H44K145	78	72	8.6	72	70	3.6	69	68	1.3	64	64	-0.8	60	61	-1.6	51	52	-1.6	43	43	-1.4	35	35	-1.5	28	28	-1.1
H44K155	75	69	9.0	70	67	3.8	66	66	1.4	62	62	-0.8	57	58	-1.6	49	50	-1.6	41	41	-1.4	33	33	-1.5	26	26	-1.1
H44K165	73	67	9.3	68	65	3.9	64	63	1.5	60	60	-0.8	55	56	-1.6	47	48	-1.6	39	40	-1.4	31	32	-1.5	25	25	-1.0
H44K175	71	65	9.6	66	63	4.1	62	62	1.5	58	58	-0.8	53	54	-1.7	45	46	-1.6	37	38	-1.4	30	30	-1.5	23	24	-1.0
H44K185	69	63	9.9	64	62	4.2	61	60	1.6	56	56	-0.8	52	53	-1.7	44	45	-1.6	36	36	-1.4	29	29	-1.5	22	22	-1.0
H44K195	68	62	10.1	62	60	4.4	59	58	1.7	54	55	-0.8	50	51	-1.7	42	43	-1.6	35	35	-1.4	27	28	-1.5	21	21	-0.9
H44K205	66	60	10.4	61	58	4.5	58	57	1.7	53	53	-0.8	49	50	-1.7	41	42	-1.6	33	34	-1.4	26	27	-1.5	20	20	-0.9
H44K215	65	59	10.7	60	57	4.6	56	55	1.8	52	52	-0.8	47	48	-1.7	40	40	-1.6	32	33	-1.4	25	26	-1.5	19	19	-0.8
H44K225	64	57	11.0	58	56	4.8	55	54	1.9	50	51	-0.8	46	47	-1.8	39	39	-1.7	31	32	-1.4	24	25	-1.4	19	19	-0.8

Note. (a) D^{FE} and D^{cal} stand for the deflection values obtained by the finite element method and the Winkler model, respectively (unit: mm); (b) $D^{\%}$ represents the relative deviation of the D^{FE} and D^{cal}.
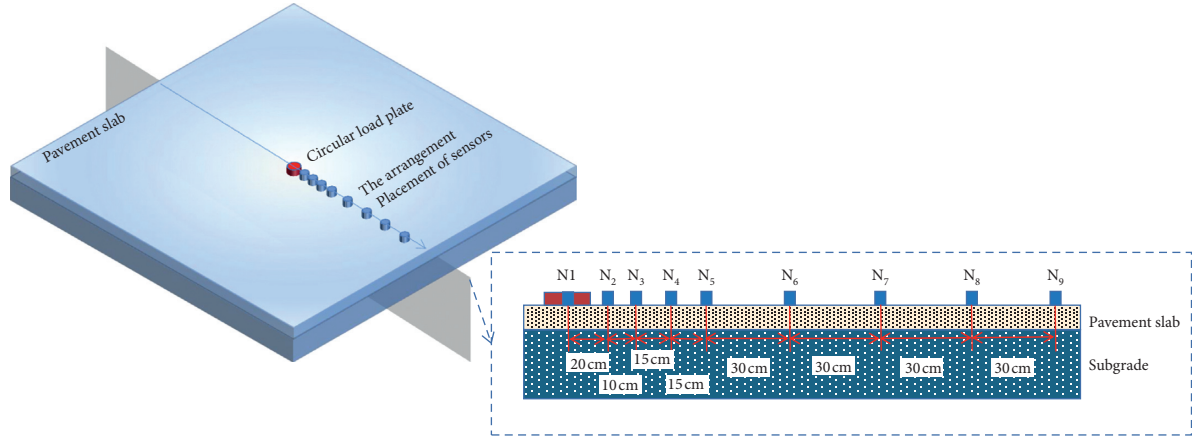
FIGURE 1: Layout of measuring points.

(a)

(b)
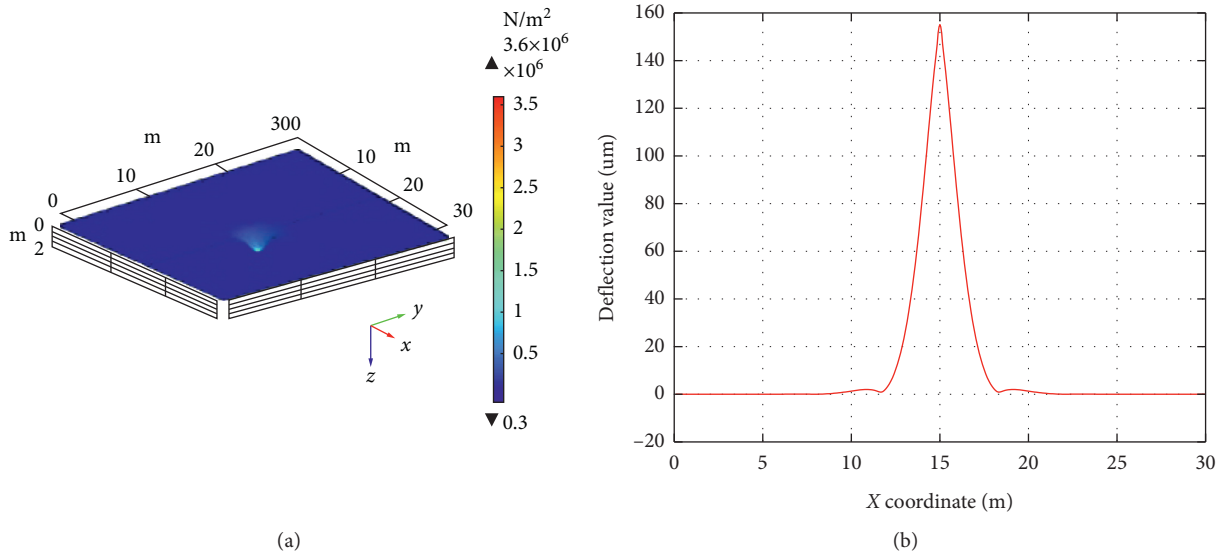
FIGURE 2: FE model of pavement thin slab. (a) Stress of concrete slab. (b) Displacement under H28K125 working condition.

TABLE 2: Parameters adopted in the parametric study.

Parameter	Value
Slab thickness h (mm)	20–44 at an interval of 4
Modulus of subgrade reaction k (MN/m^3)	15–225 at an interval of 10

$$w(r) = \frac{qR}{kl} \int_0^\infty \frac{J_0\left((r/l)t\right) J_1\left((R/l)t\right)}{1 + t^4} dt, \quad (1)$$

where $w(r)$ represents the deflection value at the distance of r away from the load center (m); q is the circular uniform load (Pa); R stands for the radius of load acting surface (m); l represents the radius of relative stiffness (m), which can be calculated by equation (2) according to Ioannides [12]; J_0 is the zero-order Bessel function; J_1 is the first-order Bessel function; r is the distance of a measurement point away from the load center (m); and t stands for the integral variable.

$$l = \left(\frac{Eh^3}{12\left(1 - \mu^2\right)k}\right)^{1/4}, \quad (2)$$

where E represents the elastic modulus of pavement slab (Pa) and μ represents Poisson's ratio.

2.4.2. Verification. To evaluate the accuracy of the FE model, the FE results were compared with the corresponding theoretical deflection values calculated with MATLAB under 154 working conditions according to the Winkler foundation model formula, as shown in Table 1. Only part of deflection data were selected to illustrate the difference of theoretical and simulated value of deflections, as depicted in Figure 3. The variables D^{FE} and D^{cal} represent the deflection values obtained by the numerical simulation and theoretical calculation, respectively.
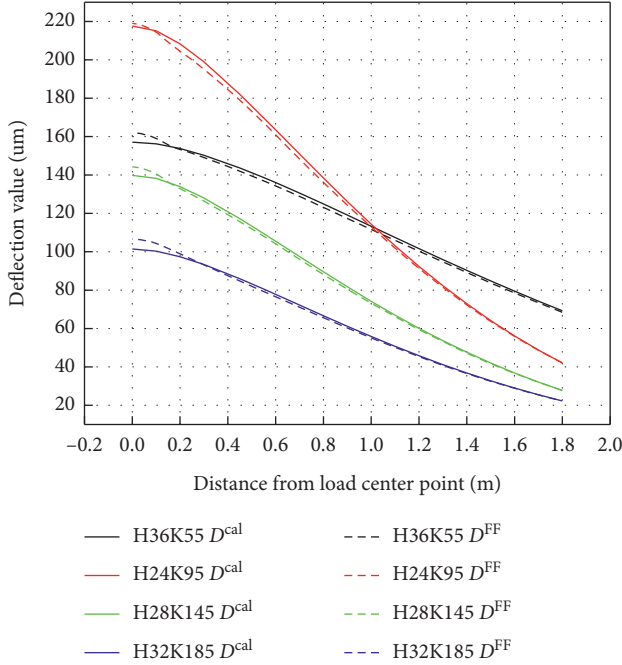
FIGURE 3: Comparisons of deflections between FE simulations and theoretical calculations.

It can be seen from Table 1 and Figure 3 that the difference between the simulated value and the theoretical value is rather small, and the deviations of the points within 20–150 cm away from the load center are even lower than 5%. Moreover, the deviation decreases first and then increases with the increment of slab thickness, and it increases with the modulus of subgrade reaction. For the slab with a thickness of 0.24–0.40 m, the deviations are all lower than 10%. However, when the slab thickness exceeds or is lower than a specific value and with the increment of the modulus of subgrade reaction, the deviation between the two methods gradually increases. For example, when the thickness of the slab is 0.44 m, the maximum deviation of the measurement point in the load center is 10.96%, and the deviation of the measuring point at the location of 180 cm away from the load center is 11.82% on the slab with the thickness of 0.2 m. The reason is probably that the Winkler foundation model was initially developed based on the thin slab theory, and the thick slab may be squeezed vertically at the loading point, resulting in the measurement deviation. The accuracy of the predicted solution may be extensively degraded for the slab with a relatively high modulus of subgrade reaction. Furthermore, there was no interaction between different points, as assumed in the Winkler foundation model. However, weak interactions can be detected in the FE model. When the thickness of the slab was relatively thin, the cumulative deviation may bring a significant error for the farthest point away from the loading point with the increase of the modulus of subgrade reaction due to the weak interaction. Therefore, to ensure the accuracy of verification and the rationality of the model parameters being relative to the engineering application, it is suggested that the optimal range of the slab thickness is 0.24–0.40 m.

3. Refined Deflection Basin Area Index Method

3.1. General Description. Ioannides [12] has illustrated that the deflection basin area index A_w (see equation (3)) was a geometric property of the deflection basin, which can be calculated based on the by dividing the basin into several fine trapezoids as shown in Figure 4. Then, A_w is normalized by the deflection value w of the designated measuring point, which can be applied to describe the geometric information of the deflection basin:

$$A_w = \frac{s}{2w} \left[w_0 + 2 \left(w_1 + w_2 + \cdots w_{n-1} \right) + w_n \right], \qquad (3)$$

where s represents the distance between two adjacent measuring points (m); w is the deflection of the designated measuring point (m); and w_i is the deflection of measuring point i (m).

Based on the elastic foundation slab model theory, the deflection basin area index method is a back-calculation approach that determines the pavement structural parameters as per the deflection value. The back-calculation process can be stated as follows. According to equations (1) and (2), the deflection value at a certain point is determined by the calculations of qR/k and $1/l \int_0^\infty (J_0 ((r/l)t)J_1 ((R/l)t)/1 + t^4) dt$. However, it is difficult to calculate the modulus of subgrade reaction k and the radius of relative stiffness l in practical engineering simultaneously. To separate these two variables, the deflection basin area index A_w becomes a necessity, and the relationship between A_w and l can be established. Then, according to the expression of the deflection coefficient $w(l)$, the equations of the modulus of subgrade reaction k and the elastic modulus of pavement slab E are also available, which are induced by the following equations:

$$k = \frac{qR}{w(r_0)} w(l), \qquad (4)$$

where $w(r_0)$ is the deflection value at r_0 away from the load center (m) and $w(l)$ stands for deflection coefficient which is equal to $1/l \int_0^\infty (J_0 ((r/l)t)J_1 ((R/l)t)/(1 + t^4)) dt$.

$$E = \frac{12 \left(1 - \mu^2 \right) k l^4}{h^3}. \qquad (5)$$

3.2. Existing Deflection Basin Area Index Methods

3.2.1. Method Introduction. So far, the conventional deflection basin area index methods with satisfactory accuracy mainly include MH/T 5024-2009 [13], Strategic Highway Research Program (SHRP) 4-in, SHRP 5-outer, US Air Force (USAF) 6-outer, and SHRP 7-in method [24]. It should be noted that the number represents the number of measuring points, and the following label of "in" and "outer" means the near-side measuring points (measurement ranges within the load center) and far-side measuring points (measurement ranges beyond the load center), respectively. Figure 5 shows the layout schemes of measuring points of several theories mentioned above.
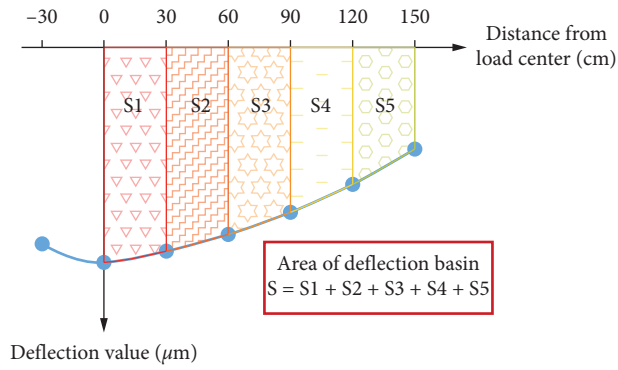
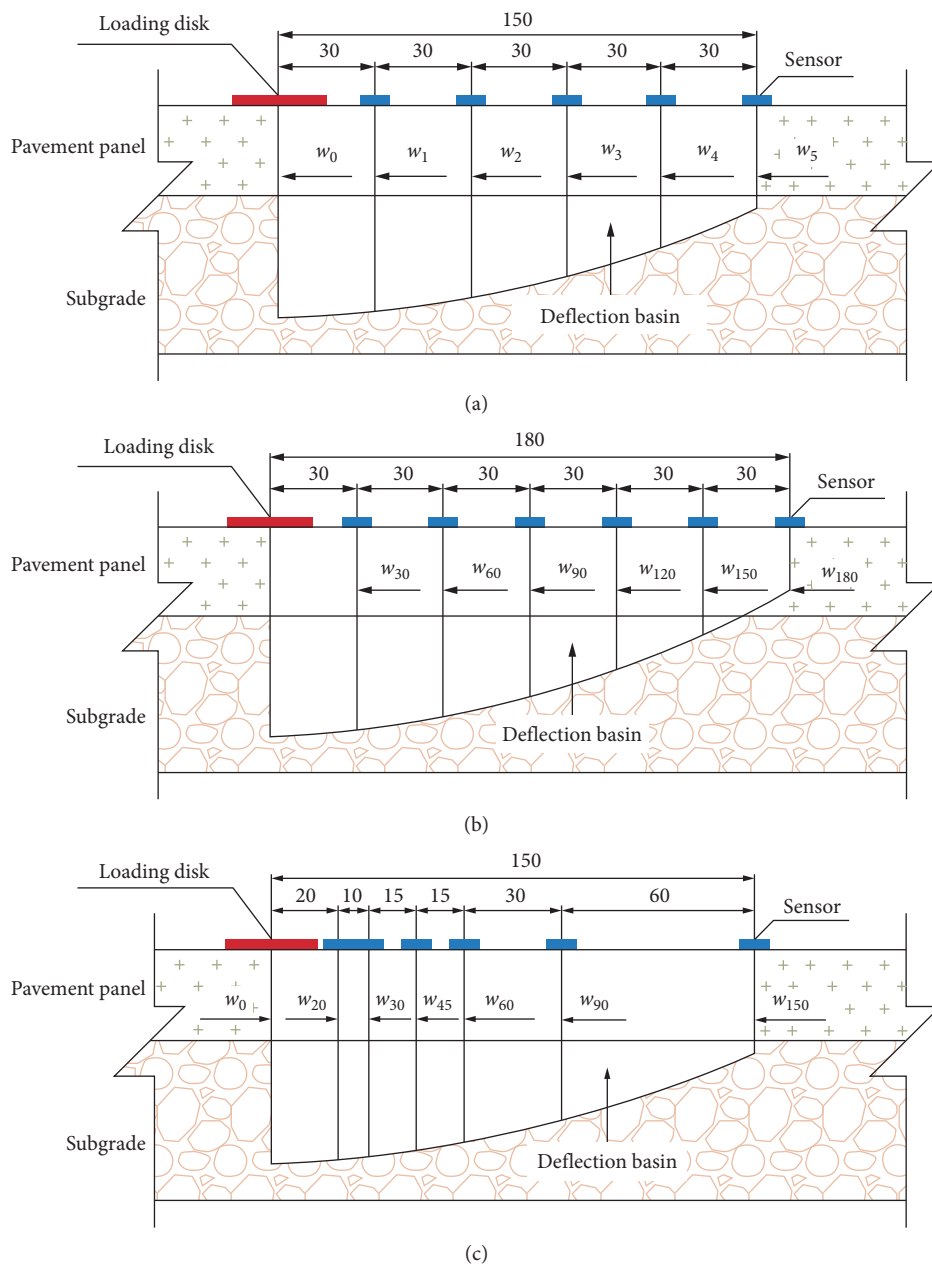Figure 4: Calculation diagram of the deflection basin area.

(a)

(b)

(c)

Figure 5: Layout schemes of measuring points. Layout scheme of (a) MH/T 5024-2009 [13], (b) Cheng et al. [19], and (c) SHRP 7-in [24].

Cheng et al. [19] have analyzed the accuracy of back-calculation of the five deflection basin area index methods mentioned above for pavement structural parameters and reported that the results of the far-end measuring points were more accurate. Furthermore, it has also been observed that sufficient measuring points and a reasonable form of best-fitting formula can significantly improve the accuracy of prediction. In addition, for the reason that most of the existing methods cannot incorporate the deflection information of each measurement point, Lin et al. [15] developed a revised deflection basin area index method to overcome this deficiency using the point-by-point fitting method [9] based on the traditional deflection basin area index method. The results revealed that the new method can provide more reasonable back-calculation results. However, this method requires multiple iterations of the distribution, which makes the calculation process quite complicated.

3.2.2. Method Evaluation. Based on the database mentioned above, the accuracy of the methods of MH/T 5024-2009 [13], SHRP 7-in [24], Cheng et al. [19], and Lin et al. [15] is systematically evaluated in this section. Nine groups of representative working conditions are compared. The results are presented in Figure 6 and Table 3. It should be noted that the calculated value of the modulus of subgrade reaction k is adopted to assess the accuracy.

As illustrated in Figure 6, although the methods of SHRP 7-in [24] and MH/T 5024-2009 [13] adopted similar layout schemes on the near-end measuring points, smaller back-calculation deviations are detected for the former method. This is because that the measuring points in SHRP 7-in [24] method are arranged intensively near the loading point, where the slope of deflection basin curve is significantly changed to fully capture the shape of deflection basin, resulting in a higher accuracy compared with MH/T 5024-2009 [13]. Since the far-end measuring points were used in Cheng et al. [19] method to conduct the back-calculation process, the predicted errors decrease obviously due to the reason stated before. For these methods except for Lin et al. [15], the deflection value of a specific measuring point was applied to standardize the deflection basin area index A_w. Thus, when the information of the specific measuring point is inaccurate, considerable errors of the predicted results may emerge, and the back-calculation process may become unstable as well. Moreover, if the deflection value normalizes the deflection basin area index at different measuring points, multiple-solution problems need to be considered as well. To avoid these potential problems, Lin et al. [15] have calculated the back-calculation results by minimizing the deviations as the objective function, which exhibits the best performance among all selected methods, as represented in Figure 6. However, low efficiency and complex calculations faced by this method means that it cannot be applied directly in practical engineering.

3.3. Proposed Method. To balance the accuracy of prediction and calculation complexity, seven locally intensive far-end measuring points were adopted with the positions of 30 cm,

45 cm, 60 cm, 90 cm, 120 cm, 150 cm, and 180 cm away from the load center, as shown in Figure 7. Besides, the average $\overline{w}$ of all the above points was applied directly to determine the deflection basin area index A_w and the resulting modulus of subgrade reaction k was recalculated as well (equations (6)–(8)). The most evident advantage of this method was that the information of deflection of all measuring points can be considered to make the predicted results more accurate and stable and to avoid the multiple-solution problem effectively.

$$A_w = \frac{0.15}{2\overline{w}} \left[w_{30} + 2w_{45} + 3w_{60} + 4\left(w_{90} + w_{120} + w_{150}\right) + 2w_{180}\right],$$
(6)

where w_j is the deflection of measuring point j (m) and j represents the distance from the load center (m).

$$\overline{w} = \frac{1}{7}\left(w_{30} + w_{45} + w_{60} + w_{90} + w_{120} + w_{150} + w_{180}\right), \quad (7)$$

$$k = \frac{qR}{\overline{w}} w(l). \tag{8}$$

Based on the deflection results from FE simulations under different working conditions (including different modulus of subgrade reaction k and different thickness of pavement slab h), the expression on the radius of relative stiffness l was obtained by regression analyses [25] with equations (2) and (6), as presented in equation (9); next, the deflection coefficient $w(l)$ was regressed through equations (8)–(9), as presented in equation (10). Figures 8 and 9 show that the trend almost coincides with the simulation results with R^2 being equal to 0.9927 and 0.9995, respectively. It should be noted that, under all working conditions, the deflection results of the slab with a certain thickness are represented by the same label, and the number following the letter "H" refers to the thickness of the slab. X represents all working conditions under this plate thickness.

$$l = 0.0036e^{\left(A_w^{4.60338}\right)} + 0.52495, \tag{9}$$

$$w(l) = 0.1945e^{(-1.90595l)} + 0.00908. \tag{10}$$

4. Comparison with Engineering Data

4.1. Data Source. An airport in northern China was selected to obtain practical deflection results. The runway is 2200 m in length and 45 m in width, including two vertical contact lanes and six parking aprons. The airport is located on the frozen soil area, and the soil layers are topsoil/miscellaneous fill, fine sand, silty clay, and bedrock (moderately and strongly weathered granite) [26], respectively. The runway of the airport has a severe frost boiling problem due to the freeze-thaw effect and constant impact loads. Thus, the HWD deflection test has been carried out on the existing pavement to assess the safety grade of the airport, as shown in Figure 10, which covered all functional regions, as listed in Table 4.
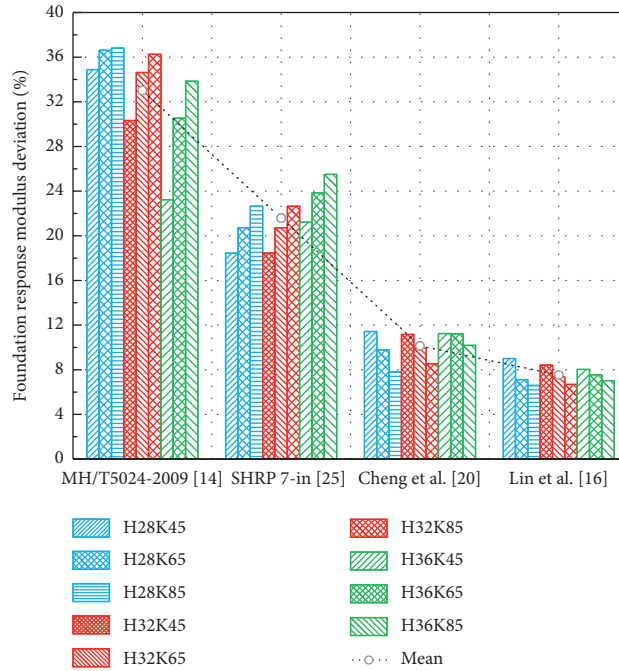
FIGURE 6: Deviation comparison of existing deflection basin area index methods.

TABLE 3: Comparison of existing deflection basin area index methods.

Number	MH/T 5024-2009 [13] (%)	SHRP 7-in [24] (%)	Cheng et al. [19] (%)	Lin et al. [15] (%)
H28K45	34.89	18.45	11.43	9.01
H28K65	36.62	20.72	9.77	7.12
H28K85	36.81	22.65	7.8	6.59
H32K45	30.33	18.46	11.16	8.42
H32K65	34.63	20.72	9.92	7.34
H32K85	36.26	22.65	8.54	6.69
H36K45	23.22	21.22	11.25	8.03
H36K65	30.53	23.83	11.21	7.55
H36K85	33.85	25.50	10.18	7.02
Average	33.02	22.06	10.38	7.51
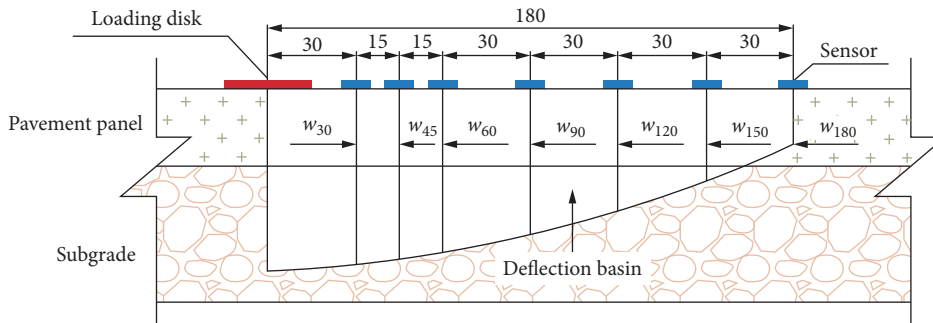
FIGURE 7: Layout scheme of measuring points in the proposed method.

4.2. Verification Results. To verify the rationality of the proposed method, the actual deflection data of each functional area of the airport were randomly selected to examine the back-calculation accuracy of the new proposed approach and three other methods developed by MH/T 5024-2009 [13], Cheng et al. [19], and Lin et al. [15]. Based on the measuring data of deflections, the deflection basin area index A_w can be determined by equation (6). Then, the radius of relative stiffness l and the deflection coefficient $w(l)$ were obtained by the proposed equations as well, and the modulus of subgrade reaction k and elastic modulus of pavement slab E can also be derived by equations (8) and (5), respectively.

$$l = 0.0036 \times e^{A_w^{4.60338}} + 0.52495$$
$$R^2 = 0.99272$$

□ H20-X   ◇ H36-X
○ H24-X   ◁ H40-X
△ H28-X   ▷ H44-X
▽ H32-X

FIGURE 8: Relationship between A_w and l.

$$\omega(l) = 0.1945 \times e^{-1.90595l} + 0.00908$$
$$R^2 = 0.99947$$

□ H20-X   ◇ H36-X
○ H24-X   ◁ H40-X
△ H28-X   ▷ H44-X
▽ H32-X
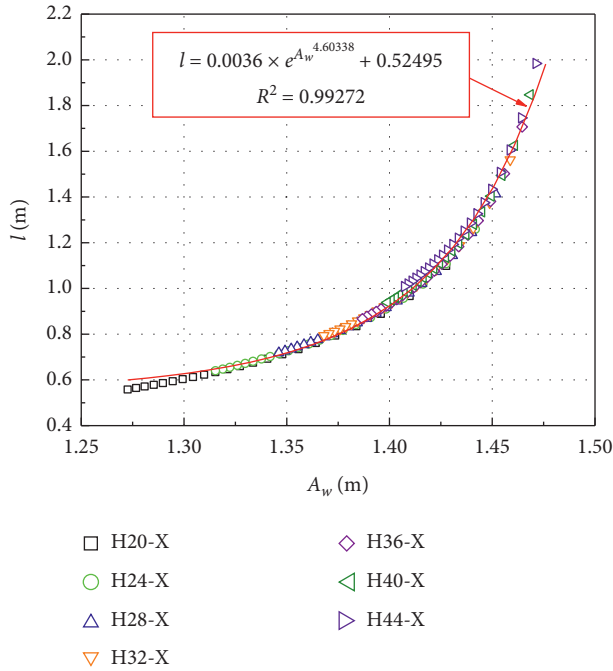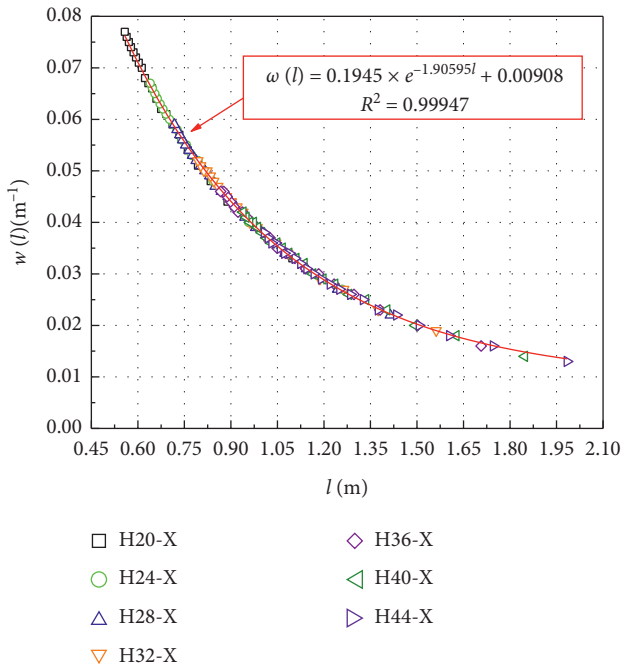
FIGURE 9: Relationship between l and $\omega(l)$.

FIGURE 10: Schematic diagram of HWD deflection measurement.

TABLE 4: Information of pavement structure for the airport.

Region	Functional area	Pavement type	Load (kN)
Runway	1800 m from east to west 400 m from west to east	Cement concrete	70
Contact lane	A contact lane B contact lane	Cement concrete	70
Parking apron	A parking apron B parking apron	Cement concrete	70

■ Proposed   ▼ Lin et al. [16]
● Cheng et al. [20]   ▲ MH/T 5024-2009 [14]
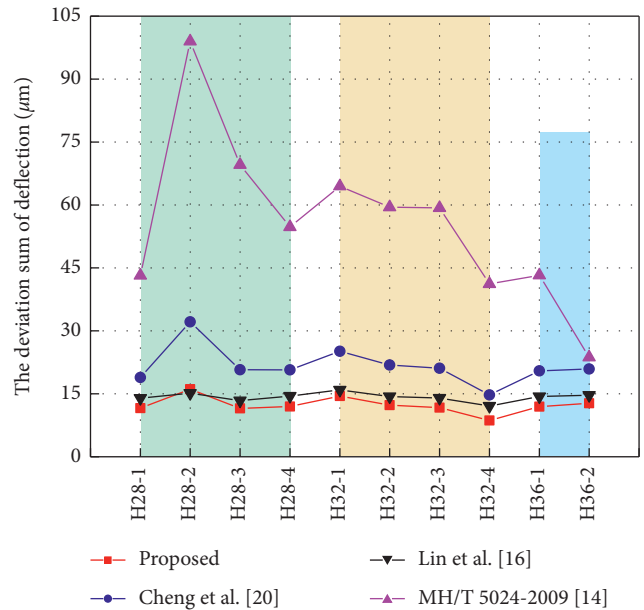
FIGURE 11: The deviation sum of deflection.

Therefore, the theoretical value of deflection calculated by equation (1) as per the above structural parameters was adopted to compare it with the actual measurement value, and the difference between the two values is shown in Figure 11 and Table 5.

As shown in Figure 11, the methods developed by Cheng et al. [19] and MH/T 5024-2009 [13] possess a lower accuracy and unstable predictions, which indicates that the information of the specific measuring point adopted to standardize A_w may have a great impact on the back-calculation results in the conventional deflection basin area index methods. For the proposed method and method developed by Lin et al. [15], more stable results can be obtained because all measuring points are considered. Moreover, the new method proposed in this study exhibits the better performance with the lower predicted errors and

TABLE 5: Verification of four methods.

Measuring point	w_0 (mm)	w_{20} (mm)	w_{30} (mm)	w_{45} (mm)	w_{60} (mm)	w_{90} (mm)	w_{120} (mm)	w_{150} (mm)	w_{180} (mm)	Elastic modulus E (GPa)				Modulus of subgrade reaction k (MN/m^3)				Sum of errors (um)			
										Proposed	MH/T5024-2009 [13]	Cheng et al. [19]	Lin et al. [15]	Proposed	MH/T5024-2009 [13]	Cheng et al. [19]	Lin et al. [15]	Proposed	MH/T5024-2009 [13]	Cheng et al. [19]	Lin et al. [15]
H28-1	125	118	115	107	100	84	69	56	42	43.67	40.50	45.28	39.46	63.42	61.71	60.83	67.43	11.58	43.21	18.88	13.96
H28-2	185	178	174	164	155	133	111	90	74	33.61	33.49	35.97	32.57	35.86	32.28	33.49	38.18	16.10	99.01	32.14	15.14
H28-3	133	128	125	118	110	94	78	63	48	45.00	43.96	45.95	42.23	52.63	47.86	50.77	54.44	11.53	69.58	20.73	13.38
H28-4	125	118	116	108	101	86	72	57	45	45.73	43.16	47.55	44.52	59.66	56.49	56.96	63.44	11.98	54.76	20.71	14.48
H32-1	135	127	125	117	110	94	79	64	51	30.58	27.73	31.84	29.94	51.65	49.91	49.10	54.81	14.46	64.47	25.14	15.92
H32-2	116	110	108	102	96	82	68	58	45	37.33	33.97	38.83	33.28	56.78	54.49	53.95	64.47	12.29	59.48	21.87	14.36
H32-3	128	122	119	112	105	89	74	61	48	30.97	29.33	32.90	31.04	55.68	52.44	52.43	58.04	11.72	59.31	21.10	14.00
H32-4	109	104	101	95	88	74	61	49	37	33.07	32.08	34.81	30.44	72.12	67.81	68.72	75.13	8.66	41.18	14.72	12.09
H36-1	107	103	100	96	90	78	69	58	48	34.50	31.14	36.32	32.89	50.47	50.33	47.58	54.93	11.93	43.25	20.48	14.34
H36-2	113	109	106	102	97	84	73	63	53	33.69	32.45	36.63	35.57	45.65	45.67	42.23	43.81	12.73	23.72	20.91	14.69

higher computed efficiency compared with the method developed by Lin et al. [15], which is more convenient for the practical engineering application.

5. Conclusions

FE modeling was adopted to simulate the pavement structure in this study, and the study on parameter was also carried out to develop a new deflection basin area index. The main conclusions that can be drawn as follows:

(1) By comparing the deflection values gained from FE simulation with the theoretical values calculated by the Winkler foundation response model, increasing deviations are observed with the increment of the modulus of the subgrade reaction when the pavement slab is either too thick or thin. Thus, considering the accuracy of the FE method and the actual demands of practical engineering, the suitable range of slab thickness for pavement structural parameters in the back-calculation process is suggested to be 0.24–0.4 m.

(2) Based on the established database, the back-calculation results of several existing deflection basin area index methods reveal that the increase of local measuring points under the same layout scheme can improve the accuracy of back-calculation results. Moreover, using the average deflection of all measuring points instead of a specified point during the normalized procedure, the back-calculation will become more stable, and the multiple-solution problem can also be alleviated.

(3) According to the deflection database obtained by FE simulation under different working conditions, a refined deflection basin area index method is proposed. The actual measuring data from an airport in northern China is applied to verify the rationality of the new method. Comparisons between the test results and theoretical predictions illustrate that the new method possesses a higher accuracy and efficiency, which may provide valuable guidance for the practical engineering application.

Data Availability

The data used in this paper are all from the finite element simulation and engineering measurement mentioned in the study.

Conflicts of Interest

The authors declare that there are no conflicts of interest regarding the publication of this study.

Acknowledgments

References

[1] C. Guo and F. Wang, "Case study on quick treatment of voids under airport pavement by polymer grouting," *Journal of Materials in Civil Engineering*, vol. 32, no. 7, Article ID 05020006, 2020.

[2] K. Gopalakrishnan and M. R. Thompson, "Pavement moduli variation under heavy aircraft trafficking," *Proceedings of the Institution of Civil Engineers—Transport*, vol. 159, no. 3, pp. 117–125, 2006.

[3] J. Roussel, C. Sauzéat, H. D. Benedetto, and M. Broutin, "Numerical simulation of falling/heavy weight deflectometer test considering linear viscoelastic behaviour in bituminous layers and inertia effects," *Road Materials and Pavement Design*, vol. 20, pp. 1–15, 2019.

[4] M. Broutin and A. Sadoun, "Advanced modelling for rigid pavement assessment using HWD," *Transportation Research Procedia*, vol. 14, pp. 3572–3581, 2016.

[5] S. R. Amin and L. E. Amador-Jiménez, "Backpropagation neural network to estimate pavement performance: dealing with measurement errors," *Road Materials and Pavement Design*, vol. 18, no. 5, pp. 1218–1238, 2017.

[6] T. F. Fwa, C. Y. Tan, and W. T. Chan, "Backcalculation analysis of pavement-layer moduli using genetic algorithms," *Transportation Research Record: Journal of the Transportation Research Board*, vol. 1570, no. 1, pp. 134–142, 1997.

[7] K. Loganathan, M. M. Isied, A. M. Coca, M. I. Souliman, S. Romanoschi, and S. Dessouky, "Development of comprehensive deflection parameters to evaluate the structural capacity of flexible pavements at the network level," *International Journal of Pavement Research and Technology*, vol. 12, no. 4, pp. 347–355, 2019.

[8] E. Camacho-Garita, R. Puello-Bolaño, P. Laurent-Matamoros, J. P. Aguiar-Moya, and L. Loria-Salazar, "Structural analysis for APT sections based on deflection parameters," *Transportation Research Record: Journal of the Transportation Research Board*, vol. 2673, no. 3, pp. 313–322, 2019.

[9] M. I. Darter, K. T. Hall, and C. M. Kuo, *Support under portland Cement concrete Pavements*, Transportation Research Board, Washington, DC, USA, 1995.

[10] L. J. Sun, S. Hu, and X. N. Zhang, "Intertial point on deflection basin of concrete pavement and asphalt pavement," *Journal of Highway and Transportation Research and Development*, vol. 18, no. 3, pp. 1–5, 2001, in Chinese.

[11] J. Zhu and L. J. Sun, "Determination of optional back-calculation point for three layer structure modulus back-calculation of asphalt pavement," *Journal of Tongji University*, vol. 45, no. 2, pp. 203–208, 2017, in Chinese.

[12] A. M. Ioannides, "Dimensional analysis in NDT rigid pavement evaluation," *Journal of Transportation Engineering*, vol. 116, no. 1, pp. 23–36, 1989.

[13] CAAC (Civil Aviation Administration of China), *Technical Specifications of Aerodrome Pavement Evaluation and Management MH/T 5024-2009*, China Civil Aviation Publishing House, Beijing, China, 2009, in Chinese.

[14] AASHTO (American Association of State Highway Transportation Officials), *AASHTO Guide for Design of Pavement Structures*, AASHTO, Washington, DC, USA, 1993.

[15] X. P. Lin, J. Yuan, J. M. Ling, and Z.-M. Tan, "Improved deflection basin area parameters back calculation method for rigid pavement," *China Journal of Highway and Transport*, vol. 22, no. 3, pp. 14–19, 2009, in Chinese.

[16] J. M. Ling, S. F. Liu, and J. Yuan, "Improved AREA back-calculation method for rigid pavement and its regression

model," *Journal of Tongji University*, vol. 46, no. 12, pp. 1683–1689, 2018, in Chinese.

[17] L. K. Ma, M. Li, J. S. Pang, and C. Huang, "Evaluation of transverse cracks for semi-rigid asphalt pavements using deflection basin parameters," *Transportation Research Record: Journal of the Transportation Research Board*, vol. 2673, no. 2, pp. 358–367, 2018.

[18] J. Xu, Z. Shen, S. Yang, X. Xie, and Z. Yang, "Finite element simulation of prevention thermal cracking in mass concrete," *International Journal of Computing Science and Mathematics*, vol. 10, no. 4, pp. 327–339, 2019.

[19] G. Y. Cheng, X. J. Wang, and M. Y. Liao, "Improvement of deflection basin area index method based on solid element," *Journal of Highway and Transportation Research and Development*, vol. 36, no. 4, pp. 15–20, 2019, in Chinese.

[20] R. S. Chen, B. M. Tang, and J. K. Qin, "Comparison of two foundation models under the rigid pavement slab," *China Journal of Highway and Transport*, vol. 3, no. 2, pp. 1–10, 1990, in Chinese.

[21] J. Yuan, *Research on Parameters Back Calculation Method for Airport Rigid Pavements*, Tongji University, Shanghai, China, 2008, in Chinese.

[22] MOHURD (Ministry of Housing and Urban-Rural Development of the People's Republic of China), *Code for Geotechnical Investigations of Urban Rail Transit GB 50307-2012*, China Planning Press, Beijing, China, 2012, in Chinese.

[23] R. R. Costigan and M. R. Thompson, "Response and performance of alternate launch and recovery surf aces that contain layers of stabilized material," *Transportation Research Record*, vol. 1986, pp. 57–71, 1986.

[24] US FAA (Federal Aviation Administration), *Use of Nondestructive Testing in the Evaluation of Airport Pavements AC 150/5370-11B*, US Department of Transportation, Washington, DC, USA, 2011.

[25] C. Zhu, M. He, M. Karakus, X. Zhang, and Z. Guo, "The collision experiment between rolling stones of different shapes and protective cushion in open-pit mines," *Journal of Mountain Science*, vol. 18, no. 5, pp. 1391–1403, 2021.

[26] Q. Yin, J. Y. Wu, C. Zhu, M. C. He, Q. X. Meng, and H. W. Jing, "Shear mechanical responses of sandstone exposed to high temperature under constant normal stiffness boundary conditions," *Geomechanics and Geophysics for Geo-Energy and Geo-Resources*, vol. 7, no. 2, 2021.

Research Article

Model of Seismic Wave Field Excited by Horizontally Distributed Charge

Xu Qian (ID) and Wang Zhong-Qi

State Key Laboratory of Explosion Science and Technology, Beijing Institute of Technology, 100081 Beijing, China

Correspondence should be addressed to Xu Qian; chinaxuqian@126.com

The amplitude-frequency characteristics of seismic wave field excited by an explosive source can directly affect the accuracy of seismic prospecting. To reveal the laws by which the horizontally distributed charge excites the amplitude-frequency characteristics, a method to calculate seismic wave field excited by horizontally distributed charge was studied in this paper. By taking the spherical cavity source model as the basis, the superposition method was applied to obtain the approach of calculating seismic wave field excited by horizontally distributed charge. Compared with numerical simulation, the error of this method was controlled under 7%. As a matter of fact, the distributive charge can effectively reduce the impact on ground vibration and increase the downward seismic wave energy. The charges that are horizontally distributed with 1 m interval can enhance the seismic wave resolution excited by explosive source. The research shows that the established theoretical model can correctly describe the amplitude-frequency characteristics of the seismic wave field excited by horizontally distributed charges.

1. Introduction

Explosive is the main seismic source that excites the seismic waves artificially in oil and gas prospecting. Gas with high temperature and high pressure would be produced at the moment of explosion and act directly on the geomaterial, resulting in severe damage and forming the blasting cavity in the areas adjacent to the explosive area. With the development of blast wave, the overpressure value drops rapidly till below the failure strength of geomaterial, forming seismic wave in geomaterial [1–6]. Among the above, the explosive source properties can affect the size and acting time of gas detonation pressure; and, as a matter of fact, different types of explosives can form different blasting cavities. In addition, the shape of the charge can also affect the geometrical shape of the blasting cavity. Since the properties of the detonation cavity determine the characteristics of the seismic waves, it can be deemed that the explosive source has significant impacts on the characteristics of seismic waves.

To study the process in which the explosive source forms seismic waves, Jeffreys was the first to establish a cavity vibration model in one-dimensional space, answering questions about full space cavity under spherical pulse [7]. Sharpe studies the wavelets generated by explosion in a closed spherical space, through which he obtained the analytical solution of the pressure elastic wave on the wall of blasting cavity [8]. Targeting at the point-source explosion theoretical model, Blake obtained the analytical solution of elastic waves of non-Poisson body based on Sharpe's study results [9]. Xiao, based on the spreading characteristics of spherical waves in isotropic medium, obtained the amplitude and waveform of spherical waves produced by explosive source [10, 11]. Ding and Zhen studied blasting vibration by equivalent load model and found that the theoretical results are in line with the actual situation [12]; Lin and Bai obtained the pressure solution in the blasting cavity according to the explosion process of explosives in rock and soil [13]. The spherical cavity source models can establish the relationship between the explosion pressure and elastic cavity radius with the seismic wave field. Since these methods simplify the process of explosive source exciting the seismic waves, they cannot build up the direct relationship between the explosive source characteristics and the amplitude-frequency characteristics of seismic wave field. Targeting at this problem,

Yu et al. developed a cavity source model and established the theoretical model for the process in which explosive source excites seismic wave field [14]. This method describes how the explosive source forms the seismic waves, sets up the relationship between initial parameters of explosive source and seismic wave field, and is able to describe the full-field seismic wave characteristics of spherical charge.

Although the seismic source model of spherical cavity can describe the formation and changes of the seismic wave field excited by explosive blasting, multiple sections of cylindrical charges would be adopted as seismic sources. Since the characteristics of the seismic wave field generated by spherical charge and cylindrical charge are different, the traditional seismic source model of spherical cavity is not suitable for describing the seismic wave field produced by cylindrical charge. Heelan analyzed the seismic wavelet excited by finite-length cylindrical charge and obtained the far-field solution of the seismic wave excited by cylindrical charge [15]. As for this method, the detonation pressure at the time of explosive blasting was applied on the excitation medium along the length direction of the cylindrical charge. It directly solves the seismic wave field formed by infinite-length cylindrical charge but cannot describe the seismic wave field characteristics excited by finite-length cylindrical charge. Starfield and Pugliese deemed the cylindrical charge as superposition of multiple short cylindrical charges, thus to solve the blasting stress field at the end of the cylindrical charge when the explosion happens. The calculation results were basically in line with the experimental testing results [16]. Long et al. obtained the development process of the cavity machine formed by cylindrical charge by means of experiment and numerical simulation [17]. On the basis of Yu's results, Li et al. proposed the seismic wave field model of finite-length cylindrical charge by superposition of spherical charges [18, 19]. Hu et al., based on the theory of elastic wave propagation, obtained the relation between the seismic wave field of delayed source and the type of charge, quantity of charge, and interval of charge column by field experiment [20]. Huang et al. figured out the impacts of delayed time of cylindrical charge on seismic wave field from their experimental study conducted on cylindrical charge [21]. However, the above methods are usually used to study the seismic wave characteristics formed by distributive charges through experiments or numerical simulation methods and cannot clearly describe the theoretical relations between horizontally distributed charges and seismic wave field. In order to achieve refined prospecting and control seismic wave characteristics by adjusting the explosive source excitation plan, it is necessary to establish the model for horizontally distributed charges exciting seismic wave field.

In this paper, the whole process in which the explosive source excites the seismic waves was analyzed and the different stages of seismic wave field excited by explosive source were summarized firstly. Considering the spatial structure of the charge, a method for calculating the seismic wave field excited by the horizontally distributed charged was proposed. Meanwhile, on-site experiment was carried out to verify the applicability of this calculation model and further analyze the evolution process in which the horizontally distributed charges excite and form the seismic wave field.

2. Analysis on Process of Explosive Source Exciting Seismic Waves

The process of explosives from blasting to finally forming elastic waves in the distance is accompanied by a series of chemical and physical changes. The energy keeps attenuating during the transmission process due to various dissipation mechanisms, showing the evolution from the powerful blast waves to elastic waves finally. This process is composed of four stages: hydrodynamic stage, geomaterial crushing stage, dynamic expansion stage, and elastic wave propagation stage [22–24]. Meanwhile the medium would have irreversible deformation under the strong explosion effects during the attenuation process, so that the geomaterial near the explosive source shows certain fluid properties under the impacts of huge energy. At the moment of explosion, a wave front could be pushed out from inside the explosion cave, which is in a shape the same as the explosive. With the development of the blast wave, its peak stress attenuates rapidly during the outward propagation process until below the ultimate failure strength of the geomaterial. At this moment, the geomaterial turns from fluid stress state to the elastic-plastic stress state; and the attenuation of the stress wave continues until its peak value falls below a certain value, and the geomaterial transforms from the plastic state to the elastic state. In this case, the explosive source forms the explosion cavity area, plastic area, and an elastic area in sequence when it blasts in geomaterial along the energy transformation direction. However, due to the geometrical difference between the cylindrical charge and the horizontally distributed charge, the development processes of these areas vary to some certain extent: the nearby areas of the cylindrical charge are similar to the shape of the charge, but, with the increase of distance from explosive source, the seismic wave fields excited by cylindrical charge are similar to those excited by distributed charges; and the seismic wave field excited by distributed charge develops from ellipsoid to a spherical shape gradually till forming wave front similar to that of the cylindrical charge. For the comparison of area shapes, see Figure 1.

3. Model for Seismic Wave Field Excited by Spherical Explosive

The model of spherical cavity seismic source can be used to describe the relationship between the explosive source and the seismic wave field. In this model, large amounts of gases with high temperature and high pressure generated at the moment of blasting act directly on the geomaterials and form blasting cavity. Since the gas pressure inside the cavity is far greater than the geomaterial strength, the geomaterial near the explosives shows fluid property under huge pressure, so that the blasting cavity can be deemed as expanding in incompressible flow. With the propagation and
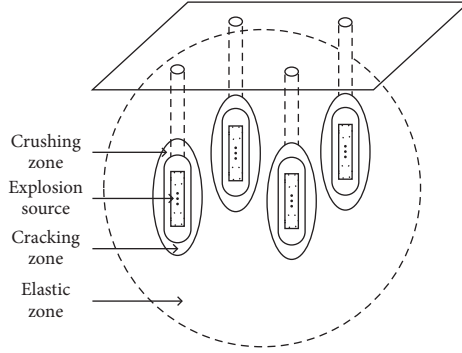
FIGURE 1: Explosive zoning of horizontally distributed charge in geomaterial.

attenuation of blast waves in medium, the blast waves keep attenuating till below the medium failure strength at place which is certain distance away from the explosive source. At this time, the excitation medium shows elastic properties. Yu supposed that the detonation process and blast cavity are formed instantaneously. Then, under the condition that the soil medium is incompressible and the property change is ignored, a quasi-static model for predicting the blast cavity of the spherical charge was established, through which the blast cavity radius and the plastic zone radius excited by the spherical charge in geomaterial can be obtained.

Radius of blast cavity is

$$b_* = a_0 \left(\frac{P_0}{-(c/\varphi) + (\sigma_* + (c/\varphi))L^{(4f/3(1+f))}} \right)^{(1/3\gamma)} \sqrt[3]{\frac{2\mu}{3\sigma_*}}, \tag{1}$$

where

$$L = \frac{\mu}{\sigma_* [1 + \ln(\sigma_*/\sigma_0)]}. \tag{2}$$

Radius of plastic zone is

$$b_0 = \left(\frac{\sigma_*}{\sigma_0} \right)^{(1/2)} b_*, \tag{3}$$

where a_0 is the spherical charge radius, P_0 is the initial blasting pressure of the explosive, γ is the explosive expansion index, φ is the cohesion of the soil medium, c is the internal friction angle of soil medium, σ_* is the compressive strength of the soil medium, σ_0 is the tensile strength of the soil medium, and μ is the lame coefficient (shearing modulus in elastic medium).

The linear radial strain and hoop strain are introduced according to the spherical symmetry and linear theory to simplify the motion equation as follows:

$$\frac{\partial^2 u}{\partial r^2} + \frac{2}{r} \frac{\partial u}{\partial r} - 2\frac{u}{r^2} = \frac{1}{c^2} \frac{\partial^2 u}{\partial t^2}. \tag{4}$$

The solution of this equation can describe the forced vibration of the particle under viscous damping, and its general form is

$$U(r,t) = e^{-(\eta^2 \tau / \rho_{soil} c b_*)} \left[\left(\frac{Pb_*^2 c}{\eta \kappa r^2} - \frac{\eta P b_*}{\kappa \rho_{soil} c r} \right) \sin \frac{\eta \kappa \tau}{\rho_{soil} c b_0} + \frac{Pb_*}{\rho_{soil} c r} \cos \frac{\eta \kappa \tau}{\rho_{soil} c b_0} \right], \tag{5}$$

where

$$\eta^2 = \frac{2(1 - 2\sigma)\rho_{soil} c^2 + 3(1 - \sigma)\gamma P}{2(1 - \sigma)},$$

$$\kappa^2 = \frac{2\rho_{soil} c^2 - 3(1 - \sigma)\gamma P}{2(1 - \sigma)}, \tag{6}$$

$$\tau = t - \frac{r - b_0}{c}.$$

The main frequency of vibration in the above equation can be expressed as

$$f_1 = \frac{\omega}{2\pi}$$

$$= \frac{\eta \kappa}{2\pi \rho_{soil} c b_0} \tag{7}$$

$$= \frac{\sqrt{(8\rho_{soil} c^2 - 9\gamma P)(4\rho_{soil} c^2 + 9\gamma P)}}{12\pi \rho_{soil} c b_0}.$$

Vibration amplitude can be expressed as

$$A_0 = e^{-(\eta^2 T / \rho_{soil} c b_0)} \frac{P}{\eta \kappa} \frac{b_0^2}{2\rho_{soil} c^2 r}. \tag{8}$$

4. Method to Calculate Seismic Wave Field Excited by Horizontally Distributed Charges

The horizontally distributed charge is composed of cylindrical charges with equal lengths arranged at equal intervals along the axial direction of the cylindrical charge. Supposing that each cylindrical charge is equivalent to the superposition of multiple spherical charges, the horizontally distributed charge can be regarded as a multilevel continuous spherical charges superimposed at intervals. Since different sections of cylindrical charges are of different spatial positions, different spherical equivalent charges have different positions relative to a certain point in the space, and vibration directions of designated positions excited by each charge are different, we need to decompose the vibration resulting by each spherical charge. Then, we should superimpose, respectively, at x-direction, y-direction, and z-direction to finally obtain the resultant velocity. However, each section of cylindrical charge shall satisfy the following conditions: (1) The total volume of the charge is equal to the total volume of all spherical charges. (2) The total length of the charge is equal to the sum of the diameters of all spherical charges. (3) The continuity of the detonation process and the equivalent spherical charge interval of all sections of cylindrical charges shall be zero.

As shown in Figure 2, the vibration velocity of the seismic wave excited by No. n spherical equivalent explosive in No. m section at point A in the space should be $U_{mn}(r,t)$, the velocity component in the x-direction should be $U_{mnx}(r,t)$, the velocity component in the y-direction should be $U_{mny}(r,t)$, and the velocity component in the z-direction should be $U_{mnz}(r,t)$; then

$$U_{mnx}(r,t) = U_{mn}(r,t)\frac{L_{mnx}}{r_{mn}},$$

$$U_{mny}(r,t) = U_{mn}(r,t)\frac{L_{mny}}{r_{mn}}, \quad (9)$$

$$U_{mnz}(r,t) = U_{mn}(r,t)\frac{L_{mnz}}{r_{mn}},$$

where L_{mnx}, L_{mny}, and L_{mnz} are the distances between No. n spherical equivalent charge in No. m section and point A in three directions; r_{mn} is the actual distance between No. n spherical equivalent charge in No. m section and point A in three directions.

Then the velocity components of vibration velocity of No. m section of cylindrical charge at point A in x-direction, y-direction, and z-direction, namely, $U_{mx}(r,t)$, $U_{my}(r,t)$, and $U_{mnz}(r,t)$, are, respectively,

$$U_{mx}(r,t) = U_{m1x}(r,t) + U_{m2x}(r,t) + \cdots + U_{mnx}(r,t),$$

$$U_{my}(r,t) = U_{m1y}(r,t) + U_{m2y}(r,t) + \cdots + U_{mny}(r,t),$$

$$U_{mz}(r,t) = U_{m1z}(r,t) + U_{m2z}(r,t) + \cdots + U_{mnz}(r,t).$$

$$(10)$$

Then the velocity components of vibration velocity of the whole horizontally distributed charge at point A in x-direction,
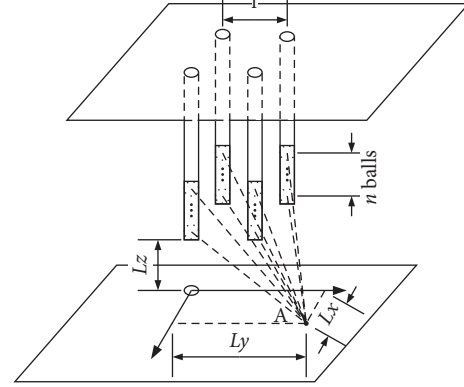
Figure 2: Horizontally distributed excitation scheme.

y-direction, and z-direction, namely, $U_x(r,t)$, $U_y(r,t)$, $U_z(r,t)$, are, respectively,

$$U_x(r,t) = U_{1x}(r,t) + U_{2x}(r,t) + \cdots + U_{mx}(r,t),$$

$$U_y(r,t) = U_{1y}(r,t) + U_{2y}(r,t) + \cdots + U_{my}(r,t), \quad (11)$$

$$U_z(r,t) = U_{1z}(r,t) + U_{2z}(r,t) + \cdots + U_{mz}(r,t).$$

Then the resultant velocity is

$$U(r,t) = \sqrt[3]{U_x(r,t)^3 + U_y(r,t)^3 + U_z(r,t)^3}. \quad (12)$$

The amplitude-frequency characteristics of the seismic waves excited by the horizontally distributed charge are closely related to the interval between all charges. Proper interval could produce greater energy. By overlapping the peak pressure of blast wave excited by the first section of cylindrical charge to the peak value of blast wave excited by the second section of cylindrical charge, we could obtain the best superposition effects.

5. Verification of the Model for Seismic Wave Field Excited by Horizontally Distributed Charges

Due to the special geometric structure of the horizontally distributed charges, the seismic waves that it excites in the soil vary in horizontal and vertical directions. In the area near the charge, stress wave front will spread outwards based on the basic shape of each section of the charge. With the geometric divergence and the propagation of seismic waves in the soil, seismic waves show different characteristics in the horizontal and vertical directions. In order to verify the effectiveness of the method for calculating the seismic wave field excited by the horizontally distributed charge, three different excitation schemes were applied in this study to make comparison on the theoretical calculation results and the numerical simulation results of the seismic wave field excited by the horizontally distributed charge in the axial and radial directions. For the detailed excitation parameters, please see Table 1.

The results calculated by the theoretical model are compared with the results obtained by the finite element

TABLE 1: Excitation scheme of axially distributed explosives.

SN	No. of cylindrical charges	Mass of each section of cylindrical charge (kg)	Interval between cylindrical charges (m)	Total charges (kg)	Delayed time (s)	Excitation direction
1	4	1	0.03	4	0	Top
2	4	1	1	4	0	Top
3	4	1	2	4	0	Top

software Autodyn, among which the soil medium parameters and TNT explosive characteristic parameters are shown in Tables 2 and 3.

The standard JWL equation for ideal detonation products was adopted as the TNT state equation:

$$P = C_1\left(1 - \frac{\omega}{r_1 v}\right)e^{-r_1 v} + C_2\left(1 - \frac{\omega}{r_2 v}\right)e^{-r_2 v} + \frac{\omega e}{v}, \quad (13)$$

where e is the detonation energy, and C_1, C_2, R_1, R_2, and ω are the parameters of state equation; please see Table 3.

Ideal elastic-plastic model was applied for soil medium. The state equation is

$$P = k\mu, \quad (14)$$

where $\mu = (\rho/\rho_0) - 1$ and k is the bulk modulus.

von Mises strength model was applied as the strength model of soil medium:

$$(\sigma_1 - \sigma_2)^2 + (\sigma_2 - \sigma_3)^2 + (\sigma_3 - \sigma_1)^2 = 2\sigma_s^2 = 6G^2, \quad (15)$$

where σ_s is yield strength, G is the shearing modulus, and the parameters shown in Table 2 were used for soil medium.

To analyze the functions of distributed seismic sources, three types of calculation models were established targeting at the centralized 4 kg charge, 4×1 kg charge (1 m × 1 m), and 4×1 kg charge (2 m × 2 m), respectively, for conducting comparative analysis on their theoretical calculation results and numerical simulation calculating results. Figure 3 shows three types of charges on a same plane. Figure 3(a) is the centralized charge, Figure 3(b) shows charges with 1 m interval, and Figure 3(c) shows charges with 2 m interval.

Figure 4 shows the changes of soil plastic deformation due to impact pressure in scheme I (centralized). Explosives explode in the soil and produce shock waves that travel outwards in a cylindrical shape. The plastic deformation area of the soil is also cylindrical. It appears as a ring on a horizontal section, the plastic deformation area increases gradually with time, and there is a volume upper limit.

Figure 5 shows the changes of soil plastic deformation due to impact pressure in scheme II (1 m × 1 m). Every explosive charge explodes in the soil and produces shock waves that travel outwards in a cylindrical shape. The plastic deformation area of the soil is also cylindrical, and it appears as a ring on a horizontal section. The plastic deformation area increases with time. When $t = 0.8$ ms, the plastic area around the adjacent gun holes is connected. When $t = 1.4$ ms, all the soils between the 4 holes are plastically deformed. When the shock wave passes completely, the soil is unloaded and its properties are restored to an elastic state, but the elastic state is different from the initial state.

Figure 6 shows the changes of soil plastic deformation due to impact pressure in scheme III (2 m × 2 m). Every explosive charge explodes in the soil and produces shock waves that travel outwards in a cylindrical shape. The plastic deformation area of the soil is also cylindrical, and it appears as a ring on a horizontal section. When $t = 0.8$ ms, the plastic deformation area increases with time. The plastic area reaches its maximum volume when $t = 1.2$ ms. When the shock wave passes completely, the soil is unloaded and its properties are restored to an elastic state, but the elastic state is different from the initial state.

The explosives in scheme I (Centralized) explode in the soil to produce the smallest area of plastic deformation. The plastic deformation areas of the explosives in schemes II (1 m × 1 m) and III (2 m × 2 m) are approximately equal at the initial moment ($t < 0.8$ ms) when they explode in the soil. However, due to the closer distance between the explosives in scheme II (1 m × 1 m), in the moment (8 ms < t < 14 ms), the area of soil deformation near the center part of the area is smaller, which causes the plastic deformation of the moment scheme II (1 m × 1 m) to be smaller than the area of scheme III (2 m × 2 m).

Figure 7 shows the comparison between the theoretical calculation results and the numerical simulation results of the maximum vibration velocity of the seismic waves excited by three different excitation schemes. As for the comparison of the maximum vibration velocities calculated based on theory and numerical simulation at the places with the same distance to explosive center, in horizontal direction, significant errors appear when the central axis horizontal distance is within 5 m, reaching about 3%–7%; the error between the two decreases with the increase of distance to explosive center. When the distance of shaft centers enlarges to over 8 m, the error would be within 3%. On the vertical direction of the central axis, the error between the two is within 5%. It can be figured out that the two values vary greatly on horizontal direction. That is because the end effects when the equivalent spherical vibrations are superimposed on the horizontal direction lead to greater theoretical calculation result. With the increase of distance to explosive center, the effect of the geometric structure decreases gradually, so that the gap at farther distances gradually decreases.

Distributed charges can effectively reduce the impacts on ground vibration. The greater the interval between charges, the more significant the shock absorption effect. This is mainly because when the charges are arranged close to each other, the blasting cavities that the charges formed at the time of detonation would be superimposed, which increases the disturbance to the ground. With the increase of the

TABLE 2: Parameters of soil.

σ_* (MPa)	σ_0 (MPa)	μ (GPa)	c	φ (kPa)	ρ_{soil} (kg·m³)	K (MPa)	G (MPa)	σ_s (MPa)
13	2	0.147	0.115	11.8	1840	245	147	22

TABLE 3: Parameters of TNT.

C_1 (GPa)	C_2 (GPa)	R_1	R_2	ω	ρ (kg·m⁻³)	D (m·s⁻¹)	E (J·m⁻³)	P_{CJ} (GPa)	P_0 (GPa)
373.7	3.747	4.15	0.90	0.35	1650	6930	$6.0×10^9$	21	9.82

(a)

(b)

(c)
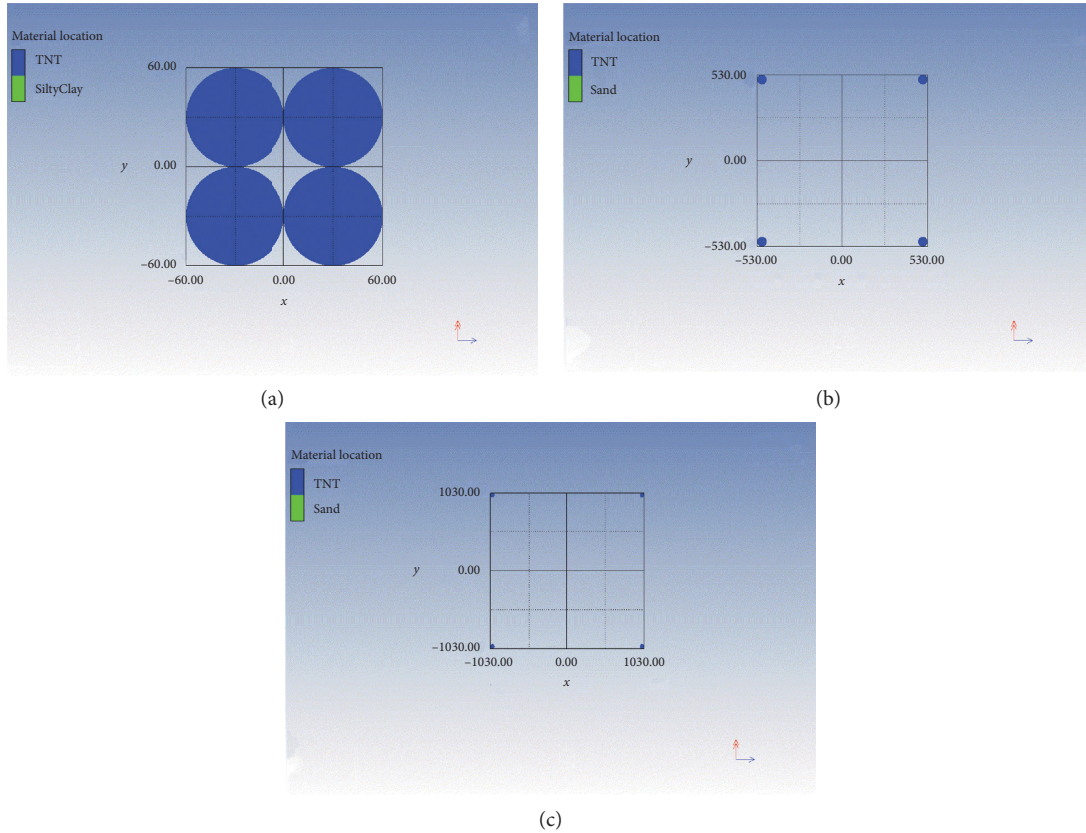
FIGURE 3: Charges with different intervals on the same plane (observed at depth of $z = -1$ m). (a) Centralized charge. (b) Charge with 1 m interval. (c) Charge with 2 m interval.

interval, the plastic zones formed by the charges are separated, which reduces the disturbance to the ground. Besides, the distributed charge can effectively improve the vibration velocity of downward propagation. Such phenomenon is also related to the interval between charges. When applying proper interval, the downward-propagated seismic waves excited by the charges would also be superimposed, thereby increasing the amplitude of the seismic wave.

6. Discussion

The geometric structure of the horizontally distributed charge determines that the characteristics of the seismic wave field in area near the explosive source are different at the axial direction and the radial direction. In order to study the development status of the seismic wave field excited by the horizontally distributed charges, the seismic wave fields

at the vertical and horizontal directions of the central axis of the centralized charge and the horizontally distributed charge were studied in this paper; and, for the three conditions of centralized charge, charges with 1 m interval, and charges with 2 m interval, their seismic wave amplitude-frequency characteristics at places 12 m away from central axis along both the vertical and horizontal directions were solved according to the spherical-cylindrical conversion model (Figure 8).

At the place with 12 m distance along the horizontal direction, the maximum vibration velocities of the centralized charge, charges with 1 m interval, and charges with 2 m interval are, respectively, 0.20 m/s, 0.15 m/s, and 0.05 m/s, the main frequencies are 125 Hz, 105 Hz, and 55 Hz, and the frequency bandwidths are 120 Hz, 95 Hz, and 48 Hz, respectively. The seismic waves excited by centralized charge are greater than those formed by distributed charges
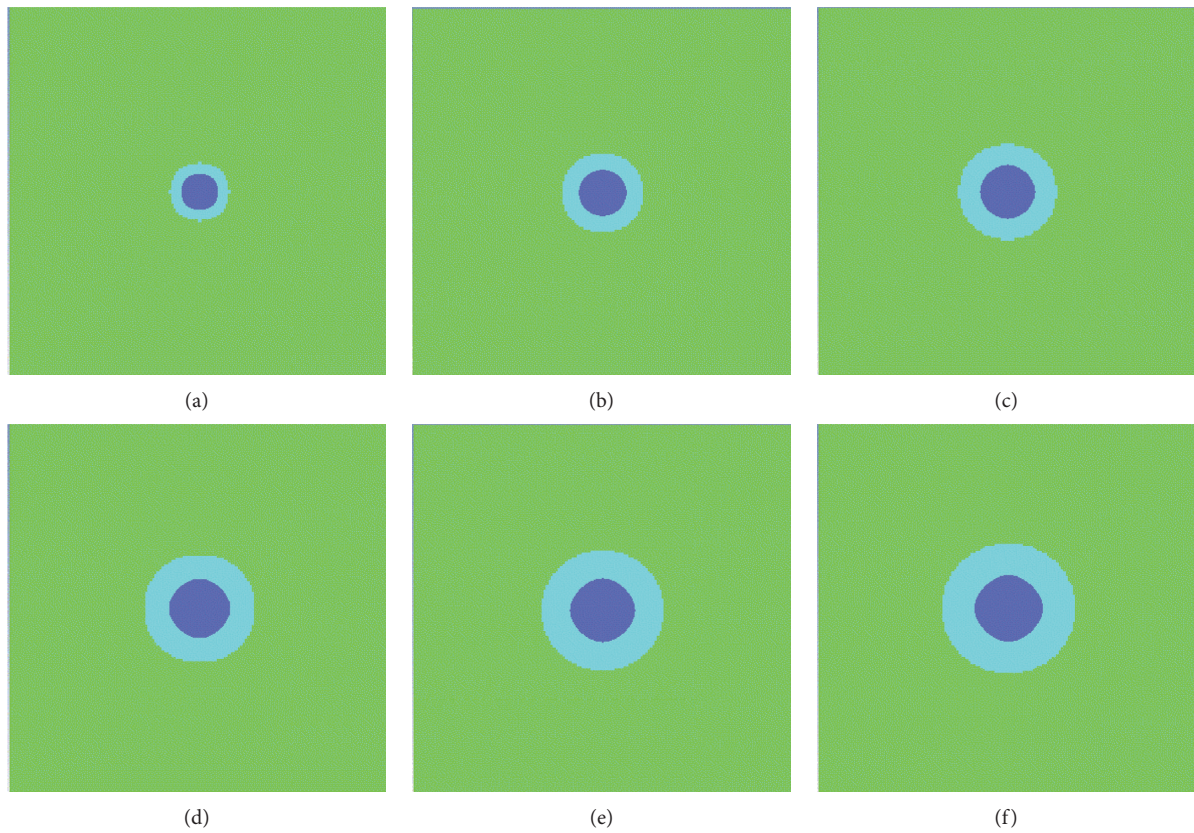
FIGURE 4: A diagram of soil plasticity changes in the horizontal cross section of explosive explosion in scheme I (centralized). (a) 0.2 ms, (b) 0.4 ms, (c) 0.6 ms, (d) 0.8 ms, (e) 1.0 ms, and (f) 1.2 ms.
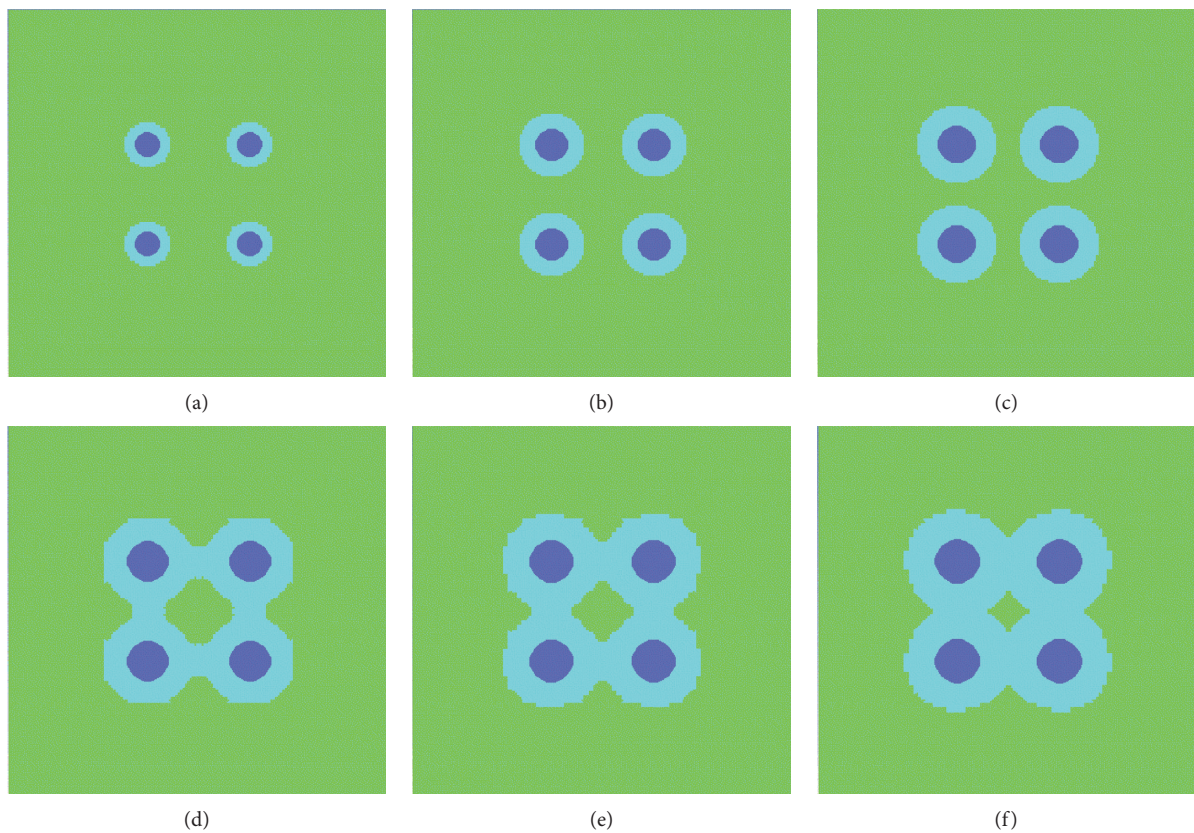
FIGURE 5: A diagram of soil plasticity changes in the horizontal cross section of explosive explosion in scheme II (1 m × 1 m). (a) 0.2 ms, (b) 0.4 ms, (c) 0.6 ms, (d) 0.8 ms, (e) 1.0 ms, and (f) 1.2 ms.
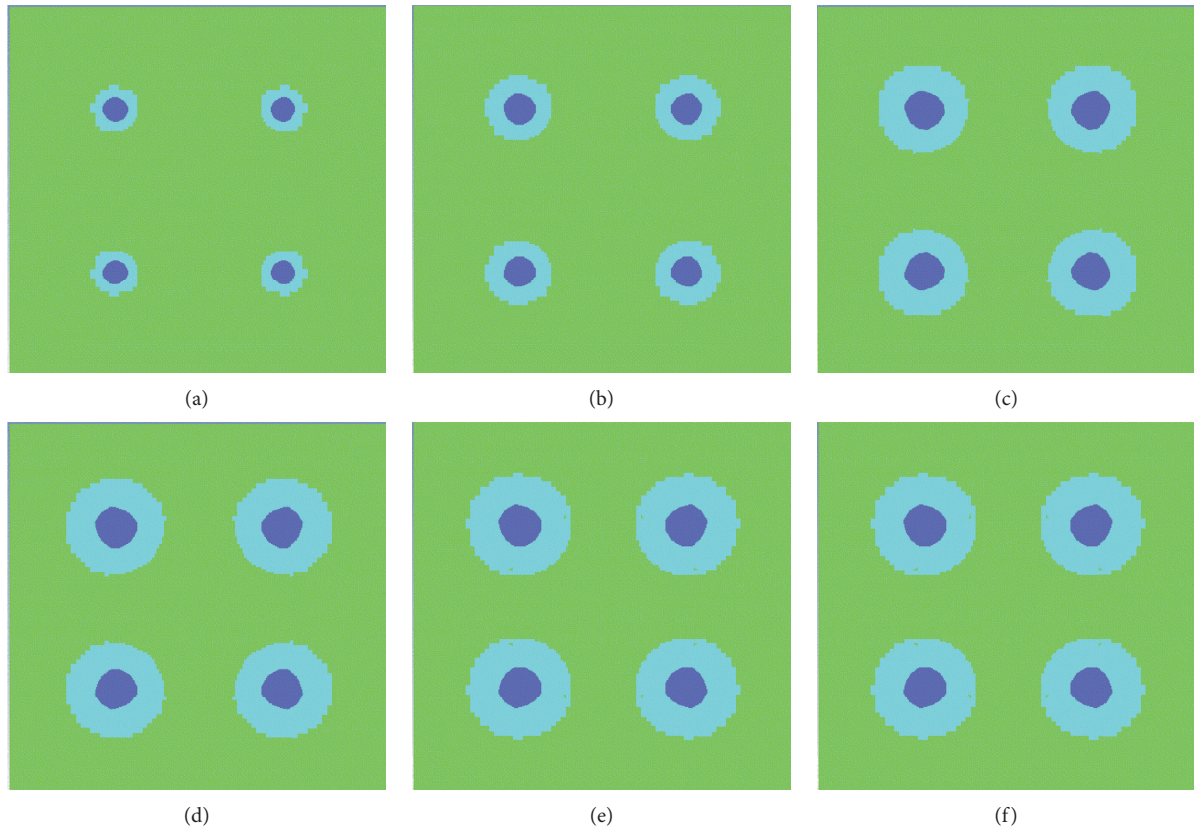
FIGURE 6: A diagram of soil plasticity changes in the horizontal cross section of explosive explosion in scheme III (2 m × 2 m). (a) 0.2 ms, (b) 0.4 ms, (c) 0.6 ms, (d) 0.8 ms, (e) 1.0 ms, and (f) 1.2 ms.
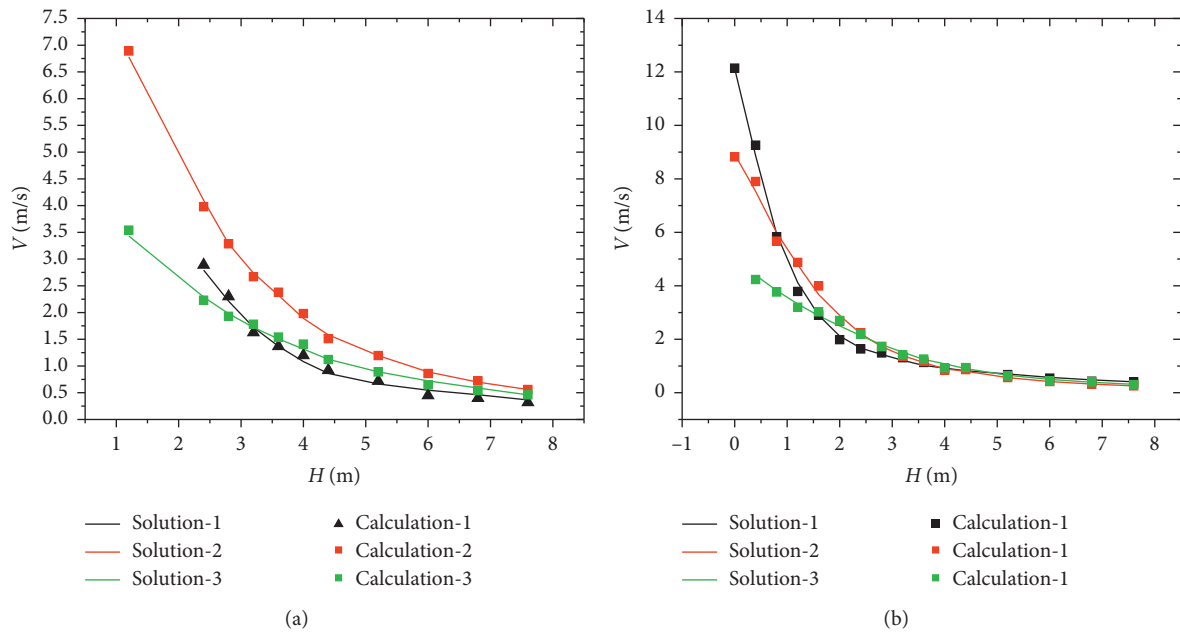
FIGURE 7: Comparison on max. vibration velocity of different excitation schemes.

in both the energy and frequency. The energy and frequency of seismic waves formed by charges with 2 m interval are both greater than those formed by charges with 1 m interval. The main reason is that the seismic wave time difference resulting by charge interval on horizontal direction makes the peak value zones of seismic waves formed by all equivalent charges unable to be superimposed, so that "the greater the charge interval, the lower the max. vibration
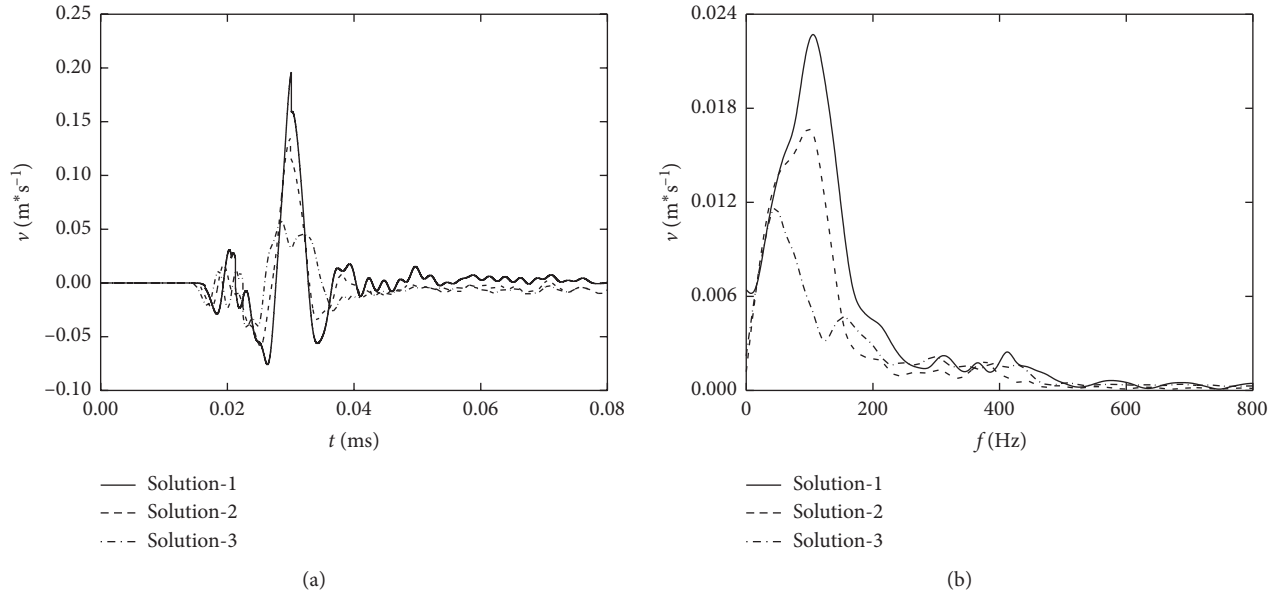
FIGURE 8: Waveform and frequency at place 12 m away from the central position at horizontal direction.
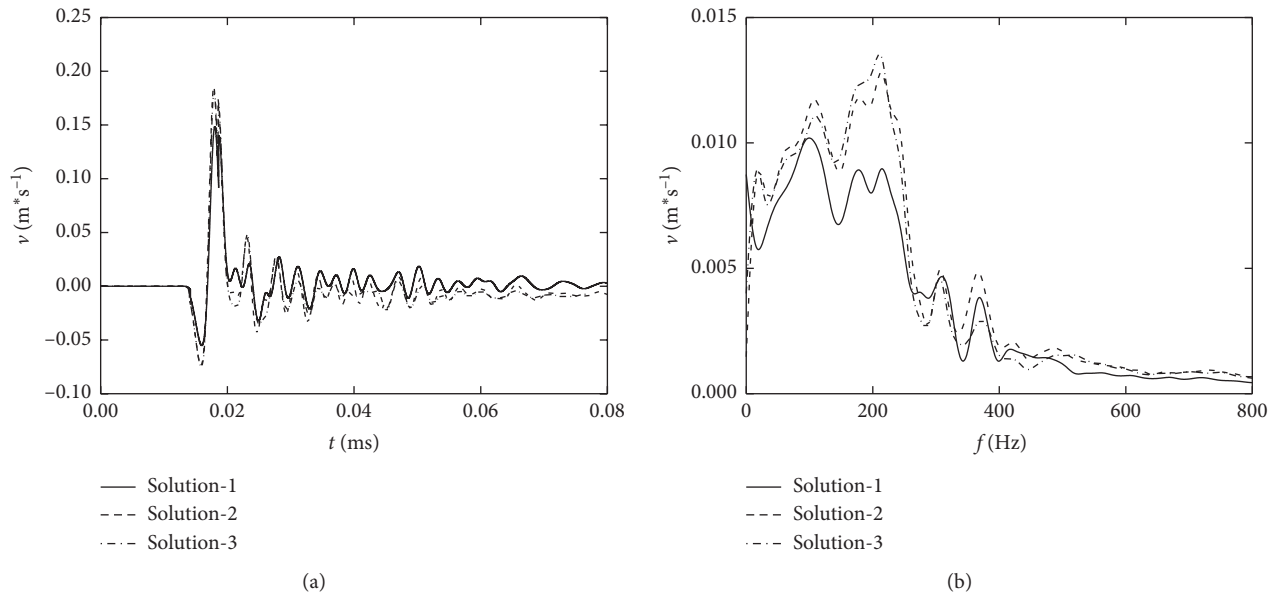
FIGURE 9: Waveform and frequency at place 12 m away from the central position at vertical direction.

velocity of the seismic wave"; and, in the transverse direction, the radius of the plastic zone formed by centralized charge must be smaller than that formed by distributed charges. With the increase of the charge interval, the sum of the plastic zones would be increased. Therefore, the greater the charge interval, the lower the frequency of the seismic wave (Figure 9).

At the place 12 m away along vertical direction, the maximum vibration velocities of the centralized charge, charges with 1 m interval, and charges with 2 m interval are, respectively, 0.15 m/s, 0.17 m/s, and 0.19 m/s, the main frequencies are 105 Hz, 125 Hz, and 120 Hz, and the bandwidths are 100 Hz, 125 Hz, and 122 Hz, respectively. It can be found

that the energy and frequency of the seismic wave formed by the centralized charge are less than the energy and frequency of the seismic wave formed by the distributed charge. The energy and frequency of the seismic wave excited by charges with 2 m interval are less than those that formed the distributed charge with 1 m interval. The reason for this phenomenon is that the radius of the plastic zone that formed along the vertical direction when the charge is exploded will not deviate due to the difference of the distribution of the charges. The time difference caused by the interval between the cylindrical charges will still affect the superposition of the peak vibration velocities of the seismic waves, so as to lead to different peak value vibration velocities formed by distributed charges.

7. Conclusions

To clarify the relationship between the horizontally distributed cylindrical charge and the seismic wave field, the spherical cavity seismic source model was taken as the basis, and the method of replacing cylindrical charges by equivalent superposition of multiple spherical charges was applied to propose the approach of calculating the seismic wave field excited by horizontally distributed charges and establish the model for seismic wave field excited by horizontally distributed charges. Traditional models for spherical charge explosive source and the cylindrical charge explosive source cannot accurately describe the seismic wave field characteristics excited by distributed charges during seismic prospecting. But the model proposed in this paper overcomes this setback and provides theoretical basis for conducting the refined prospecting and production.

Two methods of numerical simulation and on-site test were applied to verify the applicability of the theoretical model. The results of the numerical simulation calculation show that, in the radial direction, the error of calculation results between the theoretical model and the numerical model is within 7%; and, along the horizontal direction, the error of calculation results between the theoretical model and the numerical model is within 3.4%. This indicates that the distributed charges can effectively reduce the impact of ground vibration and increase the energy of seismic waves propagating downwards.

At the detonation moment of the horizontally distributed charge, the seismic wave fields formed near the explosive show differences along horizontal and vertical directions. Under the condition of the same horizontal distance, the vibration velocity along the horizontal direction reduces with the increase of explosive interval. When the horizontal distance is set to be 12 m, the maximum vibration velocity of the centralized charges, charges with 1 m interval, and charges with 2 m intervals would be 0.20 m/s, 0.15 m/s, and 0.05 m/s, respectively, the main frequencies are 125 Hz, 105 Hz, and 55 Hz, and the bandwidths are 120 Hz, 95 Hz, and 48 Hz. When the vertical distance is set to be 12 m, the maximum vibration velocity of the centralized charges, the charges with 1 m interval, and the charges with 2 m interval would be 0.15 m/s, 0.17 m/s, and 0.19 m/s, respectively, the main frequencies are 105 Hz, 125 Hz, and 120 Hz, and the bandwidths are 100 Hz, 125 Hz, and 122 Hz, respectively. The results show that the horizontally distributed charges with 2 m interval are the most satisfactory choice to achieve the goal of improving explosive source seismic wave resolution by adjusting the excitation form of explosive source.

Data Availability

The data are available and included within this article; readers can access the data supporting the conclusions of this study.

Conflicts of Interest

The authors declare that there are no conflicts of interest.

Authors' Contributions

The manuscript was approved by all authors for publication.

Acknowledgments

References

[1] Y. Wang, W. K. Feng, R. L. Hu, and C. H. Li, "Fracture evolution and energy characteristics during marble failure under triaxial fatigue cyclic and confining pressure unloading (FC-CPU) conditions," *Rock Mechanics and Rock Engineering*, vol. 54, no. 2, pp. 799–818, 2021.

[2] Z. G. Tao, C. Zhu, M. C. He et al., "A physical modeling-based study on the control mechanisms of negative Poisson's ratio anchor cable on the stratified toppling deformation of anti-inclined slopes," *International Journal of Rock Mechanics and Mining Sciences*, vol. 138, p. 104632, 2021.

[3] C. Zhu, M. He, M. Karakus, X. Zhang, and Z. Tao, "Numerical simulations of the failure process of anaclinal slope physical model and control mechanism of negative Poisson's ratio cable," *Bulletin of Engineering Geology and the Environment*, vol. 80, no. 4, pp. 3365–3380, 2021.

[4] B. Li, R. Bao, Y. Wang, and C. Zhao, "Permeability evolution of two-dimensional fracture networks during shear under constant normal stiffness boundary conditions," *Rock Mechanics and Rock Engineering*, vol. 54, no. 3, pp. 1–20, 2021.

[5] Q. Wang, H. K. Gao, B. Jiang, S. Li, M. He, and Q. Qin, "In-situ test and bolt-grouting design evaluation method of underground engineering based on digital drilling," *International Journal of Rock Mechanics and Mining Sciences*, vol. 138, Article ID 104575, 2021.

[6] Q. Wang, Q. Qin, B. Jiang et al., "Mechanized construction of fabricated arches for large-diameter tunnels," *Automation in Construction*, vol. 124, Article ID 103583, 2021.

[7] H. Jeffreys, "On the cause of oscillatory movement in seismograms," *Geophysical Journal International*, vol. 2, no. 2, pp. 407–416, 1931.

[8] J. A Sharpe, "The production of elastic waves by explosion pressure. I. Theory and empirical field observations," *Geophysics*, vol. 2, no. 7, pp. 144–154, 1942.

[9] F. G. Blake, "Spherical wave propagation in solid media," *The Journal of the Acoustical Society of America*, vol. 2, no. 24, p. 211, 1952.

[10] J. H. Xiao and W. T. Sun, "Seismic wavelet generated by point explosive source," *Oil Geophysical Prospecting*, vol. 6, no. 32, pp. 809–817, 1997.

[11] J. H. Xiao, "Argument on wave equation of spherical wave," *Oil Geophysical Prospecting*, vol. 2, no. 36, pp. 160–172, 2001.

[12] H. Ding and Z. M. Zhen, "Blasting vibration equivalent load model," *Scientia Sinica Techologica*, vol. 1, no. 33, pp. 82–90, 2003.

[13] D. C. Lin and C. H. Bai, *The Effect of Explosion Earthquakes*, Geological Publishing House, Beijing, China, 2007.

[14] C. L. Yu, Z. Q. Wang, and W. G. Han, "A prediction model for amplitude-frequency characteristics of blast-induced seismic

waves," *Geophysics: Journal of the Society of Exploration Geophysicists*, vol. 83, no. 3, pp. 1–56, 2018.

[15] P. A. Heelan, "Radiation from a cylindrical source of finite length," *Geophysics*, vol. 18, no. 3, pp. 685–696, 1953.

[16] A. M. Starfield and J. M. Pugliese, "Compression waves generated in rock by cylindrical explosive charges: a comparison between a computer model and field measurements," *International Journal of Rock Mechanics and Mining Sciences & Geomechanics Abstracts*, vol. 1, no. 5, pp. 65–77, 1968.

[17] Y. Long, X. S. Lin, and L. P. Xu, "Experimental research on growth process of the cavity of a strip-shaped explosive charge exploding in soil," *Explosion and Shock Waves*, vol. 3, pp. 227–235, 1988.

[18] P. Y. Li, Z. Q. Wang, and Q. Xu, "Calculation method for characteristic size of blasting cavity of finite length cylindrical charges in soil," *Explosion and Shock Waves*, vol. 12, no. 39, pp. 100–108, 2019.

[19] C. L. Yu and Z. Q. Wang, "Quasi-static model for predicting explosion cavity with spherical charges," *Explosion and Shock Waves*, vol. 2, no. 37, pp. 249–254, 2017.

[20] L. X. Hu, D. K. Yang, B. S. He et al., "Theoretic analysis of delayed blast," *Oil Geophysical Prospecting*, vol. 1, no. 37, pp. 33–38, 2002.

[21] W. Y. Huang, S. L. Yan, S. R. Lv et al., "The research and application of the low detonation velocity and elongated source charge," *Explosive Materials*, vol. 4, pp. 18–22, 2005.

[22] X. J. Yang, J. M. Wang, C. Zhu, M. C. He, and Y. Gao, "Effect of wetting and drying cycles on microstructure of rock based on SEM," *Environmental Earth Sciences*, vol. 78, no. 6, p. 183, 2018.

[23] L. Ban, C. Zhu, C. Qi, and Z. Tao, "New roughness parameters for 3D roughness of rock joints," *Bulletin of Engineering Geology and the Environment*, vol. 78, no. 6, pp. 4505–4517, 2019.

[24] A. Li, F. Dai, Y. Liu et al., "Dynamic stability evaluation of underground cavern sidewalls against flexural toppling considering excavation-induced damage," *Tunnelling and Underground Space Technology*, vol. 112, Article ID 103903, 2021.

Research Article

Discussion on Advanced Seepage Reduction Characteristics of Working Face under Seepage-Damage Coupling

Feisheng Feng ⓘ,[1] Jiqiang Zhang ⓘ,[1] Zhen Yang ⓘ,[2] Dongdong Pang,[1] and Jing Zhang[1]

[1]*State Key Laboratory of Mining Response and Disaster Prevention and Control in Deep Coal Mine,*
 Anhui University of Science and Technology, Anhui, Huainan 232001, China
[2]*College of Information Science and Engineering, Henan University of Technology, Zhengzhou 450001, China*

Correspondence should be addressed to Zhen Yang; 593797596@qq.com

The water burst of roof on working face has been one of the significant geotechnical engineering problems that needs to be urgently resolved. The coupling effects of seepage and damage on the amount and intensity of water inrush from the roof are critically important. In this paper, the seepage-damage coupling mathematical model of the aquifer in the working face is studied, and the seepage-damage coupling mechanics model at different stages of the aquifer is established. Under the coupling of permeability and damage, the water-soil characteristics of the aquifer in the 101163 working face of Mindong were numerically simulated by establishing the constitutive relation between vertical stress and permeability coefficient. The numerical results show that the stress concentration factor of the mining stress field gradually increases with the coal seam mining. The water-flowing fractured zone of the overburden is close to the communication of the quaternary aquifer. When the coal seam is excavated 250–300 m. Three free surfaces appear in the groundwater pressure field, and a large falling funnel is formed to establish a deep flow S-well well flow model. The research on the mining stress field and seepage field is carried out in combination with the Jakob formula. It is found that two sectors with reduced permeability of the fan surface are formed in front of the work. The variation law of the apocalyptic permeability infiltration under different mining distances, different coal seam thicknesses, different water pressures, and different roof management modes is studied systematically. The research indicates that the seepage flow under the condition of seepage infiltration of the lower aquifer should be between 50% and 100% of the traditional calculation method. The research results can help to deepen the understanding of the process of water inrush under the coupling of stress and seepage.

1. Introduction

Water inrush from roof is an important factor influencing coal mine safety production. Study on characteristics of rock seepage-stress coupling and on characteristics of advanced seepage reduction of working face in mining engineering has important theoretical and application value. A large number of Chinese experts and scholars have carried out a lot of experiments and theoretical researches in this regard [1, 2], mainly on permeability coefficient and permeability law of rock under mining stress coupling and numerical simulation research for the establishment of rock permeability evolution model and seepage-stress coupling model. Many experts and scholars have also established different rock seepage coupling models from the perspective of mathematics and mechanics

[3–6]. The classical viscoelastic-plastic constitutive theory is used to treat the seepage field on the assumption that no damage is caused to the pore and fissure structure in the rock, which is also called the classic seepage-stress coupling model. Based on the classic seepage-stress coupling model, the more complex coupling effect caused by damage changes in the pore structure system of the rock is also studied, which is called seepage-stress damage coupling model. The research on permeability changes in coal mining in countries other than China was carried out earlier, mainly on theoretical analysis, field tests, and numerical simulations. Baghbanan et al. [7, 8] established a relation model between permeability and stress of overlying rock strata during coal mining based on the relationship between stress changes and permeability coefficients in mining strata and they calculated changes of

permeability coefficient of overlying rock before and after mining. Fang et al. [9] used EDEM to simulate the influence of stress on permeability and the fluid flow pattern in fractured rock mass is studied when the pore size of fracture is related to the trace length of fracture. Ghabezloo et al. [10] found that the water flow from fissure decreased significantly with the increase of the fracture normal stress through laboratory experiments and came up with empirical formulas for the permeability coefficient, stress, and fissure parameters. Heiland et al. [11, 12] studied the relationship between rock porosity, permeability, and effective stress of different rock types and different pore types. Li et al. [13–16] revealed the relationship between the permeability coefficient and stress of fractured rock mass.

In recent years, scholars have made great efforts in the research on the path and mechanism of mine inrush. Various theoretical and mathematical models have played a good role in coal mine safety production. Scholars proposed complex rock seepage-stress coupling models including fracture mechanics model and damage mechanics model. However, these models failed to simulate the characteristics of complex composite rock masses and the entire process of fissure and water inrush induced by coal mining. The instability of rock mass and abrupt change of seepage flow are caused by the evolution of stress-seepage coupling system, so the stress-seepage coupling model of rock mass needs to be further optimized and different permeability should be adopted for rocks in different damage stages and in different regions. In particular, the confined hydraulic structure characteristics and coupling mechanism of aquifers in different locations are not clear and traditional numerical simulation constitutive models and damage criteria are not fully justified. In this paper, the geological conditions of the coal-bearing sandstone aquifer in Mindong Mining Area were taken as the research object to explore scientific issues such as the establishment of a coupled mechanical evolution model of the aquifer above the coal seam on the working face at 101163 and the establishment of a numerical model under the coupling of stress and seepage, to expound the evolution of seepage characteristics of confined aquifers and migration law of groundwater flow field and conduct a comprehensive study of the advanced seepage reduction characteristics of the working face under the coupling of stress and seepage.

2. Analysis of Mechanism of Coupling between Mining Stress and Seepage

2.1. Analysis of Seepage Characteristics of Mining-Induced Fractured Rock Mass. With the development of fissures,

working face can be divided into three areas from top to bottom, virgin rock area, fissure area, and caving area, as shown in Figure 1.

When aquifer I is in the original rock area, the mode of action of groundwater on rocks is disintegration and degradation. When aquifer II is in the mining-induced fissure area, the action mode of groundwater on rocks is shear action. When aquifer III is in the craving zone, the rock of the aquifer collapses as the mining face is exploited. As a result, the circulation channel of the aquifer is broken and the water in the aquifer in the craving area directly enters the working surface vertically to gushing water direction. The water in the aquifer on both sides enters the working surface in the form of lateral recharge and the advance bearing pressure leads to a change of permeability of aquifer and fissure shape.

2.2. Study on Influence of Mining Stress on Seepage Field.
Figure 2(a) is a composite bearing layer composed of soft rock overburden and aquifer. Before the initial fracture, the composite bearing layer will be subject to the gravity of the overlying rock and the water pressure of the aquifer. The aquifer represented by the lower layer is composed of medium conglomerate. Therefore, the aquifer mainly contains solid conglomerate and internal cracks and pores. A microunit is selected at the interface between aquifer and aquifer. The fracture is affected by rock pressure of rock and water pressure above the rock. For virgin rock area, under the mining and water pressure, water inrush in coal seam is the development of rock stratum and the expansion of various structural panels at different angles from the floor. If the aquifer floor is not collapsed, we can still believe that the reason of water inrush lies in the expansion of various structural planes at different angles within the rock. It is most dangerous when joint or fissure is at 90° from the floor. Assuming that the cracks are elliptical, the adjacent cracks do not affect each other, and the local variation of material properties is ignored, the open cracks are subjected to internal water pressure and external stress, as shown in Figure 2.

Major semiaxis of the fissure is set as a and the minor semiaxis of the fissure is set as b. According to the mechanics of elasticity, the solution formula for the stress value at any point on the fissure is (1).

$$\sigma_1 = \frac{\sigma_y \left[1 + 2m\,\sin^2\,\alpha - m^2\cos^2\,\alpha\right]}{m^2\cos^2\,\alpha + \,\sin^2\,\alpha} + \frac{\sigma_x \left[m(m+2)\cos^2\,\alpha\right]}{m^2\cos^2\,\alpha + \,\sin^2\,\alpha} + \frac{\tau_{yx}\left[2(1+m)^2\cos\,\alpha\,\sin\,\alpha\right]}{m^2\cos^2\,\alpha + \,\sin^2\,\alpha}, \tag{1}$$
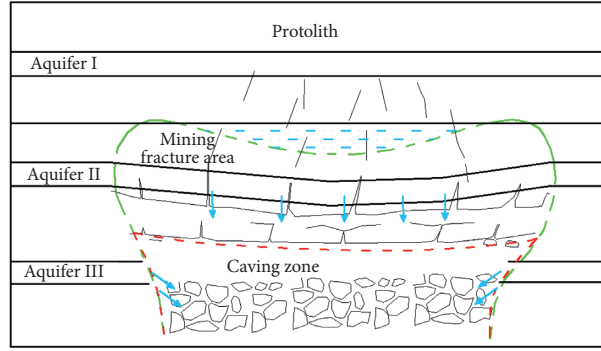
FIGURE 1: Rock mass fracture development map.

(a) (b)
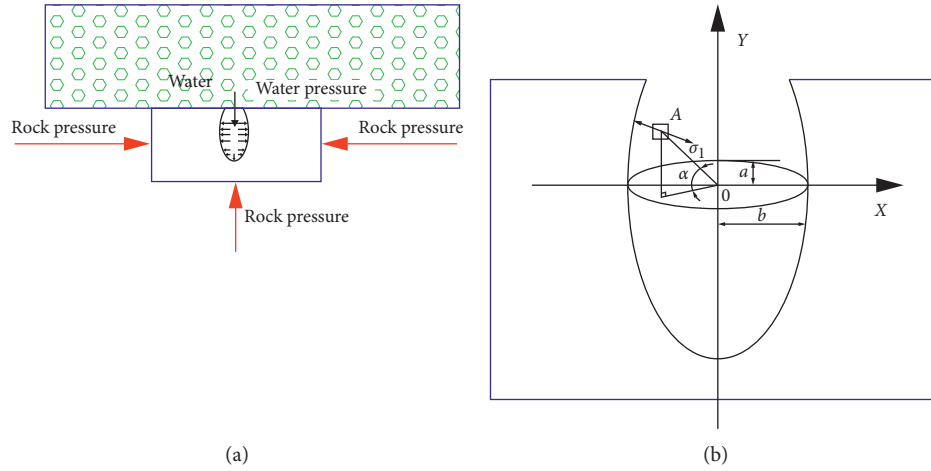
FIGURE 2: Schematic diagram of internal water pressure and external stress on fissure. (a) Schematic diagram of external stress on fissure. (b) Enlarged diagram of internal stress on fissure.

where σ_1 is the shear stress at point A, σ is the stress resultant on fissure, a is the eccentric angle, m is the number of strata from aquifer to surface, σ_x is the x direction normal stress, σ_y is direction normal stress, and τ_{yx} is shear stress.

The fissure unstable propagation meets the Griffith strength criterion, in order to simplify the calculation when considering that the bottom water-proof layer of the goaf is a uniform and horizontal cross-fixed plate. The entire water-proof layer is curved downward from the center of the circle, the roof is open fissure, and the bottom is fracturing fissure. The middle height of the plate can be considered as the contact surface where the fractures meet. The critical water pressure value is

$$P_w = R\left[\frac{8\left(L_x^2 + L_y^2\right)}{\left(L_y^2 - L_x^2\right)^2} + \frac{1}{L_y^2}\right]h_2^2 + \gamma h_2 - Q, \qquad (2)$$

where P_w is the critical water pressure, R is the tensile strength of the rock formation, h_2 is the thickness of the effective water-proof layer, γ is the unit weight of the rock formation, Q is the pressure of the mine, L_x is the periodic weighting length, and L is the length of the working face.

During mining, fissure will appear in fissure area and then gradually develop. Groundwater in the confined aquifer enters fissures and produces seepage forces in the fractured rock mass, including hydrostatic pressure and hydrodynamic pressure. The hydrodynamic pressure is mainly resulted from the lateral recharge of the aquifer, causing groundwater to fill the fissure space and interact with the overlying rock layer continuously. As a result, the gravity of the overlying rock layer acts on the bending zone in the form of hydraulic pressure through the rock layer above the bending zone. The change stress of the rock mass will affect the structure of the rock mass, thus changing the permeability, which is manifested as the changes in the groundwater seepage field. The act of mining stress on the permeability coefficient can be obtained with

$$K = K_0\left\{1 - \frac{1}{2}\left(\frac{\Delta\sigma_c - \Delta\sigma_i}{E_0}\right)^{2/3}\right\}^4, \qquad (3)$$

where K is the permeability coefficient for the stress value, K_0 is the permeability coefficient under zero stress, Δ is the change of this variable, σ_i is the consolidation pressure, E_0 is

the effective modulus of the particles, and σ_c is the confining pressure.

The relationship between the permeability coefficient and the internal particles can be obtained through the Hubbert relation expression as follows:

$$K = Nd^2\left(\frac{\rho g}{\mu}\right), \tag{4}$$

where N is a dimensionless number related to the filling particles, ρ is the density, g is the acceleration of gravity, μ is the coefficient of kinetic viscosity, and d is the average particle size.

The Bai. M's method [17] is used to evaluate the influence of stress on the development of fissures. Assuming that the confining pressure and pore pressure result in effective stress, equation (5) can be expressed as the following formula with the cube model:

$$K \propto R_k^2, \tag{5}$$

where R_k is the particle radius. When the cubes are piled up, Nd^2 grams are expressed as

$$Nd^2 = \frac{1}{2}\left\{\frac{(2R)^3}{4\pi R^2}\right\}^2$$
$$= \frac{2}{\pi^2}R^2. \tag{6}$$

Equation (5) can be expressed as equation (7) in case of insufficient compaction.

$$K = \frac{2}{\pi^2}R^2\left(\frac{\rho g}{\mu}\right). \tag{7}$$

Under uniform pressure, equation (8) can be applied to obtain particle radius.

$$\Delta R = R_0\left\{1 - \frac{1}{2}\left[\frac{9(1-\nu)^2}{2}\left(\frac{\pi\Delta\sigma}{E}\right)^2\right]^{1/3}\right\}, \tag{8}$$

where ν is Poisson's ratio of the drainage of the medium. Assuming that K_0 can be obtained through experiment, the particle radius can be expressed by

$$R_0 = \pi\sqrt{\frac{K_0\mu}{2\rho g}}. \tag{9}$$

The expression of the influence of the mining stress on the seepage field can be obtained through simultaneous formulas (7)–(9) as shown in formula equation (10).

$$\Delta K = \frac{2}{\pi^2}(\Delta R)^2\left(\frac{\rho g}{\mu}\right) = K_0\left\{1 \pm \frac{1}{2}\left[\frac{9(1-\nu)^2}{2}\left(\frac{\pi\Delta\sigma}{E}\right)^2\right]^{1/3}\right\}^2. \tag{10}$$

For the caving zone, the permeability of the overlying rock is related to its porosity, and there is a direct relationship between porosity and stress which has been extensively studied [18–24]. Their relationship is

$$\Phi = (\Phi_0 - \Phi_r)\exp(\alpha_\Phi \times \sigma_v) + \Phi_r, \tag{11}$$

where Φ is the porosity of the rock under stress, Φ_0 is the porosity under the zero stress, Φ_r is the limit value of the porosity under the high-pressure stress, α_Φ is the stress influence coefficient, which can be set as $5.0 \times 10^{-8}\,\text{Pa}^{-1}$, and σ_v is the average effective stress.

$$\sigma_v = \frac{(\sigma_1 + \sigma_2 + \sigma_3)}{3} + \alpha p, \tag{12}$$

where σ_1, σ_2, and σ_3 are three main stresses, p is the water pressure in the aquifer, which is set as 3.5 MPa, and the relationship between the permeability and the porosity of the rock mass is shown in equations (13) and (14):

$$K = k_0\left(\frac{\Phi}{\Phi_0}\right)^3\frac{\gamma_w}{\mu_w}, \tag{13}$$

$$K_s = \xi_s k_0\left(\frac{\Phi}{\Phi_0}\right)^3\frac{\gamma_w}{\mu_w}, \tag{14}$$

where ξ_s is the mutation coefficient of the permeability in the plastic zone, which is set as 4.5–5.5, K_s is the permeability on plastic zone, K_0 is the permeability under the zero stress, m_2, μ_w is the coefficient of kinetic viscosity which can be set as 10^{-3} Pa·s, and γ_w is the unit weight of water, Pa/cm, which can be set as 100.

3. Numerical Simulation of Water Inrush in Working Face under the Coupling of Mining Stress Field and Seepage Field

3.1. Establishment of Constitutive Model

3.1.1. Governing Equation for Rock Mass. The effective stress in the saturated zone is

$$\sigma = \sigma' + p, \tag{15}$$

where σ is the total stress and σ' is the stress acting on the solid matrix.

Equation of solid displacement field is as follows:

$$G\nabla 2\mu + \frac{G}{1 - 2\upsilon}\nabla \times (\nabla\mu_s) - \alpha_x\nabla p = 0, \tag{16}$$

where G is the shear modulus, ∇ is gradient, α_x is the Biot coefficient, p is the underground water pressure, and G can be derived from the following formula:

$$G = 2E(1 + \nu), \tag{17}$$

where E is elasticity modulus and the Biot coefficient α_x is mainly related to the compression performance of the material, which can be derived from the following formula:

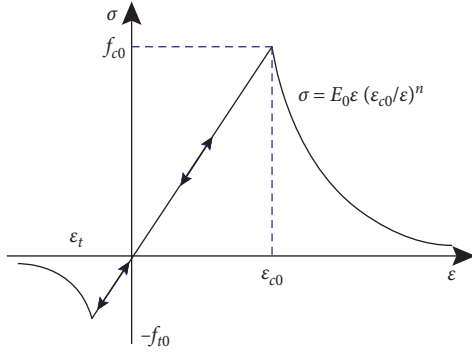$$\alpha = \frac{3(\nu_\mu - \nu)}{B(1 - 2\nu)(1 + \nu_\mu)}, \tag{18}$$

FIGURE 3: Constitutive model under uniaxial stress.

where ν_μ is Poisson's ratio of drainage of the solid component and B is the Skempton coefficient, which can be set as 0.4.

The equation of groundwater seepage field is as follows:

$$\nabla\left[\frac{\rho K}{\mu_s}\nabla p\right] = 0, \quad (19)$$

where ∇p represents the influence of the interstitial pressure produced by the fluid flow on matrix stress field and ρ is the density of fluid.

3.1.2. Stress Correlation of Permeability.
The traditional rock constitutive model under uniaxial stress [25–28] is shown in Figure 3.

As shown in Figure 3, rock experiences elastic change from 0 to fc0 at a uniaxial stress state, but the rock is actually anisotropic material with internal friction and can yield and break under high strength pressure. After undergoing the transition from elasticity to plasticity, its permeability will also increase sharply. The relation expression of the impact of plastic failure on permeability corresponds to the constitutive relationship in the figure. The formula is as equation (14).

On the basis of previous results, a study was carried out on the relationship between horizontal permeability of sandstone and stress state. Considering that the pressure loading path has been drawn up according to the trend of confining pressure of coal seam in No. III aquifer in Mindong Mining Area before the experiment, in the numerical simulation study, only the relationship between permeability and vertical pressure needs to be considered, without considering the relationship between permeability and confining pressure. Therefore, the numerical simulation can be carried out according to the following formula.

In the first stage, when $\gamma_H < \sigma_v > 1.7 \, \gamma_H$,

$$k = (-7E-08)\sigma_v^3 + (3E-06)\sigma_v^3 + 0.0001, \quad (20)$$

In the second stage, when $\sigma_v > 1.7 \, \gamma_H$,

$$k = (-2E-08)\sigma_v^3 + (8E-07)\sigma_v^3 - (2E-06)\sigma_v + 1E-04, \quad (21)$$

where σ_v is vertical stress, MPa.

3.2. Damage Criteria.
The criteria for the plastic damage of rock mass are the modified C-M criterion and the traditional tensile failure criterion.

$$\begin{aligned}
F_1 &= \alpha_1 I_1 + \sqrt{J_2} - K_1 \\
&= 0, \\
F_2 &= \sigma_3 - f_t, \\
J_2 &= \frac{1}{6}\left[(\sigma_1 - \sigma_2)^2 + (\sigma_2 - \sigma_3)^2 + (\sigma_3 - \sigma_1)^2\right], \\
\alpha_1 &= \frac{\tan\psi}{\sqrt{9 + 12\tan^2\psi}}, \\
K_1 &= \frac{3c}{\sqrt{9 + 12\tan^2\psi}},
\end{aligned} \quad (22)$$

where I_1 is the first invariant of effective stress, J_2 is the second invariant of effective stress deviation, α_1 and K_1 are the experimental constants related only to the viscous force c of the internal friction angle ψ, and f_t is the tensile strength of the rock mass. Compared with the original criterion, the modified C-M criterion puts intermediate principal stresses (σ_2) and pore pressure p into account in three-dimensional space; as a result of this, it overcomes the main shortcoming of the C-M criterion and has been widely used in the numerical analysis of rock mechanics and engineering at home and abroad. Under any stress conditions, the tensile damage criterion is a prioritized judging factor.

3.3. The Establishment of Numerical Model.
There are too many rock layers with different thickness in the Mindong Mining Area. Therefore, comprehensive histogram is adopted to replace the rock data for a certain borehole in this numerical simulation. The overlying rock that does not affect the simulation results is combined. The parameters of rock stratum and rock mechanical properties are shown in Table 1.

Based on the histogram and the length of the working face, a geometric model with a length of 800 m and a width of 358 m was established. In a vertical direction, a model was established hierarchically based on the different properties of the rock, simulating the excavation of the coal seam of 300 m.

3.4. Analysis of Numerical Simulation Results

3.4.1. Analysis of Changes of Mining Stress Field.
Figure 4 is a stress-displacement diagram at different working face lengths, from which, we can see that excavation of coal seams results in stress concentration around working face, mainly distributed on coal pillars 0–40 m away from the coal wall, where coal seam under maximum stress > roof > floor. As the length of the working face increases, the maximum stress near the coal pillar gradually increases. When the lengths of

TABLE 1: Parameter table of rock stratum and rock mechanical properties.

Rock number	Lithology	Thickness (m)	Modulus of elasticity (MPa)	Compressive strength (MPa)	Gravity density (104 N/m)	Internal friction angle (°)	Poisson's ratio	Cohesive force (MPa)
14	Overlying strata	200	4728.6	12.58	2.50	40.5	0.19	3.10
6	Middle conglomerate (aquifer)	30	6000	14.60	2.50	42	0.19	3.27
5	Mudstone	25	4300	12.38	2.52	39	0.18	3.32
4	Medium coarse sandstone (aquifer)	55	3900	12.11	2.53	40.5	0.18	3.49
2	Mudstone	10	4300	12.38	2.52	39	0.18	3.32
1	Coal seam	8	1000	4.08	1.35	38	0.28	2.13
0	Siltstone	30	4800	13.45	2.85	41.5	0.24	4.88
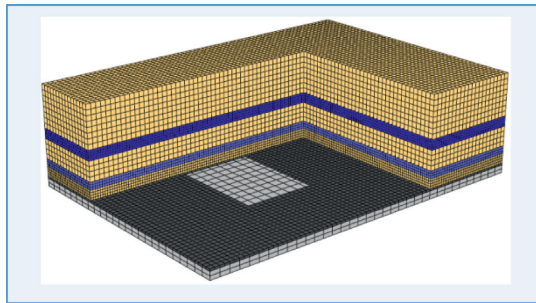
(a)
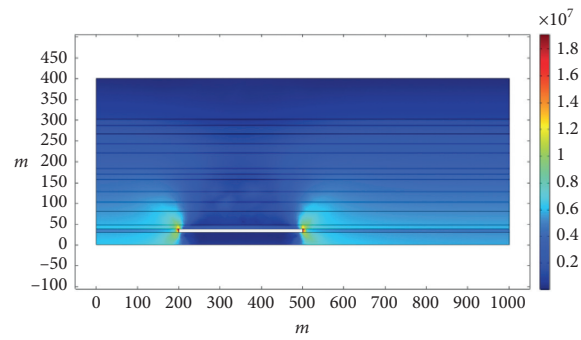
(b)
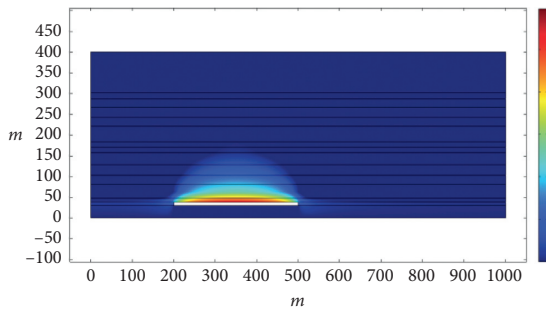
(c)
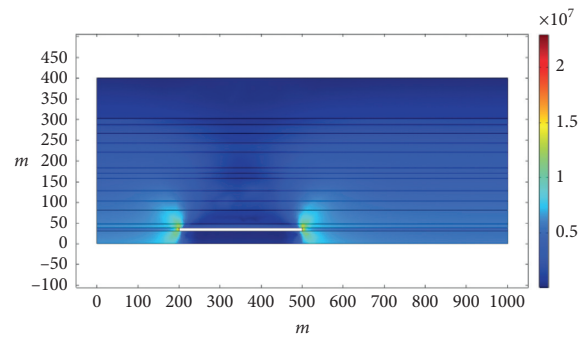
(d)
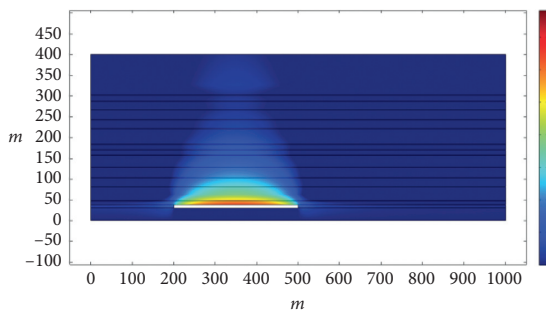
(e)
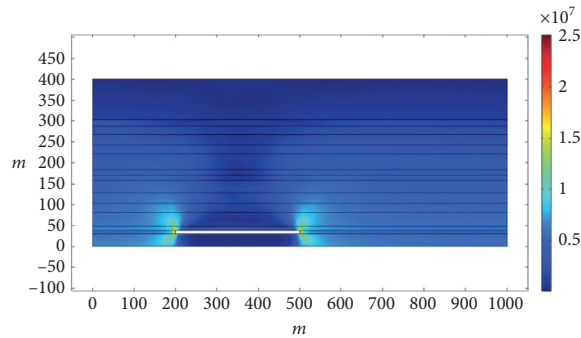
(f)

FIGURE 4: Continued.

(g)
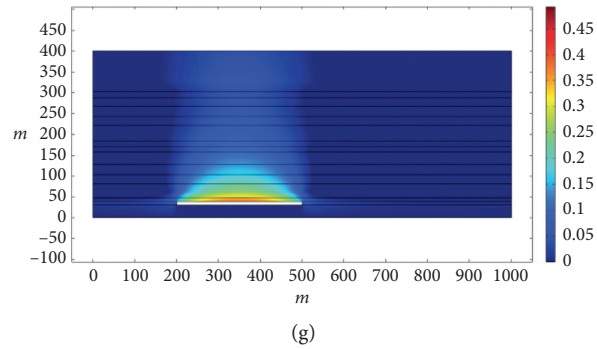
Figure 4: Stress nephogram and displacement nephogram at different working face lengths. (a) Numerical simulation geometry model. (b) Stress nephogram when working face length is 120 m. (c) Displacement nephogram when working face length is 120 m. (d) Stress nephogram when working face length is 160 m. (e) Displacement nephogram when working face length is 160 m. (f) Stress nephogram when working face length is 200 m. (g) Displacement nephogram when working face length is 200 m.

working face are 120 m, 160 m, and 200 m, the maximum stresses are 18.7 MPa, 23.2 MPa, and 25.1 MPa, respectively. The maximum value of the roof caving displacement also gradually increases, as the length of working face prolongs to 0.29 m, 0.37 m, and 0.48 m, respectively.

3.4.2. Analysis of Change Law of Groundwater Flow Field.
Considering that the purpose of the study is to research the change of the flow rate when rock is damaged, a simulation chart of inrush flow of the working surface under different conditions is made and shown in Figure 5.

It can be found that, with the working face advanced, inrush water volume reduced. The changing pattern of the inrush water is similar when the width of working face is at 120 m, 160 m, and 200 m. As the working face width increases, the inrush water flow at the working face decreases and the margin of decreases reduced. It can be considered that, with the width of the working face increasing, the caving increases, but the stress peak value is greater, and the flow rate is reduced, indicating that the water inrush path of the working face has a cascaded structure. As the local fissure closes, the amount of water inflow decreases, as the thickness of the coal seam increases, the amount of inrush water at the working surface increases. Although the increase in the thickness of the working face results in an increase in the stress concentration factor, the roof development height increases and so does the cross section of the inrush channel, resulting in the fact that an increase in the thickness of the coal seam and water inrush on the working surface increases too. This is related to the geological conditions and distribution characteristics of the aquifer. With the increase in water pressure, there are complex changes in the inrush water on the working surface and the water inrush is greatest when the water pressure is 1.50 MPa. When the water pressure is 3.50 MPa, 2.50 MPa, and 0.50 MPa, the changing curves of inrush water will cross at a later stage. All of the above indicates that, under the coupling of water pressure and rock mechanics, different effects on different inrush water volumes occur at different stages, which is consistent with the results of our previous theoretical analysis. Different

roof management methods also indicate that the filling mining not only ensures that inrush water volume decreases rapidly but also ensures that the volume of the inrush water is small. The initial inrush is mainly caused by the static water on the roof. With filling mining, we can ensure that inrush water volume is always at a low value and finally reduces to 0.

3.4.3. Study on the Change Law of Permeability in Aquifer.
As the study focuses on the change of permeability of damaged rock, a research on the relationship between different mining distances and permeability for coal seam with thickness of 8 m is carried out, as shown in Figure 6.

As shown in the figure, as the coal seam is excavated to 100 m, the permeability of the aquifer above the working face increases to about 1.6 times to 2 times of the original. At this time, the aquifer rock above the working face collapsed and the original aquifer low channel was destroyed. The water in the aquifer above the working face will all flow into the working face. In the later stage, the confined water mainly enters the working face through lateral recharge and acts on it; when the excavation reaches 200 m, the area above the working face is still the red permeability increasing zone, but two small permeability mutation areas are formed in the front and back of the working face. As the working surface advances to 300 m, we found that there is a sector permeability decreasing zone about 0–50 m in the front and back of the working face, respectively. There is an arc permeation increasing zone outside the sector permeability decreasing zone which is due to the formation of the rock structure. Leading bearing pressures are formed in the front and back of the working face, and lateral bearing pressures are formed on both sides of the work face. Leading bearing pressure and lateral bearing pressure cause vertical pressure to the aquifer around the working surface. As the horizontal distance from the coal wall of the working surface varies, the bearing pressure is different too, and so does the lateral confining pressure. Therefore, lateral permeability coefficient reduces in the aquifer within the range of the leading bearing stress
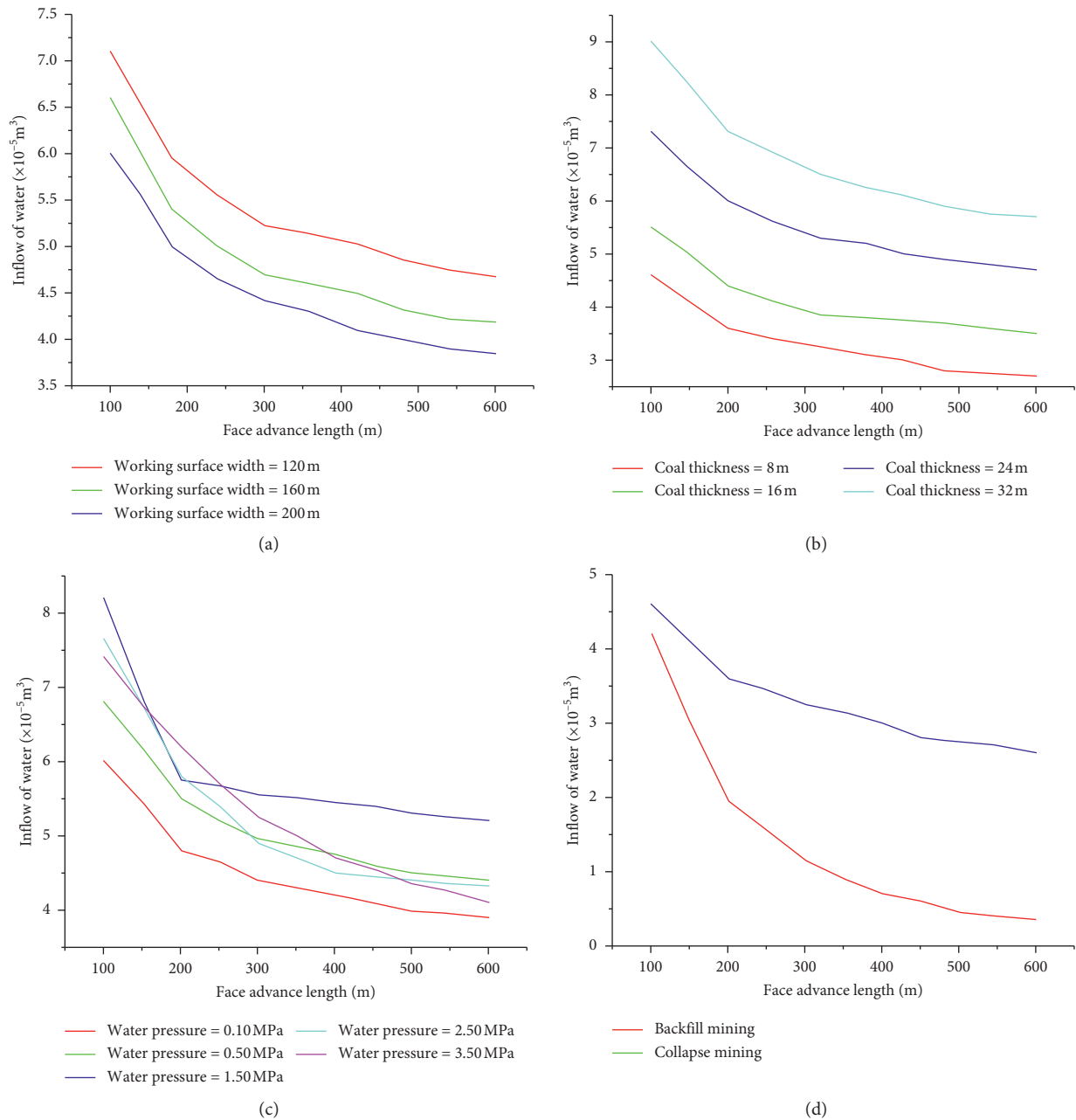
Figure 5: Inrush water flow of working face under different conditions. (a) Inrush water flow of working faces of different width. (b) Inrush water flow of working faces of different coal thickness. (c) Inrush water flow of working faces under different. (d) Inrush water flow of working face under different.

area. When the working face is at 400 m in depth, it can be found that the sector permeability reduction area has expanded to the entire aquifer section. As a result, the volume of dynamic recharge water in the aquifer is lower than that in traditional calculations. Considering that the permeability is proportional to the flow rate, the permeability is reduced by 40%–50% at a maximum if the change in head pressure is not taken into account, so the seepage flow should be between 50% and 100% of that in traditional calculation.

In order to further understand the change of the aquifer's leading permeability reduction with different coal seam

thicknesses, hydraulic pressures, and roof management methods, it has simulated the change of permeability of coal seam at the thicknesses of 8 m, 16 m, 24 m, and 32 m at the depth of 300 m. At the mining depth of 300 m, sector permeability reduction zones of different size are formed in aquifers in coal seam with different thicknesses. As the coal seam thickness increases, the area of sector permeability reduction zones decreases, which is different from the traditional view that the thicker the coal seam, the greater the leading bearing stress. From the simulation results of permeability changes under different water pressures, at the mining depth of 300 m, sector permeability reduction zones
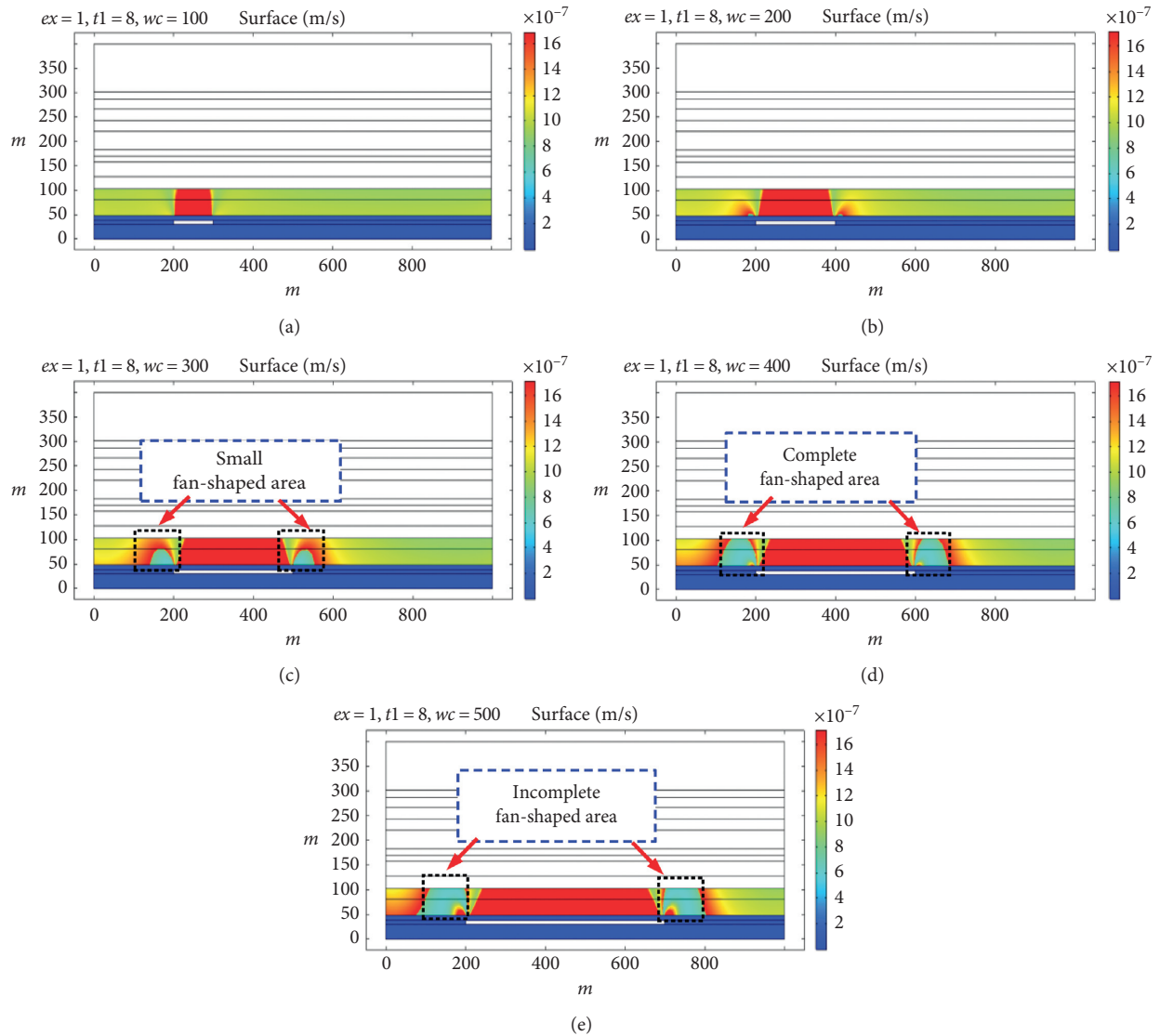
Figure 6: Variation of permeability coefficient at different depth in a coal seam of 8 m in thickness. (a) The depth of 100 m. (b) The depth of 200 m. (c) The depth of 300 m. (d) The depth of 400 m. (e) The depth of 500 m.

of different size are also formed in aquifers under different water pressures; we can see that when the water pressure increases, the area of sector permeability reduction zone gradually enlarges.

As shown in Figure 7, when the roof is managed with the direct caving method, sector permeability reduction zone is formed in the front and back of the working face. When the filling mining method is used, the gob is filled with a lag of 30 m, and the sector permeability reduction zone is not formed in the front and back of the working face. This fully verifies that the aquifer's advanced antiseepage results from the increase in the leading bearing stress.

When the confined aquifer is within the falling zone, the aquifer above the working face collapses and the circulation channel of the aquifer is damaged. Moreover, all the water in the aquifer above the working face will flow into the working face. In the later stage, the confined water mainly enters and acts on the working face by lateral

replenishment and with the working face continues to push forward. The aquifer behind the working under the ahead support pressure will form a fan permeability reduction zone, which corresponds to a curve surface infiltration increasing area outside the fan permeability reduction area. From the above analysis, it can be found that, as the mining distance, the thickness of the coal seam, the hydraulic pressure, and the roof management method vary, the sizes of the sector permeability reduction zone and the arc permeability increasing zone change. When the size of sector permeability reduction zone is larger than the height of the aquifer (since the lateral recharge of the aquifer into the working face is similar to tandem), the amount of lateral recharge water in the aquifer entering the working face reduces. Similarly, the lateral bearing pressure will also have the same effect on the coal seam side, so advanced antiseepage can be seen in the aquifer around the working face.
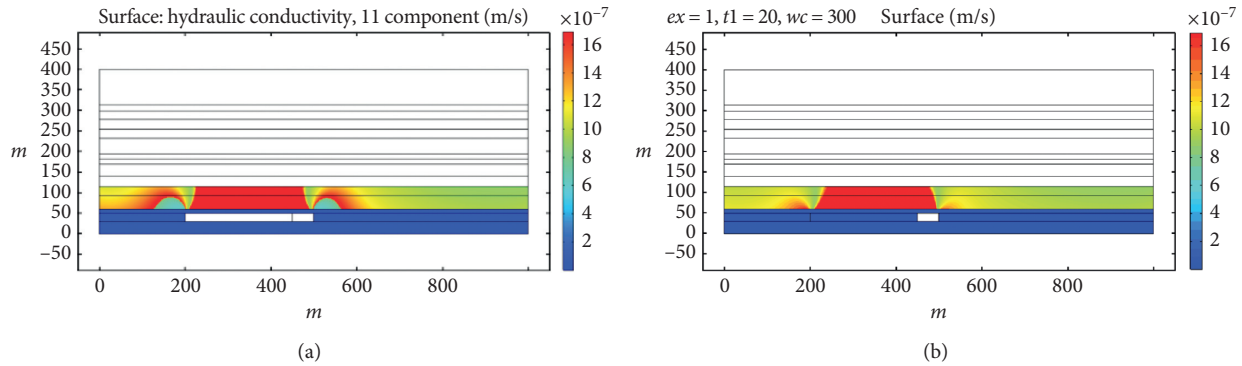
FIGURE 7: Permeability changes when roof management is not used. (a) Direct roof caving method. (b) Filling mining method.

4. Conclusions

The results obtained made it possible to draw the following conclusions:

(1) In this work, the seepage-damage coupling mathematical model of the working face roof aquifer is studied, and the seepage-damage coupling mechanical model of the aquifer in different stages is established. The variation law of the aquifer seepage leading to seepage reduction under different mining distance, different coal seam thickness, water pressure, and roof management mode is systematically studied.

(2) In the upper part of the mining fracture area, the vertical tensile stress produces transverse cracks and fissures, forming a certain subsidence space. There are many vertical cracks in the middle of the mining fracture area, which is due to the bending of the rock layer, the vertical cracks are formed by the compression at the upper end of the middle, and the vertical cracks are formed by the tension at the lower end of the middle. Finally, many transverse and longitudinal fractures are formed in the lower part of the mining fracture area. By establishing the mechanical structure model of bending bearing stratum under hydrostatic pressure, the mechanism of hydrostatic pressure of confined water on aquifuge of bending subsidence strata is studied, the relationship between overburden fracture and water pressure and mine pressure is quantified, the shear force expression of aquifuge in bending subsidence zone is obtained, and the coupling relationship between mining stress and seepage field in mining fracture area is studied. The influence expression of mining stress on seepage field is given.

(3) The numerical simulation study of the change of the mining stress field and seepage field was carried out. During the mining of coal seams, the stress concentration factor of the mining stress field gradually increased, and as a result, floor became larger than roof in stress concentration area. In this paper, leading antiseepage of the aquifer is discussed and the change of leading antiseepage of the aquifer with different mining distances, coal seam thickness, water pressure, and roof management methods is studied. The study finds that the seepage flow of the leading antiseepage of aquifer accounts for 50%–100% of that of the traditional flow.

Data Availability

This is an open-access article distributed under the Creative Commons Attribution License, which permits unrestricted use, distribution, and reproduction in any medium, provided the original work is properly cited.

Conflicts of Interest

The authors declare that there are no conflicts of interest regarding the publication of this paper.

Acknowledgments

References

[1] W. Al-Wardy and R. W. Zimmerman, "Effective stress law for the permeability of clay-rich sandstones," *Journal of Geophysical Research: Solid Earth*, vol. 109, no. B4, 2004.

[2] W. F. Bawden, J. H. Curran, J. H. Curran, and J.-C. Roegiers, Influence of fracture deformation on secondary permeability—a numerical approach," *International Journal of Rock Mechanics and Mining Sciences & Geomechanics Abstracts*, vol. 17, no. 5, pp. 265–279, 1980.

[3] N. Barton, S. Bandis, and K. Bakhtar, "Strength, deformation and conductivity coupling of rock joints," *International Journal of Rock Mechanics and Mining Sciences & Geomechanics Abstracts*, vol. 22, no. 3, pp. 121–140, 1985.

[4] M. Bai and D. Elsworth, "Modeling of subsidence and stress-dependent hydraulic conductivity for intact and fractured

porous media," *Rock Mechanics and Rock Engineering*, vol. 27, no. 4, pp. 209–234, 1994.

[5] Q. Wang, H. K. Gao, B. Jiang, S. C. Li, M. C. He, and Q. Qin, "In-situ test and bolt-grouting design evaluation method of underground engineering based on digital drilling," *International Journal of Rock Mechanics and Mining Sciences*, vol. 138, Article ID 104575, 2021.

[6] X. Liu, G. Han, E. Wang, S. Wang, and K. Nawnit, "Multiscale hierarchical analysis of rock mass and prediction of its mechanical and hydraulic properties," *Journal of Rock Mechanics and Geotechnical Engineering*, vol. 10, no. 4, pp. 694–702, 2018.

[7] A. Baghbanan and L. Jing, "Stress effects on permeability in a fractured rock mass with correlated fracture length and aperture," *International Journal of Rock Mechanics and Mining Sciences*, vol. 45, no. 8, pp. 1320–1334, 2008.

[8] F. M. R. Ferfera, J. P. Sarda, M. Boutéca, and O. Vincké, "Experimental study of monophasic permeability changes under various stress paths," *International Journal of Rock Mechanics and Mining Sciences*, vol. 34, no. 3-4, pp. 37–e1, 1997.

[9] J. Fang, L. Tian, Y. Cai, Z. Cao, J. Wen, and Z. Wen, "A mechanical model of the overlying rock masses in undersea coal mining and a stress-seepage coupling numerical simulation," *Advances in Civil Engineering*, vol. 2018, Article ID 8161498, 14 pages, 2018.

[10] S. Ghabezloo, J. Sulem, S. Guédon, and F. Martineau, "Effective stress law for the permeability of a limestone," *International Journal of Rock Mechanics and Mining Sciences*, vol. 46, no. 2, pp. 297–306, 2009.

[11] J. Heiland and S. Raab, "Experimental investigation of the influence of differential stress on permeability of a Lower Permian (Rotliegend) sandstone deformed in the brittle deformation field," *Physics and Chemistry of the Earth, Part A: Solid Earth and Geodesy*, vol. 26, no. 1-2, pp. 33–38, 2001.

[12] Y.-H. Huang, S.-Q. Yang, W.-L. Tian, W. Zeng, and L.-Y. Yu, "An experimental study on fracture mechanical behavior of rock-like materials containing two unparallel fissures under uniaxial compression," *Acta Mechanica Sinica*, vol. 32, no. 3, pp. 442–455, 2016.

[13] G. Li, Z. Jiang, C. Lv, C. Huang, G. Chen, and M. Li, "Instability mechanism and control technology of soft rock roadway affected by mining and high confined water," *International Journal of Mining Science and Technology*, vol. 25, no. 4, pp. 573–580, 2015.

[14] K.-B. Min, J. Rutqvist, C.-F. Tsang, and L. Jing, "Stress-dependent permeability of fractured rock masses: a numerical study," *International Journal of Rock Mechanics and Mining Sciences*, vol. 41, no. 7, pp. 1191–1210, 2004.

[15] J. Shao, F. Zhou, and W. Sun, "Evolution model of seepage characteristics in the process of water inrush in faults," *Geofluids*, vol. 2019, Article ID 4926768, 14 pages, 2019.

[16] Z. Tomanovic, B. Miladinovic, and S. Zivaljevic, "Criteria for defining the required duration of a creep test," *Canadian Geotechnical Journal*, vol. 52, no. 7, pp. 883–889, 2014.

[17] P. A. Witherspoon, J. S. Y. Wang, K. Iwai, and J. E. Gale, "Validity of cubic law for fluid flow in a deformable rock fracture," *Water Resources Research*, vol. 16, no. 6, pp. 1016–1024, 2010.

[18] W. A. M. Wanniarachchi, P. G. Ranjith, M. S. A. Perera, T. D. Rathnaweera, C. Zhang, and D. C. Zhang, "An integrated approach to simulate fracture permeability and flow characteristics using regenerated rock fracture from 3-d scanning: a numerical study," *Journal of Natural Gas Science and Engineering*, vol. 53, pp. 249–262, 2018.

[19] Y. Ye and G. Liu, "Porous seepage in calcirudite rock with 3-D stresses," *Journal-Tsinghua University*, vol. 47, no. 3, p. 335, 2007.

[20] C. Zhu, M. C. He, M. Karakus, X. H. Zhang, and Z. G. Tao, "Numerical simulations of the failure process of anaclinal slope physical model and control mechanism of negative Poisson's ratio cable," *Bulletin of Engineering Geology and the Environment*, vol. 80, pp. 3365–3380, 2021.

[21] D. Qiuhao, L. Xiaoli, W. Enzhi, and G. Cruciani, "Strength reduction of coal pillar after CO_2 sequestration in abandoned coal mines," *Minerals*, vol. 7, p. 26, 2017.

[22] A. Li, F. Dai, Y. Liu, H. B. Du, and R. C. Jiang, "Dynamic stability evaluation of underground cavern sidewalls against flexural toppling considering excavation-induced damage," *Tunnelling and Underground Space Technology*, vol. 112, Article ID 103903, 2021.

[23] T. H. Yang, P. Jia, W. H. Shi, P. T. Wang, H. L. Liu, and Q. L. Yu, "Seepage-stress coupled analysis on anisotropic characteristics of the fractured rock mass around roadway," *Tunnelling and Underground Space Technology*, vol. 43, pp. 11–19, 2014.

[24] M. D. Zoback and J. D. Byerlee, "The effect of microcrack dilatancy on the permeability of Westerly granite," *Journal of Geophysical Research*, vol. 80, no. 5, pp. 752–755, 1975.

[25] S. Zhang, S. F. Cox, and M. S. Paterson, "The influence of room temperature deformation on porosity and permeability in calcite aggregates," *Journal of Geophysical Research: Solid Earth*, vol. 99, no. B8, 15 pages, Article ID 15761, 1994.

[26] Y. Wang, W. K. Feng, R. L. Hu, and C. H. Li, "Fracture evolution and energy characteristics during marble failure under triaxial fatigue cyclic and confining pressure unloading (FC-CPU) conditions," *Rock Mechanics and Rock Engineering*, vol. 54, no. 2, pp. 799–818, 2021.

[27] Q. Wang, Q. Qin, B Jiang et al., "Mechanized construction of fabricated arches for large-diameter tunnels," *Automation in Construction*, vol. 124, Article ID 103583, 2021.

[28] J. Zhang, W. B. Standifird, J.-C. Roegiers, and Y. Zhang, "Stress-dependent fluid flow and permeability in fractured media: from lab experiments to engineering applications," *Rock Mechanics and Rock Engineering*, vol. 40, no. 1, pp. 3–21, 2007.

Research Article

Model for Calculating Seismic Wave Spectrum Excited by Explosive Source

Qian Xu [ID] **and Zhong-Qi Wang**

State Key Laboratory of Explosion Science and Technology, Beijing Institute of Technology, 100081 Beijing, China

Correspondence should be addressed to Qian Xu; chinaxuqian@126.com

To reveal the characteristics and laws of the seismic wavefield amplitude-frequency excited by explosive source, the method for computing the seismic wave spectrum excited by explosive was studied in this paper. The model for calculating the seismic wave spectrum excited by explosive source was acquired by taking the seismic source model of spherical cavity as the basis. The results of using this model show that the main frequency and the bandwidth of the seismic waves caused by the explosion are influenced by the initial detonation pressure, the adiabatic expansion of the explosive, and the geotechnical parameters, which increase with the reduction of initial detonation pressure and the increase of the adiabatic expansion. The main frequency and the bandwidth of the seismic waves formed by the detonation of the explosives in the silt clay increase by 23.2% and 13.6% compared to those exploded in the silt. The research shows that the theoretical model built up in this study can describe the characteristics of the seismic wave spectrum excited by explosive in a comparatively accurate way.

1. Introduction

Explosive is a common seismic source used for stimulating seismic waves artificially in seismic prospecting. It provides high-frequency and broad-frequency domain to achieve higher seismic resolution, aiming to satisfy the "smaller, thinner, and deeper" demands of seismic prospecting. Considering that the explosive source and the physical properties of the excitation medium have significant effects on seismic wave characteristics, the theoretical relationship between the explosive source and excitation medium parameters and the amplitude-frequency characteristics of the seismic waves can be established, thus to acquire the seismic waves satisfying the demands of seismic exploration by designing proper explosives excitation plan [1–6].

To study the seismic wave forming process induced by explosive source, Jeffreys et al. established a cavity vibration model in one-dimensional space, based on which a method for calculating the cavity size under spherical impact was given out [7–9]. Sharpe obtained the elastic wave analytical solution of the pressure on the wall of the spherical explosive cavity [10]. Targeting at the theoretical model of point-source explosion and based on the research of Sharpe, Blake et al. obtained the analytical solution of the elastic waves in the viscoelastic medium models of Duvall and Ricker [11–13]. Meanwhile, Sharpe also took the influences of the detonation pressure of explosive source and the seismic wave attenuation with the increase of spreading distance into consideration when making the model. The calculation results of the model were similar to the true seismic waveforms. However, for the model, the way of directly loading the detonation pressure on the cavity wall actually lacked consideration about the dynamic explosion process. Jiang [14] established the model, whose results of the calculation were compared with Blake's [11] model. For all these models, the impacts of the plastic regions on the seismic waves during the explosion process are simplified. Stevens et al. proposed the nonlinear model, which gave out a solution for explosive plastic regions [15–17]. These models can establish the relationship between explosives parameters and the seismic wave fields. However, since they all simplify the process that the explosive source excites the seismic

waves, it is impossible to establish the direct relationship between explosive source parameters and seismic wave field characteristics. Yu et al. improved the cavity source model for this problem, and established the theoretical model for the process that the explosive source excites the seismic wave field [18]. This method can be used to establish the cavity for explosive source, thus to describe the action process of the explosive source, the relationship between the initial parameters of the explosive source and the elastic wave field, and the whole-field seismic wave characteristics resulted by spherical explosives. However, these studies have not further studied the frequencies and bandwidths of the seismic waves.

Schenk and Červený studied the relationship between the density and proportion of sandy soil, and the frequency bandwidth of the seismic waves was formed during explosive detonation, based on which a fitting relationship model was acquired accordingly [19]. Through the test results of large-scale on-site tests, Wu studied the particle vibration velocity and its main frequency of the seismic waves formed by underground explosion at different positions. Wu et al. figured out, based on the above study, that the energy of high-frequency vibration attenuates sharply with the increase of distance [20]. Lin and Bai conducted time-frequency analysis on blasting vibration by the wavelet transform method, which provides a new method for the spectrum analysis of seismic waves [21]. Ling and Li analyzed the relationship between the explosive vibration band and the explosive source parameters by the wavelet method [22]. Stroujkova adopted on-site tests to analyze the seismic wave spectrum formed by different types of explosives and obtained the relationship between the low-frequency energy of the explosive seismic wave and the explosive expansion index [23]. It can be seen that the amplitude-frequency characteristics of the seismic waves are closely related to the explosive source parameters and the geotechnical medium parameters. However, these studies have not given a quantitative relationship between the seismic wave frequency characteristics and the explosive source and geophysical parameters.

If the relationship between the explosion characteristics and the amplitude-frequency of the seismic wave is established, the amplitude and frequency of the seismic waves can be controlled by selecting different types of explosives. To achieve goals of fine exploration and controlling of the seismic wave characteristics by changing the explosive source excitation plans, the model that explosive source excites amplitude-frequency characteristics of the seismic wave field must be established.

In this paper, the entire process in which the explosive source excites the seismic waves was analyzed firstly, and then, the theory that the spherical explosive source excites seismic wave field was described briefly, based on which the method for calculating the amplitude-frequency characteristics of the seismic wave field formed by explosive source was proposed accordingly. And, the applicability of this calculation model was verified through on-site experiments.

2. Creation of Seismic Wave

Explosive seismic wave is produced by the vibration of elastic cavity which is formed after medium blasting. At this stage, the seismic wave features are not related to the inelastic property of the medium. And, after being created, the seismic wave attenuates gradually with the increase of distance during the propagation process in geomaterial. Therefore, the study on frequency and amplitude rules of seismic wave field should be conducted from two perspectives: the creation of seismic wave and its propagation in medium.

The process from the explosives' detonation to the forming of seismic waves is accompanied with a series of chemical and physical changes. At the moment of blasting in geomaterial, the explosives produced abundant of gases with high velocity and pressure due to chemical reaction, which further formed the impact wave (Figure 1 (I)), directly applying on the geomaterial. Since the gas pressure is far greater than the geomaterial-confined deformation modulus, the geomaterial near the explosive source becomes liquefied under huge energy impact so that the blasting cavity can be deemed as the expansion in the incompressible fluid medium. With the development of the impact wave, the peak stress rapidly attenuates during the outwards propagation process. In this case, the impact wave converts into stress wave (Figure 1 (II) and (III)), the propagation velocity reduces sharply, and the elastic precursor with higher velocity than that of the failure wave can be separated and obtained from the plastic wave. The plastic wave peak and the wave velocity decrease with the increase of the propagation distance, but the elastic wave velocity remains unchanged. In this case, when the peak pressure of the stress wave decreases to below a certain value, the geomaterial would transform from the plastic state to the elastic state. Once the plastic wave disappears completely, the detonation wave completely turns to be an elastic wave (Figure 1 (IV)) at this moment, which is the seismic wave in general. The whole attenuation process of the blasting wave is as shown in Figure 1, in which y-direction refers to the changes of blasting wave pressure and x-direction refers to the one-dimensional detonation process.

The stress-strain curve in the geomaterial is as shown in Figure 2. The geomaterial state under the stress of the blasting wave can be divided into four parts. In the area close to the explosive, the blasting load stress is much greater than the confined deformation modulus of the geomaterial ($\sigma > \sigma_c$). And, at this time, the geomaterial shows hydrodynamic properties with the propagation of impact wave in medium, and the peak stress descends gradually. When the geomaterial stress exceeds the extreme geomaterial strength ($\sigma_c > \sigma > \sigma_b$), the geomaterial would exist in a broken form, the geomaterial deformation modulus ($d\sigma/d\varepsilon$) still enlarges with the increase of stress, and the impact wave shows the elastic wave and turns to the unsteady impact wave. Under the condition that the stress value further decreases but is still greater than the yield point ($\sigma_b > \sigma > \sigma_a$), the loading state evolves into a plastic state, having elastic-plastic waves. However, the geomaterial deformation modulus ($d\sigma/d\varepsilon$) at
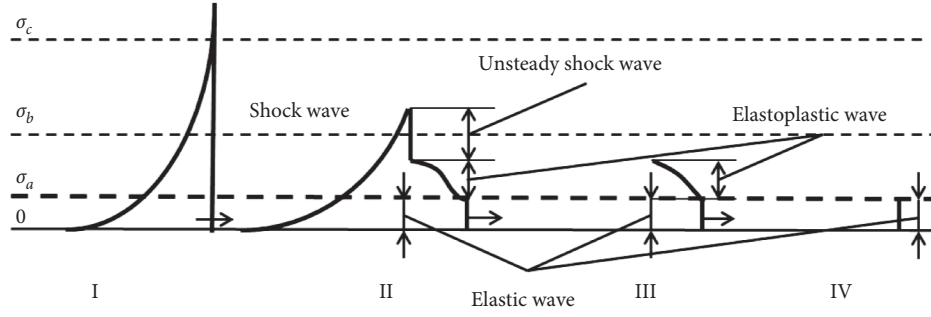
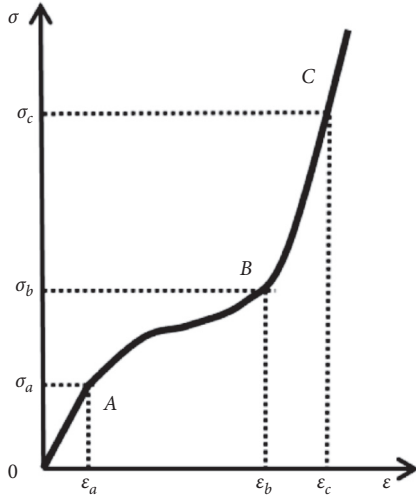FIGURE 1: Blasting wave evolution with the attenuation of the peak stress.

FIGURE 2: Stress-strain curve in the geomaterial.

that time decreases with the increase of stress. When the stress drops below the extreme elastic value ($\sigma < \sigma_a$), ($d\sigma/d\varepsilon$) is a constant while the stress wave exists in the form of the elastic wave. Therefore, in terms of energy transformation direction, the explosive source forms the blasting cavity area, inelastic area, and elastic area in sequence at the moment of explosion.

3. Analysis on Process of Explosive Source Exciting Seismic Waves

The spherical cavity seismic source model can be used to describe the relationship between the explosive source and the seismic wave field. For this model, it is supposed that when the explosion happens, the shock wave pressure excited by the explosive source for an instant would destroy the mediums in regions nearby. In the region adjacent to the explosive loading area, the energy released by explosion is far greater than the soil medium pressure and the geotechnical strength. The geomaterial shows fluid property under such high pressure. The soil medium particles will displace with the explosion shock wave, while the water and gas in the soil

medium will be extruded out, forming an explosion cavity. As the spread and attenuation in the excitable medium occur, the shock wave pressure would keep attenuating till it is below the breaking strength of the medium at position which is a certain distance away from the shocking source. However, the excitable medium still has the elastic property. Yu established the spherical satchel charge seismic wave field model under the assumption that the soil medium is not compressible, the explosion process and the cavity are formed for an instant, and the changes to the soil medium is neglected. Based on the above model, the spherical explosive blasting cavity radius and the plastic zone radius can be obtained accordingly.

The blasting cavity radius is

$$b_* = a_0 \left(\frac{P}{-(c/\varphi) + (\sigma_* + (c/\varphi))L^{4f/3(1+f)}} \right)^{1/3\gamma} \sqrt[3]{\frac{2\mu}{3\sigma_*}}, \quad (1)$$

where

$$L = \frac{\mu}{\sigma_* [1 + \ln(\sigma_*/\sigma_0)]}. \quad (2)$$

Plastic zone radius is

$$b_0 = \left(\frac{\sigma_*}{\sigma_0} \right)^{1/2} b_*, \quad (3)$$

where a_0 is the explosive radius, P is the initial blasting pressure of the explosive, γ is the adiabatic expansion, φ is the cohesion of the soil medium, c is the internal friction angle of soil medium, σ_* is the compressive strength of the soil medium, σ_0 is the tensile strength of the soil medium, and μ is the lame coefficient.

Introduce the linear radial strain and hoop strain, and simply the motion equation as follows:

$$\frac{\partial^2 u}{\partial r^2} + \frac{2}{r} \frac{\partial u}{\partial r} - 2 \frac{u}{r^2} = \frac{1}{c^2} \frac{\partial^2 u}{\partial t^2}. \quad (4)$$

The solution of this equation can describe the forced vibration of the particle under viscous damping, and its general form is

$$U(r,t) = e^{(-\eta^2\tau/\rho_{\text{soil}}cb_*)}\left[\left(\frac{Pb_*^2c}{\eta\kappa r^2} - \frac{\eta Pb_*}{\kappa\rho_{\text{soil}}cr}\right)\sin\frac{\eta\kappa\tau}{\rho_{\text{soil}}cb_0} + \frac{Pb_*}{\rho_{\text{soil}}cr}\cos\frac{\eta\kappa\tau}{\rho_{\text{soil}}cb_0}\right], \tag{5}$$

where

$$\eta^2 = \frac{2(1-2\sigma)\rho_{\text{soil}}c^2 + 3(1-\sigma)\gamma P}{2(1-\sigma)},$$

$$\kappa^2 = \frac{2\rho_{\text{soil}}c^2 - 3(1-\sigma)\gamma P}{2(1-\sigma)}, \tag{6}$$

$$\tau = t - \frac{r - b_0}{c}.$$

Seismic exploration analyzes the spectral characteristics of seismic waves from the perspectives of main frequency and bandwidth. Schenk proposed to use the mean value of the frequency at which the 0.7-times vibration amplitude value is located as the main frequency of the vibration signal, that is, $f = ((f_2 + f_1)/2)$, bandwidth $f_a = f_2 - f_1$, where f_2 and f_1 are, respectively, the frequencies at which 0.7 times of maximum vibration amplitude is located. To analyze the spectral characteristics of seismic signals, the Fourier transform can be used to quickly process time-domain signals and convert them into frequency-domain signals.

The motion velocity field of the particle of the seismic waves excited by the spherical explosive source is simplified as

$$U(t) = e^{-at}(A\cos(\omega_0 t) + B\sin(\omega_0 t)), \tag{7}$$

where

$$a = -\frac{\eta^2}{\rho_{\text{soil}}cb_*},$$

$$A = \frac{Pb_*^2c}{\eta\kappa r^2} - \frac{\eta Pb_*}{\kappa\rho_{\text{soil}}cr},$$

$$B = \frac{Pb_*}{\rho_{\text{soil}}cr}, \tag{8}$$

$$\omega_0 = \frac{\eta\kappa}{\rho_{\text{soil}}cb_*}.$$

Conduct the Fourier transform to formula (7):

$$F(\omega) = \int_0^\infty e^{-at}(A\cos(\omega_0 t) + B\sin(\omega_0 t)) \cdot e^{-i\omega t}\mathrm{d}t. \tag{9}$$

That is,

$$F(\omega) = \frac{\sqrt[2]{A^2 + B^2}\,\omega_0}{(a + i\omega)^2 + \omega_0^2}. \tag{10}$$

The velocity spectrum is

$$|F(\omega)| = \left|\frac{\sqrt[2]{A^2 + B^2}\,\omega_0}{(a + i\omega)^2 + \omega_0^2}\right|, \tag{11}$$

$$|F(\omega)| = \frac{\sqrt[2]{A^2 + B^2}\,\omega_0}{\sqrt{(a^2 - \omega^2 + \omega_0^2)^2 + 4a^2\omega^2}}. \tag{12}$$

4. Discussion

According to formula (12), it can be deemed that a and ω_0 are the main parameters affecting the spectral characteristics of the vibration at the elastic wave radius. In order to analyze the relationship between bandwidth and the parameters of a and ω_0, normalization was conducted to vibration amplitude, based on which it could be seen that when ω_0 was maintained unchanged and a increased from 50 to 150, the main frequency had no change, while the bandwidth increased from 25 Hz to 35 Hz; when ω_0 increased from 50 to 100, the main frequency of the seismic waves increased from 50 Hz to 165 Hz, while the bandwidth was remained unchanged. The laws of changes are as shown in Figure 3. This means that a affects the bandwidth, and the greater the a, the wider the bandwidth; ω_0 affects the main frequency, and the greater the ω_0, the higher the main frequency. Since a and ω_0 are closely related to explosive parameters and geotechnical medium parameters, it is necessary to analyze the influences of each explosive parameter and geotechnical medium parameter on the seismic wave frequency spectrum.

4.1. The Influences of Explosive Source Parameters on Amplitude-Frequency Characteristics. It can be figured out from formulas (1), (5), and (12) that the explosive parameters of detonation velocity D, initial detonation pressure P_0, and explosion adiabatic expansion γ will affect the seismic wave amplitude-frequency characteristics. In order to analyze the impacts of detonation velocity D and explosion adiabatic expansion γ on the amplitude-frequency characteristics of seismic waves in detail, the excitation of the explosive source in the geomaterial was taken as the basic data to verify the parameters in this paper. The explosive source is 1 kg TNT, and the geomaterial medium is silt clay. For the detailed parameters of TNT and silt clay, please refer to Tables 1 and 2.

Substitute data of Tables 1 and 2 into formulas (1), (3), (5), and (12), respectively, the data of detonation pressure, cavity, elastic area radius, and particle vibration velocity frequency and bandwidth at the elastic radius part, which are excited by the explosion of spherical explosive source in silt clay, can be obtained accordingly. In order to study the influencing laws of explosive source parameter changes on the amplitude-frequency characteristics, only a single parameter was changed while all others were maintained unchanged during the calculation process. Figures 4–9 show
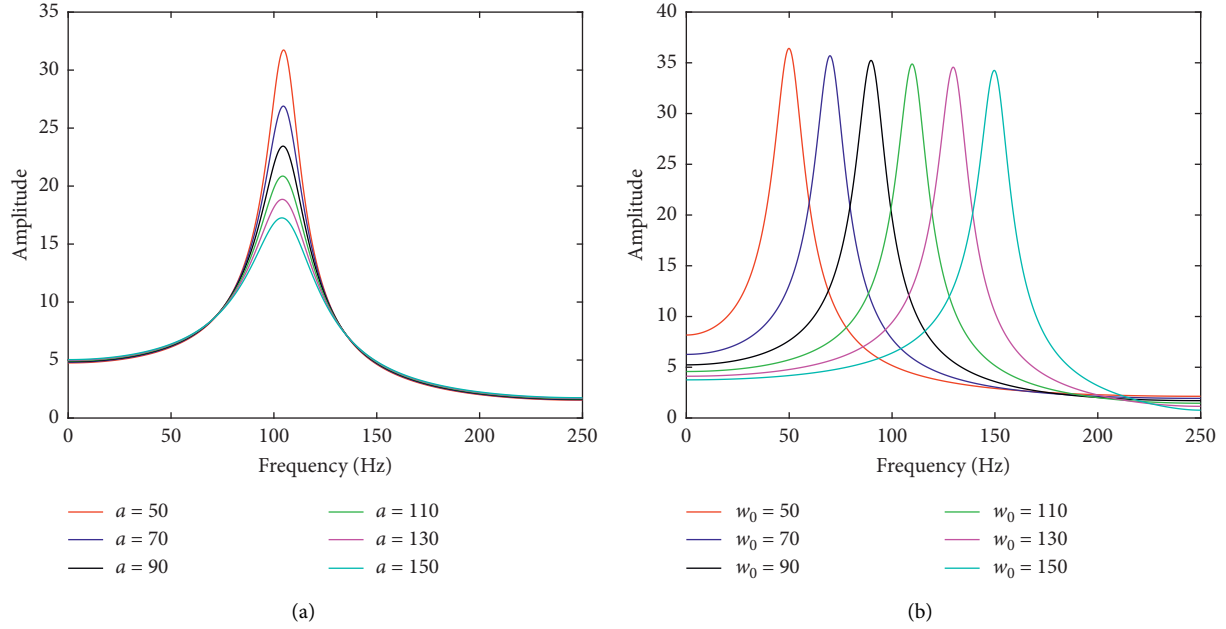
FIGURE 3: The influencing laws of a and ω_0 on the amplitude and frequency of seismic waves.

the changes of the amplitude-frequency characteristics of the seismic wave which was formed with the changes in the initial detonation pressure, adiabatic expansion, and geotechnical parameters of the explosive.

According to the research of Henrych, the detonation pressure range of conventional explosives is 5–10 GPa. In the prediction model, the detonation pressure was set to be 4, 8, and 12 GPa, and other parameters were maintained as shown in Tables 1 and 2. Figure 4 shows the frequency spectrum of the seismic wave changing with the initial detonation pressures: with the initial detonation pressure increases, the frequency of the seismic wave decreases and the frequency band becomes narrower. The size and wall pressure of the explosion cavity after the detonation is also closely related to the initial detonation pressure. The increase of the initial detonation pressure leads to an increase in the stress that the explosive source applied to the geomaterial medium at the time of detonation, thereby forming larger cavity. The greater the detonation cavity, the lower the cavity wall pressure. The enlargement of cavity size reduces the particle vibration frequency. When the initial detonation pressure increases from 4 GPa to 12 GPa, the main frequency decreases from 306.4 Hz to 240.6 Hz, and the bandwidth attenuates from 440 Hz to 350 Hz.

The adiabatic expansion of the explosives is the parameter characterizing the attenuation of the maximum stress state of the high pressure gas caused by explosion. The greater the index, the faster the attenuation. Opjiehko figured out based on the relative research that the adiabatic expansion of conventional explosives is from 1.5–3.5. In the prediction model, the adiabatic expansion was set to be 1.5, 2.5, and 3.5, respectively, while all other parameters were maintained as shown in Tables 1 and 2. Figure 5 shows the impacts of adiabatic expansion changes

TABLE 1: Parameters of TNT.

ρ (kg·m^{-3})	D (m·s^{-1})	P_0 (GPa)	γ
1650	6930	9.82	3.15

TABLE 2: Parameters of soil.

σ_* (MPa)	σ_0 (MPa)	μ (GPa)	ρ_{soil} (kg·m^3)	K (MPa)	q
13	2	0.147	1840	245	2

on amplitude-frequency characteristics of the seismic waves. With the increase of the adiabatic expansion, the main frequency of the seismic wave enlarges and the bandwidth broadens. When the adiabatic expansion increases, the velocity of blasting pressure attenuation increases, the detonation cavity size reduces, and the seismic wave frequency increases. When the adiabatic expansion increased from 1.5 to 3.5, the main frequency of the seismic waves increased from 185 Hz to 350 Hz, while the bandwidth increased from 250 Hz to 510 Hz.

To increase the frequency and bandwidth of the explosive seismic waves, explosives having larger adiabatic expansion and higher detonation pressure can be considered to increase frequency while guaranteeing no reduction of energy. Meanwhile, adding volume of explosive can increase the bandwidth and enhance the proportion of low-frequency signals and reduce the energy dispersion of the seismic waves when spreading in the geomaterial medium. This is conductive for prospecting in deeper stratum.

4.2. Impacts of Geomaterial Parameters on Amplitude-Frequency Characteristics.
By referring to the method of analyzing the impacts of explosive source parameters on seismic
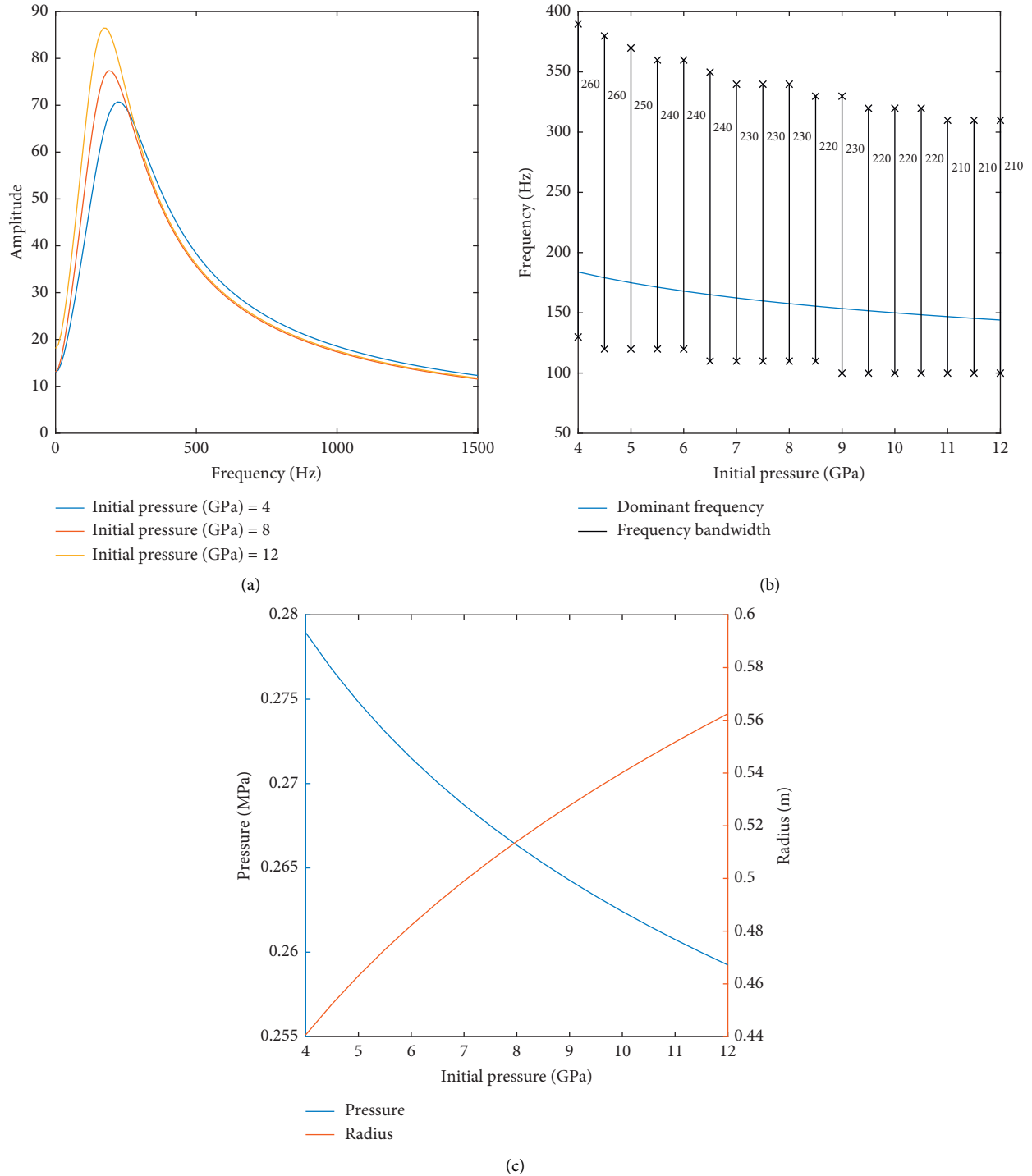
Figure 4: Impacts of initial detonation pressure changes on seismic wave frequency at elastic radius position. (a) Impacts of initial detonation pressure on velocity and frequency-amplitude characteristics of particle vibration. (b) Impacts of initial detonation pressure on velocity, main frequency, and bandwidth of particle vibration. (c) Impacts of initial detonation pressure on detonation cavity and its internal pressure.

wave spectrum, the way of changing a single parameter was adopted to analyze the impacts of geomaterial parameters on seismic waves formed by the explosive source. Among geomaterial parameters, the part having close relationship with amplitude-frequency characteristics of the seismic waves include density ρ_{soil}, compressive strength σ_* (Figure 6),

tensile strength σ_0 (Figure 7), Lame coefficient μ (Figure 8), and shear modulus G (Figure 9).

When the compressive strength of the geomaterial increases, the frequency of the seismic waves increases, the detonation volume reduces, and the frequency of the seismic waves increases. When the compressive strength of the

(a)

(b)

(c)
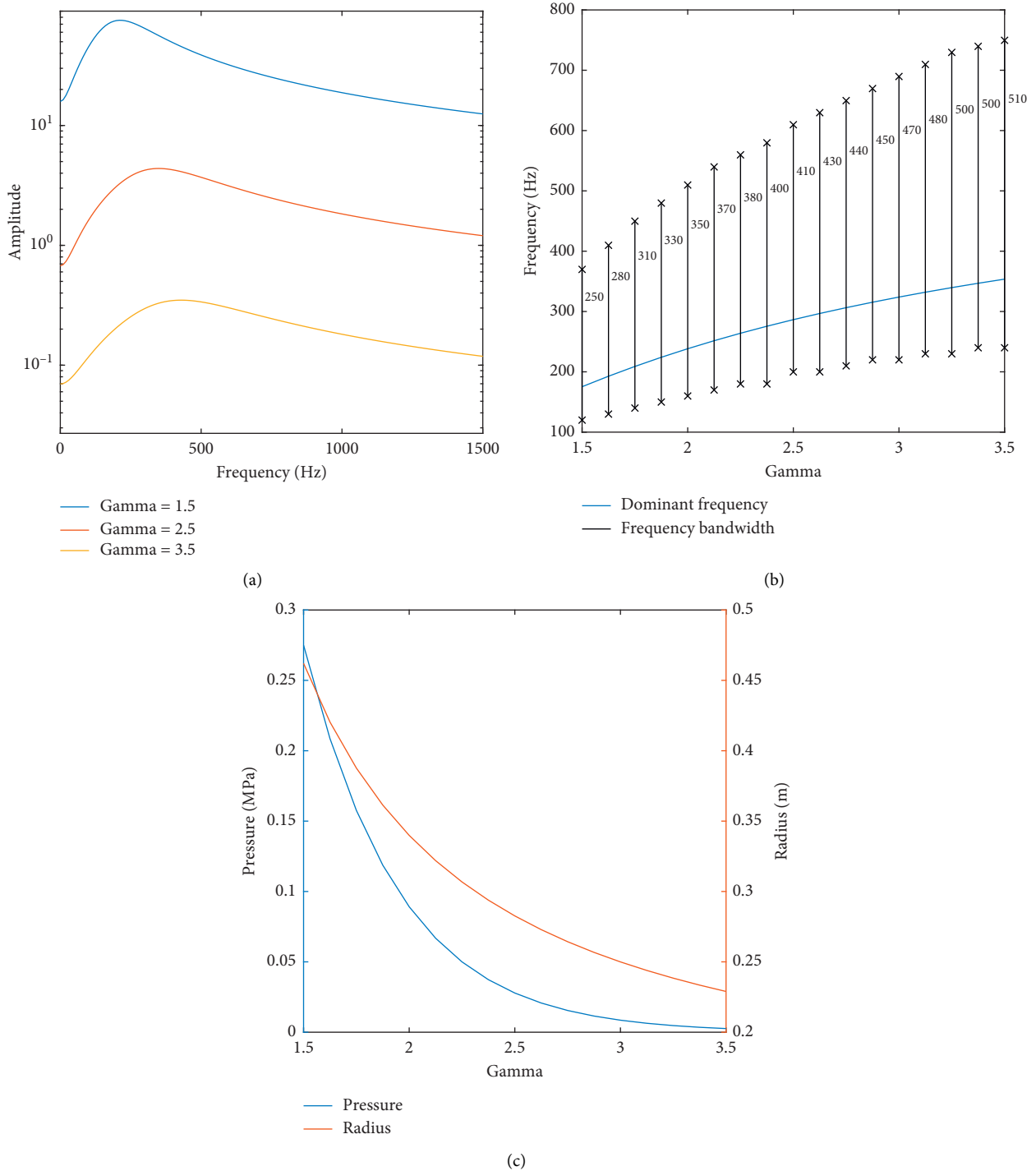
FIGURE 5: Impacts of adiabatic expansion changes on seismic wave frequency. (a) Impacts of adiabatic expansion on velocity and frequency-amplitude characteristics of seismic wave. (b) Impacts of adiabatic expansion on velocity, main frequency, and bandwidth of particle vibration. (c) Impacts of adiabatic expansion on detonation cavity and its internal pressure.

geomaterial increased from 6 MPa to 20 MPa, the main frequency of the seismic waves enlarged from 147 Hz to 252 Hz, while the bandwidth increased from 200 Hz to 320 Hz.

According to the analysis of Section 2, the spherical satchel charge would leave spherical detonation cavity in the homogeneous medium after explosion. The stress on radial direction on the cavity wall and the geomaterial compressive strength are in a balanced status; the stress on circumferential direction and the geomaterial tensile strength are in a balanced status. This is the result of co-action of tensile strength and compressive strength. Therefore, the laws of tensile strength influencing the amplitude-frequency characteristics of seismic waves are similar to those of the compressive strength. The greater

(a)

(b)

(c)

Figure 6: Impacts of geomaterial compressive strength on amplitude-frequency characteristics of seismic waves. (a) Impacts of geomaterial compressive strength on velocity and frequency-amplitude characteristics of particle vibration. (b) Impacts of geomaterial compressive strength on velocity, main frequency, and bandwidth of particle vibration. (c) Impacts of geomaterial compressive strength on detonation cavity and its internal pressure.

(a)

(b)

(c)
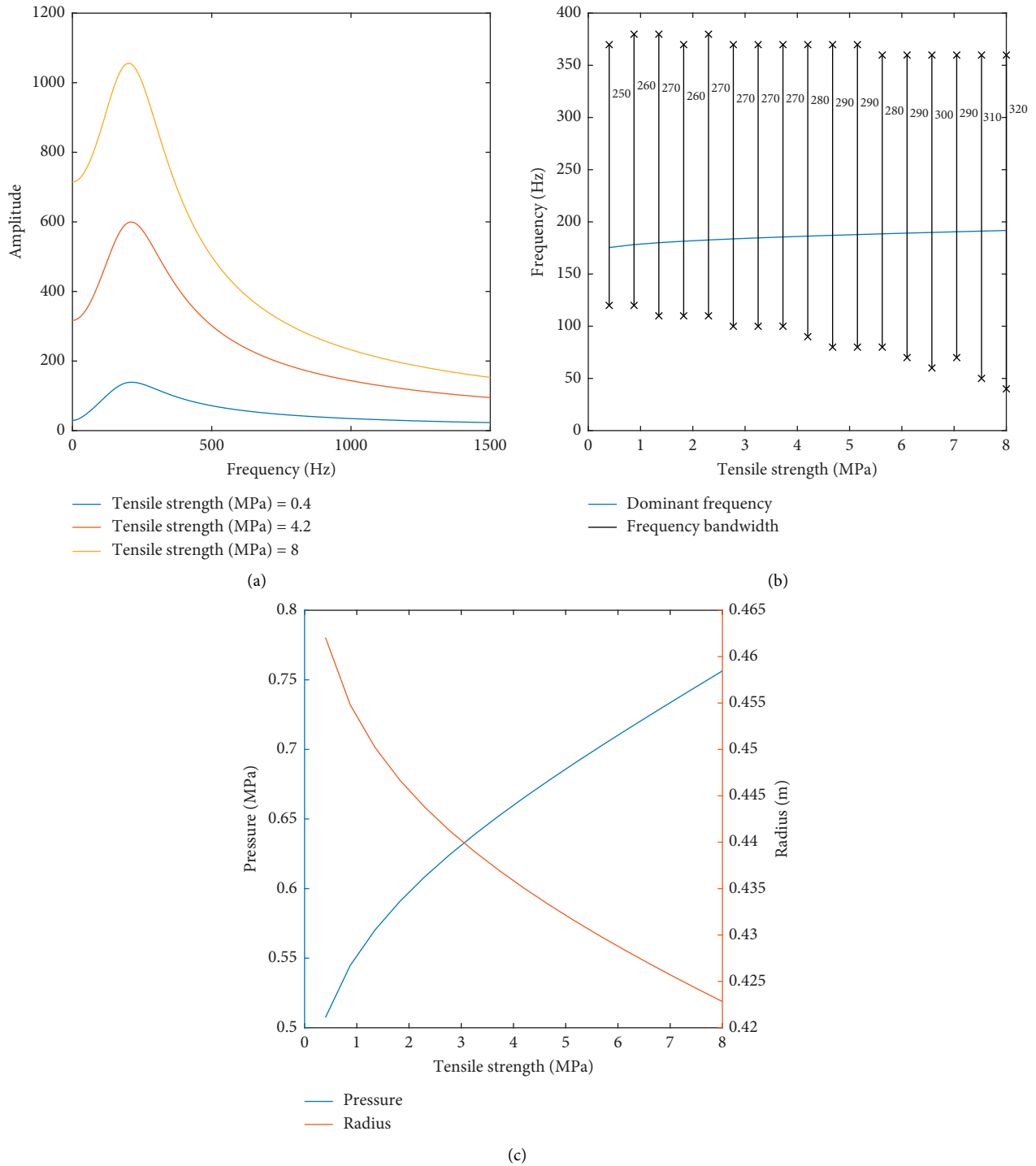
FIGURE 7: Impacts of geomaterial tensile strength on amplitude-frequency characteristics of seismic waves. (a) Impacts of geomaterial tensile strength on velocity and frequency-amplitude characteristics of particle vibration. (b) Impacts of geomaterial tensile strength on velocity, main frequency, and bandwidth of particle vibration. (c) Impacts of geomaterial tensile strength on detonation cavity and its internal pressure.

the compressive strength, the smaller the detonation cavity (Figure 8(c)) and larger the seismic wave frequency. When the tensile strength of the geomaterial increased from 0.4 MPa to 8 MPa, the main frequency of the seismic waves enhanced from 175 Hz to 190 Hz, while the bandwidth increased from 250 Hz to 320 Hz.

The greater the Lame Coefficient, the larger the detonation radius and the lower the seismic wave frequency. When the geomaterial Lame Coefficient increased from 0.2 GPa to 0.4 GPa, the main frequency of the seismic wave decreased from 175 Hz to 149 Hz and the bandwidth decreased from 250 Hz to 210 Hz.

(a)

(b)

(c)
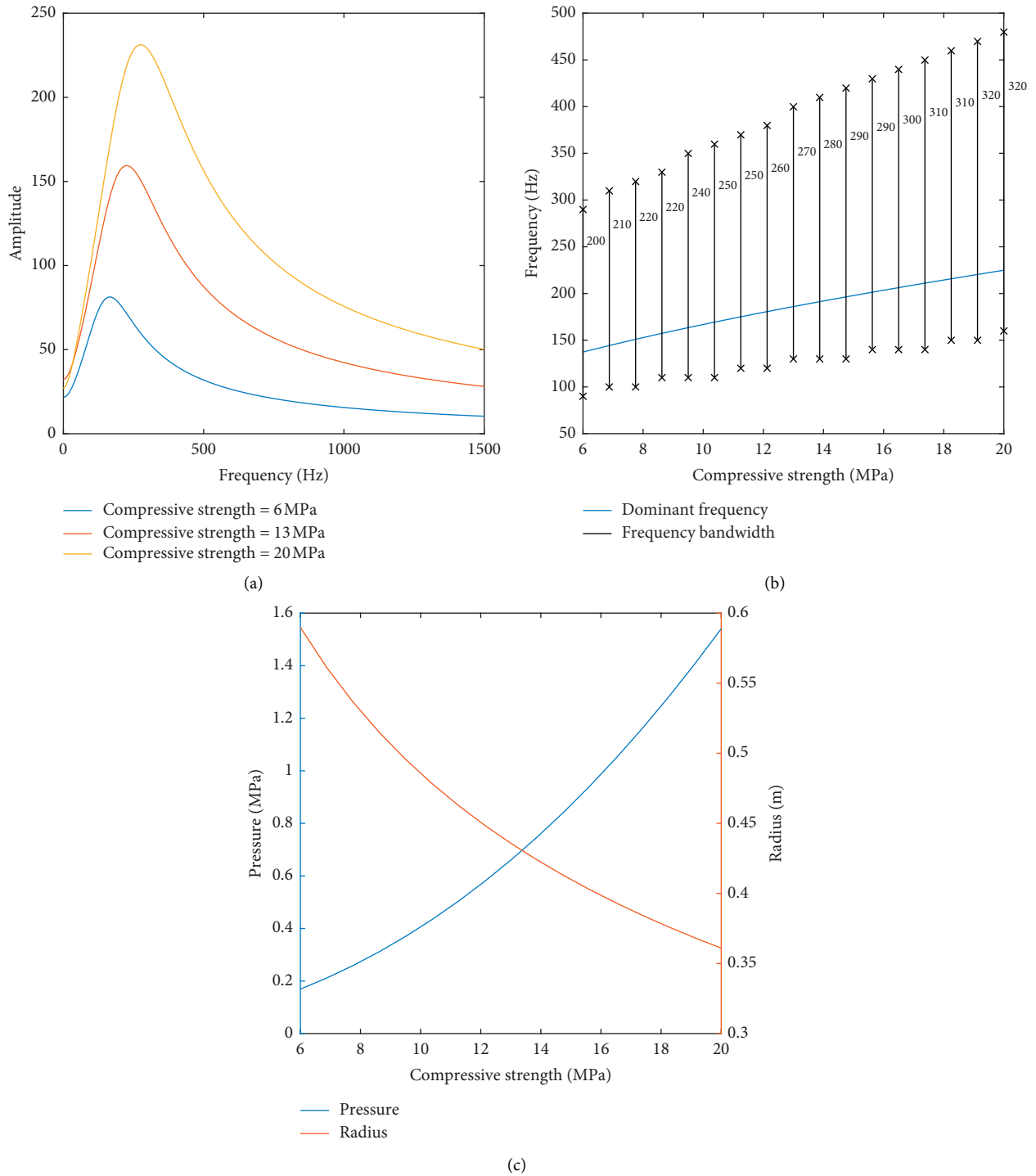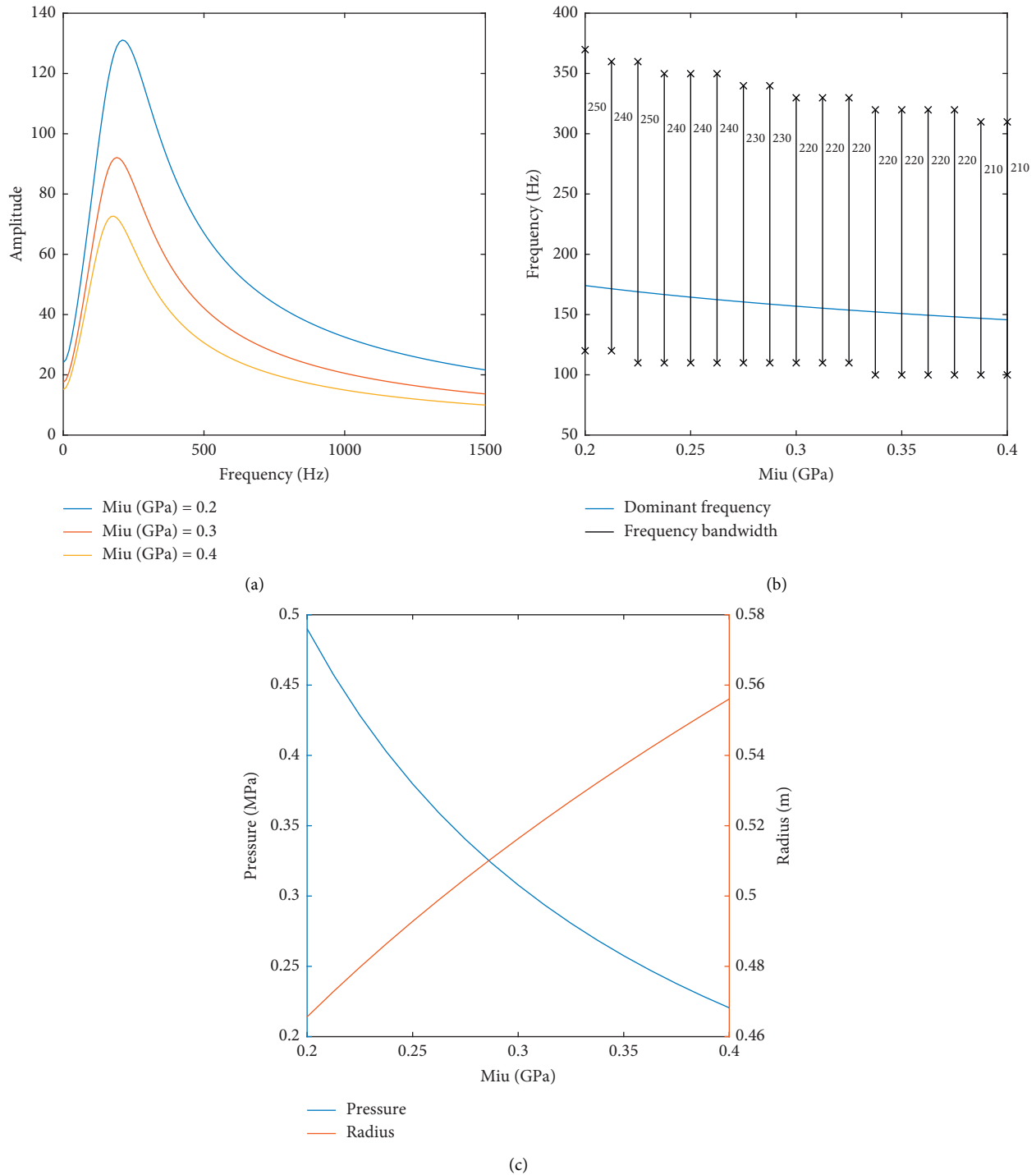
Figure 8: Impacts of geomaterial Lame coefficient on amplitude-frequency characteristics of seismic waves. (a) Impacts of geomaterial Lame coefficient on velocity and amplitude-frequency characteristics of particle vibration. (b) Impacts of geomaterial Lame coefficient on velocity, main frequency, and bandwidth of particle vibration. (c) Impacts of geomaterial Lame coefficient on detonation cavity and its internal pressure.

Although the longitudinal wave velocity of the geomaterial affects the mechanics parameters, it has nothing to do with the geomaterial strength. So, the wave velocity changes will not change the detonation cavity and its internal pressure. Under the same stress conditions, the greater the geomaterial wave velocity, the larger the elastic modulus. Under the same stress conditions, it results in smaller particle strain, shorter time required for particle rebound, and shorter vibration period,

(a)

(b)

(c)
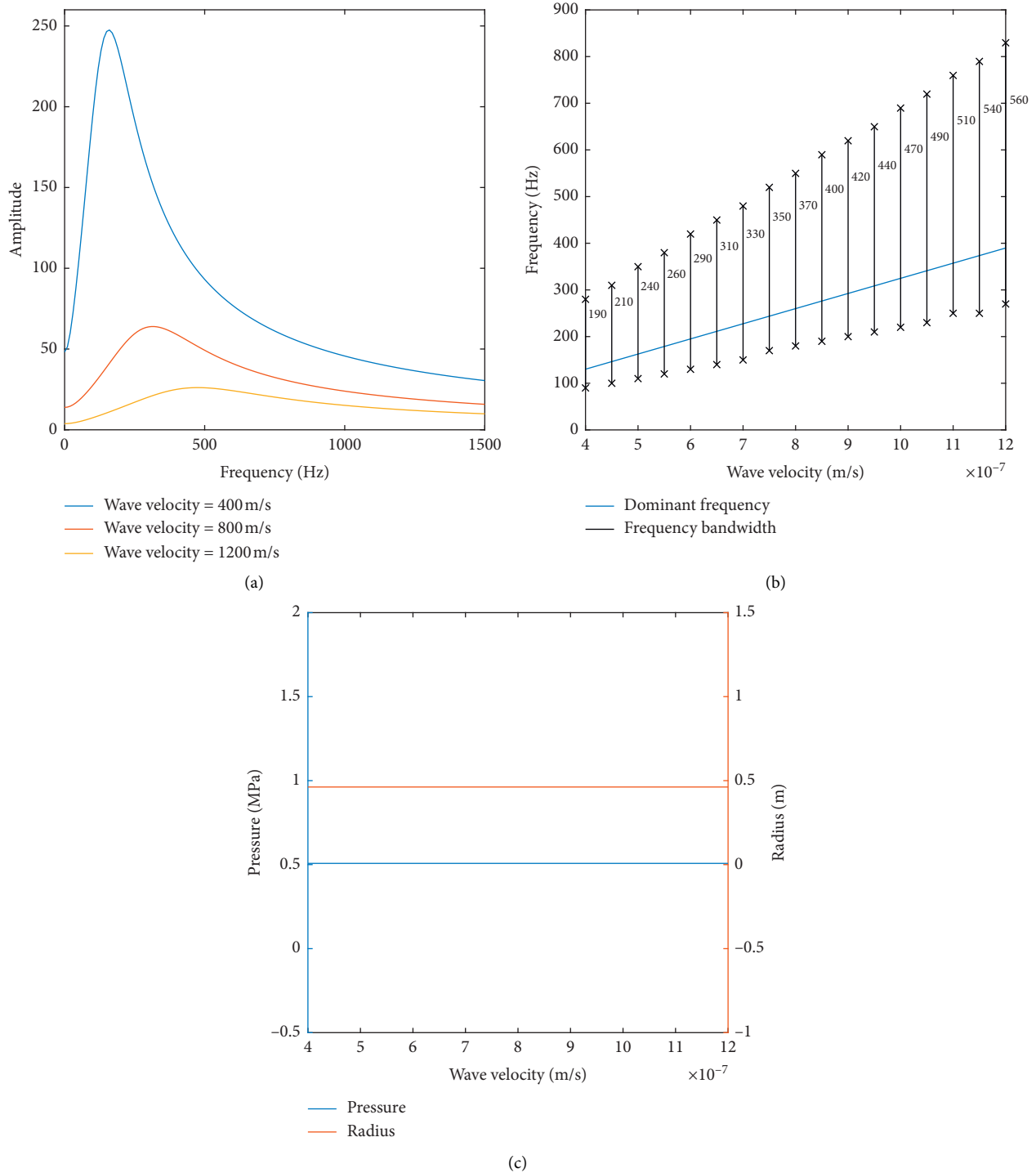
Figure 9: Impacts of wave velocity of geomaterial on amplitude-frequency characteristics parameters of seismic waves. (a) Impacts of wave velocity of geomaterial on velocity and amplitude-frequency characteristics of particle vibration. (b) Impacts of wave velocity of geomaterial on velocity, main frequency, and bandwidth of particle vibration. (c) Impacts of wave velocity of geomaterial on detonation cavity and its internal pressure.

but increased vibration frequency. Therefore, the greater the wave velocity in geomaterial, the higher the frequency of seismic waves. When the wave velocity increased from 400 m/s to 1200 m/s, the main frequency of the seismic wave increased from 130 Hz to 390 Hz, while the bandwidth increased from 190 Hz to 560 Hz.

4.3. Experimental Results' Comparison. The on-site experiment was conducted to verify the model for calculating spectrum of seismic waves excited by the explosive source. In the experiment, the AN-TNT, AN-TNT-AL, and AP-RDX-AL-G were used as seismic sources. The explosives were embedded 12 m below the ground surface. For all explosives,
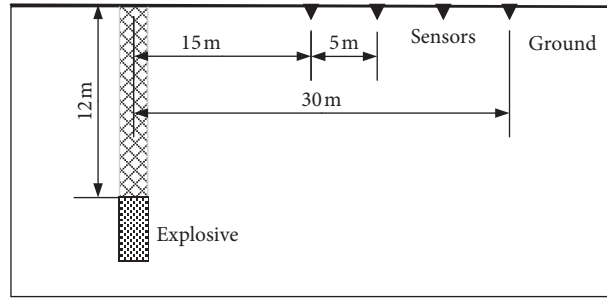
Figure 10: Layout plan of geophones.

Table 3: Initial detonation pressures and adiabatic expansion indexes of four explosives.

Explosive	Detonation pressure (GPa)	Adiabatic expansion index
AN-TNT	8.98	3.00
AN-TNT-AL	8.94	2.49
AP-RDX-AL-G	9.82	2.35
Emulsion	9.81	2.30

Table 4: Geomaterial parameters.

Geomaterials	σ_* (MPa)	σ_0 (MPa)	μ (GPa)	F	K (kPa)	ρ_{soil} (kg/m^3)	σ
Silt	6.2	0.8	0.09	0.38	25	1400	0.25
Silt clay	11.6	2	0.16	0.2	50	1600	0.25
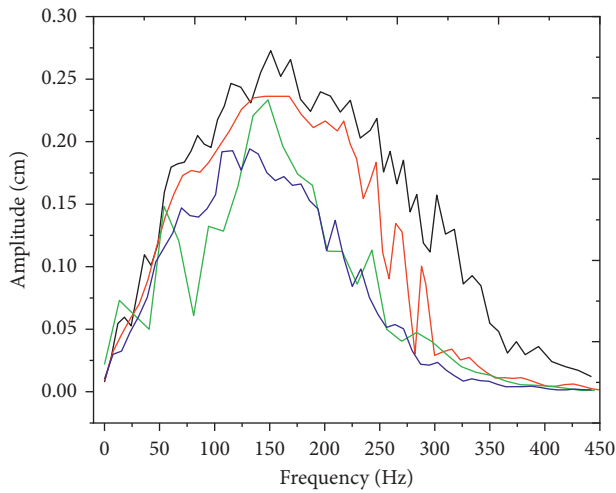
(a)
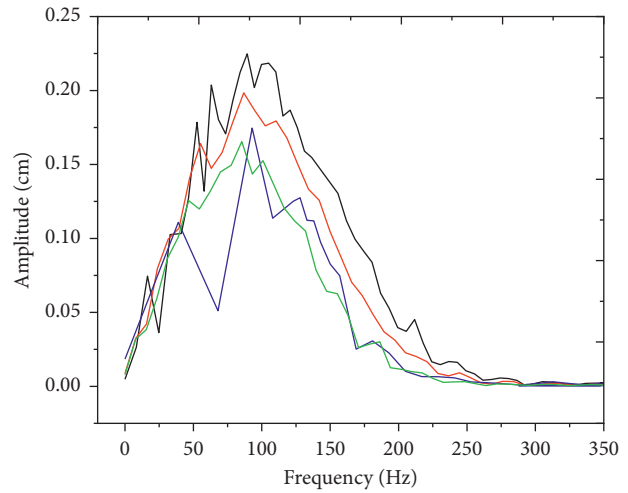
(b)

Figure 11: Continued.

(c)

(d)
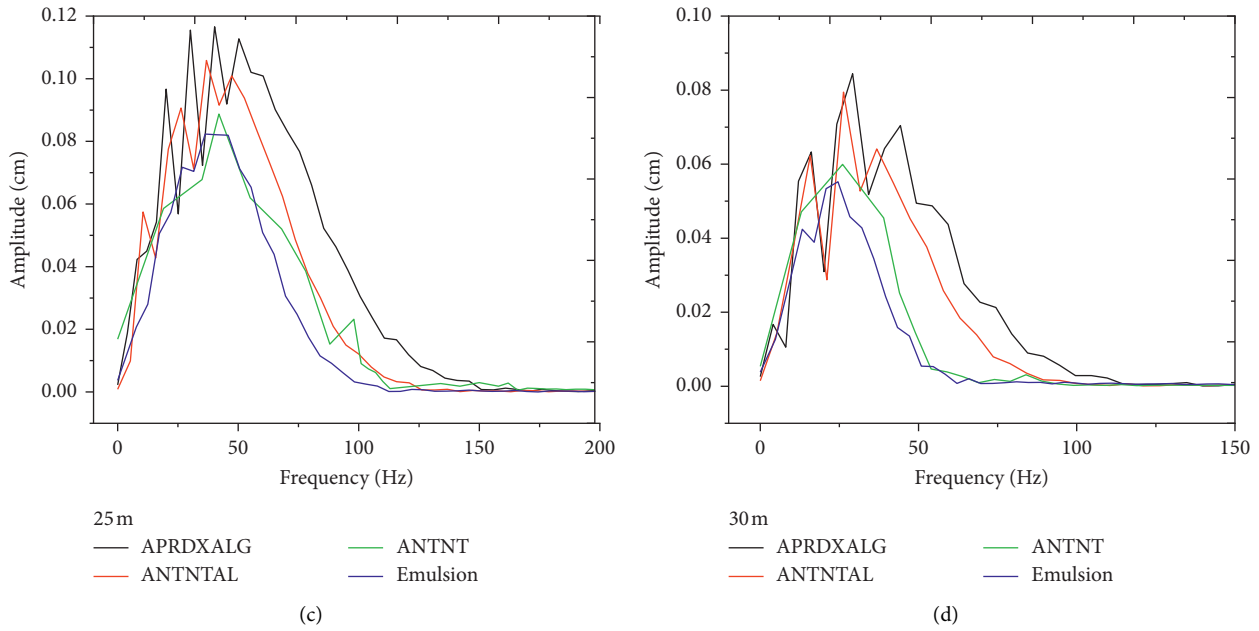
Figure 11: Spectrum of seismic waves excited by different explosives at different distances in geomaterials. (a) Spectrum comparison at 15 m position. (b) Spectrum comparison at 20 m position. (c) Spectrum comparison at 25 m position. (d) Spectrum comparison at 30 m position.

(a)

(b)
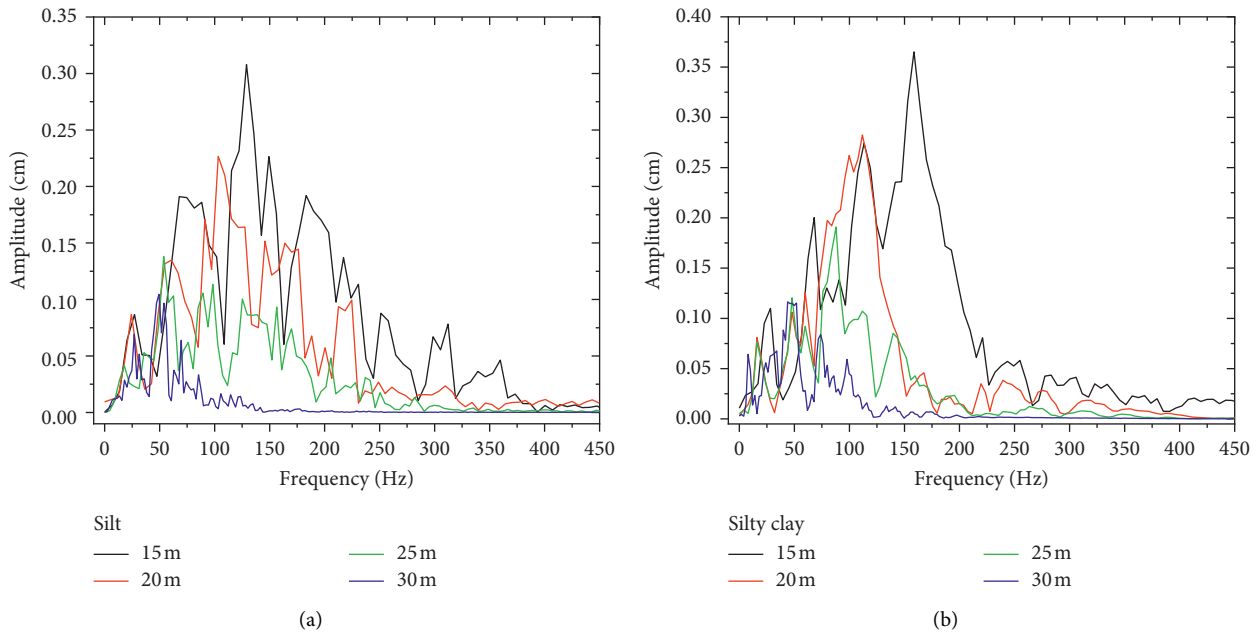
Figure 12: Spectrum comparison of seismic waves excited at different positions in different geomaterials. (a) Spectrum comparison of seismic waves excited in silt. (b) Spectrum comparison of seismic waves excited in silt clay.

the quantity of 4 kg was adopted. The sensors were embedded in 0.3 m depth with 5 m horizontal interval. And, for the deployment of the geophones, see Figure 10. The seismic waves were recorded by the 428XL digital seismograph produced by the French Sercel company. The adiabatic expansion index and the detonation pressure are as shown in Table 3. And, the geomaterial parameters are as shown in Table 4.

It can be figured out from Figure 11 that the seismic wave frequency excited by explosive with high detonation pressure is lower than the seismic wave frequency excited by conventional explosives, among which the AP-RDX-AL-G formed maximum seismic wave frequency, followed by AN-TNT-AL explosive. Besides, the AN-TNT and AN-TNT-AL showed basically the same initial detonation pressures, but the later's adiabatic expansion index is 25% higher than that

of the former, and the frequency of the later is significantly higher than that of the former, showing 11.1% main frequency increase and 9.38% increase of bandwidth. The experiment results have proved the correctness of the theoretical model, and explosives with low detonation pressure and low adiabatic expansion index excite seismic waves with higher frequency and broader bandwidth.

According to Figure 12, which shows the comparison results of the spectrum of the seismic waves excited in different geomaterials, the main frequency of the seismic wave excited in the silt clay is, respectively, 23.2%, 8.7%, 38.5%, and 10.74% higher at four positions of 15 m, 20 m, 25 m, and 30 m compared to those seismic waves excited in the silt. No matter whether it is geomaterial strength or Lame Coefficient, the silt clay is better than the silt and can excite better seismic wave. This is in line with the results obtained by the theoretical model. Therefore, in practical engineering, the explosive source excitation can be conducted in silt clay or clay instead of silt.

5. Conclusions

In order to make clear the relationship between the explosive source and the amplitude-frequency characteristics of the seismic wave, the model for predicting the seismic wave spectrum excited by the explosive source was established in this paper, which overcomes the problems that the explosive source model cannot describe the explosive source parameters quantitatively, and the geomaterial parameters have insufficient impacts on the seismic wave spectrum excited by explosives, providing theoretical basis for guiding the fine exploration and production.

This model was applied to analyze the impacts of explosive source parameters on the seismic wave spectrum. The results show that when the initial detonation pressure of the explosive increased from 4 GPa to 12 GPa, the main frequency of the seismic waves decreased from 64.1 Hz to 52.3 Hz, while the bandwidth attenuated from 62 Hz to 48 Hz; when the adiabatic expansion increased from 1.5 to 4.5, the main frequency of seismic waves increased from 65.7 Hz to 124.7 Hz, while the bandwidth increased from 55 Hz to 132 Hz. Lower initial detonation pressure and higher adiabatic expansion can effectively increase the seismic wave frequency and frequency bandwidth, thereby improving seismic exploration resolution and facilitating the detection towards deeper stratum. When the geomaterial compressive strength increased from 6 MPa to 20 MPa, the main frequency of the seismic waves increased from 147 Hz to 252 Hz, and the bandwidth increased from 200 Hz to 320 Hz. When the geomaterial tensile strength increased from 0.4 MPa to 8 MPa, the main frequency of the seismic waves enhanced from 175 Hz to 190 Hz, and the bandwidth increased from 250 Hz to 320 Hz. When the Lame coefficient increased from 0.2 GPa to 0.4 GPa, the main frequency of the seismic waves increased from 175 Hz to 149 Hz and the bandwidth increased from 250 Hz to 210 Hz. When the wave velocity increased from 400 m/s to 1200 m/s, the main frequency of the seismic waves increases from 130 Hz to 390 Hz, and the bandwidth increased from 190 Hz to 560 Hz.

The results indicate that the explosive source may excite higher seismic wave frequency and bandwidth in harder geomaterial.

In addition, on-site experiment was carried out to verify the prediction model. The detonation pressure decrease and adiabatic expansion increase of the explosives can lead to increases of the amplitude, frequency, and bandwidth. Moreover, it was also figured out from the experiment that compared to the seismic waves excited in silt, the main frequency of seismic waves excited in silt clay increased by 23.2%, 8.7%, 38.5%, and 10.74% at four positions of 15 m, 20 m, 25 m, and 30 m, while the bandwidth increased by 13.6%, 10.7%, 8.76%, and 14.3%, respectively. The experimental results show that the spectrum calculation model can describe the seismic spectrum characteristics excited by explosive blasting, which provides theoretical foundation for guiding the fine prospecting and production.

It should be noted that the prediction model in the paper simplifies the geomaterial parameters in order to quickly predict the seismic wave spectrum. However, the simplified parameters may affect the calculation of seismic wave frequency, for example, the explosion effects may result in density changes of mediums near the seismic source. Besides, the attenuation effect of seismic wave in geomaterial could also affect the amplitude-frequency characteristics of the entire seismic wave field. These factors need to be further studied in the future.

Data Availability

The data used to support the findings of the study are available within the article.

Conflicts of Interest

The authors declare that they have no conflicts of interest.

Acknowledgments

References

[1] Q. Wang, Z. Jiang, B. Jiang, H. Gao, Y. Huang, and P. Zhang, "Research on an automatic roadway formation method in deep mining areas by roof cutting with high-strength bolt-grouting," *International Journal of Rock Mechanics and Mining Sciences*, vol. 128, Article ID 104264, 2020.

[2] B. Li, R. Bao, Y. Wang, R. Liu, and C. Zhao, "Permeability evolution of two-dimensional fracture networks during shear under constant normal stiffness boundary conditions," *Rock Mechanics and Rock Engineering*, vol. 54, no. 3, pp. 1–20, 2021.

[3] Q. Wang, M. He, S. Li et al., "Comparative study of model tests on automatically formed roadway and gob-side entry driving in deep coal mines," *International Journal of Mining Science and Technology*, 2021, In press.

[4] C. Zhu, M.-c. He, M. Karakus, X.-h. Zhang, and Z. Guo, "The collision experiment between rolling stones of different shapes and protective cushion in open-pit mines," *Journal of Mountain Science*, vol. 18, no. 5, pp. 1391–1403, 2021.

[5] A. Li, F. Dai, Y. Liu, H. Du, and R. Jiang, "Dynamic stability evaluation of underground cavern sidewalls against flexural toppling considering excavation-induced damage," *Tunnelling and Underground Space Technology*, vol. 112, Article ID 103903, 2021.

[6] L. Ban, C. Zhu, C. Qi, and Z. Tao, "New roughness parameters for 3D roughness of rock joints," *Bulletin of Engineering Geology and the Environment*, vol. 78, no. 6, pp. 4505–4517, 2019.

[7] H. Jeffreys, "On the cause of oscillatory movement in seismograms," *Geophysical Journal International*, vol. 2, no. 2, pp. 407–416, 1931.

[8] Q.-X. Meng, W.-Y. Xu, H.-L. Wang, X.-Y. Zhuang, W.-C. Xie, and T. Rabczuk, "DigiSim—an open source software package for heterogeneous material modeling based on digital image processing," *Advances in Engineering Software*, vol. 148, Article ID 102836, 2020.

[9] Y. Wang, W. K. Feng, R. L. Hu, and C. H. Li, "Fracture evolution and energy characteristics during marble failure under triaxial fatigue cyclic and confining pressure unloading (FC-CPU) conditions," *Rock Mechanics and Rock Engineering*, vol. 54, no. 2, pp. 799–818, 2021.

[10] J. A. Sharpe, "The production of elastic waves by explosion pressure. I. Theory and empirical field observations," *Geophysics*, vol. 2, no. 7, pp. 144–154, 1942.

[11] F. G. Blake, "Spherical wave propagation in solid media," *The Journal of the Acoustical Society of America*, vol. 2, no. 24, p. 211, 1952.

[12] W. I. Duvall, "Strain-wave shapes in rock near explosions," *Geophysics*, vol. 2, no. 18, pp. 310–323, 1953.

[13] N. Ricker, "The form and laws of propagation of seismic wavelets," *Geophysics*, vol. 1, no. 18, pp. 10–40, 1953.

[14] J. Jiang, D. P. Blair, and G. R. Baird, "Dynamic response of an elastic and viscoelastic full-space to a spherical source," *International Journal for Numerical & Analytical Methods in Geomechanics*, vol. 3, no. 19, pp. 181–193, 1995.

[15] J. L. Stevens and G. E. Baker, "Seismic wave generation by a non-isotropic explosion source," *Journal of Geophysical Research Solid Earth*, vol. 12, no. 114, 2009.

[16] J. L. Stevens, "Analysis and simulation of chemical explosions in non-spherical cavities in granite," *Journal of Geophysical Research: Solid Earth*, vol. 111, no. 4, 2006.

[17] J. L. Stevens, T. G. Barker, S. M. Day et al., *Simulation of Teleseismic Body Waves, Regional Seismograms, and Rayleigh Wave Phase Shifts Using Two-Dimensional Nonlinear Models of Explosion Sources*, American Geophysical Union (AGU), Washington, DC, USA, 2013.

[18] C. L. Yu, Z. Q. Wang, and W. G. Han, "A prediction model for amplitude-frequency characteristics of blast-induced seismic waves," *Geophysics: Journal of the Society of Exploration Geophysicists*, vol. 3, no. 83, pp. 1–56, 2018.

[19] V. Schenk and V. Červený, "Frequency content of stress waves in the nearest zone of a spherical explosive source in gravel sandy soil," *Studia Geophysica et Geodaetica*, vol. 15, no. 3-4, pp. 421–423, 1971.

[20] C. Wu, Y. Lu, H. Hao, W. K. Lim, Y. Zhou, and C. C. Seah, "Characterisation of underground blast-induced ground motions from large-scale field tests," *Shock Waves*, vol. 13, no. 3, pp. 237–252, 2003.

[21] D. C. Lin and C. H. Bai, *The Effect of Explosion Earthquakes*, Geological Publishing House, Beijing, China, 2007.

[22] T. H. Ling and X. B. Li, "Laws of energy distribution in different frequency bands for blast vibration signals," *Journal of Central South University*, vol. 2, pp. 310–315, 2004.

[23] A. M. Starfield and J. M. Pugliese, "Compression waves generated in rock by cylindrical explosive charges: a comparison between a computer model and field measurements," *International Journal of Rock Mechanics and Mining Sciences & Geomechanics Abstracts*, vol. 1, no. 5, 1968.

Research Article

Research on the Mechanical Properties of New Double-Row Pile Supporting Structure Based on an In Situ Study

Yijun Zhou [ID],[1] **Kuiming Liu** [ID],[2] **and Fengnian Wang** [ID][2]

[1]*College of Architecture and Engineering, North China University of Science and Technology, Tangshan 063210, China*
[2]*State Key Laboratory for Geomechanics & Deep Underground Engineering, Beijing 100083, China*

Correspondence should be addressed to Fengnian Wang; wangfn_bj@163.com

According to the force characteristics of the double-row pile supporting structure, two new types of double-row piles are developed: the prestressed strong-constrained double-row piles and the recycling assembled double-row piles. A comparative field test was conducted on the support effects of the two new double-row piles and conventional double-row piles. The test site is located in a deep foundation pit of the Beijing Daxing International Airport Project. The feasibility and reliability of the two new support structures are verified. Field monitoring included section strain and bending moment of the pile body, horizontal displacement of the pile body, and vertical and horizontal displacement of the pile top. The research shows that because of the prestressed anchorage cables in the rear row piles, the prestressed strong-constrained support structure can provide better tensile performance from the rear piles, and the deformation and displacement are minimal. The recycling assembled double-row piles have similar deformation and displacement to the conventional piles. Through the connection of the steel members, the construction time can be effectively shortened. After the backfill of the foundation pit, the steel members can be recycled and the cost can be reduced.

1. Introduction

Currently, double-row pile support structures are widely used in slope engineering, hydraulic engineering, road engineering, and other fields. This type of support structure mainly consists of front row piles, rear row piles, crown top beams, and coupling beams [1, 2]. It can also be regarded as the case where the total number of piles does not change, and a single row of piles is transferred to the rear row to form parallel front and rear rows. The spatial structure system is formed by connecting several beams to the tops of the piles [3–6], as shown in Figure 1.

Many scholars have studied conventional double-row pile support structures based on the unique structural form and stress variation characteristics. Based on the classic earth pressure theory in China, the most representative one is the volume-ratio coefficient method proposed by He et al. [7]. Nie et al. [8] used a combination of model tests, numerical simulations, and field tests to systematically study the distribution of earth pressure, displacement of front and rear row piles, and bending moments of the front and rear rows of double-row piles in a foundation pit excavation. Nie et al. summed up the laws of these observations and proposed a theoretical calculation method based on the spatial effects. Based on previous research and the Winkler foundation beam theory, Zheng et al. [9] proposed a new plane element finite element model considering pile-soil interaction. Wang and Zhao [10] started with the multilayer soil arch effect of double-row piles, analyzed the mechanical properties of two types of soil arches (end-bearing arches and friction arches) at the arch foot, and derived two types of soil arches. The ultimate load-carrying capacity was then studied by analyzing the problems of landslide thrust distribution in front row piles, soil resistance in front of the piles, and spacing between the front and rear row piles.

All of the above studies are based on the traditional double-row pile support structure, and there is less research on the optimization and improvement of the traditional
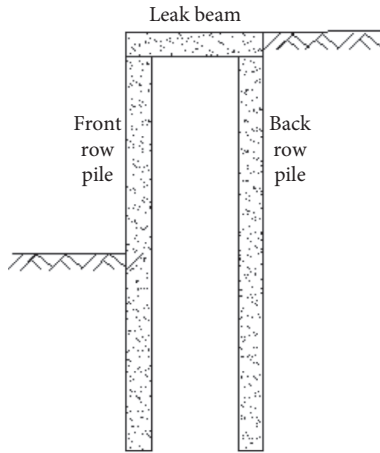
FIGURE 1: Schematic diagram of traditional double-row pile support structure.

FIGURE 2: Location of test sites.

FIGURE 3: Test site.

support structure [11–16]. It is also short of comparison of mechanical properties for supporting structures and some in situ studying [17–21]. Double-row pile supporting structure is used in mining engineering and geotechnical engineering [22–25]. At the same time, the traditional double-row pile support structure also has its drawbacks. First, because its structural form is more complex than a single row pile, the construction period is longer. Second, because it consists of two rows of piles, the project cost is much higher than that of single row piles. Therefore, based on the deficiencies of the above traditional double-row piles, according to the force characteristics of the double-row pile support structure, two new types of double-row pile support structures were developed in this study and field-tested: the prestressed strong-constrained double-row piles and the recycling assembled double-row piles. A comparative test was conducted with traditional double-row piles to verify the feasibility and reliability of the new support structures.

2. Project Overview

2.1. Test Site Overview. The test site is located in a deep foundation pit of the Beijing Daxing International Airport Project, located in Yufa town and Lixian town of Daxing District in Beijing and Guangyang District of Langfang city in Hebei province, as shown in Figure 2. The specific test area is south from the terminal building, north to the north border of the remote parking lot (Paradise Henan Coast after manual diversion), west about 250 m to the main entrance road viaduct A2, and east to the east side of South Central Axis Road about 450 m. The overall layout is one horizontal and four vertical.

2.2. Engineering Geological Conditions. The field test site is shown in Figure 3. Based on the comprehensive analysis of onsite conditions, in situ testing, and the results of the indoor geotechnical tests, the strata within the depth of the survey were divided into three categories: artificial accumulation, recent sedimentary, and quaternary sedimentary. The strata are divided into five main layers and their

sublayers according to their lithology, physical and mechanical properties, and engineering characteristics. The groundwater level is about 2 meters.

2.2.1. Artificial Accumulation Layer (1st Major Layer). The surface layer of the test field is generally covered with an artificial accumulation layer with a thickness of 0.40~1.80 m, which consists of a clayey silt soil layer, sandy silty soil fill ① layer, and slag soil $①_1$ layer. The local distribution may be thicker, as influenced by human transformation.

2.2.2. Recent Sedimentary Layers (2nd and 3rd Major Layers). Under the artificial accumulation layer, the recent sedimentary layers consist of the newly deposited sandy silt and clayey silt ② layers, silty sand and fine sand $②_1$ layers, organic clay, organic heavy silty clay $②_2$ layers, silty clay and clayey silt $②_3$ layers, sandy silt and clayey silt ③ layers, organic clay and organic heavy silty clay $③_1$ layers, fine sand and silty sand $③_2$ layers, and silty clay and clayey silt $③_3$ layers.

2.2.3. Quaternary Sedimentary Layers (4th and 5th Major Layers). Under the new sedimentary layer, the quaternary sediments are silty clay and clayey silt ④ layers, silty clay and

sandy silt $④_1$ layers, fine sand and silty sand $④_2$ layers, heavy silty clay and clay $④_3$ layers, and fine sand and medium sand $⑤$ layers.

3. New Support Structures

The prestressed strong-constrained type support is created by adding a prestressed anchor cable along the pile at the top of the rear row of piles, and the anchors are tied to the inside of the reinforcement cage. After the reinforcement cage is driven into the pile holes and the concrete of the pile has reached the strength requirements, the anchor cable is tensioned. Due to the increase in the tensile strength of the rear row of piles, the length of the front row piles can be appropriately shortened, as shown in Figure 4(a). A single prestressed anchor cable has a nominal value of 15.2 mm, and three of them are used, and the prestress value is 100 kN.

The recycling assembled type support uses detachable steel components instead of the traditional crown beams and coupling beams, while the rear row piles use steel pipe piles instead of traditional bored piles, as shown in Figure 4(b).

The numbers in Figure 4(a) represent the following: (1) front row pile, (2) crown beam of front row pile, (3) coupling beam, (4) soil between piles, (5) rear row pile, (6) crown beam of rear row pile, (7) anchor pad, (8) steel reinforcement cage, (9) prestressed anchorage cable, (10) free section of anchor cable, and (11) anchoring section of anchor cable.

The numbers in Figure 4(b) represent the following: (1) front row pile (bored concrete pile), (2) crown beam of front row pile, (3) rear row pile (steel pipe pile), (4) pile cap, (5) tie sleeve, (6) tie rod, (7) locking joint, (8) steel reinforcement cage, (9) paint layer, (10) pin shaft, and (11) keyhole.

In order to fully compare the mechanical properties of the two new types of double-row pile retaining structures and the conventional ones, the three types of piles were all cast with C30 concrete. The compressive strength of concrete was 14.3 N/mm^2, and the elastic modulus was 3×104 N/mm^2. The longitudinal reinforcement of the pile is 14 B20 HRB400 steel bars, and the stirrups are HRB400, $\phi12$ @ 200, and $\phi16$ @ 2000. The geometric design parameters of the three types of piles are given in Table 1.

4. Field Monitoring

4.1. Field Monitoring Scheme Design. The purpose of this field test is to determine the mechanical properties of the new double-row pile retaining structures in the excavation process of the foundation pit, explore the displacement and deformation behavior of the new pile types, and comprehensively evaluate the working performance of the new pile types in the field test.

In order to reveal the law of displacement and deformation of the new pile type, the changes of the conventional double-row pile supporting structures after the force deformation are compared. The test focuses on the horizontal and vertical displacement of the pile top and horizontal displacement of the pile body. The pile body deformation was monitored, as given in Table 2. Based on the abovementioned monitoring items, reliability, accuracy, and convenience were taken as criteria for the selection of monitoring instruments.

The field monitoring instruments are shown in Figure 5.

4.2. Field Monitoring Scheme Implementation. The displacement measurement point plan view of the pile tops is shown in Figure 6, and the reflective sheet site layout is shown in Figure 7.

The plan view of the inclinometer pipe is shown in Figure 8, and the site embedment plan is shown in Figure 9.

The site construction process consisted of the following steps and is shown in Figure 10.

(1) Behind the pile, a trench with a depth of 1 m, width of 2 m, and length of about 25 m was excavated for laying the steel strands. In order to minimize the disturbance of the overlying soil on the steel strands, aluminum-plastic tubes and iron tubes are sheathed outside the steel strands.

(2) At the end of the trench away from the foundation pit, a 1.5 m long steel bar was drilled into the bottom of the pit to firmly connect the steel strand to the exposed bar head as a fixed point

(3) The other end of the strand was extended to the top of the crown girder and connected to the cable-type displacement meters of the piles at the top and the rear of each pile, respectively

(4) The connections of the whole system were checked, the initial data values were collected, and the groove was carefully filled.

The strain of pile body was monitored by a vibrating wire embedded strain gauge. The strain gauges were bound to the main reinforcement of the steel reinforcement cage symmetrically, and the vertical spacing was 200 mm from top to bottom. The elevation view of the measuring point layout is shown in Figure 11, and the gauge burial is shown in Figure 12.

When the installation of each monitoring point was complete and the commissioning was correct, the initial values were collected and the excavation of the foundation pit was carried out. The pit was designed for a depth of 8 m, excavated in four steps at a rate of 2 m for each step, and the concrete was sprayed on the wall of the foundation pit after each excavation to prevent runoff between piles. After each excavation step, data acquisition was performed for each monitoring aspect three times/day (morning, afternoon, and evening) to capture the time of the initial changes in the data during excavation. The monitoring continued until the fifth day when the pit excavation was completed. The excavation process of the foundation pit is shown in Figure 13.

5. Results and Discussion

5.1. Displacement Analysis of Pile Top

5.1.1. Vertical Displacement. As shown in Figure 14, positive values on the vertical axis indicate that the top of the pile is floating and the negative values indicate that the pile top is

(a)   (b)
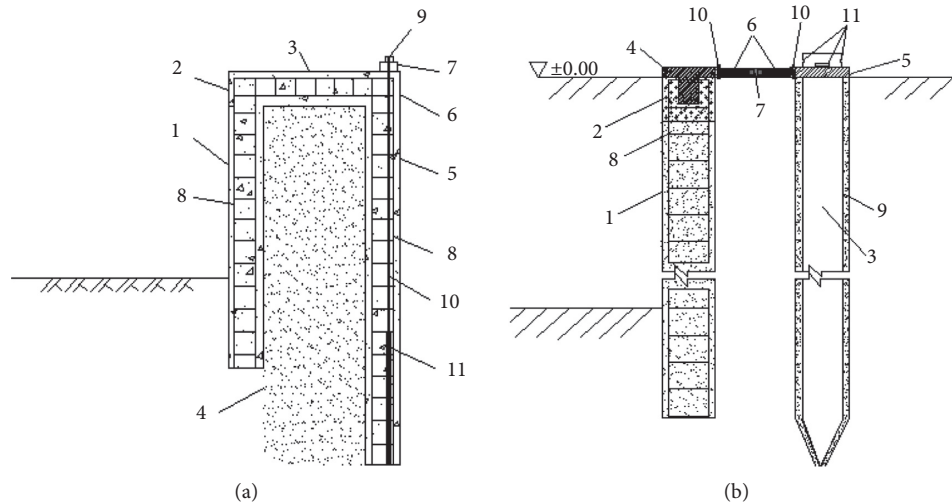
FIGURE 4: Elevation view of new double-row piles. (a) Prestressed strong-constrained double-row piles. (b) Recycling assembled double-row piles.

TABLE 1: Geometric design parameters of test piles.

Test pile type	Crown beam size (m)	Length of front and rear row pile (m)	Pile diameter (m)	Row spacing (m)	Pile spacing (m)	Depth of foundation pit (m)
Conventional	0.8×0.8	12.5/12.5	0.8			
Prestressed strong-constrained	0.8×0.8	10.0/12.5	0.8	2.4	2.0	8
Recycling assembled	—	12.5/12.5	0.8/0.6			

TABLE 2: Test procedure.

Property	Monitoring position	Monitoring quantity	Instrument
Pile strain	Conventional front and rear row pile Prestressed strong-constrained front and rear row pile Recycling assembled front row pile	Conventional pile strain gauge: five groups + one branch Prestressed strong-constrained pile strain gauge: four groups + two branches Recycling assembled pile strain gauge: five groups	Vibrating string embedded strain gauge (BGD-4200)
Horizontal displacement of pile body	Conventional front row pile Prestressed strong-constrained front row pile Recycling assembled front row pile	Three types of front row pile for a total of six	Clinometer
Horizontal displacement and vertical displacement of pile top	Conventional front and rear row pile Prestressed strong-constrained front and rear row pile Recycling assembled front and rear row pile	One of three types of front and rear piles, a total of 12 measuring points	Remote displacement automatic monitoring system, electronic total station

sinking. Before the excavation in the third step of the three types of piles, the vertical displacement of the piles at the front and rear rows was minimal. When the excavation reached the third step, the vertical displacement of the pile top appears to be floating. After the fourth excavation was completed, the vertical displacement of the pile top is basically stable, about 1 mm. The main purpose of the analysis is that with the excavation of the foundation pit, the unloading effect of the soil in front of the pile is gradually obvious, and the soil at the bottom of the pit has a certain rebound, which causes the floating phenomenon of the top and bottom of the piles. This conclusion is also consistent with the indoor physical simulation test pile top displacement changes.

(a)

(b)

(c)

(d)

(e)
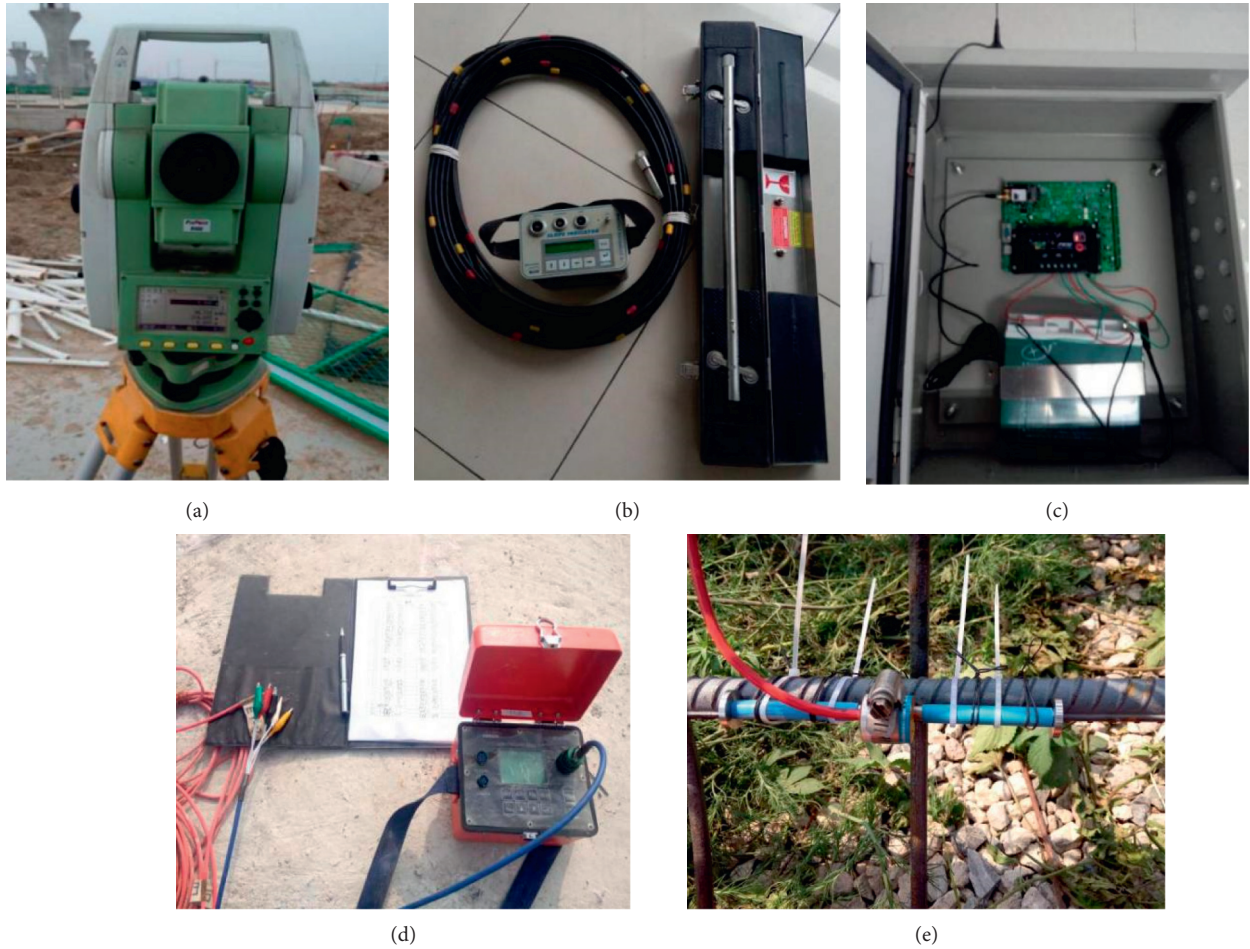
FIGURE 5: Field test monitoring instruments. (a) Electronic total station. (b) Clinometer. (c) Remote automatic displacement monitoring system. (d) Strain collector BGK408. (e) Strain gauge BGD-4200.
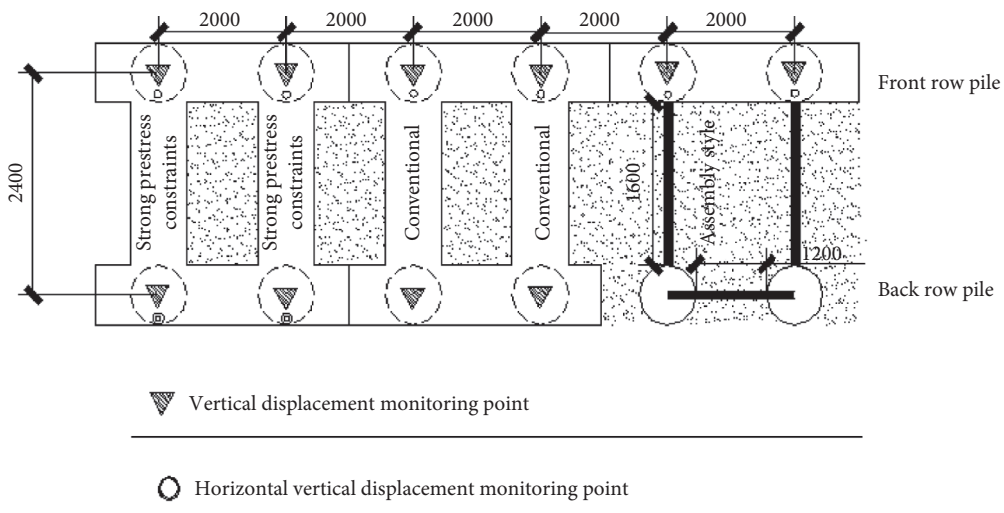
FIGURE 6: Pile top displacement measurement point plan view.

Due to the summer flood season, after the excavation of the foundation pit, heavy rainfall occurred in the test area for several consecutive days, resulting in sinking of the vertical displacements of the front and rear pile tops,

especially for the recycling assembled double-row piles. The sinking of the front row piles was −2 mm, and the sinking of the rear row piles was −3 mm. The main reason for the analysis is that the strata within the site are mainly

FIGURE 7: Reflective sheet in pile top.
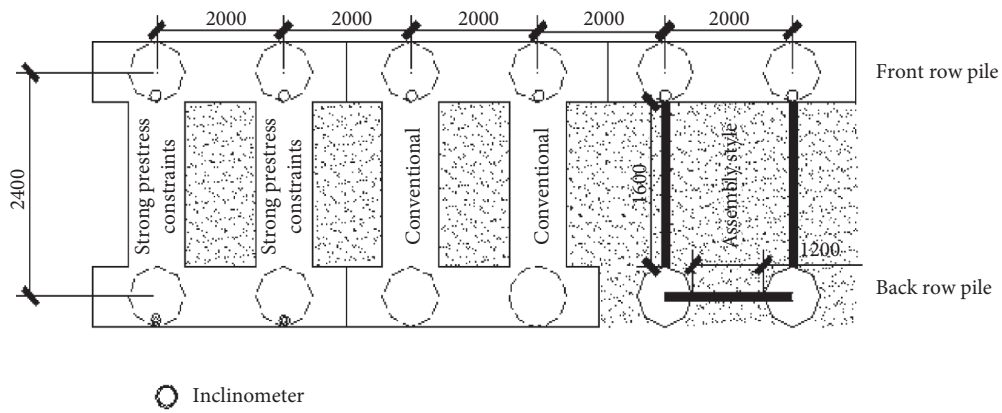
FIGURE 8: Inclinometer plan.
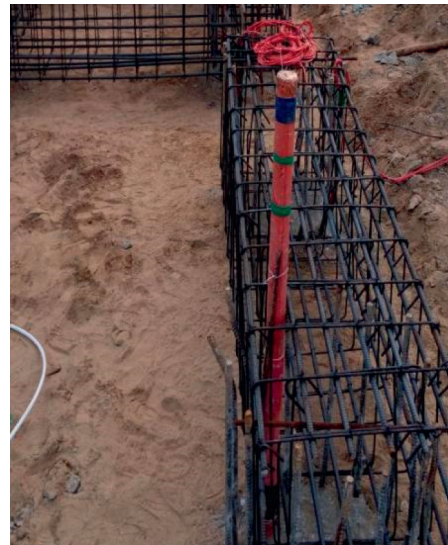
FIGURE 9: Inclinometer pipe site layout.

composed of thick clayey soil, silty soil, and sand soil, and the soil structure is relatively loose, so the engineering properties are poor. Under strong rain, the bottom of the pit is weakened with water and soil. Therefore, the pile body sinks under the tow of the soil around the pile, and since the hollow steel pipe pile is used for the recycling assembled rear pile, the weight of the pile is smaller, and the towing effect is more obvious.

(a)

(b)

(c)

Figure 10: Connection diagram of the remote displacement automatic monitoring system. (a) Relative position of the aluminum-plastic tube, iron pipe, and steel strand. (b) Fixed point connection behind the pile. (c) Connection of guyed displacement gauge on the pile top.
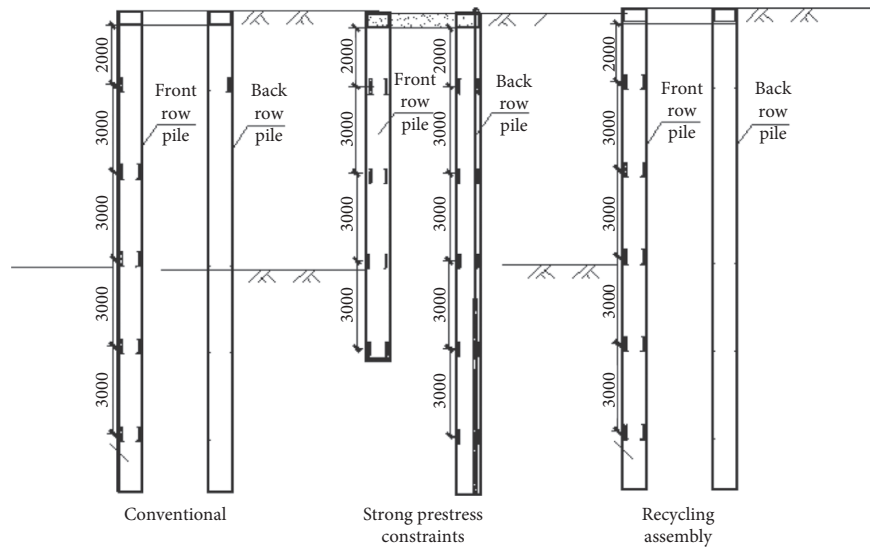
FIGURE 11: Pile strain measuring point layout elevation.

(a)   (b)

FIGURE 12: Binding and burial of strain gauges.

5.1.2. Horizontal Displacement. Positive values on the vertical axis in Figure 15 indicate displacements in the direction of the foundation pit and negative values indicate displacements in the direction away from the foundation pit. As shown, the horizontal displacement variation trends of the conventional and recycling assembled pile top are basically the same. However, for the prestressed strong-constrained pile, due to the effect of the prestressed anchor cable, the horizontal displacement of pile top has a negative value in the early stage of monitoring, which means the displacement is far away from the foundation pit. With the continuous excavation of the foundation pit, the horizontal displacement of the prestressed strong-constrained piles at the front and rear piles is gradually displaced toward the direction of the foundation pit. When the excavation of the foundation pits occurred, the horizontal displacements of the piles at the

front and rear piles all abruptly changed, which indicates that the excavation of foundation pits is the main influencing factor of the horizontal displacement of the pile tops. Moreover, as the excavation depth of the foundation pit increases, the displacement increases gradually and the displacement at the end of monitoring reaches a maximum value. Among them, the horizontal displacements of the prestressed strong-constrained front row pile, the recycling assembled type front row pile, and the conventional front row pile top were 2.52 mm, 5.78 mm, and 5.56 mm, respectively. The corresponding horizontal displacements of the rear row of piles are 1.72 mm, 4.52 mm, and 4.11 mm, respectively. The horizontal displacements of the piles at the front row of each pile are larger than those of the rear piles, which is consistent with the changing trend of the previous numerical simulation results.

FIGURE 13: Excavation process of foundation pit. (a) Excavation of 2 m. (b) Hanging net between piles. (c) Spraying concrete. (d) Excavation of 4 m. (e) Excavation of 6 m. (f) Excavation of 8 m.
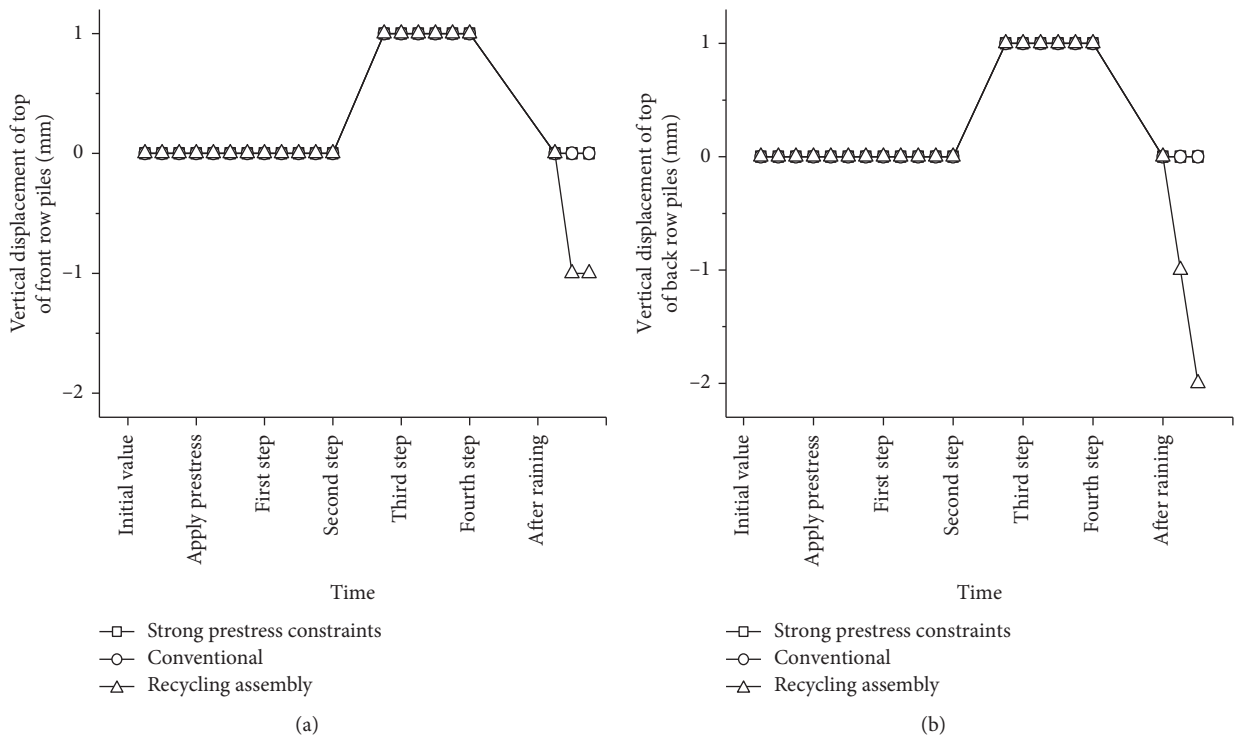
FIGURE 14: Comparison of vertical displacement time history of pile top. (a) Front row pile. (b) Rear row pile.
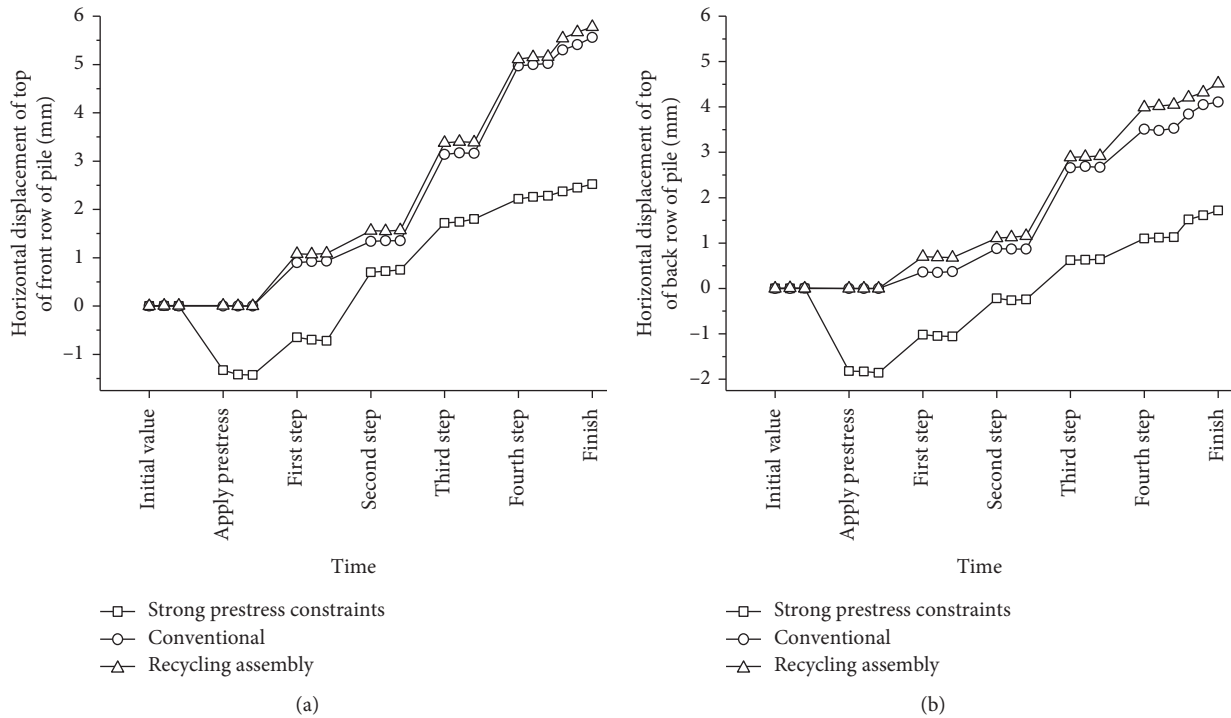
FIGURE 15: Comparison of horizontal displacement time history of pile top. (a) Front row pile. (b) Rear row pile.

5.2. Horizontal Displacement Analysis of Pile.

It can be seen from Figure 16 that as the depth of pit excavation increases, the horizontal displacement of the pile gradually increases. In the first and second excavations, the maximum displacement is at the top of the pile. During the third or fourth excavations, the maximum displacement gradually moves downward, about 2-3 m below the top of the pile. It shows that with the increase of excavation depth of the foundation pit, the crown beam of the pile gradually exerts a restraining effect.

The front row pile of the prestressed strong-constrained pile appears as negative values in the early stage of monitoring, where the maximum displacement reaches −1.82 mm. The prestressed strong-constrained front row piles showed a negative value in the initial period of monitoring, and the maximum displacement reached −1.82 mm. That is to say, displacement of the pile top produces a deviation from the side of the foundation pit relative to the initial value, and then, as the excavation depth increases, the displacement gradually changes from a negative value to a positive value and increases continuously. This phenomenon indicates that the prestressed anchor cables of the prestressed and strongly constrained rear row piles exert a certain anchorage effect on the front row piles. The tension is transmitted to the front row pile top through the coupling beam. Therefore, the displacement change process of the front row pile top gradually converts from a negative value to a positive value, and the final displacement is smaller.

After the monitoring was complete, the horizontal displacement of the pile body was as shown in Figure 17. The overall variation trend of the three pile types was basically

the same, and the curve was roughly a "right convex" type distribution. The horizontal displacement of the pile head of the recycling assembled pile is basically the same as that of the conventional pile, and their maximum displacements were 6.22 mm and 6.41 mm. The horizontal displacement of the prestressed strong-constrained front piles is less than the former two, and its maximum displacement is 3.18 mm. The results show that the prestressed strong-constrained supporting structure plays a significant role in controlling the maximum horizontal displacement of the front row piles. The horizontal displacement control effect of the front row piles of the recycling assembled supporting structure is almost the same as that of conventional piles.

5.3. Deformation Analysis of Pile

5.3.1. Strain of the Pile.

The variation of strain at the end of the excavation and at the end of monitoring is shown in Figure 18. It is shown that the strain of the front row pile at the end of monitoring is larger than that at the end of excavation for the three types of piles, but the increase is minimal. It indicates that the strain has been basically completed during the excavation.

The strain distributions of the three types of piles in the front row are basically the same, and the effect of pulling and pressing on the front and rear sides of the pile is obvious. The maximum strain is in the middle of the pile, which is about 6 m below the pile top. It shows that the binding effect of the crown beam and soil is obvious. The front row pile above the excavation face is subjected to tensile stress before the pile and compressive stress behind the pile, resulting in tensile

(a)

(b)

(c)
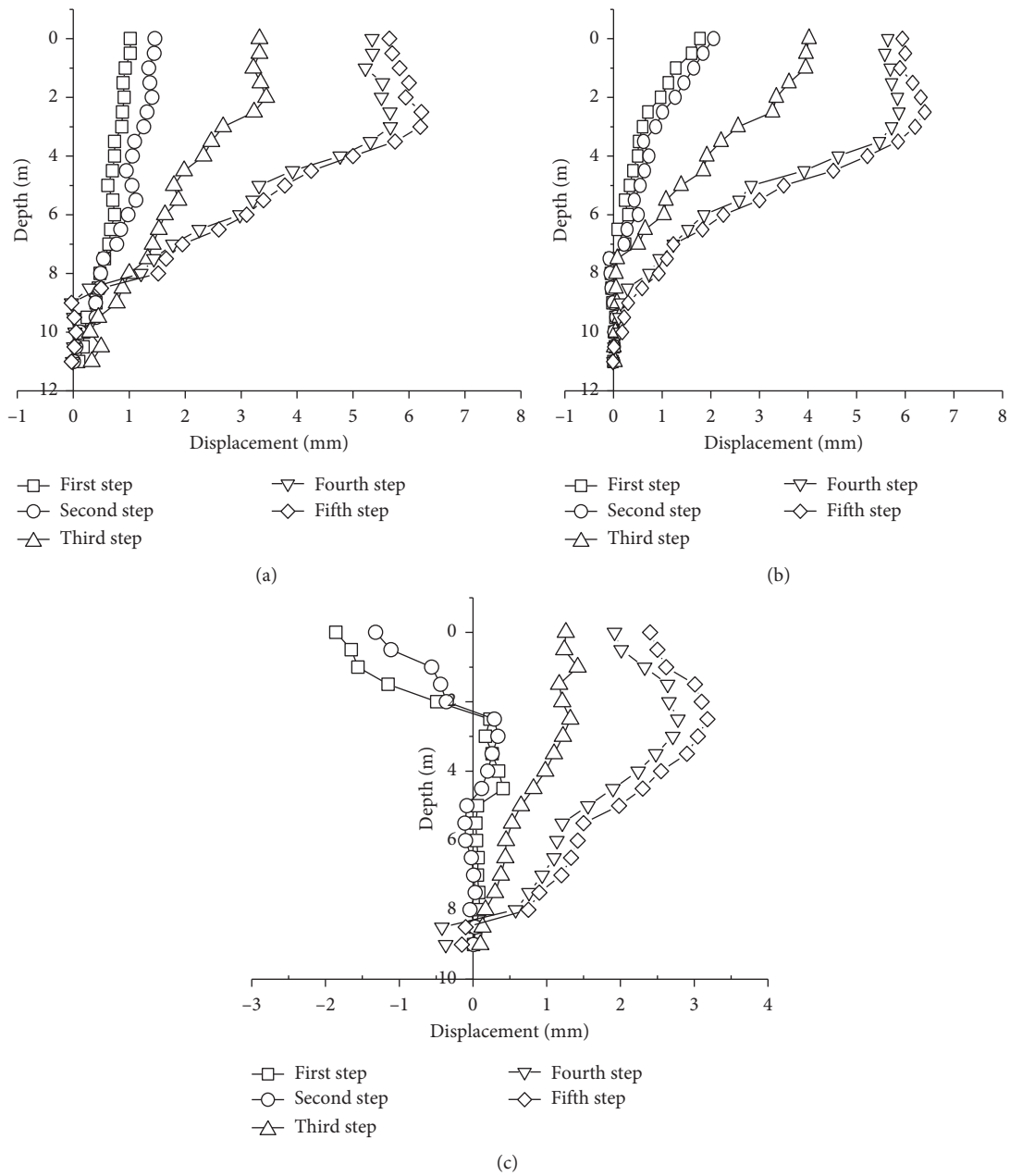
FIGURE 16: Horizontal displacement of front row piles. (a) Conventional front row pile. (b) Recycling assembled front row pile. (c) Prestressed strong-constrained front row pile.

deformation and compressive deformation; however, the tension and compression below the excavation face are the opposite. Due to the prestressing of the strong-constrained rear row pile anchors, the strain of the prestressed strong-constrained front row piles is less than that of the other two types of piles, especially at the 0–3 m position of the upper part of the pile where the effect is more pronounced.

5.3.2. Bending Moment of the Pile. It can be seen from Figure 19 that after the monitoring is complete, the bending moments of the three types of piles are basically in the same

direction, with positive bending above the excavation surface and negative bending below the excavation surface. The three types of piles all have the largest bending moment at 6 m, which shows that the crown beam and the bottom of the pile have certain restrictions on the pile body. Among them, the bending moments of the conventional type and the recycling assembled type are basically the same, and the maximum values are 70 kN·m and 78 kN·m, respectively. The prestressed strong-constrained type generated less than the first two, with a maximum value of 42 kN·m, indicating that the prestressed anchor cable with prestressed strong-constrained type rear row has a certain restraining effect on the front row of piles.
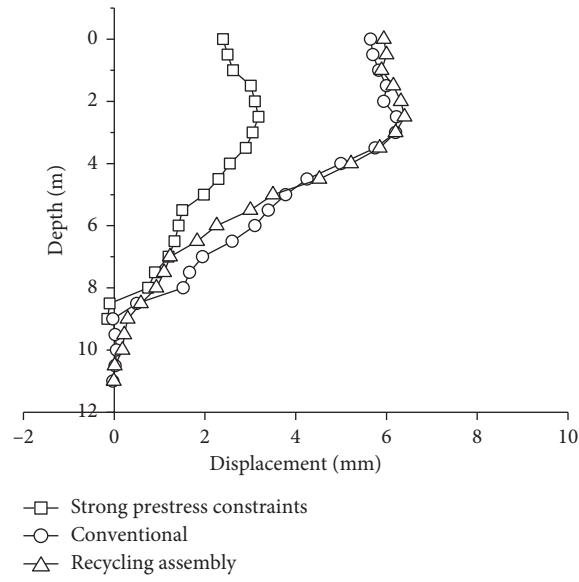
Figure 17: The comparison of horizontal displacement for three front row piles.

(a)

(b)

Figure 18: Continued.

Strain (με)

Depth (m)

—□— Front strain of prestressed front row piles
—○— Poststrain of prestressed front row piles

(c)
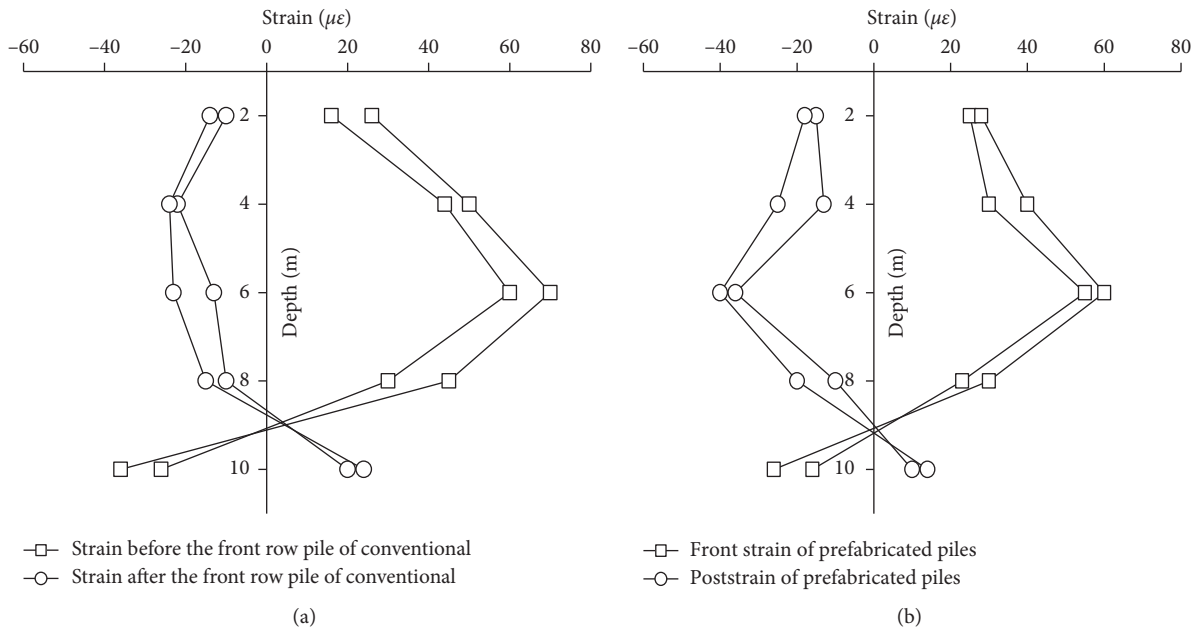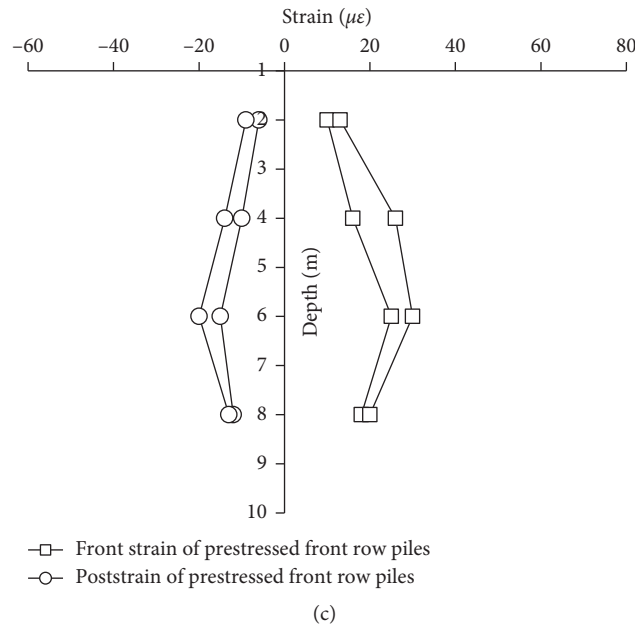
FIGURE 18: Variation of strain for front row piles. (a) Conventional pile. (b) Recycling assembled pile. (c) Prestressed strong-constrained pile.

Bending moment (kN·m)

Depth (m)

—□— Strong prestress constraints
—○— Conventional
—△— Recycling assembly
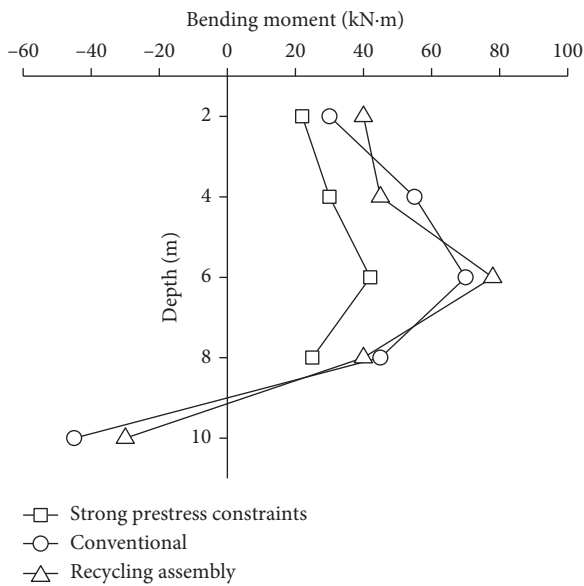
FIGURE 19: Comparison curve of bending moment.

με

Apply prestress First step Second step Third step Fourth step

Time

—□— Strain of back row pile for strong prestressed constrained
—○— Strain of back row pile for conventional

FIGURE 20: Comparison of strain at 2 m below the back row pile top.

In order to compare the deformation of the prestressed strong-constrained and conventional rear piles, strain gauges were laid at the same location of the two piles, 2 m below the top of the piles, away from the foundation pit, and the results were compared. According to the results presented in Figure 20, the conventional rear row pile has no prestressed anchor cable and the strain of the rear row pile shows an increase along with the excavation strain of the foundation pit, indicating that the conventional rear row pile is gradually subjected to tensile stress, and the main tensile strain occurs. This phenomenon is also consistent with the conclusion of the physical simulation test.

Before excavation of the foundation pits, initial strain values were collected, and prestressing was then applied to the prestressed strong-constrained rear row pile anchors. Before the first excavation, due to the effect of prestressing, the strain value continues to decrease, indicating that the rear row piles have increased pressure and that the transmission of prestress has a certain time effect; the stress gradually is balanced thereafter. After the first excavation, due to the earth pressure generated by soil unloading, the strain value gradually increases, that is, the prestressed strong-constrained rear row piles change from compression to tension. After each excavation of the foundation pit, the strain value has a certain abrupt change, and the strain value increases gradually, which means that each excavation

unloading of the soil exerts a significant tensile stress on the rear pile body. The ultimate strain value of the prestressed strong-constrained rear row pile is $13.5\,\mu\varepsilon$ and the ultimate strain value of the conventional rear row pile is $27.2\,\mu\varepsilon$, which indicate that the prestressed strong-constrained pile has a better restraining effect than the conventional one on the rear piles.

6. Conclusions

(1) The horizontal displacement of piles in the pre-stressed strong-constrained double-row piles and recycling assembled double-row piles supporting structures is basically the same as that of the conventional ones. After the foundation pit excavation is completed, the maximum horizontal displacement point appears in the upper part of the pile about 2-3 m. The displacement of the prestressed strong-constrained type in each step of excavation is smaller than that of the conventional and recycling assembled types, and the overall horizontal displacement change trend between the conventional and recycling assembled types is basically the same.

(2) For the three types of supporting structure, the horizontal displacement of the front pile top is larger than the rear row pile, which explains that the influence of the active earth pressure on the front row pile is more obvious under the unloading of the foundation pit. The horizontal displacement values of the prestressed strong-constrained front and rear row piles are all smaller than the conventional and recycling assembled ones, indicating that the prestressed strong-constrained type has a better restraining effect on the front and rear rows of pile tops. Recycling assembled piles ensure that the displacement is similar to that of the conventional piles. Steel members are used to connect rear row piles and front row piles, which effectively reduces construction time and speeds up the construction process. After the foundation pits are backfilled, steel members can be recycled to save costs.

(3) Due to the existence of prestressed anchor cables in the rear row piles, the rear row piles of the pre-stressed strong-constrained supporting structure can provide better tensile performance. At the same time, the pulling anchor effect of prestressed anchor cable can restrain the displacement and deformation of prestressed strong-constrained front row piles, and the restraint effect on the top of the front row pile is especially obvious. It shows that the prestressed strong-constrained support structure has better deformation coordination ability.

Data Availability

The data used to support the findings of this study are included within the article.

Conflicts of Interest

The authors declare that there are no conflicts of interest.

Acknowledgments

References

[1] Profession Standard of the People's Republic of China, *Technical Specification for Retaining and Protection of Building Foundation Excavation JGJ120-2012*, Profession Standard of the People's Republic of China, Taiwan, China, 2012.

[2] X. N. Gong, *Handbook for Design and Construction of Deep Foundation Pit*, China Architecture & Building Press, Beijing, China, 1998.

[3] S. L. Xing, J. S. Ye, and X. L. Yao, "Construction of bridge pile foundation finite element model and its application," *Feature Structure*, vol. 27, pp. 77–80, 2010.

[4] Y. J. Shen, H. Y. Sun, Y. Q. Shang et al., "Optimization design of double row anti-slide pile piers connection," *Chinese Journal of Rock Mechanics and Engineering*, vol. 29, pp. 3034–3038, 2010.

[5] J. F. Huang, C. G. Jiang, and S. L. Xing, "Study on finite element model of bridge pile foundation," *Road Traffic Technology*, vol. 7, pp. 161–163, 2011.

[6] G. Z. Qu and X. Q. Ye, "A new calculation method for the combined action of pile foundation and superstructure," *Hubei Water Conservancy and Electricity Generation*, vol. 3, pp. 16–18, 2001.

[7] Y. H. He, B. Yang, B. S. Jin et al., "Research and test of double row slope protection pile," *Journal of Building Structure*, vol. 2, pp. 58–66, 1996.

[8] Q. K. Nie, J. N. Hu, G. Wu et al., "Deformation and earth pressure of a double-row piles retaining structure for deep excavation," *Rock and Soil Mechanics*, vol. 155, no. 11, pp. 3089–3094, 2008.

[9] G. Zheng, X. Li, C. Liu et al., "Analysis of double-row piles in consideration of the pile-soil interaction," *Journal of Building Structure*, vol. 1, pp. 99–106, 2001.

[10] Y. Wang and B. Zhao, "Multilayer soil arching effect calculation and soil pressure analysis in double-row anti-sliding piles," *Journal of Beijing University of Technology*, vol. 8, pp. 1193–1199, 2008.

[11] Y. J. Zhou, A. J. Yao, X. Zheng et al., "Correction of earth pressure and analysis of deformation for double-row piles in foundation excavation in Changchun of China," *Advanced in Materials Science and Engineering*, vol. 2016, Article ID 9818160, 10 pages, 2016.

[12] C. Zhu, K. Zhang, H. Cai et al., "Combined application of optical fibers and CRLD bolts to monitor deformation of a pit-in-pit foundation," *Advances in Civil Engineering*, vol. 2019, Article ID 2572034, 16 pages, 2019.

[13] C. Zhu, Z. Yan, Y. Lin, F. Xiong, and Z. Tao, "Design and application of a monitoring system for a deep railway foundation pit project," *IEEE Access*, vol. 7, Article ID 107591, 2019.

[14] Q. Wang, H. Gao, B. Jiang, S. Li, M. He, and Q. Qin, "In-situ test and bolt-grouting design evaluation method of underground engineering based on digital drilling," *International Journal of Rock Mechanics and Mining Sciences*, vol. 138, Article ID 104575, 2021.

[15] N. Bella, I. Bella, and A. Asroun, "The application of equivalent age concept to sand concrete compared to ordinary concrete," *Advanced in Civil Engineering*, vol. 2016, Article ID 8940831, 7 pages, 2016.

[16] P. Colajanni, M. Papia, and N. Spinella, "Stress-strain law for confined concrete with hardening or softening behavior," *Advanced in Civil Engineering*, vol. 2013, Article ID 804904, 11 pages, 2013.

[17] Q. Wang, M. C. He, and S. C. Li, "Comparative study of model tests on automatically formed roadway and gob-side entry driving in deep coal mines," *International Journal of Mining Science and Technology*, 2021.

[18] Q. Wang, Y. Wang, and M. C. He, "Experimental research and application of automatically formed roadway without advance tunneling," *Tunnelling and Underground Space Technology*, vol. 114, Article ID 103999, 2021.

[19] A. Li, F. Dai, Y. Liu, H. Du, and R. Jiang, "Dynamic stability evaluation of underground cavern sidewalls against flexural toppling considering excavation-induced damage," *Tunnelling and Underground Space Technology*, vol. 112, Article ID 103903, 2021.

[20] X. J. Yang, J. M. Wang, C. Zhu, M. C. He, and Y. Gao, "Effect of wetting and drying cycles on microstructure of rock based on SEM," *Environmental Earth Science*, vol. 78, no. 6, p. 183, 2018.

[21] L. Ban, C. Zhu, C. Qi, and Z. Tao, "New roughness parameters for 3D roughness of rock joints," *Bulletin of Engineering Geology and the Environment*, vol. 78, no. 6, pp. 4505–4517, 2019.

[22] Q.-X. Meng, W.-Y. Xu, H.-L. Wang, X.-Y. Zhuang, W.-C. Xie, and T. Rabczuk, "DigiSim—an open source software package for heterogeneous material modeling based on digital image processing," *Advances in Engineering Software*, vol. 148, Article ID 102836, 2020.

[23] C. Zhu, M.-c. He, M. Karakus, X.-h. Zhang, and Z. Guo, "The collision experiment between rolling stones of different shapes and protective cushion in open-pit mines," *Journal of Mountain Science*, vol. 18, no. 5, pp. 1391–1403, 2021.

[24] Q. Yin, J. Y. Wu, C. Zhu, M. C. He, and Q. X. Meng, "Shear mechanical responses of sandstone exposed to high temperature under constant normal stiffness boundary conditions," *Geomechanics and Geophysics for Geo-Energy and Geo-Resources*, vol. 7, p. 35, 2021.

[25] Q. Wang, Z. Jiang, B. Jiang, H. Gao, Y. Huang, and P. Zhang, "Research on an automatic roadway formation method in deep mining areas by roof cutting with high-strength bolt-grouting," *International Journal of Rock Mechanics and Mining Sciences*, vol. 128, Article ID 104264, 2020.

Research Article

Microstructure and Dry Friction of 2205 Dual-Phase Steel during Solution Precipitation

Weijie Yang [iD],[1] **Wenjun Meng** [iD],[1] **and Xiaobing Dai** [iD][2]

[1]*School of Mechanical Engineering, Taiyuan University of Science and Technology, Taiyuan 030024, China*
[2]*Chair of Materials Handling, Material Flow, Logistics, Technical University of Munich, Boltzmannstraße 15,*
 85748 Garching, Germany

Correspondence should be addressed to Wenjun Meng; tyustmwj2021@163.com

The friction and wear tests of 2205 dual-phase steel with different solution temperatures were carried out, and the effects of solution temperature on the microstructure and friction and wear properties of the steel were determined. Results show that, as the solution temperature increases, the morphology of the austenite phase in 2205 duplex stainless steel gradually changes from fibrous strips to short rods and islands with a more uniform distribution. Additionally, the ferrite content increases with a rise in solution temperature, reaching 56.3% after solution treatment at 1160°C. It was also found that, between 1000°C and 1160°C, the friction coefficient curves of 2205 dual-phase steel and silicon nitride balls have similar characteristics. Under 100 N dry friction, with the increase of solution temperature and oxygen distribution area, the wear mechanism of 2205 dual-phase steel gradually expanded from local oxidation wear to adhesive wear and exfoliation wear.

1. Introduction

Composed of austenite and ferrite, 2205 duplex stainless steel possesses great strength and corrosion resistance. It is widely used in the petrochemical, papermaking, and petroleum industries [1–7]. Because of the presence of both austenite and ferrite, 2205 duplex stainless steel possesses the properties of both of these phases. The existence of austenite can greatly reduce the brittleness of the ferrite and also improve the weldability of the material. Ferrite improves the resistance of the material to stress corrosion, and because of the simultaneous existence of these two phases, it can also inhibit grain growth [8–13]. However, the presence of these two phases also brings some disadvantages. A higher ferrite content in stainless steel increases the brittleness of the material. Moreover, due to the difference in deformation abilities between ferrite and austenite, the properties of the material in extremely hot or cold working conditions are inferior to those of single-phase stainless steel [14, 15]. Previous studies [16–22] have found that solution treatment is one of the main factors determining the two-

phase ratio of duplex stainless steel. Different solid solution treatment processes not only cause 2205 duplex stainless steel to have different two-phase ratios but also lead to the precipitation of a secondary phase. This secondary phase often causes pitting corrosion of the steel and increases the tendency of stress corrosion cracking and corrosion fatigue cracking during usage. This in turn affects the corrosion resistance and mechanical properties of 2205 duplex stainless steel.

The mechanism of friction and wear is to explain the wear process of materials. It represents the formation of wear debris in the process of wear [23–25]. The wear mechanism can be understood by observing the worn surface. The most likely wear of duplex stainless steel in the wear process is adhesive wear, abrasive wear, and local oxidation wear. Sometimes, the duplex stainless steel will be exfoliated, worn, and abraded. The wear mechanism is also different. In the case of wear resistance of dual-phase steel, Wang et al. [26] reported the effects of dry friction and fretting amplitude in an aqueous solution on the fretting wear behavior of 2507 super-dual-phase stainless steel. The

results showed that, under dry friction, the wear mechanism changed from local oxidation wear and local fatigue wear to oxidation wear, adhesion wear, and spalling wear. In an aqueous solution, the main wear mechanisms were mild oxidation wear and abrasive wear, accompanied by fatigue wear. Wang et al. [27] prepared a high nitrogen austenite layer on the surface of dual-phase steel and obtained a high nitrogen stainless steel layer with a uniform structure and easier subsequent processing.

In practical applications, dual-phase steel will suffer material loss from friction and wear. The friction and wear properties of duplex stainless steel are affected by the solution treatment. So far, there have been few studies on the wear resistance of 2205 dual-phase steel under different solution treatment conditions. Therefore, microstructure analysis and friction and wear tests for 2205 duplex stainless steel were carried out under different solid solution treatment conditions. The wear resistance of the material was evaluated to provide an important reference for the optimization of the production process and product quality control.

2. Materials and Experiments

Table 1 displays different chemical compositions of 2205 duplex stainless steel plates with 4 mm thickness. The solution test was carried out in a muffle furnace. Solution temperatures ranged from 1000°C to 1160°C, at intervals of 40°C, and the solution holding time was 40 minutes. After being removed from the solution, the sample was directly quenched with water.

The specimens used for the electron backscatter diffraction (EBSD) study were cut along the rolling direction, and the longitudinal sections (RD-ND) of the specimens were polished using standard metallographic procedures. Then, electrolysis was carried out in 20 : 1 ethanol and perchloric acid solution, with an electrolysis voltage of 20 V and current of 1 A to ensure the removal of any surface deformations. EBSD was carried out using a ZEISS Sigma 3000 field-emission scanning electron microscope.

The wear resistance of the 2205 dual-phase steel was characterized by exploring the friction and wear properties of the material after treatment at different temperatures. Before the experiment, the solid sample to be placed in the solution was cut into a 20 mm × 10 mm × 4 mm rectangular block. Next, the surface of the sample was polished to 3000 mesh and further polished with a diamond polishing agent. The reciprocating sliding friction test was carried out under dry conditions at room temperature using an MFT-5000 friction and wear tester from RTEC Instruments. The friction and wear tests were carried out with a 0.006 mm diameter silicon nitride ball. The trace length was 0.006 mm under 100 N applied load, the wear time was 30 min, and the frequency was 1 Hz. Table 2 shows the working parameters of the experiment. After the friction and wear test, the wear trace was observed with an online three-dimensional optical profilometer. The worn surface was observed using the X-ray diffraction (XRD). It was performed by using Cu-Kα radiation. The scanning speed and the scan step size were 1°/min and 0.02°, respectively. The experimental data were processed by Jade 6.0 software.

3. Results and Discussion

3.1. Microstructure Analysis at Different Solution Temperatures.
Figure 1 shows different morphologies of 2205 duplex stainless steel at different solution temperatures. The long-strip austenite phase is gray, and its width increases from 8–12 μm at 1000°C to about 15 μm at 1160°C. The width of the austenite phase displays an obvious increase at temperatures above 1080°C, as the phase map in Figure 1 illustrates. After heating and the solid solution treatment, a local phase boundary dissolution fracture occurred in the austenite phase. Its morphology changed from fiberboard strip morphology to long rod morphology. When the solution temperature increased to 1040°C, the austenite phase with the long-rod shape transformed into a bamboo shape, and the grain/phase boundaries gradually became more regular. As the temperature increased to 1160°C, the atomic diffusion speed increases, the grain boundaries and phase boundaries of austenite and ferrite become clearer after rolling and compression, and the long-rod austenite gradually forms a regular shape through recovery and recrystallization.

Figure 2 exhibits the X-ray diffraction patterns of the 2205 duplex stainless steel surface at different temperatures. Several oxides are formed on the surface of the sample after friction and wear such as Mn_3O_4, Fe_2O_3, and Cr_2O_3. It can be seen from Figure 2(a) that the relative intensity of the diffraction peak of the worn surface increases obviously with the increase of temperature, and the peak value of the curve deviates partially. The results show that friction and wear cause some microstructure changes in the dual-phase steel such as dislocations and lattice shifts. The ferrite content of 2205 duplex stainless steel was 53.5% after solution treatment at 1000°C (Figure 2(b)). With a rise in solution temperature, the ferrite content increased. After solid solution treatment at 1160°C and subsequent water cooling, the ferrite phase content in the microstructure reached 56.3%. When the solution treatment temperature increased, a transformation in the two-phase composition occurred in the steel. It was a $\gamma \longrightarrow \alpha$ transformation, which means that ferrite in the steel increased gradually, while the level of austenite decreased [28].

3.2. Effect of Solution Temperature on Friction Coefficient.
Figure 3 displays the real-time friction coefficient of 2205 dual-phase steel with different solution treatments under 100 N dry sliding friction. It can be seen from Figure 3 that the friction coefficient curves of 2205 dual-phase steel and silicon nitride balls have similar characteristics. The friction coefficient first increases rapidly, reaches a peak value, decreases quickly, and then increases gradually towards a stable value. The entire friction coefficient curve is divided into three stages. The first stage is the initial running-in stage [29]. In this stage, the material surface

TABLE 1: Chemical composition of 2205 duplex stainless steel (wt%).

C	Cr	Mo	Ni	Si	S	Mn	P	N	Fe
0.025	21.83	3.09	5.45	0.58	0.003	1.13	0.024	0.1699	Balance

TABLE 2: Wear test parameters.

Applied load (N)	Balls	Balls' diameter (m)	Trace length (m)	Frequency (Hz)	Temperature (°C)	Total sliding distance (m)
100	Si_3N_4	0.006	0.006	1	24 ± 2	0.36

(a)

(b)

(c)

(d)

(e)

(f)

(g)

(h)

(i)

FIGURE 1: Continued.

IPF

Phase map

Recrystallization

ND

RD

δ
γ

ND

RD

Deform
Subgrain
Recrystallization

ND

RD

(j)

(k)

(l)

IPF

Phase map

Recrystallization

ND

RD

δ
γ

ND

RD

Deform
Subgrain
Recrystallization

ND

RD

(m)

(n)

(o)
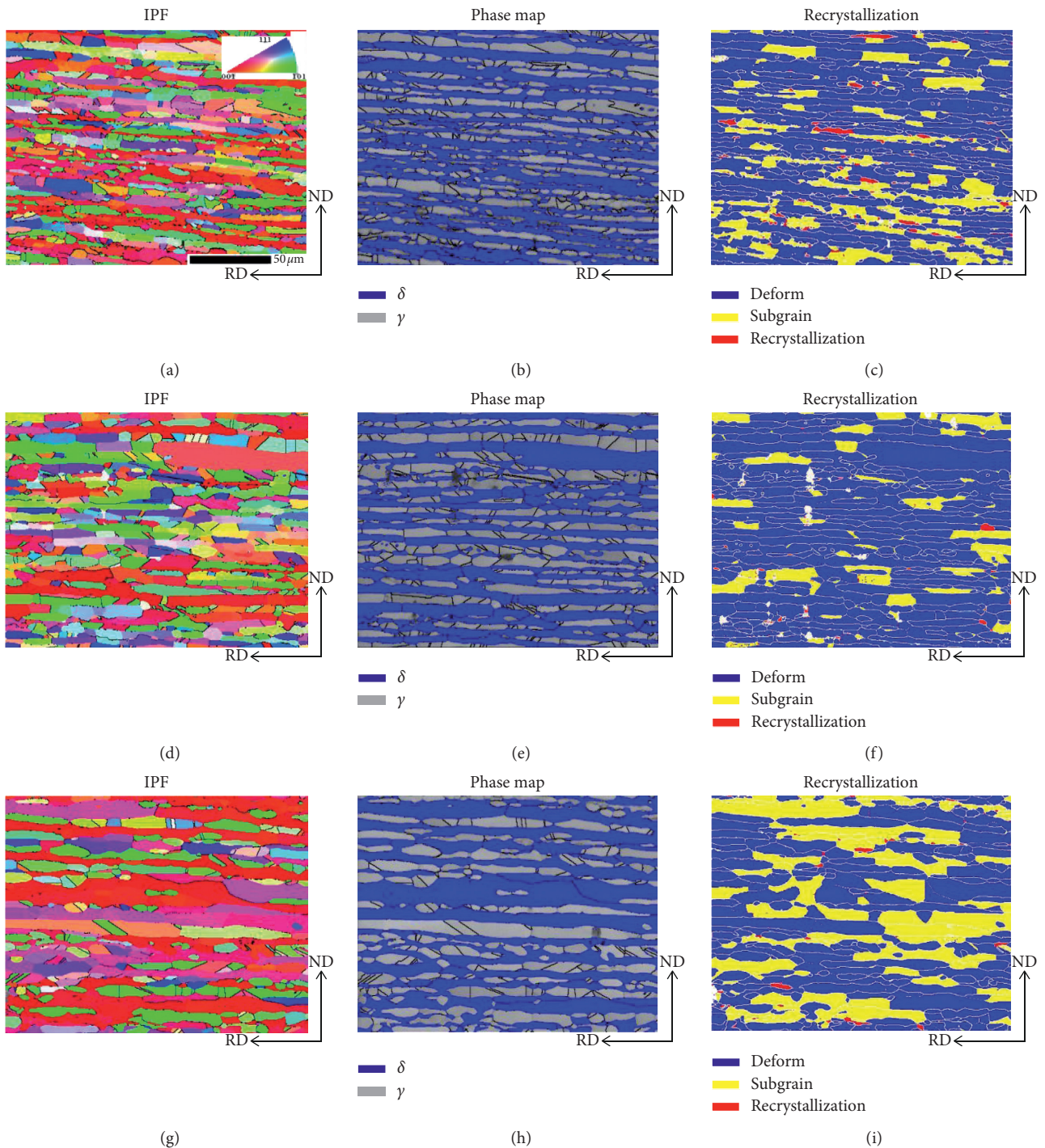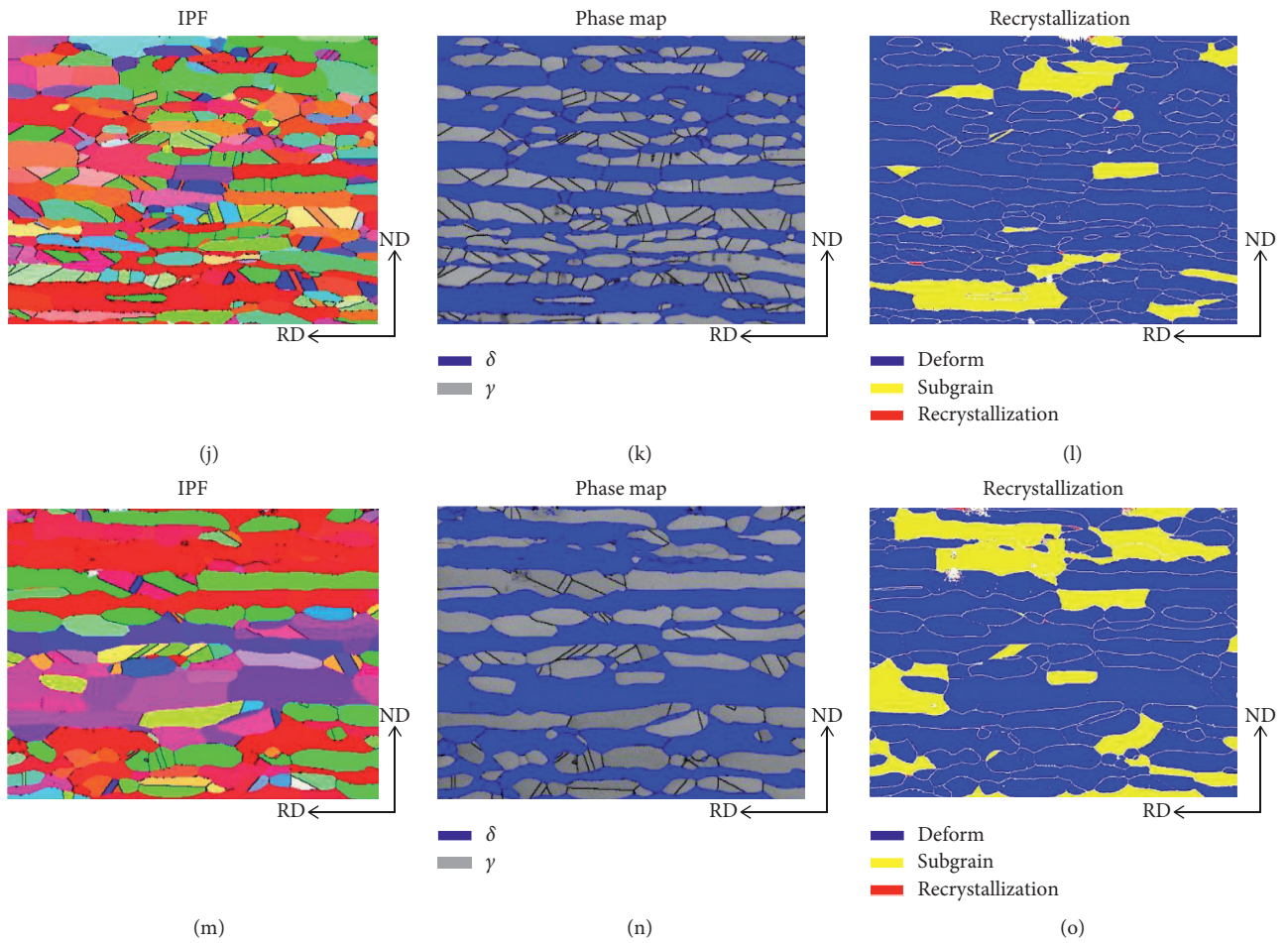
FIGURE 1: Microstructure of 2205 duplex stainless steel at different solution temperatures: (a–c) 1000°C, (d–f) 1040°C, (g–i) 1080°C, (j–l) 1120°C, and (m–o) 1160°C.
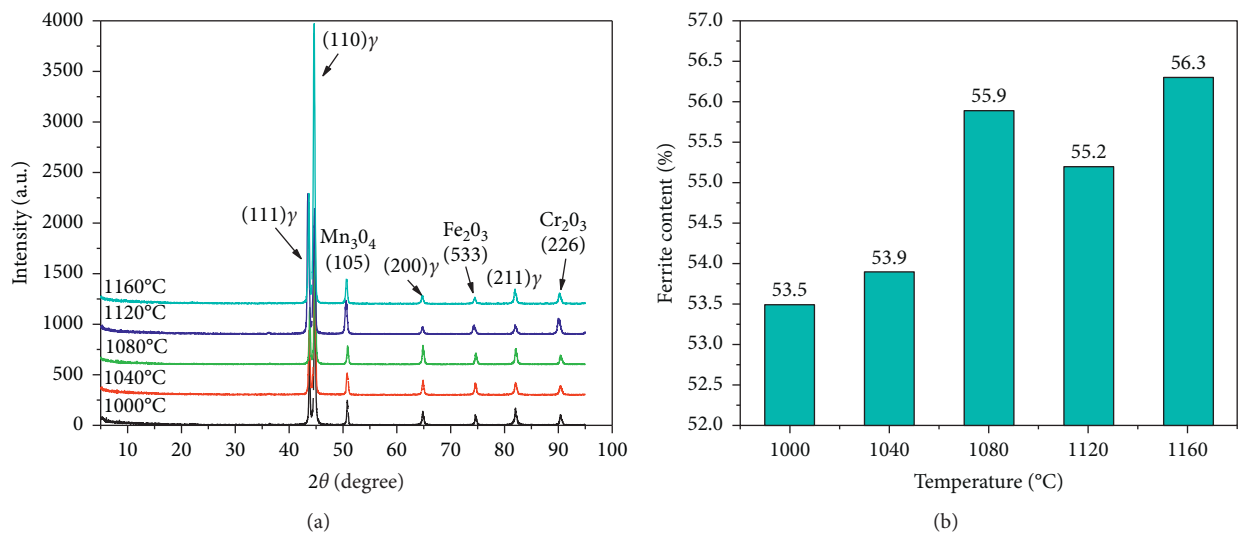

(a)

(b)

FIGURE 2: (a) X-ray diffraction patterns of the duplex stainless steel surface. (b) Ferrite phase proportion of 2205 duplex stainless steel at different solution temperatures.
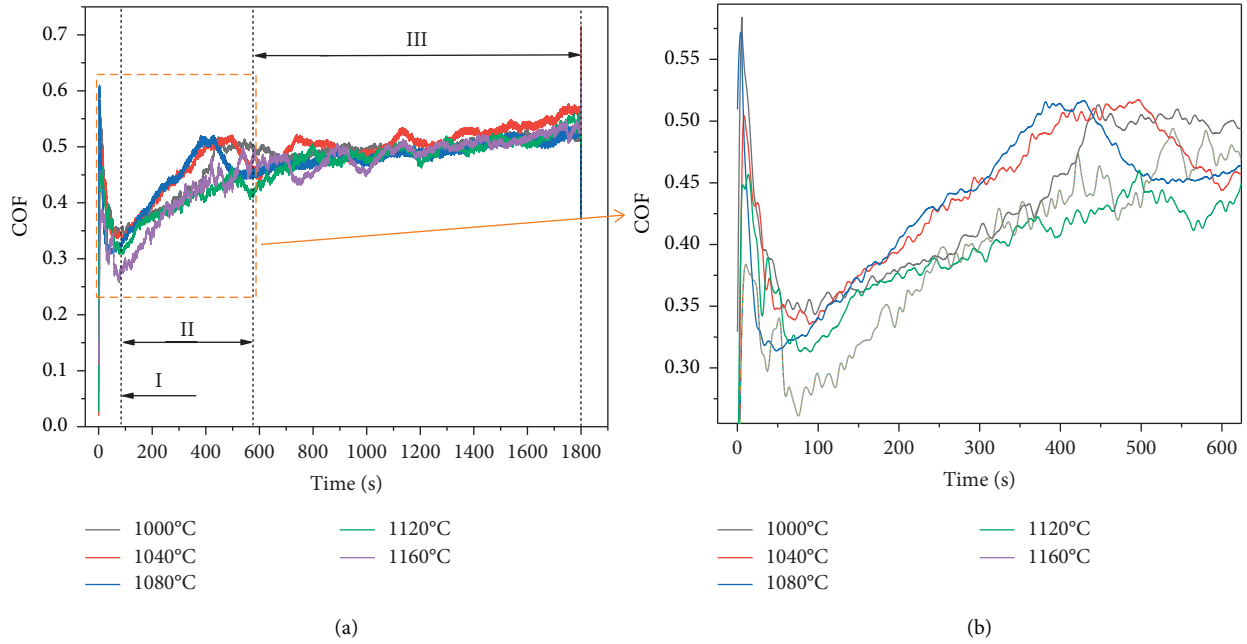
(a)

(b)

FIGURE 3: Relationship between friction coefficient and dry friction time at different solution temperatures.

has a certain roughness, so the contact area between the Si_3N_4 ball and the material surface is small. This leads to an increase in contact stress and wear rate. The subsequent decrease in the friction coefficient is due to the rapid wear of the ball and the material surface, which makes the interface smoother and the contact area smaller. Besides, the wear debris between the friction pairs acts like ball bearings to reduce the friction coefficient. In the second stage, as the friction continues to increase, the actual contact area also increases, resulting in a further increase in the friction coefficient. After about 400 s, the wear debris between the friction pairs increases to such a level that the friction coefficient decreases. In the third stage, plastic deformation leads to work hardening with the increase in the degree of wear, but the surface contact area remains almost constant. Therefore, the wear increases slowly with time [30, 31], and the friction coefficient increases slowly and stably.

In the first stage, the peak value of the friction coefficient increases along with a rise in solution temperature. This may be due to the increase in the microstructure and wear rate of 2205 dual-phase steel resulting from the solution temperature increase. As Figure 3 shows, the highest value of the coefficient at 1160°C is 0.27. In the second stage, the friction coefficient reaches a peak of 0.52 at 1040°C and 1080°C. The peak value of the friction coefficient at 1120°C and 1160°C is 0.45, which is lower than for the other solution temperatures. This is because an increase in the solution temperature results in the alloy elements in 2205 dual-phase steel dissolving in the matrix, thus improving the material strength [32]. Under the same load, the actual contact area and friction coefficient are lower. In the third stage, the friction coefficients for the five solution temperatures are all very similar and increase slowly.

3.3. Effect of Solution Temperature on the Wear Macromorphology.
Friction and wear tests were carried out on different 2205 duplex stainless steel samples. The macromorphology and cross-section morphology of the samples after the test are shown in Figure 4. Results of the friction and wear test indicate that the macrostate of wear was similar for all solution temperatures, and the depth and width were about 85–94 μm and 1.5 mm, respectively.

Figure 5 shows the wear volume of the 2205 duplex stainless steel under different solution treatment conditions. Combined with the results of the analysis on the microstructure and the friction coefficient, this situation may be due to the solution strengthening effect of the 2205 dual-phase steel that occurred with the increase in solution temperature. This causes the wear volume to decrease, and the grain growth makes the strength and wear resistance to decrease.

3.4. Analysis of the Micromorphology of Friction and Wear.
Figure 6 shows the wear morphology (from middle to edge) and surface oxygen energy spectrum distribution of dual-phase steel at different solution temperatures under dry friction conditions. By comparing this with the results shown in Figure 5, it can be seen that the wear track of the dual-phase steel under different solution temperatures is very similar, indicating that the wear mechanism of the five groups of samples is essentially the same. The reciprocal sliding of the silicon nitride ball causes the deformation of 2205 dual-phase steel and results in cutting or ploughing. Microcracks appear on the surface of the 2205 dual-phase steel under the repeated action of the contact compressive stress of the silicon nitride ball and then peel off. The cracks can be easily seen in Figure 6. At 1000°C, there is a lot of
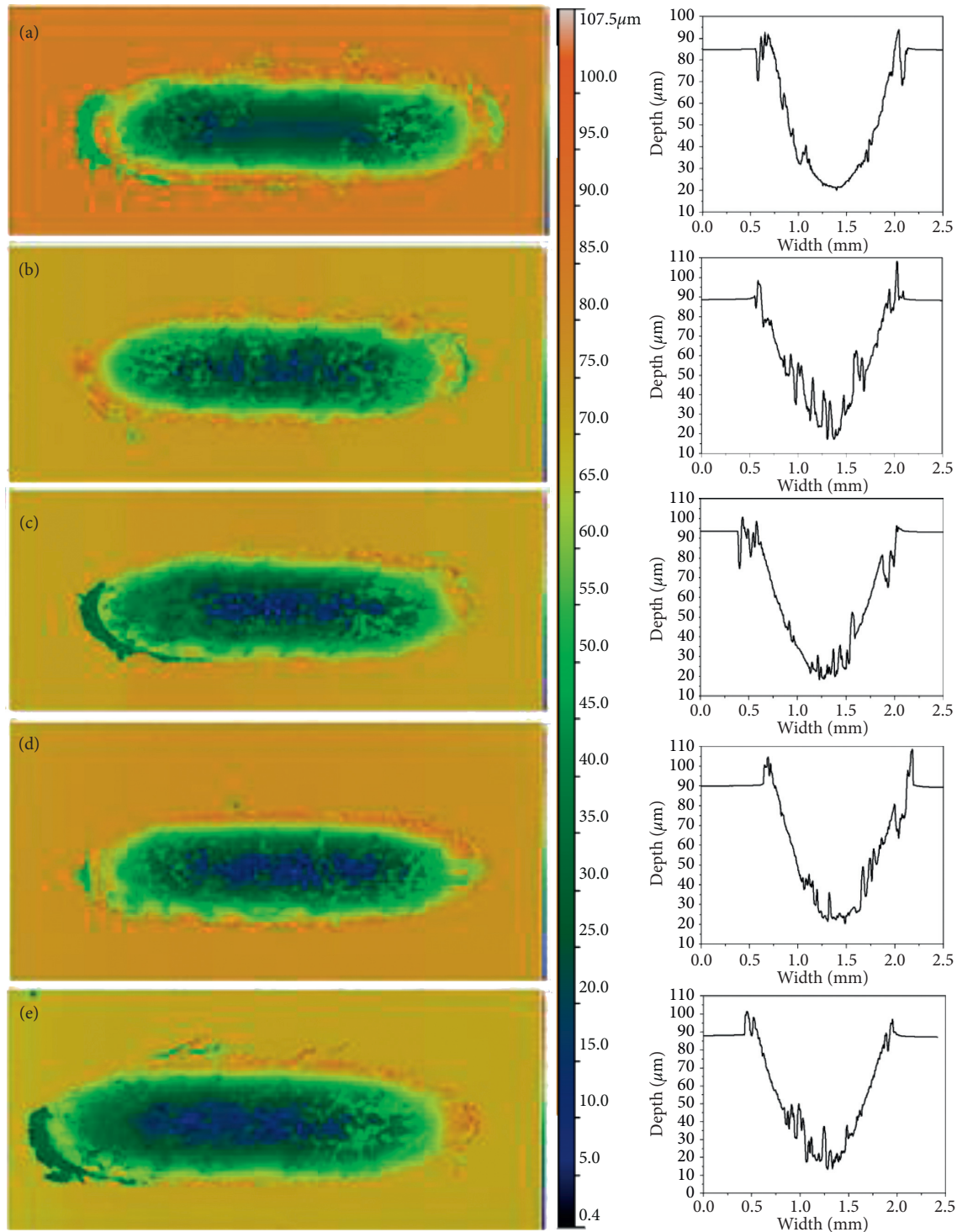
FIGURE 4: Wear macromorphology and cross-section morphology of samples at different solution temperatures: (a) 1000°C, (b) 1040°C, (c) 1080°C, (d) 1120°C, and (e) 1160°C.

spalling, and the corresponding oxygen distribution map shows that the oxygen distribution at this temperature is the least. With a rise in solution temperature, the spalling layer presents a similar morphology. When the temperature rises, oxygen in the oxygen element distribution diagram shows a steady increasing trend. When the temperature is 1160°C, the distribution area of oxygen is the largest. This may be

related to an increase in the grain size resulting from the rise in the solution temperature ranged from 1000°C to 1160°C. In the friction and wear process, the compressive stress at the contact point of the asperities on the sample surface can reach more than 4000 MPa and reach high temperatures of more than 1000°C instantaneously [33]. Coarse grains are prone to high-temperature oxidation under compressive
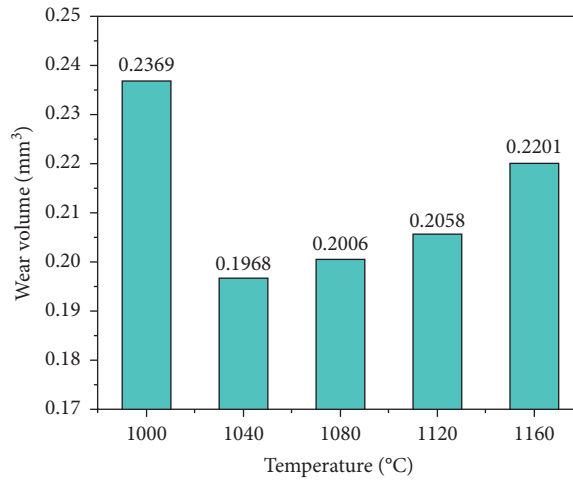
FIGURE 5: Wear volume of 2205 duplex stainless steel at different solution temperatures.
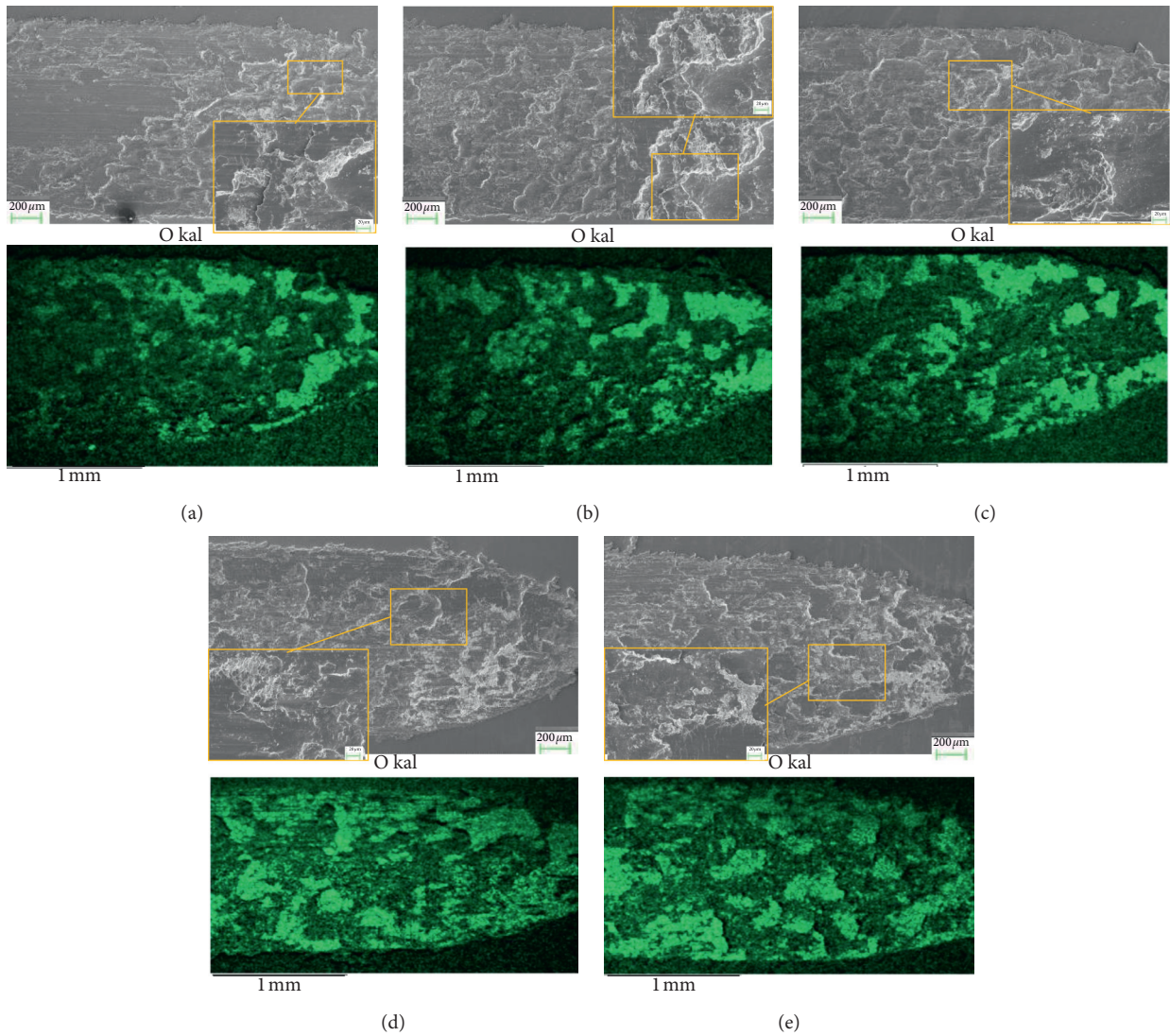
FIGURE 6: Wear morphology (from middle to edge) and surface oxygen energy spectrum distribution of dual-phase steel at different solution temperatures under dry friction conditions.

stress. Therefore, under 100 N dry friction, with the increase of solution temperature and oxygen distribution area, the wear mechanism of 2205 dual-phase steel gradually expanded from local oxidation wear to adhesive wear and exfoliation wear.

4. Conclusion

(1) As the solution temperature rises, the fiber-like austenite phase in 2205 duplex stainless steel gradually evolves into a short rod-like and island-like morphology, and the grain/phase boundaries become clearer. The content of the ferrite phase in the microstructure increases gradually, and the content of the ferrite phase can reach 56.3% at 1160°C.

(2) Results show that the friction coefficient curves of 2205 dual-phase steel and silicon nitride balls have similar characteristics between 1000°C and 1160°C. The friction coefficient first increases rapidly, reaches a peak value, and then decreases at a fast rate before gradually and stably increasing. In the first stage, the peak value of the friction coefficient falls with an increase in the solution temperature. In the second stage, the friction coefficient at 1040°C and 1080°C reaches the peak value of 0.52, while in this stage, the friction coefficient at 1120°C and 1160°C only reaches a maximum value of 0.45. In the third stage, the friction coefficients of the five samples are almost identical, and all increase slowly.

(3) Under 100 N dry friction, with the increase of solution temperature and oxygen distribution area, the wear mechanism of 2205 dual-phase steel gradually expanded from local oxidation wear to adhesive wear and exfoliation wear.

Data Availability

All the data that support the findings of this study are included within the article.

Conflicts of Interest

The authors declare that there are no conflicts of interest.

Acknowledgments

References

[1] M. B. Mampuya, M. C. Umba, K. Mutombo, and P. A. Olubambi, "Effect of heat treatment on the microstructure of duplex stainless steel 2205," *Materials Today: Proceedings*, vol. 38, pp. 1107–1112, 2021.

[2] Y. Tang, "Investigation of influence of surface roughness on pitting corrosion of duplex stainless steel 2205 using various electrochemical techniques," *International Journal of Electrochemical Science*, vol. 14, pp. 6790–6813, 2019.

[3] Z. Tao, C. Zhu, M. He, and M. Karakus, "A physical modeling-based study on the control mechanisms of negative Poisson's ratio anchor cable on the stratified toppling deformation of anti-inclined slopes," *International Journal of Rock Mechanics and Mining Sciences*, vol. 138, Article ID 104632, 2021.

[4] C. Zhu, M. He, M. Karakus, X. Zhang, and Z. Tao, "Numerical simulations of the failure process of anaclinal slope physical model and control mechanism of negative Poisson's ratio cable," *Bulletin of Engineering Geology and the Environment*, vol. 80, no. 4, pp. 3365–3380, 2021.

[5] Y. Wang, W. K. Feng, R. L. Hu, and C. H. Li, "Fracture evolution and energy characteristics during marble failure under triaxial fatigue cyclic and confining pressure unloading (FC-CPU) conditions," *Rock Mechanics and Rock Engineering*, vol. 54, no. 2, pp. 799–818, 2021.

[6] L. Jinlong, H. Jin, and L. Tongxiang, "The effect of electrochemical nitridation on the corrosion resistance of the passive films formed on the 2205 duplex stainless steel," *Materials Letters*, vol. 256, Article ID 126640, 2019.

[7] X. Yang, J. Wang, C. Zhu, M. He, and Y. Gao, "Effect of wetting and drying cycles on microstructure of rock based on SEM," *Environmental Earth Sciences*, vol. 78, no. 6, p. 183, 2019.

[8] Y. Song, S. Wang, G. Zhao, Y. Li, L. Juan, and Z. Jian, "Hot deformation behavior and microstructural evolution of 2205 duplex stainless steel," *Materials Research Express*, vol. 7, no. 4, Article ID 046510, 2020.

[9] K. Vijayalakshmi, V. Muthupandi, and R. Jayachitra, "Influence of heat treatment on the microstructure, ultrasonic attenuation and hardness of SAF 2205 duplex stainless steel," *Materials Science and Engineering: A*, vol. 529, no. 1, pp. 447–451, 2011.

[10] J. Nachazel, P. Martínek, P. Podany, and I. Polakova, "Effect of heat treatment on the microstructure of duplex stainless steel," *Applied Mechanics and Materials*, vol. 751, pp. 9–14, 2015.

[11] Q.-X. Meng, W.-Y. Xu, H.-L. Wang, X.-Y. Zhuang, W.-C. Xie, and T. Rabczuk, "DigiSim-an open source software package for heterogeneous material modeling based on digital image processing," *Advances in Engineering Software*, vol. 148, Article ID 102836, 2020.

[12] C. Zhu, M.-C. He, M. Karakus, X.-H. Zhang, and Z. Guo, "The collision experiment between rolling stones of different shapes and protective cushion in open-pit mines," *Journal of Mountain Science*, vol. 18, no. 5, pp. 1391–1403, 2021.

[13] Q. Wang, Z. Jiang, B. Jiang, H. Gao, Y. Huang, and P. Zhang, "Research on an automatic roadway formation method in deep mining areas by roof cutting with high-strength bolt-grouting," *International Journal of Rock Mechanics and Mining Sciences*, vol. 128, Article ID 104264, 2020.

[14] J. X. Zhang, W. W. Li, and Q. Y. Li, "State-of-the-art weldability of the 2205 duplex stainless steel," *Welded Pipe and Tube*, vol. 28, no. 5, pp. 6–10, 2005.

[15] Y. Mao, Y. Zheng, Y. Shi et al., "Effect of rolling deformation on microstructure and mechanical properties of 2205 duplex stainless steel with micro-nano structure," *Modern Physics Letters B*, vol. 34, no. 25, Article ID 2050269, 2020.

[16] X. J. Meng, F. Y. Meng, W. W. Song et al., "Effect of two kinds of heat treatment on corrosion behavior of 2205 duplex

stainless steel," *Corrosion & Protection*, vol. 33, no. 7, pp. 563–566, 2012.

[17] B. Li, R. Bao, Y. Wang, R. Liu, and C. Zhao, "Permeability evolution of two-dimensional fracture networks during shear under constant normal stiffness boundary conditions," *Rock Mechanics and Rock Engineering*, vol. 54, no. 1, pp. 409–428, 2021.

[18] J. C. Zheng, *Study on the Resistance to Corrosion of Duplex Stainless Steel 2205*, pp. 34–45, University of Science and Technology Beijing, Beijing, China, 2019.

[19] Q. Wang, H. Gao, B. Jiang, S. Li, M. He, and Q. Qin, "In-situ test and bolt-grouting design evaluation method of underground engineering based on digital drilling," *International Journal of Rock Mechanics and Mining Sciences*, vol. 138, Article ID 104575, 2021.

[20] Q. Wang, Q. Qin, B. Jiang et al., "Mechanized construction of fabricated arches for large-diameter tunnels," *Automation in Construction*, vol. 124, Article ID 103583, 2021.

[21] A. Li, F. Dai, Y. Liu, H. Du, and R. Jiang, "Dynamic stability evaluation of underground cavern sidewalls against flexural toppling considering excavation-induced damage," *Tunnelling and Underground Space Technology*, vol. 112, Article ID 103903, 2021.

[22] X. Wang, L. Huang, H. Wang, C. Ma, and J. Luo, "Influence of solution treatment on microstructure and properties of duplex stainless steel," *Heat Treatment of Metals*, vol. 43, no. 5, pp. 101–105, 2018.

[23] R. Djeridi and M. Ould Ouali, "Experimental modeling of wear behavior of filled elastomer SBR under dry friction-influence of roughness," *Key Engineering Materials*, vol. 640, pp. 13–20, 2015.

[24] V. Abouei, H. Saghafian, S. Kheirandish et al., "A study on the wear behaviour of dual phase steels," *Materials Science and Technology*, vol. 023, no. 1, pp. 107–110, 2007.

[25] A. Bayram and A. Uğuz, "Effect of microstructure on the wear behaviour of a dual phase steel," *Materialwissenschaft und Werkstofftechnik*, vol. 32, no. 3, pp. 249–252, 2001.

[26] M. J. Wang, Y. X. Wang, N. Fan, Q. F. Wang, and F. Y. Yan, "Fretting wear properties of 2507 super duplex stainless steel in artificial seawater," *Lubrication Engineering*, vol. 44, no. 2, pp. 24–30, 2019.

[27] Y. T. Wang, P. L. Mao, L. J. Chen, Y. B. Ren, B. C. Zhang, and K. Yang, "Fabrication technology of high nitrogen austenite layer on surface of duplex stainless steel," *Journal of Shenyang University of Technology*, vol. 3, pp. 49–52, 2007.

[28] Q. Bai and Z. Zhang, "Effect of solution treatment temperature on phase ration and mechanical properties of 2507 super duplex stainless steel," *Heat Treatment of Metals*, vol. 9, pp. 123–126, 2019.

[29] Y. Xue, S. Yan, J. Xie, Z. Feng, and J. Zou, "Contact and tribological properties of self-lubricating ellipsoidal plain bearings," *Tribology International*, vol. 140, Article ID 105840, 2019.

[30] L. Shan, Y. Wang, J. Li, X. Jiang, and J. Chen, "Improving tribological performance of CrN coatings in seawater by structure design," *Tribology International*, vol. 82, pp. 78–88, 2015.

[31] R. Yang, W. Ma, C. J. Duan et al., "Microstructure responses and deformation mechanisms of solutionized Ti-51.5 at.% Ni alloy during reciprocating sliding," *Tribology International*, vol. 140, Article ID 105816, 2019.

[32] F. Xie, J. W. Pan, and H. Yuan, "Optimizing heat treatment for a duplex stainless steel," *Transactions of Materials and Heat Treatment*, vol. 31, no. 9, pp. 68–72, 2010.

[33] S. Z. Wen and P. Huang, *Principles of Tribology* pp. 62–78, Tsinghua University Press, Beijing, China, 3rd edition, 2008.

Research Article

Effects of Bedding Geometry and Cementation Strength on Shale Tensile Strength Based on Discrete Element Method

Jiong Wang ⓘ,[1] Yang Wang ⓘ,[1] Liu Yang ⓘ,[1] Tianquan Chang ⓘ,[2] and Qingping Jiang ⓘ[2]

[1]*State Key Laboratory for Geomechanics and Deep Underground Engineering,
China University of Mining and Technology (Beijing), Beijing 100083, China*
[2]*China Research Institute of Exploration and Development, PetroChina Xinjiang Oilfield Company, Karamay,
Xinjiang 834000, China*

Correspondence should be addressed to Liu Yang; shidayangliu@cumtb.edu.cn

To study the effects of anisotropy and heterogeneity on the shale failure mode and tensile strength, Brazilian splitting tests were performed from both directions of the bedding and layer thickness. Layers containing different bedding and loading angles and layer thicknesses were obtained separately. The results show that, at 0° and 90° angles, the shale cracks grow "linearly"; at 15°, the shale cracks have "arc type" growth; and at 30°–75°, the shale-splitting displays "broken line" crack propagation. The tensile strength from 0° to 90° exhibits an increasing trend. Water has a significant softening effect on the tensile strength of shale—the higher the water content, the lower the tensile strength. In addition, a 3DEC numerical simulation was used to simulate the tests, establishing shale specimen particles with random blocks. In the shale disc, uneven parallel bedding and uniform parallel bedding were set up with different loading angles and layer thicknesses to generate simulated stress-displacement curves, and the effect of layering on shale cleavage was analyzed from a mesoscopic perspective. The tensile strength of shale with uniform parallel bedding was found to be higher under the same conditions, which is consistent with the experimental results. By comparing the experimental and simulation results, from both the macro- and mesoperspectives, the Brazilian splitting crack growth of shale is affected by bedding, displaying a process from disorder to order. This study is of great significance for further exploration of the mechanical properties of shale under loading failure.

1. Introduction

As an unconventional energy source, shale gas has attracted much attention from researchers. The development of shale gas requires large-scale hydraulic fracturing of a shale rock mass to form a fissure grid structure in the rock mass. In addition, shale bedding is well developed [1], and there are many natural fractures hidden in the rock mass with strong heterogeneity and complicated fracture propagation laws. A thorough understanding of the crack propagation law and its influencing factors when shale is stressed is of great significance. Moreover, it is helpful to control the development of the fracture network and improve the production of shale gas.

The Brazilian splitting test indirectly measures the tensile strength of rocks through compression. Owing to the simple operation and easily prepared test pieces, this test has become a universal method for measuring the tensile strength of materials. Many factors affect the experimental results. Huang et al. [2] established a Brazilian splitting mechanical model under a string load and obtained an approximate analytical solution of the internal stress of a disk. It was found that the greater the loading angle of the platform, the lower the stress concentration at the loading place, and the smaller the tensile zone in the disk. Peng et al. [3] carried out a Brazilian splitting test of rocks at alternate loading rates and found that the rock splitting strength increased with increasing loading rate. In addition, through the Brazilian splitting test, crack initiation and propagation laws when the rock splits can be observed. Teng et al. [4] conducted a Brazilian splitting test of Longmaxi shale in combination with acoustic emission and found that the bedding and loading angles affected the

shale failure mode. Du et al. [5] combined digital image correlation technology to perform the Brazilian splitting test of carbon shale at different dip angles and found that, with the increase of bedding and loading angle, the split crack initiation time increased, and the extension to penetration time decreased. Gao et al. [6] collected shale from the Yanchang Formation in Ordos and conducted a Brazilian splitting experiment to measure the brittleness index and horizontal differential stress of the shale. It was also found that fractures propagated along the natural fracture during fracturing of the shale. Furthermore, the combination of experimentation and numerical simulation can verify the crack propagation law. Bilgen Carola et al. [7] conducted a Brazilian splitting test and established two- and three-dimensional Brazilian split disc numerical models, obtaining a phase-field method that can predict crack initiation and propagation.

The discrete element method is a dynamic numerical simulation method based on deformable elements, which can simulate the shape and property changes after a block is loaded. Based on the unique separability of its basic unit, the discrete element method is more suitable for simulating plastic mechanical problems such as deformation and failure of massive and fissured media [8]. Wang et al. [9] combined the Neper program with 3DEC software to establish a demonstration model containing rigid, elastic, and fragile particles and found that the assignment of particles and the contact parameters between particles affect the macroscopic mechanical properties of rock compressive strength. Li et al. [10] used the DFN module in 3DEC to simulate the joints in a rock mass for analysis of the discontinuity of the rock material. Meanwhile, Huang et al. [11] used the PFC program to establish a discrete element model of a center-grooved Brazilian disc with different particle sizes. It was found that the larger the particle radius of the specimen, the greater the tensile strength.

Although a lot of experimental and numerical simulation research has been conducted on the extension of shale tensile cracks, there is no systematic study on the effects of the angle and layer thickness of bedding, bond strength, and natural cracks on the extension of tensile cracks. It is necessary to conduct in-depth research from the macro- and micro-perspectives. In this study, Brazilian splitting tests were conducted on shale specimens from the Longmaxi Formation in the Sichuan Basin, China, to macroscopically study the laws of shale tensile crack propagation. Further, mesomodelling was performed using 3DEC to observe the changes in shale morphology during the splitting process. Stress and displacement fields were generated for a comparative analysis with the experimental results to reveal the propagation rule of shale Brazilian split cracks under the influence of bedding and layer thickness.

2. Numerical Methodology

2.1. Basic Theory of Discrete Element Method.
As shown in Figure 1, 3DEC considers that the interaction force between the two blocks is related to the contact between the blocks [12].

For elastic deformation, suppose that the increment of the normal force vector between the blocks $\triangle F^n$ is directly proportional to the increment of the normal displacement $\triangle U^n$, and then,

$$\Delta F^n = -K_n \Delta U^n A_c, \tag{1}$$

where K_n is the normal stiffness coefficient of the joint, and A_c is the contact area between the blocks.

Similarly, the increment of the tangential force vector between blocks ΔF_i^s is

$$\Delta F_i^s = -K_s \Delta U_i^s A_c, \tag{2}$$

where K_s is the tangential stiffness coefficient of joints, and ΔU_i^s is the increment of the tangential displacement. Index i takes values of 1–3 and denotes the components of a vector in the global coordinate system.

The total normal force and total tangential force are

$$\begin{aligned} F^n &= F_0^n + \Delta F^n, \\ F_i^s &= F_{i0}^s + \Delta F^s, \end{aligned} \tag{3}$$

where F_0^n and F_{i0}^s are the initial normal force and initial tangential force, respectively.

Considering the plastic deformation of rock failure, the normal tension is greater than the tensile strength of the contact $F^n = 0$. If the Mohr–Coulomb criterion is used to calculate the shear strength, when the tangential force F_i^s exceeds $c + F^n \tan \varphi_f$, slip occurs between the blocks, and the tangential force takes the limit value at this time. This indicates that

$$\begin{aligned} F_i^s &= F_{i0}^s - K_s \Delta U_i^s A_c, && \text{if } |F_i^s| < c + F^n \tan \varphi_f, \\ |F_i^s| &= c + F^n \tan \varphi_f, && \text{if } |F_i^s| \geq c + F^n \tan \varphi_f, \end{aligned} \tag{4}$$

where c and φ_f are the contact cohesion and friction angle, respectively.

2.2. Building the Model.
The numerical simulation uses a combination of 3DEC and Neper. Neper is a free and open source software, which can realise a 3D Voronoi mosaic model and further convert it into 3DEC format code [13]. 3DEC is a three-dimensional computer numerical program based on discrete element simulation, which can calculate the deformation of rock blocks by establishing deformable blocks and different contacts [8].

First, Neper was used to generate a 3D particle mosaic and synthesize a Brazilian disc model. The simulation specification was $\Phi 50 \, \text{mm} \times 1 \, \text{mm}$. Then, the disc was imported into 3DEC, and the powerful DFN module was used in 3DEC to generate layering.

As shown in Figure 2, the shale disc was set as block Mat 1, and the upper and lower parallel loading plates were set as block Mat 2. The joint material was divided into four parts. The contact surface between the upper and lower loading blocks and the shale disc is Jmat 1. The preset bedding surface is Jmat 2. The virtual joint in the 3DEC simulation is Jmat 3 [14], and the contact surface between shale particles is Jmat 4.
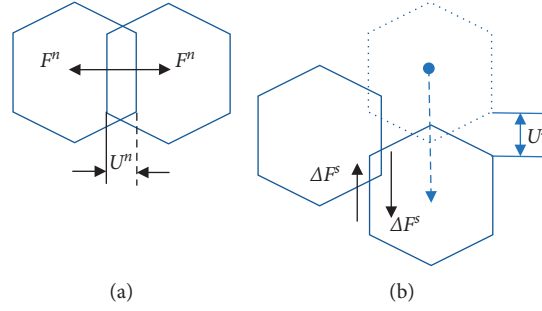
(a) (b)

FIGURE 1: Diagram of the contact relationship between blocks. (a) Normal contact. (b) Tangential contact.

(a) (b)
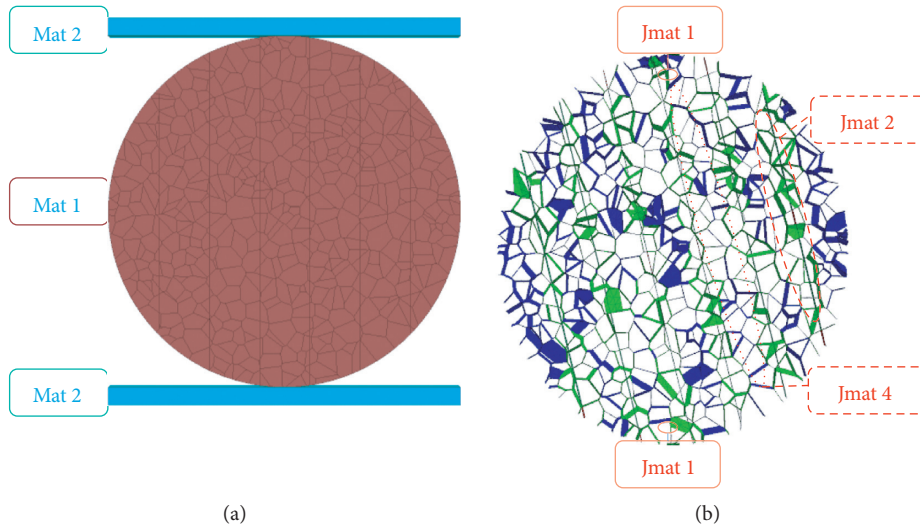
FIGURE 2: Brazilian disc model. (a) Blocks. (b) Joints.

As shown in Figures 3(a)–3(d), taking the angle between the bedding direction and the vertical loading direction as the bedding angle, a preset bedding of 0°–90° was established. The bedding was a long strip, and its length did not penetrate the disc, whereas its width was consistent with that of the disc. As shown in Figure 3(e), five observation points were set on the centerline of the disc from top to bottom at equal intervals, numbered 1–5, and point 3 is the center of the circle.

Uniformly and nonuniformly parallel bedding were established, and samples were modelled regarding the bedding direction and bedding spacing. When building the bedding models with different layers, the bedding angle was set to 0°. Set the block model to linearly elastic, while set the joints model to area contact elastic/plastic with Coulomb slip failure. Failure of joint in shear or tension results in the use of cohesion, tension, and friction residual values. The default residual values of cohesion and tension are 0. The lower boundary was fixed, and a loading speed boundary of 0.1 mm/min was set at the upper loading block node, which is consistent with the experimental loading speed. Changes in the stress field and displacement field were recorded at the five observation points.

2.3. Calibration of Microparameters.

To build the model, values must be assigned to different blocks and contacts in the model. Because the particle and bedding parameter values cannot be measured experimentally, it is necessary to first assume the parameters that need to be assigned and further adjust them according to the results.

Wang et al. [15] proposed that, in 3DEC, the joint normal stiffness K_n can be expressed as

$$K_n = \frac{7.34\sigma_n}{0.3434},$$

(5)

where σ_n is the normal stress.

Considering the operation efficiency, the stiffness value of the adjacent block is greater than 10 times the bedding stiffness value [12], which is

$$k_n \text{ and } k_s \leq 10 \left[\max\left(\frac{(K+4)/3G}{\Delta z_{\min}} \right) \right],$$

(6)

where k_n and k_s are the normal and shear stiffness of the bedding, respectively; K and G are the bulk and shear modulus of the adjacent block, respectively; and $\Delta z_{\min}$ is the minimum width of the normal direction of the adjacent block in the bedding.

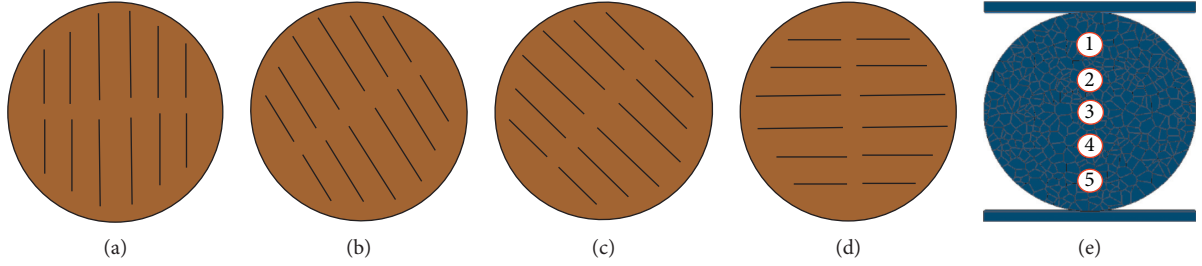FIGURE 3: Schematic of preset bedding and observation points. (a) 0°. (b) 30°. (c) 60°. (d) 90°. (e) Observation points.

According to classical rock mechanics, the bulk modulus of a block is given by

$$K = \frac{E}{3(1 - 2\mu)},\tag{7}$$

and the shear modulus is

$$G = \frac{E}{2(1 + \mu)},\tag{8}$$

where E is the bulk Young's modulus, and μ is the bulk Poisson's ratio.

The calculation results were synthesized, with reference to the relevant literature for the assignment of the microparameters of the weak surface of the rock [14, 16–21] and large numbers to the loading block to prevent deformation of the loading block. Finally, the simulation results conforming to the test rules were obtained. The calibration parameters used are listed in Tables 1 and 2.

3. Results and Discussion

3.1. Model Validation. As shown in Figure 4(a), black homogeneous shales from the Longmaxi Formation in the Sichuan Basin were taken and processed in accordance with the International Society for Rock Mechanics [22] standards and prepared into Φ50 mm × 25 mm standard-specification disc test pieces by coring, cutting, and grinding. The parallelism of the upper and lower surfaces of each test piece was controlled within 0.5 mm, and the flatness of the surface was controlled within 0.1 mm. All test pieces were stored in a dry environment at room temperature.

The Brazilian splitting test involves platform loading. To ensure that the loading direction line passes through the center of the disk, the specimen was first marked in the preapplication direction, and then the upper loading point was marked. When placing the test piece, a vertical line was used for calibration. After fixing the test piece, the lower platform was fixed, and the upper platform was applied with a loading speed of 0.1 mm/min. The stress-displacement curve of the test was recorded and observed. When a sudden stress drop was measured, the test piece formed a crack and stopped loading. The shape of the specimen after splitting is shown in Figure 4(b). The splitting crack penetrated the upper and lower loading ends and developed vertically through the center point of the disc.

TABLE 1: Block parameters.

	Density (kg/m³)	Bulk modulus (GPa)	Shear modulus (GPa)
Mat 1	2400	65.2	21.8
Mat 2	78 000 000	7780	3590

A homogeneous shale disc model without bedding was created in 3DEC software for loading, and the disc displacement field and stress field evolution were recorded.

As shown in Figures 5 and 6, similar to the experimental splitting results, the splitting crack of the homogeneous model extended vertically through the upper and lower loading ends. After splitting, the displacement field on the right side of the crack was larger than that on the left side. The analysis shows that, because of the damage to the particles at the loading end after splitting, the disk homogeneity was destroyed, and the forces on both sides were uneven, resulting in an asymmetric distribution of the stress field.

As shown in Figure 7(a), the tensile stress-main displacement curves of the center point of the test and the simulated disc were compared. During the test loading process, the vertical tensile stress at the center point increased linearly with the loading displacement. Before the splitting failure, the stress increasing trend rarely decreased. The peak value of the visible tensile stress is the "tensile strength" of the shale specimen [17]. More specifically, the tensile strength of the black shale measured by the test specimen was 7.25 MPa. The maximum stress peak at the center of the circle when the homogeneous model was split by simulation was 6.99 MPa, which was 3.59% different from the tensile strength obtained from the experiment. As shown in Figure 7(b), the split peak stresses of observation points 2 and 4, with the center of the circle as the symmetry point, are approximately 70% of the peak stress at the center of the circle, and the same symmetrical stress peaks at points 1 and 5 are the smallest, approximately 15% of those at the center of the circle. During splitting, the displacements of the five observation points were similar, and the maximum displacement was 26.2 μm at the center point.

For the bedding shale, which is also from the Longmaxi Formation, two sets of samples were further drilled from 0°, 45° and 90° bedding directions. The samples were processed to create standard test pieces, and the first group of samples was recorded as A-0, A-45, and A-90, according to the angle from small to large; the second group of samples was B-0, B-45, and B-90.

TABLE 2: Contact parameters.

	Normal stiffness (10^{14} Pa/mm)	Tangential stiffness (10^{14} Pa/mm)	Friction angle (°)	Cohesion (MPa)	Tensile strength (MPa)
Jmat 1	3.32	1.12	55	24	19
Jmat 2	3.32	1.12	45	23.36	18.25
Jmat 3	3.32	1.12	42	22	17
Jmat 4	3.32	1.12	42	22	17

(a)

(b)
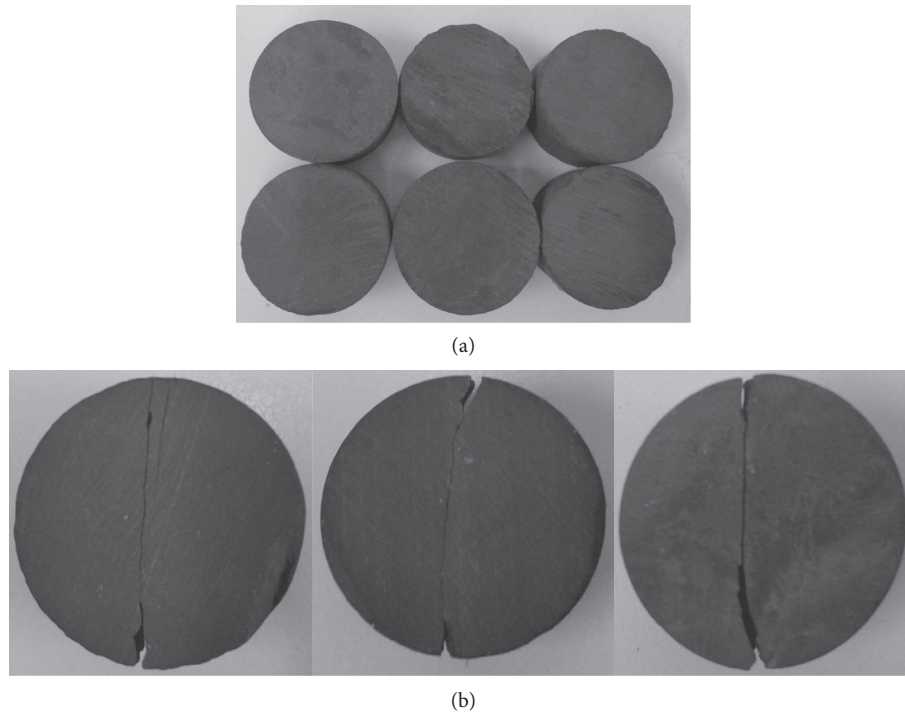
FIGURE 4: Uniform bedding specimens. (a) Before splitting. (b) After splitting.
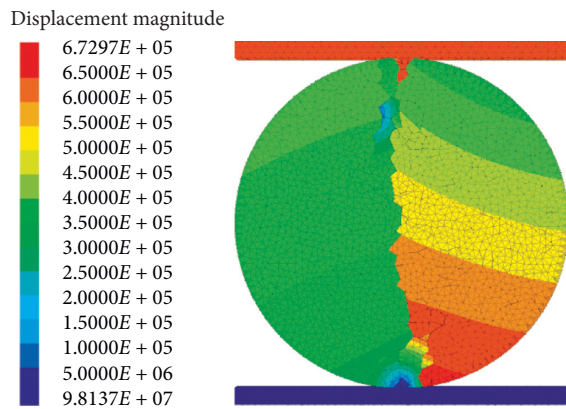
FIGURE 5: Loading displacement cloud of homogeneous model.
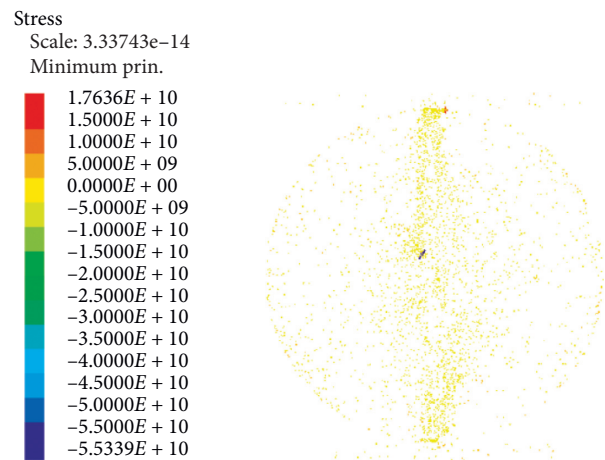
FIGURE 6: Loaded cloud of homogeneous model.

As shown in Table 3, a shale X-ray diffraction analysis was conducted to analyze the mineral composition of the test piece. The clay minerals and nonclay minerals in the two groups of shale were equivalent, each accounting for approximately 50%. Nonclay minerals have the highest quartz content, while clay minerals have the highest illite content.

As shown in Figure 8, for the specimen in the parallel bedding direction, the cracks penetrated the center of the disc along the bedding direction during splitting. Affected by the mineral composition of the specimen, when the main crack develops vertically, the other cracks will split and produce secondary cracks in the vertical direction. Meanwhile, for the test piece in the vertical bedding direction, the crack connects the upper and lower loading ends and is

(a)   (b)
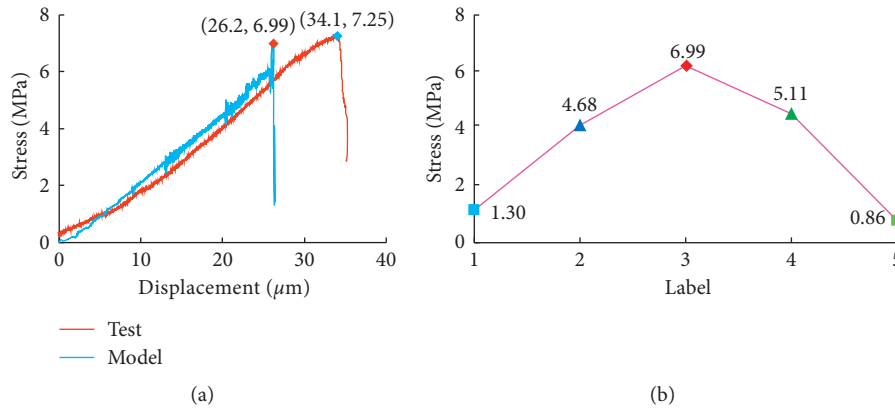
FIGURE 7: Stress-displacement curves of observation points of homogeneous model. (a) Center points of test and simulation test pieces. (b) 5 observation points of simulation test pieces.

TABLE 3: Clay mineral analysis of test specimens.

Label	Total nonclay					Total clay			
	Quartz	Plagioclase	Calcite	Ankerite/Fe-Dolomite	Pyrite	Illite/Smectite (I/S)	Illite	Kaolinite	Chlorite
A-0	25	8	3	3	2	14	25	3	15
A-45	27	10	2	4	3	13	22	3	15
A-90	30	10	2	4	3	11	22	3	14
B-0	27	9	2	4	4	6	28	4	14
B-45	25	9	1	5	7	12	25	2	13
B-90	29	11	1	5	3	10	24	1	12

(a)   (b)   (c)

(d)   (e)   (f)
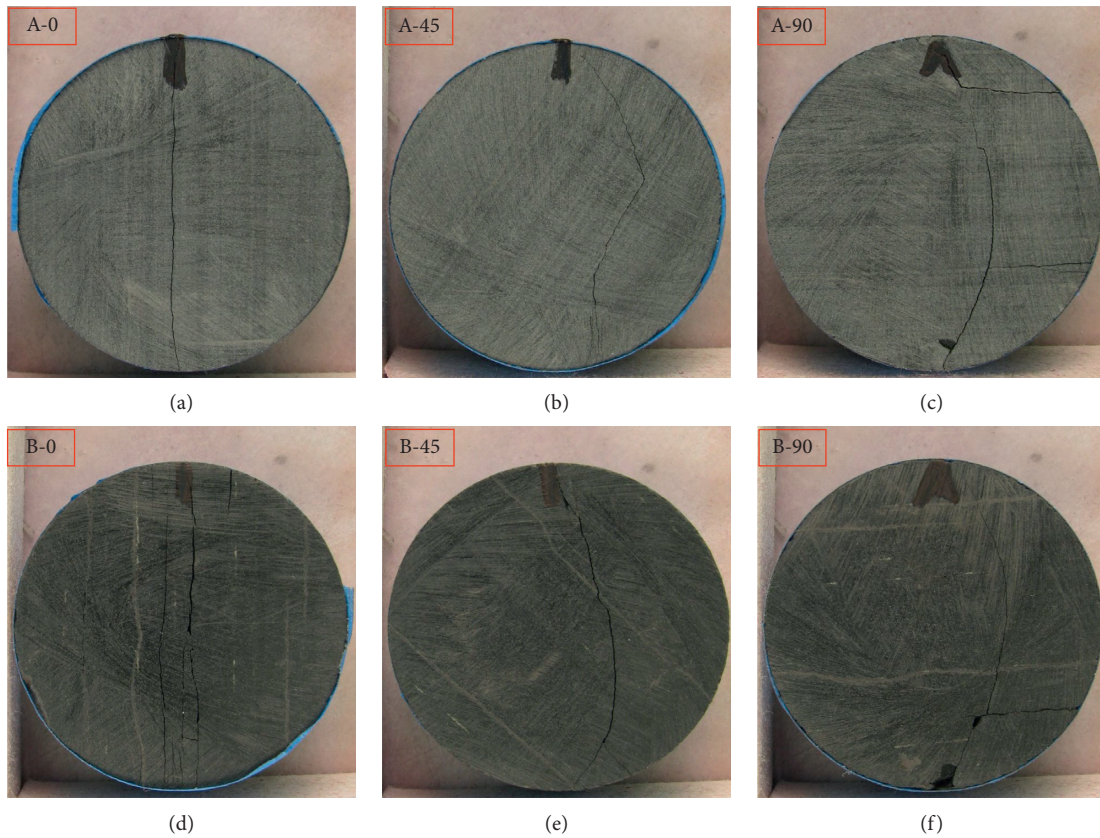
FIGURE 8: Split form of test specimen. (a) A-0. (b) A-45. (c) A-90. (d) B-0. (e) B-45. (f) B-90.

developed into an arc, reaching the maximum arc end at the lateral diameter. At 1/4 of the disk, cracks easily fork to produce lateral secondary cracks. For the 45° bedding direction, the crack connects the two loading points, forming a broken line through the specimen. The main crack first split down as an arc. During the expansion process, it folded in the parallel bedding direction under the influence of bedding. In the vicinity of the lower loading end, the arc crack developed to the lower loading point. In the tests, when the 45° and 90° bedding specimens were split, the crack did not pass through the center of the disc, indicating that the crack was tensile and damaged, and shear slip was also generated. This phenomenon reflects the influence of bedding direction on crack propagation.

As shown in Figure 9, the experimentally obtained shale tensile strength increased with the increase in the bedding and loading angle. At 90°, the tensile strength can be regarded as the tensile strength of the shale blocks. At 0°, the tensile strength can be considered as that of the bedding in the shale. The ratio of the two was 3.25 in group A and 1.5 in group B, indicating that the anisotropy of shale bedding has a significant effect on tensile strength.

3.2. Different Angles.
For different angles, as shown in Figure 10, the stress and displacement of the uniform parallel bedding disc model were changed during the loading process to obtain the corresponding stress field and displacement field. The simulation data were recorded during the loading process at the center point of the bedding, and the corresponding stress-displacement curve was obtained.

As shown in Figures 10 and 11, for uniformly parallel shale models with different bedding angles, at 0° and 90°, the split crack started to form from the upper loading end and developed in a straight line through the centerline of the disc. At 15°–60°, the crack began forming from the upper loading end and first propagated along the vertical center line under the action of vertical tension. During the expansion process, the crack was shifted by the influence of the bedding angle on the lower half of the disc. The bedding angle dominates the direction, and the crack split near the bedding at the lower loading end; the overall crack presents a "Z" broken line. At 75°, the crack began forming from the upper loading end and spread in a small-angle arc to the adjacent bedding of the lower loading section. For non-uniform parallel shale models with different bedding angles, the splitting crack trend is the same as that of the uniform parallel model. Further, it is easier to see the effect of anisotropy on crack development. When splitting at 0° and 45°, secondary cracks evolved at the lower end of the center of the circle, and the development direction was the same as that of the primary crack.

As shown in Figures 12 and 13, in the splitting stress field cloud of the shale disc model at different angles, the stress value measured at the splitting crack is larger than that measured at any other place, which basically reflects the splitting crack shape of the shale model at different angles. In general, the shale model with uniform parallel bedding exhibited a larger splitting stress value than that with uneven
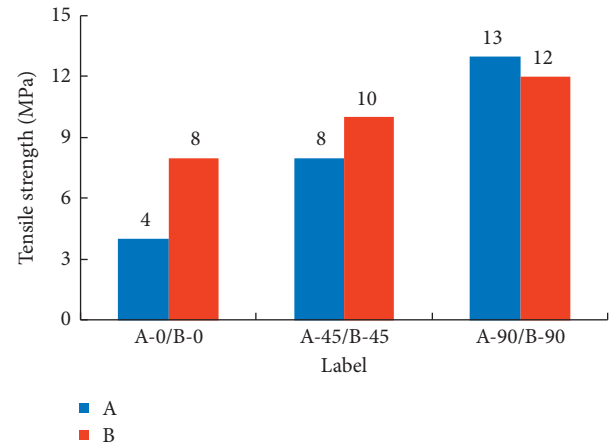

FIGURE 9: Tensile strength of test specimen.

bedding. For bedding shales with different angles, the overall value of the stress field of the 75° model is the smallest.

As shown in Figures 14 and 15, the stress-displacement curves generated at different monitoring points have the same trend: the stress first increases linearly with the displacement. Before splitting, the stress increased suddenly and then decreased at the instant of splitting. The cleavage stress was the largest at the center of the circle, followed by the stress values at symmetry points 2 and 4 near the center of the circle; and those at symmetry points 1 and 5 near the two loading ends were the smallest. The symmetrical points of the stress-displacement curves can be seen to approach each other.

As shown in Figure 16, the stress and displacement processes of the center point of the shale disc in different bedding directions were recorded. It was found that the bedding angle in the shale significantly influences its tensile strength. The tensile strength increased with the angle from 0° to 90° in a zigzag manner. For the models with uniform parallel bedding, the splitting strength was the largest at 90°, of 11.98 MPa, and the splitting strength at 0° was smaller, of 6.73 MPa. Their ratio is 1.78. For the models with uneven parallel bedding, the splitting strength was the largest at 90°, of 9.99 MPa, and the splitting strength was smaller at 0°, of 7.72 MPa. The ratio between the two is 1.29. For the 90° model, the shale particles were mainly tensioned during loading, and the splitting strength can be approximated to the tensile strength of the particle blocks, which have a large strength value. Meanwhile, for the 0° model, the weak layer of the middle shale was loaded when the load was applied. The splitting strength can be approximated to the tensile strength of the bedding surface, and the strength value is small.

3.3. Different Layer Thickness.
As shown in Figures 17 and 18, for parallel bedding shale models with different layer thicknesses, the main crack propagated vertically through the disc. As the layer thickness decreased, the number of bedding increased, and secondary cracks were generated from the middle of the crack in the bedding direction near the loading end. In Figure 18, "2 and 6" indicate the numbers

FIGURE 10: Cloud diagrams of loading displacement with uniform parallel bedding model at different angles. (a) 0°. (b) 15°. (c) 30°. (d) 45°. (e) 60°. (f) 75°. (g) 90°.
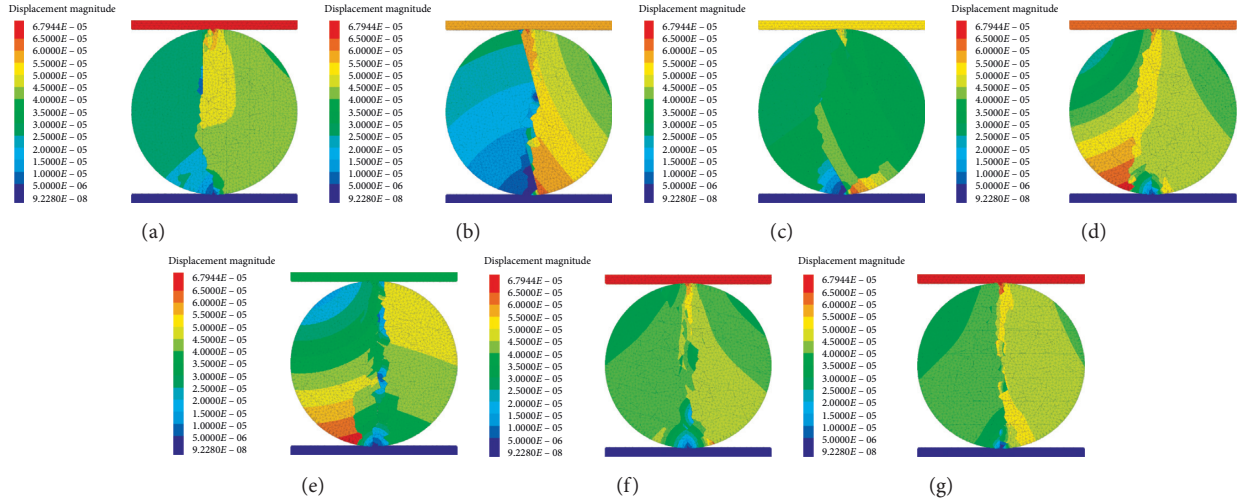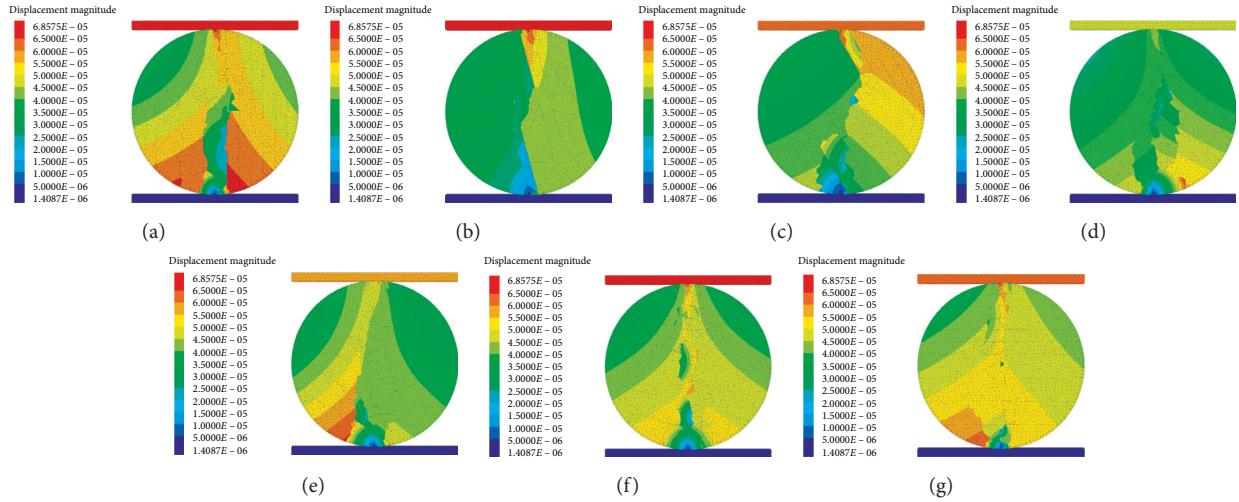

FIGURE 11: Cloud diagrams of loading displacement with uneven parallel bedding model at different angles. (a) 0°. (b) 15°. (c) 30°. (d) 45°. (e) 60°. (f) 75°. (g) 90°.
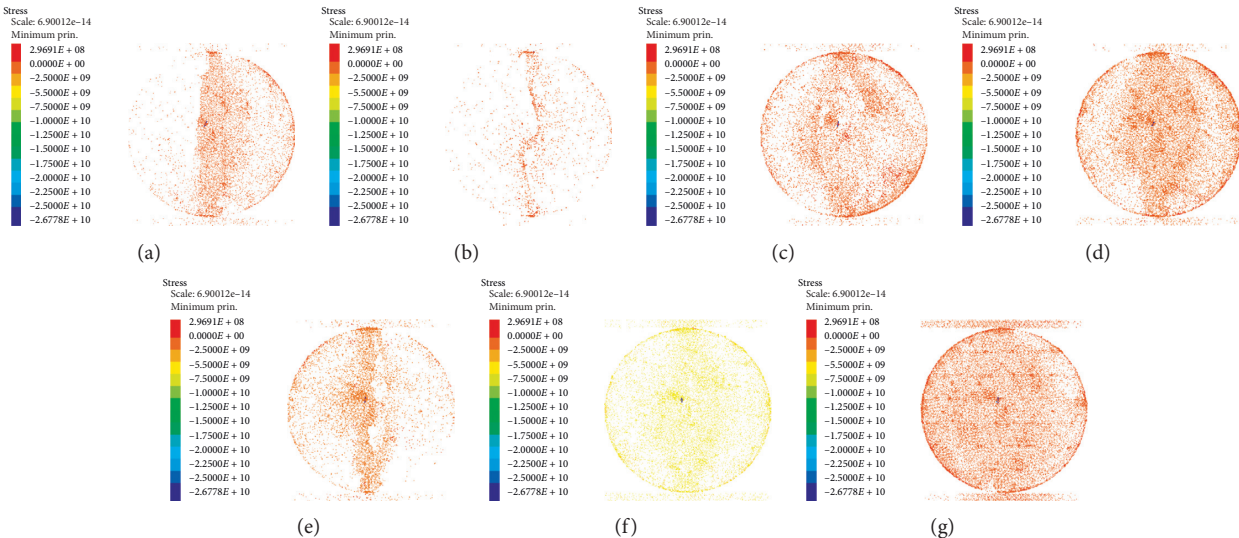
FIGURE 12: Loaded stress cloud with uniform parallel bedding model at different angles. (a) 0°. (b) 15°. (c) 30°. (d) 45°. (e) 60°. (f) 75°. (g) 90°.
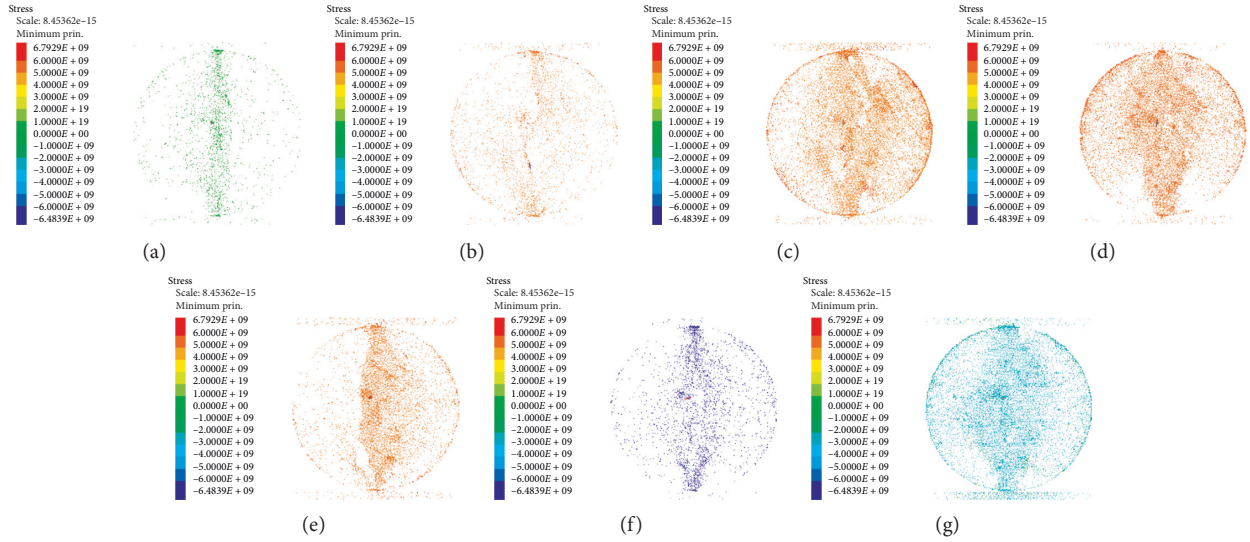
FIGURE 13: Loaded stress cloud with uneven parallel bedding model at different angles. (a) 0°. (b) 15°. (c) 30°. (d) 45°. (e) 60°. (f) 75°. (g) 90°.
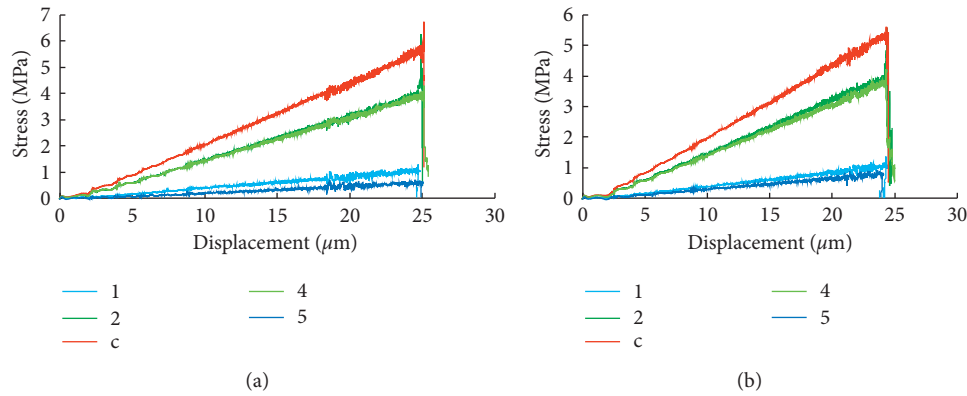
FIGURE 14: Stress-displacement curves of five monitoring points with uniform parallel bedding and different angles. (a) 0°. (b) 45°.
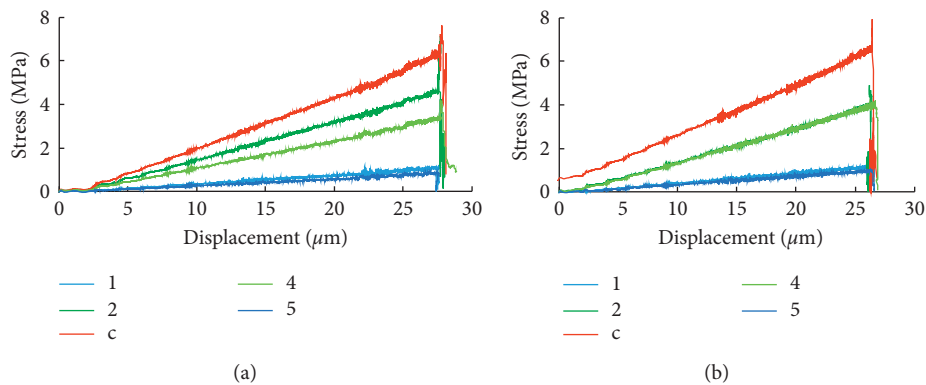
FIGURE 15: Stress-displacement curves of five monitoring points at different angles with uneven parallel bedding. (a) 15°. (b) 60°.

of beds on the left and right semidisk, respectively, of the shale model with uneven bedding.

As shown in Figures 19 and 20, the stresses at the splitting cracks with different layers of shale were more concentrated, which characterizes the vertical cracks. The numerical value of the stress field of a complete unstratified disk is small. The stress field of a model with uneven bedding is generally smaller than that of a homogeneous bedding.

As shown in Figures 21 and 22, for shales with different bedding layer thicknesses, it can be seen that as the layer thickness decreased, the number of bedding increased, and the difference between the stress-displacement curves of

(a)

(b)

FIGURE 16: Tensile strength changes of the center points of the bedding model with different angles. (a) Uniformly parallel. (b) Unevenly parallel.

(a)   (b)   (c)
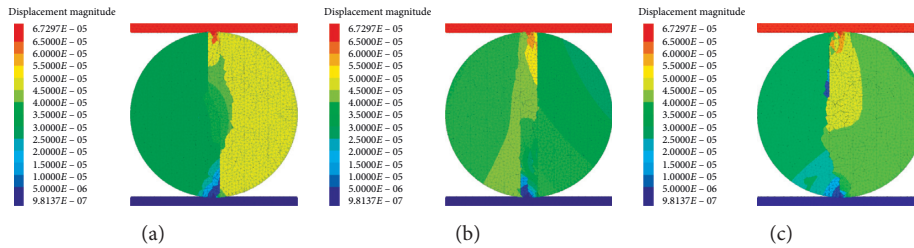
FIGURE 17: Cloud diagrams of loading and displacement with uniform and parallel bedding models with different layer thicknesses. (a) 3.6 mm. (b) 5.0 mm. (c) 7.1 mm.

(a)   (b)   (c)
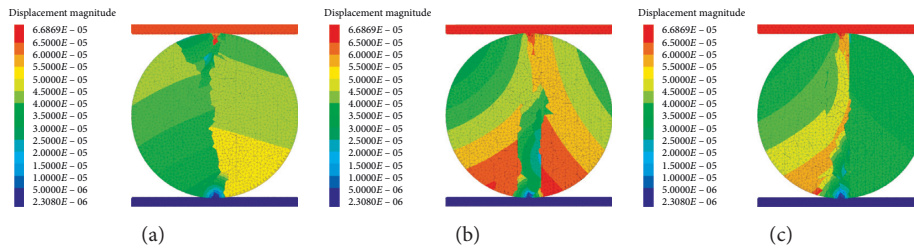
FIGURE 18: Cloud diagrams of loading and displacement of parallel bedding model with uneven layer thickness. (a) 2 and 6. (b) 6 and 12. (c) 10 and 18.

(a)   (b)   (c)
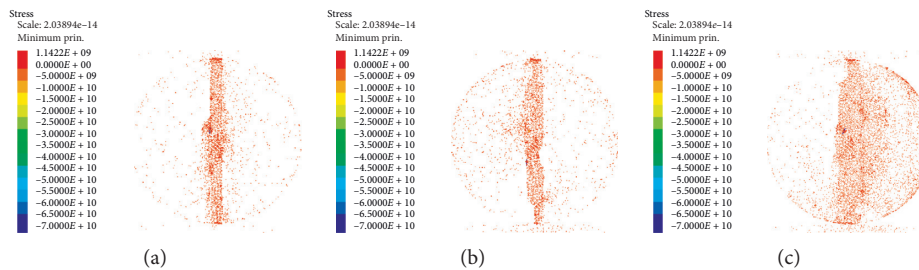
FIGURE 19: Loaded stress cloud of uniform parallel bedding models with different layer thicknesses. (a) 3.6 mm. (b) 5.0 mm. (c) 7.1 mm.

(a)   (b)   (c)
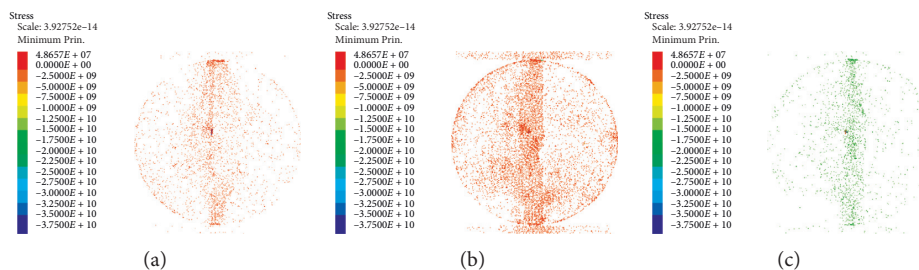
FIGURE 20: Loaded stress cloud with uneven parallel bedding models with different layer thicknesses. (a) 2 and 6. (b) 6 and 12. (c) 10 and 18.

(a)

(b)
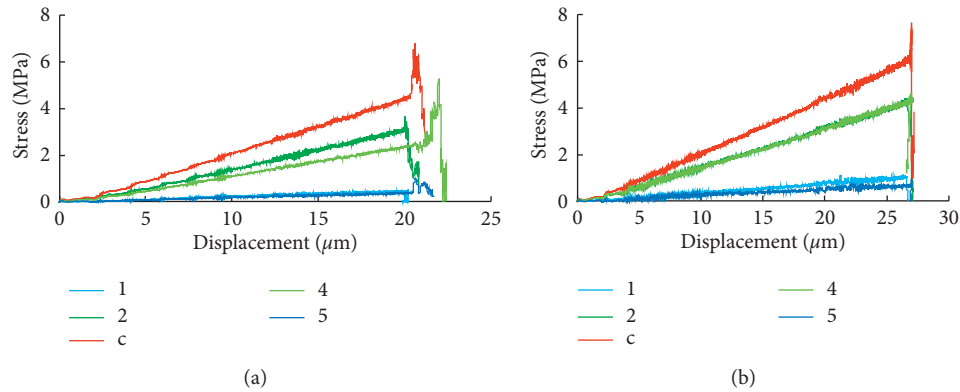
FIGURE 21: Loading stress-displacement curves of uniform parallel bedding models with different layer thicknesses. (a) 3.6 mm. (b) 5.0 mm.

(a)

(b)
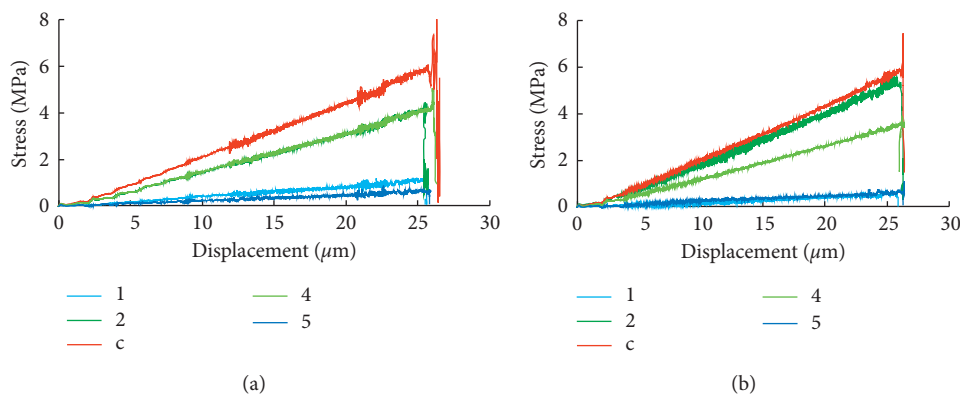
FIGURE 22: Loading stress-displacement curves of uneven parallel bedding models with different layer thicknesses. (a) 2 and 6. (b) 10 and 18.

recording points 2 and 4 became larger. For the model with a uniform parallel layer thickness of 3.6 mm, the peaks of splitting stress and splitting displacement at point 4 at the lower end are greater. For the 10 and 18 model with the most parallel uneven layering, the peak splitting stress peak at point 2 at the upper end is greater.

As shown in Figures 23 and 24, for the shale models with uniform and parallel bedding of different thicknesses, the complete disc model without bedding had the smallest center displacement value when splitting. The model with the layer thickness of 5.0 mm exhibited the largest splitting strength of 7.64 MPa, and the model with the layer thickness of 3.6 mm had the smallest splitting strength of 6.79 MPa. The ratio between the two was 1.13. For the bedding models with uneven parallel and different layer thicknesses, the stress-displacement curves of the center of each circle are not very different, and the maximum cleavage strength was 8.02 MPa in the model with the largest bedding number of "10 and 18," while the model with the bedding numbers of "6 and 12" achieved the minimum splitting strength of 6.37 MPa. The ratio between the two is 1.26. The curve first decreases and then increases. It was found that the shale first undergoes shear failure along the bedding, and the stress decreases; then, the shale particles are compressed, and the tensile stress increases. After the particle tensile strength is reached, interparticle stretching causes damage.

3.4. Bonding Strength. Studies [23] have shown that shale mainly contains minerals such as clay and quartz feldspar, and different geological shales in different regions have different proportions of mineral components. Different mineral components inevitably lead to different bonding strengths among the shale particles. Studies [24] have shown that the bonding strength between soil particles is mainly affected by cohesion. A 45° uniform parallel bedding model was established. The cohesion of each contact was changed in the same proportions of 0.8, 1.2, and 1.5 times and compared with the original ratio. The simulated bond strength between the bedding and particles differed, and the results are shown in Figures 25–28.

As shown in Figures 25 and 26, as the cohesive force between the contacts increased, the split crack decreased, and the displacement and stress at the corresponding split decreased. The smaller the cohesion, the lower the shale bond strength. With the same loading, on the one hand, the 0.8 times cohesive force model formed a through crack, and the overall disk was stressed. On the other hand, the 1.5 times cohesive force model formed dispersed fine cracks, while only the crack area was significantly stressed, and the stress value was small.

As shown in Figures 27 and 28, the stress-displacement change trends of the different contact cohesive shales were the same before splitting failure. With the increase in cohesive force, the splitting strength increased, and the

(a)   (b)
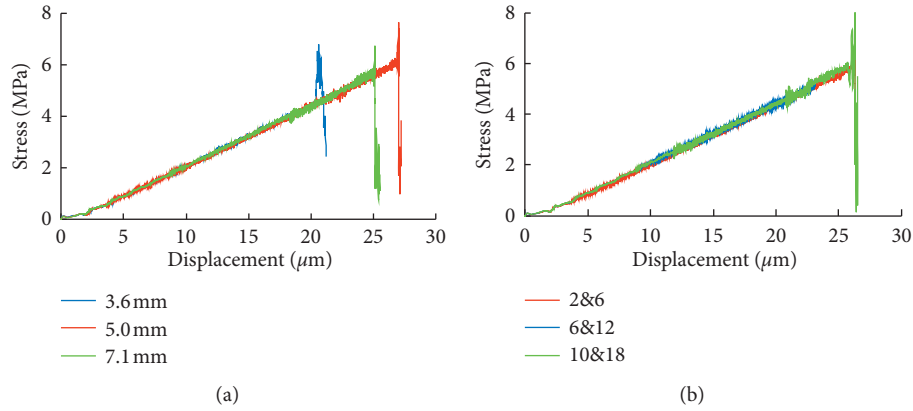
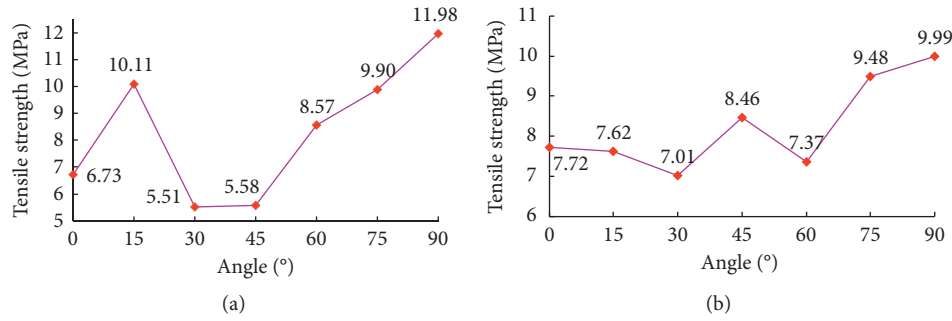FIGURE 23: Stress-displacement curves of the center point of the bedding model with different layer thicknesses. (a) Uniformly parallel. (b) Unevenly parallel.

(a)   (b)
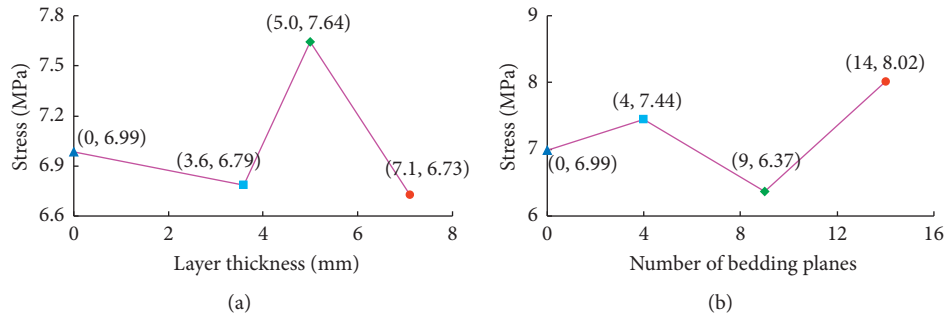
FIGURE 24: Tensile strength changes at the center of bedding models with different layer thicknesses. (a) Uniformly parallel. (b) Unevenly parallel.

(a)   (b)   (c)   (d)
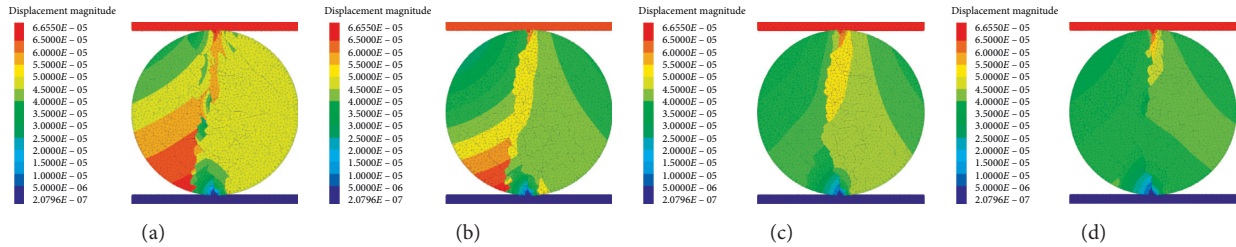
FIGURE 25: Cloud maps of splitting displacement of 45° bedding shale with different contact cohesion. (a) 0.8 times. (b) 1 time. (c) 1.2 times. (d) 1.5 times.

displacement during splitting increased; the measured ratio of the shale tensile strength between 1.5 times and 0.8 times is 2.29. This indicates that an increase in the cohesive force of each contact leads to an increase in the bond strength between the shale particles and the bedding, so that increased energy is required for shale destruction under the same load, and the corresponding shale tensile strength increases. The corresponding splitting strength change is not proportional to the cohesive force change.

3.5. Natural Cracks. As shown in Figure 29, shales with a 45°-direction crack, two 15° and 75° cross cracks, three 0°, 45°, and 90° cross cracks, and horizontal and vertical randomly distributed fracture grids were established. The models were then loaded.

As shown in Figure 30, for shale models with natural fractures, the split cracks are tortuously affected by the cracks. In the model with only one crack, the split cracks developed directly along the 45° natural crack. For the models with two or three natural cracks, the main crack split through the crack intersection. For models with natural crack grids, the cracks were clearly affected by the natural cracks and became randomly distributed along the crack grid. Random and small secondary cracks formed in the area near the natural cracks. As shown in Figure 31, the stress concentration areas easily formed at the natural cracks.
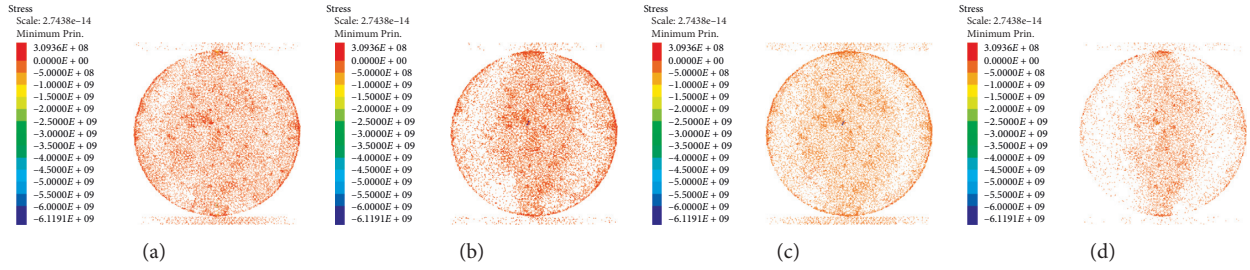
FIGURE 26: Splitting stress cloud of 45° bedding shale with different contact cohesion. (a) 0.8 times. (b) 1 time. (c) 1.2 times. (d) 1.5 times.
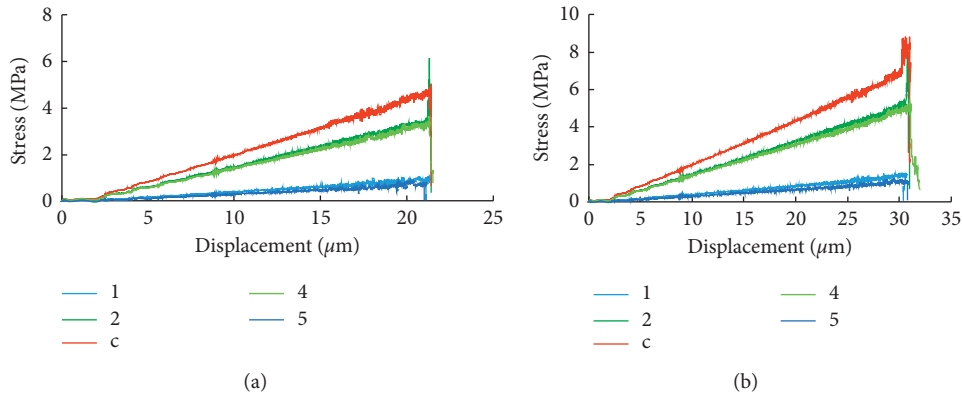
FIGURE 27: Stress-displacement changes of splitting points of 45° bedding shale with different contact cohesion. (a) 0.8. (b) 1.2.
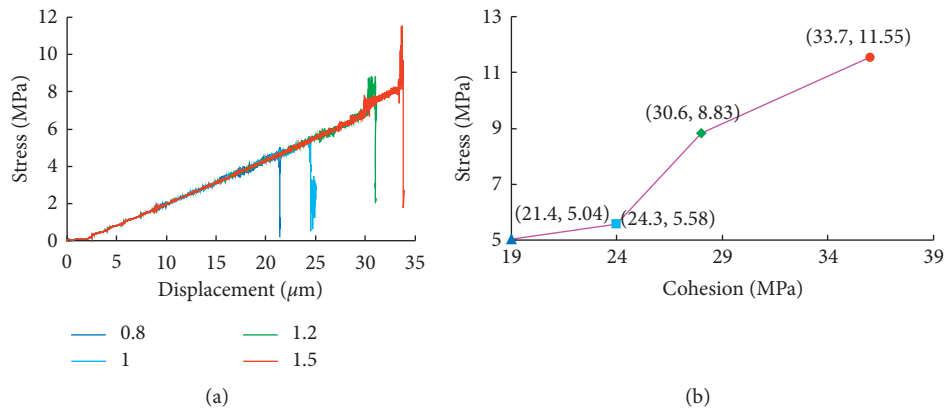
FIGURE 28: Stress-displacement changes at the center of cleavage of 45° bedding shale with different contact cohesion.
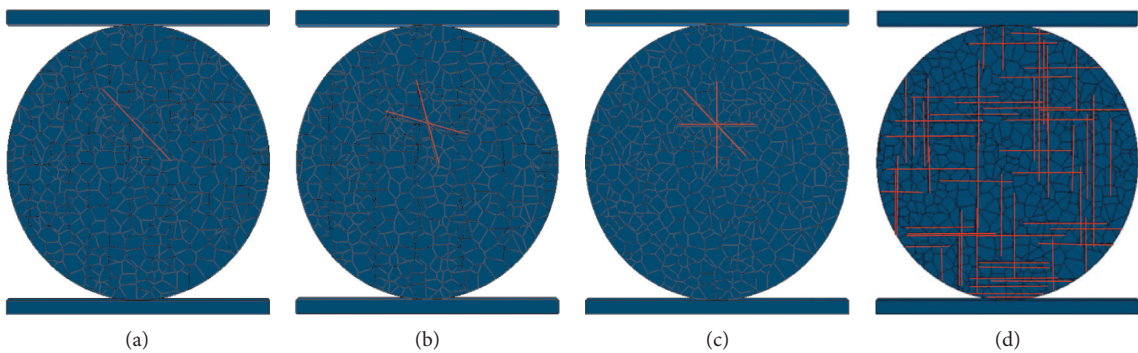
FIGURE 29: Shale model with natural fractures. (a) 1 crack. (b) 2 cracks. (c) 3 cracks. (d) Natural crack grid.
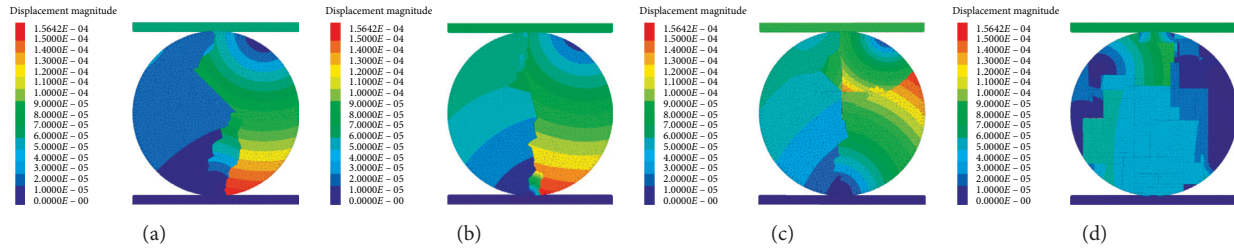
Figure 30: Splitting displacement cloud diagrams of shale with natural fractures. (a) 1 crack. (b) 2 cracks. (c) 3 cracks. (d) Natural crack grid.
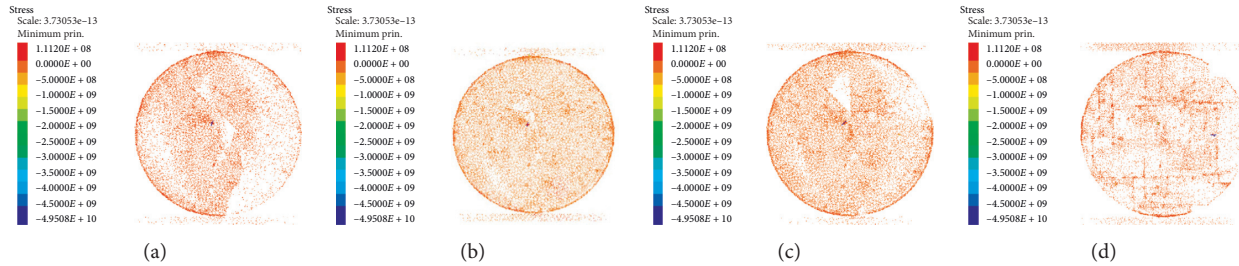
Figure 31: Splitting stress cloud diagrams of shale with natural fractures. (a) 1 crack. (b) 2 cracks. (c) 3 cracks. (d) Natural crack grid.

4. Conclusions

In this study, 3DEC and Neper software were used to establish the Brazilian splitting models of shale with different angles and layer thicknesses, combined with experimental verification to analyze the influence of bedding geometry and shale cement strength on the tensile strength. The conclusions are as follows:

(1) Bedding angles significantly affect the shale-splitting mode. At 0° and 90°, the crack penetrated the upper and lower loading sections through the center of the disk; at 15°, the crack extended through the upper and lower loading ends with an arc-shaped expansion. At 30°–75°, the crack was initiated from the top loading end and shifted from the center line to a polyline-shaped expansion.

(2) Bedding significantly affects the tensile strength of shale. For shales with different bedding angles, the ratio of tensile strength measured in the 90° and 0° directions can reach a maximum of 1.79. For shales with different layer thicknesses, the maximum tensile strength ratio can reach 1.26. Thus, shale is clearly anisotropic.

(3) Bond strength affects the tensile strength of shale. As the cohesion between the contacts increased, the shale bond strength increased, and the splitting cracks decreased. The ratio of the shale tensile strength measured by the 1.5 times and 0.8 times cohesion models was 2.29.

(4) Natural cracks affect the propagation of Brazilian splitting cracks in shale. The cracks are easily distributed along the natural cracks and form small secondary cracks around the natural cracks; stress concentration areas are easily formed at the natural cracks.

Data Availability

The data used to support the findings of this study are available from the corresponding author upon request.

Conflicts of Interest

The authors declare that they have no conflicts of interest to report regarding the present study.

Acknowledgments

References

[1] S. Liao, "Transversely isotropic shale with prefabricated cracks under brazilian tests," Dissertation, Chongqing University, Chongqing, China, 2018.

[2] Y. Huang, L. Wang, J. Chen, and J. Zhang, "Theoretical analysis of flattened Brazilian splitting test for determining tensile strength of rocks," *Rock and Soil Mechanics*, vol. 36, no. 3, pp. 739–748, 2015.

[3] S. Peng, C. Chen, J. Xu et al., "Loading rate dependency of rock stress-strain curve based on Brazil splitting test," *Journal of Rock Mechanics and Engineering*, vol. 37, no. S1, pp. 3247–3252, 2018.

[4] J. Teng, J. Tang, and C. Zhang, "Experimental study on tensile strength of layered water-bearing shale," *Rock and Soil Mechanics*, vol. 39, no. 4, pp. 1317–1326, 2018.

[5] M. Du, P. Pan, W. Ji, Z. Zhang, and Y. Gao, "Time-space laws of failure process of carbonaceous shale in Brazilian split test," *Rock and Soil Mechanics*, vol. 37, no. 12, pp. 3437–3446, 2016.

[6] R. Gao, X. Wang, and F. Jing, "Fracability evaluation of lacustrine shale in the Yanchang Formation of southeastern Ordos basin," *Energy Exploration & Exploitation*, vol. 33, no. 3, pp. 363–374, 2015.

[7] C. Bilgen, S. Homberger, and K. Weinberg, "Phase-field fracture simulations of the Brazilian splitting test," *International Journal of Fracture*, vol. 220, no. 1, pp. 85–98, 2019.

[8] X. Tong, "Analysis on construction stability of jointed tunnel based on 3DEC," *Urban Architecture*, vol. 16, no. 32, pp. 135–137, 2019.

[9] X. Wang and M. Cai, "A comprehensive parametric study of grain-based models for rock failure process simulation," *International Journal of Rock Mechanics and Mining Sciences*, vol. 115, pp. 60–76, 2019.

[10] L. Li, W. Wu, M. H. El Naggar, G. Mei, and R. Liang, "Characterization of a jointed rock mass based on fractal geometry theory," *Bulletin of Engineering Geology and the Environment*, vol. 78, no. 8, pp. 6101–6110, 2019.

[11] Y. Huang, S. Yang, Y. Ju, X. Zhou, and J. Zhao, "Study on particle size effects on strength and crack coalescence behavior of rock during Brazilian splitting test," *Journal of Central South University (Natural Science Edition)*, vol. 47, no. 4, pp. 1272–1281, 2016.

[12] Itasca Consulting Group Inc, *3DEC (Three Dimensional Distinct Element Code) Manual. [S. l.]*, Itasca Consulting Group Inc, Minnesota, MN, USA, 2013.

[13] E. Ghazvinian, M. S. Diederichs, and R. Quey, "3D random Voronoi grain-based models for simulation of brittle rock damage and fabric-guided micro-fracturing," *Journal of Rock Mechanics and Geotechnical Engineering*, vol. 6, no. 6, pp. 506–521, 2014.

[14] Z. Wang, L. Gu, Q. Zhang, S. Yue, and G. Zhang, "Creep characteristics and prediction of creep failure of rock discontinuities under shearing conditions," *International Journal of Earth Sciences*, vol. 109, no. 3, pp. 945–958, 2020.

[15] H. Wang, Y. Gao, A. Jin, and K. Zhang, "Determination of stiffness parameters of jointed rock masses with 3DEC simulations," *Journal of Rock Mechanics and Engineering*, vol. 33, no. S1, pp. 2894–2900, 2014.

[16] X. Tan and H. Konietzky, "Brazilian split tests and numerical simulation by discrete element method for heterogeneous gneiss with bedding structure," *Journal of Rock Mechanics and Engineering*, vol. 33, no. 5, pp. 938–946, 2014.

[17] X. Tan, H. Konietzky, T. Frühwirt, and D. Q. Dan, "Brazilian tests on transversely isotropic rocks: laboratory testing and numerical simulations," *Rock Mechanics and Rock Engineering*, vol. 48, no. 4, pp. 1341–1351, 2015.

[18] Z. Tao, C. Zhu, M. He, and M. Karakus, "A physical modeling-based study on the control mechanisms of Negative Poisson's ratio anchor cable on the stratified toppling deformation of anti-inclined slopes," *International Journal of Rock Mechanics and Mining Sciences*, vol. 138, Article ID 104632, 2021.

[19] C. Zhu, M. He, M. Karakus, X. Zhang, and Z. Tao, "Numerical simulations of the failure process of anaclinal slope physical model and control mechanism of negative Poisson's ratio cable," *Bulletin of Engineering Geology and the Environment*, vol. 80, no. 4, pp. 3365–3380, 2021.

[20] B. Li, R. Bao, Y. Wang, R. Liu, and C. Zhao, "Permeability evolution of two-dimensional fracture networks during shear under constant normal stiffness boundary conditions," *Rock Mechanics and Rock Engineering*, vol. 54, no. 3, pp. 1–20, 2021.

[21] L. Yang, H. Ge, X. Shi, Y. Cheng, and K. Zhang, "The effect of microstructure and rock mineralogy on water imbibition characteristics in tight reservoirs," *Journal of Natural Gas Science and Engineering*, vol. 34, pp. 1461–1471, 2016.

[22] ISRM, "Suggested methods for determining tensile strength of rock materials," *International Journal of Rock Mechanics and Mining Sciences*, vol. 15, no. 3, pp. 99–103, 1978.

[23] X. Zhao, "Numerical simulation and experimental study on three-dimensional initiation and propagation behavior of shale fracturing cracks," Dissertation, China University of Mining and Technology, Beijing, China, 2017.

[24] C. Cheng, S. Liu, Y. Wang, H. Xin, and Q. Chen, "Microscopic study of the cohesive force of cemented soil," *Journal of Rock Mechanics and Engineering*, vol. 3, pp. 322–326, 1999.

Research Article

Simulating the Formation of Blasting-Excavation-Induced Zonal Integration in Deep Tunnels with an Elastoplastic Damage Model

Qiang Gao ,[1,2] Chuanxiao Liu ,[1] Jian Zhang ,[1] and Guangtan Cheng [1]

[1]*College of Water Conservancy and Civil Engineering, Shandong Agricultural University, Tai'an 271018, China*
[2]*Research Center of Geotechnical and Structural Engineering, Shandong University, Jinan 250061, Shandong, China*

Correspondence should be addressed to Jian Zhang; 13905485295@sdau.edu.cn and Guangtan Cheng; gtcheng@sdau.edu.cn

More deep tunneling projects will be constructed due to the increasing demand of underground energy and resource. The zonal disintegration phenomena are frequently encountered with the surrounding rock of deep tunnels. To explain the mechanisms underlying the formation of zonal disintegration, an elastoplastic damage model and failure criterion are proposed in this study based on the strain gradient theory and the damage property of rock mass. A coupling calculation subroutine is thereafter developed by the ABAQUS code. The dynamic formation and development regularity of zonal disintegration in the deep tunnel are simulated by this subroutine. The radial displacement, radial stress, and tangential stress show the oscillated variation of peaks and troughs alternately. The coupling effect of the blasting load and the initial geostress transient unloading leads to the variation of alternation oscillation in the surrounding rock stress field, which is an important reason for the zonal disintegration of the surrounding rock. The morphological characteristics of fractured zones and nonfractured zones obtained from numerical simulations are in good agreement with the results from the in situ observations, which confirm the correctness and feasibility of the damage and numerical approach. The method proposed in the current study can be utilized to provide a basis for the prediction and supporting design of fractured modes.

1. Introduction

With rapid economy development and increasing demand for energy, many underground engineering applications, such as mining, traffic engineering, largescale water conservancy, and hydroelectric engineering, have entered a high-geostress and complex geological environment. The mechanical characteristics, deformation, and failure modes of deep rock masses differ from those of shallow rock masses. Zonal disintegration is a unique failure phenomenon in the deep surrounding rock, in which ruptured and nonruptured zones alternately appear in the surrounding rock of a deep tunnel [1].

The zonal disintegration phenomenon has been confirmed through many physical detection methods in the excavation of deep tunnels. The periodic rupture phenomenon was discovered through spectroscopic observations in South African 2300 m gold mine [2]. A resistivity method was used to detect the zonal disintegration in the

deep mine of Oktyabrskil (Figure 1) [3]. This phenomenon was observed by borehole television and an electrical resistivity survey in the Huainan coal mine in China (Figure 2) [4].

The zonal disintegration phenomenon was reproduced in a model test. Then 2D and 3D equivalent material model tests were carried out and the zonal disintegration of surrounding rock was observed [5]. By using cement mortar as a similar material, the model test was performed and the alternate ruptured and nonruptured zones were generated in the surrounding rock of the model tunnel under high axial pressure [6]. A 3D triaxial loading geomechanical model was used to realistically reproduce the zonal disintegration phenomenon (Figure 3) in which the variation characteristics of strain and displacement were obtained using a variety of monitoring methods [7].

For static numerical simulation, 3D realistic failure process analysis (RF-PA3D) was used to simulate the zonal disintegration phenomenon of the underground tunnel with
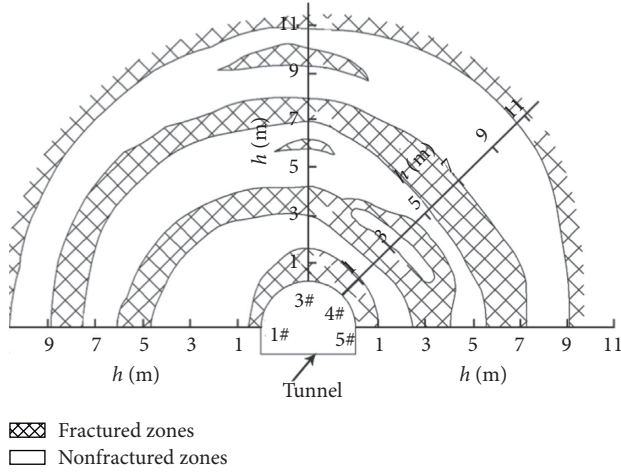
FIGURE 1: Zonal disintegration of Oktyabrskil mine in Russia.
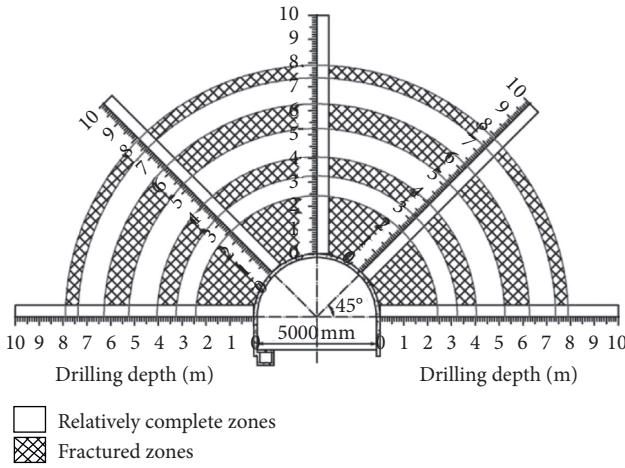
FIGURE 2: Distribution of cracked zones in Huainan mine of China.

FIGURE 3: Zone disintegration of the model test.

the increase of axial load [8, 9]. Flac3D, a finite difference method software application, was implemented to conduct a numerical simulation of zonal disintegration in deep tunnels with a strain-softening joint model [10]. For dynamic numerical simulation, the unloading of tunnel excavation was regarded as a dynamic process. A corresponding dynamic

model was set up and the Flac3D numerical code was used to simulate zonal disintegration in the surrounding deep tunnel rock [11–13]. Based on the continuous cap model suitable for dynamic properties of rock, LS-DYNA finite element software was used to simulate zonal disintegration, and it was proposed that static stress gradient and dynamic loading were the two prerequisites for the far-field fracture zone [14]. A constitutive model based on the general particle dynamics (GPD) method was proposed to investigate the zonal disintegration mechanism of isotropic rock masses around a deep circular tunnel subjected to dynamic unloading [15]. The numerical results indicated that the dynamic loads and high in situ stress are two dominant factors in the occurrence of zonal disintegration. The above dynamic load only refers to the in situ stress transient unloading and ignores the effect of blast loading on the rock mass surrounding the tunnel. There has been no lack of research on the coupling dynamic effect of the blast loading and the in situ stress transient release on the mechanical analysis of the zonal disintegration phenomenon.

Zonal disintegration in a deep tunnel is completely different from that of a shallow cavity. It is difficult to explain zonal disintegration using elastic-plastic mechanics in a continuum mechanics frame. Zonal disintegration is a special and regular strain localization phenomenon [16]. Since the strain gradient plays a controlling role in the strain localization of rock [17], its influence should be considered in the study of zonal disintegration.

An elastoplastic damage model and failure criterion were proposed based on the strain gradient theory. The zonal disintegration calculation program was written based on the dynamic finite element equations and ABAQUS finite element software. The morphological characteristics of zonal disintegration under blasting excavation were obtained through numerical simulation. This study reveals the morphological characteristics of zonal disintegration, which is used as a basis for the prediction and support control of fractured modes.

2. Elastoplastic Damage Model Based on Strain Gradient

2.1. Introduction of High-Order Stress. In the Toupin–Mindlin strain gradient theory [18–20], the total strain u_i has two parts: the conventional Eulerian strain tensor ε_{ij} and the high-order strain tensor η_{ijk}, which are deduced as

$$\varepsilon_{ij} = \frac{\left(u_{i,j} + u_{j,i}\right)}{2},$$

$$\eta_{ijk} = \partial_i \partial_j u_k = u_{k,ij}. \tag{1}$$

According to the second law of thermodynamics, the Helmholtz free energy function [18] can be expressed as

$$\psi\left(\varepsilon, \eta\right) = \frac{1}{2}\varepsilon_{ij} : E_{ijkl}^{epd} : \varepsilon_{kl} + \frac{1}{2}\eta_{ijk} : \Lambda_{ijklmn}^{ed} : \eta_{lmn}, \tag{2}$$

where σ_{ij} is a second-order Cauchy stress tensor, which is the conjugate of the Eulerian strain tensor ε_{ij}, and τ_{ijk} is set

as the third-order stress tensor which is conjugate to the strain gradient tensor η_{ijk}. The stress tensor σ_{ij} and high-order stress tensor τ_{ijk} can be derived from the free energy function corresponding to the strain tensor ε_{ij} and strain gradient tensor η_{ijk}, respectively:

$$\left.\begin{aligned}\sigma_{ij} &= \frac{\partial \psi}{\partial \varepsilon_{ij}} = E_{ijkl}^{epd}\varepsilon_{kl}, \\[2em] \tau_{ijk} &= \frac{\partial \psi}{\partial \eta_{ijk}} = \Lambda_{ijklmn}^{ed}\eta_{lmn},\end{aligned}\right\} \tag{3}$$

where E_{ijkl}^{epd} is the elastoplastic damage tensor, $E_{ijkl}^{epd} = E_{ijkl}^{e} - E_{ijkl}^{pd}$; d is the damage tensor; E_{ijkl}^{e} is the elastic tensor; E_{ijkl}^{p} is the plastic tensor determined by plastic flow law and hardening law [21]; Λ_{ijklmn}^{ed} is the sixth-order elastic damage tensor considering the strain gradient,

$\Lambda_{ijklmn}^{ed} = (1 - d)l^2 E_{ijlm}^{e}\delta_{kn}$; δ_{kn} is the Kronecker symbol; and l is the internal length parameter of the material, which is closely related to the microcracks and microdefects inside the material, whose value is generally the average aggregate particle diameter of the corresponding material [22].

2.2. Establishment of Elastoplastic Damage Constitutive Equation.
Cauchy stress σ_{ij} and Eulerian strain ε_{ij} are expressed as an incremental matrix:

$$d\boldsymbol{\sigma} = \frac{1 - \omega + \delta_{ij}\omega}{3}\mathbf{H}d\varepsilon, \tag{4}$$

where $d\sigma = \begin{bmatrix} d\sigma_{xx} & d\sigma_{yy} & d\sigma_{zz} & d\sigma_{xy} & d\sigma_{xz} & d\sigma_{yz}\end{bmatrix}^T$ and $d\varepsilon = \begin{bmatrix} d\sigma_{xx} & d\sigma_{yy} & d\sigma_{zz} & d\sigma_{xy} & d\sigma_{xz} & d\sigma_{yz}\end{bmatrix}^T$.

$\mathbf{H}$ is 6×6 matrix $\mathbf{H} = \mathbf{H}^e - \mathbf{H}^p$, and $\mathbf{H}^e$ can be written as

$$\mathbf{H}^e = \begin{bmatrix} \dfrac{E(1-v)}{(1+v)(1-2v)} & \dfrac{Ev}{(1+v)(1-2v)} & \dfrac{Ev}{(1+v)(1-2v)} & & & \\[1.5em] \dfrac{Ev}{(1+v)(1-2v)} & \dfrac{E(1+v)}{(1+v)(1-2v)} & \dfrac{Ev}{(1+v)(1-2v)} & 0 & 0 & 0 \\[1.5em] \dfrac{Ev}{(1+v)(1-2v)} & \dfrac{Ev}{(1+v)(1-2v)} & \dfrac{E(1-v)}{(1+v)(1-2v)} & 0 & 0 & 0 \\[1.5em] 0 & 0 & 0 & \dfrac{E}{2(1+v)} & 0 & 0 \\[1.5em] 0 & 0 & 0 & 0 & \dfrac{E}{2(1+v)} & 0 \\[1.5em] 0 & 0 & 0 & 0 & 0 & \dfrac{E}{2(1+v)} \end{bmatrix}, \tag{5}$$

where E is the elastic modulus and v is Poisson's ratio. $\mathbf{H}^p$ is expressed as

$$\mathbf{H}^P = \left(\frac{\mathbf{H}^e(\partial Q/\partial \boldsymbol{\sigma})(\partial F/\partial \boldsymbol{\sigma})\mathbf{H}^e}{(\partial F/\partial \boldsymbol{\sigma})\mathbf{H}^e(\partial Q/\partial \boldsymbol{\sigma}) - (\partial F/\partial \boldsymbol{\sigma})\boldsymbol{\sigma}(\partial Q/\partial \boldsymbol{\sigma})}\right), \tag{6}$$

where $F = F(\sigma, \kappa) = 0$ is the yield function, κ is plastic work, $d\kappa = \sigma d\varepsilon^p$, and Q is plastic potential function.

The high-order stress tensor τ_{ijk} and strain gradient tensor η_{ijk} are expressed as an incremental matrix:

$$d\boldsymbol{\tau} = (1 - \omega)\Lambda d\boldsymbol{\eta}, \tag{7}$$

where

$$d\boldsymbol{\tau} = \begin{pmatrix} d\tau_{xxx} & d\tau_{yyx} & d\tau_{zzx} & d\tau_{xyx} & d\tau_{yzx} & d\tau_{xzx} & d\tau_{xxy} & d\tau_{yyy} & d\tau_{zzy} & d\tau_{xyy} & d\tau_{yzy} & d\tau_{xzy} & d\tau_{xxz} & d\tau_{yyz} & d\tau_{zzz} & d\tau_{xyz} & d\tau_{yzz} & d\tau_{xzz}\end{pmatrix}^T,$$

$$d\boldsymbol{\eta} = \begin{pmatrix} d\eta_{xxx} & d\eta_{yyx} & d\eta_{zzx} & d\eta_{xyx} & d\eta_{yzx} & d\eta_{xzx} & d\eta_{xxy} & d\eta_{yyy} & d\eta_{zzy} & d\eta_{xyy} & d\eta_{yzy} & d\eta_{xzy} & d\eta_{xxz} & d\eta_{yyz} & d\eta_{zzz} & d\eta_{xyz} & d\eta_{yzz} & d\eta_{xzz}\end{pmatrix}^T. \tag{8}$$

Λ is 18×18 matrix, $\Lambda = (El^2/8(1+v))\begin{bmatrix} D_1 & D_2 \\ D_3 & D_4 \end{bmatrix}$, and D_1, D_2, D_3, D_4 can be written as

$$
D_1 = \begin{bmatrix}
21 & 6 & 6 & 0 & 0 & 0 & 0 & 0 & 0 \\
6 & 11 & 4 & 0 & 0 & 0 & 0 & 0 & 0 \\
6 & 4 & 11 & 0 & 0 & 0 & 0 & 0 & 0 \\
0 & 0 & 0 & 10 & 0 & 0 & 2 & 3 & 1 \\
0 & 0 & 0 & 0 & 7 & 0 & 0 & 0 & 0 \\
0 & 0 & 0 & 0 & 0 & 10 & 0 & 0 & 0 \\
0 & 0 & 0 & 4 & 0 & 0 & 11 & 6 & 4 \\
0 & 0 & 0 & 6 & 0 & 0 & 6 & 21 & 6 \\
0 & 0 & 0 & 2 & 0 & 0 & 4 & 6 & 11
\end{bmatrix},
$$

$$
D_2 = \begin{bmatrix}
6 & 0 & 0 & 0 & 0 & 0 & 0 & 0 & 6 \\
4 & 0 & 0 & 0 & 0 & 0 & 0 & 0 & 2 \\
2 & 0 & 0 & 0 & 0 & 0 & 0 & 0 & 4 \\
0 & 0 & 1 & 0 & 0 & 0 & 1 & 0 & 0 \\
0 & 0 & 0 & 4 & 0 & 2 & 0 & 0 & 0 \\
0 & 2 & 0 & 2 & 1 & 3 & 0 & 0 & 0 \\
0 & 0 & 0 & 0 & 0 & 0 & 0 & 2 & 0 \\
0 & 0 & 0 & 0 & 0 & 0 & 6 & 0 & 0 \\
0 & 0 & 0 & 0 & 0 & 0 & 4 & 0 & 0
\end{bmatrix},
$$

$$
D_3 = \begin{bmatrix}
3 & 2 & 1 & 0 & 0 & 0 & 0 & 0 & 0 \\
0 & 0 & 0 & 0 & 0 & 2 & 0 & 0 & 0 \\
0 & 0 & 0 & 0 & 1 & 0 & 0 & 0 & 0 \\
0 & 0 & 0 & 0 & 0 & 4 & 0 & 0 & 0 \\
0 & 0 & 0 & 0 & 0 & 4 & 0 & 0 & 0 \\
0 & 0 & 0 & 0 & 0 & 6 & 0 & 0 & 0 \\
0 & 0 & 0 & 0 & 1 & 0 & 0 & 0 & 0 \\
0 & 0 & 0 & 2 & 0 & 0 & 1 & 3 & 2 \\
3 & 1 & 2 & 0 & 0 & 0 & 0 & 0 & 0
\end{bmatrix},
$$

$$
D_4 = \begin{bmatrix}
10 & 0 & 0 & 0 & 0 & 0 & 0 & 0 & 2 \\
0 & 10 & 0 & 1 & 2 & 3 & 0 & 0 & 0 \\
0 & 0 & 7 & 0 & 0 & 0 & 1 & 0 & 0 \\
0 & 2 & 0 & 11 & 4 & 6 & 0 & 0 & 0 \\
0 & 3 & 0 & 4 & 11 & 6 & 0 & 0 & 0 \\
0 & 6 & 0 & 6 & 6 & 21 & 0 & 0 & 0 \\
0 & 0 & 1 & 0 & 0 & 0 & 7 & 0 & 0 \\
0 & 0 & 0 & 0 & 0 & 0 & 0 & 10 & 0 \\
2 & 0 & 0 & 0 & 0 & 0 & 0 & 0 & 10
\end{bmatrix}.
$$

$$\tag{9}$$

Thus, the elastoplastic damage constitutive equation based on the strain gradient can be expressed as

$$
\begin{bmatrix} d\boldsymbol{\sigma} \\ d\tau \end{bmatrix} = D \begin{bmatrix} d\boldsymbol{\varepsilon} \\ d\boldsymbol{\eta} \end{bmatrix} = \begin{bmatrix} \dfrac{1-\omega+\delta_{ij}}{3}\mathbf{H} & 0 \\[2ex] 0 & (1-\omega)\Lambda \end{bmatrix} \begin{bmatrix} d\boldsymbol{\varepsilon} \\ d\boldsymbol{\eta} \end{bmatrix}.
$$

$$\tag{10}$$

2.3. Damage Evolution Equation. It is assumed that the damage of a rock mass can be represented by an isotropic damage variable d with the use of analytical methods from continuous damage mechanics. Since the damage variable d is an internal variable, equation (10) cannot form a complete damage constitutive model. The damage criterion and damage evolution law should also be determined.

According to the mechanical properties of deep rock under high stress, the stress-strain relationship is simplified properly, as shown in Figure 4(a). The OA stage is the linear elastic stage, in which no damage occurs to the rock mass. ε_s is the yield stress and σ_s is the yield strain. The AB stage is the plastic damage stage. The original cracks are pressed, and new cracks are produced after the rock mass enters the plastic stage. ε_u is the ultimate strain. Once the deformation reaches the ultimate strain, the rock mass is completely destroyed. To describe the strain-softening of deep rock under high stress, the damage evolution of rock is determined as [23]

$$
d = d(\widetilde{\varepsilon}) = \begin{cases} 0, & \varepsilon < \varepsilon_s, \\[2ex] \dfrac{\varepsilon_u}{\widetilde{\varepsilon}} \dfrac{\widetilde{\varepsilon} - \varepsilon_s}{\varepsilon_u - \varepsilon_s}, & \varepsilon_s \leq \varepsilon < \varepsilon_u, \\[2ex] 1, & \varepsilon \geq \varepsilon_u, \end{cases}
$$

$$\tag{11}$$

where $\widetilde{\varepsilon}$ is the generalized equivalent strain containing the strain gradient [24], $\widetilde{\varepsilon} = \sqrt{(2/3)\varepsilon_{ij}\varepsilon_{ij} + l^2\eta_{ijk}\eta_{ijk}}$. The variation curve of damage variable d with equivalent strain $\widetilde{\varepsilon}$ is shown in Figure 4(b).

Thus, equations (13) and (14) constitute an elastoplastic damage model based on the strain gradient.

3. Implementation of the Model of a Deep Tunnel under Dynamic Excavation

3.1. Construction of C^1Order Element considering Strain Gradient. To implement the elastoplastic damage model with the finite element method, the influence of the strain gradient should be considered first. The interpolating shape functions of a conventional finite element generally have only first-order continuity, and the constructed elements have only C^0order continuity. The second derivative after the interpolation of the displacement field is zero, and the influence of the strain gradient cannot be considered in such elements. Therefore, it is necessary to consider finite elements with higher-order continuity, such as elements with C^1order continuity. This requires that the normal
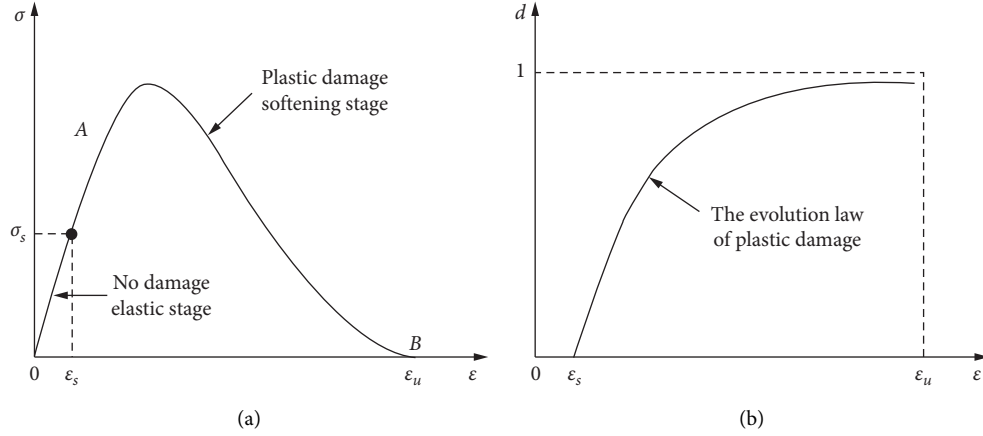
Figure 4: Nonlinear damage evolution law of rock under high stress. (a)$\sigma - \varepsilon$ curve. (b)$d - \varepsilon$ curve.

displacement and first-order partial differential maintain continuity so that the strain gradient can enter into the finite element equation.

Taking the most versatile tetrahedral element as an example, a three-dimensional general tetrahedral element with C^1 order continuity is established in Figure 5. The geometric coordinates of the node i ($i = 1; 2; 3; 4$) are (x_i, y_i, z_i). Four-node displacements can be assumed as

$$\mathbf{a} = \begin{pmatrix} \mathbf{a}_1 & \mathbf{a}_2 & \mathbf{a}_3 & \mathbf{a}_4 \end{pmatrix}^T,$$

$$\mathbf{a}_i = \begin{pmatrix} u & u_{,x} & u_{,y} & u_{,z} \end{pmatrix} v \quad v_{,x} \quad v_{,y} \quad v_{,z} \begin{vmatrix} w & w_{,x} & w_{,y} & w_{,z} \end{pmatrix}_i^T.$$

$$(12)$$

The area coordinates L_i of any point $P(x, y, z)$ within the element can be defined as

$$L_i = \frac{A_i}{V}, \quad (i = 1, 2, 3, 4), \tag{13}$$

where $A_1 = \text{Vol}(P234) A_2 = \text{Vol}(P134) A_3 = \text{Vol}(P214) A_4 = \text{Vol}(P231)$, and $V = \text{Vol}(1234)$.

Then, the above formula can be expanded as follows:

$$L_i = (-1)^{i+1} \frac{(a_i + b_i x + c_i y + d_i z)}{6v}, \tag{14}$$

where

$$V = \frac{1}{6} \begin{vmatrix} 1 & x_1 & y_1 & z_1 \\ 1 & x_2 & y_2 & z_2 \\ 1 & x_3 & y_3 & z_3 \\ 1 & x_4 & y_4 & z_4 \end{vmatrix},$$

$$a_i = \begin{vmatrix} x_j & y_j & z_j \\ x_k & y_k & z_k \\ x_l & y_l & z_l \end{vmatrix},$$

$$b_i = -\begin{vmatrix} 1 & y_j & z_j \\ 1 & y_k & z_k \\ 1 & y_l & z_l \end{vmatrix},$$

$$c_i = \begin{vmatrix} 1 & x_j & z_j \\ 1 & x_k & z_k \\ 1 & x_l & z_l \end{vmatrix},$$

$$d = -\begin{vmatrix} 1 & x_j & y_j \\ 1 & x_k & y_k \\ 1 & x_l & y_l \end{vmatrix},$$

$$(15)$$

where i, j, k, and l are in accordance with the rotation of $1 \longrightarrow 2 \longrightarrow 3 \longrightarrow 4 \longrightarrow 1$ and meet the right-handed spiral rule.

The displacement field u can be expressed as

$$u = \sum_{i=1}^{4} \alpha_i L_i^3 + \alpha_5 L_1^2 L_2 + \alpha_6 L_1^2 L_3 + \alpha_7 L_1^2 L_4 + \alpha_8 L_2^2 L_3 + \alpha_9 L_2^2 L_4 + \alpha_{10} L_2^2 L_1 + \alpha_{11} L_3^2 L_4 + \alpha_{12} L_3^2 L_1 + \alpha_{13} L_3^2 L_2 \\ + \alpha_{14} L_4^2 L_1 + \alpha_{15} L_4^2 L_2 + \alpha_{16} L_4^2 L_3. \tag{16}$$

The values of the 16 coefficients α_i ($i = 1, \ldots 16$) can be determined from the displacement u_i ($1 = 1, \ldots 4$) of the four vertices and the gradient $u_{i,x}, u_{i,y}, u_{i,z}$ ($i = 1, \ldots 4$) of the three directions.
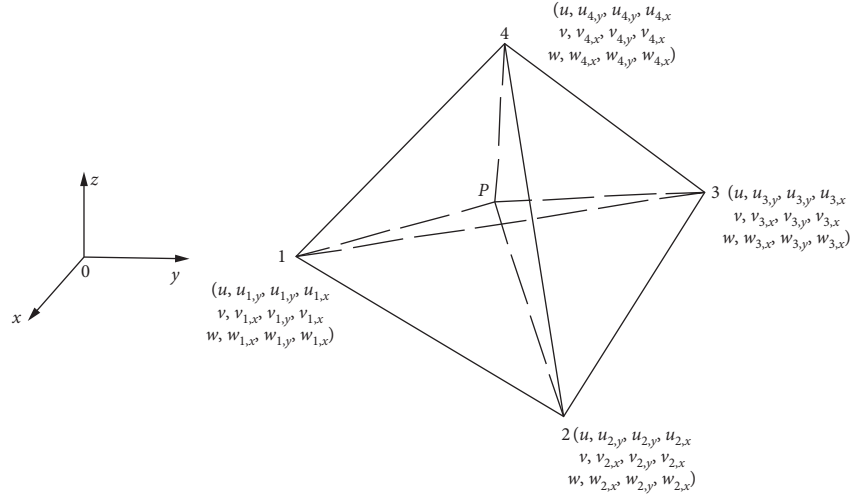
FIGURE 5: Tetrahedral elements with C^1 order continuity.

After introducing a shape function N, the displacement field in three dimensions is expressed as

$$\mathbf{u} = \begin{Bmatrix} u \\ v \\ w \end{Bmatrix} = \begin{bmatrix} N_1 & 0 & 0 & N_2 & 0 & 0 & N_3 & 0 & 0 & N_4 & 0 & 0 \\ 0 & N_1 & 0 & | & 0 & N_2 & 0 & | & 0 & N_3 & 0 & | & 0 & N_4 & 0 \\ 0 & 0 & N_1 & 0 & 0 & N_2 & 0 & 0 & N_3 & 0 & 0 & N_4 \end{bmatrix} \begin{Bmatrix} a_1 \\ a_2 \\ a_3 \\ a_4 \end{Bmatrix} = Na, \tag{17}$$

where

$$N_i = \begin{pmatrix} N_i^0 & N_i^x & N_i^y & N_i^z \end{pmatrix}$$

$$= \begin{Bmatrix} L_i^3 + \dfrac{3L_i^2}{A_i}\left(A_j L_j - A_k L_k + A_l L_l \right) \\ \\ \dfrac{6V}{A_i} L_i^2 \left(p_{kl} L_j + p_{lj} L_k + p_{jk} L_l \right) \\ \\ \dfrac{6V}{A_i} L_i^2 \left(q_{kl} L_j + q_{lj} L_k + q_{jk} L_l \right) \\ \\ \dfrac{6V}{A_i} L_i^2 \left(r_{kl} L_j + r_{lj} L_k + r_{jk} L_l \right) \end{Bmatrix}^T,$$

$$A_1 = \begin{vmatrix} b_2 & b_3 & b_4 \\ c_2 & c_3 & c_4 \\ d_2 & d_3 & d_4 \end{vmatrix},$$

$$A_2 = \begin{vmatrix} b_1 & b_3 & b_4 \\ c_1 & c_3 & c_4 \\ d_1 & d_3 & d_4 \end{vmatrix},$$

$$A_3 = \begin{vmatrix} b_1 & b_2 & b_4 \\ c_1 & c_2 & c_4 \\ d_1 & d_2 & d_4 \end{vmatrix},$$

$$A_4 = \begin{vmatrix} b_1 & b_2 & b_3 \\ c_1 & c_2 & c_3 \\ d_1 & d_2 & d_3 \end{vmatrix},$$

$$p_{jk} = c_k d_j - c_j d_k,$$

$$q_{jk} = b_j d_k - b_k d_j,$$

$$r_{jk} = b_k c_j - b_j c_k,$$

$$[0]_{1\times 4} = \begin{bmatrix} 0 & 0 & 0 & 0 \end{bmatrix}. \tag{18}$$

Strain ε and strain gradients η take the following form:

$$\varepsilon = \mathbf{B}_1 \mathbf{a} = \mathbf{L}_1 \mathbf{N} \mathbf{a},$$
$$\eta = \mathbf{B}_2 \mathbf{a} = \mathbf{L}_2 \mathbf{N} \mathbf{a}, \tag{19}$$

where L_1 and L_2 are differential operators that can be written as

$$L_1 = \begin{bmatrix} \dfrac{\partial}{\partial x} & & \dfrac{\partial}{\partial y} & & \dfrac{\partial}{\partial z} \\ & \dfrac{\partial}{\partial y} & & \dfrac{\partial}{\partial x} & \dfrac{\partial}{\partial z} \\ & & \dfrac{\partial}{\partial z} & & \dfrac{\partial}{\partial y} & \dfrac{\partial}{\partial x} \end{bmatrix}, \tag{20}$$

$$L_2 = \begin{bmatrix} \mathbf{M} & 0 & 0 \\ 0 & \mathbf{M} & 0 \\ 0 & 0 & \mathbf{M} \end{bmatrix},$$

where $\mathbf{M} = [(\partial^2/\partial x^2)\,(\partial^2/\partial y^2)\,(\partial^2/\partial z^2)\,(\partial^2/\partial x\,\partial y^2)\,(\partial^2/\partial y\,\partial z^2)\,(\partial^2/\partial x\,\partial z^2)]^T$, $0_{1\times 6} = \begin{bmatrix} 0 & 0 & 0 & 0 & 0 & 0 \end{bmatrix}^T$.

Therefore, the geometric equation considering the strain gradient can be expressed as

$$\begin{bmatrix} \boldsymbol{\varepsilon} \\ \boldsymbol{\eta} \end{bmatrix} = \mathbf{Ba} = \begin{bmatrix} \mathbf{B_1} \\ \mathbf{B_2} \end{bmatrix} \mathbf{a}, \tag{21}$$

where $\mathbf{B}$ is the strain matrix.

Finally, the element stiffness matrix of the C^1 order tetrahedral element is

$$\mathbf{K} = \iiint \mathbf{B^T DB}\,dx\,dy\,dz. \tag{22}$$

3.2. Establishment of the Dynamic Finite Element Equation. Similar to static finite element analysis, dynamic finite element analysis should establish the finite element equation. The space of the rock mass is discretized, and higher-order tetrahedral elements are constructed. The shape function and stiffness matrix of the elements are deduced. According to the dynamic equilibrium equations of each node, the Newmark-β integral method [25, 26] is adopted to solve the following motion equation:

$$[M]\{\ddot{u}\} + [C]\{\dot{u}\} + [K]\{u\} = \{P\}, \tag{23}$$

where $[M]$ is the element mass matrix; $[M] = \int_V \rho \mathbf{N}^T \mathbf{N} dV$, ρ is the density of the rock mass; $[C]$ is the element damping matrix, $[C] = \int_V c\mathbf{N}^T \mathbf{N} dV$, c is damping coefficient; $[K]$ is the element stiffness matrix; $\{\ddot{u}\}, \{\dot{u}\}$, and $\{u\}$ are the acceleration, velocity, and displacement matrices at any point in the element; and $\{P\}$ is the external loads.

Displacement at any point in the element is $\mathbf{u} = \mathbf{Na}$, where $\mathbf{N}$ is a function only of position and is not related to time t, and $\mathbf{a}$ is related to time and can be expressed as $\mathbf{a} = \begin{pmatrix} \mathbf{a}_1^t & \mathbf{a}_2^t & \mathbf{a}_3^t & \mathbf{a}_4^t \end{pmatrix}^T$. Therefore, the acceleration $\ddot{u}$ and velocity $\dot{u}$ at any point in the element are expressed, respectively, as $\ddot{u} = \mathbf{N}\ddot{a}$ and $\dot{u} = \mathbf{N}\dot{a}$ where $\cdot$ indicates a derivative with respect to time.

In the Newmark-β method, when the control parameters satisfy $\alpha = (1/2)$, $\beta = (1/4)$, the method changes to an average constant acceleration method with second-order accuracy, which satisfies the engineering requirements. Therefore, the basic assumption based on the method can be expressed as [27]

$$\begin{cases} \{\dot{u}_{t1+\Delta t}\} = \{\dot{u}_{t1}\} + \dfrac{\Delta t}{2}\left[\{\ddot{u}_{t1}\} + \{\ddot{u}_{t1+\Delta t}\}\right], \\[4mm] \{u_{t1+\Delta t}\} = \{u_{t1}\} + \{\dot{u}_{t1}\}\Delta t + \dfrac{\Delta t^2}{4}\left[\{\ddot{u}_{t1}\} + \{\ddot{u}_{t1+\Delta t}\}\right]. \end{cases} \tag{24}$$

Equation (24) can be expanded as

$$\begin{cases} \{\ddot{u}_{t1+\Delta t}\} = \dfrac{4}{\Delta t^2}\{u_{t1+\Delta t}\} - \dfrac{4}{\Delta t^2}\{u_{t1}\} - \dfrac{4}{\Delta t}\{\dot{u}_{t1}\} - \{\ddot{u}_{t1}\}, \\[4mm] \{\ddot{u}_{t1+\Delta t}\} = \{\dot{u}_{t1}\} + \dfrac{\Delta t}{2}\left[\{\ddot{u}_{t1}\} + \{\ddot{u}_{t1+\Delta t}\}\right] = \dfrac{2}{\Delta t}\{u_{t1+\Delta t}\} - \dfrac{2}{\Delta t}\{u_{t1}\} - \{\dot{u}_{t1}\}. \end{cases} \tag{25}$$

After subsisting equation (25) into equation (23) at time $t1 + \Delta t$, the expression can be arranged as

$$[\overline{K}]\{u_{t1+\Delta t}\} = \{\overline{P}_{t1+\Delta t}\}, \tag{26}$$

where $[\overline{K}]$ is the equivalent stiffness matrix, $[\overline{K}] = (4/\Delta t^2)[M] + (2/\Delta t)[C] + [K]$; $\{\overline{P}_{t1+\Delta t}\}$ is the equivalent load, $\{\overline{P}_{t1+\Delta t}\} = \{P_{t1+\Delta t}\} + [M]\{(4/\Delta t^2)\{u_{t1}\} + (4/\Delta t)\{\ddot{u}_{t1}\} + \{\ddot{u}_{t1}\}\} + [C]\{(2/\Delta t)\{u_{t1}\} + \{\dot{u}_{t1}\}\}$.

In iterative computation, the process of each time step are as follows:

(1) Calculate the equivalent load $\{\overline{P}_{t1+\Delta t}\}$ according to the operation state and external load of the node.

(2) Calculate the equivalent stiffness matrix $[\overline{K}]$ according to the node.

(3) Solve equation set (24). When the structure is in the elastic state, the equivalent stiffness matrix $[\overline{K}]$ does not change with the displacement of the node, which is a linear equation set and can be solved directly by triangular decomposition. When the structure is in the plastic state, the equivalent stiffness matrix $[\overline{K}]$ is related to the displacement of the node and must be solved through displacement iteration.

(4) Calculate the acceleration and velocity at time $t1 + \Delta t$ by equation (25).

3.3. Dynamic Incremental Variable Plastic Stiffness Iterative Method. When the structure enters the plastic stage described by the Mohr–Coulomb plasticity criterion, equation set (26) is nonlinear. The equivalent stiffness matrix $[\overline{K}]$ is related to displacement and must be solved iteratively. The dynamic incremental variable plasticity stiffness iteration method is used to solve the equation set [28].

The equivalent stiffness matrix $[\overline{K}]$ of dynamic calculation is made up of mass matrix $[M]$, damping matrix $[C]$, and stiffness matrix $[K]$. The plastic stiffness matrix $[K_P]$ is formed from $[K]$ when the element enters plasticity.

To guarantee the convergence of iteration, according to the incremental plastic stiffness iteration method, the plastic load of each time step is applied in multiple stages. In each stage of plastic load application, the overall stiffness matrix of the structure can be decomposed into two parts: elastic and plastic:

$$[K] = \iiint_v [B]^T \big([D_e] - [D_p]\big)[B]dv = [K_e] - [K_p]. \quad (27)$$

In the calculation, the elastic stiffness matrix $[K_e]$ remains unchanged, and the plastic stiffness matrix $[K_p]$ is changed according to the critical stress state imposed after each stage load. In the process of each stage of the plastic load iteration, according to the basic idea of the incremental load method, the plastic stiffness matrix is kept constant, and the displacement $\{\delta_{t1+\Delta t}\}_0$ solved by the elastic equivalent stiffness matrix $[\overline{K}_e]$ is taken as the initial displacement of the iterative calculation. The displacement value $\{\delta_{t1+\Delta t}\}$ under the incremental load at each stage is solved by the continuous correction of the displacement. The basic iterative equation for the dynamic elastoplastic finite element method is

$$\begin{cases} [\overline{K}_e]\{u_{t1+\Delta t}\} = \{\Delta \overline{P}_p\} + [K_p]\{u_{t1+\Delta t}\}, \\[2mm] [\overline{K}_e] = \dfrac{4}{\Delta t^2}[M] + \dfrac{2}{\Delta t}[C] + [K_e], \end{cases} \quad (28)$$

where $[\overline{K}_e]$ is the elastic equivalent stiffness matrix.

3.4. Calculation Method of External Load

3.4.1. Stress Decomposition. Considering the complexity of deep underground engineering, a circular tunnel is used to carry out the mechanical analysis. The blasting excavation process of a deep tunnel is accompanied by the blasting load and in situ stress transient unloading, and blasting excavation is the precondition for transient unloading of in situ stress [29]. Thus, on the one hand, the stress wave produced by the blasting load and detonation gas will cause blasting damage of surrounding rock within a certain range; and on the other hand, transient unloading of stress in a deep tunnel will cause stress redistribution of surrounding rock. Therefore, the stress field of blasting excavation in Figure 6 is decomposed into two problems:

(1) The elastoplastic stress field caused by the blasting load $P_b(t)$

(2) The elastoplastic stress field caused by the transient unloading of in situ stress $P_o(t)$

3.4.2. Blasting Load. The blasting load is actually the shock wave pressure acting on the surrounding rock after the explosion. In this paper, the change process of the blasting load is described by a triangle function (Figure 7). P_b is the equivalent peak load of the blasting load on the excavation surface and t_r and t_d are the time of the load rising and the positive pressure, respectively.

Taking full section blasting in a tunnel as the research object, the influence of the blasting load on rock mass is taken into account.

The detonation CJ model [30, 31] is used to calculate the peak load of the blasting load. For cylindrical radial uncoupled loading conditions, the equivalent peak load P_b on the excavation surface is calculated as

$$P_b = \frac{\rho_0 D_e^2}{2(1+\gamma)}\left(\frac{d_c}{d_b}\right)^{2\gamma}\frac{d_b}{S}, \quad (29)$$

where ρ_0 is the density of explosives, D_e is the detonation velocity of explosives, γ is the isentropic exponent of explosives, which is generally taken as 3, d_c is the diameter of the cartridge, d_b is the diameter of the blast hole, and S is the distance of adjacent blast holes.

When the explosion wave is propagating to the blasting hole with velocity D_e, the blasting load in the hole rises to the maximum, and the rising time t_r can be written as

$$t_r = \frac{L_1}{D}. \quad (30)$$

The blasting load is a transient load that changes with time during blasting. With explosive gas escaping, the blasting load decreases further. When the pressure of the blast hole drops to atmospheric pressure, the synchronous unloading of the excavation load is completed. The duration of the blasting load t_d is calculated as

$$t_d = \frac{L_1}{D} + \frac{\sqrt{(1/4)S^2 + L_2^2}}{C_f} + \frac{L_1 + L_2}{C_{u1}} + \frac{L_1 + L_2}{C_{u2}}, \quad (31)$$

where L_1 and L_2 are the respective lengths of the charging section and blockage section in the blast hole; C_f is the average speed of expansion driven by crack explosion loading; C_{u1} is the unloading wave speed of gas explosion; and C_{u2} is the reflected wave velocity spread from the bottom to the top of the blast hole [32].

The time history relation $P_b(t)$ of the blasting load acting on the excavation surface can be expressed as follows:

$$P_b(t) = \begin{cases} 0, & (t \leq 0 \text{ or } t \geq t_d), \\[3mm] P_b\dfrac{t}{t_r} & (0 < t \leq t_r), \\[3mm] P_b\dfrac{t_d - t}{t_d - t_r} & (t_r < t < t_d). \end{cases} \quad (32)$$

3.4.3. Transient Unloading of In Situ Stress. The unloading of in situ stress on the excavation surface [33] should satisfy the
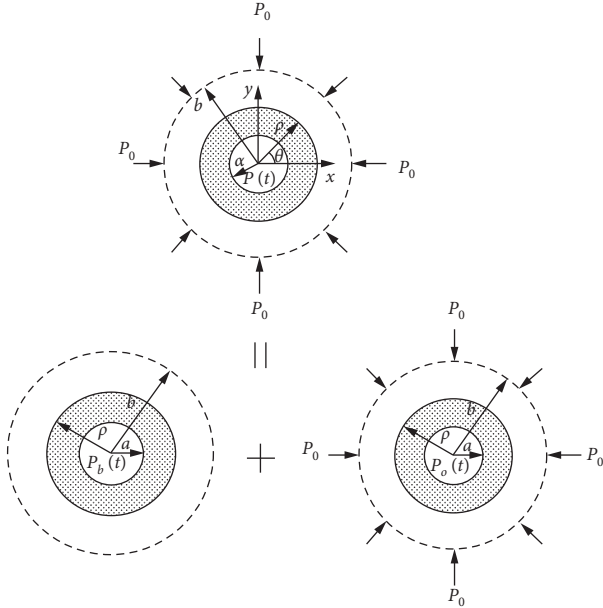
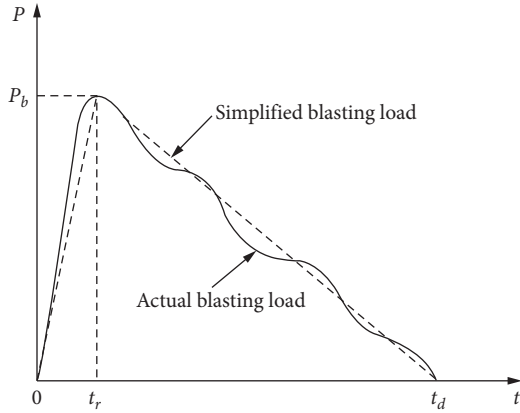FIGURE 6: Forces on circular tunnel under dynamic unloading.

FIGURE 7: Explosion load curve.

continuous stress condition, so the initial time and duration of transient unloading are determined by the blasting process. The in situ stress unloads at time t_b, defined as the moment when the blasting load decreases to the in situ stress. When the blasting load is further reduced to zero, the synchronous unloading of in situ stress is completed. $t_d - t_b$ is the duration of transient unloading of in situ stress. The transient unloading curve of in situ stress coincides with the curve of the blasting load (Figure 8).

The time history relation of the in situ stress $P_0(t)$ on the excavation surface can be written as

$$
P_0(t) = \begin{cases} P_0, & (t \leq t_b), \\ -P_0 \dfrac{t - t_d}{t_d - t_b}, & (t_b < t < t_d), \\ 0, & (t \geq t_d). \end{cases} \tag{33}
$$

3.4.4. Loading Method.
In the process of blasting excavation of an underground tunnel, the external loads $\{P\}$ imposed on surrounding rock elements are mainly divided into blasting load $\{F_p\}$, gravity loads $\{F_g\}$, and excavation loads $\{F_e\}$ [34].

According to the stress generated by blasting on rock mass elements, the blasting load $\{F_p\}$ can be obtained as

$$
\{F_p\} = \iiint_v [B]^T \{P_b(t)\} dv, \tag{34}
$$

where $\{F_g\}$ is the vertical gravity loads caused by the removed elements and can be expressed as

$$
\{F_g\} = \iiint_v [N]^T \{\rho g\} [N] dv, \tag{35}
$$

where ρ is the density of the rock mass, g is the acceleration of gravity, and $[N]$ is the shape function matrix which can be obtained by Hermit interpolation function. $\{F_e\}$, the transient unloading of in situ stress, can be expressed as

$$
\{F_e\} = \iiint_v [B]^T \{P_0(t)\} dv, \tag{36}
$$

where $[B]$ is strain matrix and $P_0(t)$ is the in situ stress of the excavation unit, obtained from equation (33).

3.5. Zonal Disintegration Damage Failure Criterion

3.5.1. Maximum Tensile Strain Criterion.
Tensile failure of surrounding rock is generally the result of strain development in the direction perpendicular to the surface of the wall. The maximum tensile strain criterion can be written as

$$
f = \varepsilon_{t\max} - \varepsilon_{tu} = 0, \tag{37}
$$

where $\varepsilon_{t\max}$ is the maximum tensile strain of a calculation element [35] and ε_{tu} is the ultimate tensile strain, which is obtained by a uniaxial tensile test or Brazilian disk test.

If $f \geq 0$, then tensile failure will occur and the element is destroyed. To maintain the integrity and continuity of the entire calculation during the numerical simulation, a small residual elastic modulus E_C is given to the element where the tensile failure occurs; usually, $E_C = 0.05E$. If $f < 0$, the tensile failure will not occur. The zonal disintegration energy damage failure criterion is used as the criterion of element failure.

3.5.2. Zonal Disintegration Energy Damage Failure Criterion.
Considering the influence of the strain gradient term, the formula for calculating the strain energy density of an element is written as

$$
\frac{dW}{dV} = \int_0^{\varepsilon_{ij}} \sigma_{ij} d\varepsilon_{ij} + \frac{1}{8} G l^2 \big(4\eta_{ijj}\eta_{ikk} + 4\eta_{iik}\eta_{kjj} \\ + 4\eta_{iik}\eta_{jjk} + 7\eta_{ijk}\eta_{ijk} + 2\eta_{ijk}\eta_{kji} \big). \tag{38}
$$

Figure 9 shows the simplified stress-strain relation curve of rock under high stress. Elastic strain energy density $(dW/dV)_s$, critical strain energy density $(dW/dV)_o$, and
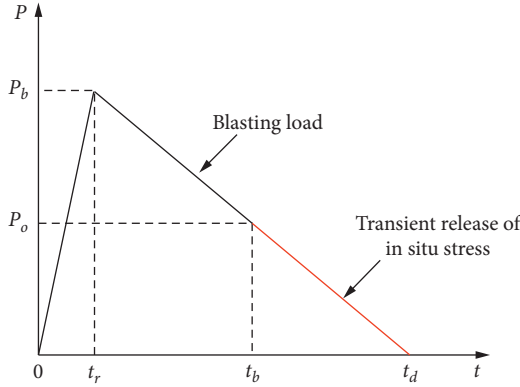
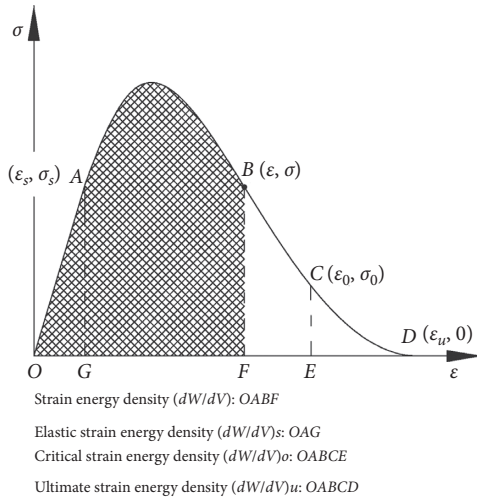FIGURE 8: Coupling effect curves of blasting load and transient release of in situ stress.

Strain energy density (dW/dV): OABF

Elastic strain energy density (dW/dV)s: OAG

Critical strain energy density (dW/dV)o: OABCE

Ultimate strain energy density (dW/dV)u: OABCD

FIGURE 9: Stress-strain relation curve of rock under high stress.

ultimate strain energy density $(dW/dV)_u$ can be calculated as [36]

$$\begin{cases} \left(\dfrac{dW}{dV}\right)_e = \displaystyle\int_0^{\varepsilon_e} \sigma_{ij} d\varepsilon_{ij}, \\[2ex] \left(\dfrac{dW}{dV}\right)_o = \displaystyle\int_0^{\varepsilon_o} \sigma_{ij} d\varepsilon_{ij}, \\[2ex] \left(\dfrac{dW}{dV}\right)_u = \displaystyle\int_0^{\varepsilon_u} \sigma_{ij} d\varepsilon_{ij}. \end{cases} \tag{39}$$

The damage failure criterion of zonal disintegration is judged by the change of the strain energy density.

(1) When $(dW/dV) < (dW/dV)_s = \int_0^{\varepsilon_s} \sigma_{ij} d\varepsilon_{ij}$ (ε_s is the yield strain in the loading process), then the element is in the linear elastic stage, and damage within the element will not occur.

(2) When $(dW/dV) \geq (dW/dV)_s$, the element enters into the plastic damage stage; microcracks in the rock mass appear and begin to expand.

(3) When $(dW/dV) \geq (dW/dV)_D = \int_0^{\varepsilon_o} \sigma_{ij} d\varepsilon_{ij}$ (ε_o is the critical strain in the loading process), the microcracks in the rock mass develop into a macroscopic crack, and there is still bearing capacity in the rock body. This is called the plastic residual stage.

(4) When $(dW/dV) \geq (dW/dV)_u = \int_0^{\varepsilon_u} \sigma_{ij} d\varepsilon_{ij}$ (ε_u is the ultimate strain in the loading process), the element is damaged to failure. In the case of tensile failure, a residual elastic modulus value is given to the failed element to maintain the integrity and continuity of the entire calculation.

3.6. Numerical Simulation Procedure. Based on the elastoplastic damage model and the energy damage failure criterion, the code for the zonal disintegration calculation was programmed with the finite element software ABAQUS and the dynamic incremental variable plastic stiffness iterative method. Figure 10 shows the flowchart of the zonal disintegration procedure.

4. Engineering Application

4.1. In Situ Monitoring Results. The deep tunnel of the Dingji Mine in the Huainan area was selected as the research object. The depth of the tunnel is 910 m, and the monitoring section size is $5,000 \times 3,880$ mm. The damaged scopes of the surrounding rock in the boreholes are depicted on the map, and the fractured areas within 0.5 m in different holes are connected to form fractured zones with different depths. The zones between the fractured zones are relatively complete (Figure 11) [37, 38].

The average ranges of the fractured zones are listed in Table 1. The inner and outer diameters are the sides near and away from the tunnel in the distance, respectively.

4.2. Determination of Calculation Parameters. The calculation parameters of the tunnel's surrounding rock are as follows: the tunnel shape is a semicircular arch; the section size is $5\,m \times 3.88\,m$; the simulation range of the calculation area is $30\,m \times 30\,m \times 30\,m$; the initial geostress is $P_0 = 23.5$ MPa; the rock density $\rho = 2.45\,g/cm^3$; the compressive strength $\sigma_c = 88.55$ MPa; the elastic modulus $E = 77.82$ GPa; Poisson's ratio $v = 0.286$; the cohesion force $c = 9$ MPa; the internal friction angle $\varphi = 43°$; the internal material length $l = 0.01$ m; the yield strain $\varepsilon_s = 0.725 \times 10^{-3}$; and the ultimate strain $\varepsilon_u = 4.65 \times 10^{-3}$.

Figure 12 shows the layout of the hole in the tunnel excavation blasting. The blasting design of the underground tunnel in the actual project is simplified, and the full section blasting is used. Only the effect of the blasting load on surrounding rock at the excavation radius (periphery holes and bottom holes) is considered. For tunneling blasting, the diameter of the blast hole is $d_b = 42$ mm and the distance of adjacent blast holes is $S = 0.3$ m; the explosive is grade-three water-gel explosive for permissible coal mine; the diameter of the cartridge is $d_c = 35$ mm, the length of the charging section is $L_1 = 1.4$ m; the length of the blockage section is L_2
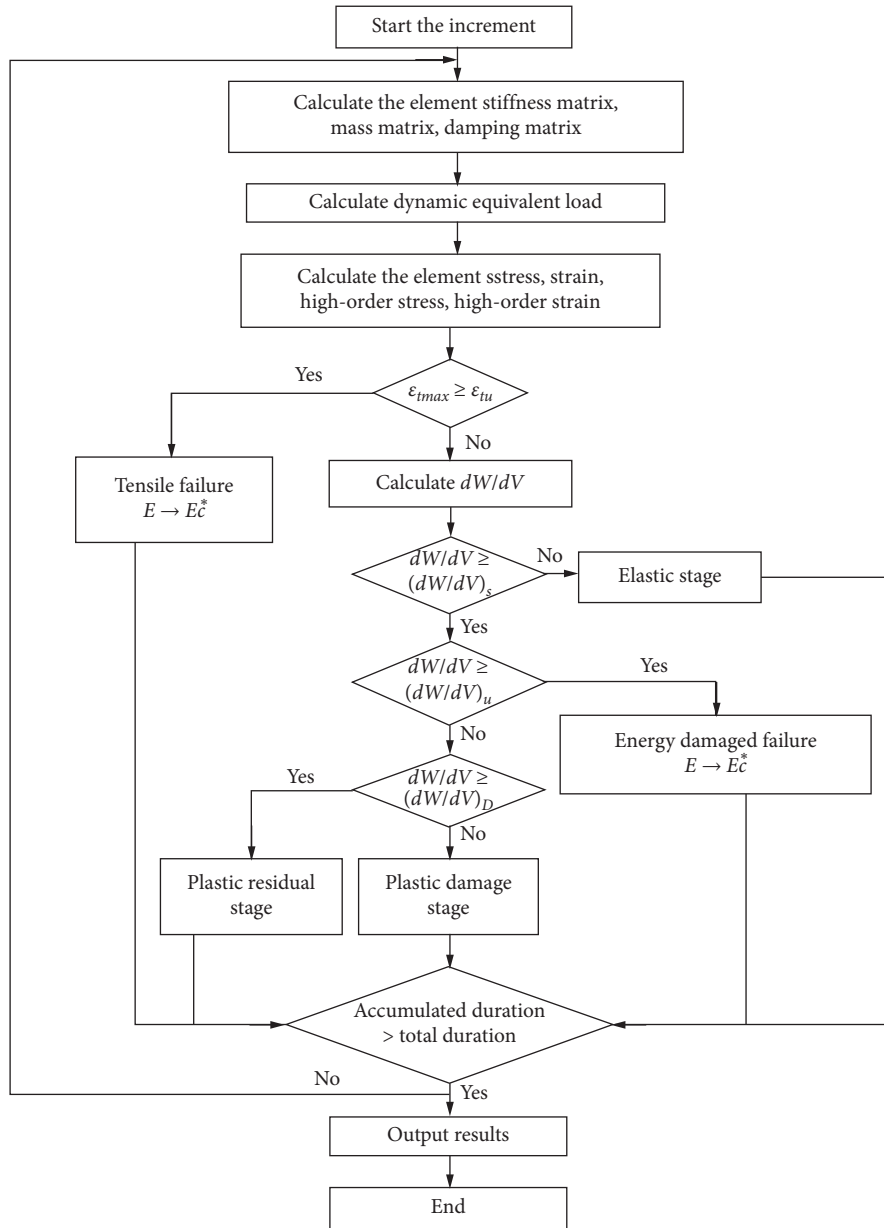
FIGURE 10: Flow chart of zonal disintegration subroutine.
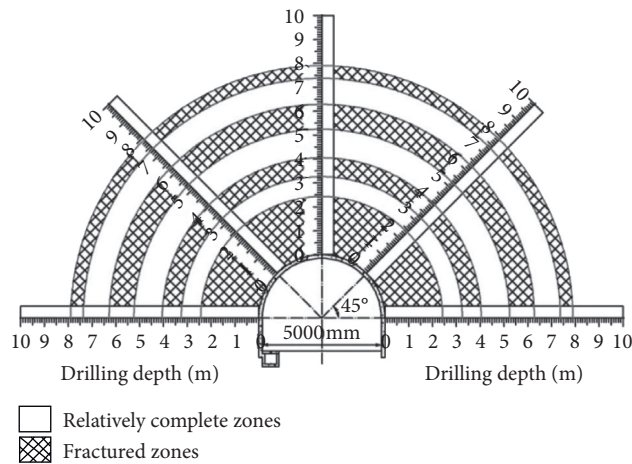

FIGURE 11: Failure distribution of model cavern after excavation.

TABLE 1: In situ test results of fractured zones.

Fractured zones number	Field measured results	
	Inner diameter (m)	Outer diameter (m)
1	2.50	4.99
2	5.75	6.55
3	7.74	8.78
4	9.87	10.40
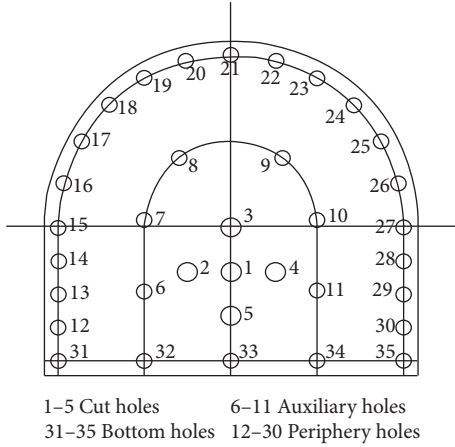
FIGURE 12: The schematic diagram of blast hole arrangement.

1–5 Cut holes 6–11 Auxiliary holes
31–35 Bottom holes 12–30 Periphery holes

$= 0.6$ m; the density of the explosive is $\rho_0 = 0.95$–1.25 g/cm^3; the detonation velocity is $D_e = 3.0 \times 10^3$ m/s; the isentropic exponent is $\gamma = 3$; and the equivalent blasting peak load on the surface of the blasting excavation can be calculated by equation (33), in which the value is $P_b = 52.75$ MPa.

It is concluded that the unloading wave speed of gas explosion C_{u1} is approximately equal to the reflected wave velocity C_{u2}, that is, $C_{u1} = C_{u2} = (1$–$1.5) \times 10^3$ m/s. The average speed of expansion driven by crack explosion loading is $C_f = 0.25\, C_L$, where C_L is the longitudinal velocity of rock mass, $C_L = 4550 \times 10^3$ m/s. According to equations (30) and (31), it can be obtained that the rise time of the blasting load is $t_r = 470\,\mu s$, the duration of the blasting load is $t_d = 5700\mu s$, and the unloading time of in situ stress is $t_b = 2130\,\mu s$.

The calculation step is determined by the demanded precision, so the initial space step is 0.01 m, and the initial time step is 10 μs.

4.3. Establishment of the ABAQUS Numerical Model.
Figure 13 shows the three-dimensional computational mesh for the selected calculation range. There are 110,360 elements and 157,837 nodes.

In the dynamic calculation, the outwardly propagating stress wave will be reflected back to the model interior at the constraint boundary of the model, causing the energy not to be dissipated outwards. As the time increases, the model elements will be completely destroyed and the result will be completely distorted. To solve this problem, a free-field boundary [39–41] is used as the boundary conditions of the
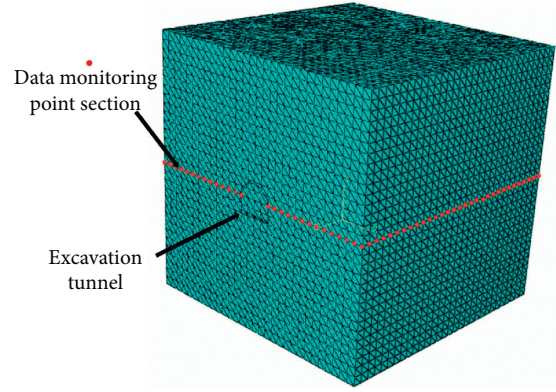
FIGURE 13: Three-dimensional computational mesh of rock mass.

computational model and the outward waves generated by the structure can be properly absorbed.

4.4. Simulation Results and Comparative Analysis.
Figure 14 shows the numerical nephogram obtained by numerical simulation.

At the time of $250\,\mu s$, the radial displacement of the tunnel reaches 4.91 cm, and a damage zone is generated within the range of about 2.05 m around the tunnel as in Figure 14(a).

At the time of $500\,\mu s$, the damage zone around the tunnel increases significantly, and the radial displacement increases to 6.85 cm as in Figure 14(b).

At the time of $2500\,\mu s$, there is a sudden increase in radial displacement at 5.5 m, where the second fractured zones occur as in Figure 14(c).

At the time of $6000\,\mu s$, the ultimate time, a third fractured zone occurs about 7.8 m away from the tunnel periphery as in Figures 14(d) and 14(e).

Figure 15 shows the stresses and displacement of the surrounding rock in a deep tunnel caused by blasting excavation. A wave phenomenon can be seen in the radial displacement, tangential stress, and radial stress of the surrounding rock. From the curves in Figure 15, the following trends can be observed.

(1) At time $t = 250\,\mu s$, the blasting load is at the rising stage; the radial stress and tangential stress in the surrounding rock near the blasting area are relatively high. With the increase of the radius, the stress decreases rapidly, and the attenuation speed decreases with the increase of the radius. The stress in surrounding rock at moderate and blasting areas tends to be gentle. When the tangential tensile stress in the surrounding rock is greater than the tensile strength, the radial tensile cracks will occur and lead to the fracture phenomenon. The radial displacement of the surrounding rock will also increase.

(2) At the time $t = 500\,\mu s$, the blasting load is around the peak load, and the stress and displacement values of the surrounding rock increase to a certain extent.

(3) At the time $t = 2500\,\mu s$, the stress oscillation of the surrounding rock appears at a moderate and remote

U, U1 (CSYS-1)
+2.722e − 02
+2.086e − 02
+1.450e − 02
+8.137e − 03
+1.778e − 03
−4.581e − 03
−1.094e − 02
−1.730e − 02
−2.366e − 02
−3.002e − 02
−3.638e − 02
−4.274e − 02
−4.910e − 02

Radial displacement

S, S11 (CSYS-1)
(Avg: 75%)
+7.374e + 07
+6.002e + 07
+4.629e + 07
+3.256e + 07
+1.884e + 07
+5.114e + 06
−8.612e + 06
−2.234e + 07
−3.606e + 07
−4.979e + 07
−6.351e + 07
−7.724e + 07
−9.097e + 07

Radial stress

S, S22 (CSYS-1)
(Avg: 75%)
+1.227e + 06
−2.433e + 06
−6.093e + 06
−9.753e + 06
−1.341e + 07
−1.707e + 07
−2.073e + 07
−2.439e + 07
−2.805e + 07
−3.171e + 07
−3.537e + 07
−3.903e + 07
−4.269e + 07

Tangential stress

Fracture
(Avg: 75%)
+9.999e − 01
+5.000e − 01
+0.000e + 00

Fractured zones

(a)

U, U1 (CSYS-1)
+1.399e − 02
+7.114e − 03
+2.389e − 04
−6.636e − 03
−1.351e − 02
−2.039e − 02
−2.726e − 02
−3.413e − 02
−4.101e − 02
−4.788e − 02
−5.476e − 02
−6.163e − 02
−6.851e − 02

Radial displacement

S, S11 (CSYS-1)
(Avg: 75%)
+8.462e + 07
+6.445e + 07
+4.429e + 07
+2.413e + 07
+3.967e + 06
−1.620e + 07
−3.636e + 07
−5.652e + 07
−7.668e + 07
−9.684e + 07
−1.170e + 08
−1.372e + 08
−1.573e + 08

Radial stress

S, S22 (CSYS-1)
(Avg: 75%)
+7.855e + 05
−2.591e + 06
−5.968e + 06
−9.345e + 06
−1.272e + 07
−1.610e + 07
−1.947e + 07
−2.285e + 07
−2.623e + 07
−2.961e + 07
−3.298e + 07
−3.636e + 07
−3.974e + 07

Tangential stress

Fracture
(Avg: 75%)
+1.000e + 00
+5.000e − 01
+0.000e + 00

Fractured zones

(b)

Figure 14: Continued.

U, U1 (CSYS-1)

+1.978e − 02
+1.287e − 02
+6.563e − 03
+2.550e − 04
+6.053e − 03
−1.236e − 02
−1.867e − 02
−2.498e − 02
−3.128e − 02
−3.759e − 02
−4.390e − 02
−5.021e − 02
−5.652e − 02

Radial displacement

S, S11 (CSYS-1)
(Avg: 75%)

+2.367e + 09
+1.878e + 09
+1.388e + 09
+8.985e + 08
+4.089e + 08
−8.068e + 07
−5.703 + 08
−1.060e + 09
−1.550e + 09
−2.039e + 09
−2.529e + 09
−3.018e + 09
−3.508e + 09

Radial stress

S, S22 (CSYS-1)
(Avg: 75%)

+7.855e + 05
−2.591e + 06
−5.968e + 06
−9.345e + 06
−1.272e + 07
−1.610e + 07
−1.947e + 07
−2.285e + 07
−2.623e + 07
−2.961e + 07
−3.298e + 07
−3.636e + 07
−3.974e + 07

Tangential stress

Fracture
(Avg: 75%)

+1.000e + 00
+5.000e − 01
+0.000e + 00

Fractured zones

(c)

U, U1 (CSYS-1)

+8.362e − 03
+4.834e − 06
+8.353e − 03
−1.671e − 02
−2.507e − 02
−3.342e − 02
−4.178e − 02
−5.014e − 02
−5.850e − 02
−6.685e − 02
−7.521e − 02
−8.357e − 02
−9.193e − 02

Radial displacement

S, S11 (CSYS-1)
(Avg: 75%)

+1.133e + 07
+7.099e + 06
+2.866e + 06
−1.367e + 06
−5.600e + 06
−9.834e + 06
−1.407e + 07
−1.830e + 07
−2.253e + 07
−2.677e + 07
−3.100e + 07
−3.523e + 07
−3.947e + 07

Radial stress

S, S22 (CSYS-1)
(Avg: 75%)

+3.106e + 06
−1.487e + 05
−3.403e + 06
−6.657e + 06
−9.912e + 06
−1.317e + 07
−1.642e + 07
−1.967e + 07
−2.293e + 07
−2.618e + 07
−2.944e + 07
−3.269e + 07
−3.595e + 07

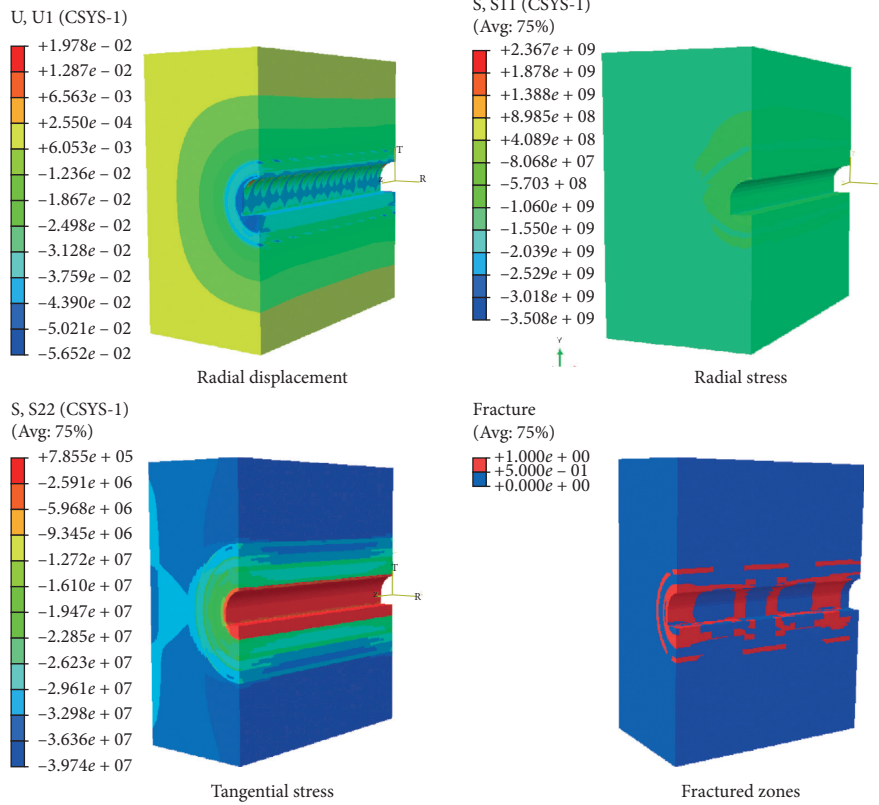Tangential stress

Fracture
(Avg: 75%)

+9.999e − 01
+4.999e − 01
+0.000e + 00

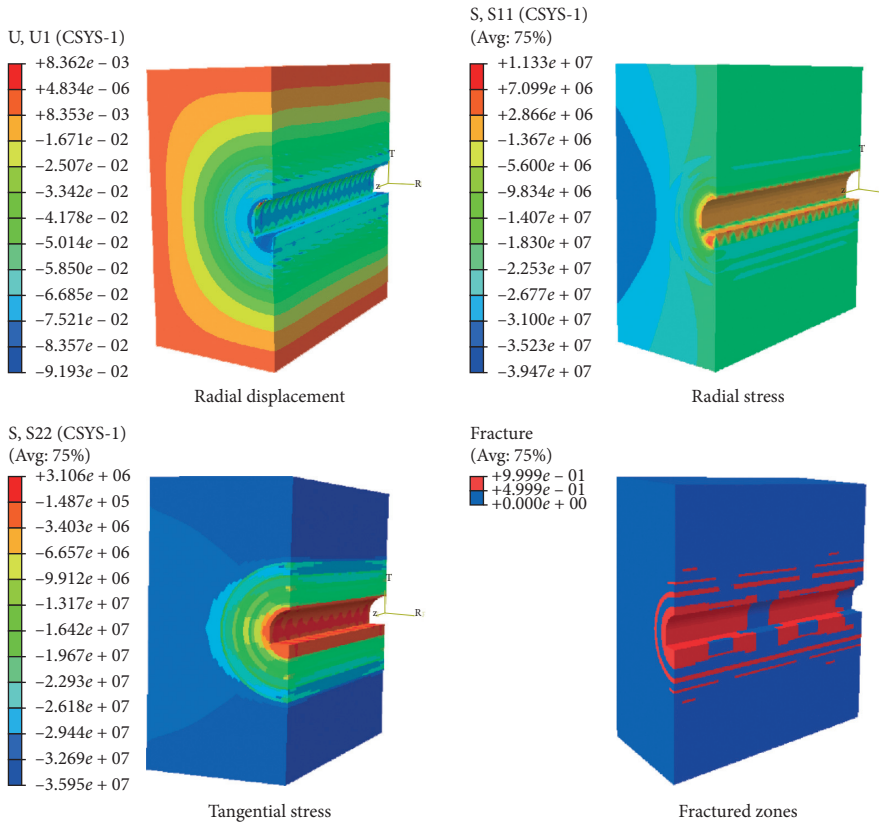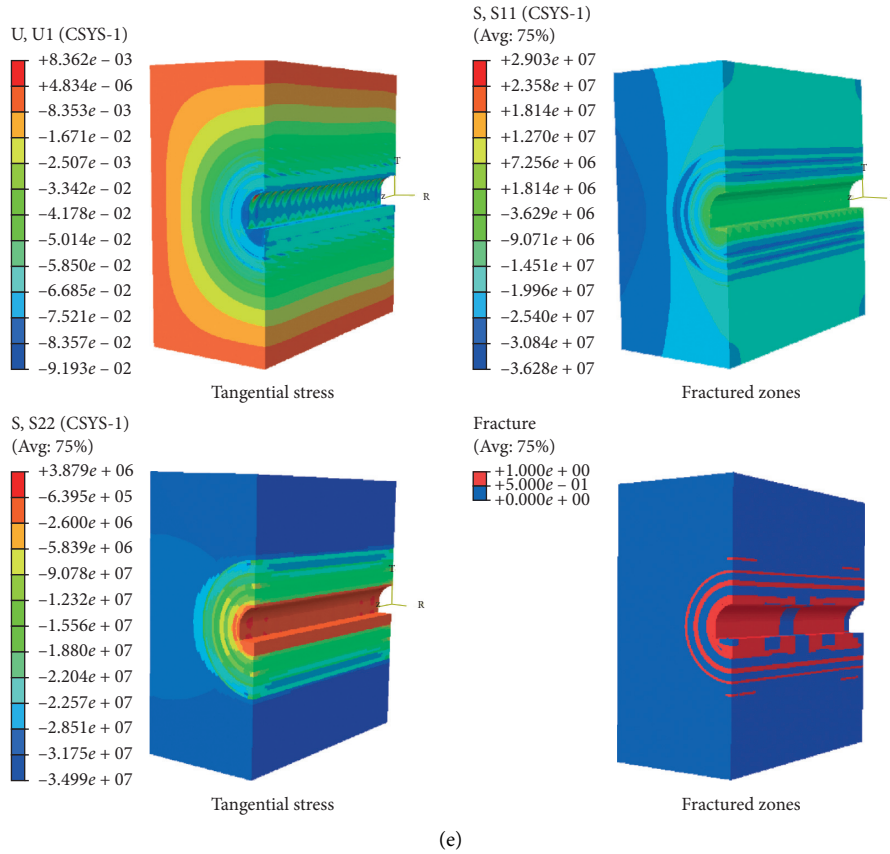Fractured zones

(d)

Figure 14: Continued.

Figure 14: Fractured zone nephogram of surrounding rock. (a)$t = 250\,\mu s$. (b)$t = 500\,\mu s$. (c)$t = 2500\,\mu s$. (d)$t = 6000\,\mu s$. (e) Ultimate time.
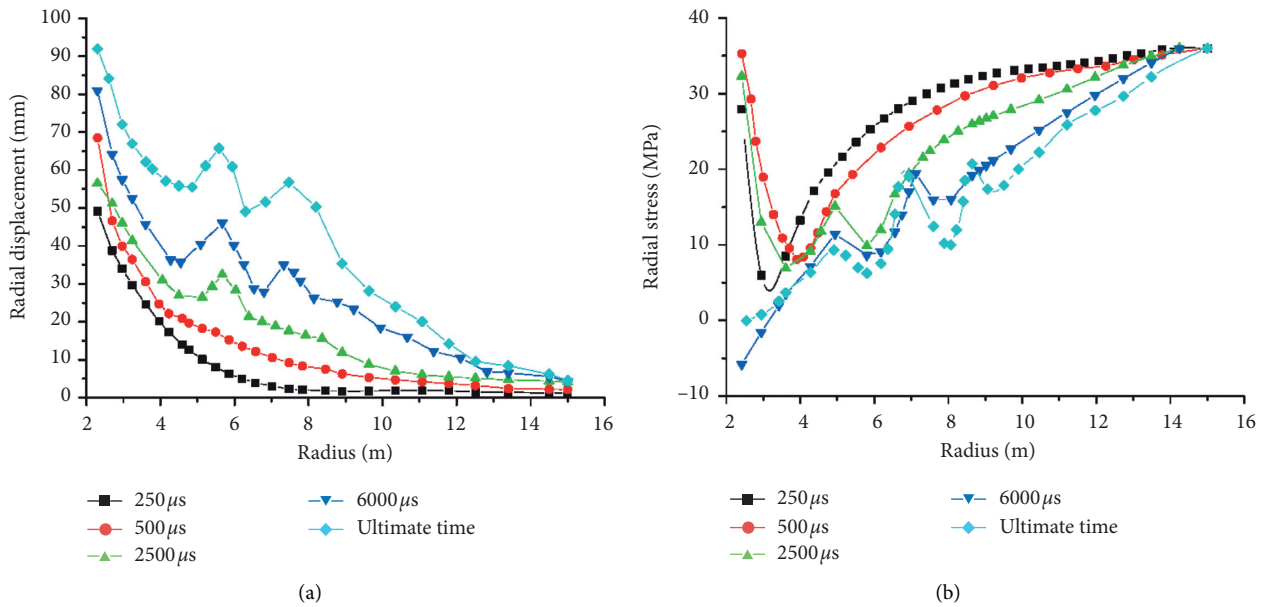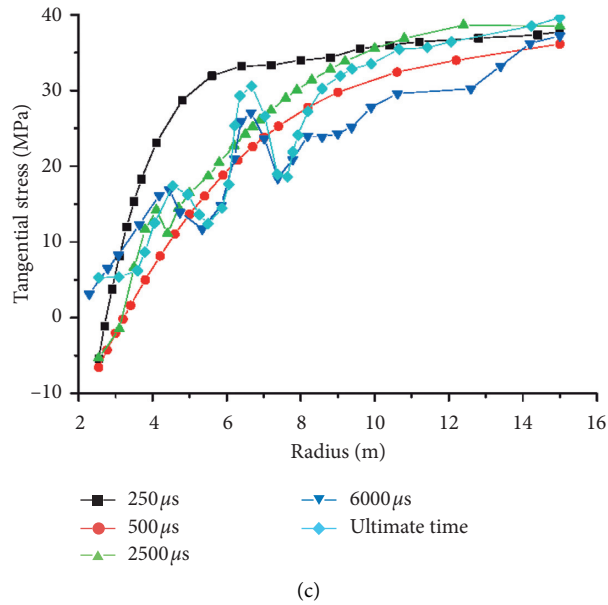

(a)

(b)

Figure 15: Continued.

(c)

Figure 15: The displacement and stress changes of tunnel surrounding rock in different times. (a) Radial displacement. (b) Radial stress. (c) Tangential stress.

distance under the interaction of blasting load and in situ stress unloading. As shown in Figures 8(a) and 8(b), the radial and tangential stress are both in the trough state at a radius of 5.65 m, and the variation of radial displacement shows a rapidly increasing trend from a radius of 5 m and reaches the peak at the radius of 5.8 m. It is known from the previous analysis that the surrounding rock in this region is damaged and the fractured zone is produced.

(4) At the time $t = 6000\,\mu s$, the unloading of the dynamic load in the tunnel is completed. The radial stress changes from tension to compression at the near region. The tangential arc crack will be generated when the stress exceeds the tensile strength of the rock mass. In the moderate and remote area of the tunnel, the stresses in the surrounding rock present a more obvious changing mode. The radial displacement increases continuously in the original fractured zone and rises rapidly in the new fractured zone.

It can be realized from the values at the ultimate time that the displacement and stresses present an oscillating mode, which is reflected in the alternate appearance of the wave peak and trough. By comparative analysis of Figures 14 and 15, the surrounding rock stresses at the relatively complete zones are in the peak ranges while the displacements are in the trough ranges; on the contrary, the surrounding rock stresses in the fractured zones are in the trough ranges while the displacements are in the peak ranges.

The numerical calculation of the fractured zones is compared with the in situ results in Figure 16. It is worth mentioning that the average radius is the mean value of the inner and outer diameter of each fractured zone, and the average width is the mean value of the difference between the internal and external diameters of each fractured zone.
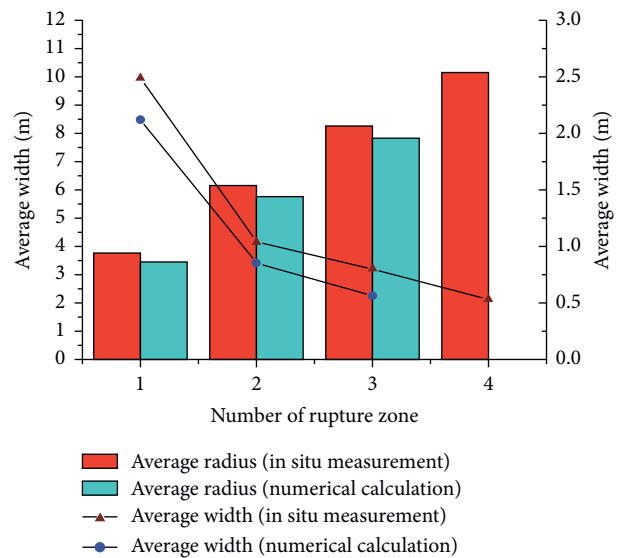
Figure 16: Width and quantity comparison in surrounding rock of tunnel.

We can conclude that the range, width, and position of the fractured zones obtained by numerical simulation are basically consistent with the field measurement results, indicating that the numerical calculation method is feasible and reliable.

5. Conclusion

The effect of strain gradient should be considered in the study of the zonal disintegration of deep tunnels.

Based on the strain gradient theory and the damage characteristics of rock mass, an elastoplastic damage model

was developed. The zonal disintegration calculation program was compiled with the dynamic finite element equation and the dynamic incremental variable stiffness iterative method, which is embedded in the finite element software ABAQUS. According to the failure criterion, the number and depth of fractured zones are obtained under the action of blasting excavation. The failure process of the surrounding rock in the deep tunnel can be observed dynamically, and the formation mechanism of the zonal disintegration phenomenon in the deep tunnel can be clearly identified.

In the numerical calculation, the radial displacement, radial stress, and tangential stress of the surrounding rock appear in the changing law of the wave peak and trough alternation. The width and quantity of the fractured zone are in good agreement with the in situ observations. The applicability of the numerical simulation method is analyzed.

When the tunnel is disturbed by blasting excavation, the coupling effect of the blasting load and the initial geostress transient unloading leads to the variation of alternation oscillation in the surrounding rock stress field, which is an important reason for the zonal disintegration of the surrounding rock.

Data Availability

The data used to support the findings of this study are available from the corresponding authors upon request.

Conflicts of Interest

The authors declare that they have no conflicts of interest.

Acknowledgments

References

[1] E. I. Shemyakin, G. L. Fisenko, M. V. Kurlenya et al., "Zonal disintegration of rocks around underground workings, Part 1: data of in situ observations," *Soviet Mining Science*, vol. 22, no. 3, pp. 157–168, 1986.

[2] M. A. Guzev and A. A. Paroshin, "Non-Euclidean model of the zonal disintegration of rocks around an underground Working," *Journal of Applied Mechanics and Technical Physics*, vol. 42, no. 1, pp. 131–139, 2001.

[3] C. Z. Qi, Q. H. Qian, M. Y. Wang et al., "Internal variable gradient plasticity model for zonal disintegration of surrounding rocks in deep tunnels," *Chinese Journal of Rock Mechanics and Engineering*, vol. 31, no. S1, pp. 2722–2728, 2012.

[4] Q. Zhang, X. Zhang, Z. Wang, W. Xiang, and J. Xue, "Failure mechanism and numerical simulation of zonal disintegration around a deep tunnel under high stress," *International Journal of Rock Mechanics and Mining Sciences*, vol. 93, no. 1, pp. 344–355, 2017.

[5] C. A. Tang and Y. B. Zhang, "Discussion on mechanism and evolution laws of fracture spacing in rock mass," *Chinese Journal of Rock Mechanics and Engineering*, vol. 27, no. 7, pp. 1362–1369, 2018.

[6] F. Q. Gao, H. P. Kang, and J. Lin, "Numerical simulation of zonal disintegration of surrounding rock mass in deep mine roadways," *Journal of China Coal Society*, vol. 35, no. 1, pp. 21–25, 2010.

[7] J. C. Gu, L. Y. Gu, A. M. Chen et al., "Model test study on mechanism of layered fracture within surrounding rock of tunnels in deep stratum," *Chinese Journal of Rock Mechanics and Engineering*, vol. 27, no. 3, pp. 433–438, 2008.

[8] X. Zhang, Q. Gao, S. Cui, and C. Duan, "Research on failure mechanism and parameter sensitivity of zonal disintegration in deep tunnel," *Advances in Civil Engineering*, vol. 2019, pp. 1–10, 2019.

[9] Z. Tao, C. Zhu, M. He, and M. Karakus, "A physical modeling-based study on the control mechanisms of Negative Poisson's ratio anchor cable on the stratified toppling deformation of anti-inclined slopes," *International Journal of Rock Mechanics and Mining Sciences*, vol. 138, no. 138, Article ID 104632, 2021.

[10] M. Beiki, A. Bashari, and A. Majdi, "Genetic programming approach for estimating the deformation modulus of rock mass using sensitivity analysis by neural network," *International Journal of Rock Mechanics &Mining Sciences*, vol. 47, no. 1, pp. 1091–1103, 2010.

[11] B. Li, R. Bao, Y. Wang, R. Liu, and C. Zhao, "Permeability evolution of two-dimensional fracture networks during shear under constant normal stiffness boundary conditions," *Rock Mechanics and Rock Engineering*, vol. 54, no. 3, pp. 1–20, 2021.

[12] W. Zhu and G. Zhang, "Sinsitivity analysis of influence of jointed rock parameters on damaged zone of surrounding rock," *Underground Space*, vol. 14, no. 1, pp. 10–15, 1994.

[13] Q. Wang, Q. Qin, B. Jiang et al., "Mechanized construction of fabricated arches for large-diameter tunnels," *Automation in Construction*, vol. 124, no. 124, Article ID 103583, 2021.

[14] R. D. Mindlin, "Micro-structure in linear elasticity," *Archive for Rational Mechanics and Analysis*, vol. 16, no. 1, pp. 51–78, 1964.

[15] Z. G. Tao, C. Zhu, M. C. He, and K. M. Liu, "Research on the safe mining depth of anti-dip bedding slope in Changshanhao Mine," *Geomechanics and Geophysics for Geo-Energy and Geo-Resources*, vol. 36, no. 6, pp. 1–20, 2020.

[16] J. W. Ju, "On energy-based coupled elastoplastic damage theories: constitutive modeling and computational aspects," *International Journal of Solids and Structures*, vol. 25, no. 7, pp. 803–833, 1989.

[17] Q. Gao, Q. Y. Zhang, X. T. Zhang, and W. Xiang W, "Zonal disintegration mechanism analysis based on strain gradient of deep surrounding rock mass under dynamic unloading effect," *Rock and Soil Mechanics*, vol. 39, no. 1, pp. 3181–3194, 2018.

[18] R. D. Mindlin, "Second gradient of strain and surface-tension in linear elasticity," *International Journal of Solids and Structures*, vol. 1, no. 4, pp. 417–438, 1965.

[19] M. Geers, R. D. Borst, and W. Brekelmans, "Strain-based transient-gradient damage model for failure analyses," *Computer Methods in Applied Mechanics & Engineering*, vol. 160, no. 1-2, pp. 133–153, 1998.

[20] N. A. Fleck and J. W. Hutchinson, "Strain gradient plasticity," *Advances in Applied Mechanics*, vol. 33, no. 2, pp. 295–361, 1997.

[21] L. Mishnaevsky, "Computational analysis of the effects of microstructures on damage and fracture in heterogeneous

materials," *Key Engineering Materials*, vol. 306, no. 2, pp. 489–494, 2005.

[22] J. Y. Shu and N. A. Fleck, "Strain gradient crystal plasticity: size-dependentdeformation of bicrystals," *Journal of the Mechanics and Physics of Solids*, vol. 47, no. 2, pp. 297–324, 1999.

[23] H. Zhu, F. Huang, and X. U. Qianwei, "Model test and numerical simulation for progressive failure of weak and fractured tunnel surrounding rock under different overburden depths," *Chinese Journal of Rock Mechanics and Engineering*, vol. 29, no. 6, pp. 1113–1122, 2010.

[24] I. Babuka and B. Q. Guo, "The h, p and h - p version of the finite element method; basis theory and applications," *Advances in Engineering Software*, vol. 15, no. 3–4, pp. 159–174, 1992.

[25] K. P. Dharmasena, H. N. G. Wadley, Z. Xue, and J. W. Hutchinson, "Mechanical response of metallic honeycomb sandwich panel structures to high-intensity dynamic loading," *International Journal of Impact Engineering*, vol. 35, no. 9, pp. 1063–1074, 2008.

[26] Y. Peng and W. B. Lu, "Study of the damage characteristics of surrounding rocks for tunnels constructed using TBM and drill-and-blast," *China Civil Engineering Journal*, vol. 42, no. 11, pp. 121–128, 2009.

[27] M. XIAO, Y. T. Zhang, J. T. Chen et al., "Numerical analysis of excavation damaged zone of underground caverns induced by excavation blasting," *Rock & Soil Mechanics*, vol. 21, pp. 145–168, 2010.

[28] Q. Gao, Q. Zhang, and W. Xiang, "Mechanism of zonal disintegration phenomenon (ZDP) around deep roadway under dynamic excavation," *Geotechnical and Geological Engineering*, vol. 37, no. 1, pp. 25–41, 2019.

[29] S. C. Li, X. Feng, S. C. Li et al., "Numerical simulation of zonal disintegration for deep rock mass," *Chinese Journal of Rock Mechanics and Engineering*, vol. 30, no. 7, pp. 1337–1344, 2011.

[30] Z. Zhang, M. Xiao, Y. Zhang et al., "Dynamic finite element analysis of large-scale complex underground caverns with three-dimensional elastoplastic damage model," *Chinese Journal of Rock Mechanics and Engineering*, vol. 29, no. 5, pp. 982–989, 2010.

[31] G. Zhang and W. S. Zhu, "Susceptibility analyses of parameters and optimization of test program," *Rock and Soil Mechanics*, vol. 14, no. 1, pp. 51–58, 1993.

[32] X. G. Lei and X. P. Zhou, "Analyses of susceptibility in the strength of parameters interrelationship of rock and soil media," *Journal of Yunnan Agricultural University*, vol. 14, no. 2, pp. 171–175, 1999.

[33] C. F. Yan, D. Y. Liu, J. H. Zhang et al., "The susceptibility analysis of reliability for the probability distribution types of parameters in strength criterion," *Chinese Journal of Rock Mechanics and Engineering*, vol. 18, no. 1, pp. 36–39, 1999.

[34] W. S. Zhu and G. Zhang, "Susceptibility analyses of parameters of jointed rock to breaking area in surrounding rock," *Underground Space*, vol. 14, no. 1, pp. 10–15, 1994.

[35] W. H. Peng, L. S. Cai, X. J. Hua et al., "Control methods of stability of zonal disintegration surrounding rock in deep rock roadway and its application," *Rock and Soil Mechanics*, vol. 35, no. 7, pp. 1957–1964, 2014.

[36] Y. Wang, W. K. Feng, R. L. Hu, and C. H. Li, "Fracture evolution and energy characteristics during marble failure under triaxial fatigue cyclic and confining pressure unloading (FC-CPU) conditions," *Rock Mechanics and Rock Engineering*, vol. 14, no. 54, pp. 799–818, 2021.

[37] Q. Qian, X. Zhou, and E. Xia, "Effects of the axial in situ stresses on the zonal disintegration phenomenon in the surrounding rock masses around a deep circular tunnel," *Journal of Mining Science*, vol. 48, no. 2, pp. 276–285, 2012.

[38] Q. Zhang and Q. Gao, "Geomechanical modeling of the stability of deep tunnel in Dingji coal mine in China," *Geotechnical and Geological Engineering*, vol. 37, no. 4, pp. 3313–3327, 2019.

[39] C. Zhu, M. C. He, M. Karakus, X. H. Zhang, and Z. G. Tao, "Numerical simulations of the failure process of anaclinal slope physical model and control mechanism of negative Poisson's ratio cable," *Bulletin of Engineering Geology and the Environment*, vol. 12, no. 80, pp. 3365–3380, 2021.

[40] Q. Wang, H. Gao, B. Jiang, S. Li, M. He, and Q. Qin, "In-situ test and bolt-grouting design evaluation method of underground engineering based on digital drilling," *International Journal of Rock Mechanics and Mining Sciences*, vol. 138, no. 2, Article ID 104575, 2021.

[41] A. Li, F. Dai, Y. Liu, H. Du, and R. Jiang, "Dynamic stability evaluation of underground cavern sidewalls against flexural toppling considering excavation-induced damage," *Tunnelling and Underground Space Technology*, vol. 112, no. 112, Article ID 103903, 2021.

Research Article

Study on Stability and Plastic Zone Distribution of Tunnel with Thin Carbonaceous Slate at Different Dip Angles

Jin Zhang (ID),[1] **Chuanhao Xi,**[1] **Qian Zhang,**[2] **and Mengxue Wang**[1]

[1]*College of Civil Engineering, Qingdao University of Technology, Qingdao 26033, China*
[2]*Beijing Key Laboratory for Precise Mining of Intergrown Energy and Resources, China University of Mining and Technology, Beijing 100083, China*

Correspondence should be addressed to Jin Zhang; zhangjin@qut.edu.cn

Carbonaceous slate is heterogeneous and anisotropic, which has a great influence on the stability of tunnel. In this paper, by means of laboratory test, field measurement, and numerical simulation, the surrounding rock stability and plastic zone distribution characteristics of the carbonaceous slate tunnel at different intersection angles are analyzed. First, combined with the Haibaluo tunnel project, Brazilian splitting and uniaxial compression tests of jointed carbonaceous slate are performed. The test results show that the tensile strength of carbonaceous slate is related to joint dip angle. When the joint angle is 0°, the tensile strength is the largest and decreases with the increase of the joint angle. The uniaxial strength of rock decreases first and then increases. Based on the discrete fracture network (DFN) technology, a calculation model is established. The calculation results show that the maximum displacement is 0.45 m, when the dip angle of the surrounding rock joint is 45°. The field measurement also shows that the dip angle of the surrounding rock joint has an important influence on the distribution of the plastic zone. When the joint dip angle is 45°, the plastic zone develops most strongly.

1. Introduction

The stability of surrounding rock plays a decisive role in the safe excavation of tunnel. In the process of tunnel excavation, when the surrounding rock is disturbed, the stress will redistribute and plastic zone would be expansion. The strength of rock mass in the plastic zone decrease obviously, the fracture expands, and the stability of surrounding rock is weak [1]. When the joints are relatively developed, the plastic sliding phenomenon is easy to occur. Previous engineering experience shows that the size of the plastic zone will have a significant impact on the stability of the tunnel and the difficulty of the support. When the area of plastic zone is larger, the stability of surrounding rock is worse, and the difficulty of roadway support is greater.

Numerical analysis has become a more and more common method in the study of surrounding rock stability. In the study by Xiang and Feng [2] based on the assumption of homogeneous isotropic ideal elastic-plastic soil, a theoretical method is proposed to predict the secondary stress field and the corresponding potential plastic zone caused by tunnel excavation near the pile foundation. Taking the calculation results as an example, the theoretical results are compared with the corresponding numerical simulation results to demonstrate the development characteristics of the plastic zone of the tunnel. Lu et al. [3] calculated the elastic-plastic stress and strain of circular tunnel in rock mass controlled by Mohr Coulomb failure criterion. The results show that the stress, strain, and failure zone in the surrounding rock are related not only to the transverse in situ stress but also to the axial in situ stress. Massinas and Sakellariou [4] provide an opportunity to quickly and accurately calculate the plastic zone and stress distribution around a circular tunnel. By using different support pressure values, tunnel designers can easily evaluate the feasibility of different design schemes, such as shotcrete shell and tunnel boring machine support pressure. Behnam et al. [5] discussed the calculation of the plastic zone of the surrounding rock of a circular tunnel under

nonhydrostatic conditions, which satisfies the Hoek Brown failure criterion, and reviewed the calculation of the plastic zone and displacement of the surrounding rock under hydrostatic conditions. Li et al. [6–8] used the method of discrete element numerical simulation to analyze the distribution characteristics of in situ stress, the control effect of support on plastic zone, and the distribution characteristics of plastic zone under water rock coupling. In the study by Annan et al. [9], in order to solve the problem of surrounding rock stability, the displacement field, stress field, and plastic zone in the construction process of CRD method were analyzed by using the method of numerical simulation and field monitoring. Shi et al. [10] derived the principal stress distribution function around a circular tunnel from elastoplastic mechanics, calculated the boundary and radius of plastic zone under different strength criteria. The results show that the variation law of plastic zone around circular tunnel under different strength criteria has the following commonalities: first, with the increase of lateral pressure coefficient, the shape of plastic zone presents the variation law of "circle ellipse butterfly." With the increase of lateral pressure coefficient, the radius of plastic zone presents exponential distribution. When the radius of plastic zone is infinite, the eigenvalues are different. In the study by Wu et al. [11–13], through induction, theoretical analysis, numerical calculation, and field measurement, the deformation characteristics, plastic zone distribution, and support control measures of large deformation tunnel in soft rock are studied. Hu et al. [14] used numerical simulation to study the phenomenon of large deformation of weak surrounding rock. At present, with the development of science and technology, some advanced numerical simulation methods for geotechnical engineering modeling are more and more common. For example, Meng et al. [15] used heterogeneous material modeling for digital image processing. At the same time, many experts also use the indoor test and similar material simulation method to carry out engineering rock failure test [16–19]. Significant progress has also been made in engineering practice [20–25].

The main methods of measuring plastic zone in engineering field include acoustic wave method, multipoint displacement meter method, geological radar method, seismic wave method, resistivity method, permeability method, borehole camera method, and radioactive element method. The acoustic method is to use the ultrasonic detector to infer the range of the plastic zone by measuring and analyzing the parameters according to the different characteristics of the ultrasonic propagation speed in the rock with different integrity [26]. The multipoint displacement meter method is to measure the displacement of surrounding rock measuring points by displacement measurement and obtain the thickness range of plastic zone through the change of displacement [27]. The ground penetrating radar (GPR) method uses the change of radar reflection wave in different media to detect the location of surrounding rock cracks and obtain the boundary of surrounding rock loose circle [28]. Seismic wave method is used to determine the range of plastic zone according to the change of wave velocity at different rock interface. Permeability method makes use of the permeability of liquid to

cracks and infiltrates the liquid into the pores. When there are more cracks in the rock mass, the permeability becomes larger. Finding out the large range of permeability can determine the range of plastic zone. Borehole camera method uses borehole detection for real-time image monitoring and acquisition to observe the fracture development in the rock mass, so as to determine the size of the plastic zone. The radioactive element method uses the characteristics of radioactive elements contained in rocks and absorbed radioactive elements to test the surrounding rock loose zone [22].

In this paper, uniaxial and Brazilian splitting tests are used to analyze the influence of different dip angles of surrounding rock joints on rock strength at laboratory scale. At the same time, the influence of dip angles is analyzed by discrete element numerical simulation. Using the method of acoustic testing, the distribution characteristics of plastic zone of tunnel surrounding rock under different dip angles are analyzed in engineering practice.

2. Engineering Geological Characteristics

Haibaluo tunnel is located on the line from Shangri La to Lijiang in Yunnan Province. Its length is 2262 m, and the maximum buried depth is 461 m. The maximum relative height difference of tunnel crossing is 540 m. The elevation of the tunnel located is 2455–2902 m. According to the internationally accepted altitude classification standard, it belongs to high altitude area, which is a typical carbonaceous slate tunnel. The vertical section is shown in Figure 1.

The tunnel is located in high altitude area with thin air, low air pressure, and poor natural conditions. The geological structure of the tunnel area is complex, and the greatest influence geological structure is Qinghai Tibet Plateau, with many active faults. Zhongdian fault and longpanqiaohou fault also have a great influence. The tunnel mainly passes through strongly and moderately weathered carbonaceous slate. The structure is mainly thin-layer and cataclastic. The joints and fissures are relatively developed with poor integrity. The local groundwater is relatively developed, and the surrounding rock is easy to soften when encountering water.

Typical carbonaceous slate samples are selected for X-ray fluorescence spectrum analysis. The main minerals in carbonaceous slate are quartz and clay minerals, and the clay minerals are mainly illite and chlorite, as shown in Table 1. The surrounding rock is soft and prone to softening and argillization when meeting with water. Affected by the geological structure, the joint angle of the surrounding rock changes greatly.

3. Influence of Different Joint Dip Angles on Rock Mass Strength

In order to comprehensively analyze the influence of joint angle of surrounding rock on rock strength, the compressive strength and splitting strength under different inclination angles are analyzed. Figure 2 is the comparison diagram of uniaxial compressive strength of rock mass under different
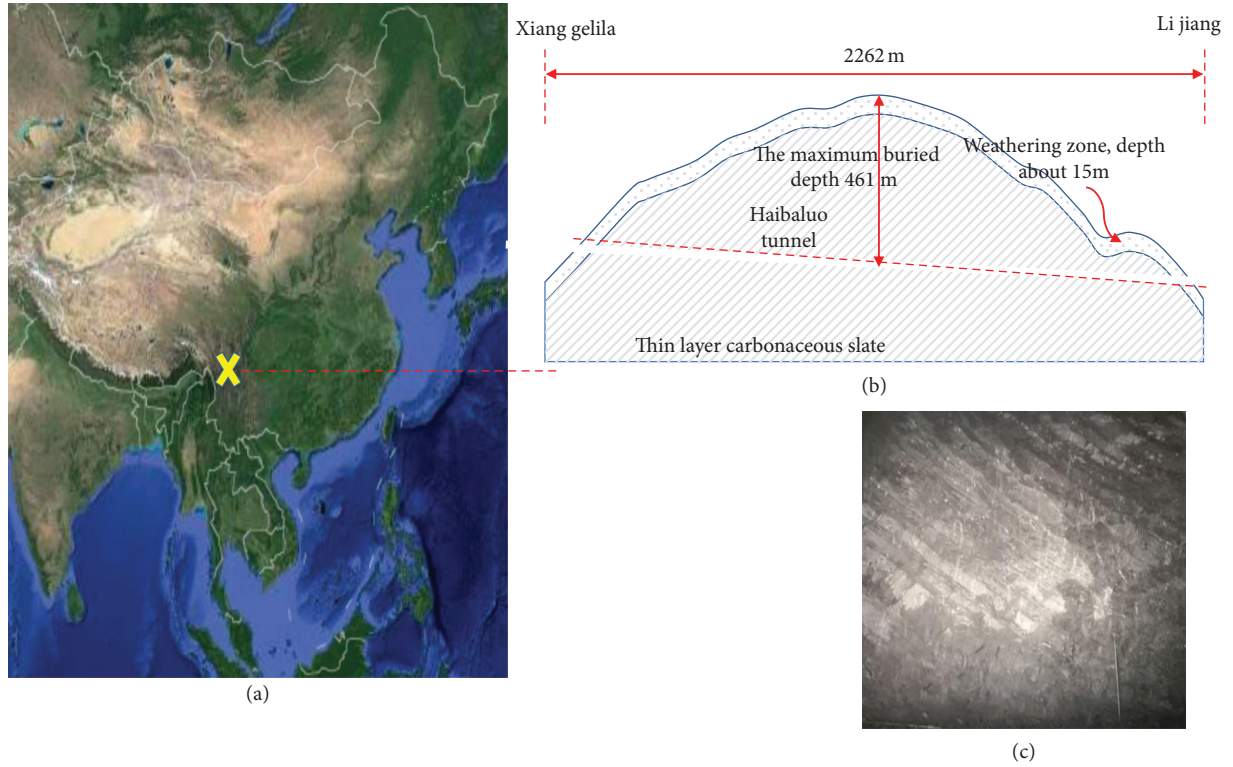
(a)

(b)

(c)

Figure 1: Tunnel construction location and geological profile. (a) Tunnel location. (b) Geological section. (c) Characteristics of surrounding rock.

Table 1: X-ray diffraction analysis of minerals.

Mineral content (%)				
Quartz	Potash feldspar	Plagioclase	Halite	Clay minerals
37.7	0.7	7.2	1.9	52.5
Relative content of clay minerals (%)				
I/S	It	K	C	C/S
—	43	—	52	—

S: smectites; I/S: illite mixed; It: illite; K: kaolinite; C: chlorite; C/S: mix of turquoise and montmorillonite.

joint dip angles. From the diagram, with the increase of joint dip angle, the uniaxial compressive strength of rock presents the pattern of first decreasing and then increasing. It is considered that the strength of rock joints is weak when the rock joints are in the range of 40° to 60°.

As a special slate, carbonaceous slate has a low sample rate due to the development of fractures and joints, so there are a few studies on its tensile properties in the current literature. Therefore, it is necessary to carry out in-depth experimental research on Brazilian splitting of carbonaceous slate.

The sample preparation of Brazilian splitting test is divided into two steps: ① select a 50 mm diameter sleeve to core and cut the disc according to the predetermined inclination angle; ② smooth the sample with a grinder. The plane along the thickness direction shall be flat to 0.01 mm, and the concave deviation shall not be greater than 0.5°, so that the processed samples can meet the requirements of relevant specifications of rock mechanics test. The experimental results are shown in Figure 3.

Through the calculation and processing of the test data, the average tensile strength is 1.49 MPa, 1.21 MPa, 1.09 MPa, 0.88 MPa, and 0.56 MPa, respectively, at 0°, 30°, 45°, 60°, and 90° inclination. The test results show that the maximum tensile strength of carbonaceous slate is when the joint dip angle is horizontal. The horizontal angle of joint angle represents that the joint inclination angle is 0°, and the strength decreases with the increase of the angle between the joint and the horizontal plane. The variance coefficient $R = 0.88$ indicates that the data is still discrete.

## 4. Numerical Calculation of Deformation Characteristics of Surrounding Rock under Different Joint Dip Angles

4.1. Model Establishment and Parameter Selection. For the numerical simulation of jointed surrounding rock, there are two kinds of analysis modes: finite element and discrete element. From the simulation principle, the 3D discrete element software is more suitable for practical engineering. The purpose of this study is finding out the relative magnitude of the influence of joint on tunnel stability under different dip angles. So, it is feasible to use 3DEC discrete element software to simulate the joint plane. In order to study the stability and plastic zone distribution characteristics of tunnels with different dip angles, five models were established in this study, which were 0° dip angle, 30° dip angle, 45° dip angle, 60° dip angle, and 90° dip angle.
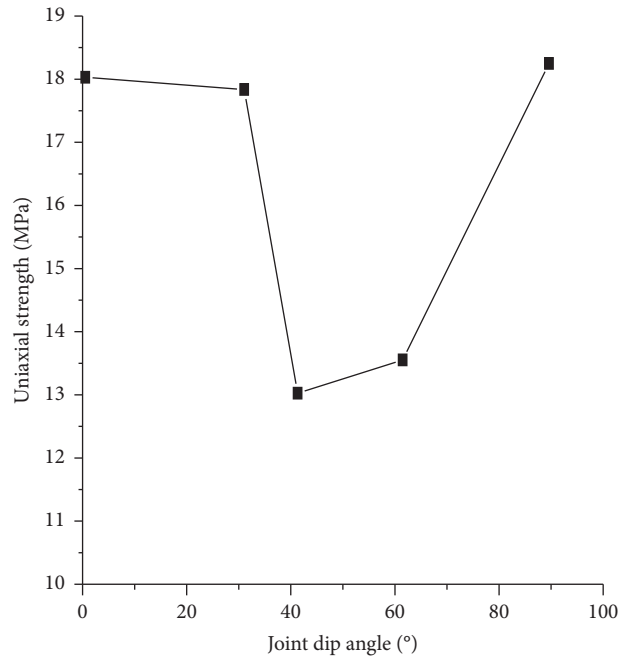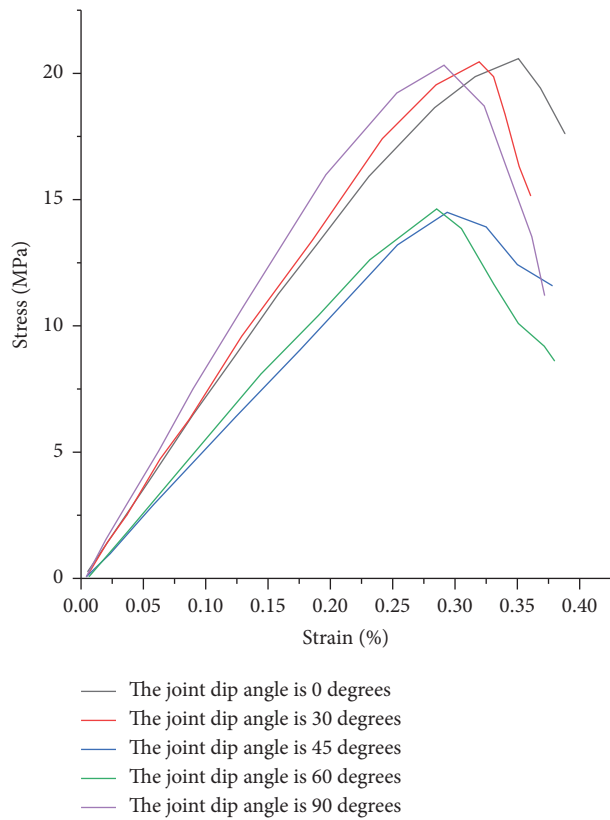
Figure 2: Influence of rock joint dip angle on uniaxial strength. (a) Uniaxial strength curve of different dip angles. (b) Rock strength under different dip angles.
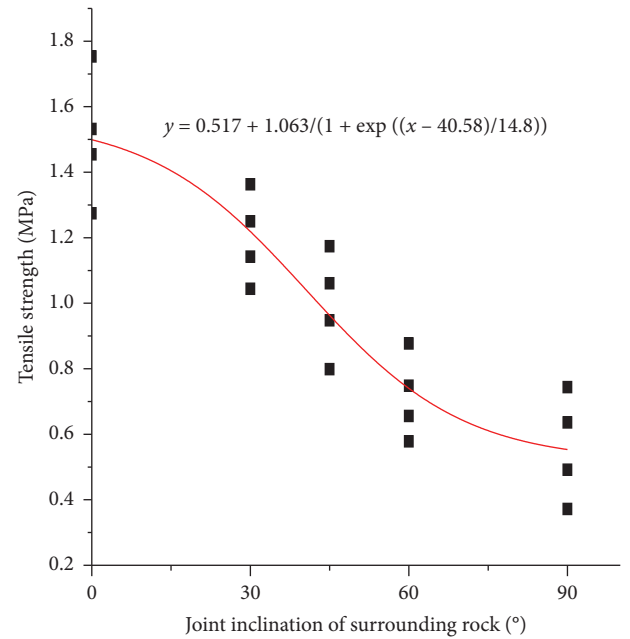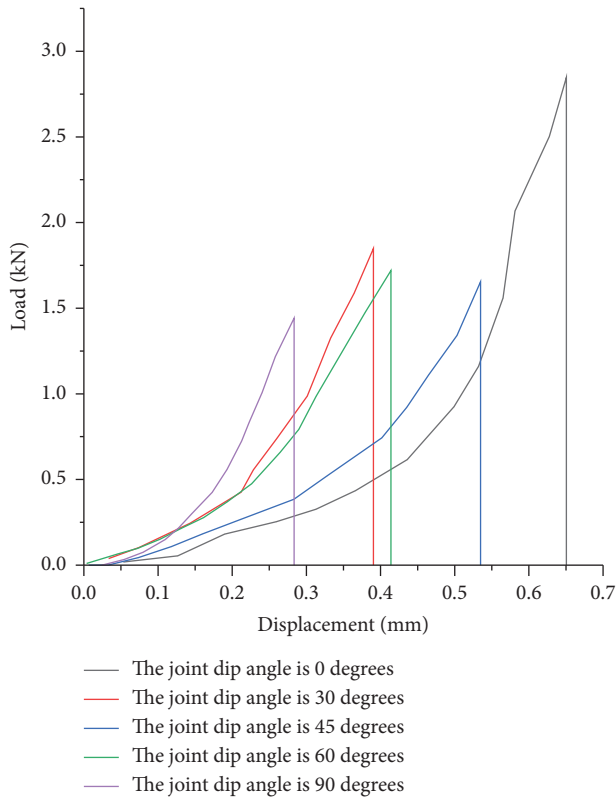
Figure 3: Influence of rock joint dip angle on tensile strength. (a) Strength curve of different dip angles. (b) Tensile strength under different dip angles.

In the process of establishing the numerical model, the plane model is used to simulate, and the size of the analysis area has a great influence on the study of tunnel surrounding rock. The model size is 50 m × 50 m, which is five times the tunnel diameter. In the numerical simulation, Mohr Columb criterion and Coulomb slip model are adopted for rock mass discontinuities. The beam element is used to simulate the initial support, and the thickness of the initial support is 350 mm. Referring to the GSI rock classification standard, combined with the numerical inversion analysis in the simulation process, the parameter values of the strength model of carbonaceous slate rock are shown in Table 2, and the model is shown in Figure 4. The horizontal stress is 15 MPa, and the vertical stress is 14 MPa.

4.2. Analysis of Numerical Simulation Results. The displacement of surrounding rock under different dip angles is shown in Figure 5. It is obvious that the joint angle has a great influence on the displacement of tunnel surrounding rock. It can be seen from the figure that, for 45° joint condition, the maximum displacement of the right spandrel of the tunnel is 0.45 m; for 0° joint condition, the maximum displacement of the junction between the free face and joint of the upper tunnel is 0.1 m; for 30° joint condition, the maximum deformation is still in the right spandrel, and the maximum displacement of the junction between the free face and joint is 0.21 m; for 60° joint condition, the maximum deformation is located at the vault, and the deformation is caused by sliding; for 90° joint condition, the maximum displacement of tunnel top is 0.22 m. When the joint angle of the surrounding rock is between 0° and 45°, the deformation of surrounding rock is mainly caused by the bending of thin plate under the action of stress. When the joint angle of surrounding rock is 60°~90°, the deformation is mainly caused by the sliding of surrounding rock along joints.

The variation of surrounding rock displacement under different dip angles is shown in Figure 5(f). It is obvious from the figure that the maximum displacement is 0.45 m under the condition of 45° joint angle. The reason for the maximum displacement at 45° joint angle is that the resultant force of horizontal stress and vertical stress is basically perpendicular to the thin plate.

5. Field Test of Surrounding Rock Plastic Zone and Support Optimization

Acoustic testing method is to judge the integrity of rock mass according to the internal relationship between the physical and mechanical indexes (strength, density, dynamic elastic modulus, etc.) of geotechnical medium and propagation speed of ultrasonic wave in geotechnical medium. If the force (stress) of rock mass is large, the density is large, the integrity of rock mass is good, and the acoustic wave velocity will be correspondingly large.

On the contrary, when the rock mass density is small, the structural plane is developed, the lithology is poor, the groundwater exists, and the acoustic wave velocity will decrease. Therefore, in the same nature of the surrounding rock, the higher the acoustic wave velocity, the better the integrity of the rock mass; the lower the wave velocity, the more broken the rock mass, the higher the existence of cracks, and even the more likely the failure. Through testing the longitudinal wave velocity of rock mass at different depths of surrounding rock, according to the change of rock mass wave velocity, the thickness of loose zone of tunnel surrounding rock can be obtained. Figure 6 is the schematic diagram of acoustic double-hole test method.

According to the wave theory in elastic-plastic medium, the wave velocity of stress wave is as follows [29]:

$$v_p = \sqrt{\frac{E(1-\mu)}{\rho(1+\mu)(1-2\mu)}}. \tag{1}$$

In the field test of the project, the rock mass integrity is evaluated by the ratio of the longitudinal wave velocity of the rock mass and longitudinal wave velocity of the undisturbed rock mass. The square of the value is the rock mass integrity coefficient, and the calculation formula is as follows:

$$L_v = \left(\frac{v_{pt}}{v_{yt}}\right)^2, \tag{2}$$

where E is the elastic modulus of medium (GPa), ρ is the density of medium (kg/m^3), u is the Poisson's ratio of medium, L_V is the integrity coefficient of loose zone, v_{pt} is the P wave velocity of rock mass in loose zone (km/s), and v_{yt} is the P wave velocity of original rock mass (km/s).

Five sections are selected to test the loose circle of the surrounding rock, and four pilot sites are arranged at the left and right side walls and spandrels of each section. No. 1 and No. 2 measuring points are symmetrically arranged 1.5 m above the upper bench excavation line of the left and right side walls. No. 3 and No. 4 measuring points are symmetrically arranged at the spandrel of the upper and lower steps. The down-the-hole drilling is adopted, the hole depth is 8.0 m, and the hole diameter is 40 mm. The dip angles of the surrounding rocks of the five sections are 0°, 30°, 45°, 60°, and 90° respectively, and the layout of the acoustic measuring holes is shown in Figure 7.

The thickness distribution of surrounding rock loose zone is shown in Figure 8. When the joint angle is 0°, the plastic zone is symmetrical. The height of the top plastic zone is about 3.3 m on the free surface. With the increase of the dip angle of surrounding rock, the shape and depth of the plastic zone have obvious changes. When the joint angle is 30 degrees, the plastic zone presents obvious asymmetry. The maximum position of the plastic zone appears in the upper left part of the tunnel, and the maximum depth is 6.2 m. When the joint angle is 45°, the maximum depth of plastic zone is 7.5 m. When the joint angle is 60°, the maximum depth of plastic zone appears in the upper right part of the tunnel, and the maximum depth is 6.1 m. When the joint angle is 90°, the plastic zone also presents symmetrical distribution, and the maximum depth of the plastic zone on the upper right is about 3.6 m.

After the tunnel excavation in layered rock mass, the depth of plastic zone in the area perpendicular to the joint

TABLE 2: Mechanical parameters of carbonaceous slate.

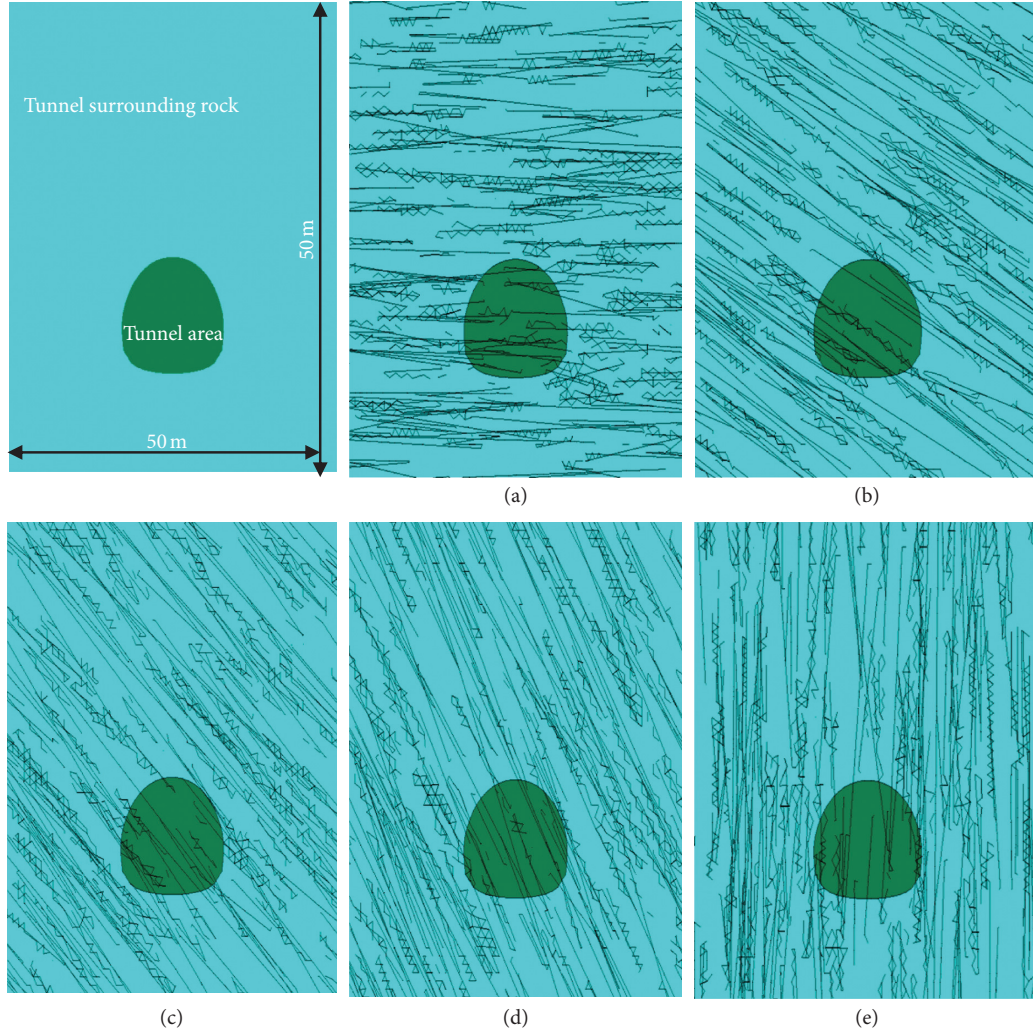| Lithology	Rock mass parameters						Structural plane parameters				
	Density (kg/m^3)	K (GPa)	G (GPa)	C^b (MPa)	φ^b	σ_t^b (MPa)	K^n (GPa)	k^s (GPa)	C^j (MPa)	φ^j	σ_t^i (MPa)
Carbonaceous slate	2423	0.49	0.26	1.58	27	0.56	28.99	11.98	3.69	28	3.32

(a)

(b)

(c)

(d)

(e)

FIGURE 4: Numerical calculation model of different surrounding rock inclination. (a) The dominant joint angle 0 degrees. (b) The dominant joint angle 30 degrees. (c) The dominant joint angle 45 degrees. (d) The dominant joint angle 60 degrees. (e) The dominant joint angle 90 degrees.

angle is larger, and the stability of surrounding rock is poor. In view of the large deformation above the arch waist of the tunnel and the characteristics of the surrounding rock when the joint angle is 45°, the length and ring distance of the bolt are optimized on the basis of the original support scheme. The support arrangement is shown in Figure 9. In the dangerous area, the anchor rod is lengthened to 7.5 m and the spacing is 1 m. In other noncritical positions, the length of anchor rod is 4 m and the circumferential spacing is 1 m.

The measured data show that the optimized bolt length can control the deformation of surrounding rock (Figure 10). It is an economical and reliable support scheme to change the layout angle of the anchor and arrange the anchor perpendicular to the bedding plane, which can better
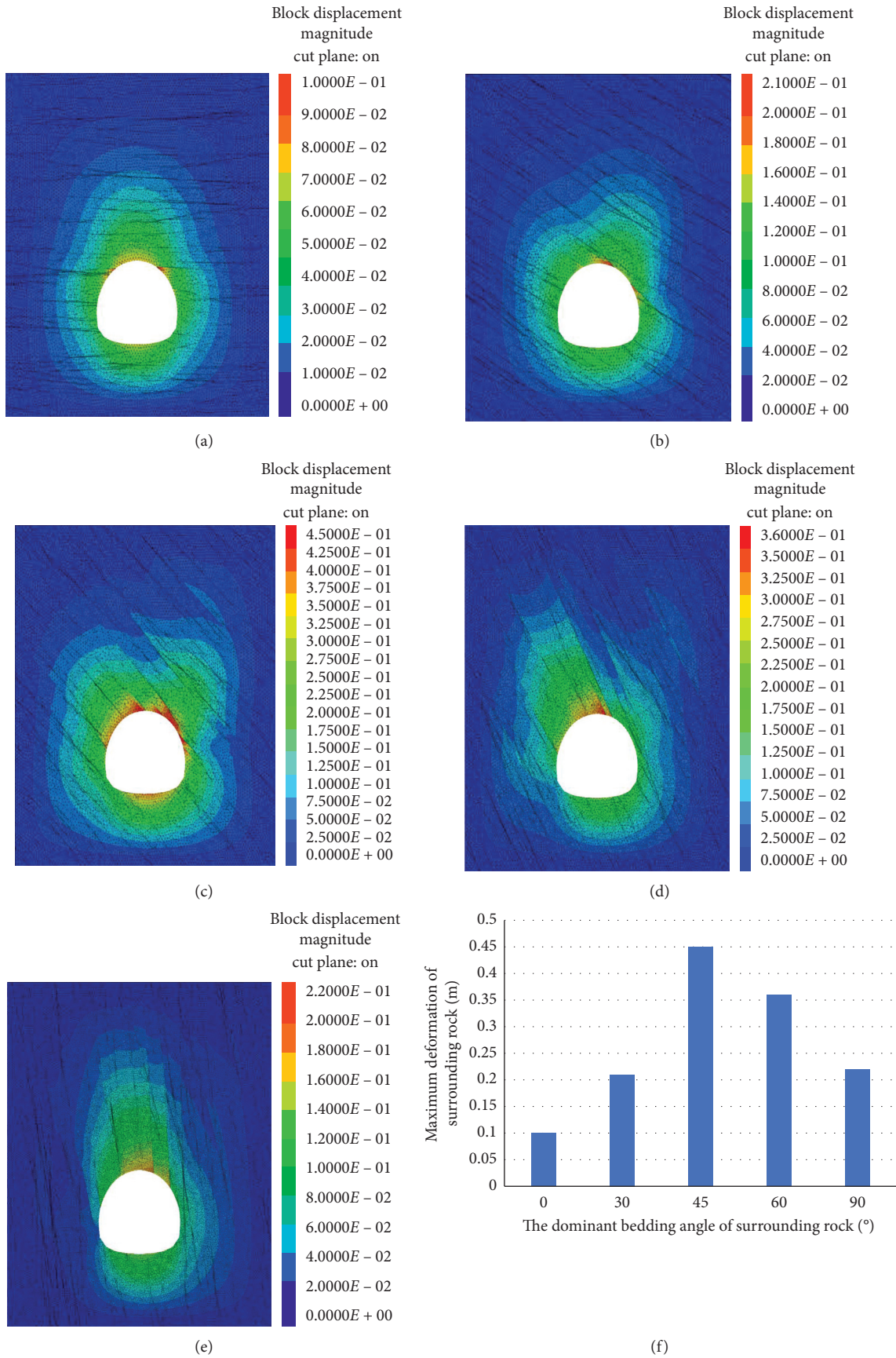
FIGURE 5: Different dip angles and deformation characteristics of surrounding rock. (a) The dominant joint angle 0 degrees. (b) The dominant joint angle 30 degrees. (c) The dominant joint angle 45 degrees. (d) The dominant joint angle 60 degrees. (e) The dominant joint angle 60 degrees. (f) Relationship between dip angle deformations of different surrounding rocks.
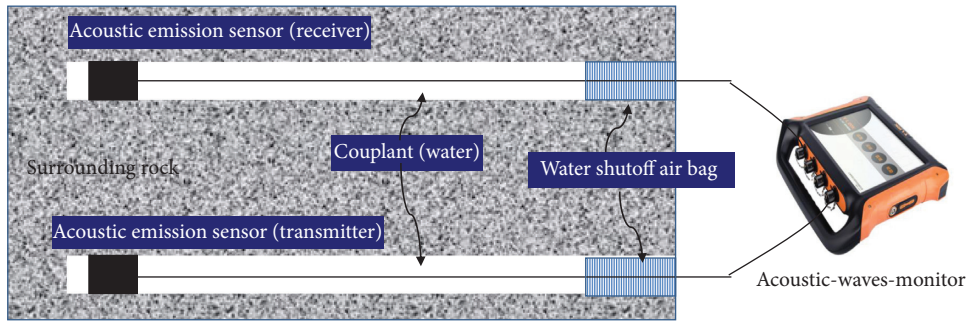
FIGURE 6: Schematic diagram of acoustic double-hole test method.

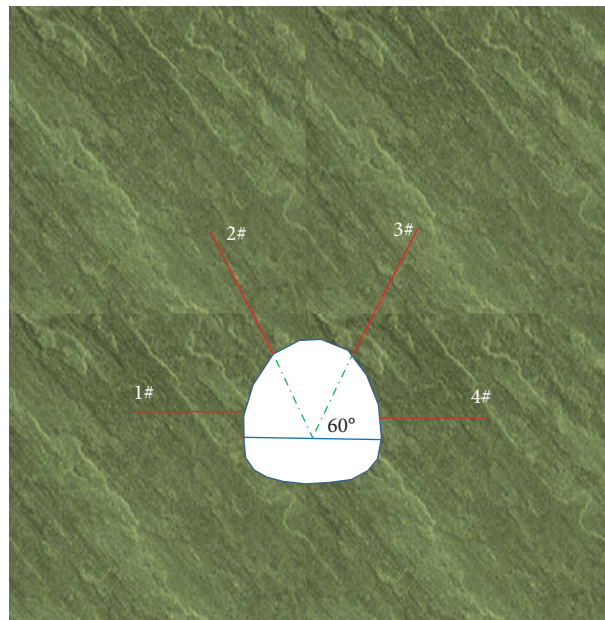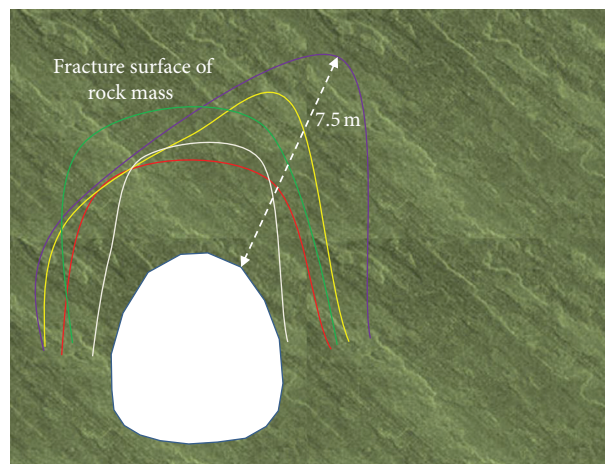FIGURE 7: Layout of acoustic measuring hole.

Bedding dip angle 0°   Bedding dip angle 60°
Bedding dip angle 30°   Bedding dip angle 90°
Bedding dip angle 45°

FIGURE 8: Distribution characteristics of plastic zone of surrounding rock.
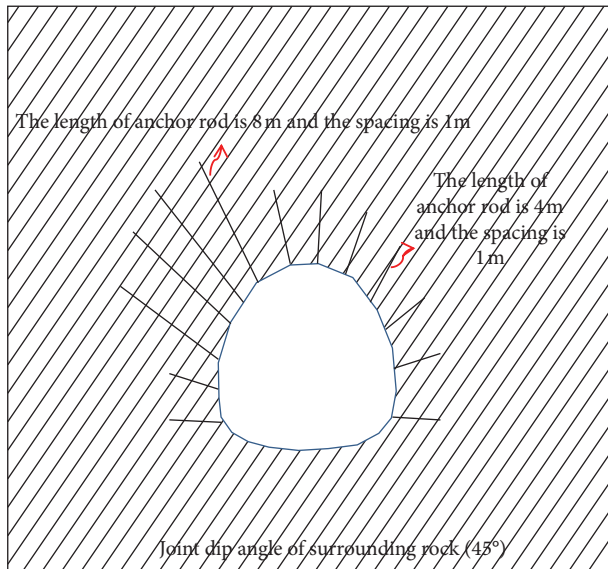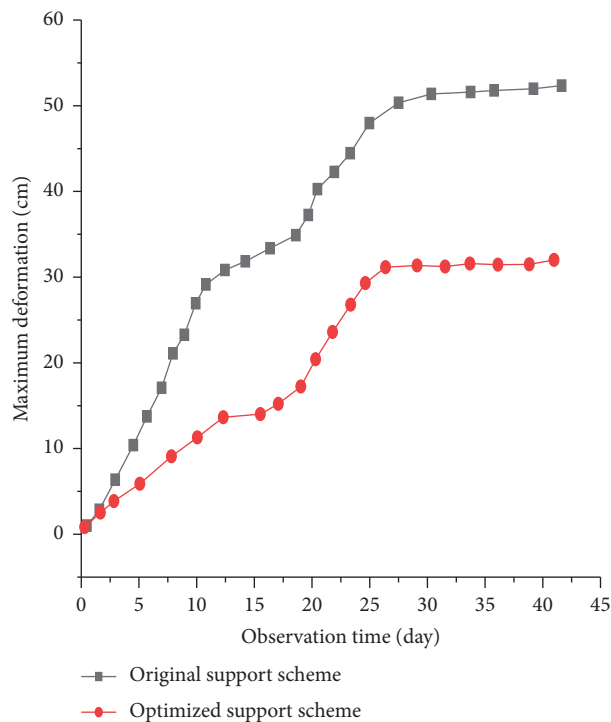
FIGURE 9: Support design optimization.

FIGURE 10: Tunnel surrounding rock deformation by optimized support.

control the deformation of surrounding rock, and is convenient for construction and cost saving.

6. Conclusion

In this paper, uniaxial compression and Brazilian splitting tests are used to analyze the strength characteristics of laboratory scale rock under different joint dip angles. Discrete element numerical simulation method is used to fully

consider the distribution characteristics of joints and fissures, and the influence of different joint dip angles on the stability of surrounding rock is analyzed. The distribution characteristics of plastic zone in practical engineering are analyzed by using acoustic wave testing instrument.

(1) The maximum tensile strength of carbonaceous slate appears when the joint angle is 0° and decreases with the increase of joint angle. With the increase of joint dip angle, the uniaxial strength of rock first decreases and then increases, and the strength of rock joint is weak in the range of 40° to 60°.

(2) According to the simulation results, the stable displacement of tunnel surrounding rock with different dip angles is analyzed, and the maximum displacement under the condition of 45° dip angle joint is obtained.

(3) The results show that the dip angle of surrounding rock has a great influence on the depth and distribution of plastic zone. When the joint dip angle is 45 degrees, the boundary between the plastic zone and the intact rock is the deepest.

Data Availability

The data used to support the findings of this study are included within the article.

Conflicts of Interest

The authors declare no conflicts of interest.

Authors' Contributions

All authors approved the manuscript for publication.

Acknowledgments

References

[1] X. Liu, Q. Fang, D. Zhang, and Y. Liu, "Energy-based prediction of volume loss ratio and plastic zone dimension of shallow tunnelling," *Computers and Geotechnics*, vol. 118, p. 103343, 2020.

[2] Y. Xiang and S. Feng, "Theoretical prediction of the potential plastic zone of shallow tunneling in vicinity of pile foundation in soils," *Tunnelling and Underground Space Technology*, vol. 38, pp. 115–121, 2013.

[3] A.-Z. Lu, G.-S. Xu, F. Sun, and W.-Q. Sun, "Elasto-plastic analysis of a circular tunnel including the effect of the axial in situ stress," *International Journal of Rock Mechanics and Mining Sciences*, vol. 47, no. 1, pp. 50–59, 2010.

[4] S. A. Massinas and M. G. Sakellariou, "Closed-form solution for plastic zone formation around a circular tunnel in half-space obeying Mohr-Coulomb criterion," *Géotechnique*, vol. 59, no. 8, pp. 691–701, 2009.

[5] B. Behnam, S. Fazlollah, and M. Hamid, "Prediction of plastic zone size around circular tunnels in non-hydrostatic stress

field," *International Journal of Mining Science and Technology*, vol. 24, no. 1, pp. 81–85, 2014.

[6] G. Li, Y. Hu, Q.-B. Li, T. Yin, J.-X. Miao, and M. Yao, "Inversion method of in-situ stress and rock damage characteristics in dam site using neural network and numerical simulation-a case study," *IEEE Access*, vol. 8, pp. 46701–46712, 2020.

[7] L. Gan, M. Weibin, T. Siming, and Z. Wenhao, "Effects of high-pretension support system on soft rock large deformation of perpendicularly crossing tunnels," *Advances in Civil Engineering*, vol. 2020, Article ID 6669120, 18 pages, 2020.

[8] G. Li, W. Ma, S. Tian, Z. Hongbo, F. Huabin, and W. Zou, "Groundwater inrush control and parameters optimization of curtain grouting reinforcement for the Jingzhai tunnel," *Geofluids*, vol. 2021, Article ID 6634513, 10 pages, 2021.

[9] J. Annan, L. Peng, and S. Hongtao, "Shallow depth of the tunnel excavation response research based on CRD method," *Procedia Engineering*, vol. 15, pp. 4852–4856, 2011.

[10] H. Y. Shi, Z. K. Ma, Q. J. Zhu, J. J. Shi, and Z. Q. Zhao, "Comparison of shape characteristics of plastic zone around circular tunnel under different strength criteria," *Journal of Mechanics*, vol. 36, no. 6, pp. 849–856, 2020.

[11] K. Wu, Z. Shao, S. Qin, W. Wei, and Z. Chu, "A critical review on the performance of yielding supports in squeezing tunnels," *Tunnelling and Underground Space Technology*, vol. 114, no. 1, p. 2021, 2021.

[12] K. Wu, Z. Shao, and S. Qin, "An analytical design method for ductile support structures in squeezing tunnels," *Archives of Civil and Mechanical Engineering*, vol. 20, no. 3, pp. 1–13, 2020.

[13] K. Wu, Z. Shao, M. Sharifzadeh, S. Hong, and S. Qin, "Analytical computation of support characteristic curve for circumferential yielding lining in tunnel design," *Journal of Rock Mechanics and Geotechnical Engineering*, vol. 13, no. 1, pp. 1–13, 2021.

[14] B. Hu, M. Sharifzadeh, X. T. Feng, W. B. Guo, and R. Talebi, "Roles of key factors on large anisotropic deformations at deep underground excavations," *International Journal of Mining Science and Technology*, vol. 31, no. 4, pp. 1–16, 2021.

[15] Q. X. Meng, W. Y. Xu, H. L. Wang, X. Y. Zhuang, and T. Rabczuk, "Digisim-an open source software package for heterogeneous material modeling based on digital image processing," *Advances in Engineering Software*, vol. 148, p. 102836, 2020.

[16] Z. Tao, C. Zhu, M. He, and M. Karakus, "A physical modeling-based study on the control mechanisms of negative Poisson's ratio anchor cable on the stratified toppling deformation of anti-inclined slopes," *International Journal of Rock Mechanics and Mining Sciences*, vol. 138, p. 104632, 2021.

[17] C. Zhu, M. He, M. Karakus, X. Zhang, and Z. Tao, "Numerical simulations of the failure process of anaclinal slope physical model and control mechanism of negative Poisson's ratio cable," *Bulletin of Engineering Geology and the Environment*, vol. 80, no. 6, pp. 3365–3380, 2021.

[18] Y. Wang, W. K. Feng, R. L. Hu, and C. H. Li, "Fracture evolution and energy characteristics during marble failure under triaxial fatigue cyclic and confining pressure unloading (fc-cpu) conditions," *Rock Mechanics and Rock Engineering*, vol. 54, pp. 799–818, 2021.

[19] B. Li, R. Bao, Y. Wang, R. Liu, and C. Zhao, "Permeability evolution of two-dimensional fracture networks during shear under constant normal stiffness boundary conditions," *Rock Mechanics and Rock Engineering*, vol. 54, no. 3, pp. 1–20, 2021.

[20] Q. Wang, H. Gao, B. Jiang, S. Li, M. He, and Q. Qin, "In-situ test and bolt-grouting design evaluation method of underground engineering based on digital drilling," *International Journal of Rock Mechanics and Mining Sciences*, vol. 138, p. 104575, 2021.

[21] Q. Wang, Q. Qin, B. Jiang et al., "Mechanized construction of fabricated arches for large-diameter tunnels," *Automation in Construction*, vol. 124, no. 3, p. 103583, 2021.

[22] A. Li, F. Dai, Y. Liu, H. Du, and R. Jiang, "Dynamic stability evaluation of underground cavern sidewalls against flexural toppling considering excavation-induced damage," *Tunnelling and Underground Space Technology*, vol. 112, p. 103903, 2021.

[23] Z. Wang, L. Gu, Q. Zhang, S. Yue, and G. Zhang, "Creep characteristics and prediction of creep failure of rock discontinuities under shearing conditions," *International Journal of Earth Sciences*, vol. 109, pp. 945–958, 2020.

[24] X. Yang, J. Wang, C. Zhu, M. He, and Y. Gao, "Effect of wetting and drying cycles on microstructure of rock based on sem," *Environmental Earth Sciences*, vol. 78, no. 6, pp. 1–10, 2019.

[25] L. Ban, C. Zhu, C. Qi, and Z. Tao, "New roughness parameters for 3d roughness of rock joints," *Bulletin of Engineering Geology and the Environment*, vol. 78, no. 6, pp. 4505–4517, 2019.

[26] Q. Bu, G. Hu, Y. Ye, C. Liu, C. Li, and J. Wang, "Experimental study on 2-d acoustic characteristics and hydrate distribution in sand," *Geophysical Journal International*, vol. 211, no. 2, pp. 990–1004, 2017.

[27] F. U. Jian-Dang, Y. Y. Zhang, and Y. N. Shi, "Method to measure and calculate deep displacement of surrounding rock based on new dual multi point gauge," *Coal Engineering*, no. 5, pp. 81–83+86, 2014.

[28] A. P. Ermakov and A. V. Starovoitov, "The use of the ground penetrating radar (gpr) method in engineering-geological studies for the assessment of geological-cryological conditions," *Moscow University Geology Bulletin*, vol. 65, no. 6, pp. 422–427, 2010.

[29] R. Liu, F. Jiang, and X. Zhang, "Measurement of dynamic elastic-plastic fracture toughness under stress wave loading," *Binggong Xuebao/Acta Armamentarii*, vol. 22, no. 1, pp. 115–119, 2001.

Research Article

Experimental Study on the Influence Mechanism of the Structural Plane to Rockbursts in Deeply Buried Hard Rock Tunnels

Guangtan Cheng ⓘ,[1,2] Jian Zhang ⓘ,[1] Qiang Gao ⓘ,[1] and Chuanxiao Liu ⓘ[1]

[1]*College of Water Conservancy and Civil Engineering, Shandong Agricultural University, Tai'an 271018, China*
[2]*State Key Laboratory of Geomechanics and Geotechnical Engineering, Institute of Rock and Soil Mechanics, Chinese Academy of Sciences, Wuhan 430071, China*

Correspondence should be addressed to Jian Zhang; zhangj614@163.com and Qiang Gao; gaoqiang@sdau.edu.cn

During the excavation of a large number of deeply buried tunnels and mining projects, rockburst disasters occur frequently due to the complex geologic environment in deep underground, including high initial geostress, adverse tectonic actions, and excavation disturbance. Many rockbursts have been found to be induced by some small-scale structural planes in the area around the tunnels during the construction of Jinping II hydropower station. In order to study the influence mechanisms of the structural plane to rockbursts, the physical simulation tests of rockbursts under biaxial stress conditions are carried out using marble samples by considering different relative positions of the structural plane with tunnels, namely, in tunnel spandrel, in tunnel sidewall, and at the intersection with the tunnel. The digital image correlation (DIC) technique is used to trace the evolution of the deformation on the surface and the rockburst process of the marble sample. The results reveal that three types of rockbursts are identified, namely, fault-slip rockburst, split bulking rockburst, and shear rupture rockburst, and their evolution processes are reproduced. The presence of small-scale structural planes in the vicinity of deep tunnels could be one of the major influence factors in triggering rockbursts. The findings could provide helpful references for predicting the development process and the design of burst-resistant measures for this type of rockbursts.

1. Introduction

As the foundation engineering construction and the resource development are progressing to greater depths, the frequency of rockburst increases remarkably. Rockburst disasters have been the significant threat to the safety construction of deep underground rock mass engineering. Besides rockbursts occurring easily in hard intact rock masses, small-scale structural planes have been found to play a significant role in inducing rockburst in deeply buried hard rock tunnels [1–5]. This type of rockburst related to structural planes is referred to as the structure-type rockburst. For instance, an extremely intense rockburst (often referred to as the 11.28 rockburst because of the date on which it occurred) took place in a drainage tunnel of the Jinping II hydropower station. As a result of this event, seven

workers were killed and a TBM machine was totally destroyed causing significant economic losses. After this rockburst, a rigid structural plane subparallel to the tunnel axis which strike NWW and dip about 50° was exposed at the boundary of the rockburst. All the rock masses beneath the structural plane were collapsed, creating a "V"-shaped failure zone, as illustrated in Figure 1 [6]. Postmortem analysis suggested that this rockburst event might be induced by the sudden sliding failure of the structural plane caused by excavation activities.

In recent decades, although extensive research studies have been conducted to investigate the mechanism of rockbursts, the influence mechanism of structural plane on rockbursts is pretty rare and still unclear. Williams [7] recorded a rockburst that is caused by the movement along an argillite bed first observed after the macroseismic
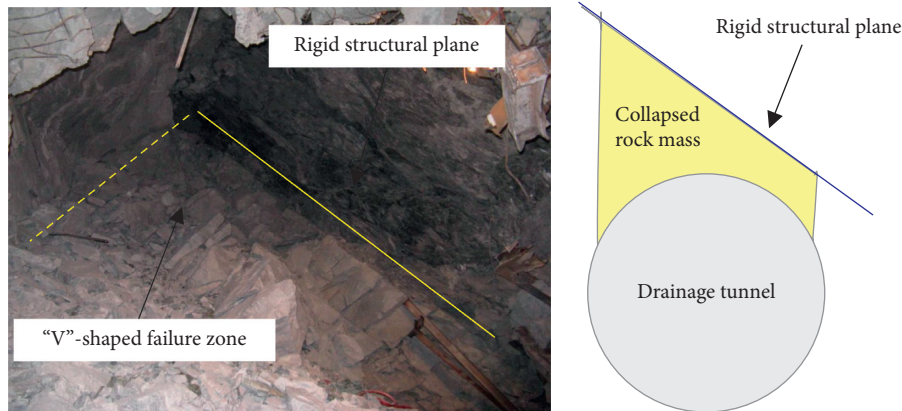
FIGURE 1: The 11.28 rockburst in drainage tunnel and exposed rigid structural plane [6].

monitoring system had been installed. Ortlepp and Stacey [8] classified the rockburst by main source mechanisms into five types: strain-bursting, buckling, face crush, shear rupture, and fault-slip. The authors supposed that the last two source mechanisms of rockbursts represented shear failure on a plane different from those of the first three and that shear failure of a plane may induce rockburst. White and Whyatt [9] suggested that slip movements of a steeply dipping fault towards a nearby stope increases stress at the margins of stopes, which resulted in rockbursts. Many researchers revealed that fault slip can generate seismic waves that could inflict rockburst [10–12]. Castro et al. [13] analysed the influences on fault slip of four possible factors, including unclamping, daylighting, stress rotation, and pillar shear. Zhang et al. [14] analysed the impact of macrogeological conditions (e.g., the tunnel depth, the fold, and the fault) on rockbursts occurring on tunnel floor at Jinping II hydropower station. Zhou et al. [15] conducted laboratory direct shear tests of structural planes with different asperity heights to explore the source mechanism of rockbursts caused by structural planes. In above studies, the rockburst mechanisms induced by the structural plane were all investigated after the rockburst event. There are rare model tests to simulate the evolution of rockbursts influenced by the structural plane.

More than 20 rockburst cases influenced by structural planes are listed and the rockburst characteristics are presented during the excavation of Jinping II headrace tunnels [1]. Numerical analyses have also been conducted to simulate the movements of fault-slip and the generated seismic waves resulting from mining activities [16–21]. To date, a number of studies have been conducted analytically and numerically to investigate the rockbursts induced by fault slip. However, the influence mechanism of small-scale structural planes on rockbursts has not been sufficiently studied.

In this paper, physical model experiments in laboratory are carried out for clear observation of the rockburst evolution process influenced by small-scale structural planes. The evolution processes are recorded simultaneously by the DIC technique. The structural-type rockburst caused by shearing is simulated by the means of UDEC software. A

discussion of the results and the future research plan in dealing with the shortage of current models is presented.

2. Model Sample Preparation and Testing Procedure

Rock masses prone to rockbursts are typically stiff, strong, and brittle, with uniaxial compressive strength of 100–400 MPa with Young's modulus > 20 GPa [22]. Therefore, the hard brittle marble materials were used as the model samples considering their burst-prone characteristics under high compressive stresses, and the basic mechanical parameters of this marble sample are listed in Table 1. The thin-plate marble samples with dimensions of 150 mm × 150 mm × 30 mm were cut from a long piece of marble collected from a building material market. A circular hole with a diameter of 30 mm served as the excavated tunnel was drilled at the center of the sample. A pinhole was drilled at the position of 5 mm away from the tunnel boundary for a thin wire getting through. The structural plane with 45 mm in length was cut with the thin wire saw about 1 mm in diameter. According to different relative positions of the structural plane and the tunnel sections, three types of model samples were prepared, as shown in Figure 2. For model samples A, B, and C, the structural plane was located in the tunnel spandrel, in the tunnel sidewall, at the intersection with the tunnel, respectively.

The model tests were carried out on the Rock Biaxial Loading and Macro-Mesoscopic Measurement System at the Institute of Rock and Soil Mechanics, Chinese Academy of Sciences. The experimental system is composed of biaxial loading system and deformation measurement system, as shown in Figure 3. The maximum loading capacity and travelling displacement are 1000 kN and 200 mm, respectively. The deformation measurement system is equipped with two high-speed cameras, two LED lights, and 3D-DIC (digital image correlation) processing software, and the measurement accuracy of strain is 10^{-5}. When the test began, a horizontal stress was first applied to 5 MPa at a rate of 0.1 kN/s and kept constant. Then a normal stress was applied until the ultimate failure of samples at a rate of 0.002 mm/s. Before the test, a random grey intensity

TABLE 1: Basic mechanical parameters of the marble used in this study.

Type of material used	σ_c (MPa)	σ_t (MPa)	E (GPa)	μ
Marble	126.06	1.63	51.59	0.23

σ_c, σ_t, E, and μ are uniaxial compression strength, the uniaxial tensile strength, elastic modulus, and Poisson ratio, respectively.
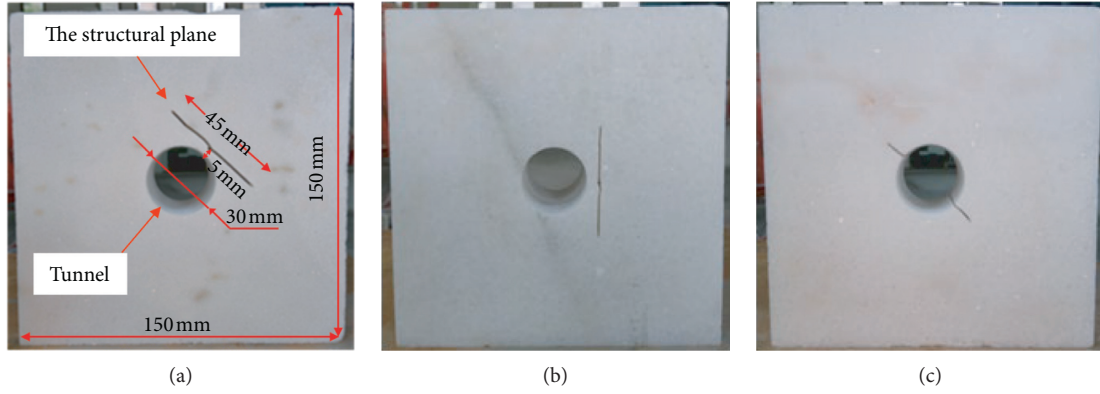

(a)   (b)   (c)

FIGURE 2: Three types of marble model samples. (a) The structural plane located in the tunnel spandrel. (b) The structural plane located in the tunnel sidewall. (c) The structural plane intersected with the tunnel.
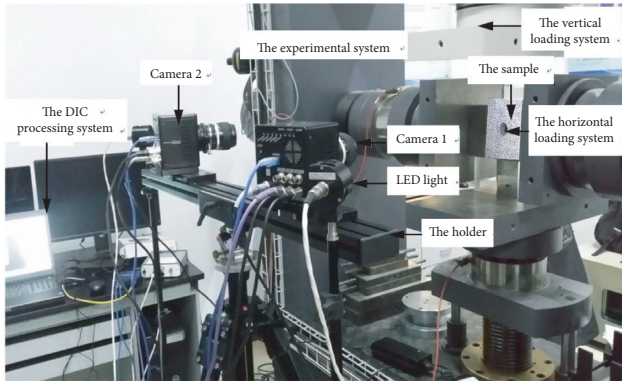

FIGURE 3: The Rock Biaxial Loading and Macro-Mesoscopic Measurement System.

distribution is made by spraying black paint and white paint onto the surface of the thin-plate sample for DIC analysis.

3. Model Test Result Analysis

3.1. Stress-Strain Curves. The axial stress versus axial strain curves of three types of model samples under biaxial pressure are illustrated in Figure 4. The results show that the stress-strain curves can be divided into four main regions and the typical points are marked on the curves: elastic deformation region, stable crack propagation region, unstable crack propagation region, and postpeak region [23]. Before the axial stress is applied, most existing, open, and appropriately oriented microcracks in the model sample are effectively closed due to the compaction of the applied horizontal stress of 5 MPa. In the initial region, the axial stress increases linearly with the increase of axial strain and

the marble sample is presumed to be a linear, homogeneous, elastic material. At the end of elastic deformation region, the curve has an inflection point and stable crack propagation begins, which indicate more microcracks start to form and propagate when the marble sample is loaded beyond the threshold at the inflection point. With the occurrence of more and more new cracks, the adjacent microcracks start to coalesce to form macroscopic fractures. After the peak stress is reached, a significant stress drop happens abruptly, indicating a sudden release of the strain energy stored in the marble sample. From the analysis of stress-strain curves and the evolution of cracks, it can be inferred that the shear failure of macrocracks may occur or even a rockburst may be induced.

Table 2 summarizes the stress and strain thresholds between different stages of stress versus strain curves shown in Figure 4 for three types of model samples. It is seen that the crack initiation threshold is approximately 0.3 times the peak stress and the onset of the crack damage starts at the stress levels of about 0.8 times the peak stress. This result is in keeping with those studies [24–27], which showed that σ_{ci}/σ_p and $\sigma_{c\,d}/\sigma_p$ are about 0.3–0.5 and 0.7–0.8 times the peak compressive strength, respectively.

The shaded area below the stress-strain curve represents the strain energy stored during the loading process in the prepeak region, as shown in Figure 4. The amount of the releasable energy could be approximately estimated by the area encompassed by the triangle below the stress-strain curve, namely, a half of σ_p times ε_p in Table 2. The peak strain of three types of model samples is 60.20, 76.93, and 90.76 ($\times 10^{-4}$), which indicate model sample A has the smallest peak strain and may be more prone to burst than model samples B and C under the same conditions.
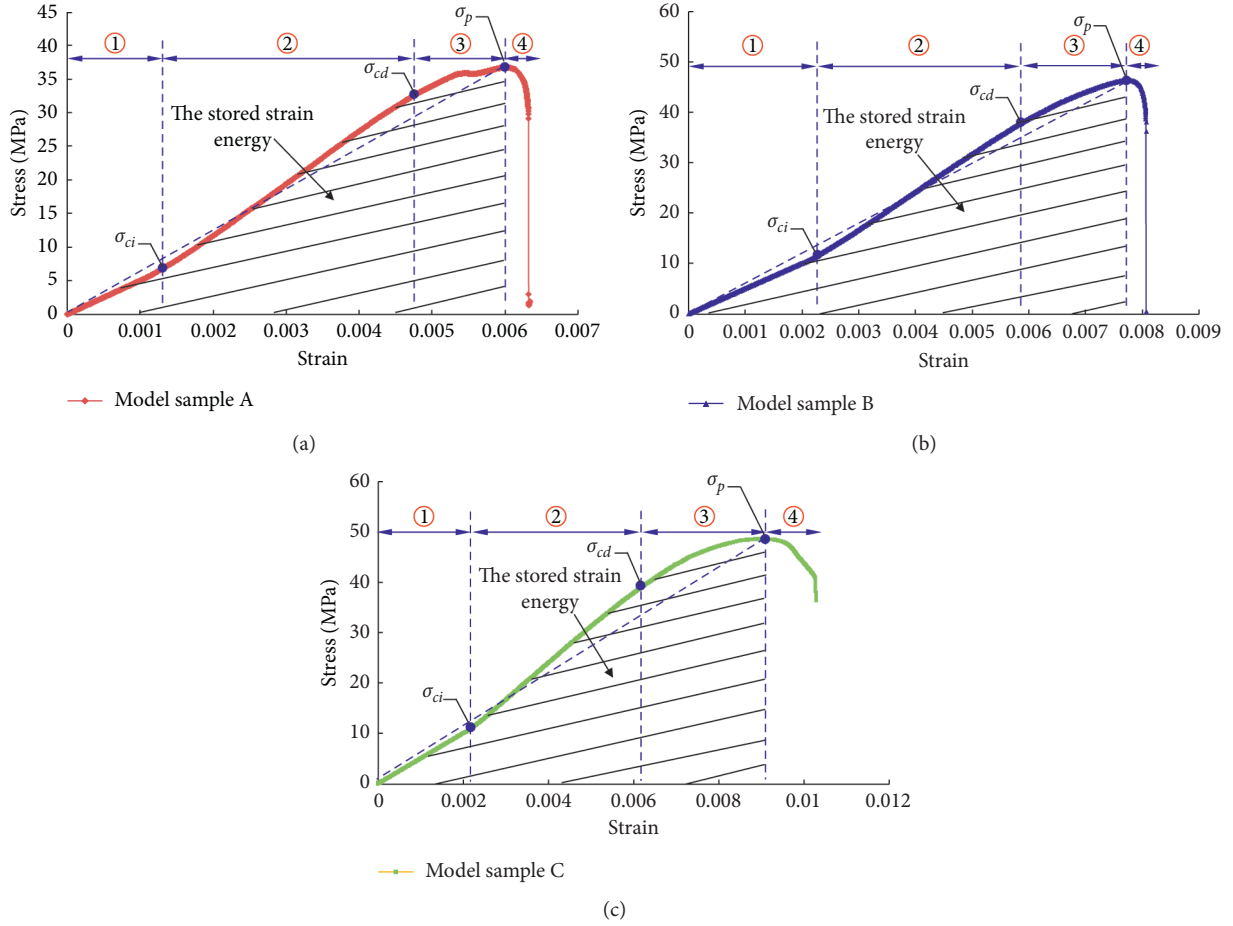
(a)

(b)

(c)

FIGURE 4: Curves of stress versus strain of three types of model samples: (a) model sample A; (b) model sample B; (c) model sample C (①, ②, ③, and ④ indicate the elastic deformation stage, stable crack propagation stage, unstable crack propagation stage, and postpeak stage) (after [23]).

TABLE 2: The stress and strain threshold between different stages of stress versus strain curves for three types of model samples.

Type of model samples	σ_{ci} (MPa)	σ_{cd} (MPa)	σ_p (MPa)	ε_p (10^{-4})	σ_{ci}/σ_p	σ_{cd}/σ_p
Model sample A	8.72	29.56	36.71	60.20	0.24	0.81
Model sample B	12.61	37.53	46.27	76.93	0.27	0.81
Model sample C	16.12	39.71	48.57	90.76	0.33	0.82

σ_{ci}, σ_{cd}, σ_p, and ε_p are the crack initiation stress, that is, the elastic limiting stress in this paper, the crack damage stress, the peak compressive strength, and the peak strain, respectively.

However, model sample C presents the biggest peak stress and also has the largest strain energy stored, followed by model samples B and A, which may result in the highest rockburst hazard after release by the rapid stress drop [16]. The results could provide meaningful references for predicting the occurrence time and intensity of structural-type rockbursts according to the attitude of the structural plane.

3.2. Evolution Processes of Structural-Type Rockbursts. The rockburst evolution processes of three types of model samples are illustrated in Figure 5. According to the influence mechanism of structural planes and the model testing results, three types of structural-type rockbursts can be reproduced using model samples A, B and C, namely, the fault-slip rockburst, buckling rockburst, and shear rupture rockburst, respectively.

The evolution process of fault-slip rockburst experienced four main stages: quiet stage, crack initiation and propagation stage, shear slip stage, and rockburst stage, as illustrated in Figure 5(a), which is corresponded with the main regions of stress versus strain curves shown in Figure 4. The quiet stage represents the closure of existing cracks and the storing of the strain energy with the initial loading. Due to the increasing axial loading and the opening of the tunnel, the tangential stress is concentrated in the surrounding area of the tunnel beneath the structural plane, while cracks are appeared at both ends of the structural plane and propagate
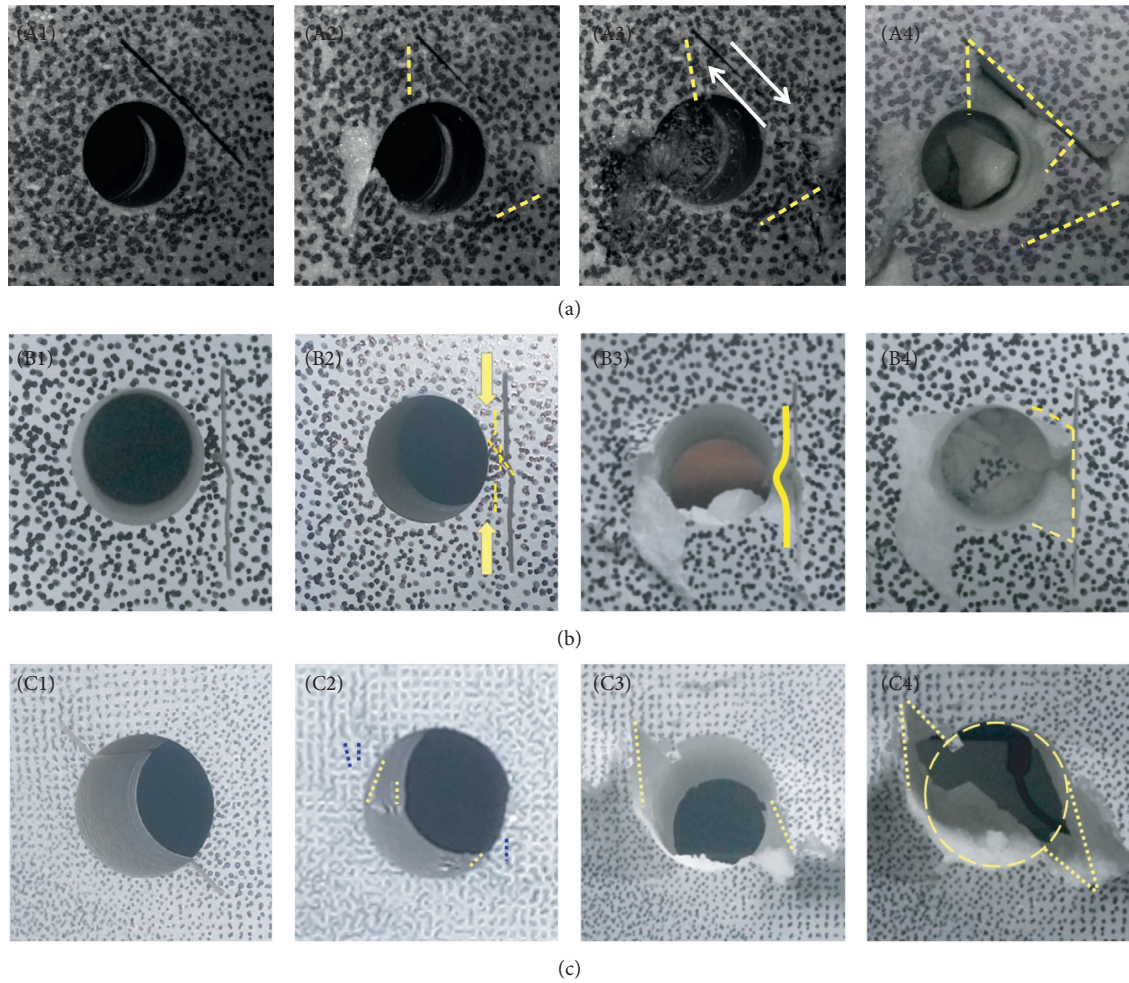
FIGURE 5: The rockburst evolution processes of three types of model samples: (a) fault-slip rockburst, (b) buckling rockburst, and (c) shear rupture rockburst.

towards the tunnel, as denoted by the yellow dotted lines in picture (A2) of Figure 5(a). When the shear stress exceeds the shearing resistance on the structural plane, shear slip initiates along the structural plane and the tensile fractures are caused in the rock masses beneath the structural plane, as shown in picture (A3) of Figure 5(a). Pictures (A3) and (A4) of Figure 5(a) show the violent ejection of rock factures towards the opening tunnel induced by the shock waves resulting from the stress drop in Figure 4 and a rockburst notch is formed after the event, as enclosed by the yellow dotted line. The final failure modes can well reflect the 11.28 rockburst occurred in deeply buried rock engineering (Figure 1).

The buckling rockburst process also involves four stages: quiet stage, crack initiation and propagation stage, splitting and bending stage, and rockburst stage, as illustrated in Figure 5(b). At the second stage, due to the influence of the vertical structural plane, the increasing axial loading can result in a rapid increase in the tangential stress between the tunnel and the structural plane. Then most of cracks with vertical orientation are caused by the axial stress concentration, as shown in picture (B2) of Figure 5(b). With the

propagation and connection of more vertical cracks, many thin rock slabs subparallel to the structural plane are generated in the right sidewall. Due to the sustained stress accumulation and sudden stress drop, the thin slabs' buckling occurs, as shown in picture (B3) of Figure 5(b). Finally, the rock slabs at the right sidewall, which are separated from the surrounding rock mass by fractures, are carried or ejected into the tunnel by the stress waves, creating a rockburst pit, as illustrated in picture (4) of Figure 5(b).

Figure 5(c) shows that the evolution process of shear rupture rockburst can be described in four stages: quiet stage, crack initiation and propagation stage, shear rupture stage, and rockburst stage. Abundant cracks appear in the surrounding rock around the structural plane under the influence of the stress concentration, as shown in picture (C2) of Figure 5(c). When shear failure occurs along the structural plane, tensile fractures appear in the lower or upper part and the released energy from stress drop may lead to their ejection into the tunnel. After the rockburst, two "V"-shaped pits are formed with the structural plane as a boundary, as enclosed by yellow dotted lines in the picture (C4) of Figure 5(c).
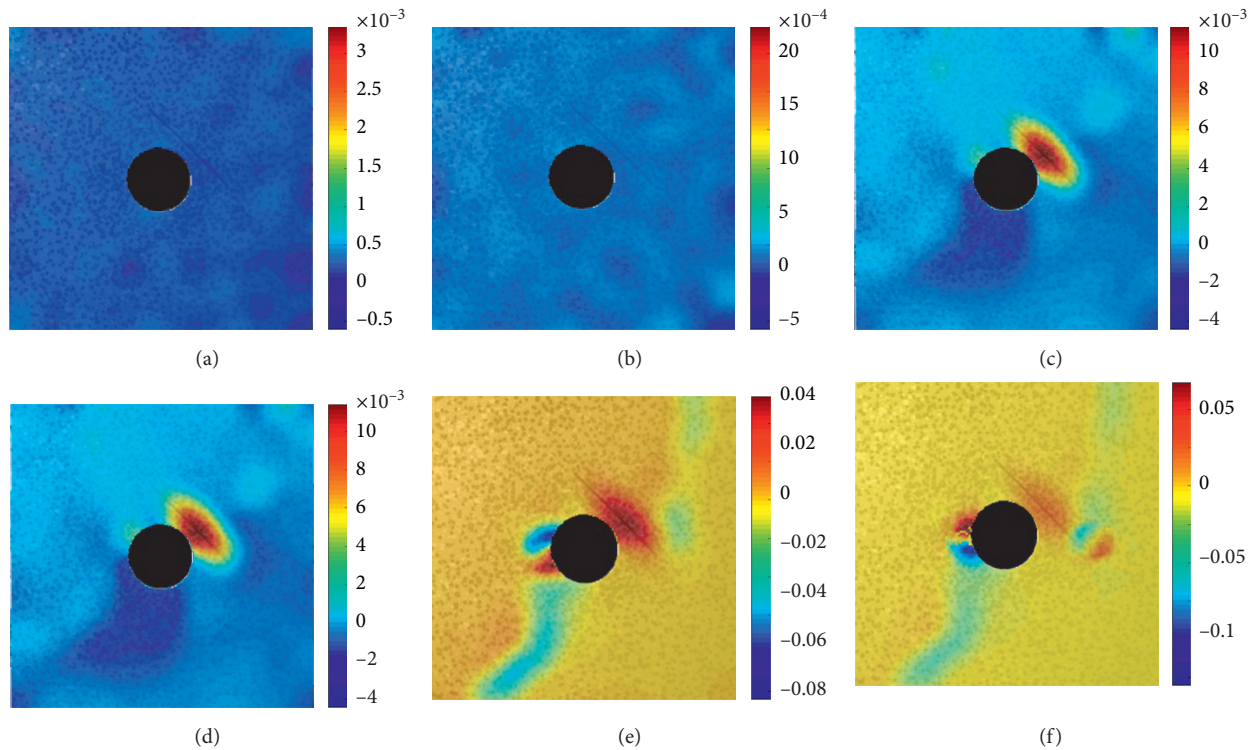
FIGURE 6: The shear strain contours of model sample A at different test stages: (a) 83 sec. (b) 87 sec. (c) 299 sec. (d) 305 sec. (e) 307 sec. (f) 308 sec.

According to the results of stress-strain curves and evolution processes, it can be concluded that the typical characteristics of structural-type rockbursts, including the location, time, intensity, and damage pit shape, are significantly affected by the control of stiff structural planes. Therefore, more attentions should be paid to the influences of the structural planes during the excavation of deep tunnels so as to prevent and mitigate rockburst damage.

3.3. Strain Fields of Structural-Type Rockbursts.

As one of the most used optical and noncontact techniques for measuring material deformations, digital image correlation (DIC) is applied to trace the deformation and rockburst process of the model samples. A sequence of high-resolution images of the sample surface is captured by two high-speed cameras at a speed of five frames per second during the test. Then the displacement field or strain field of the sample surface can be obtained at any given moment by DIC analysis. In this paper, we emphasize on understanding the influence mechanism of the structural plane on fault-slip rockburst using the DIC technique. The shear strain fields of model sample A at different temporal steps are shown in Figure 6, illustrating the evolution process of rock deformations during the whole loading test. At initial loading, Figure 6(a) presents the shear strain on the whole surface of the sample is very small and no obvious strain concentration is observed when the sample is considered in elastic state. As the loading increases, obvious shear strain localization occurs in the middle part of the structural plane, as shown in Figures 6(c) and 6(d), which

identify that the shear slip appears on the structural plane and triggers the subsequent rockburst, as shown in Figure 5(a). At the rockburst stage, as is noticed in Figure 6(f), shear strain concentration is situated at the left sidewall and beneath the structural plane, which is similar to the final failure characteristic of the sample, as shown in picture (A4) of Figure 5(a).

3.4. Numerical Analysis of 11.28 Rockbursts.

In order to reproduce the continuous-to-discontinuous process and further understand the fracture mechanism of the rockburst influenced by the structural plane, numerical analysis was carried out based on the 11.28 rockburst by using universal distinct element code (UDEC) software. For the sake of simplicity, a two-dimensional elastoplastic model was established in plane strain condition and the initial geostress condition is the same as that of the 11.28 rockburst in situ with reference to the study of Zhang et al. [28]. Figure 7 shows the evolution process of the 11.28 rockburst. In the initial step, there are no obvious fractures occurring, as shown in Figure 7(a). At the 1560th steps, large amounts of fractures occur and are localized in the tunnel vault beneath the structural plane. The local place is collapsed and some fractured rock masses are detached from the tunnel vault, as shown in Figure 7(b). Abundant broken rocks have poured into the tunnel and the final state is presented in Figure 7(c). A damage pit is generated and it is bounded by the structural plane. Comparison between the results shown in Figure 7(c) and Figure 1 indicates that the geometry of the rockburst pit
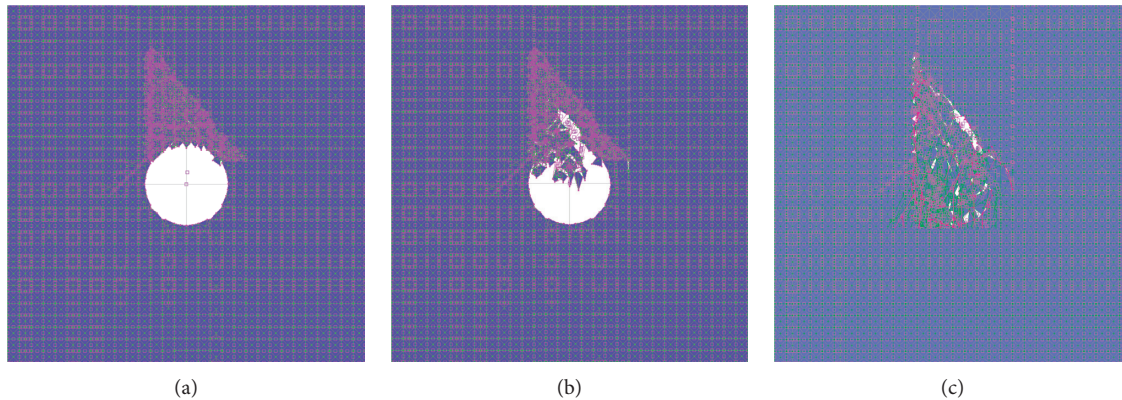
(a)   (b)   (c)

Figure 7: The evolution process of the 11.28 rockburst at different steps: (a) 150th step. (b) 1560th step. (c) 2590th step.

obtained from numerical results shows a strong agreement with the practical results of the 11.28 rockburst.

4. Discussion

For simplicity, a biaxial model test was performed using small sized marble samples with dimensions of 150 mm × 150 mm × 30 mm, which is not exactly consistent with the site conditions. For further study, a true triaxial model test will be conducted with large-scale model samples, such as 500 mm × 500 mm × 500 mm. Furthermore, a smooth structural plane is used in this study, while some scholars reported that the asperity shear of the structural plane may cause fault slip [29, 30]. Therefore, further studies need to be focused on the influence of the attitude of structural planes on rockbursts, such as surface roughness, shape, and orientation. Moreover, the tunnels were performed in this test and the influence of excavation is not considered, which need to be addressed in the future. For the sake of simplicity, we just focused on the evolution process of fault-slip rockbursts. The evolution of buckling and shear rupture rockbursts can be investigated in future research. In this article, the strain fields of structural-type rockbursts are analysed using DIC technique, and the displacement fields can also be discussed in future research.

5. Conclusions

In this study, biaxial model tests were undertaken using marble samples to investigate the influence mechanism of the structural plane on rockbursts by considering different locations of structural planes, i.e., in tunnel spandrel, in tunnel sidewall, and at the intersection with the tunnel. The failure characteristics and rockburst evolution process were traced by the digital image correlation technique. The UDEC software was used for better understanding the ejection process of the fractured rock masses during rockbursts influenced by the structural plane. The following conclusions are obtained:

(1) The stress-strain curves can be divided into four main regions: elastic deformation region, stable crack propagation region, unstable crack propagation region, and postpeak region. The stress drop in the postpeak region can release the stored strain energy, which may induce the rockburst damage.

(2) The evolution process of fault-slip rockburst (buckling rockburst or shear rupture rockburst) experienced four main stages: quiet stage, crack initiation and propagation stage, shear slip stage (splitting and bending stage or shear rupture stage), and rockburst stage, which is corresponding with the four regions of stress-strain curves.

(3) The shear moving process of the structural plane can be traced by the digital image correlation technique, which demonstrates that the shear failure of the structural plane is the main cause resulting in the fault-slip rockburst. The UDEC software can better simulate the process of the fault-slip rockburst and the results show a very good agreement with the actual 11.28 rockburst.

Data Availability

The data supporting the findings of this study are available within the article.

Conflicts of Interest

No potential conflicts of interest were reported by the authors.

References

[1] X. T. Feng, *Rockburst: Mechanisms, Monitoring, Warning, and Mitigation*, Butterworth-Heinemann, Oxfordshire, UK, 2017.

[2] A. M. Naji, M. Z. Emad, H. Rehman, and H. Yoo, "Geological and geomechanical heterogeneity in deep hydropower tunnels: a rock burst failure case study," *Tunnelling and Underground Space Technology*, vol. 84, pp. 507–521, 2019.

[3] B. Li, R. Bao, Y. Wang, R. Liu, and C. Zhao, "Permeability evolution of two-dimensional fracture networks during shear under constant normal stiffness boundary conditions," *Rock Mechanics and Rock Engineering*, vol. 54, no. 3, pp. 1–20, 2021.

[4] Q. Wang, H. Gao, B. Jiang, S. Li, M. He, and Q. Qin, "In-situ test and bolt-grouting design evaluation method of underground engineering based on digital drilling," *International Journal of Rock Mechanics and Mining Sciences*, vol. 138, Article ID 104575, 2021.

[5] Q. Wang, Q. Qin, B. Jiang et al., "Mechanized construction of fabricated arches for large-diameter tunnels," *Automation in Construction*, vol. 124, Article ID 103583, 2021.

[6] C. Zhang, X.-T. Feng, H. Zhou, S. Qiu, and W. Wu, "Case histories of four extremely intense rockbursts in deep tunnels," *Rock Mechanics and Rock Engineering*, vol. 45, no. 3, pp. 275–288, 2012.

[7] T. J. Williams, C. J. Wideman, and D. F. Scott, "Case history of a slip-type rockburst," *Pure and Applied Geophysics PAGEOPH*, vol. 139, no. 3-4, pp. 627–637, 1992.

[8] W. D. Ortlepp and T. R. Stacey, "Rockburst mechanisms in tunnels and shafts," *Tunnelling and Underground Space Technology*, vol. 9, no. 1, pp. 59–65, 1994.

[9] B. G. White and J. K. Whyatt, "Role of fault slip on mechanisms of rock burst damage, Lucky Friday Mine, Idaho,-USA,," in *Proceedings of the SARES 99: 2nd Southern African Rock Engineering Symposium. Implementing Rock Engineering Knowledge*, pp. 169–178, T.O. Hagan, Johannesburg, South Africa, Septembet 1999.

[10] W. D. Ortlepp, "Observation of mining-induced faults in an intact rock mass at depth," *International Journal of Rock Mechanics and Mining Sciences*, vol. 37, no. 1-2, pp. 423–436, 2000.

[11] W. Blake and D. G. F. Hedley, *Rockbursts: Case Studies from North American Hard-Rock Mines*, Society for Mining, Metallurgy, and Exploration, Englewood, CO, USA, 2003.

[12] A. Li, F. Dai, Y. Liu, H. Du, and R. Jiang, "Dynamic stability evaluation of underground cavern sidewalls against flexural toppling considering excavation-induced damage," *Tunnelling and Underground Space Technology*, vol. 112, Article ID 103903, 2021.

[13] L. A. M. Castro, T. G. Carter, and N. Lightfoot, "Investigating factors influencing fault-slip in seismically active structures,," in *Proceedings of the 3rd CANUS Rock Mechanics Symposium*, Toronto, Canada, May 2009.

[14] C. Zhang, X.-T. Feng, H. Zhou, S. Qiu, and Y. Yang, "Rock mass damage induced by rockbursts occurring on tunnel floors: a case study of two tunnels at the Jinping II Hydropower Station," *Environmental Earth Sciences*, vol. 71, no. 1, pp. 441–450, 2014.

[15] H. Zhou, F. Meng, C. Zhang, D. Hu, F. Yang, and J. Lu, "Analysis of rockburst mechanisms induced by structural planes in deep tunnels," *Bulletin of Engineering Geology and the Environment*, vol. 74, no. 4, pp. 1435–1451, 2015.

[16] P. E. Snelling, L. Godin, and S. D. McKinnon, "The role of geologic structure and stress in triggering remote seismicity in Creighton Mine, Sudbury, Canada," *International Journal of Rock Mechanics and Mining Sciences*, vol. 58, pp. 166–179, 2013.

[17] A. Sainoki and H. S. Mitri, "Evaluation of fault-slip potential due to shearing of fault asperities," *Canadian Geotechnical Journal*, vol. 52, no. 10, pp. 1417–1425, 2015.

[18] A. Sainoki and H. S. Mitri, "Back analysis of fault-slip in burst prone environment," *Journal of Applied Geophysics*, vol. 134, pp. 159–171, 2016.

[19] A. Manouchehrian and M. Cai, "Analysis of rockburst in tunnels subjected to static and dynamic loads," *Journal of Rock Mechanics and Geotechnical Engineering*, vol. 9, no. 6, pp. 1031–1040, 2017.

[20] C. Zhu, M. He, M. Karakus, X. Zhang, and Z. Tao, "Numerical simulations of the failure process of anaclinal slope physical model and control mechanism of negative Poisson's ratio cable," *Bulletin of Engineering Geology and the Environment*, vol. 80, no. 4, pp. 3365–3380, 2021.

[21] Z. Tao, C. Zhu, M. He, and M. Karakus, "A physical modeling-based study on the control mechanisms of Negative Poisson's ratio anchor cable on the stratified toppling deformation of anti-inclined slopes," *International Journal of Rock Mechanics and Mining Sciences*, vol. 138, Article ID 104632, 2021.

[22] L. Obert and W. I. Duvall, *Rock Mechanics and the Design of Structures in Rock*, John Wiley & Sons, New York, NY, USA, 1967.

[23] M. S. Diederichs, P. K. Kaiser, and E. Eberhardt, "Damage initiation and propagation in hard rock during tunnelling and the influence of near-face stress rotation," *International Journal of Rock Mechanics and Mining Sciences*, vol. 41, no. 5, pp. 785–812, 2004.

[24] C. D. Martin, *The strength of massive Lac du Bonnet granite around underground openings*, PhD thesis, University of Manitoba, Winnipeg, Canada, 1994.

[25] E. Eberhardt, D. Stead, B. stimpson, and R. S. Read, "Identifying crack initiation and propagation thresholds in brittle rock," *Canadian Geotechnical Journal*, vol. 35, no. 2, pp. 222–233, 1998.

[26] M. Cai, P. K. Kaiser, Y. Tasaka, T. Maejima, H. Morioka, and M. Minami, "Generalized crack initiation and crack damage stress thresholds of brittle rock masses near underground excavations," *International Journal of Rock Mechanics and Mining Sciences*, vol. 41, no. 5, pp. 833–847, 2004.

[27] Y. Wang, W. K. Feng, R. L. Hu, and C. H. Li, "Fracture evolution and energy characteristics during marble failure under triaxial fatigue cyclic and confining pressure unloading (FC-CPU) conditions," *Rock Mechanics and Rock Engineering*, vol. 54, no. 2, pp. 799–818, 2021.

[28] C. Zhang, X.-T. Feng, H. Zhou, S. Qiu, and W. Wu, "Rockmass damage development following two extremely intense rockbursts in deep tunnels at Jinping II hydropower station, southwestern China," *Bulletin of Engineering Geology and the Environment*, vol. 72, no. 2, pp. 237–247, 2013.

[29] J. A. Ryder, "Excess shear stress in the assessment of geologically hazardous situations," *Journal of the Southern African Institute of Mining and Metallurgy*, vol. 88, pp. 27–39, 1988.

[30] A. Sainoki and H. S. Mitri, "Simulating intense shock pulses due to asperities during fault-slip," *Journal of Applied Geophysics*, vol. 103, pp. 71–81, 2014.